Real World Driving Emissions from Hybrid Electric Vehicles and the Impact of Biofuels

Daisy Bess Thomas

Submitted in accordance with the requirements for the degree of
Doctor of Philosophy

The University of Leeds
School of Chemical and Process Engineering

September, 2020

The candidate confirms that the work submitted is his/her own and that appropriate credit has been given where reference has been made to the work of others.

Acknowledgements

I would like to express my thanks to all of those who have aided me throughout my PhD research project and the writing of this thesis.

First and foremost I would like to thank my three supervisors. This work would not have been possible if it were not for Dr Hu Li. I thank you for your ideas, guidance and support throughout this project. Dr Karl Ropkins, I thank you for your continued help throughout the planning, testing and data processing stages. Professor Alison Tomlin, thank you for your ideas and input.

Second, I would like to thank Dr Xin Wang, Professor Yunshan Ge and everyone else at Beijing Institute of Technology with whom I have collaborated. To Xin, in particular, I thank you for your generous donation of time, knowledge and patience to help me with my project.

Third, I would like to thank the team at the University of Bath for kindly allowing me to use their chassis dynamometer facility, and to Katie Pye and the rest of Horiba UK and Horiba Mira for generously allowing me to use their Horiba OBS-ONE PEMS equipment. I would also like to thank Scott Prichard at the University of Leeds for his technical assistance throughout this project.

Fourth, I would like to thank the Engineering and Physical Sciences Research Council (EPSRC) and the Bioenergy CDT for funding this work and giving me the freedom to design my own project. A big thank you to Jenny Jones, James McKay and Emily Bryan-Kinns in particular. Thanks also to Andy Price-Allison for lending me ‘Freddie’ the FTIR, to Richard Riley for initial help with the Prius, and to James Hammerton and Yanlong Wu for help with the DMS500.

I would also like to take a moment to thank all of my friends both within and outside the University. In particular, Charlotte Weaver, Ric Birley, Iram Razaq, Nicola Wood and Jeni Spragg on the Bioenergy CDT, for countless tea breaks and laughter. Thursday evenings would not have been nearly as fun if it were not for Dougie, Lee, Ollie, Ric, Andy, Aaron, Nando, Poppy, Katy and Jess, to name a few. I also thank other friends and family for keeping me sane, including Siân, Isis, Alan, Will, Juliette, Danny, Dean, Kelz, Christie, Megan, Kat, Greg, Mark, Jane, Bruce, and others too numerous to mention.

Finally, the biggest thank you goes to my fiancé Sam Wilson for his endless encouragement and support throughout my PhD. I could not have done it without you. Thank for proofreading this thesis, and similarly, extra thanks to my mother Siân Thomas, sister Isis Thomas and future father-in-law William Wilson for additional proofreading help.

Abstract

In order to reduce CO_2 emissions it is important to consider hybrid electric vehicles (HEVs) and the increased blending of biofuels with conventional fuels, whilst ensuring that type approval test procedures are robust enough to protect local air quality. This thesis investigates the behaviour and emissions of an HEV. Modal regulated and unregulated pollutant emissions including particle number (PN) and size distribution (PNSD) were captured. Chassis dynamometer testing, including those following type approval New European Drive Cycle (NEDC) and World-harmonised Light Duty Test Cycle (WLTC) procedures and cycles, are compared with on-road Real Driving Emissions (RDE) and non-compliance, real-world on-road testing. The variations in drive cycle properties are investigated, followed by an investigation of HEV behaviour and the resultant emissions from these different tests. Various characteristics of HEVs that make them different to conventional internal combustion engine vehicles are then studied in unprecedented detail. Finally, the effect of biofuel blends of 5% ethanol (E5), 10% ethanol (E10), and 10% n-butanol (B10) with gasoline (E0) on the HEV emissions is investigated.

This work found that the frequency of vehicle stops (and hence engine re-start events) had the greatest impact on HEV CO and PN emission factors, while test cycle distance (and hence cold start penalty) had the greatest impact on HEV CO_2 and NO_x emission factors, across test cycles. CO_2, CO, NO_x and PN were 9%, 66%, 58% and 71% lower from the RDE than the WLTC. The urban section of the RDE was found to be unrepresentative of a real world city-centre drive cycle in this regard. The HEV PNSD was dependent on drive style, with engine re-ignition events having a unimodal maximum at 50nm, and constant engine operation having a bimodal PNSD with maxima at 15nm and 110nm. The three-way catalyst (TWC) was found to light-off very fast – within approximately 50s – for the HEV, despite slow warm-up times due to engine inactivity, and displayed good resistance to de-lighting during periods of engine-off. Emissions of CO, PN, ammonia and methane were associated with periods of fuel enrichment on engine re-ignition, while NO_x, N_2O and other unregulated pollutants were unaffected. Tests fuelled with E10 and B10 had 28% and 22% lower respective CO emissions over the WLTC than E0, with lower vehicle speeds exhibiting the greatest decrease. E10 and B10 led to 24% and 18% respective decreases of NO_x over the RDE, while E10 and B10 led to 41% and 21% decreases in PN over the WLTC, compared to E0.

Table of Contents

List of Tables

List of Figures

List of Abbreviations

A/F	Air/fuel ratio
ABE	Acetone-butanol-ethanol
AC	Alternating current
ARTEMIS	Assessment and Reliability of Transport Emission Models and Inventory Systems
BEV	Battery electric vehicle
CH_4	Methane
CI	Compression-ignition
CLD	Chemiluminescence detector
CLEVeR	(University of Bath) Centre for Low Emissions Vehicle Research
CO	Carbon monoxide
CO_2	Carbon dioxide
CO_2e	Carbon dioxide equivalent
COPD	Chronic obstructive pulmonary disease
COV	Coefficient of variation
CPC	Condensation particle counter
CSEE	Cold start extra emissions
CV	Conventional vehicle
CV	Conventional (internal combustion engine) vehicle
CVS	Constant volume sampler
CVT	Continuously variable transmission
DC	Direct current
DfT	Department for Transport
DTC	Diagnostic trouble codes
E	Ethanol (specific only to Table 2.8 in Chapter 2)
ECU	Engine control unit
EGR	Exhaust gas recirculation
EPA	Environmental Protection Agency
EU	European Union
EUDC	Extra-urban drive cycle
FID	Flame ionization detector
FQD	Fuel quality directive
FTIR	Fourier transform infrared
FTP	Federal Test Procedure
FWHM	Full width at half maximum
GDI	Gasoline direct injection

GHG	Greenhouse gas
GMD	Geometric mean diameter
GPF	Gasoline particulate filter
GPS	Global positioning system
GTR	Global technical regulation
GWP	Global warming potential
H_2	Hydrogen
H_2O	Water
HC	Hydrocarbon
HEPA	High-efficiency particulate air
HEV	Hybrid electric vehicle
ICCT	International Council on Clean Transportation
ICE	Internal combustion engine
ILUC	Indirect land use change
IMEP	Indicated mean effective pressure
IPA	Isopropyl alcohol
IPSD	Integrated particle size distribution
IR	Infra-red
LHV	Lower heating value
LUC	Land use change
MAW	Moving averaging windows
MHEV	Mild hybrid electric vehicle
MPG	Miles per gallon
MY	Model year
N_2O	Nitrous oxide
NA	Naturally aspirated
NDIR	Non-dispersive infra-red
NDUV	Non-dispersive ultra-violet
NEDC	New European Drive Cycle
NH_3	Ammonia
NMHC	Non-methane hydrocarbons
NMVOC	Non-methane volatile organic carbon
NO_2	Nitrogen dioxide
NO_x	Oxides of nitrogen
NTE	Not-to-exceed
O_2	Oxygen
O_3	Ozone
OBD	On-board diagnostic
PAH	Poly-aromatic hydrocarbon

PEMS	Portable emissions measurement system
PFI	Port fuel injection
PHEV	Plug-in hybrid electric vehicle
PM	Particle mass
PMP	Particle measurement programme
PN	Particle number
PNC	Particle number counter
PNSD	Particle number size distribution
ppm	Parts per million
RDE	Real Driving Emissions
RED	Renewable Energy Directive
RPA	Relative positive acceleration
RPM	Revolutions per minute
SAO	Smooth approach orifice
SI	Spark injection
SO2	Sulphur dioxide
SOC	State of charge
SPN	Solid particle number
TOC	Total organic carbon
TWC	Three-way catalytic converter
UDC	Urban Drive Cycle
UDDS	Urban Dynamometer Driving Schedule
UK	United Kingdom
USB	United States (of America)
ULEV	Ultra-low emission vehicle
UoB	University of Bath
USB	Universal serial bus
UTC	Coordinated universal time
$v.a_{pos}[95]$	95^{th} percentile of the positive product of velocity and acceleration
VOC	Volatile organic compound
VPR	Volatile particle remover
VSP	Vehicle specific power
VVT	Variable valve timing
VVT-i	Variable valve timing with intelligence
WLTC	Worldwide Harmonized Light Vehicle Test Cycle
WLTP	Worldwide Harmonized Light Vehicle Test Procedure

Chapter 1
Introduction

1.1 Background and motivation

There has been a great increase in the use of road vehicles over the last half century. As an example, between the years 1960 and 2000, the number of cars per 1000 people in the United Kingdom (UK) grew from less than 10 to 400 (Uherek et al., 2010). Road transportation accounted for around 21% of total greenhouse gas (GHG) emissions from the UK in 2017, with 75% of this transportation coming from passenger cars (Clarke and Ainslie, 2019). The effect on the anthropogenic greenhouse effect is increasing with time, due to an increase in the average size and power of vehicles, as well as an increase in the mileage travelled and the addition of energy-consuming comfort systems, such as air conditioning, within cars (Uherek et al., 2010). Compounding this is the fact that other sectors are decarbonising faster, meaning that the proportion of GHGs arising from transportation is increasing with time (Clarke and Ainslie, 2019). Colvile et al. (2001) stated that 60-65% of life-cycle GHG emissions for gasoline cars arise from carbon dioxide (CO_2) exhaust emissions, while 10% are from non-CO_2 exhaust emissions. The manufacture of the car contributes a further 10%, while the extraction, refinery and transportation of the fuel to run the car gives 15-20% of the total life cycle emissions. From these values it is clear that exhaust CO_2 emissions are a very important factor to consider.

In the 1980s, the global atmospheric effects of transport CO_2 emissions were an increasing cause for concern, and toward the end of the 20th century the Rio summit of 1992 first concluded that climate change is a serious problem. The Kyoto Protocol of 1997 made the first international agreement to make some small reductions in GHG, leading to an increased uptake of diesel cars over gasoline cars in Europe because of the lower CO_2 emissions of the former. However, there was an unexpected result: the diesel car produced large quantities of particulate matter and Nitrogen dioxide (NO_2), widely believed to be responsible for increasing the incidence of cardiovascular and respiratory diseases, as well as making asthma worse. The increased uptake of diesel encouraged by the policies in Europe meant that there was a notable decrease in air quality (Uherek et al., 2010).

Many polluting gases and particles are released by road transportation that negatively affect atmospheric composition, decreasing air quality (Uherek et al., 2010). There are cancer-inducing Hydrocarbon (HC) components within exhaust gases, particularly poly-aromatic hydrocarbons (PAHs), benzene and 1,3-butadiene (Colvile et al., 2001). Another main pollutant from automobiles is CO, which reduces the oxygen-carrying capacity of the blood and can lead to cardiovascular disease. NO_2 emissions, as mentioned above, are a major pollutant, being a precursor of ground-level ozone (O_3) and other photochemical pollutants (Sillman, 1999) which worsen asthma symptoms, increase emergency respiratory problems and damage crops (Colvile et al., 2001). As a result of this decline in urban air quality combined with increasing knowledge of health risks, air pollution is a major international concern (Colvile et al., 2001).

These pollutants are released in closer proximity to humans than many other emission sources, making them more dangerous for health (Colvile et al., 2001). This is particularly the case in cities, where rapid urbanisation has resulted in both an increase in emissions and population density (Gurjar et al., 2008). The health effects of urban vehicle emissions are of great concern, with a dense concentration of vehicles emitting in densely populated areas (Colvile et al., 2001). This is becoming more problematic as a growing proportion of the world's population are living in these environments (Gurjar et al., 2008), increasing the relative impact of transport on health (Schauer, 2015) and forcing people to demand cleaner air (Gurjar et al., 2008).

In the last few decades the reported emissions from road transport have been drastically reduced. Carbon monoxide (CO) and non-methane volatile organic compounds (NMVOC) have both fallen by factors of at least two in many European countries, while nitrogen oxides (NO_x) and particulate mass (PM) have also decreased (Uherek et al., 2010). However, evidence suggests that even the air quality in well-controlled regions is still posing a health risk (Schauer, 2015), with over 90% of Air Quality Management Areas in the UK being a response to transport related emissions (Chatterton et al., 2006). It is clear that work to reduce harmful pollutant emissions is vitally important (Uherek et al., 2010).

The legislation restricting the pollutant emissions from vehicles has mainly acted at the point of 'type approval', with new vehicle types and models having to pass chassis dynamometer tests before they are allowed to be sold to the

public (Vlachos et al., 2014). Since the 1990s, a set of European Union (EU) emission standards for light duty and heavy duty gasoline and diesel vehicles have been launched for EU type approval testing (known as 'Euro standards'). The Euro standards limit the distance-specific mass emissions (g/km) of certain regulated pollutants for new vehicles on the market, and have become more stringent with time. The test cycle and procedure has also changed with time, in the attempt to further limit emissions. The New European Drive Cycle (NEDC) that was used for type approval was replaced by the Worldwide Harmonised Light Vehicle Test Procedure (WLTP) and Worldwide Harmonised Light Vehicle Test Cycle (WLTC) because the NEDC was deemed unrepresentative of 'real-world' driving and too easy to manipulate (Marotta et al., 2015). More recently, a supplementary on-road test called the Real Driving Emissions (RDE) test has been added alongside the WLTC as a means to protect against so-called 'cycle beating' on the fixed chassis dynamometer test cycles that led to the 'Dieselgate' scandal of 2015 (Johnson, 2016).

Over the past decades, there have been a plethora of technological advancements in the light duty transport industry aimed at reducing GHG emissions (Reichmuth et al., 2013). 'Light-weighting' is one of the simplest approaches used to decrease fuel consumption, where high tensile strength materials are used in a smaller quantity to decrease the mass of the car (Miyanishi, 2010). This technique also allows the car engine to be downsized, further improving the efficiency (Reichmuth et al., 2013). Another way to enable downsizing is by advanced turbocharging (Johnson, 2012). Tyre improvements also aid efficiency by decreasing the rolling resistance of the car (Pasaoglu et al., 2012), while engine technology changes such as the multi-valve, variable valve timing, exhaust gas recirculation, electronic throttle control and turbo charging are all widely used today to improve engine thermal efficiency (Yao et al., 2011). Another effective improvement is the reduction of power used during engine idling, such as idle stop-and-go or 'stop-start' technology (Shancita et al., 2014). The above changes have all contributed to vast improvements in vehicle efficiency. However, these alone are not enough to meet the legislated fleet-wide emissions limits for CO_2 that manufacturers have to meet (Reichmuth et al., 2013).

A significant change to vehicle technology that attempts to reduce GHG emissions is increased powertrain electrification. Electrified vehicles include hybrid electric vehicles (HEVs), plug-in hybrid electric vehicles (PHEVs) and

battery electric vehicles (BEVs). Each type has both efficiency and GHG advantages over conventional internal combustion engine (ICE) spark ignition (SI) vehicles, particularly in urban areas. Currently, non-plugin HEVs, also called Not Off Vehicle Charging HEVs (NOVC) still make up the majority of electrified vehicle licences, as shown in Figure 1.1. These vehicles will be those referred to as simply 'HEVs' in the rest of this thesis, as opposed to 'PHEV' for the plug-in variety. Of these HEVs, the Toyota Prius has been the most common generic model on roads in Great Britain (Parry, 2019). However, despite their increased uptake, little research has been conclusive as to the pollutant emission levels from these new hybrid technologies.

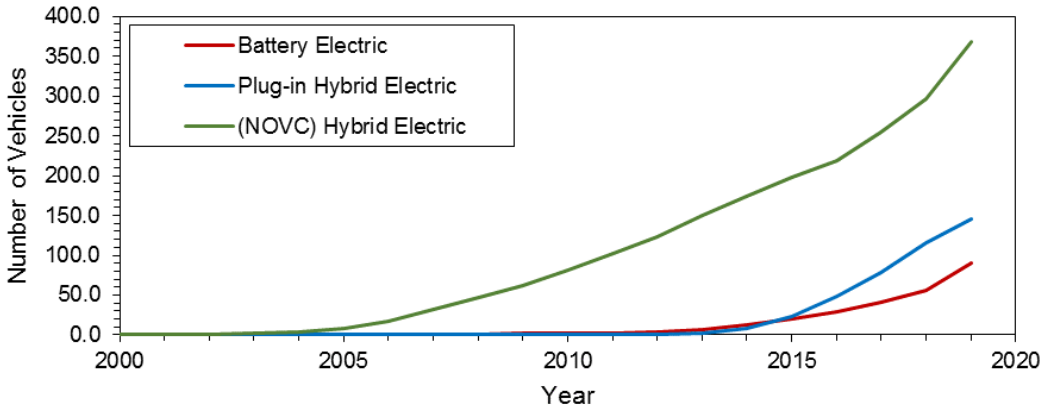

Figure 1.1 Number of UK licenced electrified vehicles per year by technology type. Made from the 'Cars(VEH02)' dataset (Department for Transport and Driver and Vehicle Licensing Agency, 2020).

Another method currently being employed worldwide to limit global warming is the use of biofuels. These fuels have the potential to produce lower net GHG emissions due to the fact that the CO_2 released on biofuel combustion was captured from the atmosphere by the biomass very recently (Colvile et al., 2001). The biofuel most commonly used as a substitute for gasoline in light duty SI passenger cars today is ethanol, though other biofuels, such as butanol, are possible alternatives. A great advantage to the use of these biofuels is that they can be used in current engine technologies (Anderson, 2012). Biofuels can be blended in low quantities with conventional fuels for use without any modification, or in higher quantities given some engine modification (Johansson and Åhman, 2002). The use of 10% ethanol (E10) with gasoline has been shown to decrease particulate matter and CO emissions significantly, while little change in NO_x was seen. However, some unregulated pollutants such as acetaldehyde have significantly increased for some vehicles tested (Hernandez et al., 2014).

For gasoline powered cars, the adoption of the three-way catalyst greatly reduces the emissions of NO_x, HC and CO (Colvile et al., 2001). This catalyst is generally a combination of platinum, palladium and rhodium. The catalyst aids the oxidation of HC and CO while also promoting the reduction of nitrogen monoxide (NO) to nitrogen and oxygen. The operational window is narrow for these reactions, with a near-stoichiometric air-fuel ratio required for successful pollutant abatement (Faiz et al., 1996). However with so many cars on the roads these pollutants, and others, are still causing problems to health, and with new technologies and fuels on the horizon it is vital that the emission of these pollutants is as low as possible. The investigation of emissions from HEVs, including those running on increased proportions of biofuel blends is therefore of the utmost importance. Approaching this investigation in the context of type approval test procedures is an effective way of not only assessing the performance of these new technologies, but also assessing the adequacy of the type approval test procedure.

1.2 Research aims and objectives

The aims of this work are to investigate the regulated and unregulated pollutant emissions from HEVs and examine the effect that the use of biofuel blends with gasoline have on these emissions. In addition, the legislated type approval testing procedures will be investigated and compared to other real-world driving tests: The differences between reported emissions under different types of testing will be studied, in order to assess whether the type approval HEV testing is representative of real-world HEV emissions. The specific objectives are defined and presented in Chapter 2 Section 2.11.

1.3 Thesis outline

This thesis is comprised of eight chapters. Chapter 1 gives the background to the research topic, introduces the aims and objectives of the research and details the structure of the thesis. Chapter two provides a literature review into all relevant fields directly related to the aims and objectives of the research. Chapter three outlines the methodologies used for the research presented in this thesis, including testing, processing and analysis. Chapter four provides an in-depth investigation into the type approval procedure, comparing and contrasting the test properties and reported results that arise from the NEDC, WLTC and RDE tests, with particular focus on HEVs. Chapter five focuses on

the RDE test in particular, comparing this with real-world driving. Chapter six investigates HEV behaviour in detail, and quantifies how this behaviour impacts the resultant pollutant emissions. Chapter seven studies the pollutant emissions resulting from HEVs fuelled with ethanol and butanol biofuels blended in low percentages with gasoline, compared to pure gasoline and the currently adopted blends. Chapter eight concludes the thesis findings and discusses possibilities for future work.

Chapter 2
Literature Review

2.1 Introduction

This literature review will investigate the concept of HEVs and biofuel blending as a means to minimise CO_2 emissions and therefore reduce the transportation industry's contribution of GHGs to global warming. The wide range of harmful pollutant emissions that result from combustion will then be introduced with the formation mechanisms, health impacts and environmental impacts of each discussed. Emission abatement technologies currently in use for SI vehicles will then be covered, followed by a discussion of relevant emission measurement technologies. The literature review will provide a brief history of EU type approval legislation as well as a detailed presentation of current regulations at the time of writing.

The literature focusing on HEV behaviour and emissions will then be reviewed, paying particular attention to any gaps in the current state of knowledge. Finally the literature on tailpipe emissions resulting from low percentage ethanol and n-butanol blends with gasoline in SI vehicles, including HEVs, will be reviewed, paying particular attention to research gaps that exist in this field.

2.2 Engine and powertrain fundamentals

2.2.1 Spark ignition internal combustion engine

The SI ICE was first developed in the 1860s, though these engines have evolved greatly since their inception (Heywood, 1988). Over the past 60 years this evolution has particularly focused on minimising the emission of pollutants and increasing fuel efficiency.

Conventional ICE vehicles (CVs) can provide reliable performance over a long driving range because of their use of energy-dense liquid fuels. However, they also have poor fuel economy and produce damaging levels of pollutants. The poor fuel economy is due to a range of factors, including heat loss via exhaust gases, a mismatch of energy fuel characteristics with real-world driving conditions, wastage of the vehicle's kinetic energy on braking, wastage of energy during engine idling and low efficiency of hydraulic transmission under transient conditions (Pollet et al., 2012).

2.2.2 Hybrid and electric powertrains

Electrified vehicles can be of higher efficiency than ICEs due to extra energy saving techniques possible, such as regenerative breaking. During a deceleration event, the regenerative brakes work by putting the vehicle's motor into reverse mode, running backwards (Poullikkas, 2015). The electric traction motor experiences opposing torque from the motor resistance as current is induced in the motor coils (Prajapati et al., 2014). The wheels and motor are coupled, and so this opposing torque is transferred to the wheels, slowing the wheels down to decelerate (Poullikkas, 2015). This process also works when the car is coasting (Prajapati et al., 2014). Regenerative brakes are most effective at lower speeds and stop-start circumstances. When additional braking is required for harsher deceleration, friction brakes are also applied (Poullikkas, 2015). The use of an electric motor is also better for the initial acceleration from standstill because electric motors produce maximum torques instantaneously at the lowest motor speeds, providing far better response and low speed acceleration (German, 2015). There are three main types of electrified vehicle in commercial production (Poullikkas, 2015); HEVs, PHEVs and BEVs. These will be explained in the following subsections.

2.2.3 Hybrid electric vehicles (HEVs)

HEVs use ICEs in combination with one or more electric motors connected to a battery pack (M. Sabri et al., 2016). These are not the plug-in type; they have no way to externally charge the battery. The main purpose of the electrification is to enable the reduction of engine size and power as any further power needs can be met by the motor, thereby reducing fuel consumption (Bayindir et al., 2011). HEVs utilise the advantages afforded by both ICEs and EVs: They are able to improve efficiency by downsizing the engine, employing regenerative braking, and utilising stop-start technology (German, 2015). Additionally, the engine speed (revolutions per minute (RPM)) can be decoupled from the wheel speed, allowing the engine to be run at lower speeds where it is more efficient (Pollet et al., 2012). An alternator is usually employed to generate electrical power for auxiliary systems in an ICE vehicle, which works by creating electricity in a stationary coil of wires (stator) when an electric field spins inside it. An alternator has some parts that can easily wear with age, and a separate starter motor is required to provide the initial charge to start the engine (Viorel et al., 2004). In an HEV, however, this system can be replaced by a more efficient motor/generator system. Similarly,

less efficient mechanical water and oil pumps can be replaced by electrical ones (German, 2015). One downside of HEVs is their increased cost compared to CVs, due to the expensive components. There are various configurations of HEVs (series hybrid, parallel hybrid, and series/parallel hybrid), which will be discussed in the following subsections.

2.2.3.1 Series hybrids

The simplest kind of HEV is the series hybrid. Figure 2.1 outlines the components within the system. The ICE produces rotary motion in a shaft, which is then used to generate electricity in a generator (Pollet et al., 2012). This electricity can be passed through a motor to produce torque, thereby turning the wheels, with any surplus electricity stored in a battery (Prajapati et al., 2014). The series hybrid therefore has no mechanical connection between the ICE and the wheels (Bayindir et al., 2011), allowing the engine to run at optimum RPM and throttle setting for maximum fuel efficiency, even at standstill (Pollet et al., 2012). This ability for highly controlled ICE operation also allows for superior emissions control (Fuhs, 2009).

There are also disadvantages to the series configuration. The mechanical energy from the ICE is converted twice before it reaches the wheels, and each of these conversions wastes some energy (Prajapati et al., 2014). The required generator is also very heavy (Fuhs, 2009), decreasing efficiency further. Meanwhile, the expensive components necessary also make this a more expensive technology than parallel hybrids (Prajapati et al., 2014). For these reasons, series technology is mostly used in heavy vehicles, military vehicles and buses (Bayindir et al., 2011).

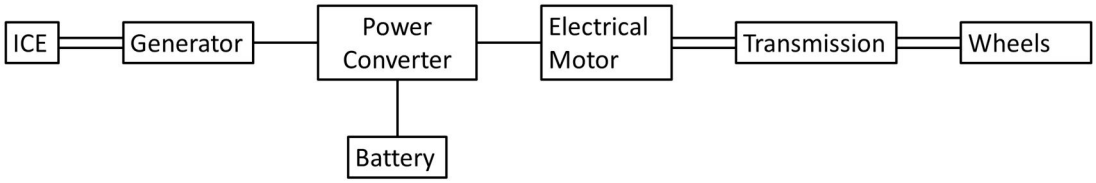

Figure 2.1 Series hybrid configuration (Prajapati et al., 2014).

2.2.3.2 Parallel hybrids

Parallel hybrids have the mechanical output from the ICE and the electric output from the motor connected in parallel to drive the wheels (Bayindir et al., 2011). This is done through a transmission as in a conventional car, to match the engine speed with the drive shaft speed. In this case a three shaft continually variable transmission (CVT) is usually employed (Fuhs, 2009). As

a result of this configuration, there is no need for an alternator or generator as there is in the series HEV, which makes the parallel hybrid lower weight (Fuhs, 2009). The car can generally use either ICE power only, motor power only, or a combination of both, depending on the needs of the vehicle (Pollet et al., 2012). Figure 2.2 shows a simple schematic diagram of the components.

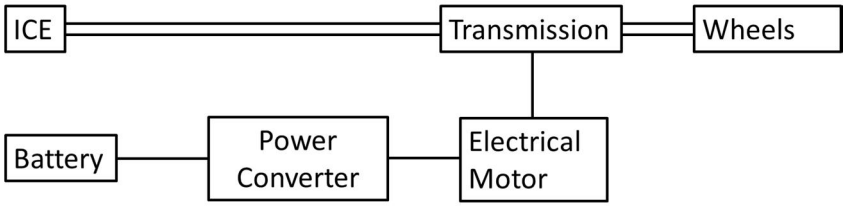

Figure 2.2 Parallel hybrid configuration (Prajapati et al., 2014).

Compared to the series hybrid, the parallel hybrid needs fewer propulsion devices, and a downsized ICE and smaller motor can be used. Additionally, there is less conversion of energy occurring than in the series hybrid, which also improves efficiency. The electric-only mode is useful for stop-start conditions, and changes in torque demand are met with a faster response time (Fuhs, 2009). In the most common strategy, the ICE is operating at almost constant power output and the maximum efficiency point (Bayindir et al., 2011). However, unlike the series hybrid, the parallel hybrid does have variations in engine speed depending on the drive requirements, taking the engine out of its optimum operational efficiency. The variability in engine throttle setting inevitably makes the control of emissions harder (Fuhs, 2009). In addition, there are extra powertrain parts required such as clutches and transmission, and because of the need for a direct mechanical connection between ICE and drive shaft, engine placement is less flexible (Fuhs, 2009).

2.2.3.3 Series-parallel or ‘power-split’ hybrids

As the name suggests, a series-parallel or ‘power split’ hybrid incorporates features of both series and parallel hybrid technologies. The series-parallel hybrid has one more mechanical link than the series hybrid, and one more generator than the parallel hybrid (Prajapati et al., 2014). They have a power split device, consisting of a planetary gear set as shown in Figure 2.3. This couples the ICE, generator and motor. The ICE is linked to the planet gears, the generator to the sun gear and the outer ring gear transmits torque to the differential. The motor is also linked to the ring gear via a motor speed reduction gear, so that it is able to add torque to the system. Because of this setup, the engine is able to operate at optimum efficiency for each speed. As

there is no gear changing involved, the ICE operation is less transient, lying between the parallel and series configurations (Bayindir et al., 2011). The series-parallel vehicle is particularly good at optimising efficiency for city driving, but this advanced technology is also costly (German, 2015).

The power-split technology is used in the Toyota Prius (Pollet et al., 2012). This type of system offers greater flexibility than either the series or the parallel hybrid technologies, and has been the most popular HEV type for passenger cars (Parry, 2019).

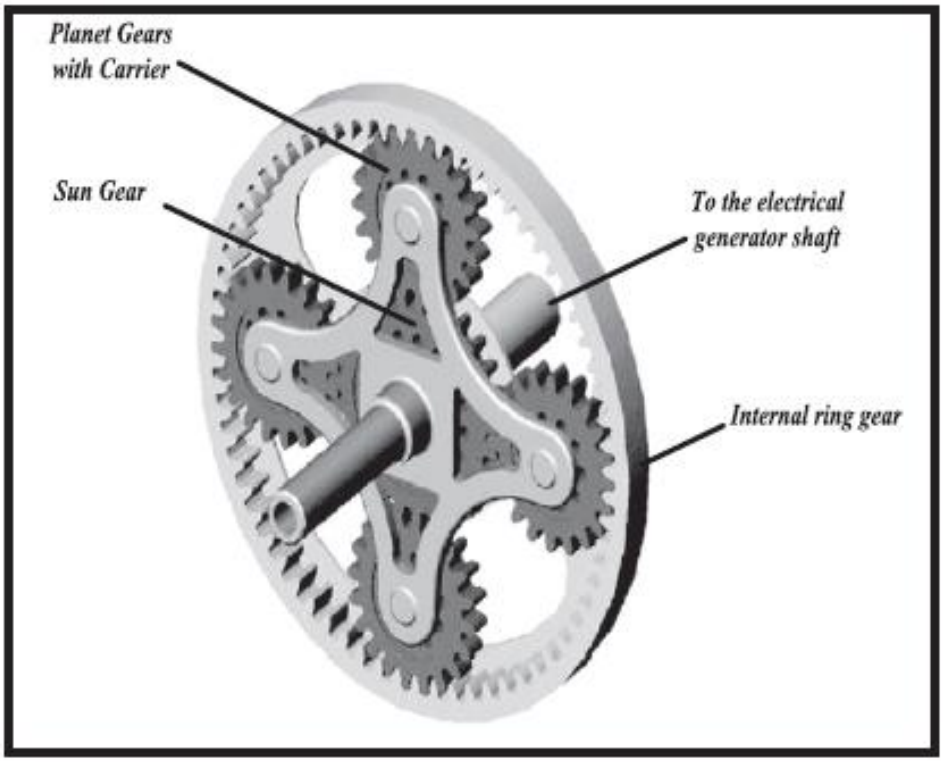

Figure 2.3 A Planetary gear system. Source: Bayindir et al. (2011).

2.2.4 Plug-in hybrid electric vehicles (PHEVs)

PHEVs are HEVs that have a battery storage system of at least 4 kWh (HEVs having 1-5 kWh), a means of recharging the battery externally, and the ability to drive at least 16 km (whereas HEVs generally only last a few kilometres) in electric mode (Pollet et al., 2012). Figure 2.4 shows a simple schematic diagram of the components. The PHEV ability to charge the battery externally means that the car can be more selective about when to run the ICE, resulting in lower tailpipe GHG emissions, which translate into lower overall GHG emissions provided that the externally produced electricity was formulated in a renewable manner (Poullikkas, 2015). Some studies have calculated that

PHEVs offer reductions of 25-55% NO_x, 35-65% GHG and 40-80% fuel consumption compared to conventional HEVs (Amjad et al., 2010).

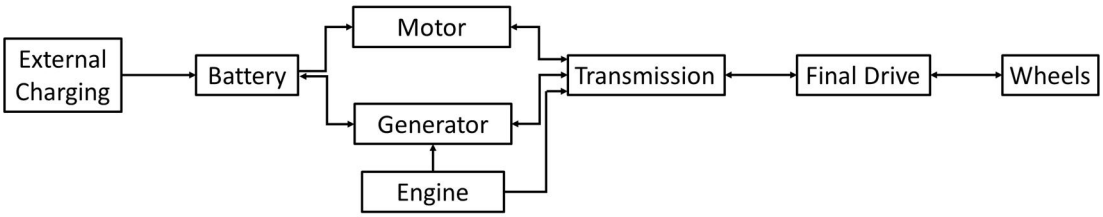

Figure 2.4 Schematic diagram of a PHEV system (Prajapati et al., 2014).

2.2.5 Future prospects

The government has set a vision for all cars and vans to be zero emission vehicles by 2050 (Department for Transport et al., 2015), aiming for all new cars sold by 2035 to be Ultra Low Emission Vehicles (ULEVs) (BBC, 2020) of less than 75gCO_2/km (Department for Transport, 2016c). However, the government maintains that it is not their responsibility to identify and support specific technologies at this early stage of development, so are backing those deemed most promising by the industry consensus. The HEV has proven to be one of the most successful of these alternative technologies (Parry, 2019).

It is widely believed that electrification will be at the core of the long-term decarbonisation plan, with increased hybridisation an important intermediary step in this direction (Office for Low Emission Vehicles, 2013). Conventional HEV technologies can offer GHG emissions savings in the region of 15-25% over comparative ICE vehicles, so will not be able to deliver the full GHG savings required, but are an important step while electric vehicle technology is still improving (Office for Low Emission Vehicles, 2013). Data provided in an International Council on Clean Transportation (ICCT) report shows that the percentage uptake of these vehicles has undergone a steady increase since their market introduction (ICCT, 2015). HEVs therefore play an important role, with a large proportion of the vehicle population predicted to be hybrid by 2030, as demonstrated by Figure 2.5 (IEA, 2011). Until charging infrastructure is improved, PHEVs will not dominate the market. Of the HEVs, Toyota's series-parallel (power-split) vehicles such as the Toyota Prius have been the most popular (Parry, 2019), evidenced by Figure 2.6.

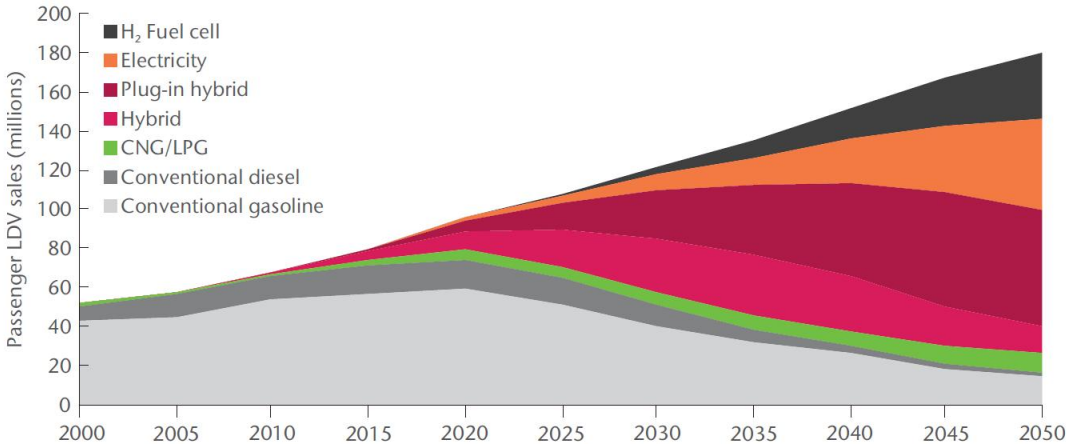

Figure 2.5 Annual light-duty car sales by technology type (IEA, 2011).

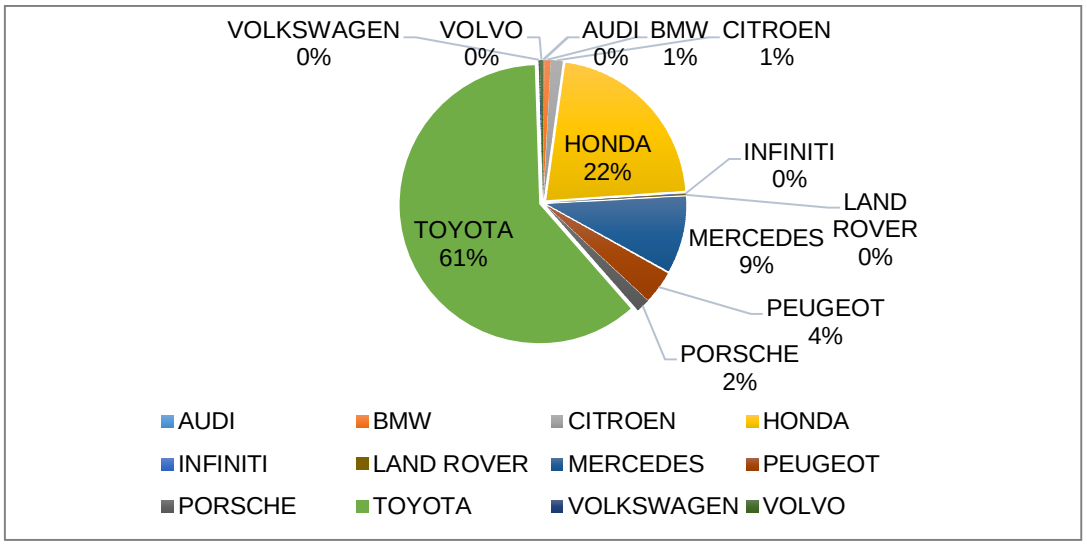

Figure 2.6 UK licenced HEV make shares in 2014. Made from the Cars(VEH02) dataset available at GOV.UK.

2.3 Biofuels for SI vehicles

2.3.1 Fuel requirement for SI engines

Under the Renewable Energy Directive (RED), a target of 10% for the percentage of renewable energy used in transport fuels was set for 2020, with much of this met through the use of biofuels (Department for Transport, 2017). Additionally, another EU directive, the Fuel Quality Directive (FQD), imposed the obligation for fuel suppliers of land transport to decrease the life cycle GHG emissions of their fuel by at least 6% by 2020 (Department for Transport, 2017). The EU Directive 2018/2001 has set a further obligation on fuel suppliers to ensure that the share of renewable energy within the final consumption of energy in the transport sector is at least 14% by 2030. Within this target, there are additional requirements for increasing GHG savings from

the renewable fuels used, and also a minimum contribution from advanced biofuels and biogas that increase with time. This is to ensure that the increased quantities of biofuels are not made from raw materials from land with high carbon stock, so that they actually give good savings in GHG emissions.

In order to help meet these requirements in the UK, there is a percentage of renewable fuels ('obligation percentage') that must be incorporated into the fuel mix of all suppliers selling above 450,000 litres of fuel per year (Department for Transport, 2019). The Department for Transport (DfT) envisions that higher blend percentages of renewable fuels will be used in the future, as outlined in Table 2.1. In order to achieve this, 10% ethanol blended with gasoline, or 'E10', is being introduced to replace E5 previously used, with the transition expected to occur in 2021 (Department for Transport, 2020). However, crop sources of biofuels can cause indirect land-use change (ILUC) elsewhere to account for the lost agricultural land, resulting in deforestation, habitat destruction and the release of additional CO_2 into the atmosphere. Due to the restrictions surrounding crop-based fuels, additional gasoline-additive fuels are being considered to compliment ethanol use, such as n-butanol (Department for Transport, 2016a).

Table 2.1 Biofuel trajectory targets set out by the DfT. Source: Department for Transport (2019).

Obligation period	Specified amount, as share of fossil fuel, by volume	Specified amount, as share of total fuel, by volume [13]
1 Jan 2019 - 31 Dec 2019	9.289%	8.50%
1 Jan 2020 - 31 Dec 2020	10.803%	9.75%
1 Jan 2021 - 31 Dec 2021	11.235%	10.1%
1 Jan 2022 - 31 Dec 2022	11.607%	10.4%
1 Jan 2023 - 31 Dec 2023	11.857%	10.6%
1 Jan 2024 - 31 Dec 2024	12.107%	10.8%
1 Jan 2025 - 31 Dec 2025	12.360%	11.0%
1 Jan 2026 - 31 Dec 2026	12.613%	11.2%
1 Jan 2027 - 31 Dec 2027	12.867%	11.4%
1 Jan 2028 - 31 Dec 2028	13.122%	11.6%
1 Jan 2029 - 31 Dec 2029	13.378%	11.8%
1 Jan 2030 - 31 Dec 2030	13.636%	12.0%
1 Jan 2031 - 31 Dec 2031	13.895%	12.2%
1 Jan 2032 - 31 Dec 2032 (and subsequent obligation periods)	14.155%	12.4%

2.3.2 Ethanol

2.3.2.1 Fuel properties

The properties of a fuel vary depending on its composition. Gasoline consists of a mixture of many different compounds, the composition of which varies from sample to sample. This variation, though not greatly affecting the elemental composition, causes variation in the physical properties of the fuel (Schobert, 2013). Nonetheless, properties of gasoline fuel – and its blends with ethanol – have been characterised in many studies. Table 2.2 gives some important properties for gasoline and ethanol fuels.

Table 2.2 Selected properties of gasoline and ethanol. Information gathered from Canakci et al. (2013)[1], Varde et al. (2007)[2], Schobert (2013)[3] and Liu et al. (2019)[4].

Property	Gasoline	Ethanol
Density (kg/m^3 at 15°C) [1]	750.8	809.9
Kinematic viscosity (mm^2/s and 40°C) [1]	0.494	1.221
Research octane number [4]	93.1	107
Motor octane number [1]	85	89.7
Latent heat of vaporisation (kJ/kg) [1]	180-373	840
Autoignition temperature (°C) [1]	370	464
Lower heating value (LHV) (MJ/kg) [4]	32.9	21.3
Stoichiometric A/F ratio (kg/kg) [2]	14.56	8.95
LHV at stoichiometry (MJ/kg; MJ/m^3) [2]	2.84; 3.4	2.69; 3.3
Flammability limits (volume % in air) [3]	1.4 – 76	4.3 – 19
Flash point (°C) [3]	-43 – -39	12.8
Octane number (R+M)/2 [2]	87	99
Vapour pressure (kPa) [4]	55 – 103	18
Water solubility (wt% at 20°C) [3]	0.009	infinite

In the UK, cars manufactured since 2005 are compatible with E10 (Lonza et al., 2011). The Society of Motor Manufacturers and Traders estimated that in 2011, 88% of gasoline cars in UK were E10 compatible, while 12% – 2.5 million cars – were either confirmed non-compatible (1.6 million cars) or were of unknown compatibility (900,000 cars) (UK Department for Transport, 2013). The Department for Transport has estimated current and future car numbers based on this data, assuming different rates of decline for differently aged cars. Their results are displayed in Figure 2.7. For 2020, the total number of incompatible cars has been estimated at 460,000. It is clear that as time progresses, the larger portion of non-compatible cars will be the older vintage cars, which are generally used far less and whose users often choose to use

pure-gasoline ‘super unleaded’ fuel anyway (UK Department for Transport, 2013). These predictions indicate that E10 should be fairly readily taken up by consumers.

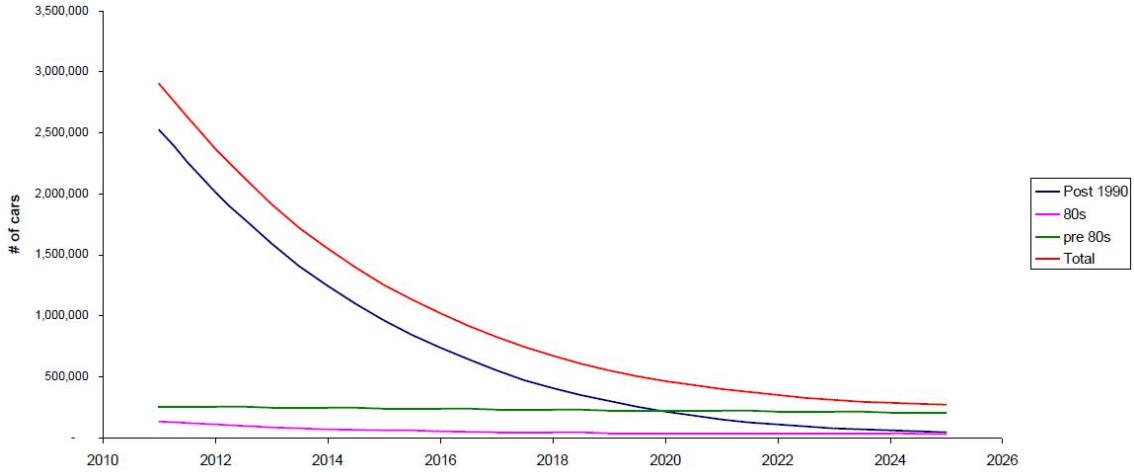

Figure 2.7 Estimated rate of decline of non-E10-compatible cars. Source: UK Department for Transport (2013).

In the following sections, ethanol use with gasoline will be considered, covering the combustion in engines and resultant emissions. When discussing technical results, there will be a focus on E5 and E10 blends where possible, but work on other blend ratios will also be included for completeness where required.

2.3.2.2 Combustion characteristics

This section covers the differences in combustion properties between ethanol and gasoline. Ethanol is an octane booster, and so can replace other additives used to boost the octane number of gasoline (da Silva et al., 2005). Due to its octane boosting nature, higher compression ratios are possible without the fuel auto-igniting and causing knock (Eyidogan et al., 2010). Higher thermal efficiencies and pressures inside cylinders have therefore been achieved in the past with the use of this fuel; this can help to negate the impacts of the lower heating value of ethanol compared with gasoline (Hernandez et al., 2014). More aggressive turbocharging, in combination with downsizing, is also possible when using ethanol-containing fuel; this would further increase fuel efficiency (Anderson et al., 2012).

A study presented in Al-Hasan (2003) into the effects of ethanol blends on an SI engine revealed that brake power, brake thermal efficiency and volumetric efficiency increased by mean average values of 8.3%, 9% and 7% respectively. This is because E10 is a more oxygenated fuel, improving

combustion and hence thermal efficiency (Hsieh et al., 2002a; Agarwal, 2007; Costagliola et al., 2013; Varol et al., 2014; Masum et al., 2015). Brake specific fuel consumption, however, decreased by a mean average value of 2.4%, indicating that the improvements due to ethanol do not completely negate their inferior heating value.

With regard to fuel consumption, there is general consensus in the literature that ethanol blends induce higher fuel consumptions, due to ethanol's decreased LHV (Liu et al., 2019). Al-Hasan (2003) saw increased break specific fuel consumption with ethanol blending, demonstrating that with the lower energy content of the ethanol, the engine needs to use more fuel in order to produce the same wheel power as gasoline (Eyidogan et al., 2010). Al-Hasan (2003) found that volumetric efficiency also increases. The break thermal efficiency however increases (Al-Hasan, 2003; Eyidogan et al., 2010) due to the improved combustion and thermal efficiency (Hsieh et al., 2002a; Agarwal, 2007; Costagliola et al., 2013; Varol et al., 2014; Masum et al., 2015). Hsieh et al. (2002) also found that torque output slightly increases with ethanol addition, but is rather insensitive to the percentage ethanol. This trend was mainly seen in the low throttle opening and high engine speed conditions, where gasoline traditionally operates slightly fuel-rich. The reason given was that the addition of ethanol produces a leaning effect to increase the air-fuel equivalence ratio, bringing it closer to stoichiometric and thus improving the combustion and allowing higher torque.

2.3.2.3 Engine component interactions

According to a report published by the American Petroleum Institute (Foster et al., 2011), many manufacturers have concerns that ethanol blends greater than E10 risk damaging engine components. Potential issues include materials' compatibility and durability, the drivability of the vehicles, tailpipe and evaporative emissions, and issues with on-board diagnostic (OBD) systems (Anderson et al., 2009).

The addition of ethanol to gasoline can reduce driveability and 'cold start' performance, because of the higher heat of vaporisation of ethanol blends. The increased volatility of ethanol blends may also lead to higher chances of vapour locking issues (Wyman, 1996). A very important consideration when discussing the use of ethanol blends in vehicles also pertains to the possibility of undesirable reactions between the ethanol fuel and the engine. This includes corrosion, increased engine deposits, phase separation (Khuong et

al., 2016), and also unfavourable compounds being formed via reactions with oxygen (Santos, 2012) or lubricating oil (Costa and Spikes, 2014) during combustion. Deformation of a material surface due to repeated sliding contact is called wear, and this occurs when acid forms on a surface. The accumulation of metal particles such as iron, aluminium and copper due to the ethanol corroding engine components produces sludge, which can result in oxidation of the lubricant and corrosion of engine components. Wear and sludge reduce the lubrication properties of the lubricant, reducing engine component lifespans (Khuong et al., 2016). Some fuel dilution in lubricants is common for engines, but because of its higher boiling point and latent heat of vaporisation, ethanol has a higher tendency to reach the crankcase and dilute the engine oil located there (Wattrus, 2013). This is particularly the case under cold start conditions, so is worse for short trips where the car is warming up for much of the journey as the ethanol is not evaporated from the oil.

Due to the various differences in chemical and physical properties of ethanol compared to gasoline, it is a widely held view within the industry that without further modifications to the vehicles, there is a limit to the quantity of ethanol that can be safely blended into gasoline. This is currently 10% in the EU, according to the fuel quality Directive 2009/30/EC.

2.3.2.4 Environmental impact and life cycle assessment

Ethanol can be produced through fermentation of many different crops including wheat, sugar beet, sugarcane and corn (Agarwal, 2007). The CO_2 released on combustion is recycled into organic tissues during the growth of additional crops for ethanol production (Sadeghinezhad et al., 2014). Agarwal (2007) estimates a net removal of CO_2 from the atmosphere.

There are, however, various concerns over the introduction of biofuels. One of these is the potential harm that could result if biofuels are irresponsibly produced, because the production of the biofuel is just as important as how it is used. Significant quantities of fossil energy can still be used during the production process, and this must be closely scrutinised (Agarwal, 2007). Another very important consideration with first generation biofuel crops such as ethanol is the rich agricultural land required for growth, which competes for land that could be used for food (Sadeghinezhad et al., 2014) and competes for water (Sheehan, 2009). Soil degradation is another potential issue that can result from the vast crop cultivation that is necessary for intensive ethanol production (Agarwal, 2007). The vast use of fertilisers in the growth of these

crops is also a concern, with the N_2O emissions that result impacting the climate (Crutzen et al., 2008). Land use change is another area where the carbon cost is only just starting to be fully comprehended, and so if a change is to be made to grow biofuel crops, this must also be carefully considered (Sheehan, 2009).

There have been many life cycle assessments (LCAs) performed in the past for ethanol, including those based on wheat. Wheat is a particularly popular ethanol feedstock in northern Europe because it has the highest yield of the cereal crops, of which the UK is the largest producer (Yan and Boies, 2013). The literature to date is mixed, with the RTFO default value for European wheat ethanol given as 44 g CO_2 equivalence (CO_2e) CO_2/MJ. Yan and Boies (2013) conducted a LCA of UK-based wheat ethanol using RTFO inputs, and found that the GHG intensity of this fuel could span the range from 40-110 gCO_2eMJ^{-1} when land use change (LUC) emissions and sources of uncertainty are taken into account. Valin et al. (2015) calculated that wheat ethanol production contributed 34 gCO_2e/MJ from LUC alone, ignoring agricultural production and chain emissions. Sustainable Transport Solutions Ltd (2008) calculated that wheat ethanol production in the UK has a CO_2 intensity of 60.6 gCO_2/MJ, equal to a 28.6% reduction compared to UK gasoline at 84.8gCO_2/MJ, while Edwards et al. (2011) presented a 59.2 g/MJ CO_2e GHG emission (a 31.0% reduction compared to European gasoline at 85.8 gCO_2/MJ). Borrion et al. (2012) conducted well-to-wheel LCAs for E15 and E85 fuels, and calculated reductions of 15% and 73% GHG emissions respectively, compared to standard gasoline. The functional unit they chose was the amount of fuel to drive 1km in a small passenger car, so they accounted for the inherently lower energy density of ethanol compared to gasoline in their study. This study also emphasised that although ethanol use gives GHG savings, it has little effect on other environmental issues such as acidification and water depletion.

The above LCAs demonstrate that although there is much disagreement as to the exact GHG saving that ethanol can provide due to the different methods used to conduct the LCAs, there is a consensus that it does have the potential to offer considerable savings as long as responsible practises are maintained throughout the process.

2.3.1 Butanol

2.3.1.1 Fuel properties

The medium-term industry trend regarding road transport appears to be to produce drop-in biofuels compatible with existing technologies. Butanol is another biofuel with the ability to blend with gasoline. Butanol has been suggested as a more compatible fuel than ethanol for the gasoline refuelling infrastructure, due to the fact that it is not water soluble and therefore, unlike ethanol, it can be transported in existing pipelines (Bergthorson and Thomson, 2015). Like ethanol, butanol is regarded as an octane booster when added to gasoline, allowing higher compression ratios and greater spark advance by lowering risk of engine knock, which increases thermal efficiency (Yang et al., 2009). N-butanol also has higher energy density than ethanol, improving fuel economy, and lower vapour pressure, reducing vapour lock issues and evaporative emissions (Liu et al., 2019).

There has therefore been increased interest in butanol research recently, to assess the environmental, performance and emissions characteristics of this fuel and its blends with gasoline. Table 2.3 outlines some key properties of n-butanol, alongside those of ethanol and gasoline.

Table 2.3 Selected physical and chemical properties of n-butanol compared to gasoline and ethanol. Source: Liu et al. (2019).

Fuel	Gasoline	Ethanol	n-Butanol
Molecular formula	C_2–C_{14}	C_2H_5OH	C_4H_9OH
Molecular weight (g/mol)	110.8	46.07	74.12
Research octane number	93.1	107	96
Density at 20 °C (g/mL)	0.745	0.789	0.81
Lower heating value (MJ/L)	32.9	21.3	26.9
Laminar flame burning speed at 1 bar, 390K (cm/s)	52	63	57
Viscosity at 20 °C (cSt)	0.4–0.8	1.52	3.35
Surface Tension at 20 °C (mN/m)	20–25	22.39	24. 6
Vapor Pressure (kPa)	55–103	18	4.08
Boiling point (°C)	35–210	78	117
Latent heat of vaporization (kJ/kg)	180–373	840	546
H/C ratio	1.8	3	2.5
O/C ratio	0	0.5	0.25
Stoichiometric A/F ratio	14.56	8.95	11.13
Stoichiometric CO_2 (kg/L, fuel)	2.38	1.51	1.93

The production of butanol has a long history. Production of butanol from biomass was first recorded in 1861 when Louis Pasteur fermented sugars to n-butanol (Jones and Woods, 1986). Between 1930 and 1940, the production of n-butanol reached commercial scales using the bacterium *Clostridium*

acetobutylicum to convert sugars into a mixture of acetone, n-butanol and ethanol. This is commonly referred to as the acetone-butanol-ethanol (ABE) process, and can use a wide range of feedstocks that include waste products and crops that do not displace food crops (Weber et al., 2011). Other processes used to produce butanol after 1940 were less environmentally friendly, such as those utilising petroleum (Sarathy et al., 2014). Recently, significant work has been done to genetically manipulate industrial bacteria such as Escherichia coli to enable them to produce butanol (such as Shen and Liao (2008), Atsumi et al. (2008), Nielsen et al. (2009)), while other work has looked at increasing the efficiency of organisms already capable of producing butanol (such as Lee et al. (2008), Jiang et al. (2009)). For more detailed information about butanol, its production and prospects as a biofuel, see Nigam and Singh (2011). There are several isomers of butanol; n-butanol, 2-butanol, iso-butanol and tert-butanol (Yang et al., 2014), but only n-butanol will be discussed in detail in this thesis.

2.3.1.2 Combustion characteristics

Addition of n-butanol into gasoline can result in shorter ignition delay, faster combustion and better combustion stability (Liu et al., 2019). The latent heat of butanol is greater than gasoline, but lower than ethanol, so the combustion temperatures within the cylinder can be lower than gasoline (Elfasakhany, 2014). The majority of previous literature reports that butanol addition to gasoline generally results in improved combustion stability (Dernotte et al., 2010; Zhang et al., 2014), but little comparison against ethanol blends has been performed. However, Elfasakhany (2014) discussed the combustion characteristics of low blends of n-butanol/gasoline, finding that B10 gave lower engine torque, brake power, in-cylinder pressure and volumetric efficiency than pure gasoline. They concluded that the performance of n-butanol blends is lower than gasoline due to its higher latent heat of vaporisation and lower calorific value, which could be improved by modification of the ignition time and increase of the compression ratio. They do, however, suggest that low blends, of B10 and below, can be used with minimal decrease in performance.

With regard to fuel consumption specifically, the literature points to slightly increased fuel consumption compared to gasoline, because of butanol's lower heating value (Liu et al., 2019). However, this increase is much smaller than for ethanol, due to the fact butanol's LHV lies between that of ethanol and gasoline. Additionally, it has been theorised by Liu et al. (2019) that the higher

latent heat of butanol compared to gasoline lowers combustion temperatures, decreasing heat loss. This, combined with the extra oxygen in the butanol molecule, improves the efficiency of combustion.

2.3.1.3 Engine component interactions

It has been shown that n-butanol generally has better compatibility and lower corrosion to the engine system than that of ethanol (Liu et al., 2019). Overall, Singh et al. (2015) and Liu et al. (2019) conclude that butanol blends can be used as a partial replacement for pure gasoline in low percentage blends without any significant sacrifice of engine performance or hardware modification in existing SI transportation engines. The ASTM standard D7862-13 for butanol blending in the USA covers blends from 1-12.5% for n-butanol, iso-butanol and 2-butanol, indicating that blends up to B12.5 can be readily used in SI engines without the need for modification.

2.3.1.4 Environmental impact and life cycle assessment

With butanol, as with any biofuel, it is important to assess its total environmental impacts. Wu et al. (2008) assessed the life-cycle energy and greenhouse gas emissions that arise from the use of corn-based n-butanol, suggesting that a 39-56% energy saving and 32-48% GHG emission reduction would result when compared to gasoline. The large uncertainties associated with these values demonstrate the importance of the entire process of cultivation, processing and utilisation of biofuels. The paper did not conduct a sensitivity analysis, which would have been a useful uncertainty indicator given the number of independent variables in such LCAs. However, the study used reliable methods and data values, and any assumptions were outlined. It should be remembered that the paper only assessed n-butanol production from corn, which is not the only possible method for producing this fuel, and so is not necessarily an accurate assessment of all n-butanol production. Formation of n-butanol from waste products, for example, may prove to give more optimistic figures for both energy savings and emission reductions.

Pfromm et al. (2010) conducted a LCA to compare n-butanol production with ethanol production. This study used the LHV of the liquid fuel products per unit mass of feedstock as the base for comparison, and also assessed the carbon mass balances and economics resulting from both corn and cellulosic feedstocks. It concluded that at this time, ethanol is a more attractive alternative fuel than n-butanol if the ABE process in its current state is used.

This is despite the fact that butanol transportation uses existing pipelines, due to the small and remote production volumes limiting the advantage. The main reason for this economic disadvantage was that the yield of n-butanol is too low compared to ethanol to be advantageous, and would have to be doubled in order to compete economically with ethanol. This could be achieved in the future, and so it is still worthwhile to research n-butanol combustion and emissions.

Several studies have conducted life cycle assessments of butanol blends compared to ethanol blends, and most conclude that, with current technology, butanol has higher life-cycle emissions than ethanol (for example Pfromm et al. (2010), Hu et al. (2015)). Tao et al. (2014), however, conducted analyses of n-butanol and iso-butanol separately in comparison to ethanol, and found that while iso-butanol a greater lifecycle GHG emissions than ethanol, n-butanol had similar GHG emissions. There is clearly some disagreement concerning the lifecycle emissions from butanol. Considering the research currently being performed into the production of butanol, the attractiveness of butanol as an alternative fuel in the future may improve with changes to production technologies. Butanol, particularly n-butanol, is therefore a worthy research focus.

2.4 Types of emissions, their formation and impacts

There are many different forms of emissions that arise from power systems such as road vehicles. The most common air pollutants are outlined in the following sections. Primary pollutants are those directly emitted, while secondary pollutants are formed in the atmosphere, and include those such as ozone and secondary particles (Uherek et al., 2010). The health impacts related to the individual types of emissions from road transport have been widely assessed, as outlined in the review article by Curtis et al. (2006). The different pollutants released from transport and their associated health effects will be discussed below, followed by a discussion of the resulting global effects. It should be noted that a major hurdle in the quantification of health impacts from pollutants is the fact that people are exposed to relatively low levels of many different pollutants over a long time period, making it difficult to attribute any resulting problems to specific pollutants (Colvile et al., 2001).

2.4.1 Carbon monoxide (CO)

Carbon monoxide is produced during incomplete combustion, which occurs particularly in mobile combustion sources such as road vehicles (Godish, 1997). When this occurs, some of the fuel is only oxidised to CO, with some volatile hydrocarbon vapour and carbonaceous particles also emitted alongside (Colvile et al., 2001). The overall fuel conversion process during combustion consists of conversion of a primary fuel into smaller intermediate hydrocarbons, followed by oxidation to aldehydes and ketones, then to CO. Finally this CO is oxidised to CO_2 in reaction 1 (Sher, 1998).

$$CO + OH \leftrightarrow CO_2 + H \quad (1)$$

When this final step is not able to proceed due to a lack of oxygen, CO emissions result. This occurs when the mixture is fuel-rich, or if the expansion of burnt gases is too fast. CO emissions are therefore usually only important during cold start and harsh acceleration, when fuel enrichment is employed (Sher, 1998). The lower the efficiency of combustion, the colder the weather, or the higher the altitude, the more CO is produced (Brook et al., 2004). CO has a half-life of 1-2 months in the atmosphere, and can travel thousands of kilometres from its point of origin (Akimoto, 2003).

2.4.2 Nitrogen oxides (NO_x)

NO_x, namely NO and NO_2, is produced by combustion. The formation of these two species is strongly correlated with high combustion temperatures, high oxygen concentration and low reaction residence time (Canakci et al., 2013). In stoichiometric SI engines, the production of NO_2 is negligible (Vallero, 2008).

NO is formed when the high flame temperatures of combustion decompose molecular nitrogen and oxygen in the air, which recombine to produce NO. The main route for NO formation occurs via the Zeldovich-Kech mechanism, also known as the thermal route, given in reactions 2, 3 and 4 (Sher, 1998).

$$N_2 + O \leftrightarrow NO + N \quad (2)$$

$$N + O_2 \leftrightarrow NO + O \quad (3)$$

$$N + OH \leftrightarrow NO + H \quad (4)$$

In this reaction scheme, oxygen atoms behind the propagating flame front initiate decomposition of molecular nitrogen to form NO and atomic nitrogen (N). The atomic nitrogen is then able to decompose any molecular oxygen to

give more NO, and more atomic oxygen (O). Finally, the reaction of atomic nitrogen with a hydroxyl radical becomes the major sink for N. This reaction mechanism is highly endothermic, so the equilibrium concentration of NO is highest at the highest temperatures (Vallero, 2008).

In addition to the thermal route, there are other proposed routes. The most important of these is the 'prompt' route, occurring at a lower activation energy than the thermal route. This route involves the reaction of a CH radical with N_2, given in reaction 5 (Vallero, 2008).

$$CH + N_2 \rightarrow HCN + N \quad (5)$$

In general, the formation of NO is greater when the temperature of the burned gas, particularly the peak temperature, is higher. NO concentrations decrease under the following engine conditions because they lower combustion temperatures (Sher, 1998):

- Higher levels of dilution (from e.g. exhaust gas recirculation (EGR) or ambient moisture)
- Delayed spark timing
- Decreased engine speed
- Decreased engine load
- Decreased compression ratio

The second most important variable after temperature is oxygen concentration. NO production increases with higher oxygen concentration. This means that the peak in NO occurs when the air-fuel ratio is slightly on the lean side of stoichiometric, rather than at stoichiometry where the highest peak temperatures are achieved (Sher, 1998).

2.4.2.1 Environmental impacts of nitrogen oxides (NO_x)

Road traffic emissions of NO_x contribute to nitrogen deposition and acid rain. Reactive nitrogen sources (such as nitrogen oxides) accumulate in the atmosphere, water and ground (Schauer, 2015). NO_2 combines with OH to produce nitric acid, as shown in reaction 6 (Uherek et al., 2010). This is highly water-soluble and so increases nitrogen deposition.

$$NO_2 + OH \rightarrow HNO_3 \quad (6)$$

2.4.3 Hydrocarbons (HCs)

Like CO, hydrocarbon (HC) emissions from combustion engines result from incomplete combustion. This can occur in the case of fuel enrichment, poor mixing, or early quenching of the combustion processes (Vallero, 2008). HCs can go on to produce photochemical smog under strong sunlight (Canakci et al., 2013). The composition and quantity of HCs in the exhaust gases depend on many parameters, including the nature of the fuel and the conditions within the combustion chamber. Volatile organic compounds (VOCs) are formed from unburnt or partially burnt fuel, and are particularly toxic, as detailed below. VOCs are organic compounds that have boiling points of between 50°C and 260°C (Sarigiannis et al., 2011). They can include simple hydrocarbons, but also other species with more complex compositions. VOC emissions from all types of combustion sources are dominated by those from gasoline engines (Schauer, 2015) and so are very important to control as they are still a major air pollution problem in urban centres. These chemicals can also travel significant distances in air (Curtis et al., 2006). Harmful VOCs commonly occurring from road transport include aromatics such as BTXS (benzene, toluene, xylenes, styrene), aldehyde carbonyl compounds such as formaldehyde, acetaldehyde and acrolein (Sarigiannis et al., 2011), as well as other toxic organic molecules such as acetic acid and ethanol, including hydrocarbons such as n-hexane and 1,3 butadiene (George et al., 2015).

2.4.4 Greenhouse gases (GHG) including CO_2

If enough oxygen is available within the engine, the hydrocarbon fuel will be completely oxidised to give water and CO_2 (Heywood, 1988). Around 99% of the carbon within gasoline is typically converted into CO_2 in engines. Vehicles also produce other greenhouse gases such as methane (CH_4) and nitrous oxide (N_2O) (EPA, 2014). These gases absorb infrared radiation emitted by the earth's surface and the clouds, and then re-emit this from a level where the temperature is colder than the surface. This acts to trap part of the absorbed energy, effectively warming the earth's surface (Houghton et al., 1996). These three chemicals have different global warming potentials (GWPs) through time, as outlined in Table 2.4. Methane is released as unburnt hydrocarbons (Zervas and Panousi, 2010). The production of N_2O during combustion is limited, but the three-way catalytic converter (TWC) can act as a catalyst for its formation (Bielaczyc et al., 2014).

Table 2.4 Average lifetimes and GWPs of GHG emitted from vehicles. Source: Intergovernmental Panel on Climate Change (2014).

Species	**Lifetime (years)**	**Global Warming Potential**	
		(20 years)	(100 years)
CO_2	(Variable)	1	1
CH_4	12.4	84	28
N_2O	121.0	264	265

2.4.5 Ammonia (NH_3)

Ammonia (NH_3) emissions are connected to the use of a TWC in SI ICEs, and can be produced through a mechanism involving NO and hydrogen (H_2), just after catalyst 'light-off' (Suarez-Bertoa et al., 2017). This is generally enhanced by rich combustion conditions, where higher CO and H_2 concentrations and reductive conditions promote the reaction (Whittington et al 1995, Czerwinski et al 2010). NH_3 can lead to eutrophication of water and acidification of soil, which have negative impacts on nitrogen-containing ecosystems (Suarez-Bertoa et al., 2017).

2.4.6 Particulate matter

Atmospheric particulate matter consists of particles suspended in the atmosphere that are typically less than 60μm in diameter (Schauer, 2015). These are generated in several different ways, including from transportation. Gu et al. (2011) found 25% and 40% of the total particulate matter in a particular German town were from new and old traffic emissions respectively. From this information, it seems clear that traffic is a major source of particulates in urban environments (Vu et al., 2015).

The precise size distribution of particulate matter coming from a vehicle depends on factors such as the type of engine, fuel and exhaust after-treatment devices, in addition to the vehicle operating mode, test method and atmospheric conditions at the time of measurement (Vu et al., 2015). The type of fuel used has been found to have a significant effect on the particle concentration and size distribution. The operating mode of an SI engine strongly affects the number and mass concentrations of the resulting particulate matter, but does not seem to affect the size distribution (Li et al., 2013). The size distribution from SI engines can be markedly different from diesel engines, in that the former generally has a unimodal distribution while the latter has a bimodal distribution (Vu et al., 2015).

There are three main size ranges seen in vehicle exhaust, as shown in Figure 2.8. Particles less than 100nm in diameter are generally categorised as nucleation mode (Eastwood, 2008). Nucleation mode particles are widely believed to be formed from volatile material, such as VOCs originating from fuel and lubricant oil, though some research suggests that some particles may be partly solid (Raza et al., 2018). Accumulation mode particles have been the most widely studied, and have been found to consist of a collection (agglomerate or aggregate) of smaller primary particles (spherules) of sizes ranging from 30nm to 50nm (Eastwood, 2008). Accumulation mode particles are generally considered to consist of soot particles formed when fuel molecules undergo pyrolysis at high temperatures (Raza et al., 2018). The size of these accumulation mode particles mainly depends on how many spherules they consist of. The agglomerate surface is coated by a layer of liquid or semi-liquid material that is of a different composition to the bulk (Eastwood, 2008). Particles between 100nm to 900nm are generally categorised as accumulation mode. However, some authors have classified the boundary between nucleation mode and accumulation mode as being closer to 50nm (Raza et al., 2018). Particles over 900nm in diameter are categorised as belonging to the coarse mode, which is usually insignificant from motor exhaust. Coarse mode particles are formed from nucleation and accumulation mode particles combining together on the surfaces of the exhaust pipe, or from the degradation of materials therein (Eastwood, 2008).

The distribution of particle sizes seen in the atmosphere is influenced by processes such as nucleation, coagulation, condensational growth, plume dilution and vertical mixing (Turco and Yu, 1999). The particulate atmospheric lifetime differs significantly with particle size. Nucleation modes have short lifetimes due to rapid coagulation and condensational growth, and coarse particles also have a short lifetime due to rapid gravitational settling (Vu et al., 2015). This means that these particles have much more localised impacts (Wróbel et al., 2000; Uherek et al., 2010). Particles in the accumulation mode, however, can travel vast distances as their dimensions leave them less likely to undergo either of the above processes giving them lifetimes of weeks or months (Uherek et al., 2010). The strongest impacts still lie on local scales because of the increased concentrations close to the source.

Ultrafine particles below 100nm are associated with adverse health and environmental impacts and yet they make almost no contribution toward PM measurements. These particles can penetrate further into the lungs before

they are deposited on the surface, making them far more likely to pass into the bloodstream (Raza et al., 2018). Until recently, particle number (PN) emissions were not regulated for SI vehicles, but the Euro 6c regulations limited PN to $6.0x10^{11}$ particles/km for gasoline direct injection (GDI) vehicles specifically.

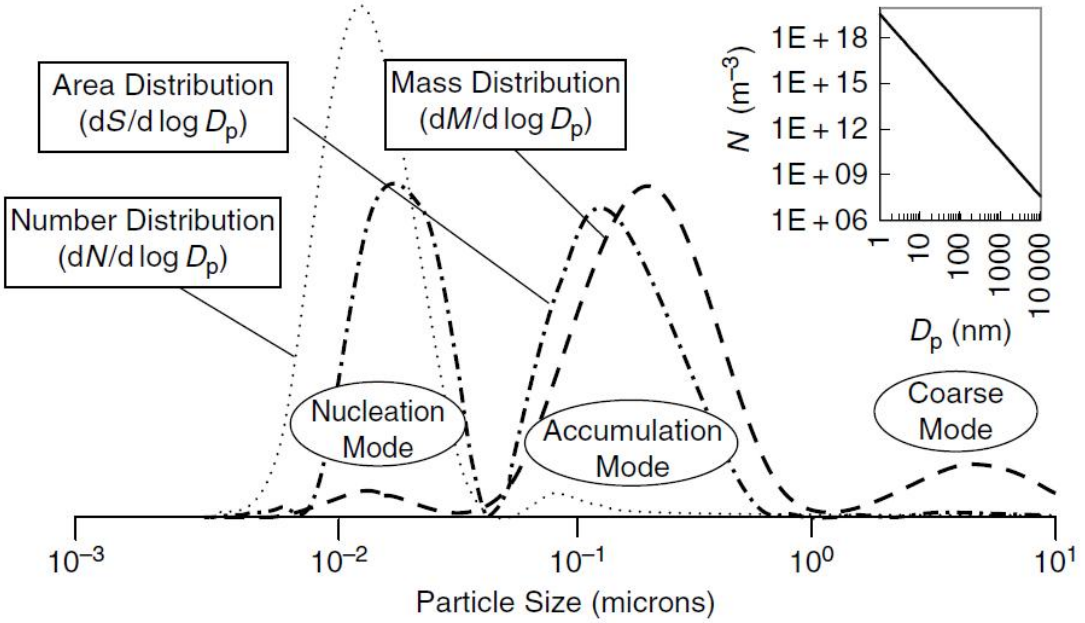

Figure 2.8 Generalised size distributions for typical particles emitted by ICEs. Source: Eastwood (2008).

During cold start, a globally rich mixture ensures that the charge can be ignited as evaporation is essentially incomplete and unreliable, making the engine susceptible to stalling. This makes films of liquid fuel accumulate on the combustion chamber walls, igniting capriciously and burning long into the expansion stroke (sooty pool fires) (Eastwood, 2008). Generally, poor air-fuel mixing increases the proportion of smaller particles (the more homogeneous, the larger the particles seen), which means that during cold start, we are likely to see a distribution of smaller particles (Raza et al., 2018). Giechaskiel et al. (2015) compared the PN emissions of cold and hot start test cycles of a GDI SI engine, confirming higher PN emissions under the cold start tests.

For harsh acceleration, the same fuel enrichment may be applied (Eastwood, 2008). Also, at high engine speed conditions, the exhaust temperatures can increase so fuel enrichment may be used to protect the TWC and other engine components from thermal stress (Nose et al., 2013). Though these two scenarios often take place in hot start conditions meaning the fuel is fully

vaporised and there is no pool fire, rich burn still leads to soot and hence PN (Eastwood, 2008).

In addition to purposeful fuel enrichment, deviations away from stoichiometry can occur due to fuel being deposited on the inside of the intake port of port fuel injection (PFI) SI vehicles, rather than going into the combustion chamber. This is not a problem during steady state operation as the oxygen sensor will compensate. However, during transient operation, these reservoirs can be problematic, as lean operation will be followed by rich operation due to improper fuelling management. When shifts in engine operation occur, the temperature of the inlet valve can change, altering the accumulation and evaporation of fuel reservoirs and hence the amount of soot seen at the tailpipe. In addition, if liquid fuel ligaments or droplets of the order 100-200µm are able to enter the cylinder and cannot be vaporised quickly enough, they will burn with a sooty flame (Eastwood, 2008). Particle number has been related to lambda in an exponential relationship by Maricq et al. (1999), given in equation 1.

$$PN = 8.18 \times 10^{8} \times e^{(160-\lambda)^2} \quad (1)$$

Generally, one can conclude that for a gasoline SI engine, the cold start period must be as short as possible and the mixture must be as stoichiometric and homogeneous as possible, in order to limit PN emissions.

Exhaust flows containing particulate matter are subject to a wide range of forces, including diffusion, turbulent impaction, thermophoresis and electrostatic forces. The most dominant of these is thermophoresis for submicron particles (Abarham et al., 2010). Thermophoresis is the motion of particles down a gas temperature gradient (Mensch and Cleary, 2019). In hotter regions, the gas molecules have greater energy and more velocity, so the collisions are more vigorous compared to in cooler regions. If a temperature gradient is present, then there will be a net pressure force from the hotter side of a particle, pushing it in the direction of the colder side (Abarham et al., 2010). Inside an exhaust pipe during cold start there will exist a temperature gradient between the hot exhaust gases and the cold exhaust pipe, so particles will be pushed to the walls of the pipe (Mensch and Cleary, 2019). This force is more important at the edges of a convective flow, where the velocities are lower, than in the centre where bulk transport will dominate. Particles will then stick to the cold exhaust pipe due to adhesive forces (Eastwood, 2008), having been pushed toward it by thermophoresis. Studies

have shown that thermophoresis depends mostly on the primary particle diameter rather than overall particle size because this force is a surface phenomenon (Abarham et al., 2010). Deposition of particles will also occur on systems within the exhaust pipe, such as a cold catalyst or silencer, and indeed this has been seen in previous studies (Andrews et al., 2002). These deposition effects can mean that particulate matter can stay within the exhaust system of a vehicle and not exit the tailpipe, particularly during low load, cold start driving.

Vehicles have been seen to eject a large quantity of particulate matter as a result of the release of previously captured particles from the exhaust pipe walls (Andrews et al., 2002). This re-entrainment of particles into the exhaust flow occurs when the fluid shear or vibration forces exceed the adhesion forces, causing particles to break off and re-enter the flow. This often occurs once the exhaust system has warmed up and the load on the vehicle increases, such as during an acceleration to higher speeds. The particles that are re-entrained are not necessarily of the same form as those that were originally captured at the walls; the deposits agglomerate on the surface and then fracture along fault lines that create secondary particles that can be of considerably greater size than those captured (Eastwood, 2008). Of course, the number concentration would be oppositely affected in this case, with much lower particle numbers detected.

2.4.7 Health impacts of pollutants

The health impacts of the various pollutants presented in the sections above have been well documented in previous literature, including books such as Godish (1997b) and reviews such as Curtis et al. (2006), so will only be outlined in this section.

CO is bad for human health because it reduces the oxygen-carrying capacity of the blood (Godish, 1997). Exposure to CO and VOCs has been linked to asthma (Wong et al., 2001; Lee et al., 2002; Pénard-Morand et al., 2005), while both CO and NO_x have been linked to chronic obstructive pulmonary disease (COPD), upper respiratory infections, myocardial infarctions and strokes (Ritz et al., 2002; D'Ippoliti et al., 2003; Metzger et al., 2004; Peel et al., 2005). NO_x and PN have been associated with lung cancer (Vineis et al., 2004) while CO, VOCs and PN have all been associated with higher rates of pre-term birth and foetal/infant death (Vassilev et al., 2001; Liu et al., 2003;

Sagiv et al., 2005). NH_3 increases the amount of particulate matter, as it is a precursor of secondary inorganic aerosols.

Particulate matter from vehicles is considered a major source of harmful particles in urban atmospheres (Vu et al., 2015). The particle number size distribution (PNSD) is an important factor to incorporate into considerations of particulate matter health risks because the ability of particles to penetrate deeply into the lung depends on their size (von Klot et al., 2005). Particles less than 10μm (PM_{10}) or 2.5μm ($PM_{2.5}$) are normally considered the most dangerous, as they are small enough to penetrate these areas of the lung (Curtis et al., 2006). It has been suggested that $PM_{2.5}$ gives a better indication of the health effects as this size range can penetrate deepest into the lungs (Uherek et al., 2010). Ultrafine particles, with aerodynamic diameters of less than 100nm, have been suggested as some of the most dangerous types (Myung and Park, 2012).

2.5 TWCs and gasoline particulate filters (GPFs) for emissions abatement

2.5.1 Three way catalytic converters (TWCs)

In order to reduce emissions, ICE vehicles utilise technologies that convert harmful gaseous pollutants from the engine exhaust into non-polluting chemicals. For SI vehicles, this comes in the form of three-way catalytic converters (TWCs). These TWC systems induce oxidation and reduction reactions for CO, unburnt hydrocarbons and NO_x. The TWC oxidises CO and HCs with oxygen (O_2) found in the atmosphere, as shown in reactions 8 and 9 (Granger and Parvulescu, 2011).

$$CO + \frac{1}{2}O_2 \rightarrow CO_2 \quad (7)$$

$$C_xH_y + \left(x + \frac{y}{4}\right)O_2 \rightarrow xCO_2 + \frac{y}{2}H_2O \quad (8)$$

The TWC reduces NO with hydrogen, CO and HC in the exhaust gas, as shown by reactions 10-12 (Granger and Parvulescu, 2011).

$$NO + H_2 \rightarrow \frac{1}{2}N_2 + H_2O \quad (9)$$

$$NO + CO \rightarrow \frac{1}{2}N_2 + CO_2 \quad (10)$$

$$\left(2x + \frac{y}{2}\right)NO + C_xH_y \rightarrow \left(x + \frac{y}{4}\right)N_2 + xCO_2 + \frac{y}{2}H_2O \quad (11)$$

An important characteristic of these TWCs is their requirement of near-stoichiometric air-fuel ratios for combined conversion of all three pollutants. The other important property is the need for the temperature to reach a certain minimum in order for the TWC to light-off and catalyse the conversion reactions. The temperature at which this occurs is generally agreed to be 200-250°C in the literature, depending on properties of the TWC under study and the pollutant in question (Gao et al., 2013; Watling and Cox, 2014; Yan et al., 2019). Figure 2.9a and Figure 2.9b display these behaviours.

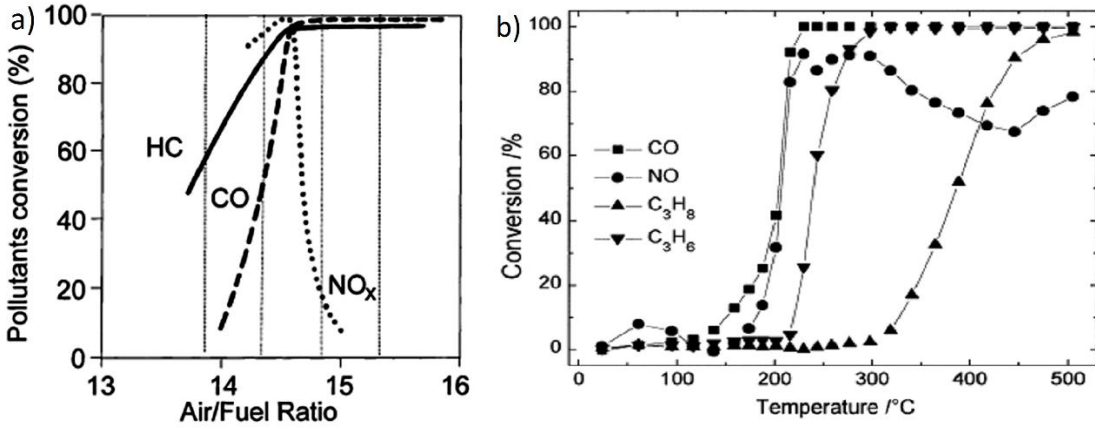

Figure 2.9 TWC conversion efficiency with air/fuel ratio and temperature, for different pollutants. Adapted from Granger and Parvulescu (2011).

2.5.2 Gasoline particulate filters (GPFs)

Gasoline Particulate Filters (GPFs) are increasingly being used to minimise PN emissions arising from SI vehicles. Because the current Euro 6 regulations only prescribe PN limits to SI vehicles powered by GDI engines, the uptake of GPFs has thus far been mainly limited to SI vehicles utilising this GDI technology (Joshi, 2020) and are not a focus of this thesis.

2.6 Emission measurement technologies

2.6.1 Gaseous pollutant measurement

There are a wide range of different instruments that have been created for the purpose of gaseous automotive emissions measurement. Those that are relevant to this thesis will be discussed in this section.

2.6.1.1 Laboratory-based certification equipment

The Global Technical Regulation (GTR) No. 15 for WLTC test procedures outlines the emission measurement requirements for this type approval procedure (United Nations, 2014). Firstly, the exhaust must be diluted to avoid

water condensation. A full flow dilution system shall be used, whereby the total vehicle exhaust is continuously and homogeneously diluted with ambient air using a constant volume sampler (CVS). One of the most common configurations is given in Figure 2.10 (Otsuki et al., 2015). The total volume of the exhaust gas/dilution air mixture must be measured, and a continuously proportional sample of the volume must be collected for analysis. The concentrations of gas compounds are then determined by the sample concentrations corrected for the concentrations in the dilution air. The advantage of this technique is that it does not rely on the exhaust flow rate being measured directly, and the emissions concentrations are averaged so the resultant emissions are more accurate (Adachi and Nakamura, 2013).

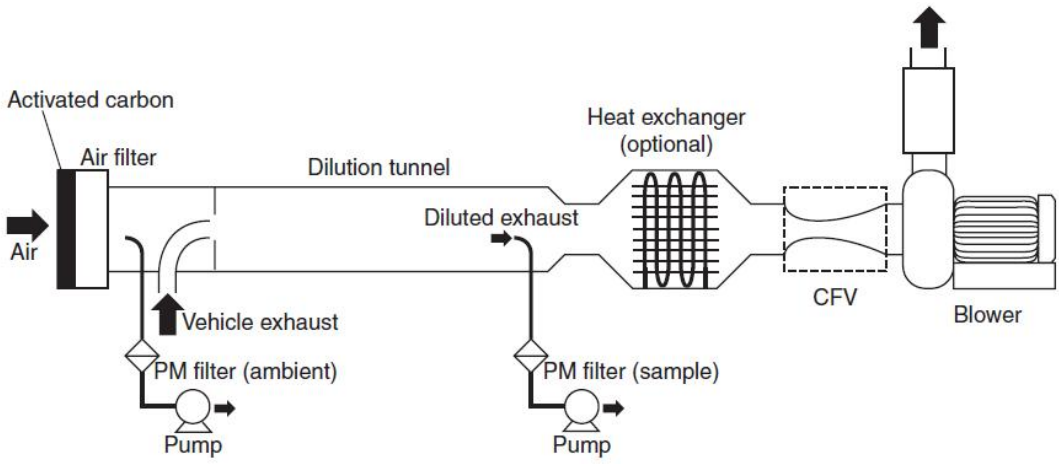

Figure 2.10 A full flow dilution CVS configuration. Source: Otsuki et al. (2015).

The permitted measurement principles for various pollutants are outlined in GTR 15 (United Nations, 2014). CO and CO_2 shall be detected by non-dispersive infrared (NDIR), while hydrocarbons (HC) shall be detected by a flame ionization detector (FID). Methane must be detected by either a gas chromatograph combined with a FID, or a FID with a non-methane cutter. NO_x and NO shall be analysed using a chemiluminescence detector (CLD) or non-dispersive ultra-violet resonance absorption (NDUV) detector. NO_2 can be determined by subtraction of NO concentration from the NO_x concentration, or by a specific NO_2 analyser (NDUV or quantum cascade laser) measuring a continuous concentration from the diluted exhaust.

2.6.1.2 Portable emission measurement system (PEMS) equipment

For on-road emissions measurements, portable emission measurement systems (PEMS) have been developed. For portable equipment to be fit for

purpose, it must be of small size, light weight, low power consumption and safe to operate.

2.6.1.2.1 Horiba OBS-ONE

In response to the increased need for high-accuracy PEMS equipment, Horiba developed their OBS-ONE PEMS system, measures the concentrations of regulated pollutants. CO and CO_2 are detected by a heated NDIR detector. These signals are compensated by water (H_2O) measurement using an optimised algorithm. NO and NO_x are detected by a heated dual CLD. The NO_2 concentration is then calculated as the difference between NO_x and NO concentrations. Ambient air is used as the source of ozone so no additional gas bottle is required. The CLD signal is compensated by CO_2 and H_2O signals to ensure accurate values. Other standard signal measurements of the Horiba OBS-ONE PEMS include exhaust and atmospheric temperature and pressure, atmospheric humidity, global positioning system (GPS) inputs and engine control unit (ECU) inputs.

The OBS-ONE unit also comes with a tailpipe attachment, from which the sample points for the gas and particulate (‘GA’ and ‘PN’) units are placed. A pitot flow meter is incorporated into this attachment, so that mass emissions can be calculated from the concentration values measured. Finally, a thermocouple is integrated so that the exhaust gas temperature can be recorded. The pitot tube measures the differential pressure between the total pressure facing the flow direction and the static pressure at 90° to the flow. This value is known to be proportional to the square of the gas flow velocity, which itself is proportional to the average gas flow rate in a tailpipe because the gas is all flowing in the same direction within a limited space. Care must be taken to account for pulsation effects when the engine of the vehicle is idling, as this negative flow will also be measured (Adachi and Nakamura, 2013).

2.6.1.2.2 AVL M.O.V.E

The AVL M.O.V.E system is another leading PEMS instrument suitable for certification RDE testing. Like the Horiba system, it utilises a NDIR analyser for CO_2 and CO measurement. However, NO and NO_2 measurement is performed using a NDUV analyser, which allows NO and NO_2 to be measured simultaneously without the need for a converter. An electrochemical oxygen (O_2) sensor, OBD reader, GPS unit, weather station, batteries and EFM

attachment can also be integrated in the same manner as the Horiba OBS-ONE.

2.6.1.3 FTIR

A Fourier Transform Infrared (FTIR) spectrometer utilises the property that most chemical compounds show unique absorption spectra in the infrared region, in proportion to their concentration (Adachi and Nakamura, 2013).

An infrared (IR) source produces broad band IR radiation that is modulated by a Michelson interferometer, so that it becomes an interference beam (Adachi and Nakamura, 2013). The interference beam passes through the sample cell where sample gas absorbs certain wavelengths of the IR broad band radiation, transmitting the rest. The system detects the transmitted radiation as an interferogram, and digitises the signal as an output. Software must then be used to perform a mathematical Fourier transform on the digitised modulated signal to produce an absorbance spectrum, which is then compared to a background spectrum made before the measurements started (Daham et al., 2005). The spectrum of sample gas usually includes many overlapping absorption peaks derived from many compounds showing absorption in the mid-infrared region, but by applying a multivariate analysis to this sample spectrum, the contributions of these multiple components can be deduced (Adachi and Nakamura, 2013). The FTIR software is then able to determine the concentrations of the different components present, based on absorption data from previous gas calibrations (Daham et al., 2005).

As the path length of the gas through the sample cell increases, so does its absorbance, so longer path lengths will give a greater signal-to-noise ratio, which is particularly useful when measuring low concentration gas components. However, the longer the path length, the greater the response time of the instrument and the lower the frequency of sampling that is possible. There is therefore always a compromise that must be made when applying this measurement technique to transient emissions measurement.

One limitation of the FTIR technique is that it is unable to measure diatomic molecules and noble gases. This is due to the fact that they do not absorb infrared radiation (Daham et al., 2005). However, the FTIR is very effective in the measurement of a wide range of pollutants, especially hydrocarbon species, making it useful in the study of unregulated pollutants, particularly during biofuels research. The SAE standard J2992 outlines the FTIR as an

approved technique for automotive measurement of CO_2, CO, NO, NO_2, N_2O, CH_4, NH_3 and formaldehyde.

2.6.2 Particle number (PN) measurement

Regulations were first introduced to monitor the PM of particulate emissions. However, as the technology available has improved, the light duty sector has been able to turn its focus to the PN emissions. The Particle Measurement Programme (PMP) was launched in 2001 with the aim to develop a more sensitive and precise measurement methodology for the PN, and in 2007, the Solid Particle Number (SPN) measurement method based on the counting of solid particles above 23nm in size was introduced (Giechaskiel et al., 2014).

The nucleation of volatile fractions depends strongly on the condition of the exhaust dilution air and dilution ratio. As a result, the formation of particles smaller than 20nm electrical mobility diameter is heavily influenced by these conditions. The choice to count only solid particles greater than 23nm was therefore made in the interest of measurement repeatability and reproducibility, because it is difficult to ensure that the exhaust sample conditions remain strictly constant (Otsuki et al., 2015). The EU SPN measurement method consists of a volatile particle remover (VPR) upstream of a particle number counter (PNC). This was integrated into the European light-duty automotive emission control regulations in 2009.

There are many different ways to detect particulate matter from vehicle exhaust gases today, and a few main ways to detect the size distribution of these particles. With regard to PN, some of these adhere to the strict criteria of the PMP SPN method, while others are suitable for non-certification emissions research. Those used within the current work will be discussed in the following sections.

2.6.2.1 Condensation particle counter (CPC)

One of the most common technologies used as the PNC of a PMP system is the condensation particle counter (CPC) (Otsuki et al., 2015). This consists of a saturator, a condenser and a detector. Within the saturator lies a working fluid (often butanol), that is induced into a super-saturated vapour phase by heating. The particles pass through this section and mix with this vapour. After this, the particles pass through the condenser of lower temperature, which induces the working fluid to condense onto the particles. The particles grow to a uniform diameter of around 10µm whereby they can be counted

consistently by the detector. The detector consists of a laser and a photodetector. When particles pass in front of the laser, the scattered light is detected as a pulse of the photodetector. In the case of multiple particles being detected by one pulse, a coincidence correction is applied to calculate the particle number of that pulse.

2.6.2.2 Electrical mobility measurement (e.g. Cambustion DMS500)

The Cambustion DMS500 system discriminates particle sizes according to the particles' charge to aerodynamic drag ratio, so the classification is based on electrical mobility. Figure 2.11 gives a schematic diagram of the DMS500. The particles pass through a diffusion charger which imparts a charge proportional to the surface area of that particle. This charger uses a single fine tungsten wire as the ion source, with the sample flow kept from touching this wire by a grid. The aerosol enters a chamber with a high voltage electrode in the centre that repels the particles toward electrode rings on the outer wall. The classification of particles is purely dependent on their electrical mobility, the known flow speed and the applied electric field. The particle charge level is a product of the ion density from the tungsten wire and the residence time of the particles in the aerosol. Therefore, the particle number distribution with size can be deduced by an inversion algorithm. An area-weighted spectrum can be determined if the particles' fractal dimension is known (Reavell et al., 2002). The PN value can be determined from the current arriving at the array of electrometer electrodes from the flux of charged particles (Price et al., 2006).

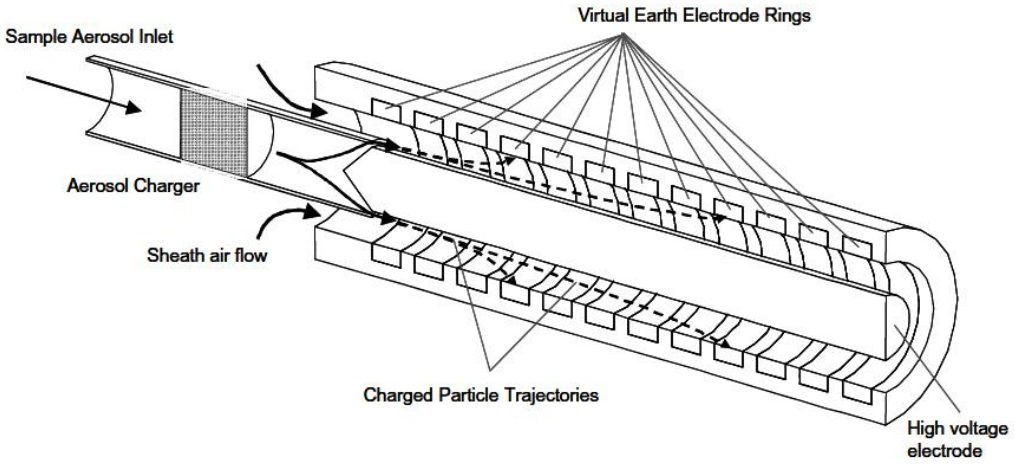

Figure 2.11 Schematic diagram of the DMS500 system. Source: Reavell et al. (2002).

The DMS500 software accounts for the difference in particle charging between agglomerates and spheres (Cambustion, 2009), so if a density is assumed, the mass-weighted spectrum can be estimated (Reavell et al., 2002). It should be noted that the high charging levels can lead to some particles of a similar size range becoming multiply charged, meaning that although they have the same size, they are collected at different axial locations (Reavell et al., 2002).

2.6.2.3 PEMS equipment for PN

For PN PEMS to be fit for purpose, it must be of small size, light weight, low power consumption and safe to operate. There are two main detection methods employed to this end: CPC and diffusion charging. Of the main three regulatory PEMS manufacturers, Horiba and Sensors use a CPC method and AVL use a diffusion charger method.

2.6.2.3.1 Horiba OBS-ONE PN

The instrumentation of the Horiba OBS-ONE PN depicted in Figure 2.12 is outlined in detail in Kim et al. (2017). It consists of a primary diluter, heated transfer pipe, 350°C heated catalytic stripper, secondary diluter and CPC. At the primary diluter, the ICE exhaust is diluted by the diluent. This diluent is actually ICE exhaust gas that has been filtered by a high-efficiency particulate air (HEPA) filter, dehumidified by a desiccant dryer, heated to prevent water condensation, and then recirculated. The exhaust then enters the cyclone pre-classifier which removes particles larger than 1µm, before continuing to the catalytic stripper. The catalytic stripper's high temperature ensures vaporisation of any volatiles, while the oxidation catalyst can effectively remove hydrocarbons and adsorb sulphates which have been known to generate small re-condensed particles at the CPC inlet. After the catalytic stripper, the gas passes through a second diluter before entering the CPC. The dilution ratios of the diluters are controlled by an orifice flowmeter at the diluent.

The Horiba PN sensor meets safety requirements by using isopropyl alcohol as the working fluid of the saturator. This is because isopropyl alcohol is a relatively benign chemical compared to the n-butanol normally used, but still with effective condensational growth properties. The only downside to the use of this fluid is that if too much water from the sample gas dissolves into this alcohol, the particle-counting sensitivity is reduced faster compared to n-butanol. To combat this problem, this working fluid is only used for short

periods of measurement time, and is delivered in a cartridge. The size of the instrument is minimised by the use of orifice flowmeters rather than larger flowmeter types, and the differential pressure of these, absolute pressure and gas temperature is monitored to ensure correct dilution ratios. The primary dilution ratio is kept constant by the rotation rate of the pump, while the secondary dilution ratio is kept constant by a fixed orifice.

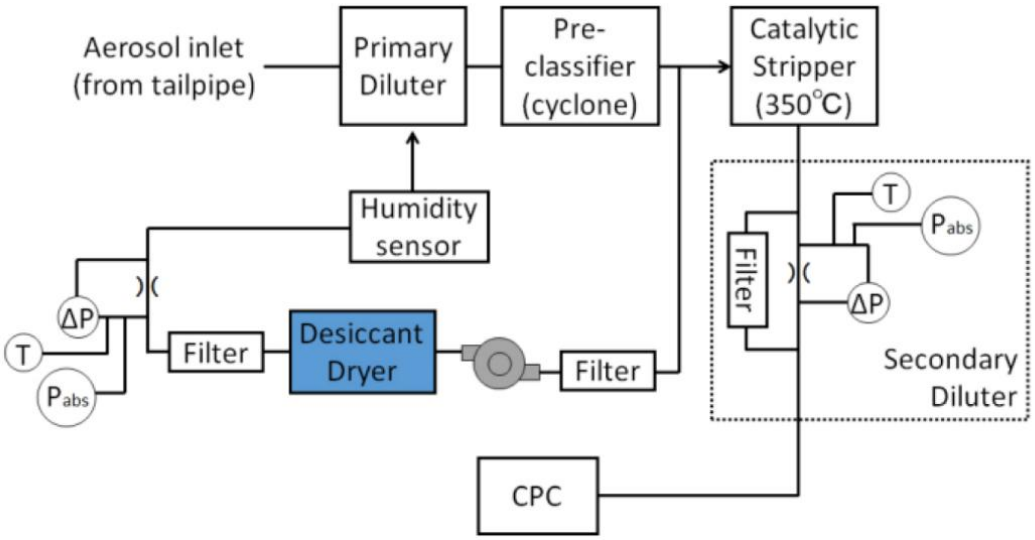

Figure 2.12 Flow diagram of Horiba OBS-ONE PN. Source: Kim et al. (2017).

2.6.2.3.2 AVL M.O.V.E PN PEMS

The AVL M.O.V.E PN PEMS utilises an Advanced Diffusion Charger technology, involving a diffusion charger following a VPR with a catalytic stripper (Giechaskiel et al., 2016). A primary diluter using hot air at 150°C dilutes the sample in a 2:1 ratio, and then the sample passes through an evaporation tube with a catalytic stripper (both held at 300°C), followed by a secondary diluter at 60°C which dilutes the sample 3:1 (Schwelberger et al., 2019). This diluted sample is then transferred to the particle detector through a 1.3m, 60°C heated line. Within the detector, particles are first charged in a positive unipolar diffusion charger, which charges the particles proportional to the particle size. The measured current is therefore not only dependent on the number of particles present, but also on the particle size distribution, and therefore in order to minimise the effects of the latter, the sample is then passed through an electrostatic precipitator to which a pulsating electric field is applied (Schriefl et al., 2019). The resulting modulation in the charge state of the sampled aerosol is subsequently detected in a Faraday cage electrometer (Schwelberger et al., 2019).

2.7 Exhaust emission legislation

2.7.1 Emission standards

There has been a long history of legislative policies to reduce the emissions from cars (Tutuianu et al., 2015). The European Union has played a particularly important role in the control of vehicular emissions in the UK. The purpose of EU transport policies has been to decrease both GHG and pollutant emissions, thereby tackling both climate change and air quality problems. The pollutants which are regulated by the 'Euro emissions standards' are CO, NO_x, HC, PM and PN, while dedicated regulations limit the average CO_2 emissions for a given manufacturers vehicle fleet (European Commission, 2017). These are collectively referred to as 'regulated emissions' in the rest of this thesis. With all other pollutants being referred to collectively as 'unregulated emissions'

There are three main legislated steps to the emissions control method; type approval, conformity of production and in service conformity (Vlachos et al., 2014). The type approval test ensures that any new vehicle designs adhere to the aforementioned emission standards (AVL Emission Testing Systems, 2016). Since the 1990s a set of European Emission Standards for light duty and heavy duty gasoline and diesel vehicles have been launched for EU type approval testing. The standards limited the mass emissions per kilometre of certain regulated pollutants for new vehicles on the market, and have become more and more stringent over time. Emission limits for class M positive ignition engines under Euro 5 and Euro 6 regulation are summarised in Table 2.5. It shows the limits required of gasoline and diesel powered vehicles, for varying categories of vehicle. All other emissions are termed 'unregulated emissions'. Cars are only considered to be certified if they have performed below the limits set out in the regulation. Laboratory testing on a chassis dynamometer is used to verify the vehicles' performance, allowing for good repeatability (Els, 2013).

Table 2.5 EU emission standards for Euro 5 and 6 SI vehicles set out in Regulation (EC) 715/2007 and Regulation (EC) 692/2008 respectively.

Standard	CO (mg/km)	THC (mg/km)	NMHC (mg/km)	NOx (mg/km)	PM* (mg/km)	PN* (#/km)
Euro 5	1000	100	68	60	4.5	-
Euro 6	1000	100	68	60	4.5	6.0×10^{11}

* Particulate mass and number limits, where applicable, shall apply only to SI vehicles with direct injection engines.

2.7.2 The New European Driving Cycle (NEDC) test cycle

From Euro 3 up until Euro 6, Europe employed the NEDC for the certification of cars (Marotta et al., 2015). The NEDC test lasts for 19 minutes and 40 seconds and is split into parts One and Two, which run without interval. Part One consists of four repeated urban driving cycles (UDC) while one extra-urban drive cycle (EUDC) constitutes Part Two (United Nations, 2012). Changes in speed are achieved with gentle accelerations and decelerations. The speed trace of the NEDC test is provided in Figure 2.13. Emissions sampling commences from engine-start (a cold start), and values are then averaged over the whole cycle to give a final result (Vlachos et al., 2014). The test is done on a chassis dynamometer, with the rolling resistance of the car calculated during a road load test and then used to replicate real driving. The car is allowed to coast from a high speed down to stationary, and the length of time and distance over which this occurs is used to calculate the air and road resistance of the car. This information then determines the load on the chassis dynamometer, changing how easy it is for the car to turn the wheels. Full details can be found in Regulation No 101 of the Economic Commission for Europe of the United Nations (UN/ECE).

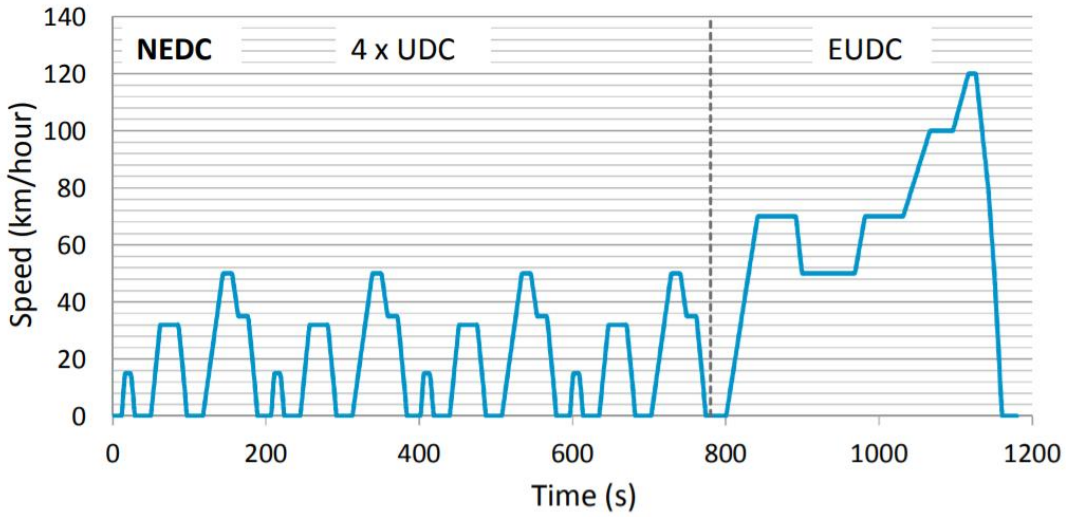

Figure 2.13 Speed trace of the NEDC. Adapted from Fontaras et al. (2017).

The NEDC test had several disadvantages which have been widely discussed in the literature. The NEDC test procedures are considered outdated for current vehicle technologies and unrepresentative of real-world driving, as well as too lax, allowing car manufacturers to ‘play the system’ to their advantage and give emissions values that can never be achieved in the real world (Tutuianu et al., 2015; Ciuffo et al., 2015).

A report by Dings (2013) outlined in great detail exactly why the NEDC test was insufficient. There are various different areas in which weaknesses in the test allowed manipulation of results. First is the fact that the test is unrepresentative of real-world driving conditions. This means that new technologies were developed to reduce emissions during the test, but these strategies proved less effective once the car was driven in the real world. For example, stop-start technology to switch off the engine when stationary produced a significant decrease in CO_2 emission during the test. This is because vehicles are stationary for 20% of the cycle, but in the real world, this is an unlikely percentage, so higher CO_2 emissions resulted. The test was also unrepresentative of real-world conditions due to new energy-intensive auxiliary systems that are not required to be running during the test. These include air conditioning, heated seating, and navigation and media systems. The speeds and accelerations involved in the test are also much lower than those common in real-world driving. The top speed of the test, 120 km/h, is only held for a matter of seconds, and is lower than the maximum speed allowed on many European roads today. Loopholes within the test were exploited by vehicle manufacturers, such as allowing the battery to deplete, reducing weight and friction, and playing on lax tolerances such as gear change regime. Vehicle manufacturers were also able to make large savings in NEDC fuel consumption by minimising resistance during the road load testing. The European Commission have estimated that 40-50% of the net CO_2 emission reduction between 2002 and 2010 was due to the exploitation of test flexibilities such as these (Kadijk et al., 2012).

The difference between NEDC test emission values and real-world emission values increased with time, indicating that the problems associated with the NEDC test were growing in magnitude. The average difference between realistic road load values and those used for NEDC tests jumped from 9% in 2001 for Euro 3 (Hooftman et al., 2018), to 19% for Euro 4 (2005) vehicles and 37% for Euro 5 (2009) vehicles (Kadijk et al., 2012). Mock et al. (2012) showed that the NEDC test was underestimating the CO_2: By 2015, the gap had risen to approximately 42% (Hooftman et al., 2018). Kadijk et al. (2012) covered in detail the many weaknesses of the NEDC test procedure.

2.7.3 Other cycles

The other main tests being used globally are the Japanese (JC 08) test cycle and the American federal test procedure (FTP-75). The JC 08 consists of

mainly low velocities to simulate driving in congested city areas (Ciuffo et al., 2015). The United States (US) designed the FTP-75 cycle from real measurements in Los Angeles, so covers a wider range of driving types and has more rapid accelerations, but is still not complete enough to cover all possible driving situations as was based on driving in a specific region of US (Tutuianu et al., 2015). The Assessment and Reliability of Transport Emission Models and Inventory Systems (ARTEMIS) also designed a set of driving cycles and procedures called the Common Artemis Driving Cycles (CADC) (Fontaras et al., 2008).

The driving cycles discussed above all vary in their diversity and ability to recreate real-world conditions, due to differences in the representativeness and completeness of the tests (Marotta et al., 2015). Different test cycles and procedures will produce varying emission results, making it difficult to fully understand the real contribution of vehicles to emissions. Evidence indicates that the more aggressive test procedures produce, on average, higher CO_2 results that are more representative of real-world driving (Dings, 2013). The variation in results impacts the ability of policy makers to design appropriate measures for emissions reduction (Tutuianu et al., 2015), and for collaboration and exchange of information between different testing authorities (United Nations, 2014). In addition, the fact that most vehicle manufacturers produce cars for a global market with different testing regimes means that they have to optimise the vehicles for each region in which they are to be sold. This is a burden for vehicle design and increases costs. There was therefore strong interest in harmonizing vehicle emission test procedures and performance requirements on the global scale from all both; regulators and vehicle manufacturers (United Nations, 2014).

2.7.4 The Worldwide Harmonised Light Vehicle Test Procedure (WLTP) and Worldwide Harmonised Light Vehicle Test Cycle (WLTC)

The World Forum for the Harmonization of Vehicle Regulations (WP.29) of the United Nations Economic Commission for Europe (UNECE) launched a program in 2009 to develop a new world-harmonised test cycle and procedure (Ciuffo et al., 2015). They aimed to develop a cycle that represented average worldwide driving characteristics, and to have it tested using a world-harmonised type approval testing procedure. The final WLTC considers cycle driveability, with different cycles for lower driving capabilities or lower

maximum speed if the vehicle would have to use an unusually high proportion of full-throttle driving to match the speed trace. Additionally, an algorithm accounting for the characteristics of individual vehicles is used to determine gear shift points along the speed trace. The WLTC is not a single cycle, but a set of different cycles (WLTC Classes 1, 2 and 3) to be used on different vehicles with different power/weight ratios. WLTC cycle Class 3 is for vehicles with higher power/weight ratios, and includes the majority of European cars (Ciuffo et al., 2015). Figure 2.14 displays the speed trace of WLTC Class 3. Full details can be found in UNECE Global technical regulation No 15 (GTR 15).

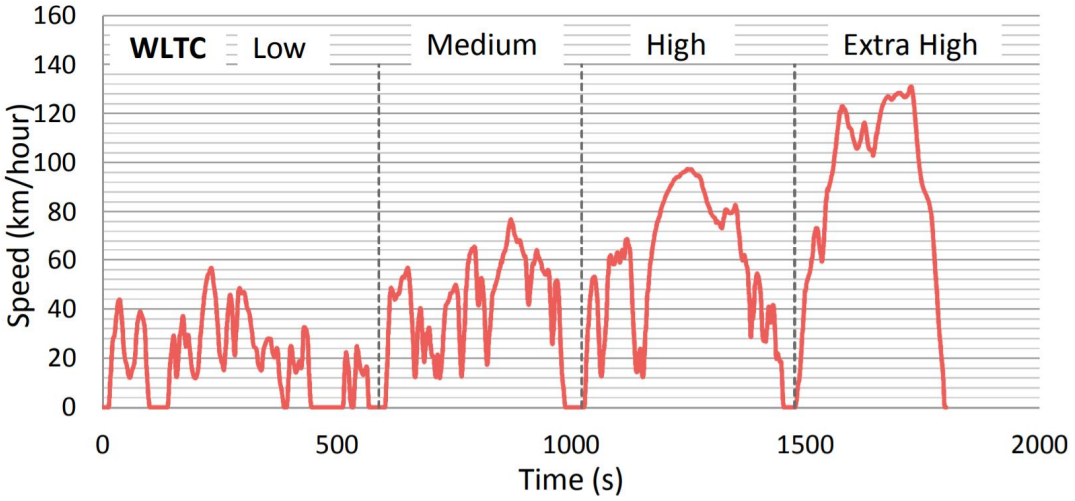

Figure 2.14 Speed trace of the WLTC class 3b cycle. Source: Fontaras et al. (2017).

This harmonised test procedure can potentially reduce costs for vehicle manufacturers as it allows vehicle design to be performed on a more globally unified scale and allows simplified administrative procedures. The higher representation of real-world driving conditions offered by the WLTP will force manufacturers to make design changes that are more effective at cutting emissions in the real world, and allow for more accurate consumer information about vehicle efficiency (Addendum 15 : Global technical regulation No. 15 - Worldwide harmonised Light vehicles Test Procedure, 2014).

2.7.5 WLTP comparisons with NEDC

The WLTC has been implemented in the Euro 6c type approval regulation currently in action and differs from the NEDC by having more aggressive driving styles and a greater range of engine operating points (Kageson, 1998). Table 2.6 displays some key characteristics of both NEDC and WLTC tests

(Marotta et al., 2015). Sileghem et al. (2014) compared the NEDC, WLTC and CADC results for a range of CVs. The relative positive acceleration (RPA) with vehicle speed was higher for the WLTC than the NEDC, and a much wider range of acceleration values were covered. However, the authors found that even the WLTC did not cover enough engine operating points; finding extra CO emissions on the CADC from an area of the engine map not covered by the WLTC.

Table 2.6 Key parameters of the NEDC and WLTC (Marotta et al., 2015).

Parameter	**NEDC**	**WLTP**
Duration (s)	1180	1800
Distance (km)	11.03	23.27
Average speed (km/h)	33.6	46.5
Maximum speed (km/h)	120.0	131.3
Stop duration (%)	23.7	12.6
Constant driving (%)	40.3	3.7
Acceleration (%)	20.9	43.8
Deceleration (%)	15.1	39.9
Average positive acceleration (m/s^2)	0.59	0.41
Maximum positive acceleration (m/s^2)	1.04	1.67
Average positive “speed·acceleration” (m^2/s^3)	1.04	1.99
Maximum positive “speed·acceleration” (m^2/s^3)	9.22	21.01
Average deceleration (m/s^2)	−0.82	−0.45
Minimum deceleration (m/s^2)	−1.39	−1.50

The literature contains extensive comparisons between the emission results of NEDC and WLTP tests. Marotta et al. (2015) and May et al. (2014a) both found that the increased robustness of the WLTP against manipulation will lead to an increase in resultant CO_2 when compared to NEDC type approval values. However a broader study by Pavlovic et al. (2016) found that this generally was only the case for vehicles under 1200 kg test mass, while there was little change or reduction of CO_2 from vehicles with higher test mass (due to increased power-to-mass ratios). Pavlovic et al. (2016) identified the increased vehicle drag – rolling resistance and air resistance – of the WLTP cycle as the largest factor contributing to the increased values, due to the increased velocities and road load coefficients of the WLTP. A more recent study utilising five SI (three GDI and two PFI) vehicles presented in Valverde et al. (2019) agrees with these results.

There is also general consensus that total hydrocarbon (THC or HC) and/or non-methane hydrocarbon (NMHC) emission results are lower under the

WLTP compared to the NEDC according to Marotta et al. (2015), May et al. (2014a), Merkisz et al. (2016a) and Valverde et al. (2019). The CO and NO_x emission results varied across the vehicles tested. In general, higher values of both pollutants were seen under the WLTP than the NEDC by Marotta et al. (2015) and Valverde et al. (2019), while Merkisz et al. (2016a) saw a significant increase (over double) for NO_x and a small decrease for CO. The limited results of May et al. (2014a) agree more with Merkisz et al. (2016a), with higher NO_x results and lower CO results occurring under the WLTC.

These results suggest that the pollutants of greatest emission under cold start (such as THC) decrease under the WLTP due to the cycle's proportionately shorter duration of cold start. Meanwhile, those pollutants of greater emission under high engine load (such as NO_x) see an increase under the WLTP due to the increase in those conditions in the WLTC. CO is less closely aligned with engine load and more strongly associated with cold start. However, Marotta et al. (2015) infer from their results that at the highest WLTC load points some low power-to-mass ratio vehicles are likely tuned to a low air-to-fuel ratio resulting in high CO emissions. This would explain the mixed results between studies, although the theory was not substantiated in the literature.

With regard to PN, May et al. (2014a) found an increase in emissions from the WLTP compared to the NEDC for their combined PFI and GDI SI vehicle, and this is also the general conclusion of Valverde et al. (2019), though the difference in results was small. There is an interplay between the smaller proportion of cold start in the WLTC driving PN emissions down, and the higher loads of the WLTC driving PN emissions up. Based on the results currently in the literature, it appears that the higher loads of the WLTC are the greater force, resulting in generally increased PN compared to the NEDC.

The only literature found to compare pollutant emissions from NEDC and WLTC testing of HEVs was Duarte et al. (2016) and Kim et al. (2019). Duarte et al. (2016) studied CO_2, HC and NO_x emissions (no CO or PN results were presented). However, this study was not actually performing these test cycles, but on-road cycles designed to have the same (VSP-based) driving styles as the respective test cycles. Kim et al. (2019) found that as the test cycle changes from NEDC to WLTP, the resultant NO_x, CO, THC and CO_2 emissions decreased, while PM increased. PN was not studied.

2.7.6 Chassis dynamometer test cycles compared to on-road testing

In 2006, Pelkmans & Debal (2006) found that the emissions resulting from the NEDC can be different from those emissions produced in real traffic. Since then, much research has been performed on this topic, alongside improvements to PEMS emission testing capabilities. For their model year (MY) 2006 SI vehicle, Merkisz et al. (2010) found that only CO_2 increased under on-road driving when compared to the NEDC, while CO, NO_x and HC decreased. Merkisz et al. (2010) also compared the UDC section of the NEDC against similar sections of urban on-road driving, and the EUDC against higher-speed on-road driving. Both showed higher CO_2, and slightly lower NO_x, on the road compared to the NEDC, while HC and CO decreased under on-road urban driving and increased under extra-urban driving. The authors attribute these differences to different vehicle cruising parameters of vehicle speed and acceleration and, to a lesser extent, the different ambient conditions.

Weiss et al. (2011) tested a range of different diesel and gasoline vehicles including one SI HEV on four different on-road driving routes, compared to the NEDC. They found that the HEV reported higher levels of CO and THC and lower NO_x over the NEDC than on the on-road driving routes. May et al. (2014b) found that an SI vehicle emitted larger CO, NO_x, CO_2 and PN emissions but comparable HC emissions over on-road testing compared to the NEDC, the WLTC and random chassis-dynamometer cycles. The findings of Giechaskiel et al. (2015) also indicate that the PN emissions (of a GDI vehicle) are greater on the road compared to on chassis dynamometer WLTC tests. Clearly there is some disagreement regarding the effects of the chassis dynamometer compared to real roads. This is due to different test cycles, procedures and test vehicles being used, causing high variability. None of the literature published thus far has directly compared a particular on-road test velocity trace with a repeat test of the same velocity trace on a chassis dynamometer. This leaves a gap in the research to study the effect of the chassis dynamometer in detail.

2.7.7 Real driving emissions (RDE) testing

Although the WLTC test more accurately replicates the types of behaviours seen in real-world driving than the NEDC, it still carries the same disadvantages of any standard laboratory test cycle. One disadvantage of this

is that these laboratory test cycles cannot adequately cover the wide range of ambient and driving conditions seen in real-world vehicle use (Vlachos et al., 2014). This means that while vehicles may comply with emission limits in laboratory tests, they could have substantially higher emissions on road under conditions outside those tested (Weiss et al., 2011). These standard cycles are also very predictable, allowing car manufacturers the possibility of 'cheating' the tests, most notably in the VW scandal of 2015 (Johnson, 2016).

It was therefore deemed necessary for a complimentary test – the Real Driving Emissions (RDE) test utilising PEMS – to be formulated alongside the WLTC to address the above issues. This RDE element using PEMS has been brought into EU legislation (Department for Transport, 2016b). The RDE test was introduced gradually, in packages, allowing time for the industry to adapt to new requirements, and allowing any modifications to be made. This evolution will be summarised in the following subsections.

2.7.7.1 RDE Package 1

The first package – Commission Regulation (EU) 2016/427 (European Commission and Council of the European Union, 2016a) – generally described the RDE PEMS test procedure, including test equipment requirements, trip characteristics, data evaluation tools, vehicle selection and reporting requirements (Hooftman et al., 2018).

The PEMS had to consist of analysers determining the concentrations of pollutants in the exhaust gas, at least one instrument to measure exhaust volume flow rate, a GPS system to determine position, altitude and speed of the vehicle, and an energy source independent of the vehicle to power the PEMS. For full details see Commission Regulation (EU) 2016/427.

The trip could last 90-120 minutes and had to be performed on public roads in real traffic during working hours. There is a set of conditions that the trip had to adhere to. These conditions were separated into moderate and 'extended'. If extended conditions had been used then the final emission factor was divided by a factor of 1.6. The conditions were:

- The test must be performed under ambient conditions of $0°C \leq T \leq 30°C$ or 'extended conditions' of $-7°C \leq T \leq 0°C$ or $30°C \leq T \leq 35°C$
- The test must be performed at a moderate altitude of less than or equal to 700 metres above sea level, or an 'extended altitude' of $700m \leq$ altitude $\leq 1300m$

The test consisted of at least 16km driven for each of three portions of different driving styles, defined according to their instantaneous speed. The distance-based percentages of the total drive were also defined. They had to be conducted in the order given below:

- 29% - 44% urban operation, characterised by velocities up to 60 km/h
- 23% - 43% rural operation, characterised by velocities between 60 and 90 km/h
- 23% - 43% motorway operation, characterised by velocities over 90 km/h

The average speed of the urban section was 15km/h and 30km/h. Stop periods (<1km/h) accounted for at least 10% of the urban time duration, and several stop periods of greater than 10s had to occur, while no single stop could occupy more than 80% of total stop time. The motorway driving had to properly cover the range between 90-100km/h, and be above 100km/h for at least 5 minutes. The vehicle speed could not normally exceed 145km/h (160km/h for no more than 3% of the motorway driving time). The auxiliary systems such as heating and air conditioning were to be used as they would in real life, while the maximum payload of the vehicle was 90% of the maximum vehicle weight. Additionally, there had to be no more than 100m altitude difference between the start and finish points of the test.

Once the above requirements were satisfied for a test, the instantaneous concentration values were converted into instantaneous mass emission values using knowledge of the exhaust mass flow, with the calculations laid out in Commission Regulation (EU) 2016/427 Appendix 4. The method of data time alignment was outlined (European Parliament and Council of the European Union, 2016).

The dynamic conditions had to be verified using one of two methodologies, before weighted emissions were calculated from these. The two methodologies available in Packages 1 and 2 of the RDE legislation were called Moving Averaging Window (MAW) and Power Binning. The Power Binning method was not included in later RDE Package regulations and hence was not used for the current work, so will not be covered further.

For the MAW method the second-by-second mass emissions data were averaged over moving averaging windows into g/km. The length of the windows was determined by a reference quantity of CO_2; the time taken for half the quantity of CO_2 emitted during the WLTC test to be emitted. The

window then moved forward by the same increments as the measurement interval. The value of average CO_2 emissions for each window were recorded and compared to a reference CO_2 curve, while the windows were also categorised into three speed classes: urban (v < 45km/h), rural (v ≥ 45-80km/h) and motorway (v ≥ 80-145 km/h). The emissions were calculated as a weighted average of the windows' distance-specific emissions separately for the urban, rural and motorway categories, and the complete trip. The calculation could be run from the first point forwards or the last point backward. The following data points were excluded from the calculation of the CO_2 mass emissions and the distance of averaging windows in Package 1 of the legislation:

- The periodic verification of the instruments or the zero drift verifications
- Cold start (first 5 minutes after initial combustion engine-start, or the time until the engine coolant temperature first reaches 70°C as long as this time period is less than 5 minutes)
- Durations with vehicle speeds under 1km/h
- Durations where the vehicle engine is switched off

The software tool that performs the MAW processing was developed by the JRC and is called EMROAD (Hooftman et al., 2018). The test was deemed 'complete' when it is comprised of at least 15% each of urban, rural and motorway windows, out of the total number of windows. The test was 'normal' when at least 50% of the windows were within the primary tolerance (normally ±25%) defined for the characteristic curve. If the minimum requirement of 50% of windows within tolerances was not met, the upper positive tolerance was be increased by steps of 1% until the 50% target was reached, though the tolerance itself could not exceed 30%. The windows were weighted with reference to their similarity to the reference CO_2 curve, and then total emissions from the test, per km, along with the average concentrations, were calculated from the normal windows.

2.7.7.2 RDE Package 2

RDE Package 2, published only one month after Package 1, built on the first package to include more political outcomes, such as the determination of the conformity factors and the timetable for implementation (ICCT, 2017). Further technical calculations were also introduced, such as the addition of dynamic boundary conditions and altitude change limitations. Full details can be found

in European Commission Regulation (EU) 2016/646 (European Commission and Council of the European Union, 2016b).

Regarding trip requirements, a few changes were made. The stop percentage in the urban mode had to be between 6-30% of the urban driving time, rather than simply >10% previously. The average speed of the urban section changed from 15-30km/h in RDE 1 to 15-40km/h in RDE 2. Additionally, if a stop lasted longer than 180s, the 180s following this stop was excluded from the evaluation. With regard to altitude, a new smoothing technique was introduced. There was also a new upper limit on cumulative positive altitude gain of 1200m/100km. The overall excess or insufficiency of drive dynamics during the trip was ensured by requiring satisfaction of certain dynamic calculations (the product of positive velocity and acceleration, and RPA).

2.7.7.3 RDE Package 3

Package 3, contained within Commission Regulation (EC) 2017/1154 (European Commission and Council of the European Union, 2017), incorporated many important changes to the RDE test. The data analyses included the cold start section of the drive, any periods where the combustion engine is turned off while the vehicle is moving, and the 180s following a stop of longer than 180s, so these sections were also newly incorporated into the emissions calculations. In the case of engine deactivation any recorded values were set to zero in post-processing. Any stop greater than 300s in the urban section voided a trip in Package 3. Additionally, the maximum speed during the cold start period was set at 60 km/h, in order to prevent the ability of manufacturers to quickly heat the catalyst to light off immediately after test start. PN was also included in the not-to-exceed (NTE) limits defined in Package 2.

In the MAW technique, the weighting function for the entirety of the test, including cold start emissions, was set to 1. Additionally, the MAW calculation had always to be run from the first point forward. The rest of the MAW analysis remained the same, except that for NOVC-HEVs, if the minimum requirement of 50% of windows within tolerances was not met the upper positive tolerance could be increased by steps of 1% until the 50% target was reached, though the tolerance itself could never exceed 50%.

2.7.7.4 RDE Package 4

The fourth and final package of RDE regulation, released in full on 5th November 2018, was incorporated into Regulation (EU) 2018/1832 (European Commission and Council of the European Union, 2018). This package had important changes to the data processing and more strict NTE limits (Hooftman et al., 2018).

The raw emissions were used to calculate the final emission value, rather than with the MAW or Power Binning methods. The calculation of final emission results was performed using an evaluation factor RF_k defined depending on the relationship between the RDE and WLTC CO_2 results (see 2018/1832 for further details).

The MAW alone was still used to verify test normality (there was no completeness requirement) but the window CO_2 calculation method was unweighted, simply integrating the instantaneous mass emissions, while the CO_2 characteristic curve thresholds tightened. The MAW still excluded periods with vehicle speed < 1km/h and periodic verification of instruments.

2.7.8 The effects of RDE regulations on reported emissions

As the RDE legislation packages have been introduced, there has been keen interest in the impacts of the RDE test on reported emissions. Varella et al. (2017) compared CO_2 and NO_x results arising through the use of the MAW and power binning RDE analyses (techniques permitted in Package 2 of the RDE legislation), and a vehicle specific power (VSP) binning method. They found that the different analysis techniques had different trends across the three powertrain technologies studied (CI, SI and HEV) and concluded that neither MAW nor power-binning accurately reflected HEVs behaviours. However, they did not compare the processed results to the raw data. Clenci et al. (2017) studied how the aggressiveness of the RDE driving style can impact the emissions, while staying within the boundaries required by the (Package 2) RDE regulation on an SI vehicle. They confirmed that a more aggressive style increases all regulated pollutant emissions from the vehicle, particularly NO_x and PN, from two repeated tests of each of eco-style and sport-style RDE. Donateo and Giovinazzi (2018) conducted a study into the repeatability of RDE tests, performing 4 repetitions of a pre-designed test route. Using a stop-start technology diesel vehicle the authors presented various dynamic parameters and regulated pollutant emission results. It is

arguable that four repetitions (only three of which satisfied all test criteria) is too small a number for a comprehensive analysis.

Varella et al. (2019) studied the RDE results for two different PFI SI vehicles resulting from use of the MAW technique compared to the raw RDE data, and found that the CO_2 and NO_x results from the MAW were always higher than those of the raw data across a sample of five different tests, averaging to approximately 6% and 31% difference for CO_2 and NO_x respectively. These authors also performed a small study into the contribution of cold start, calculating 25% and 55% higher CO_2 and NO_x for 300s of cold start compared to 300s of comparable warm start driving for these two PFI vehicles. Valverde et al. (2019) also investigated the impact of cold start on RDE results, comparing the first 300s of a cold start RDE test against the urban RDE as a whole, with five different SI vehicles (3 GDI, 2 PFI). These results show an approximate 30% cold start-specific increase for CO_2, but little variation for NO_x, demonstrating some variability in published results. Their study also incorporated PN and CO for which there were approximately 500% and 650% increases for the first 300s compared to the urban RDE section respectively. Neither Varella et al. (2019) nor Valverde et al. (2019) extended their analysis to calculate the impact over RDE test results as a whole. However, Merkisz et al. (2019) calculated the percentage changes from inclusion of cold start into a single RDE test (7.8% and 1.9% CO, 5.9% and 1.3% NO_x, and 5.1% and 0.2% PN emissions increases for urban and total RDE, respectively) of a GDI vehicle. No such up-to-date investigations for HEVs has been found in literature to date, and few studies with a statistically significant number of repeated tests are available.

2.7.9 RDE comparisons with WLTC and NEDC

Merkisz et al. (2016) conducted an extensive study into the NEDC, WLTC and RDE (Package 2) results from a wide range of SI and diesel vehicles of Euro 5 and 6 standards. Their average results indicate that for both Euro 5 PFI and Euro 6 GDI vehicles, the THC, NMHC, CO and NO_x results are lower from the WLTC than the NEDC, and that for Euro 6 GDI vehicles, the WLTC gave comparable (marginally higher) PM and (marginally lower) PN results to the NEDC. The RDE gave even lower THC, CO and NO_x results than the WLTC for both Euro 5 PFI and Euro 6 GDI vehicles, but higher PM and markedly higher PN values resulted for the Euro 6 GDIs. However, as the RDE tests were conducted according to the Package 2 regulation, these results are not

representative of the final version of RDE test in operation today. Additionally, no HEVs were incorporated into this study, leaving a gap of knowledge for the behaviour of these vehicles. This study does not directly compare engine demands of the NEDC, WLTC and RDE, but Clenci et al. (2017) plot the torque versus speed of a gasoline engine to show how much broader the demands of the WLTC and RDE are than the NEDC. Again, this type of analysis was not performed for an HEV.

With regard to the vehicle dynamic requirements of the RDE, WLTC and NEDC tests, Donateo & Giovinazzi (2018) show that the vehicle speed versus acceleration curve of the WLTC again covers a much greater area than the NEDC, particularly for positive values of acceleration. The RDE appears to cluster around certain velocity values for rural and motorway velocities (the cruising speed limits for these roads), but covers a wide range of speeds in urban driving, and a wide range of acceleration values, comparable to the WLTC. The maximum speeds and accelerations were greatest for the WLTC in this case, but the maximum product of speed and acceleration was on the RDE, while the lowest accelerations and products of speed and acceleration were found for the NEDC. This study also demonstrated that the RPA values with vehicle speed cover a wider distribution on the RDE than the WLTC, with the NEDC having the narrowest distribution. The engine load versus engine speed of the diesel test vehicle was also studied by Donateo & Giovinazzi (2018), showing that a far larger area of the load/speed map is covered by the RDE than the WLTC in this case, for four repeated RDE tests, while the WLTC covered a larger area than the NEDC. This analysis was not performed for any HEVs, so it is not clear how the engine behaviour of an HEV on RDE testing will compare with the NEDC and WLTC. As with Clenci et al. (2017) and Merkisz et al. (2016), the RDE tests performed by Donateo & Giovinazzi (2018) were according to Package 2 of the legislation, so out of date. However, given the nature of the changes between Package 2 and 4, these differences will not be substantial. The authors above acknowledge that a larger number of RDE test repeats are necessary for robust inferences about the resultant emissions.

A thorough evaluation of the emissions from the Package 4 RDE test against the NEDC and WLTC was performed by Valverde et al. (2019) using three GDI and two PFI Euro 6b vehicles. Results showed that for both CO_2 and NO_x, the NEDC test gave the lowest values, followed by the WLTC and then the RDE. For PN, the three tests gave more comparable results, with the RDE

having a slightly lower mean value than the NEDC and WLTC. CO data was not presented. The causes of the differences seen between cycles were not thoroughly investigated or verified using transient data, leaving room for more exploration and validation. It is noteworthy that the RDE results presented by Valverde et al. (2019) are not entirely compliant with the Package 4 regulation as no weighting functions or correction factors were used. The data presented for the RDE for each vehicle was only from two repeats, which given the issues with repeatability of RDE tests (as discussed in Donateo & Giovinazzi (2018)), may have been insufficient for a reliable conclusion. Varella et al. (2019) demonstrate this point with their wide-ranging CO_2 and NO_x results from five repeated (Package 2) RDE tests driven by different drivers and driving styles, for each of two different PFI SI vehicles. Some RDE tests resulted in NO_x emissions below that of the WLTC certification value, and some above. For CO_2, however, most RDEs gave slightly lower values than the WLTC. Of all the literature to date comparing characteristics of the new RDE test with WLTC and NEDC, no work on HEVs has been found, leaving a gap in knowledge for this vehicle type.

2.8 Hybrid electric vehicle (HEV) behaviour and emissions

HEVs present a useful technology that bridges the gap between CVs powered only by ICEs, and BEVs powered only by electricity stored in a battery. Previous work has focused on the behaviour of HEVs and the details of their emissions profile; this work will be discussed in the following subsections.

2.8.1 Comparisons of HEVs with ICEs

Many previous studies have investigated the potential CO_2, regulated gases and PN emissions of HEVs in comparison to CVs. Graham (2005) conducted one of the first studies into emissions from seven different vehicles (three diesel, three GDI, one First Generation Toyota Prius HEV) and found that the HEV had the lowest emissions (NO_x, THC, CO, PM), lowest specific reactivity, lowest non-methane organic gas ozone forming potential and lowest fuel consumption. The same emission trends, with the addition of lower NMHC, were also observed by Christenson et al. (2007). This was a study into the fuel consumption and transient emissions of four HEVs compared to one conventional SI ICE. They performed chassis dynamometer testing over five transient cycles and two steady-state cycles at two temperatures (20°C and -18°C), with no engine parameters measured.

Fontaras et al (2008) performed lab NEDC and real-world ARTEMIS testing on two HEVs to investigate CO_2 and fuel economy benefits of HEVs. This study utilised emission factors in order to elucidate comparisons with data already available on CVs. They showed that the fuel economy benefit peaked during urban driving, observing up to 60% reductions compared to CVs. Over higher speeds, however, the benefit was lower. Zahabi et al. (2014) came to similar conclusions based on a wide study of many different HEVs and CVs in real use, as did Holmén and Sentoff (2015) when they compared the on-road CO_2 benefits of a hybrid and conventional Toyota Camry. They found the CV produced CO_2 emissions larger than the HEV by a factor of 4.5 in urban, 2.5 in rural, and 1.4 in motorway driving modes. They also found that, generally, the CO_2 benefit decreased as VSP increased.

Liu and Frey (2015), meanwhile, tested the hot-start real-world emissions of 100 different SI vehicles, including five HEVs, using PEMS equipment on a test route designed to cover a wide range of VSP points. Emissions of CO_2, CO, HC and NO_x were measured at 1Hz frequency for each of 14 preselected power modes. This study also found that HEVs had lower emission rates than CVs, and confirmed this for a range of engine loads, not just the cycle-average rate, for which a 63% average decrease was seen. For CO in particular, average emission rates were 76% lower for the HEVs. Wu et al. (2015) investigated the fuel consumption, CO_2, CO and NO_x emissions of a Second Generation and Third Generation Toyota Prius in on-road PEMS experiments. They compared their measured emission factors with those of SI vehicles from a previous study and found that the CO emissions were similar, while the fuel consumption, THC, NO_x and CO_2 were substantially reduced. This CO result is in disagreement with Liu and Frey (2015). However, the comparison of Wu et al. (2015) is less reliable, as the vehicles being compared were not of the same emissions standard or of similar vehicle properties. The study was also unable to test high speed conditions above 80km/h, and so does not cover motorway conditions.

The findings of O'Driscoll et al. (2018) support the CO_2 and NO_x findings of previous literature (CO was not measured), with the two HEVs tested having lower hot-stabilised CO_2 and NO_x on average than the 72 CVs tested over a wide-ranging cold start drive cycle. At motorway speeds, however, the HEVs had similar CO_2 emission rates to the CVs. The small sample size of HEVs in this wide fleet study should not be overlooked. Bielaczyc et al. (2018) found that HEVs had statistically significant CO_2 and CO emission benefits. The

HEV had 46% and 8% of the distance-specific CO_2 and CO emission rates of the comparable CV, from hot-stabilised testing. HEV NO_x and HC emissions were 83% and 30% of the comparable CV, but absolute values were too low to give statistical significance. A more recent study by Huang et al. (2019) however concluded that hot stabilised on-road CO pollutant emissions from an HEV were consistently higher than that of its CV counterpart, while CO_2 emissions were lower and THC remained similar. This study utilised a small number of non-RDE compliant routes and did not have any cold start, but covered a range of urban, rural and motorway driving styles.

A common issue with many of the above comparisons is that the HEVs tested were not directly comparable to the CVs tested, giving less reliability to these results. Of those that are comparing appropriate HEV and CV combinations, there is little work incorporating cold start into the testing for gaseous pollutants. Additionally, though there are some on-road studies, there is no work testing on RDE compliant drive cycles. There are clearly some research gaps regarding the gaseous pollutant emission patterns of HEVs.

With regard to HEV PN emissions Christenson et al. (2007) studied several different HEV PN emissions and PN size distributions, compared to a CV. The CV was a Smart Car, which was not comparable to any of the HEVs tested. This paper was the first found to mention a PN penalty when HEVs undergo an engine-restart though, which is a behaviour that will be studied in more detail in following sections. Wei and Porter (2011) also found emissions spikes on engine-restart events from their study of cold start chassis dynamometer test cycles, and additionally through the investigation of the cold start period, were able to infer that the HEV did not suffer from increased PN emissions during cold start. However, the CV used for comparison was a completely different vehicle type (much heavier, with a much larger engine), rendering direct comparisons unreliable.

Robinson and Holmén (2011) compared the on-road hot-stabilised PN emission rates and size distributions of an HEV 2010 Toyota Camry with its CV counterpart, along a particular city driving route. They found significant spikes in PN emissions when the HEV engine restarted during the testing, which was not witnessed for the CV, resulting in two times greater PN emission rates for the HEV compared to the CV. They theorised that the spikes were due to fuel enrichment, but due to lack of lambda data could not confirm this theory. Their results showed average size distributions for each

run indicating that, while the CV consistently showed three distinct particle modes (10, 50 and 400nm), the HEV had a broader distribution with only two distinct modes (50 and 400nm) indicating a lack of nuclei particles. They theorised that this could either be due to the high PN events allowing more coagulation and adsorption of particles, or decreased combustion efficiency resulting in larger particles. However, they did not investigate further. Conger and Holmén (2015) also studied the hot-stabilised on-road PN emission rates for the same two vehicles presented in Robinson and Holmén (2011), but this time characterised emission rates from urban, rural and motorway driving modes. They found that the PN emission rates of the HEV were 1.8 times greater than that of the CVs in urban modes, but 2.4 times lower during motorway modes (comparable results in rural modes). They were able to study the air-to-fuel ratio for a single test and confirmed fuel enrichment was present on engine-restart. However, this was not quantified, and no further investigation using OBD or sensor information was performed to probe these events deeper.

As with gaseous pollutants, a common issue with many of the above PN comparisons is that the HEVs tested were not directly comparable to the CVs tested, giving less reliability to these results. Of those that are comparing appropriate HEV and CV combinations, there is little work incorporating cold start or the RDE test. For PN, at least, Kontses et al. (2020) remedies this. Kontses et al. (2020) compared on-road PN emissions from (cold start) RDE-compliant tests of a PFI HEV with conventional GDI and PFI vehicles. This study concluded that the total PN emissions of an HEV PFI were smaller than the comparable CV PFI. In fact, Kontses et al. (2020) found that the CV PFI had even greater emissions than the CV GDI, which is an even-more surprising result given the opposite trend in previous literature (Joshi, 2020). Kontses et al. (2020) indicated that the cold start PN penalty is lower for HEVs than CVs, which agrees with the findings of Wei and Porter (2011).

2.8.2 Effect of the test cycle used on HEV emissions

As the type approval emissions legislation has evolved, many research groups have studied the effects of the changes on resultant reported emissions. They have done so using the different test cycles and associated procedures, both comparing between test cycles and between on-road or ‘real-world’ results. Pelkmans and Debal (2006) and Merkisz et al. (2010) both studied results from a range of test cycles - including NEDC - against on-road results of CVs,

while May et al. (2014) incorporated the WLTC into the same type of investigation. Others focused only on comparisons of NEDC and WLTC (Marotta et al., 2015; Giechaskiel et al., 2015; Pavlovic et al., 2016). By 2016 the RDE test, in its earlier package forms, was being included into comparison studies (examples include Merkisz et al. (2016), Clenci et al. (2017), Donateo and Giovinazzi (2018) and Valverde et al. (2019)). All of the studies referenced above were measuring emissions only from conventional SI and compression ignition (CI) vehicles, and were discussed in Section 2.7. Other studies have looked at how the type approval tests affect reported emissions from HEVs; these results will be discussed in the paragraphs below.

Rask et al. (2010) performed testing on a Third Generation Toyota Prius, of the same model year (MY 2010) as the main research vehicle studied in this thesis. In this report, the authors monitored the fuel economy over various different US regulatory chassis dynamometer cycles, including the Urban Cycle, Highway Cycle and US06 cycle. These three cycles gave miles per gallon (MPG) fuel consumption values of 70, 67 and 44 respectively, demonstrating the large variation in fuel economy (and therefore CO_2 emissions) that is possible over different cycles. With only one repeat of each cycle discussed it is difficult to confirm that all of this difference is from cycle variability itself, but it is assumed that this was a large contributing factor.

Weiss et al. (2011) performed on-road testing with early PEMS of a wide range of vehicles, comparing results to the NEDC certification values. One HEV was tested: a second generation Toyota Prius. Their results indicated that on-road NO_x emissions were higher than the NEDC values, while the CO and THC were both lower (though all vehicles had very low absolute values of all three pollutants over all tests, giving low statistical significance). The on-road CO_2 was largely comparable to NEDC results. Duarte et al. (2014) also compared NEDC with on-road results, this time testing a Third Generation Toyota Prius. A PEMS device tested on-road emissions, covering a wide range of speed behaviours, and the results were compared to NEDC certification emissions data. Tailpipe emissions of CO_2, CO, HC, NO and O_2 were measured continuously, along with OBD values of vehicle speed, engine speed, load, airflow mass, manifold absolute pressure, intake air temperature, throttle position, coolant temperature and hybrid battery state of charge (SOC). They calculated a 3.2% decrease in the fuel consumption on the road compared to the NEDC, whereas they calculated that CO and NO_x increased by 18% and

26% respectively. However, this study only utilised four hours of experimental data, leaving the need for more comprehensive on-road testing.

Sileghem et al. (2014) and Kim et al. (2019) both tested a range of vehicles, including one HEV, over the NEDC and WLTC to compare emissions between cycles. Sileghem et al. (2014) tested a vehicle with very similar characteristics to the Third Generation Toyota Prius, but did not present individual vehicle results. Kim et al. (2019) presented results from their HEV test, concluding that as the test cycle changes from NEDC to WLTP, the resultant NO_x, CO, THC and CO_2 emissions decrease, while PM increases. The opposite trend of NO_x and CO_2 was witnessed for the CVs, while the same trend was seen for CO, THC and CO_2. PN was not studied. These results are not entirely reliable, however, due the small scale (only 1 HEV tested, and only 1 of each cycle). In addition, there is no mention of treatment of the hybrid battery SOC. It is assumed that the official procedures, as laid out in the NEDC and WLTP regulations, were followed but this is unconfirmed. Cubito et al. (2017) also directly compared CO_2 emissions from an HEV running the NEDC and WLTC on a chassis dynamometer, in full accordance with the respective test procedures. The net change in SOC over the tests was accounted for in the manner prescribed by the EU regulations in order to obtain a truly representative value for each cycle. The CO_2 emissions going from NEDC to WLTC increased from 76g/km to 94g/km (30% increase). They also found that the specific energy demand increased by about 50% and electric drive reduced by about 13%. As will be discussed in the following section, cold start is important for any drive cycle. For the HEV tested by Cubito et al. (2017), for example, the effect of the cold start on CO_2 emissions decreases from 12% for the NEDC to 4% for the WLTC. This is due to the higher power demand inducing a more rapid warm-up of the HEV, and the increase in total cycle length reducing the overall cold start impact.

Duarte et al. (2016) investigated emission differences between HEV and CVs with a focus on how the testing method and cycle used affects the two types of vehicles. They investigated the fuel consumption, CO_2, HC and NO_x emissions performance of 16 different vehicles, two of which were conventional SI and three were HEVs. PEMS were used to achieve ‘on-road’ estimates of the NEDC and WLTC results, by simulating the driving patterns required of those tests. Results were then compared to the certification values for each car.

Duarte et al. (2016) found that fuel consumption for the on-road NEDC decreased compared to NEDC certification values for only one vehicle, and it was one of the HEVs. The HEVs in general had the lowest fuel consumption and CO_2 emission values. The lowest percentage decrease from NEDC certification to experimental CO_2 emissions was for the HEVs, while two of the HEVs were also the only vehicles to have decreases in NO_x emissions. In CVs, the mechanical link between ICE and wheels means that if the vehicle is operating off-cycle, then the ICE must operate off-cycle, and an emissions penalty will result. However, because HEVs are able to disengage these two parts, the ICE can be maintained within a narrower load and RPM range under the same demands, meaning that the emissions penalty may be lower. Duarte et al. (2016) conclude that their results suggest that off-cycle operation, with its greater range of engine RPM and load values, has a greater effect on emissions even than cold start operation. For SI vehicles, fuel consumption and CO_2 emissions were 6% lower under the on-road WLTC cycles compared to the on-road NEDC cycle. This decrease is attributed to a lower amount of time being spent in low VSP modes for the WLTC cycle where ICEs are less efficient. However, for the HEVs, there was an approximate 5% increase in these values. This indicates that HEVs lose the advantage of full electric drive under high power demands. HC and NO_x results for the CVs were lower for the WLTC than the NEDC cycles, while results were less distinct for the HEVs, with less change seen between cycles. Though Duarte et al. (2016) present a thorough investigation of the differences between NEDC and WLTC on chassis dynamometer compared to on-road, a more direct methodology for analysis of road/chassis dynamometer effects could be performed by instead recording the velocity profile of an on-road test cycle and repeating it on a chassis dynamometer.

As the new packages of the RDE test have been released, some studies have focused on aspects of this legislation. Varella et al. (2019) and Suarez-Bertoa et al. (2019) both conducted thorough analyses of how various boundary conditions of the RDE affect the reported emissions from the RDE, but neither of these specifically study the effect of package changes on resultant emissions, or incorporate HEVs into the range of vehicles studied.

Kontses et al. (2020) is the only article found to study the effects of changing RDE packages and boundary conditions on the resultant RDE reported emissions. This work focused only on PN emissions. They found that the incorporation of cold start into the official RDE procedure in Package 3 acted

to increase emissions by 11.9%, which was a smaller percentage increase than seen for the CVs in general. No investigation into the effects of elimination of MAW processing, or elimination of vehicle stop and engine stop, was performed. This work did, however, compare the RDE against a more dynamic on-road driving style, and found that the increased power demand of the dynamic driving conditions minimised engine stop-start events and hence resulted in decreased PN emissions. With regard to PN size distribution, Robinson & Holmén (2011) inferred from their on-road city driving investigation that the PN size distribution changes little over the route for a given vehicle type. However, given the limited range of driving modes investigated in this work, the PN size distribution over different test modes and cycles is worthy of more investigation.

From a review of the literature, it is clear that though there are some studies focused on the emissions effect of legislation changes going from NEDC through to WTLC, there are fewer regarding the RDE and its various packages, boundary conditions, and comparisons with NEDC and WLTC. There is also little investigation of HEV emissions over the RDE test cycle, particularly for gaseous pollutants. There is also scope to further investigate the effects of driving on a real road compared to a chassis dynamometer, to quantify how type approval results are affected by this.

2.8.3 HEV cold start behaviour effect on emissions

The effects of cold start are very important on emissions behaviour, as has already been mentioned. Because of the different operational behaviour of HEV engines, this is an important characteristic to investigate. A number of studies have focused on the emissions of vehicles during cold start (for example Suarez-Bertoa et al. (2017), Merkisz et al. (2019), Varella et al. (2019) and Valverde et al. (2019)), but only a handful have focused on the effects of cold start on HEVs specifically. These are discussed below.

Rask et al. (2010) studied the cold start behaviour of a Third Generation Toyota Prius, of the same model year (MY 2010) as the main research vehicle utilised in this thesis. In this report the authors monitored the fuel economy, engine speed, fuel rate, engine oil temperature and battery power over the Environmental Protection Agency (EPA) urban dynamometer driving schedule (UDDS). This schedule lasts 1369s in low speed stop-start driving styles. In order to compare cold and hot behaviour this test was performed from a cold start and then repeated with a warm engine, following a 10 minute soak period.

The fuel economy for the cold start test was 63 MPG while that for the warm start was 70 MPG. This 10% difference is lower than the 15% difference found in a previous study of the Second Generation Toyota Prius performed by the same authors; they attribute this improvement to enhanced cold temperature fuel economy. This newer vehicle displays similar amounts of engine-on operation between cold and warm starts, though the choice of engine speeds is slightly different. The first 200s of the two tests cause the majority of total difference seen, with the vehicle in cold start selecting a much more constant engine speed during this period than during the warm start. This prescribed fuelling rate lasts approximately 50s and is likely used to warm the catalyst in a manner deemed to minimise cold start emissions. After this period, the vehicle appears to have warmed sufficiently to display similar behaviour between cold and warm tests, though the battery current remains lower throughout. The paper does not quantify battery SOC, or attempt to account for the differences in battery capacity between the cold and hot start tests in their discussion of fuel economy.

This prescribed fuelling rate period was quantified by Anderson et al. (2014) as taking approximately 60s, while they found that fuelling rates do not fully converge with warm start test iterations until 1300s, in agreement with Rask et al. (2010). Comparison against three other CVs revealed the Prius to generally have the longest duration of cold start effects, which the authors attribute to the additional time needed to recapture battery energy spent by the Prius to meet demands during cold start. They also noted, however, that cycle aggressiveness is a significant factor determining the length of the cold start effect. CO_2, NO_x and THC emissions were measured over repeated tests, showing that the cold start peaks in NO_x and THC abate after approximately 100s of the UDDS cycle, but that NO_x emission spikes can be induced later for cold start tests during transient events, particularly if the engine has been turned off. No direct comparison of cold start regulated emissions was performed between vehicles, and no CO or PN data was presented. With regard to CO_2 and fuel consumption, the authors found that the Prius displays the worst fuel consumption penalty of the small range of vehicles tested, consuming 21.8% more fuel on the cold start iteration of the UDDS than the iteration immediately following. This paper does not outline how the battery SOC was managed, nor is there any quantification of battery SOC over the test. This is significant as SOC affects engine behaviour and emissions, as will be discussed in Chapter 6 Section 6.4.

Alvarez and Weilenmann (2012) conducted laboratory testing of the cold start extra emissions (CSEE) on five HEVs recording regulated pollutant emissions, fuel consumption and CO_2 emissions over a cold start chassis dynamometer driving cycle developed within the ARTEMIS research project to have repeating subcycles. They did this by comparing cold start subcycles with the equivalent hot start subcycles. Before each test, the SOC was set to maximum. This was chosen to ensure that no recharging process was commenced by the ICE during the vehicle cold start, so that no additional CO_2 emissions distorted the envisaged CSEE values. The method they used for determining the cold start sections was to compare the CO_2 emissions between tests rather than measure the system temperatures. These results were then compared to their previous work done on CVs using the same method (Weilenmann et al., 2009).

Alvarez and Weilenmann (2012) found that the average regulated pollutant CSEEs of the HEVs were reduced by 30%-85% (across varying ambient temperatures) compared to CVs, indicating that HEVs have good cold start emission performances. This is theorised to be due to the ability of the electric drivetrain to assist the ICE by providing drive energy, allowing adjustment of the ICE operation during cold start to heat up the TWC more efficiently, while avoiding peak load demands and hence pollutant spikes. In contrast, the fuel consumption and CO_2 emissions were found to be similar to CVs, with some HEVs exceeding the average seen for CVs at ambient temperatures. This is because the quantity of fuel used to heat the TWC remains the same, so because the hot stabilised behaviour of HEVs is lower generally, higher relative CSEEs are seen during this cold start warm-up phase. Zahabi et al. (2014) conducted a wide study of real-world behaviour across 74 different vehicles, including HEVs, and also found that cold start was more dominant for HEVs compared to CVs. Significant drops in the CSEEs for particular tests were attributed to HEVs going into full-electric mode during cold start, resulting in minimised CO_2 emissions and fuel consumption. This behaviour is more likely to result if high initial SOCs are used, as in Alvarez and Weilenmann (2012), rendering the conclusions of the paper inapplicable to real-world HEV driving where journeys starting with full SOC do not generally occur for non-plugin HEVs (Duarte et al., 2014). Further cold start investigation is therefore necessary, to sample a more realistic range of initial SOC values.

With regard to PN emissions Kontses et al. (2020) measured cold and hot start PN emissions over RDE tests and found that total PN emission factors

per km dropped from $6.6x10^{11}$#/km to $5.9x10^{11}$#/km. This 10% decrease was much smaller than the average 27% decrease for the three PFI CVs tested. This difference is explained when studying the percentage total emissions that arise during the cold start period of the RDE test, compared to the rest of the urban section, the rural section and the motorway section. The proportion is much lower for the HEV than the other comparable CVs, with the rest of the urban section dominating. Kontses et al. (2020) attribute this to HEV stop-start behaviour occurring throughout urban and rural sections. No dedicated study into the size distribution of cold start HEV emissions has been found in the available literature to date.

With regard to unregulated pollutants, Suarez-Bertoa and Astorga (2016) conclude from their study of a PHEV and mild HEV (MHEV) that emissions of ethanol and acetaldehyde were present during cold start. However they do not quantify this relationship with the properties of an individual cold start, nor do they discuss any other unregulated pollutant emissions during cold start specifically.

Though these papers have some limitations, there is a general consensus that HEVs display quite different cold start behaviour to CVs, including similar or higher CO_2 emissions and fuel consumption penalties, but lower gaseous and PN pollutant emission penalties. However, there are still gaps in the research for accurate quantification and explanation of these effects for HEVs. There is also a distinct lack of HEV PN size distribution work, and further research required into the unregulated pollutant emissions from HEVs during cold start.

2.8.4 Effect of ambient conditions on emissions

Some previous studies have investigated ambient conditions and their effect on emissions from HEVs. Christenson et al. (2007) showed that low ambient temperatures had a greater detrimental effect on the HEVs than the CVs. The results of Zahabi et al. (2014) confirm that ambient conditions are important factors in the fuel consumption and CO_2 emissions values, and affect HEVs to a greater degree than ICEs. The effects on other pollutant emissions were not investigated. Fontaras et al (2008) conclude that vehicle fuel consumption is affected by the battery, the capacity of which (and hence vehicle efficiency) is greater at higher ambient temperatures. In contrast to this, Alvarez and Weilenmann (2012) concluded from their investigation that during hot phase driving, differences in ambient temperatures have no observed effect on the battery performance. Fontaras et al (2008) concluded from their study that the

effect of temperature on NO_x, HC and CO can be considered negligible. However, Suarez-Bertoa and Astorga (2018) present arguably the most comprehensive investigation into the effect of ambient temperature on HEV behaviour and emissions, concluding that CO_2, CO, NO_x, THC and NH_3 are all somewhat affected by cold ambient temperatures, and more so than CVs. However, only one HEV was tested in this campaign and the vehicle type did not have a comparable CV.

2.8.5 Effect of power demand to engine and vehicle specific power (VSP) on emissions

Much work has been conducted into the emission effects that changes in demand have on HEVs. Christenson et al. (2007) looked at the transient emissions of HEVs with respect to vehicle speed and load, and found that more transient cycles gave higher fuel consumption for HEVs, particularly for the more aggressive cycles. However, they found that emissions of CO, THC and NO_x were not always related to speed and/or acceleration, suggesting a load-levelling effect of the HEVs. These emissions also varied depending on combustion and catalyst temperatures, which were not recorded.

However, Liu and Frey (2015) found that their distance-based HEV emission factors (CO_2, CO, HC and NO_x) did vary with cycle average speed, reaching a minimum at speeds of 40-60 mph and increasing either side. Conversely, Wu et al. (2015) found that the correlation coefficients between CO_2 emission factors and average speeds of micro-trips in their study was poor, indicating that the CO_2 emission factors are almost insensitive to driving conditions. This was attributed to a reliance on the electric motor, the advantage of regenerative breaking and the need to recharge the battery. For NO_x, the emission factors actually decreased as the average speed decreased, unlike for SI vehicles where the opposite was true. THC emission factors decreased as the average speed increased, similar to SI vehicles. The reliability of this study is difficult to ascertain, however, as little information regarding the testing process and number of repeats was given.

VSP is a useful indicator of the demands on the engine, and has been widely used in the literature for the comparison of emissions output against vehicle activity. A full explanation of VSP is given in Jimenez-Palacios (1999), but the general definition is given by equation 2.

$$VSP = v\left[1.1a + 9.81\left(\frac{r}{100}\right) + 0.132\right] + 0.000302v^3 \qquad (2)$$

Where *VSP* is the calculated vehicle specific power (kW/ton), *v* is the vehicle speed (m/s), *a* is the vehicle acceleration (m/s^2), and *r* is the road grade (%).

VSP can play a big role in emission models (Frey et al., 2009). Wu et al. (2015) and Liu and Frey (2015) have both found that average emission rates for pollutants generally rose with increasing VSP for every operating mode, and emissions generally rose with increasing vehicle speed. Duarte et al. (2014) split their HEV trips up into 14 discrete VSP modes to compare fuel consumption across VSP modes. They found that fuel consumption and CO_2 emissions increased with power demand, particularly for higher VSP modes when the ICE is permanently on. Similarly, CO increased with VSP mode, probably caused by fuel enrichment leading to incomplete fuel oxidation. However, with no lambda sensor measurements, they were unable to substantiate this assumption. Regarding NO, they found that higher VSP modes increased NO concentrations.

Holmén and Sentoff (2015) used PEMS to compare real-world fuel consumption and tailpipe CO_2 emissions of a 'Toyota Synergy Drive' HEV with a CV of the same make and model. Their work focused on comparisons between the two vehicles for similar road types and road grades. They used the same VSP classes to characterise drive sections, and investigated fuel consumption and CO_2 emission values for these in order to compare HEVs with CVs. They found that emission rates of CO_2 increased linearly with positive VSP for both of their tested vehicles, and were very low for negative VSP values. The added CO_2 benefit brought by the HEV decreased as a log function of VSP until a crossover point, at which the normally lower CO_2 emission rate of the HEV became greater than that of the ICE. This crossover occurred at lower values of VSP as the vehicle speeds increased, confirming that the benefit of HEV technology lies mainly within the lower speed drive modes. Only at the highest power and highest speeds did the HEV CO_2 emission rate supersede that of the ICE. The higher CO_2 benefit in urban driving is expected, due to the higher proportion of stop-start driving. During VSP<0 events, this benefit is greatest. Conger and Holmén (2015) acknowledge that the VSP does not take into account the hybridisation effects of the vehicle, and so is not a fully accurate way to compare between the two technologies.

Frey (2018) presented some example data for fuel use rate and CO emissions with VSP for a range of 50 different gasoline engines, indicating that CO_2

emissions increase almost linearly with VSP, while CO only increases substantially at the very highest VSP values. This paper also states that HC emission rates, like CO_2, increase fairly linearly. NO_x emission rates, however, tend to increase non-linearly with increasing VSP, like CO. Notably, no data is presented for HEVs.

A series of papers (Varella et al., 2017; Varella et al., 2019) outlines the ways in which a VSP method could be used as an alternative to the MAW processing method for characterising and calculating the emissions of RDE trips with reference to the WLTP, including discussion of HEV results. However, as this methodology has not thus far been translated into the RDE legislation, it will not be discussed further here. There is clearly a gap in the research around HEV pollutant emissions trends with VSP, with no consensus on how HEV pollutant emissions are affected by VSP, or whether there is a more representative property to indicate emission rates for HEVs.

2.8.6 Effect of engine-off/on events (stop-start behaviour)

Particular attention has been given to the impact of engine-off events on vehicles, and due to the operating procedure of many HEVs, these vehicles have received specific attention in this regard. Zhai et al. (2011) developed a modal tailpipe emissions model under hot stabilised conditions for the First Generation Toyota Prius, paying particular attention to stop-start behaviours. Their experimental results found that the engine is disengaged at combinations of low acceleration and low-to-moderate speed, or moderate acceleration and low speed. Engine-off events are therefore highly speed-dependent. Zhai et al. (2011) confirmed that the HEV engine is frequently off in congested urban areas due to the low speeds and frequent stops. They concluded that increased penetration of HEVs into the urban fleet would be beneficial to air quality in urban areas, but did not appear to incorporate emissions from engine-restart events into their calculations.

However, the potential for negative impacts from engine starts is not new (Kittelson, 1998). Discussion around HEV engine-restart events has been evident since their emergence. Ng et al. (2001) studied the engine-restart characteristics of a Toyota Prius and Honda insight, noting that bursts in HC can result. While the engine-off events in HEVs decrease CO_2 emissions to ambient levels, high HC, THC and PN emissions have been detected during engine re-ignition after a period of engine-off operation (Christenson et al., 2007; Robinson and Holmén, 2011; Wei and Porter, 2011). Robinson and

Holmén (2011) theorised that the increased PN seen is due to enrichment of the air-fuel ratio by the HEV on engine-restart. Conger and Holmén (2015) subsequently validated this, estimating a two second enrichment duration for each engine-restart from a single 50km test incorporating urban, rural and motorway drive modes and containing 187 individual engine-restarts. More recently, Kontses et al. (2020) witnessed the same trend for spikes in PN on engine-restart, attributing them mainly to fuel enrichment, but also to engine temperature decreases. However, no substantial evidence to back these assumptions is given. As previously mentioned, Robinson and Holmén (2011) studied PN size distributions of an HEV 2010 Toyota Camry, and found a broad distribution, with two distinct modes (50 and 400nm), indicating a lack of nuclei particles. However, they conducted no investigation into the size distributions of engine re-ignition events and therefore there is a gap in the literature surrounding the size distribution of HEV ignition and re-ignition events.

Duarte et al. (2014) studied the effect of engine off events on CO and NO_x emissions. They found that the longer the engine-off event, the greater the emissions index (ratio of emissions to fuel mass) increase during the restart, compared to the period preceding the engine-off event. They assume this is due to decreased catalyst efficiency due to cooling but do not confirm this or quantify the effects. This conclusion is in disagreement with that of Prati et al. (2018) who, in their limited study of stop-start technology vehicles, concluded that if stationary for longer than 10s, it is better to have the engine off.

With regard to unregulated pollutants, Suarez-Bertoa and Astorga (2016) studied a selection of transient unregulated emissions of a PHEV and MHEV over the WLTP cycle, noting that NH_3 emissions are correlated with rich combustion events, but did not investigate any relationship between engine-restarts and NH_3, or any other unregulated pollutants.

Clearly, there is consensus that the engine re-ignition events cause differences in emissions compared to CVs. Few studies have tried to quantify this effect in detail, or, for gaseous pollutants, even evidence the mechanisms behind their production during engine-restarts. Very little research into the unregulated pollutants has been conducted thus far, leaving room for an investigation of how engine-restarts affect these pollutants.

2.8.7 Effect of HEV battery state of charge (SOC)

The SOC may have an important influence on HEV emissions; this too has been investigated in the literature. Fontaras et al (2008) also found that the change in SOC over a drive affects the fuel economy and CO_2 emissions, with negligible effect on the regulated pollutant emissions, but further details are not given for any of these parameters. This is, however, the same conclusion that both Loiselle et al. (2010) and Favre et al. (2013) came to from their studies of HEVs over several different chassis dynamometer drive cycles. Loiselle et al. (2010) also reports no common trend in CO, while Favre et al. (2013) also report no common trend across cycles for NO_x, PN or HC.

More recently, Duarte et al. (2014) looked closely at the effect of battery SOC on hybrid behaviour and emissions. They found that the higher the SOC, the higher the likelihood of the vehicle entering pure electric-drive mode, and the lower the emissions. However, the low number of test hours in this study makes these results less reliable. City driving has been shown to enable some significant recharging of the battery at relatively high VSP, but the authors concede that the result may be route-specific due to steep road grades (Holmén and Sentoff, 2015). The effect of driver behaviour on SOC and regenerative braking should always account for road grade, and warrants further investigation. Cubito et al. (2017) tested an HEV at 30% and 70% SOC over both NEDC and WLTC test cycles. In both cases, the high initial SOC resulted in slightly lower overall CO_2 emissions rates, equating to a 6g/km decrease over each test. However, the authors note that in all four cases, there was a net charging of the battery over the test cycle, rendering the quoted CO_2 differences unreliable. No pollutant emissions were reported in this study.

Suarez-Bertoa and Astorga (2016) conclude from their study of a PHEV and MHEV that emissions of NO_x, CO, CO_2 and NH_3 are much higher for a PHEV starting the WLTC at 88% SOC compared to 100% SOC, but no correlation was found with the MHEV studied.

2.8.8 Summary of HEV emissions literature

A review of the published literature in the field of HEV emissions reveals that though much research has already been performed, there remain significant areas not yet fully investigated. The new RDE legislation has not been thoroughly compared to the NEDC and WLTC test cycles, with limited investigation into how the chassis dynamometer differs from on-road testing

conditions. The evolution of the RDE legislation and the effects on the emissions has also been relatively untouched in the literature thus far, owing to the novelty of the most recent Package 4. With regard to cold start, a thorough investigation and quantification of cold start emissions, along with parameters such as catalyst temperature and efficiency, and fuel enrichment, has yet to be conducted on an HEV. Additionally, a study of unregulated emissions, or of the size distribution of PN emissions during the cold start period for an HEV has not yet been performed. Engine power demand and VSP is an area of interest for the study of emissions, but for HEVs this proves less clear-cut, so further work in this area is needed. Though many papers have found various emissions spikes on engine-restarts, many investigations failed to identify and characterise the properties causing these spikes. Though this is not so much the case for PN, there is still limited knowledge about the size distribution of PN during these important re-ignition events. Of the literature available, none appear to have studied in detail whether there is any pattern for unregulated emissions during engine-restarts. This, too, is worthy of further investigation.

2.9 Emissions from ethanol and butanol blends

Alongside increased electrification, the increased use of biofuels is regarded as one of the ways in which the transport industry can reduce its carbon footprint. However a change in fuel may lead to a change in the pollutant emissions. It is important to fully investigate and quantify these changes.

2.9.1 Ethanol blend emissions compared with gasoline

As discussed earlier in this chapter, ethanol is regularly blended into gasoline as an additive in order to enhance combustion properties and lower the net CO_2 emissions from transport. There have been many previous studies assessing the emissions characteristics of ethanol-gasoline blends with respect to pure gasoline, and those deemed the most suitable will be discussed further. Only blends up to 30% ethanol will be considered in this review of literature, as blends any higher can show other characteristics not representative of the lower blend ratios (Chen et al., 2011; Jin et al., 2017).

2.9.1.1 CO emissions from ethanol blends

A large number of previous studies have investigated the CO emissions resulting from ethanol blending, and the trend in the literature thus far has

generally pointed toward a decrease in emissions with ethanol blending (for example Costagliola et al. (2013), Elfasakhany (2017), Hsieh et al. (2002) and Varol et al. (2014) utilising PFI research engines). Of the chassis dynamometer studies, Guerrieri et al. (1995), Karavalakis et al. (2012), Ratcliff et al. (2013) and Saikrishnan et al. (2017) also agree on a general trend of decreasing CO emissions with ethanol blending, though the model years of the vehicles used in Guerrieri et al. (1995) and Karavalakis et al. (2012) mean results may not be applicable to modern vehicle technologies. The correlations presented by Saikrishnan et al. (2017) were weak, giving less reliability to their conclusion. Finally, Jin et al. (2017) presented decreased CO emissions from GDI vehicle FTP-75 testing of 30+% ethanol, but higher emissions for E10. On-road measurements are sparse, with the most relevant being that of Hernandez et al. (2014). Hernandez et al. (2014) tested three PFI vehicles at 40km/h steady velocity driving, and reported a CO decrease with low percentage ethanol blends.

The vast majority of these studies attributed the decreased emissions to the oxygen contained within the ethanol molecule (Hsieh et al., 2002a; Agarwal, 2007; Costagliola et al., 2013; Varol et al., 2014; Masum et al., 2015). The oxygen molecule contributes to a ‘leaning effect’ within the combustion chamber, allowing more complete combustion and thereby reducing CO emission. In fact, He et al. (2003) even states that the oxygen atom in ethanol is even more effective at improving combustion in rich mixtures than that in air. Saikrishnan et al. (2017) adds another reason: that the high molecular diffusivity and high flammability limit improves the mixing process and hence the combustion efficiency. However there is no complete consensus on this matter, with Li et al. (2017) finding that CO increases with ethanol blends in a PFI research engine. They attribute this increase to the higher heat capacity products from alcohol combustion lowering the combustion temperature and slowing down the oxidation process of CO, as well as to the shorter combustion time of biofuels leading to insufficient oxygenation time for CO. This theory is supported by decreased combustion temperatures within the GDI cylinder measured by Zhang et al. (2014), and decreased exhaust gas temperatures reported in Canakci et al. (2013), Eyidogan et al. (2010) and Varol et al. (2014).

Li et al. (2017) found CO was increased at stoichiometric conditions but decreased at rich conditions. This is likely due to the leaning effect of ethanol mentioned previously. Li et al. (2017) discussed the competing factors of

leaning effect, reduced combustion temperature, and decreased combustion duration as all affecting overall CO results. In line with this, there are also studies that were unable to draw a firm conclusion on the matter, either because the results were mixed regarding conditions and fuel blends, or because all results were too close in value to be statistically significant. These include Agarwal (2007) and Varde et al. (2007) using PFI research engines, and Vojtisek-Lom et al. (2015) and Liu et al. (2019) from GDI chassis dynamometer studies. In a study investigating only the cold start emissions of an SI engine, Chen et al. (2011) conclude there is little impact from E5 and E10 on CO emissions during engine-start, but a clear decreasing trend for higher blends E20-E40.

There has been some evidence in the literature of the trend in CO emissions between ethanol blends and gasoline changing with respect to the engine or vehicle operating conditions. Canakci et al. (2013) found distinct decreases in CO with their ethanol blends when their PFI vehicle was run at 80km/h on a chassis dynamometer, but then found similar results or even increases at the higher velocity of 100km/h. They postulated that at low vehicle speeds, the mixing is not as complete, and therefore the extra oxygen in ethanol can help reduce emissions to a greater degree at lower speeds. Interestingly, the opposite trend is presented by Liu et al. (2009) for their GDI on a chassis dynamometer. During the low speed phase of the NEDC they witnessed increased E20 with respect to E0, and then observed comparable results during the high speed phase. However, this latter test was from cold start, unlike the former, and so the lower combustion temperature caused by the increased latent heat of ethanol may have had a stronger effect on CO during cold start, leading to increased emissions.

Clearly there is still some disagreement within the literature, with little work based on realistic driving behaviours and cold start performance, particularly for PFI vehicles.

2.9.1.2 NOx emissions from ethanol blends

The relevant literature considered for this thesis has been unable to decisively conclude a relationship between NO_x and ethanol. This is either because of mixed trends or statistically insignificant differences between the fuels under testing (Hsieh et al., 2002a; Karavalakis et al., 2012; Costagliola et al., 2013; Ratcliff et al., 2013; Agarwal et al., 2015; Vojtisek-Lom et al., 2015; Saikrishnan et al., 2017). By comparing older and newer vehicles within their

test vehicle set, Karavalakis et al. (2012) were able to substantiate their assertion that the small difference arising from gasoline versus ethanol-blended fuels in newer vehicles was likely to be due to the newer vehicles' ECUs being able to more effectively adapt to changes in the fuel combustion properties. Hsieh et al. (2002) concluded that NO_x output depends on the equivalence ratio, rather than the ethanol content of a fuel.

Of those with a clear trend, Li et al. (2017) found that NO_x emissions from their PFI research engine at steady state engine RPM decreased with addition of 10% and 30% ethanol to gasoline and Canakci et al. (2013) also found decreased NO_x from E5 and E10 for their PFI SI vehicle. Liu et al. (2019) found decreased NO_x from NEDC testing of their GDI vehicle on E20 and Broustail et al. (2012) found decreased NO_x from 25% ethanol blended into iso-octane, but it should be noted that the latter was not mixed with gasoline. Jin et al. (2017) presented slightly increased NO_x emissions from GDI vehicle FTP-75 testing of E10. In a study investigating only the cold start emissions of a PFI SI engine, Chen et al. (2011) concluded that there was little impact from E5 and E10 on NO emissions during engine-start, but a clear decreasing trend for higher blends E20 – E40. Li et al (2017), Canakci et al. (2013), Costagliola et al. (2013), Agarwal et al. (2015) and Saikrishnan et al. (2017) all attribute lower NO_x results to a lowering of peak temperature, combustion temperatures and burnt gas temperatures, resulting from higher latent heat, lower heating value and the extra oxygen content brought by ethanol. The work of Varde et al. (2007) substantiates these assertions, finding that higher flow rates of the ethanol blends are also a contributing factor, resulting in decreased adiabatic flame temperatures according to simulations.

Masum et al. (2014), Furey and King (1980) and Guerrieri et al. (1995) on the other hand all found increased emissions from their chassis dynamometer tests. As previously mentioned, the older technologies employed by the vehicles tested are not comparable to those on the roads today. Wallington et al. (2016) disqualifies vehicles produced before the year 2000 from the review of literature for this reason. Accordingly, Furey and King (1980) and Guerrieri et al. (1995) will not be discussed further. Masum et al. (2014) attributed their increased NO_x emission for E20 to higher combustion temperatures, corroborated by their increased exhaust gas temperatures. They also asserted, like Canakci et al. (2013), that the extra oxygen of ethanol in the combustion chamber enables easier oxidation of nitrogen in the air.

Canakci et al. (2013) found that NO_x emissions were more decreased with ethanol blending at lower vehicle speeds, with trends converging at higher speeds. Canakci et al. (2013) did not directly address the disparity in their work, but a dependence of NO_x formation on residence time is mentioned. It could therefore be inferred that higher flow rates and engine speeds may limit the time available for oxidation reactions to occur, but this is unconfirmed. Liu et al. (2019), however, found the opposite trend; results were more similar in the low speed phase of the NEDC and then E20 had lower emission factors in the high speed phase. The authors did not discuss this result further. However, direct study of NO_x emissions with vehicle speed showed mixed, closely aligned results, indicating that the NEDC cold start may be having a levelling effect on this influence, due to cold combustion temperatures for both fuels.

2.9.1.3 HC emissions from ethanol blends

The general consensus in literature to date is that low percentage blends of ethanol into gasoline result in decreased HC emissions. This is the conclusion of PFI research engine data presented in Agarwal et al. (2015), Broustail et al. (2012), Elfasakhany (2017), Hsieh et al. (2002), Li et al. (2017), Masum et al. (2014), Saikrishnan et al. (2017) and Varol et al. (2014), and PFI chassis dynamometer data presented in Guerrieri et al. (1995), Canakci et al. (2013) and Liu et al. (2019). In a study investigating only the cold start emissions of an SI engine, Chen et al. (2011) conclude that there is little impact from E5 and E10 on HC emissions during engine-start, but a clear decreasing trend for higher blends E20 – E40. As with CO, there is a consensus in the literature that the reason for decreased HC emission is due to the additional oxygen within the ethanol molecule improving combustion by lowering the stoichiometric air/fuel ratio and increasing the actual air/fuel ratio.

Canakci et al. (2013) and Liu et al. (2019) both found decreased HC emissions at low vehicle speeds, with emission rates converging as speed increased. Canakci et al. (2013) found that at 100km/h there was a small decrease in HC emissions, whereas Liu et al. (2019) found that their results fully converged at 90km/h. Liu et al. (2019) attributes this to the fact that as the speed increases, the increased gas flow in the cylinder enhances the homogeneity and the combustion rate increases, reducing HC emissions. Price et al. (2007) found that HC emissions were dependent on the load of their GDI research engine; at low loads ethanol blend emissions were much lower than those from

gasoline, particularly with rich fuel mixtures. At high load, however, the ethanol blends gave higher emissions. Through fast in-cylinder temperature measurements, it was inferred that the likely reason for the latter effect was due to the additional fuel necessary of the ethanol blends at higher loads (due to their lower heating value (Liu et al., 2019)) saturating the charge, leading to incomplete vaporization and liquid droplets remaining which cause HC emissions.

Some literature did not find any conclusive trend for HC emissions (Costagliola et al., 2013; Varol et al., 2014), while Karavalakis et al. (2012), Vojtisek-Lom et al. (2015) and Jin et al. (2017) found very slight increases in HC emission from transient chassis dynamometer cycles. Hernandez et al. (2014) presented mixed results from on-road PEMS work. These latter results indicate that transient cycles do not generally show the clear THC relationships that steady state testing has historically tended toward.

2.9.1.4 PN emissions from ethanol blends

The literature suggests that PN emissions from SI vehicles utilising ethanol blends in gasoline are lower than those fuelling with pure gasoline. Of research engine studies, this was the conclusion reached by Costagliola et al. (2013) using a PFI engine, and Hergueta et al. (2018), Price et al. (2007), Zhang et al. (2014) and Cho et al. (2015) using GDI engines. Cho et al. (2015) thought that as ethanol fuel blends possess lighter HC chains and a lower distillation temperature, the fuel droplets would more easily evaporate and thereby form a more homogeneous air-fuel mixture, reducing total PN emissions. In addition, Liu et al. (2019) stated that the oxygenated fuel improves combustion, which in turn reduces aromatic (e.g. PAH) contents in the fuel, limiting soot formation. This extra oxygen is also able to help oxidise any soot that has formed, again reducing PN at the tailpipe. Cho et al. (2015) noted increased PN from ethanol blends versus gasoline during the cold start section of the drive only, for approximately the first 20s. This could be due to higher latent heat of vaporisation and lower vapour pressure of ethanol causing slower evaporation, poorer homogeneity and therefore worse cold start combustion performance (Luo et al., 2015).

Costagliola et al. (2013), Luo et al. (2015), Zhang et al. (2014) and Cho et al. (2015) found a general pattern of decreasing particle size with E10 blending; they found decreasing accumulation mode particle numbers alongside increasing nucleation mode particle numbers under ethanol blending.

Hergueta et al. (2018) saw a distinct lack of agglomerates from E25 compared to gasoline. Costagliola et al. (2013) pointed out that the nucleation mode was still lower for ethanol blends than gasoline however, which they explained by the higher volatile fraction of gasoline compared to E10 leading to more of the small volatile particles. Price et al. (2007) saw little difference in PN size distribution at lower ethanol blend values for their GDI SI engine, but at an ethanol percentage higher than those currently under study (E85), they saw a decrease in accumulation mode particles, particularly under fuel-rich conditions. They postulated that the presence of oxygen in the fuel molecule reduces the concentrations of key intermediate species required for the formation of aromatic soot precursors.

Luo et al. (2015) found increases in PN from ethanol blends at low loads (but decreases at medium and high loads, in line with general literature trends). The authors postulated that at low load, low speed conditions, ethanol's higher viscosity and poorer vaporization properties resulted in poorer homogeneity and so additional smaller particles, but at higher speeds there was better mixing and less time for particle nucleation, so this effect was not so influential. The chassis dynamometer work available also tends toward some dependence on engine operating mode. Liu et al. (2019) found that at low and intermediate speeds the PN emissions from ethanol blends of their GDI vehicle decreased, but at high speeds the emissions increased. Overall, however, Liu et al. (2019) found a strong decrease in PN over the NEDC cycle, as the ethanol blend PN emissions became greater only at velocities above approximately 100km/h for this vehicle. Jin et al. (2017) found that results from the FTP-75 cycle agreed with these steady state test results; phase 1 of the FTP-75 showed E10 with lower PN than gasoline, but phases 2 and 3 showed increases (it is worth noting that E30+ showed marked decreases). Overall, as with Liu et al. (2019), decreased PN resulted from the E10. Vojtisek-Lom et al. (2015) measured emissions from a GDI vehicle both on chassis dynamometer and on-road, and found that while the PN values were comparable on the chassis dynamometer, they were lower on the road. The road route utilised contained a portion of uphill motorway driving; this is where the majority of total emissions for each test were produced. Since this type of driving would be high load, high speed, the fact that it led to lower emissions for ethanol blends agrees with the previous findings mentioned above.

2.9.1.5 Unregulated emissions

The effects of ethanol blending into gasoline are varied across different species. There is some general consensus in the literature to date that most toxic unregulated emissions are decreased under ethanol blending, including VOCs, and HCs (Jin et al., 2017). There are some exceptions, however: carbonyl species, namely aldehydes originating from partial oxidation or incomplete combustion of ethanol, have been shown to increase (Karavalakis et al., 2012). Additionally, ethanol emissions have (unsurprisingly) been shown to increase under ethanol blending (Agarwal et al., 2015).

Of the aldehydes, acetaldehyde is the species most reliably increased with ethanol blending, with consensus in Agarwal et al. (2015) and Costagliola et al. (2013) from PFI research engines and Guerrieri et al. (1995), Karavalakis et al. (2012) and Ratcliff et al. (2013) from PFI chassis dynamometer studies. No relevant reliable study has been found to produce a decrease in acetaldehyde, but Varde et al. (2007) and Broustail et al. (2012) have given inconclusive results (the latter of which was ethanol blended into iso-octane, not gasoline). The literature has a range of views on formaldehyde, however. Increases were presented by Agarwal et al. (2015) and Costagliola et al. (2013) from research engines, and Ratcliff et al. (2013) from chassis dynamometer testing. However, Broustail et al. (2012) found a decrease with respect to iso-octane, while Guerrieri et al. (1995) and Karavalakis et al. (2012) had inconclusive formaldehyde results. Given the age of the vehicles used in the two latter studies, and the different fuel of Broustail et al. (2012), the results indicating increased formaldehyde emissions are viewed as having greater reliability. Acrolein was seen to decrease by Ratcliff et al. (2013), while for the ketones acetone, generally sees decreased emissions under ethanol fuelling (Karavalakis et al., 2012; Ratcliff et al., 2013).

With regard to the hydrocarbons, Agarwal et al. (2015) and Broustail et al. (2012) both agree that acetylene and ethylene emissions decrease with ethanol. Agarwal et al. (2015) also reports lower emissions of propene, but increases of propane. Most hydrocarbon emissions are lower because the higher oxygenation of ethanol fuel improves the combustion completeness and decreases the formation of these pollutants, but Agarwal et al. (2015) states that propane is produced more readily from ethanol than gasoline, hence the increase in this case.

Methane is particularly important due to its global warming potential, and there have been a range of results for this compound. Broustail et al. (2012) presented a decrease of methane with ethanol blending, while Agarwal et al. (2015) and Costagliola et al. (2013) reported mixed results. Jin et al. (2017), meanwhile, presented increased methane emissions from ethanol blends. N_2O is an even stronger greenhouse gas, and is currently also unregulated by legislation. One of the only previous studies found to measure N_2O found decreased emissions from ethanol fuel blends (Agarwal et al., 2015).

With regard to VOCs, Agarwal et al. (2015), Karavalakis (2012) and Jin et al. (2017) all report decreased emissions of 1,3-butadiene from ethanol blends, while Costagliola et al. (2013) and Ratcliff et al. (2013) both have inconclusive results. Like propene, 1,3-butadiene is only produced during the combustion process (Ye et al., 1997) and so it is expected that the oxygenation of ethanol will improve combustion completeness and decrease emissions. Agarwal et al. (2015), Broustail et al. (2012) and Jin et al. (2017) all reported decreased benzene, while Karavalakis (2012) reported mixed results for the BTEX compounds generally. Most VOCs are present as components within gasoline or are produced from components within gasoline, so the decreased proportions of gasoline in ethanol blends means VOC emission decreases are expected (Agarwal et al., 2015; Jin et al., 2017).

2.9.2 Butanol blend emissions compared to gasoline and ethanol blends

There have been many previous studies assessing the emissions characteristics of n-butanol/gasoline blends with respect to pure gasoline and ethanol/gasoline blends. Only blends up to 30% n-butanol will be considered in the review of literature, as blends any higher can show other characteristics not representative of the lower blend ratios (Chen et al., 2011; Jin et al., 2017). Some studies test individual butanol isomers whereas others refer to the fuel as simply ‘butanol’ and do not specify the isomer. Only those studies utilising n-butanol specifically will be incorporated into this literature review as the isomers have different thermodynamic properties and combustion characteristics to one another (Szwaja and Naber, 2010), resulting in different emissions characteristics. The n-butanol will simply be referred to as “butanol” in this and all subsequent chapters.

2.9.2.1 CO emissions from butanol blends

The previous literature into CO emissions resulting from butanol/gasoline blends – in comparison with pure gasoline and comparable ethanol/gasoline blends – shows varied results. Of the PFI research engine studies available, Costagliola et al. (2013), Dernotte et al. (2010), Gu et al. (2012) and Varol et al. (2014) all agree on a trend of decreasing CO emissions under butanol blending compared to gasoline. Of those that compared their results with ethanol, Costagliola et al. (2013) found the emissions more decreased than ethanol, while Varol et al. (2014) found mixed results; at low engine RPM, CO emissions were greater than those of ethanol, while at high RPM, they were lower than ethanol. Costagliola et al. (2013) attributes lower CO emissions to the higher oxygen content of the alcohol fuels allowing more complete combustion.

As with ethanol blends, there was also evidence of some dependence on engine speed and load. Elfasakhany (2014) and Elfasakhany (2017) presented decreased CO emissions from B10 for their PFI engine with respect to gasoline (and E10) at low engine speeds, but then at higher engine speeds Elfasakhany (2014) saw results comparable with gasoline, while Elfasakhany (2017) witnessed an increase (while E10 still induced a decrease) with respect to gasoline. This trend is in direct disagreement with the previous work of Varol et al. (2014), which showed larger decreases from B10 (and, equally, E10) at higher engine speeds than at lower engine speeds. The range of engine speeds covered by Elfasakhany (2017) is much narrower, and covers the speed range in which Varol et al. (2014) saw a reversal of the relationship between butanol and ethanol. Singh et al. (2015) found similar CO emissions to gasoline at low engine speeds from their PFI research engine, but found marginally higher CO emissions at higher speeds. This is in closer agreement with the results presented by Elfasakhany (2014) and Elfasakhany (2017). Singh et al. (2015) attributes the increased emissions at higher speeds to the decrease in time available for combustion to take place, which is also stated by Liu et al. (2019).

Hergueta et al. (2017) found greater CO emission from B33 in their GDI research engine at low load (compared to E5 “gasoline”) but then decreased emissions at high load, so these results are in closer agreement to those of Varol et al. (2014). At high load, they attribute the decreased emissions to greater combustion stability from the more favourable characteristics of B33;

higher oxygen content and shorter carbon chain length. They experimentally verified the greater combustion stability with a lower coefficient of variation (COV) of indicated mean effective pressure (IMEP) and higher exhaust temperatures (indicating higher combustion temperatures). They attributed the higher CO emissions at low load to an increase in the effect of butanol's physical properties – higher viscosity and lower heat of vaporization impacting spray atomization and mixing – suggesting that these caused a decrease in overall combustion efficiencies.

Some studies could not make a firm conclusion about the effects on CO emissions from butanol blends due to mixed results and results that were not statistically significant in difference. This includes Broustail et al. (2012) from a steady state PFI test engine, and Ratcliff et al. (2013) from a large PFI vehicle chassis dynamometer test cycle.

Of the chassis dynamometer studies that were able to reach a conclusion, there were again mixed results. Two studies utilising GDI vehicles concluded CO emission reductions under butanol use. Vojtisek-Lom et al. (2015) found comparable results during the urban and rural sections of the Artemis drive cycle (with statistically insignificant differences to ethanol blending), but approximately half the CO emissions of both gasoline and ethanol on the motorway section. More recently, Liu et al. (2019) presented decreased B10 CO emissions at 20km/h (compared to gasoline, and to a lesser extent, E10), comparable results between 40-80km/h for all three fuels, and then slightly increased results up to 120km/h (with E10 slightly higher than B10). These two results are again in direct conflict with each other. Both GDI vehicles where turbocharged, but that of Liu et al. (2019) was slightly larger and certified as China V, whereas that of Vojtisek-Lom et al. (2015) was Euro 6 certified. Additionally, Liu et al. (2019) used steady state driving for the speed comparisons, whereas Vojtisek-Lom et al. (2015) was using the relevant phase of a transient drive cycle. However, Liu et al. (2019) also presented NEDC test data with a similar trend: CO over the UDC from B25 was lower compared to gasoline, whereas the EUDC was comparable to gasoline. One (Euro 3) PFI vehicle has shown increased emissions from a NEDC chassis dynamometer testing than gasoline. Kalita et al. (2016) present (~20%) increased emissions under B10 fuelling compared to E0 gasoline. They attributed their increased CO to the poorer evaporation rate of butanol, inhibiting fuel atomization and therefore combustion.

Clearly there are many different competing factors that are causing a lot of disagreement between studies. Liu et al. (2019) agreed with Costagliola et al. (2013) and Singh et al. (2015) that the higher oxygen content of the alcohol fuels allows for more complete combustion, but also point to the lower volatility of butanol becoming a more significant factor when the mixing of air and fuel is uneven at lower speeds. At higher speeds, Singh et al. (2015) attributed increased emissions to the decrease in time available for combustion to take place, which is also stated in Liu et al. (2019). Overall, the literature points to similar or decreased emission results from butanol blends compared to gasoline. The trends with engine and vehicle conditions are more mixed. The studies utilising GDI engines give contrasting views with regard to the effects of both engine speed and load on butanol blend emissions compared to gasoline, whereas the PFI studies generally show increasing CO emissions with increasing engine load and speed.

With regard to comparisons with ethanol, the literature generally points to either similar or decreased CO emissions from butanol blends compared to ethanol blends. Again, this is due to multiple competing factors: the volatility of ethanol is greater than butanol, and its viscosity is lower, so it will be less negatively impacted by these properties than butanol. However, the latent heat of vaporization is higher for ethanol, which also negatively impacts combustion, particularly at low speeds and loads. Additionally, OH radicals form more easily with the longer molecular chain of n-butanol compared to ethanol, and OH is a strong oxidant to oxidise CO (Liu et al., 2019).

2.9.2.2 NOx emissions from butanol blends

As with ethanol, the literature has weak or mixed results regarding the effect of butanol blending on NO_x emissions from SI vehicles. Two previous PFI research engine studies – Broustail et al. (2012) (utilising iso-octane as a gasoline surrogate) and Gu et al. (2012) – present decreased NO_x emissions from their butanol blends (though the results of Gu et al. (2012) for B10 blends are mixed). Each study only probed a single engine speed value. Hergueta et al. (2017) also presented decreased NO_x emissions from their GDI engine research, but noted that the decrease is mainly at low load, with medium loads showing no significant change from gasoline. Hergueta et al. (2017) claimed that butanol's shorter carbon chain length and higher oxygen content are generally helping to reduce the emissions. With specific regard to the difference in behaviours with load, they hypothesised that butanol's lower

adiabatic flame temperature and marginally lower heat release rate at the end of the combustion phase could reduce the local temperatures compared to gasoline. They noted, however, that at higher loads increased homogenisation and stability would allow higher combustion temperatures and heat release rates, eliminating this effect from the butanol blends.

Two GDI chassis dynamometer studies indicated some dependence of vehicle speed on the impact butanol has on NO_x emissions. Through steady state driving at a range of velocities, Liu et al. (2019) concluded that at low to intermediate speeds (40-70km/h) the NO_x emissions are comparable between B20 and E0 (as well as E20), but at higher speeds, B20 (and E20) had slightly lower emissions. Liu et al. (2019) also tested according to the NEDC procedure, and presented a ~10% decrease in NO_x emissions to gasoline from their butanol blends during the UDC section of NEDC, and a ~14% decrease during the EUDC. The E20 results showed slightly less decrease from gasoline than the B20 for this drive cycle. Liu et al. (2019) and Singh et al. (2015) both attributed the decreased emissions to the high latent heat of vaporization butanol, resulting in lower combustion and in-cylinder temperatures, which in turn reduced NO_x formation.

Vojtisek-Lom et al. (2015) stated that their B25 NO_x results did not provide statistically significant comparisons with gasoline. They presented a very small increase in NO_x emissions during the urban and rural phases of the Artemis drive cycle, and slight decrease in the highway phase. Emissions of B25 were comparable with E15 for urban and motorway sections, but slightly elevated for the rural section. Inconclusive NO_x results were presented from PFI test engine research by Costagliola et al. (2013), Dernotte et al. (2010) and Kalita et al. (2016). The latter presented higher results for B5, but lower results for B10 and B20. Similar results between butanol and gasoline (and ethanol) blending were also presented from a large PFI engine vehicle running the LA92 test cycle of a chassis dynamometer in Ratcliff et al. (2013). Finally, Singh et al. (2015) found comparable NO emissions under B5 and B10 use from their medium duty PFI research engine at lower engine speeds, but slightly increased emissions at higher engine speeds. At higher butanol blending percentages, however, they saw emission decreases.

With regard to the difference between butanol and ethanol, Broustail et al. (2012) and Ratcliff et al. (2013) saw greater NO_x emissions from butanol blends than ethanol blends, while Costagliola et al. (2013) found small

reductions in NO_x from butanol blends compared to ethanol blends. Liu et al. (2019) found no statistically significant difference in NO_x at 20% biofuel blending ratios, but found that ethanol had the smallest NO_x emissions for higher blends. Liu et al. (2019) attributed this pattern to ethanol having the highest latent heat of vaporization, hence the greatest combustion temperature decreases.

2.9.2.3 HC emissions from butanol blends

As with ethanol, the general trend in literature is for decreasing HC emissions resulting from butanol blends, compared to gasoline. Of the available PFI test engine research, Broustail et al. (2012) (using iso-octane as a gasoline surrogate), Elfasakhany (2017), Gu et al. (2012) and Varol et al. (2014) showed decreased HC emissions from butanol blending, while Singh et al. (2015) found a small increase. Costagliola et al. (2013) and Dernotte et al. (2010) showed little correlation from their PFI engine studies, while Elfasakhany (2014) found mixed results: lower HC emissions compared to gasoline were seen at low engine speeds, but little change was seen at higher engine speeds. With regard to chassis dynamometer PFI studies, Kalita et al. (2016) indicated an increase in HC emissions from butanol blends, making the overall picture even more mixed. Kalita et al. (2016) attributed this to the incomplete vaporisation of the butanol blends within the combustion chamber, decreasing combustion efficiency.

GDI emission research has also generally highlighted lower HC emissions. Hergueta et al. (2017) showed lower THC emissions from B33 than gasoline at both high and low load values from a GDI research engine, which they attributed to butanol's shorter carbon chain length and higher oxygen content. The decrease in emissions was greatest at high load, which the authors attributed to the higher combustion temperatures and heat release rates allowing greater oxidation rates of THC during the combustion and exhaust stages. At low load, it is possible that these effects were somewhat counteracted by the poor butanol spray and mixing properties that occurred. Liu et al. (2019) found from their steady state chassis dynamometer GDI testing that THC emissions from butanol blends decreased at low vehicle speeds, but were more comparable to gasoline at higher vehicle speeds. However, over the NEDC they found that THC emissions were slightly lower than gasoline over the UDC but more comparable over the EUDC. This indicates that the vehicle has different behaviours over transient cycles

compared to steady state driving. Vojtisek-Lom et al. (2015) found from their Artemis cycle that the HC emissions of butanol blends compared to gasoline were comparable over the urban section, higher over the rural section, and then lower over the motorway section. Clearly there is some disagreement about the individual effects of speed on the HC emissions arising from butanol blends compared to gasoline for these vehicles. Liu et al. (2019) postulated that as the speed increased, the increased gas flow in the cylinder enhanced homogeneity and the combustion rate increased. Therefore the added benefit from the oxygenated fuels had less overall impact and all HC emission levels converged for the fuel blends. This effect would also explain the findings of Elfasakhany (2014).

When comparing HC emissions arising from butanol blends with iso-octane to those from ethanol blends with iso-octane, Broustail et al. (2012) found that the butanol results were higher than those of ethanol blends, while Costagliola et al. (2013) and Varol et al. (2014) found slight decreases from butanol blends with gasoline compared to ethanol blends with gasoline. Varol et al. (2014) noted that although ethanol has a higher oxygen content than butanol, their trend may be explained by the lower heat of vaporisation and higher heating value of butanol compared to ethanol. Elfasakhany (2017) found that B10 HC emissions had a dependence on engine speed; much lower HC than E10 at 2600rpm but higher HC than E10 at 3400rpm. Elfasakhany (2017) asserted that engine speed significantly influenced the gas-phase reactions of butanol fuel blends. Liu et al. (2019) found butanol THC emissions were higher than ethanol at low speed, but comparable with those of ethanol at medium and high speeds. However, Liu et al. (2019) also found that during the UDC, B20 emissions were lower than E20, but over the EUDC both were comparable. This latter result is supported by Vojtisek-Lom et al. (2015), who presented decreased HC emissions from butanol compared to ethanol over the urban section of the Artemis cycle but comparable results over the rural phase, and only slightly lower results over the motorway phase. Overall, there is clear indication of decreased HC emissions from butanol blends when compared to ethanol blends across a wide range of studies.

2.9.2.4 PN emissions from butanol blends

As with ethanol blending, there is a broad consensus in the literature that butanol blends have lower PN emissions than gasoline. This was the case of PFI test engine studies presented by Costagliola et al. (2013) and Gu et al.

(2012), GDI test engine studies presented by Hergueta et al. (2017) and Hergueta et al. (2018), and chassis dynamometer GDI vehicle research by Liu et al. (2019) and Vojtisek-Lom et al. (2015). No chassis dynamometer PFI vehicle studies probing the PN emissions resulting from n-butanol blends compared to equivalent ethanol blends or E0 have been found at the time of writing. There does not appear to be the same level of dependence on engine load and speed (Costagliola et al., 2013) as has been seen for some of the gaseous pollutants, as PN emissions from butanol blends have been widely reported to have reduced compared to gasoline across all conditions. Gu et al. (2012) attributed their decreased PN results to improved cylinder combustion, as well as a decreased fraction of aromatic hydrocarbons from butanol fuel. Vaporisation of light components in gasoline can leave heavy fractions such as aromatics prone to soot precursor formation during the expansion stroke (Hergueta et al., 2018). Hergueta et al. (2017) pointed to butanol's shorter carbon chain length and higher oxygen content, and Hergueta et al. (2018) added increased laminar flame speed to the list of probable reasons. Costagliola et al. (2013) attributed some of the PN decrease of butanol to its lower volatile fraction compared to gasoline, leading to fewer of the small volatile particles.

There is not total agreement between studies about the comparison of butanol blends with ethanol blends. Costagliola et al. (2013) found that PFI B10 PN emissions were lower than E10 and Hergueta et al. (2018) showed lower GDI B33 PN emissions than E25 PN. Vojtisek-Lom et al. (2015) also presented strong evidence of decreased PN from B25 compared to E15 using both Artemis drive cycle and on-road test data from a GDI vehicle. Liu et al. (2019) found that B20 PN emissions from their GDI vehicle were higher than E20 at 20km/h speed, comparable to E20 at 40-90km/h, and lower than E20 at 120km/h. However, over the NEDC cycle, they found that B20 results were higher than E20 for both the UDC and the EUDC. Liu et al. (2019) attributed the decreased PN from E20 (compared to E20) to the higher oxygen content than butanol further suppressing the formation of soot and oxidising soot that forms, resulting in lower emissions of PN. Also, a higher viscosity indicates that the in-cylinder mixing may be worse. Vojtisek-Lom et al. (2015) summarised the physical properties of butanol that could have contributed to higher PN emissions: lower vapour pressure, lower octane number, higher boiling point and higher viscosity. However, most test evidence points to a decrease in PN from butanol blends, which could be due to butanol's higher

latent heat of vaporisation (Vojtisek-Lom et al., 2015; Liu et al., 2019). Hergueta et al. (2018) also postulated that the higher in-cylinder pressure and exhaust temperatures that were observed during butanol combustion processes can promote further soot oxidation and post-oxidation, decreasing PN.

With regard to PN size distribution, Gu et al. (2012) and Vojtisek-Lom et al. (2015) saw no significant change between fuels for their respective PFI and GDI engines. Hergueta et al. (2017), Hergueta et al. (2018), Costagliola et al. (2013) and Zhang et al. (2014) all indicated that the size distribution shifts toward smaller diameters for butanol blends, due to a decrease of accumulation mode particles. Hergueta et al. (2017) theorised that the extra oxygen in the biofuels reduced the soot formation rate and increased soot oxidation, decreasing PN. Decreased PN in the exhaust, in turn, decreases the number of particle interactions that can occur, leading to lower levels of surface growth, coagulation and aggregation processes, thereby minimising the accumulation mode particles. They also stated that the accumulation mode particles have a close relation to the PAH content, which is reduced in butanol blended fuels, decreasing the numbers of accumulation mode PN. Costagliola et al. (2013) mentioned that their E10 and B10 blends both also have a lower contribution of ultra-fine particles than gasoline for their PFI engine, which they theorised was due to the lower volatile fraction of butanol compared to gasoline, leading to fewer of the small volatile particles.

Hergueta et al. (2017) and Hergueta et al. (2018) found a shift to the smallest diameters for both biofuels, being slightly greater for ethanol. They noted that the size of particulate matter depends on the competition between nucleation and oxidation mechanisms during the fuel combustion process. Hergueta et al. (2018) partly attributed ethanol’s higher emissions and shift to smaller particle diameters to the greater quantity of fuel in the combustion chamber (higher fuel consumption) meaning more small particles were formed. The shift to larger diameters combined with the lower total concentration of PN indicates that the results could be due to a greater amount of nucleation and agglomeration occurring for the butanol compared to ethanol. On the other hand, Zhang et al. (2014) found that B10 shifted to even smaller diameters than E10 from their GDI engine, but did not suggest a reason for this.

2.9.2.5 Unregulated emissions from butanol blends

There is limited research available into the unregulated emissions from SI vehicles using low percentage butanol blends in the literature. From the available literature, there appears to be a significant similarity between the behaviour of butanol blends with those of ethanol blends, when compared to gasoline.

Of the aldehydes, acetaldehyde generally shows increased emissions from butanol blends compared to gasoline (as confirmed by Costagliola et al. (2013) from a 1.6L PFI research engine, Kalita et al. (2016) from a Euro 3 1.2L PFI vehicle running a hot start NEDC on a chassis dynamometer, and Ratcliff et al. (2013) from a 2009 MY 3.6L PFI vehicle running the LA92 test cycle). There is less consensus regarding acetaldehyde emissions from butanol blends compared to ethanol blends: Costagliola et al. (2013) saw decreased acetaldehyde emissions from butanol blends, while Ratcliff et al. (2013) presented increased emissions from their work. As was the case for ethanol, the literature displays a range of views on the formaldehyde emissions from butanol. Broustail et al. (2012) witnessed a small increase in formaldehyde emissions from 10% butanol blends with iso-octane, compared with pure iso-octane, while Costagliola et al. (2013) and Ratcliff et al. (2013) witnessed more reliable increases. Kalita et al. (2016), however, presented decreases in their work. With regard to the comparisons of butanol blends against ethanol blends for formaldehyde emissions, Broustail et al. (2012) saw little difference, Costagliola et al. (2013) saw decreases, and Ratcliff et al. (2013) saw increases, compared to ethanol. Acrolein was seen to increase for butanol blends by Kalita et al. (2016) but decrease slightly by Ratcliff et al. (2013). Of notable ketones, acetone was seen to decrease under butanol blending by Ratcliff et al. (2013) but increase by Kalita et al. (2016). Ratcliff et al. (2013) found the decrease to be on a par with equivalent ethanol blends.

With regard to the hydrocarbons, there are again mixed results. Acetylene appears to decrease with regard to both gasoline and ethanol (Broustail et al., 2012; Costagliola et al., 2013). However there is disagreement about ethylene, with Broustail et al. (2012) finding decreased emissions but Kalita et al. (2016) presenting increased emissions against gasoline. Both agreed that ethylene emissions from butanol were higher than ethanol. Methane has shown a tendency to decrease under butanol blends, both with respect to gasoline (or its surrogates) and ethanol blends (Broustail et al., 2012;

Costagliola et al., 2013). Notably, N_2O has not been well discussed in literature thus far.

Costagliola et al. (2013) presented total VOC emission trends for both ethanol and butanol blends with gasoline, showing slightly decreased results for B10, while the results for E10 remained comparable with gasoline. This study also investigated individual VOCs, and presented an increase in benzene from butanol fuels, in contrast to the decrease presented for E10. This is in disagreement with Broustail et al. (2012), who presented a decrease in benzene from butanol blends. Ratcliff et al. (2013), meanwhile, found little change. Ratcliff et al. (2013) also probed 1,3-butadiene emissions from butanol, and found that the results were comparable to both gasoline and ethanol. All of the investigations into individual VOC species that have been mentioned have similar values between butanol and gasoline. As the reasons given for changes in ethanol VOC emissions also apply to butanol, this fact is unsurprising. Costagliola et al. (2013) do not attempt to explain their total VOC decrease witnessed for butanol.

2.9.3 Emissions from HEVs using biofuel blends

The investigation of both regulated and unregulated pollutants from HEVs is very important, as it allows prediction of their impact on total emissions from the transport sector, and how further adoption of these technologies may effect air quality and climate change. Specifically, it is important to understand how the new technologies introduced in HEVs may impact the emissions output under different conditions of operation. As bioethanol use in transportation is increasing from E5 to E10 in the UK, and alternatives such as butanol are being investigated, it is also important to study the effect of the use of these alternative fuels within hybrid systems. Only one previous paper studying this topic was found from an extensive literature search.

Suarez-Bertoa and Astorga (2016) measured both the regulated and unregulated emissions from a mild parallel HEV and a series-parallel PHEV over the certification WLTC test cycles, comparing the use of E5 and E10. The emissions measured were CO_2, CO, NO_x, NMHC, THC, NH_3, acetaldehyde and ethanol, given in Table 2.7. The following subsection is dedicated to discussing the results of Suarez-Bertoa and Astorga (2016).

2.9.3.1 HEV biofuel emissions comparisons

This subsection is dedicated to discussing the results of Suarez-Bertoa and Astorga (2016). Their PHEV displayed lower CO concentrations under E10 use compared to E5 use, while their mild HEV showed higher concentrations. This indicates that the PHEV is showing similar behaviour to the CVs discussed in Section 2.9.2.1, while the mild HEV showed the opposite. For NO_x, the concentrations increased slightly for E10 compared to E5 for the higher temperature condition, whereas the opposite relationship was true for the lower temperature. However, the uncertainty margins were too large to draw reliable conclusions. The results for CVs also showed closely aligned, mixed results. The THC results were comparable (mild HEV) or slightly lower (PHEV) for the E10 tests than the E5 tests, in line with the previous literature for ICEs.

Ethanol and acetaldehyde emissions presented during the cold start section until catalyst light-off at all tested conditions, but dipped below detectable levels once catalyst optimal operating temperature was reached. The emission of these pollutants was greater for E10 blends than E5 blends, comprising 10% and 5% of THC emissions respectively. The two vehicles showed opposite trends in NH_3 emission when comparing fuels. The PHEV displayed lower NH_3 concentrations under E10 use compared to E5 use, while the mild HEV showed higher concentrations. CH_4 levels were slightly lower or comparable for the E10 compared to the E5 tests.

Table 2.7 Regulated and unregulated emission factors over the WLTC cycle at 23°C. Adapted from Suarez-Bertoa and Astorga (2016).

	PHEV		**Mild HEV**	
	E5	**E10**	**E5**	**E10**
THC (mg)	9 ± 2	6.8 ± 0.1	12.9 ± 0.8	13 ± 1
CH_4 (mg)	1 ± 1	0.7 ± 0.1	1.0 ± 0.1	1.2 ± 0.1
NMHC (mg)	7.8 ± 0.6	6.1 ± 0.0	11.9 ± 0.7	11 ± 1
CO (mg)	80 ± 22	62 ± 4	206 ± 23	238 ± 25
NO_x (mg)	0.4 ± 0.7	0.5 ± 0	7 ± 2	7.8 ± 0.3
NH_3 (mg)	7 ± 4	1.9 ± 0.6	6.1 ± 0.3	8.0 ± 0.0
Ethanol (mg)	0.3 ± 0.3	0.8 ± 0.1	0.6 ± 0.1	0.7 ± 0.0
Acetaldehyde (mg)	0.1 ± 0.0	0.2 ± 0.1	0.2 ± 0.1	0.2 ± 0.1

The results of this paper are a valuable indication of the effect of ethanol addition into the hybrid fuel system, but there are some weaknesses. The tests were performed from full battery SOC to represent a ‘best case scenario’,

though additional testing at 88% SOC was performed to investigate the difference this makes to the emissions output. The lower initial SOC increased emissions for the PHEV but made no difference to the mild HEV. Given that most HEVs tend to maintain their charge in the region of 60% (Duarte et al., 2014), the approach may have altered the emission results and therefore requires further investigation.

Only a mild HEV and PHEV were tested, leaving a gap in the results for full HEVs. There was no investigation of PM or PN levels, which is an important feature of HEVs to investigate. In addition, the test was not performed on-road, and so did not account for real-world artefacts such as road grade. Only the WLTC cycle was used, and so only a certain set of engine load and speed operating conditions was utilised. Additionally, no investigation was performed into the causes of any emissions spikes, including the cold start behaviour and OBD vehicle operating conditions. Finally, the paper did not investigate any other biofuels such as butanol, and the effects that these have on emissions from HEVs. There is clearly scope for more investigation in this research area.

2.9.4 Summary of biofuel emissions

This section of the literature review has investigated the effects of blending ethanol and n-butanol into gasoline in the low percentages that will not adversely affect the workings of the combustion engine system. A summary of the literature findings are provided in Table 2.8. Overall, the literature notes decreased CO emissions from conventional SI vehicles when ethanol and butanol blends are used, compared to E0 neat gasoline. There is no such consensus regarding HEVs though, with the only study available giving mixed results for different HEVs. The results for NO_x and THC for both fuels are more mixed for both CVs and HEVs, with no firm consensus across the available literature, but generally close results between all three fuels.

There is a firm consensus in the literature regarding strong reductions in PN for CVs from both ethanol and butanol blends, compared to gasoline. Additionally, there is widespread agreement regarding a decreasing mean particle diameter with increasing biofuel blends, due to fewer accumulation mode particles, but no firm consensus around which biofuel causes the larger shift. Thus far only conventional PFI and GDI SI vehicles have been investigated, with a gap in the literature surrounding the PN emissions from HEVs.

With regard to toxic unregulated pollutants, the consensus for CVs is for generally decreased emissions of these pollutants from ethanol and butanol blends. Where there is general agreement that both acetaldehyde and formaldehyde increase under ethanol blending, there is only agreement that acetaldehyde increases under butanol blending, with mixed views regarding formaldehyde. As was discussed in section 2.8, HEVs can have quite different engine behaviours, meaning that this conclusion is not necessarily transferrable to this alternative technology vehicle. The only literature investigating unregulated pollutants from HEVs studied a narrow range of pollutants, leaving many other species yet to be investigated.

Table 2.8. Summary table of biofuel emission literature results

Article	Fuels of interest	Experimental device	Test Parameters	E5-E30 fuel resultant tailpipe emission results compared to ("vs.") pure gasoline (E0)	B5-B30 fuel resultant tailpipe emission results vs. E0 (and equivalent ethanol/gasoline blends ("E"))
Agarwal et al. (2015)	E0, E5, E15	PFI research engine	2500rpm @ various torques	~CO, ↓THC, ~NOx, ~CH_4, ~C2H6, ↑propane, ↓iso-butane, ↓ethylene, ↓acetylene, ↓propene,↓1,3-butadiene, ↓benzene, ↑acetaldehyde, ↑formaldehyde, ~acetic acid, ↑ethanol, ~acetic acid, ~SO_2,~NH_3, ↓N_2O, ~methane	-
Broustail et al. (2012)	E0, E25/iso-octane75	PFI research engine	2000rpm @ 3 & 5 bar IMEP	↓CO, ↓HC ↓ethylene, ↓methane, ↓acetylene, ↓benzene, ↓formaldehyde, ~↑acetaldehyde	~CO, ↓THC (↑ vs. E),↓NOx (↓vs. E), ↓ethylene & methane (↓ vs. E), ↓acetylene (↓ vs. E), ↓benzene (↓ vs. E), ↓formaldehyde (↑ vs. E), ~↑acetaldehyde (~ vs. E)
Canakci et al. (2013)	E0, E5, E10	PFI on chassis dynamometer	80 & 100 km/h @ various wheel powers	↓CO at low velocity, ↓NOx, ↓THC at 80km/h, inconclusive CO, ↓NOx, ~↓THC at 100km/h	-
Cho et al. (2015)	E0, E5, E10, E15, E20	GDI research engine	2000 rpm, varying injection pressure and timing	↓PN, ~ size distribution (except E10: secondary maximum at 23nm seen)	-
Costagliola et al. (2013)	E0, E10, E20, E30, B10	PFI research engine	various load and engine RPM points	↓CO, ~THC, ~NOx, ↓PN, ↑formaldehyde, ↑acetaldehyde, ~1,3-butadiene, ~methane, ~acetylene, ~VOC	↓CO, ~THC (↓vs. E), ~NOx (↓vs. E), ↓PN (↓vs. E), ↑formaldehyde (↓E), ↑acetaldehyde (↓ vs. E), ~1,3-butadiene, ↓methane, ↓acetylene (↓vs. E), ↓VOC (↓vs. E)
Dernotte et al. (2010)	E0, B20, B40	PFI research engine	2000rpm (highway driving), varying load	-	↓CO, ~THC, ~NOx
Elfasakhany (2014)	E0, B3, B7, B10	PFI research engine	2600-3400 rpm	-	↓CO at lower RPM, ~CO at higher RPM, ↓THC at lower RPM, ~ THC at higher RPM
Elfasakhany (2017)	E0, E3, E7, E10, B3, B7, B10	PFI research engine	WOT @ 2600-3400 rpm	↓CO, ↓UHC	↓CO @ low RPM, ↑CO @ high RPM (overall ↓CO(↑ vs. E)), ↓UHC (↓vs. E @ 2600rpm, ↑ vs. E @ 3400rpm)
Gu et al. (2012)	E0, B10, B30	PFI research engine	3000rpm, varying loads	-	↓CO, ↓NOx, ↓HC, ↓PN, ~ PNSD
Guerrieri et al. (1995)	E0, E10, E12, E14, E17, E20	6 PFI on chassis dynamometer	FTP-75	↓CO, ↑NOx, ↓THC, ↑acetaldehyde, ~formaldehyde	-
Hergueta et al. (2017)	E0, B33E5	GDI research engine	2100rpm, at both low load and medium load	-	↑CO @ low load, ↓CO @ high load, ~↓THC @ low load, ↓THC @high load ↓NOx @ low load, ~NOx @ medium load, ↓PN, ↓PNSD
Hergueta et al. (2018)	E0, E25, B33	GDI research engine	2100rpm, at medium load (urban WLTC)	↓PN	↓PN (↓PN vs. E)
Hernandez et al. (2014)	E0, E5, E15	3 PFI (MY 2004-2008) on-road	40km/h steady speed driving	↓CO, ~↓NOx, ↓THC	-
Hsieh et al. (2002)	E0, E5, E10, E20, E30	PFI research engine	various engine speeds and throttle positions	↓CO, ↓THC, ~NOx	-

Jin et al (2017)	E0, E10, E30	GDI on chassis dynamometer	FTP-75	↑CO (E10 only, ↓E30+), ↑NOx, ↑THC, ↓PN (urban), ↑PN (rural & motorway), ↑ethylene, ↑methane, ↓acetylene, ↓benzene, ~↓formaldehyde, ↑acetaldehyde, ↓1,3-butadiene	-
Kalita et al. (2016)	E0, B5, B10, B20	PFI on chassis dynamometer	hot start NEDC	-	↑CO, ↑HC ~NOx (↑B5, ↓B10/20), ↓NOx, ↑acetaldehyde, acrolein, acetone, ↓formaldehyde
Karavalakis et al. (2012)	E5.7, E10, E20	7 PFI on chassis dynamometer	-	↓CO, ~NOx, ~↑ THC, ↑acetaldehyde, ~formaldehyde, ↓BTEX,↓1,3-butadiene	-
Li et al. (2017)	E0, E10,E30	PFI research engine	3 & 5 BMEP, 1200rpm	↑CO (λ=1) , ↓CO (λ<1), ↓THC, ↓ NO_x	-
Liu et al. (2019)	E0, E20, B20	GDI on chassis dynamometer	steady speed testing & NEDC	Steady state: ↑CO @ low speed, ~↓CO @ high speed, ↓THC (at low speed, ~THC at high speed), ~NO_x @ low/med speed, ↓NO_x @ high speed, ↓PN @ low/med speed, ↑PN @ high speed, ↑FC. NEDC: ↑CO, ↑THC, ↓NO_x, ↓PN, ↑FC	Steady state: ↓CO (↓ vs. E) @ low speed, ~↑CO at high speed (~E)), ↓THC (@ low speed (↑vs. E), ~THC @ high speed (~ vs. E)), ~NO_x @ low/med speed, ↓NO_x @ high speed (~vs. E), ↓PN (@ all speeds), ↑FC(↓vs. E20). NEDC: ↓CO, ~↓NO_x, ↓THC, ↓PN (↑vs. E20), ~FC(↓vs. E20)
Luo et al (2015)	E0,E20	GDI research engine	1000-3500 rpm, varying loads	↑PN @ low load, ↓PN @ higher load	-
Masum et al. (2014)	E0, E20	PFI research engine	WOT, varying RPM	↓CO, ↑NO_x, ↓HC	-
Price et al. (2007)	E0, E10, E30	GDI research engine	1500 rpm	↓PN, ↓ accumulation mode PN, ↓HC @ low load, ↑HC @ high load	-
Ratcliff et al. (2013)	E0, E16, B17	PFI on chassis dynamometer	LA92 test cycle	↓CO, ~ NO_x, ~MMOG, ↑formaldehyde,↑acetaldehyde,~1,3-butadiene, ↓toluene	~ CO (↑ vs. E), ~ NO_x & ~NMOG, ↑formaldehyde (↑ vs. E) & ↑acetaldehyde (↑ vs. E), ~1,3-butadiene (~ vs. E), ~↓benzene (~vs. E), ↑ethylene (↑ vs. E), ↓ toluene, ↓acetone (~ vs. E)
Saikrishnan et al. (2017)	E0, E5, E10, E15	PFI research engine	2000rpm over various torques	↓CO, ↑NO_x, ↓THC	-
Singh et al. (2015)	E0, B10, B20	PFI research engine	1500, 2500, 3500 and 4500 rpm, over varying torques	-	~↓CO, (↑ @ higher RPM), ~↑THC, ~↑ NO_x
Suarez-Bertoa and Astorga (2016)	E5, E10	PFI HEV on chassis dynamometer	WLTC	~↓CO, ~↑NO_x, ~↓THC, ~NH_3, ↑ethanol, ~↑acetaldehyde	-
Varde et al. (2007)	E0, E10, E22	PFI research engine	1500 & 2500 rpm, varying torque	~CO, ~↓NO_x, ~THC, ~acetaldehyde	-
Varol et al. (2014)	E0, E10, B10	PFI research engine	1000-4000 rpm, constant break torque	↓CO, ↓THC	↓CO (~CO vs. E), ↓THC (↓THC vs E)
Vojtisek-Lom et al. (2015)	E0, E15, B25	GDI chassis dynamometer & on road (PN only)	Artemis cycle	~CO, ~NO_x, ~↑THC urban/rural, ~PN (engine), ↓PN on-road)	↓CO&HC motorway (~urban and rural) (↓CO &HC vs. E), ↑THC urban/rural (↓THC than E15 urban, ~rural), ↓ PN, ~ PN size distribution, ~↑NO_x urban(~vs. E)&rural (↑vs. E), ~↓ rural & highway(~vs. E)
Zhang et al. (2014)	E0, E10, E20, B10, B20	GDI research engine	2000rpm, 210Nm torque.	↓PN, ↓ accumulation mode PN	↓PN, ↓ accumulation mode PN

2.10 Research questions

The literature review above has outlined gaps in the current state of knowledge for many different related research areas. The effect that the RDE test has on reported emissions compared to both the WLTC type approval test, and real-world on-road driving, has still not been fully investigate. Further work is also required into HEV behaviour and the resultant emissions, including the use of low percentage biofuel blends with gasoline in these vehicles. The research questions to be addressed by the current work are:

1. How do the properties and emissions resulting from an HEV tested on the RDE compare with the WLTC and NEDC tests?
2. How have the different packages of RDE legislation changed the properties of that test and the reported emissions, and does the final RDE package sufficiently represent the behaviour and emissions seen in urban centres?
3. What behaviours specific to HEVs alter the emissions profile for these vehicles, and how?
4. How will the adoption of E10 fuel from E5 change the emissions from HEVs, and is B10 a viable alternative biofuel blend in terms of pollutant emissions?

2.11 Refined research aims and objectives

The refined research aims and objectives for this thesis will now be presented, in order to fill these research gaps.

2.11.1 Overall aim

The overall aim of this work is to investigate the regulated and unregulated pollutant emissions from HEVs, including those using biofuel blends, and to probe how effective the legislated WLTC and RDE tests are at representing their pollutant emission levels.

2.11.2 Objectives

The following objectives have been set:

1. Investigate HEV drive properties, characteristics and reported emissions resulting from RDE testing compared to legislative type approval test cycles (WLTC and obsolete NEDC), and to real-world on-road driving.

2. Investigate the effect that different packages of RDE legislation have on reported emissions of an HEV.
3. Study in detail the different elements of an HEV that make its behaviour different from a CV, and quantifying the effect that these behaviours have on the emissions.
4. Investigate the impact that the use of low percentage ethanol and butanol blends have on the emissions from an HEV.

2.11.3 Tasks

In order to achieve the overall aim and objectives, the following specific tasks have been identified:

1. Design a test route in and around Leeds that satisfies all of the criteria required of a legislative RDE test, with good repeatability.
2. Perform NEDC, WLTC and legislative RDE testing of an HEV, studying differences in the drive dynamics of the tests and the effect this has on the hybrid behaviour of the vehicle, such as engine behaviour and TWC temperatures.
3. Quantify the regulated gaseous pollutant results, as well as PN, PNSD and CO_2 results, from the above test types, to see how the test procedure and boundaries affect reported emission results for HEVs.
4. Analyse RDE tests according to each of the RDE packages that have been released with time, in order to assess the effects that the packages have on the reported emission factors.
5. Compare the drive characteristics and emissions of the urban section of the RDE test against rush hour congested real-world city driving, to assess whether the RDE is accurately capturing this type of driving where the greatest air quality health impacts are occurring.
6. Perform a real-world drive and then repeat the resultant speed trace on a chassis dynamometer, to assess what impact the use of a chassis dynamometer has on the vehicle and emissions.
7. Analyse the repeatability of multiple RDE tests using the same vehicle and route, in order to assess how this compares to other on-road driving.
8. Investigate the temperature profile and conversion efficiency of an HEV TWC during cold start driving to see how the reduced engine activity of an HEV affects the TWC and resultant emissions of CO, NO_x and THC.

Similarly, study whether engine-off periods during driving allow the TWC temperature to decrease lower than light-off temperatures.

9. Study the engine behaviour of an HEV, investigating how engine re-ignition events affect the emissions of regulated and unregulated gaseous pollutants, as well as PN, including size distribution.
10. Assess the repeatability of HEV behaviour during testing, to assess the reliability of certification emission values for HEVs under the current legislative test procedures.
11. Assess whether the hybrid behaviour of an HEV is similar under the use of E0, E5, E10 and B10 fuel mixtures.
12. Compare emissions of regulated and unregulated pollutants (including PN) and fuel consumption under the use of E0, E5, E10 and B10 fuel mixtures, to assess the effects that use of these biofuels has on emissions from an HEV.

Chapter 3
Methodology

3.1 Introduction

This chapter will present the research methodologies used in this work. It will detail the research vehicles, equipment, calculations of those parameters not directly measured, and further processing and analysis of the data. The main research vehicle used in this thesis is a Third Generation Toyota Prius. Specifications of this vehicle will be presented first, along with the details of other instrumentation on board the vehicle for all of the testing. The methods of fuel preparation and specifications of this fuel will then be outlined. The University of Bath (UoB) chassis dynamometer test cell and equipment used for most of the chassis dynamometer tests will be introduced next, followed by the equipment used for the certification RDE and other on-road testing performed with the Horiba OBS-ONE PEMS. Next, the additional testing (WLTC and RDE testing at test centres in China on vehicles other than the Third Generation Toyota Prius research vehicle) will then be detailed. Finally, the data processing methodologies and calculations used to attain the data and results presented in this thesis will be outlined.

3.2 Toyota Prius research vehicle and instrumentation

The vehicle utilised for the majority of research presented in this thesis was a Third Generation Toyota Prius, of model year 2010 and Euro 5 emission compliance. The vehicle was purchased from a registered Toyota dealer in 2014 with 26,000 miles on the odometer (Riley, 2016), and was used as a research vehicle thereafter. At the commencement of the current research, the vehicle had 30,000 miles on the odometer and underwent an extensive service at a Toyota registered garage. Figure 3.1 displays the NEDC results from this research vehicle, in a test it underwent directly prior to the tests presented in this thesis. The vehicle was fuelled with pure gasoline (E0) for this test. The results show that the vehicle emissions performance is very good, with all pollutants far below their respective limits.

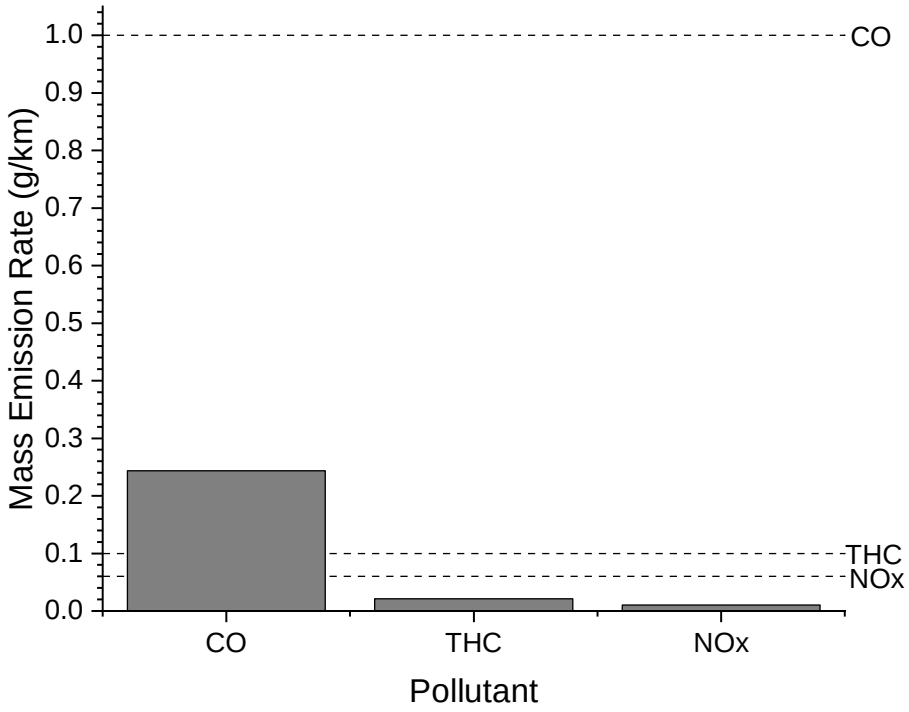

Figure 3.1 NEDC test results from Toyota Prius research vehicle, with applicable Euro 5 limits indicated.

This vehicle is outlined in detail by the Argonne National Laboratory report presented in Rask et al. (2010). The Toyota system features an Atkinson-cycle engine, two electric motors and a power-split device that is used to control the flow of energy between the electric and mechanical parts of the vehicle. The fuel economy and emission benefits are achieved through regenerative breaking, stop-start (also called 'idle stop-and-go') technology, electric operation at low loads, electric assist and optimised engine operation. Fuel economy is further increased by the addition of an electric water pump and exhaust heat recirculation system, which allows exhaust gas heat to be absorbed by the engine coolant to minimise thermal energy loss when desired. Table 3.1 below provides some basic specifications of the Toyota Prius.

This vehicle was commissioned as an emissions research vehicle for this work, and as such, some modifications were made to the vehicle. The equipment and instrumentation that was used with this research vehicle for all relevant testing will be detailed in the following subsections.

Table 3.1 Specifications of Third Generation Toyota Prius (Rask et al., 2010).

Vehicle	Toyota Prius 3rd Generation, Model Year 2010
Gasoline engine type	Aluminium double overhead cam (DOHC) 16-valve, 4-cylinder
Engine displacement	1.8 litres (1798 cc)
Engine bore x stroke (mm)	80.5 x 88.4
Engine compression ratio	13
Valvetrain	Four valves per cylinder with Variable Valve Timing with intelligence (VVT-i)
Induction system	Sequential multi-point EFI with Electronic Throttle Control System with intelligence (ETCS-i)
Ignition system	Electronic, with Toyota Direct Ignition (TDI)
Injection	Port fuel injection (PFI)
Intake	Naturally Aspirated (NA)
Engine power output	73 kW @ 5200 rpm
Torque	142 Nm @ 4000 rpm
Emission rating	Euro 5
Electric motor type	Permanent magnet AC synchronous motor
Electric motor power	60 kW
Electric motor torque	207 Nm
Electric motor voltage	650V maximum
Traction battery type	Sealed Nickel-Metal Hydride (Ni-MH)
Traction battery power	36 hp (27 kW)
Traction battery voltage	201.6V
Hybrid system net power	134 hp (100 kW)
Front suspension	Independent MacPherson strut with stabilizer bar
Rear suspension	Torsion beam
Steering	Electric Power Steering (EPS); rack-and-pinion with electric power-assist
Overall vehicle height/width/length (mm)	1490.98/ 1744.98/ 4460.24
Wheelbase (mm)	2700
Track (front/rear, mm)	1524/1518.92
Curb weight (kg)	1379.8
Seating capacity	5
Passenger volume (m^3)	2.65
Luggage capacity (m^3)	0.61
Fuel tank (l)	54

3.2.1 Sample points and thermocouples

A set of three sample points were welded into the exhaust system of the research vehicle, as shown in Figure 3.2. Sample point 1 was placed just before the inlet to the first TWC, to measure engine-out emissions (S1).

Sample point 2 was placed just after the outlet of the second TWC, to measure catalyst-out emissions (S2), and sample point 3 was placed just prior to the tailpipe, to measure tailpipe emissions (S3). Each sample point consisted of a piece of stainless steel tubing ¼" (6.35mm) inserted perpendicularly into the exhaust pipe, with three 3.3mm diameter holes equidistantly on the sampling probe across the diameter of the exhaust pipe, and an angled cut open end, all aligned facing the direction of exhaust flow for optimum sampling efficiency. Figure 3.3a and Figure 3.3b show photographs of the sample probe (S1) as an example.

Six K-type thermocouples were placed around the catalyst system and at the tailpipe to measure the exhaust temperature profile at 1Hz frequency, also shown in Figure 3.2. Thermocouples were placed to measure the gas temperature immediately prior to the TWC (T1), the TWC front-face temperature (T2) (both shown in Figure 3.3a and 3.3b), the gas temperature between the two TWC blocks (T3), the TWC rear-face temperature (T4) and the gas temperature immediately after the catalyst (T5). Finally, thermocouples were placed at the tailpipe to record the tailpipe temperature (T6), and under the rear bumper to measure the ambient air temperature out of direct airflow.

The sample lines and thermocouple wiring were all routed along the exhaust pipe, insulated in titanium heat wrap, and entered the cabin of the vehicle through a hole in the boot area. The thermocouple lines were connected to a data logger (Omega IOtech Personal Daq56, hereafter referred to as 'PDAQ') which logged the outputs to a laptop. The sample points emerged into the boot for easy attachment to sampling lines of emissions measurement equipment, and had blanking plugs to be screwed on if a sampling line was not in use.

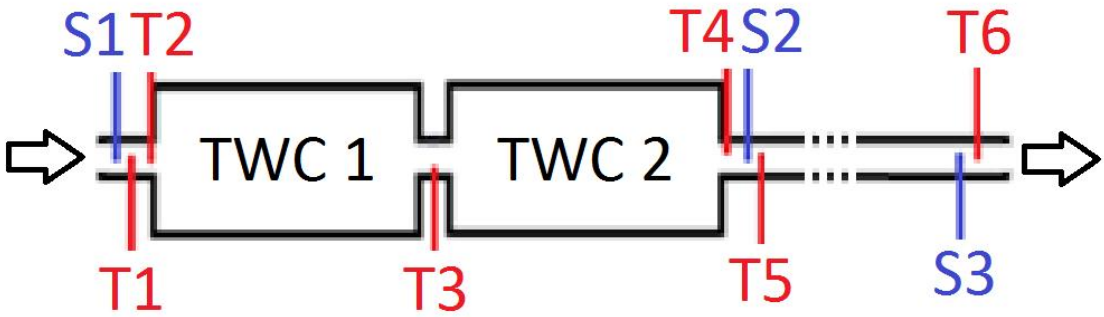

Figure 3.2 Diagram of thermocouple (T1-6) and sample point (S1-3) setup around the catalysts and at the tailpipe, with exhaust gas flow direction indicated by the arrows.

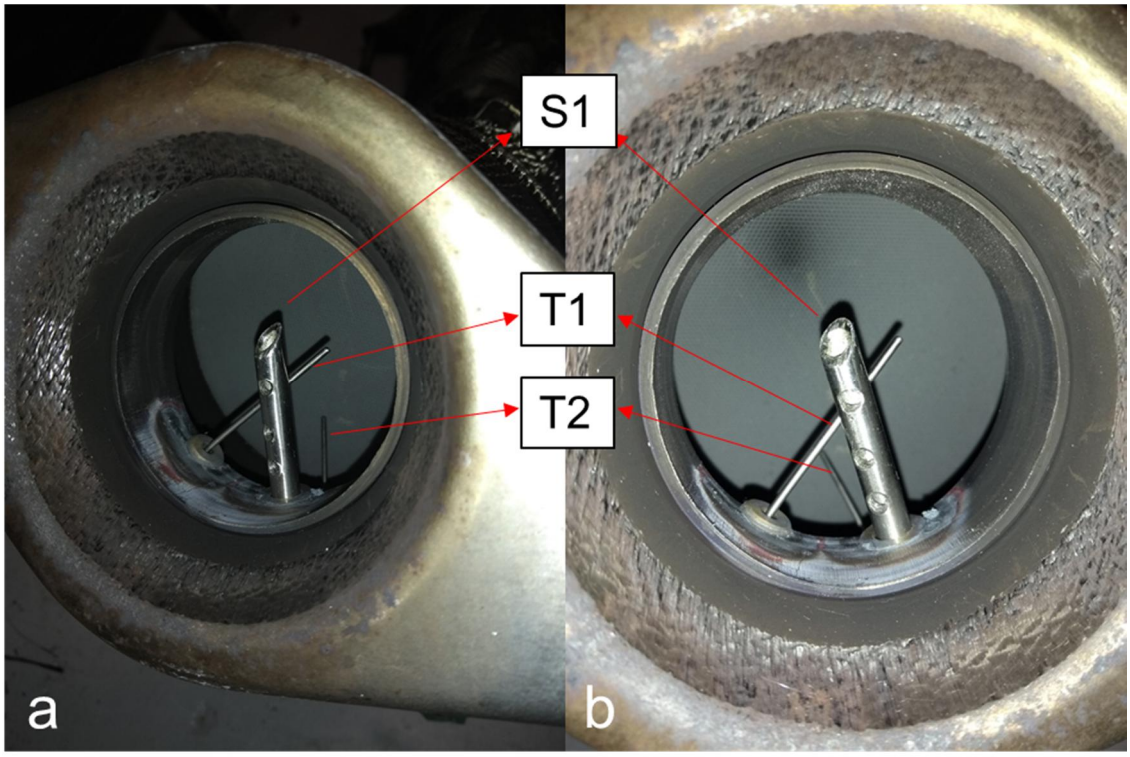

Figure 3.3 Photos (a and b) demonstrating the sample probe with inlets, and positions of sample probe S1, pre-TWC thermocouple T1 and TWC front-face thermocouple T2.

3.2.2 Power supply unit

A set of batteries were placed into the rear foot-wells of the Toyota Prius research vehicle to power the on-board equipment, allowing the vehicle's 12V power supply to remain unused during testing (ensuring no additional power was drained from the vehicle). The battery setup consisted of two 655HD Yuasa Cargo Heavy Duty 12V, 125Ah Batteries connected in series, together connected in parallel to two EXV140 Enduroline 12V, 142Ah Leisure Batteries also connected in series. This gave an overall capacity of 267Ah at 24V output, which was then inverted from direct current (DC) to alternating current (AC) by a Studer AJ 2400-24 inverter and used to power a 12-way multi-socket. A photograph of the power supply unit placement within the vehicle is provided in Figure 3.15 on page 121.

3.2.3 Horiba OBS 1000

A Horiba OBS 1000 MEXA-720 NO_x analyser was placed in the vehicle for 1Hz measurement of NO_x concentration and air/fuel ratio. This equipment was complete with a small tailpipe attachment for these non-extractive sensors in combination with a pitot exhaust flow measurement device. Table 3.2 gives

the measurement principles, ranges and accuracies of the measured properties.

Table 3.2 Horiba OBS-1000 (MEXA-720 and Pitot tube) measurement ranges and accuracies.

Measured Property	Measurement principle	Range and accuracy of measurement
NO_x	ZrO_2 sensor	0 - 1000 ppm: within +/- 30 ppm NO_x 1001 to 2000 ppm: within +/- 3% of readings 2001 to 3000 ppm: within +/- 5% of readings
Air/fuel ratio (A/F)	ZrO_2 sensor	9.50 A/F to stoichiometry: within +/- 0.35 A/F At stoichiometry: within +/- 0.15 A/F Stoichiometry to 20.00 A/F: within +/- 0.40 A/F 20.01 to 30.00 A/F: within +/- 0.90 A/F 30.01 to 40.00 A/F: within +/- 1.70 A/F 40.01 to 50.00 A/F: within +/- 2.60 A/F 50.01 to 60.00 A/F: within +/- 3.70 A/F 60.01 to 200.00 A/F: effectively +/- 0.5 vol% O_2

3.3 Research fuel preparation and use

For all testing performed by the University of Leeds Toyota Prius research vehicle, one of four different fuels was used. These were a pure gasoline (referred to as E0), a 10% by volume blend of ethanol in pure gasoline (referred to as E10), a 10% by volume blend of pure n-butanol in gasoline (referred to as B10) and a 5% ethanol market gasoline from a petrol station in Leeds (referred to as E5). The E0 used throughout this research, and for blending the E10 and B10, was a research grade RON 95 pure gasoline was ordered from Coryton Advanced Fuels. See Table 3.3 for some important properties of this fuel.

The E10 and B10 blends were made by splash blending ethanol and n-butanol into the E0 until each respectively contributed 10% of the fuel blends. A graduated container was used to ensure accurate quantities, and blends were made in 5L batches (each with 4.5L E0 and 500ml of ethanol and butanol respectively). Both the ethanol and butanol used were absolute, extra-pure (99+% purity) bottles purchased from Fisher Scientific Ltd and manufactured by Fisher Chemical.

The fuelling methodology was designed to ensure the entire fuel tank and fuelling system was purged of the old fuel. For all testing types, the entire tank was drained as fully as possible by a fuel pump attached to a connection in

the fuel return line under the vehicle bonnet. Approximately 2L of the new fuel was then poured into the fuel tank, and this process was repeated with the drained fuel from each iteration being deposited in a waste fuel container. This whole process was repeated three times to ensure the tank and fuel delivery lines were flushed, before the desired quantity of fuel for testing was finally added. After this, the vehicle was driven a short distance (approximately 1 mile), either on the chassis dynamometer or on roads, to ensure that the new fuel had completely flushed out the old fuel, and to give the ECU some time to adjust to the new fuel type and its different combustion properties.

Table 3.3 Properties of the research grade gasoline used as the E0 during this project.

Test	Method	Unit	Limit		Result
			Min	Max	
Appearance	Visual		Report		C&B
RON	EN ISO 5164		Report		95.0
MON	EN ISO 5163		Report		85.6
Density @ 15°C	EN ISO 12185	kg/L	Report		0.7397
DVPE @ 37.8°C	EN 13016-1	kPa	Report		66.2
Sulfur	EN ISO 20846	mg/kg	-	10.0	6.7
PIONA					
Paraffins	ASTM D6730 mod	% v/v	Report		17.3
Isoparaffins	ASTM D6730 mod	% v/v	Report		33.6
Olefins	ASTM D6730 mod	% v/v	-	18.0	10.9
Naphthenes	ASTM D6730 mod	% v/v	Report		2.8
Aromatics	ASTM D6730 mod	% v/v	-	35.0	35.0
Unknowns	ASTM D6730 mod	% v/v	Report		0.4
Benzene	ASTM D6730 mod	% v/v	-	1.00	0.29
Oxygenates					
Methanol	ASTM D6730 mod	% v/v	-	0.1	<0.1
Ethanol	ASTM D6730 mod	% v/v	-	0.1	<0.1
MTBE	ASTM D6730 mod	% v/v	-	0.1	<0.1
ETBE	ASTM D6730 mod	% v/v	-	0.1	<0.1
Other	ASTM D6730 mod	% v/v	-	0.1	<0.1
Oxygenates - Total	ASTM D6730 mod	% v/v	Report		<0.1
Carbon	ASTM D6730 mod	% m/m	Report		86.80
Hydrogen	ASTM D6730 mod	% m/m	Report		13.20
Oxygen	ASTM D6730 mod	% m/m	Report		0.00

3.4 University of Bath chassis dynamometer testing

3.4.1 Test vehicle and instrumentation

The Toyota Prius described in Section 3.2 was utilised for the UoB chassis dynamometer test project, with some additional instrumentation that will be described in the following subsections.

3.4.1.1 HEM OBD data logger

An OBD data logger was used to collect ECU information from the vehicle during testing. This was a HEM Data Corporation OBD Mini-logger, which will be described in this section. The logger connects directly into the OBD port of the Toyota Prius, on the underside of the dashboard to the right hand side of the steering wheel. This unit logs to a 1GB micro-SD card which can then be removed to read the data. A very wide range of parameters are available for logging, including a database of Toyota Prius specific enhanced OBD parameter IDs purchased from HEM Data Corporation. Figure 3.4 shows a photograph of the HEM OBD mini-logger, while Table 3.4 displays the parameters that were selected for logging at 1Hz frequency in the current project.

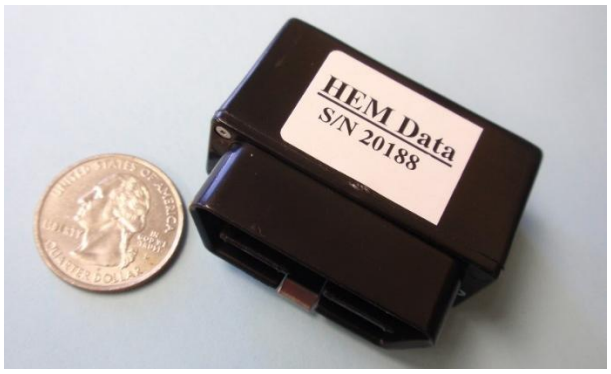

Figure 3.4 Photograph of the HEM OBD mini-logger. Source: HEM Data (2020).

Table 3.4 Parameters collected by HEM OBD Mini logger, with measurement units, where applicable.

Parameter Name	**Units**
A/C consumption power	W
Absolute load value	%
Absolute throttle position	%
Accelerator pedal position	%
Actual engine torque	Nm
AF lambda B1S1	
Air conditioning request	
Air flow rate from mass air flow censor	g/s
Ambient air temperature	Deg C
Atmosphere pressure	kPa
Auxiliary battery temperature	C
Bank 1 - Sensor 1 lambda (wide range O_2S) 1D	
Bank 1 - Sensor 1 O_2 current (wide range O_2S)	mA
Bank 1 - Sensor 1 O_2 voltage (wide range O_2S)	v
Bank 1 - Sensor 2 O_2 voltage	v

Barometric pressure	kPa
Batt pack current value	A
Battery voltage	V
Calculated load value	%
Catalyst temperature: bank 1 sensor 1	C
Catalyst temperature: bank 1 sensor 2	C
Commanded EGR	%
Commanded equivalence ratio	
Cruise requested driving force	kN
Diagnostic trouble code (DTC) count	Count
DTC numbers	hex
EGR step position	step
Engine coolant temperature	C
Engine idling request	
Engine RPM	RPM
Engine stop request	
Engine warm up request	
Fuel cut condition	
Fuel system status	Bitmapped
Generator (MG1) revolution	rpm
Generator (MG1) torque	Nm
Generator torque	Nm
HV start condition	
Hybrid battery pack remaining Life	%
Idle fuel cut	
Ignition advance	deg
Injection volume (cylinder1)	ml
Intake air temp	Deg C
Intake manifold absolute pressure	kPaA
Long-term fuel trim bank 1	%
Main batt charging request	
Motor (MG2) revolution	rpm
Motor (MG2) torque	Nm
Regenerative brake torque	Nm
Relative throttle position	%
Requested driving force	N
Requested power	W
Requested regenerative brake torque	Nm
Requested engine torque	Nm
Short term fuel trim - bank 1	%
State of charge (all Batteries)	%
Target air-fuel ratio	
Target EGR position	%

Throttle idle position	
Time since engine-start	Sec
Vehicle load	%
Vehicle speed sensor	km/hr

3.4.2 Chassis dynamometer test facility and in-house equipment

The UoB Centre for Low Emissions Vehicle Research (CLEVeR) allowed the use of their chassis dynamometer test cell for this project. The tests were performed on a 4WD AVL RoadSimTM 48” chassis dynamometer, within a test cell capable of temperature and humidity control. A near full frontal width road speed fan was placed approximately one metre in front of the vehicle for representative cooling of the full powertrain system.

There was a wide range of equipment employed to monitor the emissions during the tests performed. The tailpipe emissions were fed directly into a Horiba CVS-7100 system with bag sampling (3 bags) for total mass emissions. Two Horiba MEXA stack analysers (MEXA ONE and MEXA 7400) were employed to measure pre- and post- catalyst exhaust concentrations of CO_2, CO, NO_x, O_2 and THC at 10Hz frequency. An AVL SESAM i60 FTIR fast dual stream analyser was also placed on the tailpipe and pre-catalyst sample points, both measuring at 1Hz frequency. A Cambustion DMS500 fast particle size spectrometer owned by the University of Leeds placed at the tailpipe provided additional PN and PNSD data at 5Hz. The Horiba smooth approach orifice (SAO) and CO_2 tracer capability each also enabled exhaust flow determination and hence transient mass emission calculation, which could be compared back to the total bag mass emission results. The chassis dynamometer setup is outlined in Figure 3.5, the detection methods used by each of the pieces of apparatus are outlined in table Table 3.5 and the gas component species and their measurement ranges selected from the AVL SESAMi60 FTIR are given in Table 3.6.

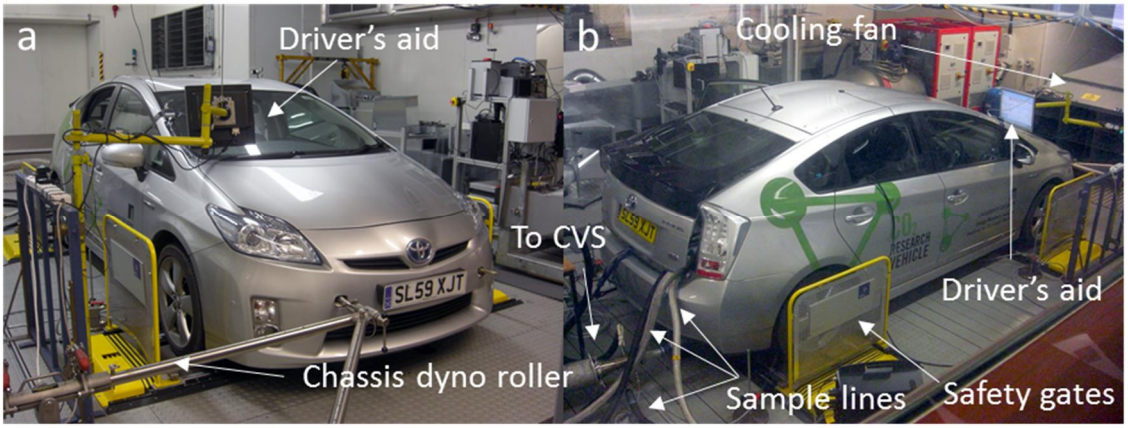

Figure 3.5 Labelled photographs (a and b) of the research vehicle on the chassis dynamometer at UoB CLEVeR facility.

Table 3.5 Emissions measurement systems employed.

Apparatus	Gas Component	Measurement Principle	Range of Measurement
Horiba MEXA 7400 and Horiba MEXA ONE	NO	Chemiluminescence Detector (CLD)	0-10 ~ 0-10000 ppm
	NO_2	Chemiluminescence Detector (CLD)	0-10 ~ 0-10000 ppm
	CO	Non-dispersive Infrared (NDIR) detector	0-0.5 ~ 0-12 vol%
	CO_2	Non-dispersive Infrared (NDIR) detector	0-0.5 ~ 0-20 vol%
	O_2	Magnetopneumatic detector	0-1 ~ 0-25 vol%
	THC	Flame Ionisation Detector (FID)	0-10 ~ 0-20000 ppmC
AVL SESAM i60	See Table 3.6	Fourier transform infrared spectroscopy (FTIR)	See Table 3.6
Cambustion DMS-500	PN	Condensation particle counter (CPC)	5nm-1µm

Table 3.6 Selected gas components and measurement ranges of the AVL SESAM i60 FTIR. Source: AVL (2020).

Species	Range (ppm)	Species	Range (ppm)
Acetylene, C_2H_2	0-1000	Formaldehyde, HCHO	0-1000
Ammonia, NH_3	0-1000	Methane, CH_4	0-1000
Carbon dioxide, CO_2	0-200000	Methanol, CH_3OH	0-1000
Carbon monoxide, CO	0-100000	Nitrogen dioxide, NO_2	0-1000
Ethane, C_2H_6	0-1000	Nitrogen monoxide, NO	0-10000
Ethanol, C_2H_5OH	0-1000	Nitrous oxide, N_2O	0-1000
Ethene, C_2H_4	0-1000	Sulphur dioxide, SO_2	0-1000
		Water, H_2O	0-250000

3.4.3 Overall test cell configuration

The configuration of the systems listed in the previous sections is given in Figure 3.6. The two available Horiba MEXA stack analysers and AVL FTIR analysers were placed one each in the pre-catalyst and tailpipe sampling positions to allow an investigation into the catalyst efficiency, while the DMS500 was placed at the tailpipe to allow deeper investigation into the tailpipe emissions.

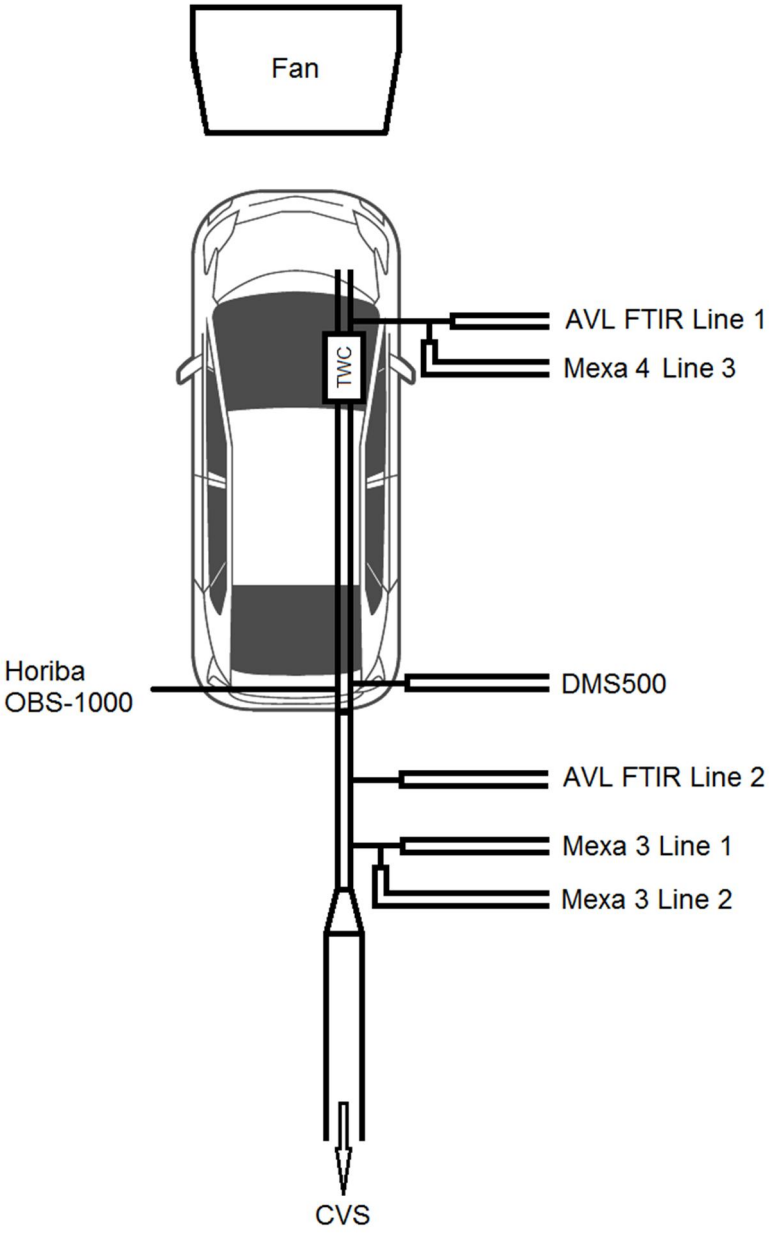

Figure 3.6 Configuration of emissions measurement systems used for the chassis dynamometer testing.

"Mexa 3" is the MEXA 7400 and "Mexa 4" is the MEXA ONE. The two AVL FTIR lines connect to a single AVL SESAM i60 FTIR fast dual stream analyser.

3.4.4 Test procedure and cycles

All tests were driven by the same trained test driver. The chassis dynamometer was warmed up according to the manufacturer's instructions at the beginning of each day of testing. The various pieces of equipment were turned on and any preparations for testing were performed as necessary, according to user manuals.

3.4.4.1 NEDC

Two cold start NEDC cycles were conducted largely in accordance with the NEDC procedures. The main purpose of these tests was to confirm that the research vehicle was operating normally, particularly with regard to emissions abatement. A secondary purpose was to allow a comparison of NEDC with WLTC for this HEV. The vehicle was fuelled with pure gasoline (E0) for both tests.

3.4.4.2 WLTC

The World Harmonized Light Duty Test Procedure (WLTP) was largely followed in the preparations for the WLTC testing, however there were some small divergences so the procedure will be outlined below. The hybrid battery SOC was conditioned to 67.8% at the end of the previous day, while the smaller 12V battery was not manipulated. The vehicle was then turned off and was soaked overnight in a temperature of 23°C and humidity of approximately 35%. The WLTC tests were performed from cold start the next morning after all the instruments were warmed up, calibrated, set sampling and logging. The equipment was left to run continuously for the duration of the test, and stopped after the test finished. The driving was done using a human driver, and there were no violations for the tests performed. Once the test was completed, the bag samples were analysed. The test cell and equipment was then prepared for the next test.

The WLTC version 3 was used for the WLTC tests. Figure 3.7 displays the speed trace of this test cycle. The WLTC tests were performed with E0, E10 and B10 fuel blends. One cold start test was performed for E0, three for E10 and two for B10, with additional warm start tests to further prove reliability.

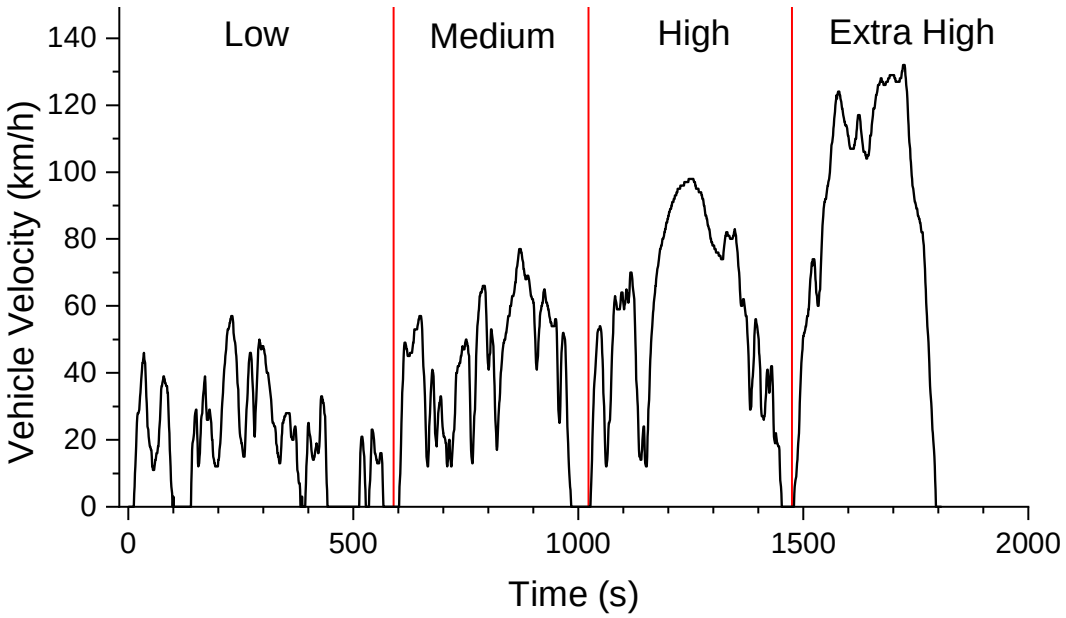

Figure 3.7 Velocity profile of the WLTC (version 3) used during this project.

3.4.4.3 Shortened RDE

A test cycle was designed on roads in and around the city of Leeds, UK, and the speed trace was then repeated on the chassis dynamometer. This test cycle adhered to very strict requirements for optimum conversion into a chassis dynamometer test cycle. Firstly, it had to be no longer than 2430s total duration, and to allow the urban, rural and motorway sections to each to be captured by individual bags, the length of each of these sections was not more than 810s. Additional limits on the aggressiveness of the dynamics were also present, but normal driving fell within these limits. A route, shown in Figure 3.8, was designed that satisfied all of these requirements, for which the resulting velocity trace is displayed in Figure 3.9.

With reference to Figure 3.8, the vehicle left the Energy Building at point 1, travelled along Cemetery Road and turned right onto Clarendon Road. At point 2 the vehicle turned right onto A660 and travelled down this road until point 3 where it turned onto Blackman Lane before heading back along Blenheim Terrace (A660) up past the Parkinson Building to Rampart Road (point 4). The vehicle then performed a circuit around the Cinder Moor, turning left at the end of Rampart Road onto Woodhouse Street, left again onto Cliff Road, left onto A660. The vehicle continued south east on A660, and continued on this road until point 5, where it turned east onto the Inner Ring Road (A64 (M)). At point 6 the vehicle exited the Inner Ring Road onto New York Road, and continued to point 7 where it turned right on to Marsh Lane.

The vehicle continued on Marsh Lane, leading to A61 at point 8 and A63 at point 9 (also called Pontefract Lane). At point 10 the rural phase commenced, and the vehicle crossed over Knowsthorpe Gate Roundabout, Thornes Farm Roundabout (11) and Bell Wood Roundabout (12) to the East Leeds Link Interchange (M1 Junction 45) (point 13), at which point it turned East onto the M1 Northbound. The vehicle went up to Junction 46 and (point 14) and back to Junction 45, at which point the rural section ended. The motorway section started at point 15 and consisted of the vehicle travelling up to Junction 47 (point 17) and back down, exiting the motorway and finishing the test at point 18 on Junction 45.

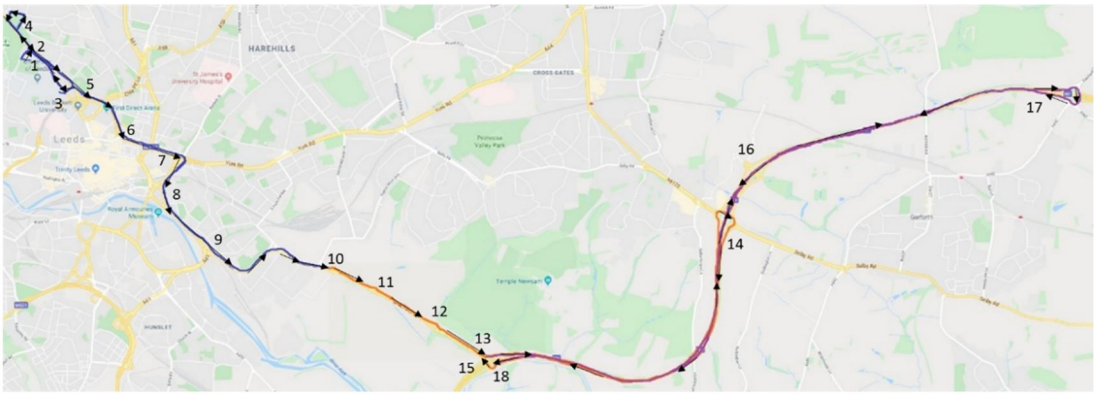

Figure 3.8 Map of the shortened RDE route driven on the road for repetition on the chassis dynamometer.

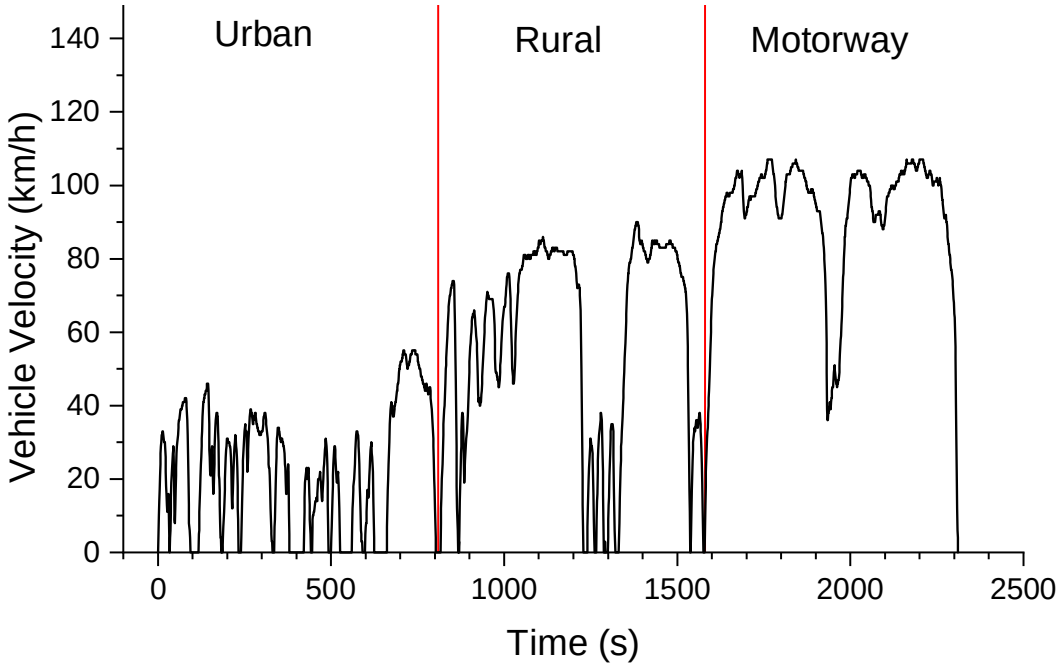

Figure 3.9 Velocity profile of the shortened RDE route driven on the road for repetition of the chassis dynamometer.

For the shortened RDE tests, the same procedure as described above for the WLTC was followed, except for the initial SOC of the vehicle hybrid battery. In order to investigate the influence of initial battery SOC, a range of 3 different SOCs were selected and used for each fuel type. These were 52.2%, 60.0% and 67.8% for across fuel types E0, E10 and B10. All shortened RDE tests were from a “warm start”, with initial engine coolant temperature of 50±3°C (maximum deviation range was 13°C and standard deviation was 7.7°C across all tests, with no linear trend in temperature with initial SOC suggesting low bias impact on the results).

In addition to these chassis dynamometer tests, two E10-fuelled shortened RDE tests were performed on the chassis dynamometer as a replica of the original on-road velocity profile attained in Leeds. This involved utilising the same initial SOC of 67.1%, ambient temperature of 10°C and initial engine coolant temperature of 34±1°C, matching those parameters of the original on-road test. This allowed a comparison between on-road and on-chassis dynamometer behaviour, including CO_2 emissions and NO_x emissions from the Horiba OBS 1000.

3.5 Leeds certification RDE testing and real-world driving

3.5.1 Test vehicle and instrumentation

The Toyota Prius described in Section 3.2 was used to perform certification RDE testing (according to Package 4 of the legislation) and other on-road testing. The additional vehicle instrumentation will be described in the following subsections. The total weight of the vehicle with all instrumentation on-board was approximately 1800kg (measured by Horiba Mira), which is at the maximum gross vehicle weight for this vehicle.

3.5.1.1 GPS tracker

A GPS tracking unit produced by Racelogic was utilised to accurately log the movement of the vehicle at 20Hz frequency. The VBOX Lite II module has GPS input from an antenna placed on the roof of the vehicle, and analogue output to the PDAQ recording the thermocouple temperatures around the exhaust system (see Section 3.2.1) to allow for reliable time alignment between the GPS information and the temperature information. A CAN02 module was connected to the VBOX Lite II, with inputs from the vehicle ECU via a Vehicle Can Bus (VCI) module, and an Inertial Measurement Unit

(IMU03) module. The IMU03 can provide highly accurate measurements of pitch, roll, and yaw rate using three rate gyros. The GPS tracker was placed on the centre of the roof of the vehicle at its highest point, while the IMU03 module was fixed to the chassis floor in the centre of the vehicle, according to the manufacturer's instructions. The units were all powered by a mains adapter plugged into the multi-socket, which came from the on-board batteries outlined in Section 3.2.2. The parameters recorded by the Racelogic equipment are displayed in Table 3.7 along with the specific unit from which each parameter originated.

Table 3.7 Parameters recorded by the Racelogic VBOX equipment. GPS speed is measured from the GPS tracker of the VBOX, while vehicle speed is calculated by the vehicle ECU.

Number of Satellites	VBOX II Lite
GPS coordinated universal time (UTC) (s)	VBOX II Lite
Latitude (°)	VBOX II Lite
Longitude (°)	VBOX II Lite
GPS Speed (km/h)	VBOX II Lite
Heading (°)	VBOX II Lite
Height (m)	VBOX II Lite
Brake Pedal Position (%)	VCI
Vehicle Speed (km/h)	VCI
Pitch Rate (°/s)	IMU

3.5.1.2 Horiba OBS-ONE PEMS

A Horiba OBS-ONE PEMS system was installed into the research vehicle. This included the OBS-ONE GS and PN units for gaseous and particulate emission measurement along with a central control (CC) unit and B-size pitot tube with thermocouple and sample points that interfaced with the CC via a pitot flow meter module (PF) unit. Electricity was supplied to the equipment through a power supply (PS) unit. In addition to these units, there was an OBD connector, GPS tracker, and weather station. Fuel consumption was calculated based on fuel data input by the user.

A photograph of the configuration is given in Figure 3.10, while the pitot tube tailpipe attachment configuration is detailed in Figure 3.11. Table 3.8 gives the measurement principles and ranges for different components of engine exhaust measured by the Horiba OBS-ONE. Table 3.9 gives general physical specifications of the equipment, while Table 3.10 details the workings of the PN unit specifically. The PEMS system was installed, secured and operated

according to the manufacturer's instructions, and an overview of this is displayed in Figure 3.12 and Figure 3.13.

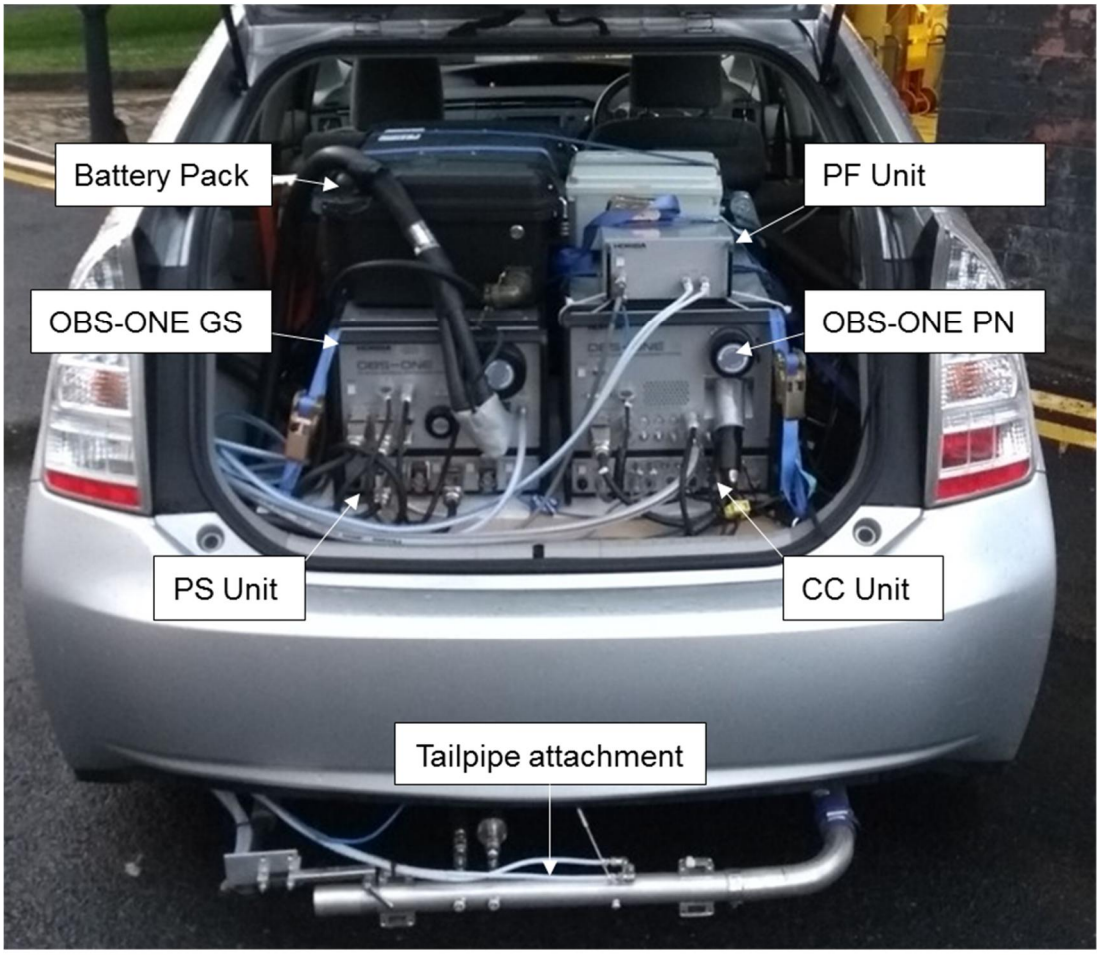

Figure 3.10 Horiba OBS-ONE equipment installed into the Toyota Prius research vehicle.

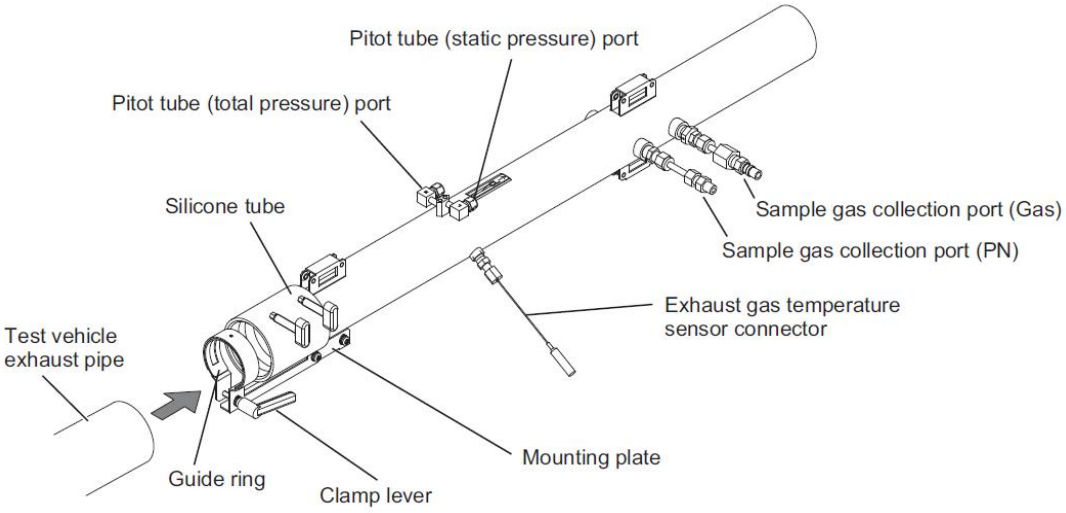

Figure 3.11 Horiba pitot tailpipe attachment diagram. Source: Horiba (2017).

Table 3.8 Measurement principles and ranges for different components/ properties of engine exhaust measured by Horiba OBS-ONE.

	Measurement Principle	**Measurement Range**
CO	Heated NDIR	0-0.5 to 0-10 vol%
CO_2	Heated NDIR	0-5 to 0-20 vol%
NO, NO_x, NO_2[1]	Heated CLD	0-100 to 0-3000 ppm
Sampling Method	Wet measurement	-
Exhaust Flow Rate	Pitot flow meter	0-4.5 m3/min
PN	Condensation particle counter (CPC)[2]	0 ～ 5×10^7 particles/cm^3 Diameters 23～1,000 nm

[1] NO_2 calculated as NO_x – NO, [2] Isopropyl alcohol a special grade reagent (99.5%) working fluid

Table 3.9 General specifications of the Horiba OBS-ONE GS and PN units.

Horiba OBS-ONE Unit	**GS**	**PN**
Power Supply	DC 24 V	
Power Consumption (Max.)	Approx. 0.25 kW	
Mass	Approx. 32 kg	Approx. 18 kg
Battery	Deep-cycle, sealed lead battery of DC 24 V 35 Ah (5 hour rate), operation time approx. 3 hours	
Operating Condition	Temperature: -10 ～ 40 °C, Altitude: 0 to 2,000 m above sea level, Relative humidity: less than 80% (No condensation)	

Table 3.10 Further specifications of Horiba OBS-ONE PN unit.

Particle size range	Detection efficiency <60% at 23nm, >60% at 50nm, limited to 1µm by inlet cyclone
Dilution ratios	Primary: 10, Secondary: 9
Flow rate	Sample flow 0.7 L/min
Catalytic stripper	>99.8% of 30nm geometric mean diameter (GMD) polydisperse tetracontane and 128nm GMD emery oil at 350°C

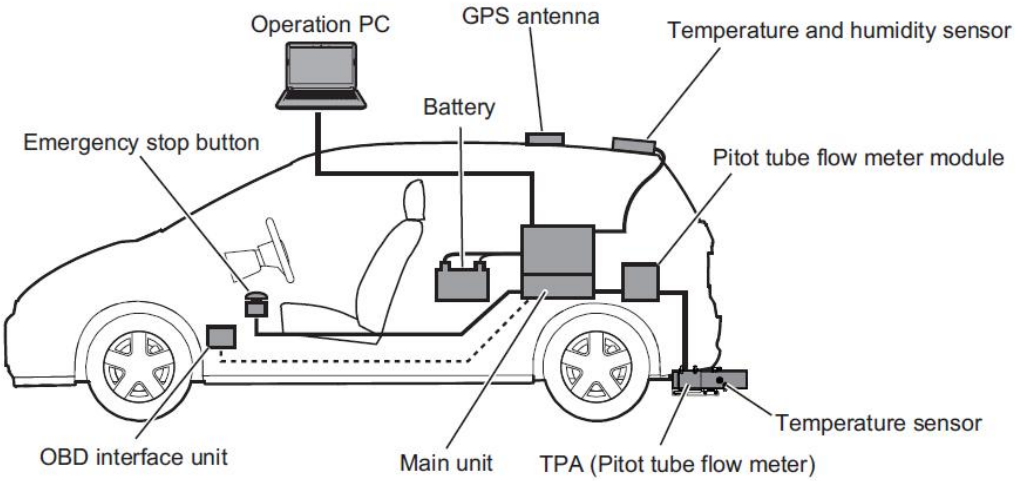

Figure 3.12 Configuration of the Horiba OBS-ONE LDV specification. Source: Horiba (2017).

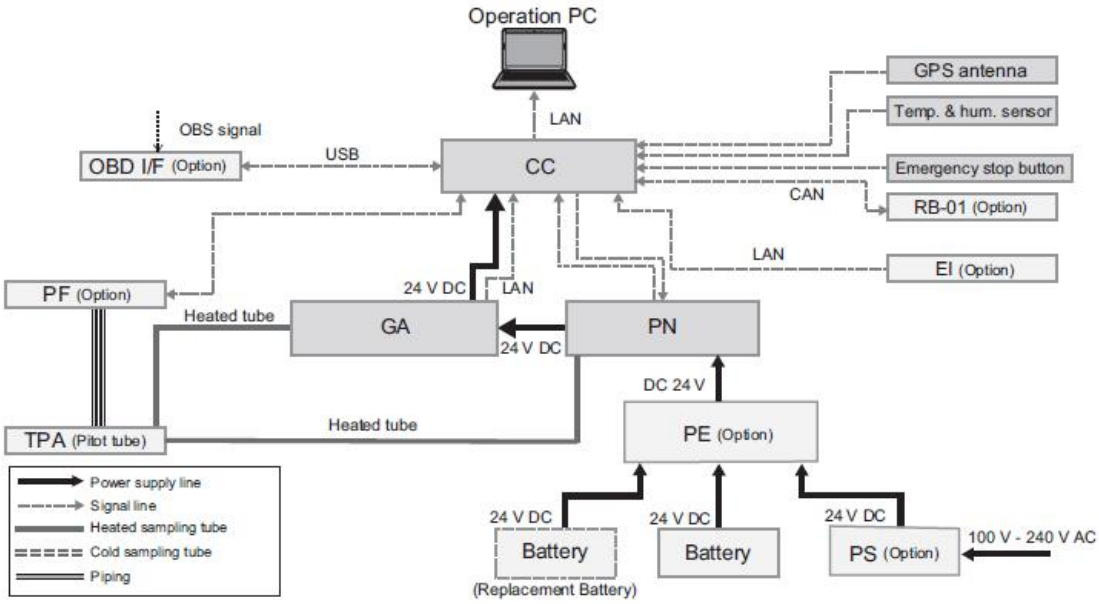

Figure 3.13 Connection diagram, showing how the various Horiba OBS units are connected. Source: Horiba (2017).

Prior to each test, the instrumentation was turned on and warmed up until each unit reached its target operating temperature (the sampling system, filter and cell operate in a window between 90-100°C, while the detector operates between 50-70°C and the NOx converter operates between 200-240°C). The laptop associated with the unit was also switched on, and the Horiba software used to interface with the instrumentation was opened. During the warm-up time, other preparations could be made. First, all the sample lines were blown through using compressed air to ensure no blockages existed. This was done at the connection point to the PEMS GS and PN units. The sample lines were

disconnected and then compressed air of approximately 2 bar was blown in the direction of the sample probes into the pitot tube attachment. Next, the isopropyl alcohol (IPA) cartridge was recharged with IPA. The cartridge was removed from the PN unit and placed within an alcohol fill capsule of isopropanol for a few minutes. Excess drips were removed and the cartridge was then locked back into its slot on the PN unit. A new NH3 scrubber filter was also inserted into the GA unit. Each desiccant dryer was used for a small number of tests, until their weight increased by a certain value outlined by the manufacturer. At this point it was changed for a fresh desiccant dryer while the old one was dehumidified.

A vacuum decay check was performed on the GS unit, whereby a blanking plug was attached to the end of the GA sample line and the unit then attempted to draw sample. If there were any leaks in the system, these would be inferred by a lack of resulting vacuum, and the GS would fail the vacuum decay check. A PN functionality check was performed by attaching a HEPA filter to the end of the PN sample probe. Once the functionality check was commenced, the unit drew ambient air through the HEPA filter and measured the PN values continuously. If the value was above a certain threshold of 100 #/cm^3, then the PN unit failed the functionality check.

Once the equipment was fully warmed, the calibration was performed. This was done by connecting alpha grade span and zero gas bottles (ordered from The BOC Group to adhere to strict Horiba requirements) to the span and zero inputs on the GA. A pressure of approximately 1 bar was set on the regulator, and a regulator inside the GA further limited the pressures entering the unit. Calibration was performed just before and just after each test, with the ambient conditions for each kept as similar as possible between calibrations.

The initial processing of the test data was performed on a laptop connected to the PEMS system, using the NA DIAdem HoribaPP software program. This software produced reports summarising important properties of the trip.

3.5.1.3 Horiba RDE CoDriver

The STARS Horiba RDE CoDriver software was utilised from a small tablet during the RDE tests as a means to assess the progress of each test in real-time. As explained in Chapter 2 Section 2.7.7, the test had to adhere to several different dynamic requirements for each phase, as well as the distance for each phase being at least 16km. The drive proportion of urban, rural and

motorway sections was displayed, along with the RPA and 95th percentile of the positive product of velocity and acceleration (v.a_{pos}[95]) of those drive modes. Figure 3.14 shows this application in use. This allowed any necessary adjustments to be made to the driving style in order to ensure RDE test compliance.

Figure 3.14 User interface of the STARS co-driver software. Source: Horiba (2020).

Information panel shows instantaneous velocity, whole trip distance and time and dynamics of each drive portion.

3.5.1.4 Gasmet DX4000 FTIR

A Gasmet DX4000 was attached at the tailpipe sample point for emissions sampling. This analyser has a similar setup to that used for UoB chassis dynamometer testing, with FTIR unit, sampling unit, and heated lines. The resolution was 8cm^{-1} and the heated lines were maintained at 180°C to prevent condensation. The multi-pass sample cell has a path length of 5m (longer than that of the AVL SESAM i60, meaning resolution at high sampling frequencies is more difficult), and is made of gold and rhodium coated aluminium. The detector is a thermos-electrically cooled mercury cadmium telluride detector, and the IR source is SiC ceramic operated at 1550K (Gasmet Technologies, 2013). The species reported by this FTIR are provided in Table 3.11. The FTIR was strapped onto one of the rear passenger seats, with sample probe routed to the sample point S3 at the tailpipe. The exhaust was vented outside the vehicle through a hole in the boot compartment. The FTIR unit was powered by the batteries outlined in Section 3.2. A photograph of the setup is given in Figure 3.15.

Table 3.11 Selected components and measurement ranges of the Gasmet DX4000 FTIR.

Species	Range (ppm)	Species	Range (ppm)
Acetaldehyde, CH3CHO	0-200	Formaldehyde, CHOH	0-100
Acetylene, C2H2	0-100	Hexane, C6H14	0-500
Ammonia, NH3	0-500	Methane, CH4	0-1000
Benzene, C6H6	0-500	Nitrogen dioxide, NO2	0-5000
Butadiene, C4H6	0-100	Nitrogen monoxide, NO	0-2000
Carbon dioxide, CO2	0-300000	Nitrous oxide, N2O	0-500
Carbon monoxide, CO	0-10000	Propane, C3H8	0-500
Ethane, C2H6	0-500	Sulphur dioxide, SO2	0-1000
Ethanol, C2H5OH	0-500	Water vapour, H2O	0-200000
Ethylene, C2H4	0-500	Acetic acid, C2H4O2	0-500

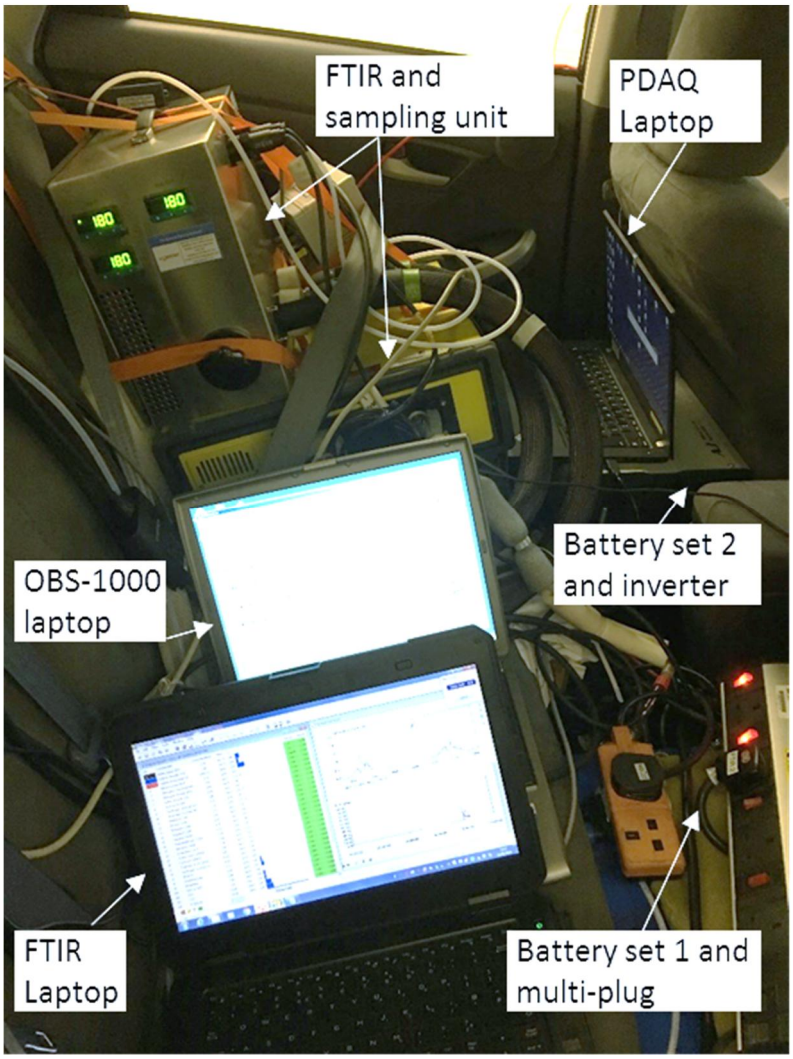

Figure 3.15 Photograph of the Toyota Prius research vehicle rear cabin with the experimental equipment indicated.

3.5.2 Test routes and procedures

3.5.2.1 Certification RDE route

A route around the city of Leeds that adhered to the requirements of the regulatory RDE test was designed. This was done using a ‘trial and error’ methodology, checking whether permutations of ‘trial’ RDE routes passed the criteria according to the instructions in the RDE regulations (European Commission and Council of the European Union, 2017) using vehicle speed and altitude data from the VBOX GPS unit. When a route was found that repeatedly passed the RDE criteria, this was chosen as the final route to be repeated for RDE testing with PEMS equipment.

All RDE tests were driven from cold start, with the vehicle left to soak in ambient temperatures for at least six hours prior to test start. The route commenced near the garage where the vehicle was prepared, and the vehicle manually pushed to this starting point in the neutral gear ‘key on, ignition off’ state, in order to achieve cold start. The whole route is outlined on the map in Figure 3.16, with blue lines representing urban driving, orange representing rural driving, and purple representing motorway driving. Repeats of urban sections occurred where the numbers 1 to 5 are displayed on the map. Sections 1 and 2 were each driven 4 times in total, while sections 4 and 5 were each driven twice, to perform the full RDE test cycle.

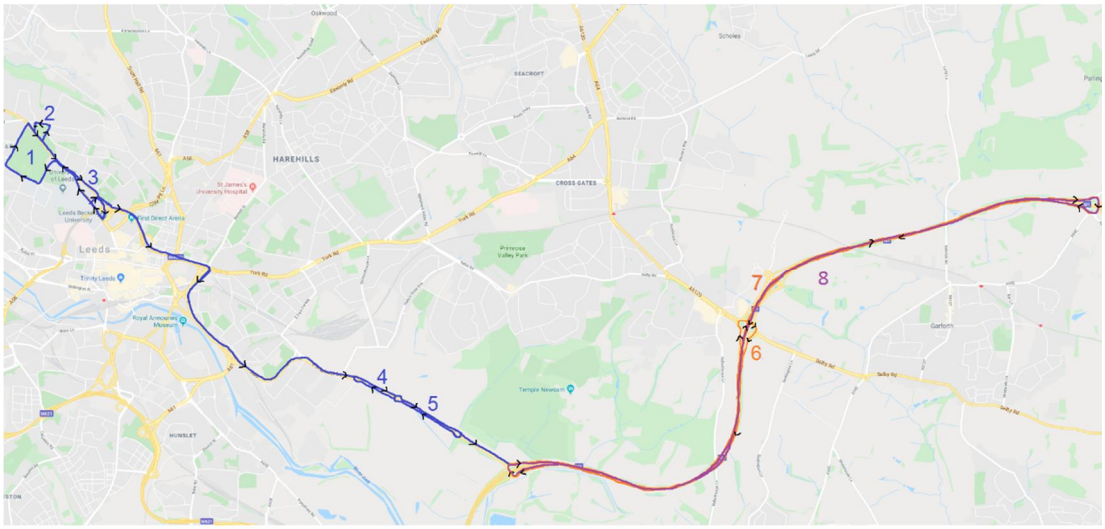

Figure 3.16 RDE drive route used for testing.

Blue lines represent urban driving, orange represents rural driving, and purple represents motorway driving.

A closer map of the urban section is given in Figure 3.17. Point 1 is the garage. The vehicle was pushed from point 1 to the traffic lights at point 2, and the test

started five seconds before the traffic lights at the crossroads turned green. The vehicle then traversed Blackman Lane to turn right onto Woodhouse Lane (point 3). The vehicle then turned right at the end of Woodhouse Lane to (point 4) to take Blenheim Terrace (A660) up past the Parkinson Building to Clarendon Road (point 5). Turning left onto Clarendon Road, the vehicle performed 4 repeats around Woodhouse Moor (points 5, 6, 7, 8, 5 etc.) until on the fourth repeat, at point 10, the vehicle turned left off A660 onto Rampart Road. The vehicle then performed 4 circuits around the Cinder Moor, turning left at the end of Rampart Road onto Woodhouse Street, left again onto Cliff Road, left onto A660 and left back onto Rampart Road. On the fourth circuit, at point 11, the vehicle continued south east on A660, and continued on this road until point 12, where it turned east onto the Inner Ring Road (A64(M)). The vehicle exited the ring road onto New York Road, and continued to point 13 where it turned right on to Marsh Lane. The vehicle continued on Marsh Lane, leading to A61 at point 14 and A63 at point 15 (also called Pontefract Lane). At point 16 the vehicle traversed straight over Knowsthorpe Gate Roundabout, but at the following roundabout (Thornes Farm Roundabout) the vehicle turned 180° (point 17) and went back up to Knowsthorpe Gate Roundabout where it turned 180° again (point 18). Travelling south east on A63 the vehicle traversed straight over Thornes Farm Roundabout (point 19) to continue down to Bell Wood Roundabout (point 20) where the vehicle turned 180° to head north west again toward Thornes Farm Roundabout. At point 21, the vehicle turned 180° at Thornes Farm Roundabout to head south east again. At point 22 the vehicle traversed straight over Bell Wood Roundabout to the East Leeds Link Interchange (M1 Junction 45), at which point it turned East onto the M1 Northbound. This was the end of the urban phase.

Referring back to Figure 3.16, the rural phase consisted of driving up from Junction 45 to 46 and back down (number 6), then up from Junction 45 to 47 and back down to Junction 45 (number 7). On re-entering the M1 eastbound, the motorway phase commenced, which consisted of driving twice up to Junction 47 and back down to Junction 25 (number 8, repeated). The driving speeds for these were suitable to the section of RDE test phase that they were completing.

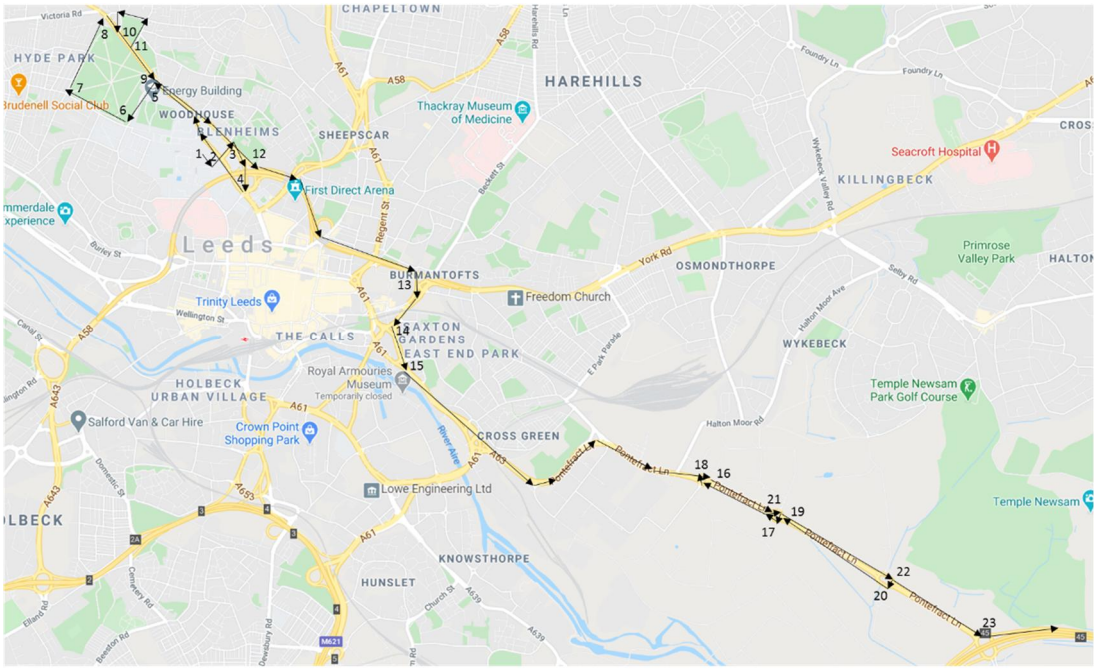

Figure 3.17 Urban section of RDE given in more detail.

3.5.2.2 Real-world driving routes

In addition to this RDE route, some other non-certification routes were driven to study the emissions behaviour of driving styles not necessarily covered by the RDE legislation, namely those in highly congested driving conditions. To do this, two different routes were chosen. The first (hereby called ‘City Centre’ route) was a drive around Leeds city centre four times during morning and evening rush hour (between 8-9am, and 5-6:30pm), and the second (hereby called ‘Headingley’ route) was a drive north out of the city along a main exit road during the evening rush hour (between 5-6:30pm). The drive cycles are outlined in Figure 3.18 and Figure 3.19 respectively. Both of these tests were performed from cold start, to simulate typical conditions on a vehicle used only for commuting on a working day.

As shown in Figure 3.18, the City Centre route was performed around the centre of Leeds. It commenced from within a garage located on Lodge Street (point 1). All emissions and vehicle behaviour tracking systems were switched on at least five seconds before the ignition was activated. After this, the vehicle was driven out of the garage, then placed into park while the garage door was closed behind it. The vehicle was then driven to the end of the Lodge Street and across the intersection ahead, in the same direction as for the RDE test. The vehicle turned right onto the A660 (point 2) and continued through point 3 until the crossroads with Merrion Street (point 4), where it turned left and

travelled east along Merrion Street until it met new Briggate (point 5). The vehicle followed the road to the left, and then headed onto New York Road at the following intersection (point 6). At the end of New York Road the vehicle turned right onto the A61 (point 7) which is part of the Inner Loop Road. The vehicle followed the Loop Road onto Kirkgate (8), The Calls (9), Call Lane (10) and Swinegate before heading past the Railway Station (11) on Bishopgate Street and then on to Quebec Street (12). The vehicle then turned right onto King Street (13) and East Parade, before turning right onto Great George Street (14) to get back to Merrion Street (15). The vehicle commenced a further three of these Inner City Loops (points 4 to 15). At the end of the fourth loop, the vehicle turned left back onto Woodhouse Lane until Lodge Street (point 16), where it went back to the garage (point 17).

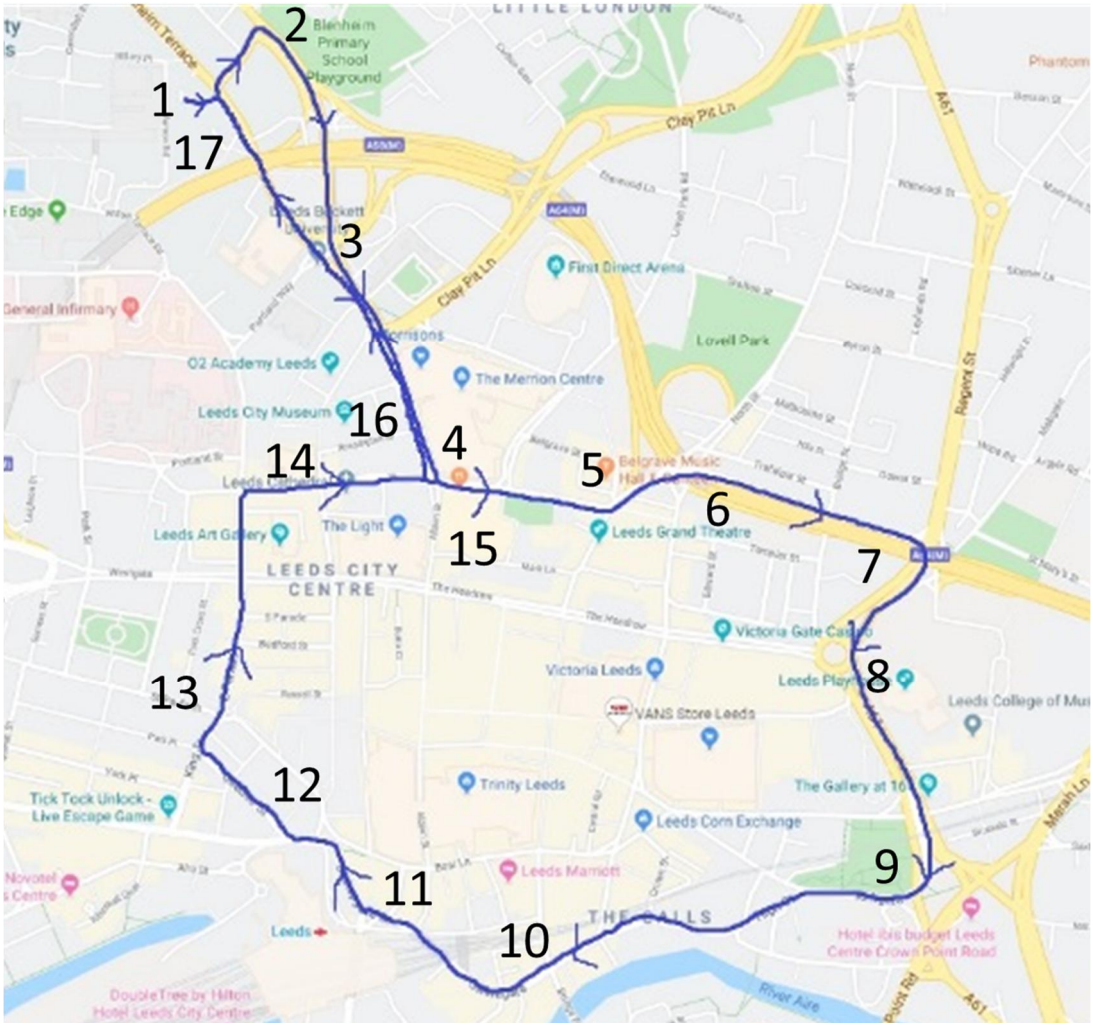

Figure 3.18 City Centre test route. Four circuits of the loop depicted were performed.

The Headingley route displayed in Figure 3.19 commenced from the garage (point 1). At the end of Lodge Street, the vehicle turned left onto Blenheim

Terrace (point 2) and followed this road onto the A660 out of Leeds through Headingley on urban roads (4) until it reached the roundabout intersection with the dual carriageway Ring Road (A6120) at point 5. The vehicle turned right at the roundabout onto the A6120 (point 6) and continued until the next roundabout, located at the intersection with the A61 (point 7). The vehicle turned around at this roundabout, and then headed back west along the A6120 and at point 8 turned back onto A660 toward the garage in the same manner in which it arrived, except at point 9 it continued on the A660 a short distance and turned right onto Blackman Lane (point 10) to arrive back to Lodge Street.

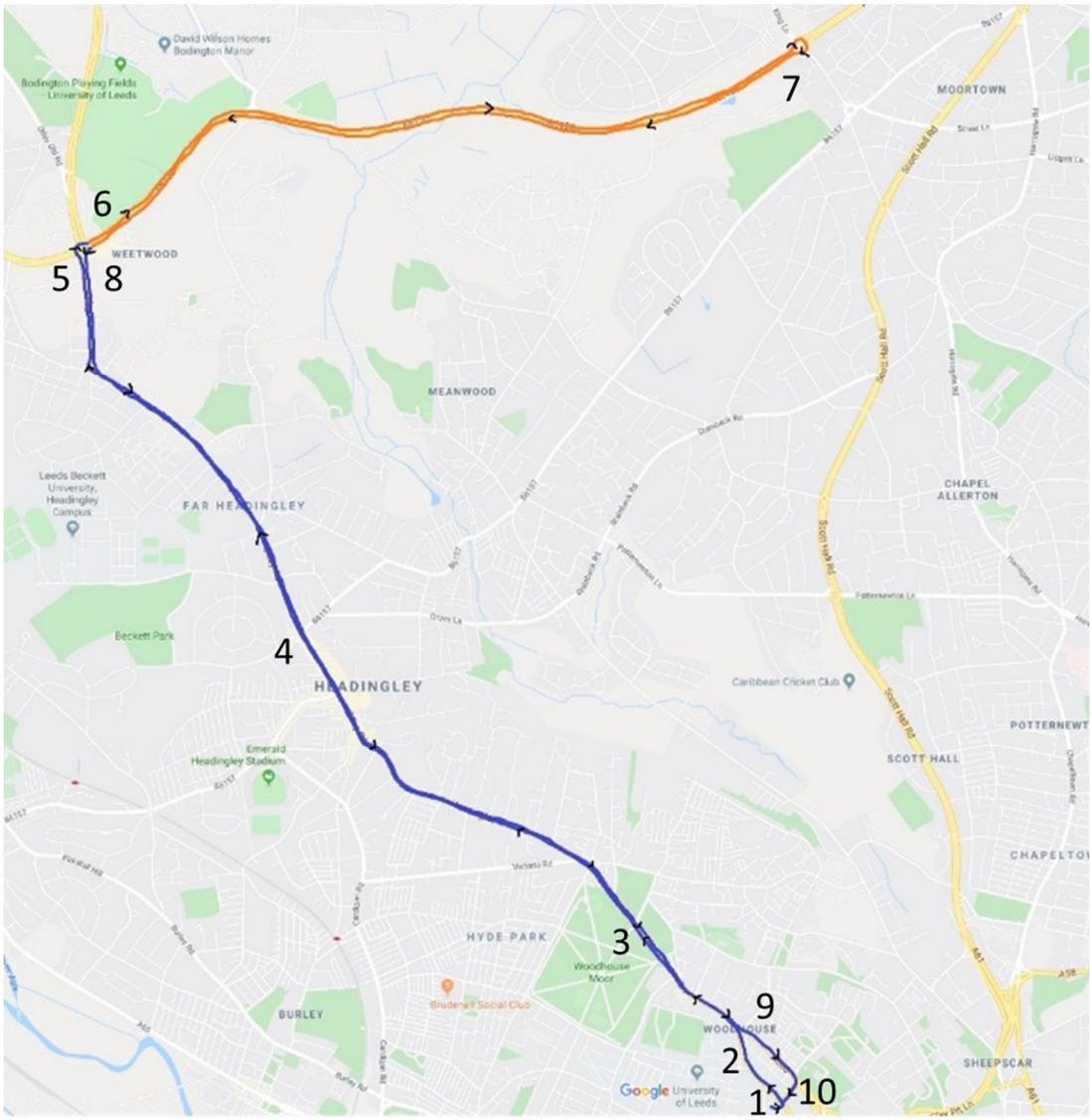

Figure 3.19 Headingley route.

The blue section denotes typically congested driving while the orange section denotes a dual carriageway, allowing a rural driving style.

3.5.2.3 Testing conditions

All tests were performed by the same driver, and took place within a three week time frame. The ambient conditions were largely similar across tests, except for some precipitation variations. Details of ambient conditions for each individual test are detailed in Table 3.12.

Table 3.12 Full details of on-road ambient conditions for Leeds certification RDE testing and real-world driving tests.

Test No.	Fuel	Route	Ambient temp (°C)	R.H	Pressure	Altitude	Precipitation
1	B10	RDE	18.2	56.3	100.3	71	Rain
2	B10	City Centre	13.6	95.3	100.2	44.5	Rain
3	B10	RDE	14.7	76.4	100	70	Rain
4	B10	RDE	13.6	72.2	101	70.1	Dry (wet ground)
5	B10	RDE	16.7	51.4	101.6	69.7	Dry
6	B10	RDE	15.7	62.4	101.5	70.7	Showers
7	E5	RDE	16.2	59.2	101.5	70.9	Dry
8	E10	RDE	12.5	89.2	101.4	70	Showers
9	E10	RDE	11.9	78.2	101.4	70.9	Light showers
11	E10	RDE	11.2	87.4	100.2	69.2	Dry (wet ground)
12	E10	RDE	13.2	93.4	100.3	72	Rain
13	E10	City Centre	13.9	90.4	100.7	52.5	Rain
14	E10	RDE	16.3	63.9	100.6	70.9	Dry
15	E10	RDE	13.7	90.3	100.6	70.7	Rain
16	E0	RDE	17.6	50	100.6	69.8	Dry
17	E0	RDE	16.2	43.7	100.9	70.2	Dry
18	E0	RDE	18.8	43.1	101.4	71.8	Dry
19	E0	City Centre	20.2	35.4	102	47.5	Dry
20	E0	RDE	20.7	44.1	101.8	71.1	Dry
21	E0	RDE	21.6	50.9	101.6	69.7	Dry
22	E0	RDE	18.4	59.4	101.7	70.2	Dry
23	E5	RDE	15.5	90.7	101.5	70.7	Rain
24	E5	RDE	17.4	88.2	101.3	70.7	Dry
25	E5	RDE	21.0	82	101.3	70.8	Dry
26	E5	RDE	14.1	96.5	101.8	70.2	Heavy rain
27	E5	RDE	14.1	89.7	102	71.1	Showers
28	E5	City Centre	13.4	85.7	103	51.9	Dry
29	E5	City Centre	16.4	69.4	103.2	44	Dry
30	E5	City Centre	13.8	72.1	103.3	47.7	Dry
31	E5	Headingley	24.8	48.6	102.3	98.9	Dry
32	E5	City Centre	15.3	68.4	102.8	47.6	Dry
33	E5	Headingley	23.5	53.6	101.7	95.9	Dry
34	E5	City Centre	17.0	65.2	101.6	46.1	Dry
35	E5	Headingley	20.8	48.6	101.4	95.5	Dry
36	E5	City Centre	18.7	49.4	102.5	46.7	Dry

3.6 Other research vehicles, test facilities and drive cycles used

Some data that was gathered from other research facilities will also be presented in the results sections of this thesis. This data will be labelled as such where presented. This section will outline the test methodologies and procedures for the research facilities producing this data.

3.6.1 China WLTC and RDE testing

Certification testing was performed in China at test facilities located in Beijing and Xiamen. A range of gasoline fuelled SI vehicles and HEVs were selected to perform one certification WLTC and one certification RDE test each. RDEs were in compliance with the Package 2 of RDE regulation; European Commission (EC) Regulation 2016/427. The vehicles were all light duty vehicles of class M1. Table 3.13 summarises some key characteristics of these vehicles, while Table 3.14 gives the time-averaged ambient conditions the RDE and WLTC tests performed, and selected drive properties of the RDE tests for each vehicle in each location. All values reported were measured during testing, unless otherwise indicated. All tests performed were under dry ambient conditions.

Table 3.13 Key characteristics of the test vehicles used.

Vehicle	Toyota Prius	Toyota Corolla	Toyota Prius	Toyota Corolla	Honda XRV	Toyota Camry	Toyota Highlander	Peugeot 308	VW Passat	Skoda Octavia
Powertrain	HEV	HEV	HEV	ICE	ICE	ICE	ICE	ICE	ICE	ICE
Engine Capacity (L)	1.8	1.8	1.5	2.0	1.5	2.0	2.0	1.2	1.8	1.6
Maximum Power (kW)	100	100	82	90	96	108	162	100	118	81
Maximum no. People	5	5	5	5	5	5	7	5	5	5
Emission Compliance	Euro 5	China-6	Euro 4	Euro 5	Euro 5	Euro 5	Euro 5	Euro 5	Euro 5	Euro 5
Injection	PFI	PFI	PFI	PFI	DI	PFI	PFI+DI	DI	DI	PFI
Transmission	CVT	CVT	CVT	CVT	CVT	4AT	6AT	6AT	7DCT	6AT
Curb Weight	1379	1302	1350	1285	1205	1510	1925	1305	1580	1250
T or NA	NA	NA	NA	T	NA	T	-	T	NA	T
After-treatment	TWC	TWC	TWC	TWC	TWC	TWC	TWC	TWC	TWC	TWC
HEV Battery Type	NiMH	NiMH	NiMH	n/a	n/a	n/a	n/a	n/a	n/a	n/a

Table 3.14 The ambient conditions and drive properties of RDE tests performed in China.

Test Vehicle	Toyota Prius	Toyota Corolla HEV	Toyota Corolla	Honda XRV	Toyota Camry	Toyota Highlander	Peugeot 308	VW Passat	Skoda Octavia
Location	Beijing	Beijing	Xiamen	Beijing	Xiamen	Beijing	Xiamen	Xiamen	Xiamen
Ambient temp (°C)	5.75	29.05	25.95	10.25	21.26	15.05	21.35	27.65	27.64
R.H. (%)	37.9	29.4	41.5	23.1	57.23	28.7	56.8	50	50.94
Pressure (kPa)	102.9	101.8	101.8	103	101.7[a]	102.2	101.8	101.6	101.55[a]
Altitude (m)	24.8	28.2	17.4	30.2	18.93[b]	29.7	17.6	21.8	18.93[b]
Average velocity (km/h)	38.8	48.0	51.7	47	43.92	34.1	45.2	48	44.95
Total distance (km)	72.407	76.406	82.364	75.892	80.18	68.094	82.454	82.256	78.4
Total duration (s)	6720	5726	5733	5813	6316	7181	6563	6166	6194
Stop duration (s)	1310	909	490	772	922	2616	773	618	796
Stop period number (#)	32	26	12	25	23	27	18	22	15
Maximum speed (km/h)	114.31	112.38	115.59	114.18	114.06	123.09	115.88	117.81	112.10

[a] values inferred from the RDE official report for that vehicle, [b] values estimated as the average value for all other trips in that location.

3.6.1.1 RDE test procedure

The RDE testing was performed using certification PEMS equipment. Seven of the tests were performed using the Horiba OBS-ONE PEMS equipment, while two of the tests (Toyota Camry, Skoda Octavia) were performed using the AVL M.O.V.E PEMS iS equipment. The Horiba OBS-ONE equipment has already been introduced in Chapter 2 Section 2.6 and detailed in Chapter 3 Section 3.5.1.2. The AVL M.O.V.E has been introduced in Chapter 2 Section 2.6. More detailed properties of the AVL M.O.V.E PEMS are given in Table 3.15 (AVL, 2010).

Table 3.15 Properties of the AVL M.O.V.E PEMS. Source: AVL (2010).

Operating temp	-10°C to 45°C
Dimensions	Approx. 482,6mm x 356mm x 540mm/ 670 mm
Weight	Approx. 50kg
Power demand	22.5 to 27V DC, approx. 450W
Sample flow rate	< 3.5 l/min
Measurement Range	NO/ NO_2: 0 to 5,000 ppm (NO), 0 to 2,500 ppm (NO_2) CO/ CO_2: 0 to 5 vol% (CO), 0 to 20 vol% (CO_2) PN: 0 – $3x10^7$ #/cm^3
Accuracy	CO: 0 to 1,499 ppm: ±30 ppm abs., 1,500 ppm to 49,999 ppm: ±2% rel.; CO_2: 0 – 9.99 vol%: ± 0.1 vol% abs., 10 - 20 vol%: ±2% NO: 0 – 5,000 ppm: ±2% rel. NO_2: 0 – 2,500 ppm: ±2% rel. PN: 0 – $3x10^7$ #/cm^3: ± 300 #/cm^3

For each test, the PEMS equipment was placed into the rear of the vehicle, with the tail-pipe attachment and heated sample probe connected to the tail pipe as per the corresponding manufacturer instructions. A GPS antenna and an ambient temperature and humidity sensor were placed on the roof of the vehicle, while an OBD interface unit was connected to the OBD port. These sensors were all connected to the main gas sensor unit via universal serial bus (USB) cables. The equipment was connected to batteries external to the engine. The equipment was then warmed up and calibrated according to the manufacturer's instructions before testing was commenced.

Each test was performed according to the RDE test procedure guidelines set out in Commission Regulation (EU) 2016/427 (with the exception of the Toyota Corolla, which commenced from warm start). The tests were performed in two different Chinese cities – Beijing and Xiamen – with the test route used in each of the two locations being self-consistent, given in Figure 3.20 and Figure 3.21 respectively.

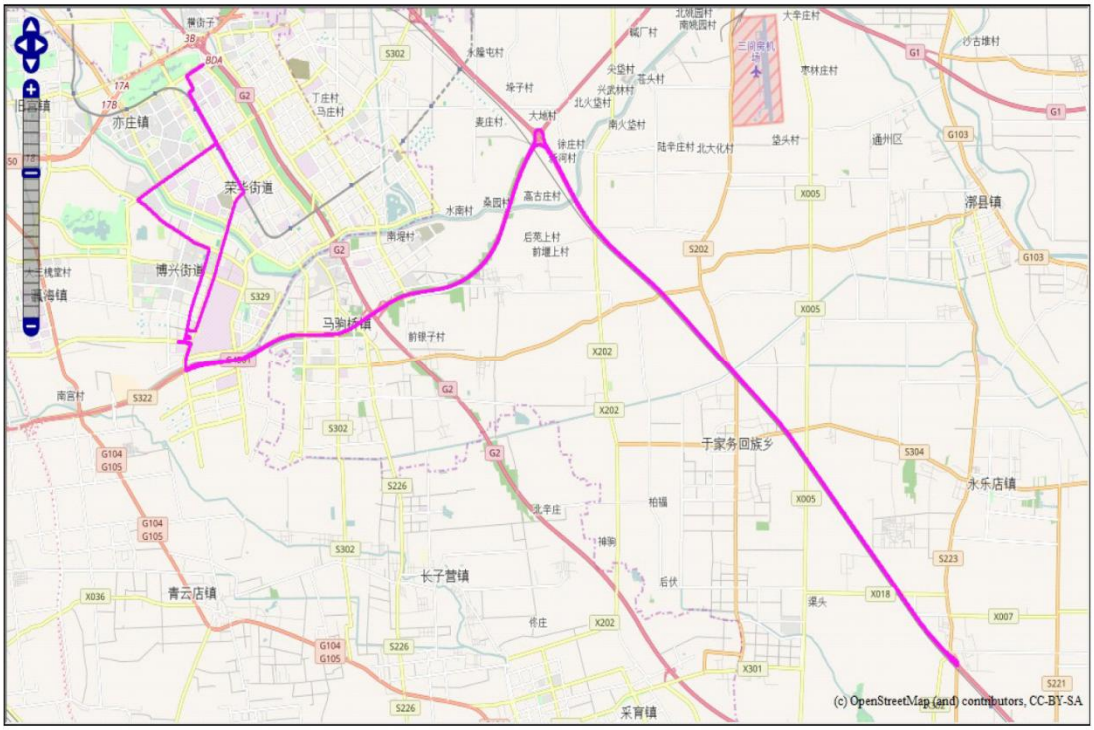

Figure 3.20 Map of the route used for Beijing RDE tests.

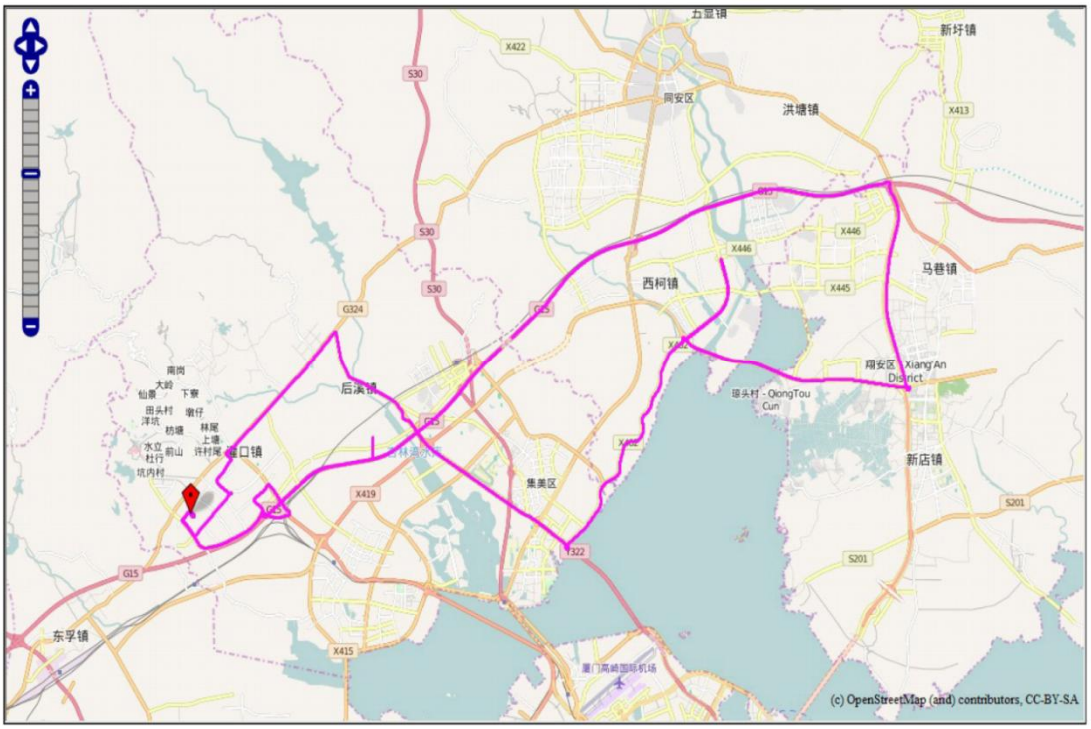

Figure 3.21 Map of the route used for Xiamen RDE tests.

3.6.1.2 WLTC test procedure

The WLTC tests were conducted at two different vehicle emissions testing facilities, one in Beijing and one in Xiamen. The standard test procedure for WLTC testing (WLTP) as outlined in Regulation (EC) 715/2007 and its supplements was used for each test. Cold start tests were performed for each vehicle following the legislated soak period. At the Beijing facility, the chassis dynamometer used was a MAHA ECDM-48L-4WD, the constant volume sampler was a Horiba CVS 7400 and the bag gas emissions were analysed with a Horiba MEXA 7400LE analyser. At the Xiamen facility, the chassis dynamometer used was an AVL 4WD Emission CD (1ASM150K-8), the constant volume sampler was an AVL CVS i60 and the exhaust analyser was an AVL AMA i60. The WLTC data presented in this thesis for each vehicle has been attained from the WLTC report for that particular vehicle.

3.7 Ambient conditions across testing

A summary of the different drive cycles and the average ambient conditions of these across repeated tests is provided in Table 3.16.

Table 3.16 Properties of different drive cycles used. Uncertainties are standard errors calculated from the distribution of tests.

Test Cycle	NEDC (UK)	WLTC (UK)	Shortened RDE (UK)	RDE (UK)	City Centre (UK)	Headingley (UK)	WLTC (China)	RDE (China)
Test Type	Chassis Dyno	Chassis Dyno	Chassis Dyno	On-road	On-road	On-road	Chassis Dyno	On-road
Ambient temp (°C)	22.65 ± 0.7	22.65 ± 0.7	22.65 ± 0.7	16 ± 0.6	14.85 ± 0.8	22.85 ± 1	23.85 ± 0.5	19.85 ± 3
R.H. (%)	25.7 ± 1	25.7 ± 1	25.7 ± 1	70 ± 4	70 ± 6	50 ± 2	48.5 ± 0.05	43.3 ± 5
Pressure (kPa)	100.1 ± 0.2	100.1 ± 0.2	100.1 ± 0.2	100 ±0.6	102 ± 0.4	102 ± 0.3	101.1 ± 0.3	102.2 ± 0.2
Altitude (m)	185	185	185	72 ± 1	47 ± 1	96 ± 1	24 ± 2	24 ± 2

3.8 Data processing

The majority of data processing and analysis was performed in R (R Foundation for Statistical Computing, Vienna, 2011), with some additional analyses performed in Microsoft Excel. Graphical representation was performed in R, Microsoft Excel and OriginPro (OriginLab Corporation, 2020). R is a free software environment for statistical computing and graphics. This programming language allows for processing and manipulation of very large datasets, many of which would be of too large a file size for spreadsheet-based software programmes to handle (such as Microsoft Excel).

3.8.1 Time alignment

The data collected in China was already time-aligned by the in-house software. For the tests performed in the UK, the alignment of signals coming from different pieces of equipment was performed using the 'pems.utils' package in R (Ropkins, 2012). Each set of signals from a particular piece of equipment was aligned to another piece of equipment using a shared signal where possible, or two signals already known to have a close relationship, if not possible.

For the data from the UoB chassis dynamometer facility, the University in-house equipment was confirmed to be already aligned. The data from the HEM was aligned to this via matching of the exhaust flow rates calculated for each (and checked by comparing vehicle velocity traces). The OBS1000 was then aligned to these using the exhaust flow rate measurement. The engine-out and tailpipe FTIR data was aligned by matching of CO_2 traces, and these were also then together aligned to the CO_2 from the MEXA stack units within the UoB in-house dataset. Finally, the PDAQ temperatures and DMS500 PN values were aligned to engine RPM from the HEM, matching signal increases

for both to the engine-start and engine-restart events as indicated by the RPM signal.

For the data from the Horiba OBS-ONE RDE and other on-road testing in Leeds, the Horiba OBS-ONE GS and PN units were automatically aligned, along with GPS and ECU information, by the Horiba software. The VBOX data was aligned to the Horiba data via matching of the vehicle speed traces, and the PDAQ also had an analogue input of this VBOX velocity, so was aligned in the same way. The OBS-1000 data was aligned to this through matching of exhaust flow rates, while the Gasmet DX4000 FTIR was aligned via matching of CO_2 signals, or, if this was not reliable for a particular test, then using either CO or NO signals instead.

3.8.2 Data corrections

After alignment, the FTIR datasets were corrected for noise, which involved calculating the mean maximum of the noise and deleting any signal less than two times this magnitude. The exception to this technique was ammonia, whereby a smoothing function was used.

There are four parts to the WLTC cycle outlined in the legislation: low, medium, high and extra high. However, the UoB chassis dynamometer had only three individual bags for diluted exhaust collection. Therefore, the decision was taken – for the sake of comparability between different WLTC cycles (and for parity with the RDE cycle) – for the second and third phases (medium and high speed) to be combined into one for the China data with 4 phase bag results. All subsequent presentation of WLTC data is with three phases, rather than four, for comparability. The NEDC data was split into three parts for the same reasons. The first two iterations of the UDC cycle were part 1, the second two iterations of the EDC were part 2, and the EUDC cycle section was part 3.

3.8.3 Gaseous pollutant mass and total PN emission calculation

The mass emission value calculations of the regulated pollutants from the UoB chassis dynamometer testing were performed following the procedure in the WLTC legislation (Commission Regulation (EC) 2017/1151), and so will not be reproduced in detail here. The results were compared to the mass emissions calculated by the in-house equipment and found to have good parity. The mass emission of FTIR component species for both chassis dynamometer and RDE testing was performed following the same general

procedure, using data book values for the density of each gas species. The cumulative modal CO_2, CO, NO_x and THC were compared against bag sample values, to verify reliability. The DMS500 values of total and size-distributed particle number were calculated as the product of the number concentration and the tailpipe exhaust flow rate.

3.8.4 PM calculations from PN measurements

An Integrated Particle Size Distribution (IPSD) method can be used to calculate particle mass emissions where gravimetric measurement is not available, or not reliable, such as is the case for very low emission vehicles (Momenimovahed and Olfert, 2015). This method estimates PM concentrations from PNSD and effective density values, and has been show as a reliable alternative to gravimetric measurement techniques (Liu et al., 2009). The calculation is given in equation 3.

$$M_{IPSD} = \sum_i \rho_{eff,i} \times \left(\frac{4}{3}\pi\left(\frac{D_{p,i}}{2}\right)^3\right) \times n_i \qquad (3)$$

Where ρ_{eff} is the effective density, D_p is the effective diameter of the particle and n_i is the total number of particles scanned in that channel of size i.

Aerodynamic diameter increases with increasing density, unlike the electrical mobility diameter, so the two diameter classifications are not equivalent. Effective density calculations based on one method are not necessarily going to be representative if applied to PN results from the other method, when trying to calculate a mass values from particle number values (DeCarlo et al., 2004).

The effective density is often defined as the ratio of the measured particle mass to the particle volume calculated by assuming a spherical particle with a diameter equal to the measured diameter (DeCarlo et al., 2004). The structure of particulate matter means that the density is not constant with diameter. Particulate matter from combustion engines is constructed from a combination of solid particles and condensed semi-volatile material (Momenimovahed and Olfert, 2015). The solid fraction is mostly soot consisting of small, nearly spherical primary particles which have coagulated into polydisperse agglomerates forming a range of different shapes and sizes of particle (Maricq and Xu, 2004). The semi-volatile material may condense onto the surface of these solid particles, or fill voids within the structure of the agglomerates, between chains of primary particles. It is commonly believed that larger agglomerates made of a greater number of primary particles will

have more void spaces within the structure, meaning that as the effective diameter increases, the effective density decreases (Momenimovahed and Olfert, 2015). This has been verified by many studies (Quiros et al., 2015), and is an important consideration because it means that a single density value should not be used to calculate the mass from all diameters within a PNSD measurement.

An alternative estimation of effective density can also be made by comparing measurements of mobility diameter and aerodynamic diameter for a given sample, in a method outlined in detail by DeCarlo et al. (2004). Some studies have employed this technique, such as the work of Maricq and Xu (2004) whereby the density of GDI exhaust particles was calculated for various different diameters. The exhaust in the current work was measured by a DMS500 analyser, which, as previously discussed, classifies particles according to their electrical mobility diameter. Therefore, it was deemed sensible, in this case, to use an effective density that has been calculated from the comparison of electrical mobility diameter and particulate mass. Many studies have previously calculated the effective density of exhaust particulate samples in this manner. By far the most commonly studied exhaust to be characterised is diesel exhaust. However, diesel exhaust and gasoline exhaust do not have the same properties likely due to the soot from each technology having a fundamentally different structure (Momenimovahed and Olfert, 2015).

The most widely researched SI vehicle type in current literature is the GDI vehicle, due to larger quantities of particulate matter produced by this injection strategy making research in this area both more technically feasible, and more valuable to society. The work by Quiros et al. (2015), claims to be the first literature research to present particle effective densities measured for gasoline PFI vehicles. This work compared PNSD results from a tandem DMA – Centrifugal Particle Mass Analyser to conventional gravimetric PM results to calculate effective density values suitable for use in an IPSD method. The study found that the densities of PN from PFI technologies are indeed different to those from GDI technologies, with the PFI density distributions having a higher mass-mobility scaling exponent and therefore greater particle effective density for larger sizes. Quiros et al. (2015) conclude that this indicates that particulate emissions more spherical in nature occur from PFI engines than GDI engines. They find results similar across a few drive modes, and conclude that a new category of particle effective density can be defined that will be

suitable for use with other PFI vehicles with similar emissions abatement technologies as those utilised in the study. Further comparison work with a wider range of PFI test vehicles and drive cycles needs to be made, before this latter statement can be made confidently. In their conclusion Quiros et al. (2015) agree with this sentiment, stating that the IPSD method should be re-evaluated over transient test cycles. They present the generic particle effective density function as in equation 4, with a constant c and mass-mobility scaling exponent D_m that can be empirically derived. The PFI density function they subsequently calculate from their results is given in equation 5, and by substituting the effective density function, ρ_{eff}, in equation 6, the practical mass equation of equation 7 is derived. This equation can be used to calculate the PM from particulate number densities over a range of different effective electrical mobility diameters, d_p. Quiros et al. (2015) found that density values generally plateaued below around 55nm, so recommended using the value calculated for a diameter of 55nm for those particles smaller than this diameter.

$$\rho_{\text{eff}} = 1000 \times c \times {d_p}^{D_m - 3} \quad (4)$$

$$\rho_{\text{eff}} = 2400 \times {d_p}^{-0.33} \quad (5)$$

$$\rho_{\text{eff}} = \frac{m_p}{\left(\frac{\pi}{6}\right) {d_p}^3} \quad (6)$$

$$M_{\text{p}} = \frac{\pi}{6} \times 2400 \times {d_p}^{2.67} \quad (7)$$

The manufacturers of PNSD equipment will often outline methods for the estimation of mass from number distributions. TSI (2006) recommend using a default value of 1.2 g/cc for their SMPS software, while the DMS500 have configured a more detailed methodology for diesel particles involving separate handling of the accumulation mode particles using an empirically-derived relationship. For GDI engines, Cambustion (2009) recommend a simple spherical calibration assuming unit density close to water – i.e. *Mass (mg)* = $5.20 \times 10^{-16} \times {d_p}^3$ *(nm)* – but there is no recommendation available for PFI engines (Cambustion, 2009). In light of this, it can be considered that the mass equation presented above – derived from the findings of Quiros et al. (2015) – is most suitable for the current work. Therefore in the results sections the method used to calculate PM values where they are presented is that presented in equation 7.

3.8.5 Verification of RDE route, test result validity, and calculation of reported results across RDE packages

Verification of the RDE route and test result validity was performed for each test, following the instructions in the RDE regulations (European Commission and Council of the European Union, 2017), and so will not be reproduced in detail here. Figure 3.22 below gives an overview of this process, including the Steps A-C for checking an RDE test. The checking of the main trip (Step A), trip dynamics and cumulative altitude gain (Step B) was performed using a script written by the author in R with the VBOX GPS and ECU speed data, and also automatically by the Horiba software using the Horiba GPS data. The 'trip dynamics' in this case refer specifically to the $v.a_{pos}[95]$ and RPA that were mentioned in Chapter 2 Section 2.7.7. The verification of trip validity against the vehicle CO_2 characteristic curve was performed automatically by the Horiba software, using data related to the vehicle and fuel that was supplied to the program by the user. As explained in Chapter 2, this validity requirement ensures that the average CO_2 emissions over the different speed points of the RDE drive are comparable to those of its WLTC, thereby checking that the vehicle on the RDE was behaving in a similar manner to the WLTC.

For the data gathered in China, the results were processed according to RDE Package 2 legislation, Package 3 legislation and Package 4 legislation in order to study the differences in reported results between packages. In each case, the guidelines of the relevant EU regulation were followed for the data processing (see Chapter 2 Section 2.7.7 for more details).

The calculation of RDE results was conducted and presented according to different packages of RDE regulation that have been released sequentially. The methodology outlined in the regulation for each package was followed to do these calculations, and so will not be reproduced here. The percentage change of properties and reported results is calculated as in equation 8.

$$Percentage\ change = \frac{new\ result - old\ result}{old\ result} \times 100 \qquad (8)$$

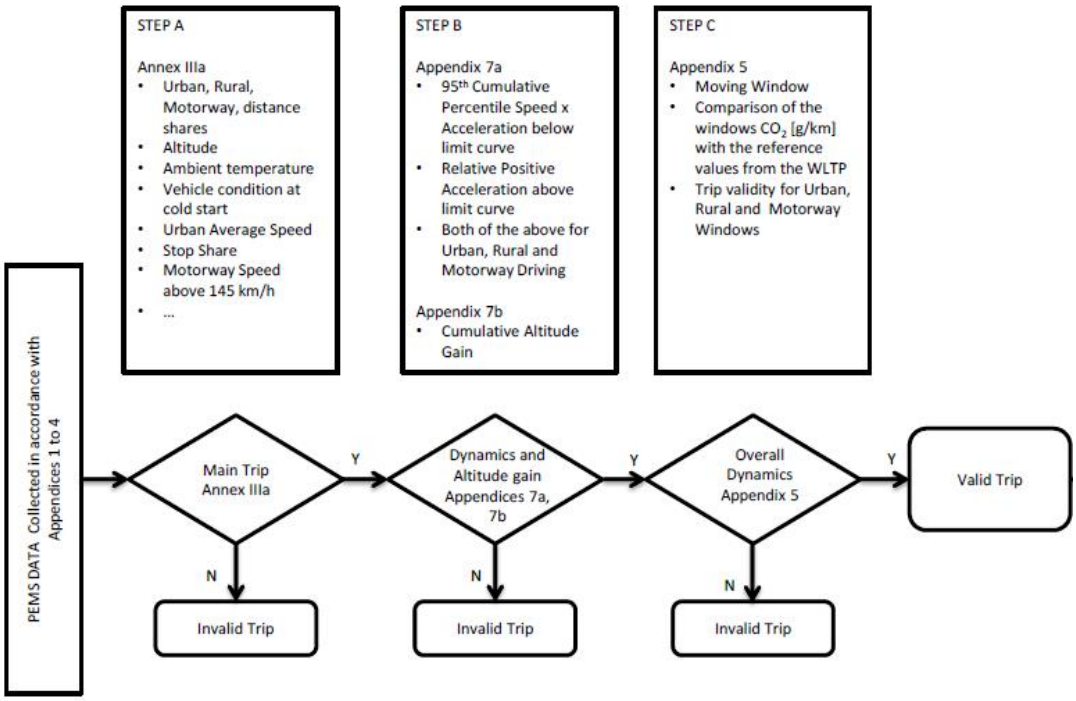

Figure 3.22. Verification of trip validity. Source: European Commission and Council of the European Union (2017).

3.8.6 Further calculations

3.8.6.1 Coefficient of variation (COV)

Where presented, the COV is the standard deviation normalised to the mean value, and is calculated according to equation 9.

$$COV = \frac{\sigma}{\mu} \tag{9}$$

Where σ is the population standard deviation and μ is the population mean, given in equations 10 and 11 respectively.

$$\sigma = \sqrt{\frac{\sum(x_i - \mu)^2}{N}} \tag{10}$$

$$\mu = \frac{\sum x_i}{N} \tag{11}$$

Where, N is the size of the population and x_i is each value from the population.

3.8.6.2 VSP calculation

The instantaneous VSP was calculated for the RDE and other on-road tests, using the method defined by Jimenez-Palacios (1999), given in equation 12.

$$VSP = v\left[1.1a + 9.81\left(\frac{r}{100}\right) + 0.132\right] + 0.000302v^3 \tag{12}$$

Where *VSP* is the calculated vehicle specific power (kW/ton), *v* is the vehicle speed (m/s), *a* is the vehicle acceleration (m/s^2) and *r* is the road grade (%).

The road grade was calculated from the GPS height data and smoothed in the manner outlined in Appendix 7b of the RDE regulation Package 4 (European Commission and Council of the European Union, 2017). This smoothing was done by the correction of instantaneous altitude data; if the difference in height between 1 second satisfied the relation given in equation 13, then the values were filled in with the previous valid value, such that all height differences were lower than this threshold.

$$|h(t) - h(t-1)| > \frac{v(t)}{3.6 \times \sin(45°)} \quad (13)$$

Where *v* is the velocity (km/h) of the vehicle during that period.

3.8.6.3 RPA calculation

The relative positive acceleration (RPA) was calculated using the method of May et al. (2014) outlined in equation 14, which itself was taken from methods used to characterize vehicle trips in the development of the WLTC.

$$RPA = \frac{\sum_{i=1}^{n} a_i v_i \Delta t}{s} \quad (14)$$

Where a_i is the acceleration at time step *i* if a_i is greater than 0m/s^2, v_i is the vehicle speed at time step *i* (m/s), Δt is the time increment and *s* is the distance travelled (m).

3.8.6.4 TWC efficiency calculation

The TWC conversion efficiency is calculated for CO, NO_x and THC pollutants by comparing engine-out emissions to tailpipe emissions for that pollutant. Equation 15 gives this calculation.

$$TWC\ efficiency = \frac{Engine\ out\ emission - Tailpipe\ emission}{Engine\ out\ emission} \times 100 \quad (15)$$

3.8.6.5 Mean TWC and gas temperature calculation

A mean TWC temperature is presented, which is calculated as the arithmetic mean of the two TWC block temperatures, as given by the ECU. The mean TWC gas temperature, where given, is calculated as the mean of the gas temperature readings just prior to the first TWC, between the two TWC blocks,

and just after the second TWC (referring to Figure 3.2 this is thermocouples T1, T3 and T5).

3.8.6.6 Calculation of uncertainties

Unless otherwise stated, all uncertainties given in the results chapters are standard errors calculated from the distribution of results. The standard error is the standard deviation of the mean value, normalised against the number of tests performed, as given in equations 16 and 17.

$$SE = \frac{\sigma}{\sqrt{N}} \tag{16}$$

$$\sigma = \sqrt{\frac{\sum(x_i - \mu)^2}{N}} \tag{17}$$

Where *SE* is the standard error, σ is the population standard deviation, *N* is the size of the population, x_i is each value from the population and μ is the population mean.

3.9 Summary

This chapter has detailed the experimental methodologies utilised in this work. The following four Chapters will discuss the results of this work, starting with an investigation of the type approval procedures in Chapter 4.

Chapter 4
Impact of type approval test cycles on emissions

4.1 Introduction

This chapter will compare and contrast the dynamic properties of the NEDC, the WLTC and repeats of an RDE test cycle adhering to all RDE Package 4 requirements (outlined in Chapter 2 Section 2.7). The effect of dynamic conditions on the behaviour of an HEV will be investigated and the resultant emissions quantified. Finally, the PN size distribution of an HEV across test cycles will be studied to assess the suitability of the currently legislated 23nm PN size cut-off. This chapter begins to answer Objective 1 as outlined in Section 2.11 of Chapter 2, by satisfying Tasks 2 and 3.

4.2 The NEDC, WLTC and RDE test cycles

As discussed in Chapter 2 Section 2.7, the WLTC and its associated test procedure replaced the NEDC as the EU light duty test procedure. This was partly in order to make the type approval procedure more closely aligned with realistic driving behaviours. The RDE was introduced as a supplementary procedure toward this end.

In order to assess the success of this aim, this section explores the drive properties of the NEDC, WLTC and RDE test cycles. Though previous research has investigated these test cycle drive properties and emissions (for example Marotta et al. (2015), Sileghem et al. (2014), May et al. (2014a), Pavlovic et al. (2016), Merkisz et al. (2016), Clenci et al. (2017), Donateo & Giovinazzi (2018) and Valverde et al. (2019)), little previous work has focused on HEVs.

It should be remembered that the RDE test has a far greater degree of freedom than the chassis dynamometer test cycles, and so the conclusions below are indicative only; they are only directly applicable to the test cycle designed as part of this research, not necessarily representative of all RDE test cycles generally.

4.2.1 Drive cycle properties

This section explores the drive properties of the NEDC, WLTC and RDE test cycles. Figure 4.1 below displays example velocity and engine speed traces from the three test cycles under study: the NEDC, WLTC and RDE. Though

the RDE test cycle presented is a single example speed trace, it is generally representative of all RDE tests presented in this section due to the very high repeatability of the RDE test route. The figures are plotted on the same scale axes, to elucidate the differences in test length and dynamics.

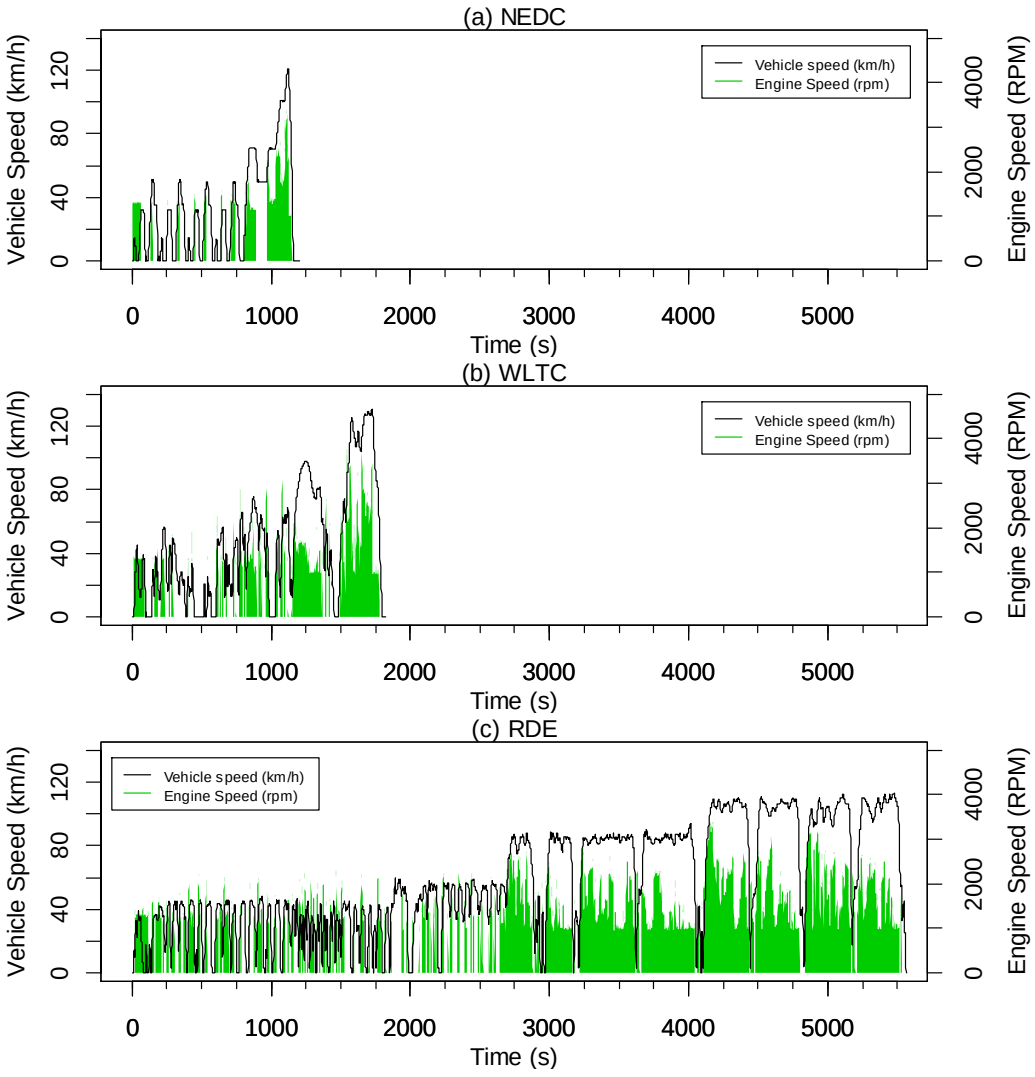

Figure 4.1 (a) NEDC, (b) WLTC, and (c) example RDE speed traces, along with examples of engine speeds of the HEV.

Table 4.1 displays some key dynamic properties that have a bearing on the resultant emissions of the three different test cycles. Due to the high repeatability of the NEDC and WLTC cycles, data from a single test was deemed suitable (the standard deviations between repeats were negligible). For the RDE test, however, average values from 23 repeats of the same RDE test route are given, along with uncertainties calculated as the standard errors. By comparing the $v.a_{pos}[95]$ with the tests presented in Clenci et al. (2017), it was confirmed that the RDE tests presented in the current work are generally

representative of common driving habits. It should be noted that the NEDC test had an initial SOC of 65.5% and finished the test with 60% while the WLTC test had an initial SOC of 67.8% and finished the test with 67.4%. The RDE tests finished with an average SOC 6.41±0.6% higher than they started. For these three tests, the final SOC is closely related to the vehicle behaviour just prior to test finish. The fact that the RDE has a prolonged duration of high speed driving followed by deceleration to stop, allows more charging of the battery.

Table 4.1 A range of dynamic properties from the NEDC, WLTC and RDE tests for HEV.

	NEDC	**WLTC**	**RDE**
Distance for urban drive (%)	50.5	37.7	32.7 ± 0.2
Distance for rural drive (%)	27.3	25.6	32.1 ± 0.2
Distance for motorway drive (%)	22.2	36.7	35.3 ± 0.2
Total distance (km)	11.023	23.25	90.9 ± 0.4
Stoppage time (urban) (%)*	31.9	20.9	14 ± 0.7
Number of stops per km (total)*	1.45	0.43	0.4 ± 0.01
Number of stops per km (urban)*	2.88	1.14	1.22 ± 0.05
Time for coolant to reach 70°C (s)	984	850	526 ± 18
Time stopped in first 300s (s)*	109	55	49 ± 2
Average urban speed (km/h)	21.2	25.8	29.4 ± 0.3
Average rural speed (km/h)	71.8	72.9	80.9 ± 0.3
Average motorway speed (km/h)	105.5	110.7	104.9 ± 0.2
Urban v.a_{pos}[95] (m^2/s^3)	7.1	11.6	7.8 ± 0.1
Rural v.a_{pos}[95] (m^2/s^3)	8.39	13.1	13.7 ± 0.4
Motorway v.a_{pos}[95] (m^2/s^3)	9.31	14.7	10.4 ± 0.3
Urban RPA (m/s^2)	0.46	0.51	0.33 ± 0.004
Rural RPA (m/s^2)	0.25	0.29	0.15 ± 0.003
Motorway RPA (m/s^2)	0.23	0.24	0.1 ± 0.002

*Here “stop” refers to a vehicle velocity of less than 1km/h.

The NEDC has the highest percentage of distance in urban drive, followed by the WLTC and then the RDE. This RDE, meanwhile, has the highest percentage of distance covered by rural drive, followed by the NEDC and then the WLTC. Finally, the WLTC has the greatest percentage of motorway distance covered, followed by the RDE then the NEDC. The RDE has the lowest percentage time stopped, followed by the WLTC and then the NEDC, and the same is true of the number of stops per kilometre of total test cycles. When considering only urban driving, the RDE has slightly higher values than the WLTC, but the NEDC has over double the number of stops per kilometre. The total time stopped during the first 300s of the cycles is 105s for NEDC,

followed by the WLTC at 55s and then the RDE at 49s. The average speed of urban and rural sections is the highest for the RDE, followed by the WLTC and then the NEDC, but the RDE has the lowest motorway average speed. With regard to $v.a_{pos}[95]$, the WLTC appears the most aggressive in the urban section, while the RDE has slightly higher $v.a_{pos}[95]$ in the rural section, but lower $v.a_{pos}[95]$ in the motorway section. For all phases, the NEDC has the lowest $v.a_{pos}[95]$ values. With regard to RPA, the RDE has the far lower values for all phases, followed by the NEDC and WLTC.

Table 4.2 displays some vehicle and engine properties resulting from the differences in dynamic parameters between the three tests. As with Table 4.1, single NEDC and WLTC run results were used for these cycles, while the RDE was characterised using average values from 23 repeats, with uncertainties calculated from the standard error of the distributions.

The engine is activated for different proportions of time for different tests, due to variations in the proportion of time with the vehicle stationary. The RDE has the largest percentage of both time and distance spent with the engine on in both urban phase and over the duration of the test. This is followed by the WLTC, with NEDC having the lowest quantities of engine-on activity. The same conclusion regarding the WLTC compared to NEDC was stated in Cubito et al. (2017) in their study of a similar type of HEV. With regard to engine restarts, the WLTC has the highest number per km for both urban phase and the whole test. In the urban phase, this is followed by the RDE, with the NEDC having the lowest number of engine restarts. When considering the whole test, however, the RDE test has the lowest number of restarts per km. As a result of this engine behaviour, the engine coolant temperature takes longest to reach 70°C for the NEDC, followed by the WLTC and then the RDE.

Table 4.2 A range of engine-behaviour parameters resulting from the NEDC, WLTC and RDE tests.

	NEDC	**WLTC**	**RDE**
Engine-on in urban drive (% of time)	19.6	28	39.7 ± 0.6
Engine-on whole cycle (% of time)	35.5	50.8	63.7 ± 0.5
Engine-on in urban drive (% of distance)	24.8	38.8	49.3 ± 0.5
Engine-on whole cycle (% of distance)	62.2	77.2	83.4 ± 0.2
Engine restarts per km (urban) (#/km)	2.88	5.02	3.28 ± 0.06
Engine restarts per km (total) (#/km)	1.45	1.89	1.07 ± 0.02
Time for coolant to reach 70°C (s)	984	850	526 ± 18

Figure 4.2a and Figure 4.2b display the VSP distributions from the NEDC and WLTC, showing that a wider range of VSP values is achieved from the WLTC. These can be compared with the average VSP distributions from 23 repeated RDE tests given in Figure 4.2c. The VSP distribution from these RDE tests is far more varied, with a much wider range of values. This finding is in agreement with Duarte et al. (2016) regarding their (non-RDE) on-road testing, as shown in Figure 4.3.

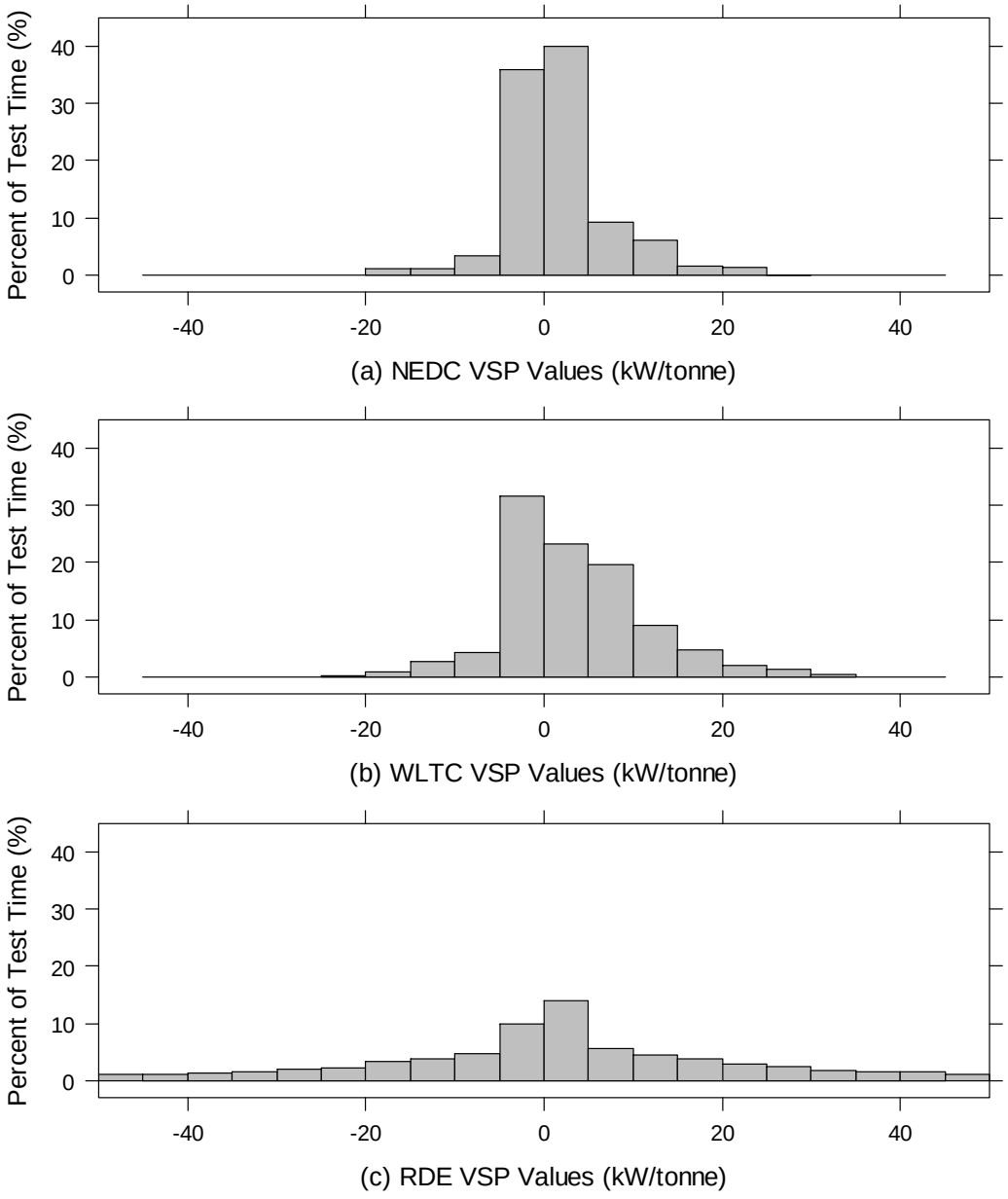

Figure 4.2 VSP distribution histograms of (a) the NEDC, (b) the WLTC and (c) average RDE tests.

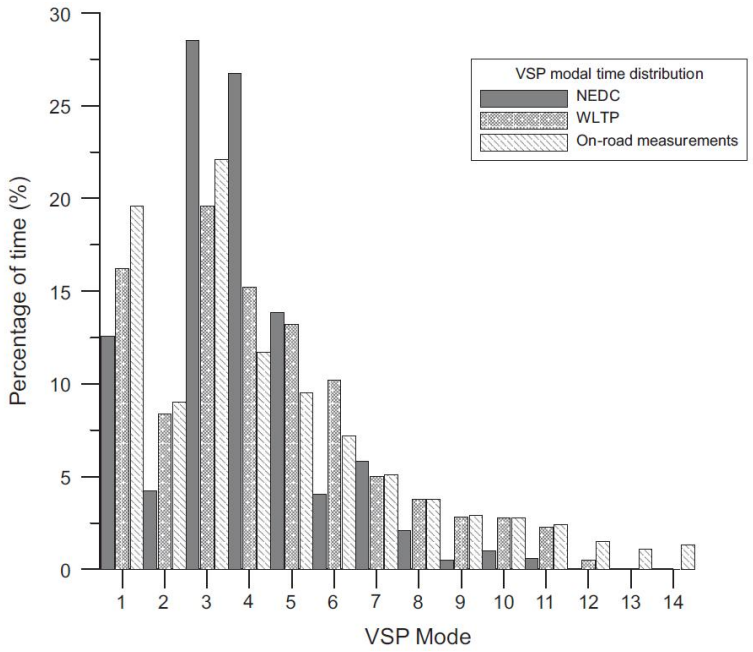

Figure 4.3 Comparison of NEDC, WLTC and on-road measurements VSP modal time distribution presented by Duarte et al. (2016).

Figure 4.4 plots torque against engine speed for the NEDC test, the WLTC test and a shortened RDE-style test. It shows that the range of engine operating parameters is similar for the three different tests, but with more operating points sampled by both the RDE and WLTC than the NEDC. The WLTC appears to cover the widest range of operating points, demanding the highest engine speed and torque combinations. This is in general agreement with the engine maps presented in Clenci et al. (2017), as can be seen by comparison with Figure 4.5. The shape of the maps, however, are markedly different for the HEV compared to the previous study, covering a narrower area than the SI engine presented by Clenci et al. (2017). This is because of the HEV ability to operate at more optimum engine conditions thanks to the motor's contribution.

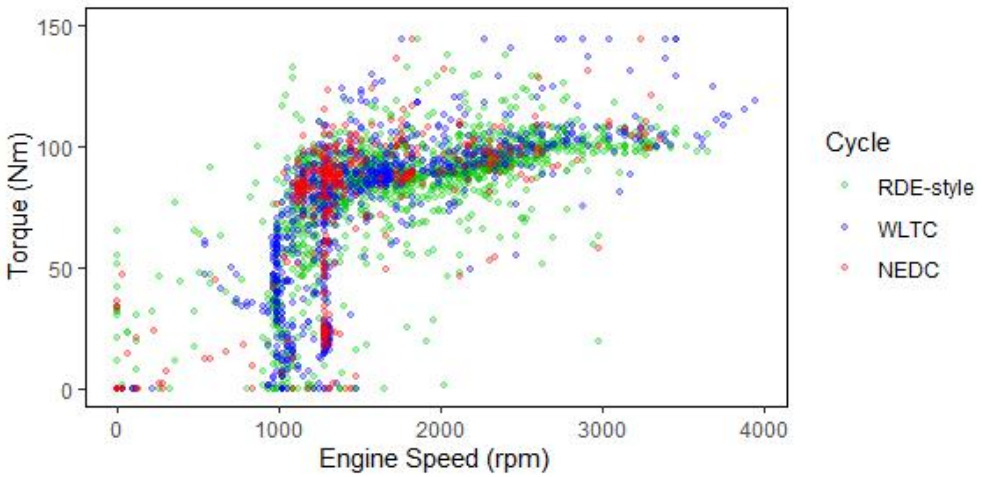

Figure 4.4 Engine torque and engine speed points covered one test of the RDE–style on-road cycle, WLTC cycle, and NEDC cycle.

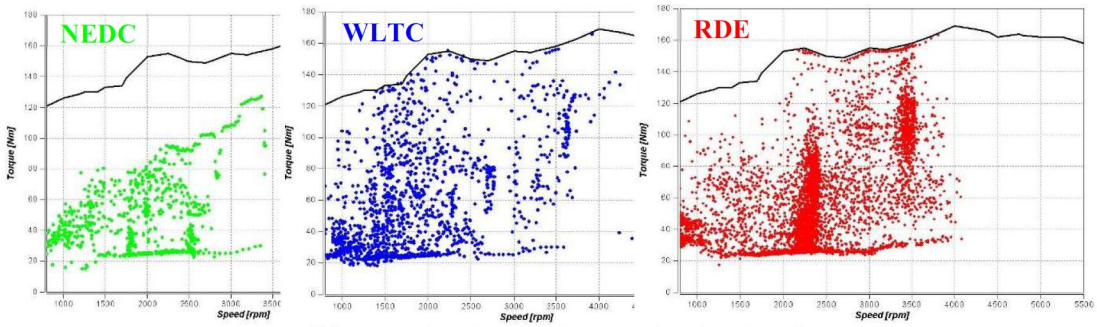

Figure 4.5 Engine operating points for NEDC, WLTC and RDE presented by Clenci et al. (2017).

Figure 4.6 plots engine load against engine speed at 1Hz resolution for a set of seven RDE tests and seven WLTC tests, along with a single NEDC test. The same number of RDE and WLTC tests are plotted in order to avoid bias in the perceived range of engine points covered by the two different types of test. This was not possible for the NEDC test due to insufficient repeats, so Figure 4.7 displays a random sample of four different single RDE and WLTC tests plotted alongside the NEDC test, in order to perceive how the three tests differ in their demands on the engine. It is clear that the NEDC test covers only a very limited range of engine operating points and the WLTC is a large improvement on the NEDC in this respect, covering a far broader range of points. This is in agreement with the general consensus of previous literature, such as Donateo & Giovinazzi (2018). Little work to date has focused on the difference between the RDE and WLTC for an HEV; the next paragraph will discuss this in detail.

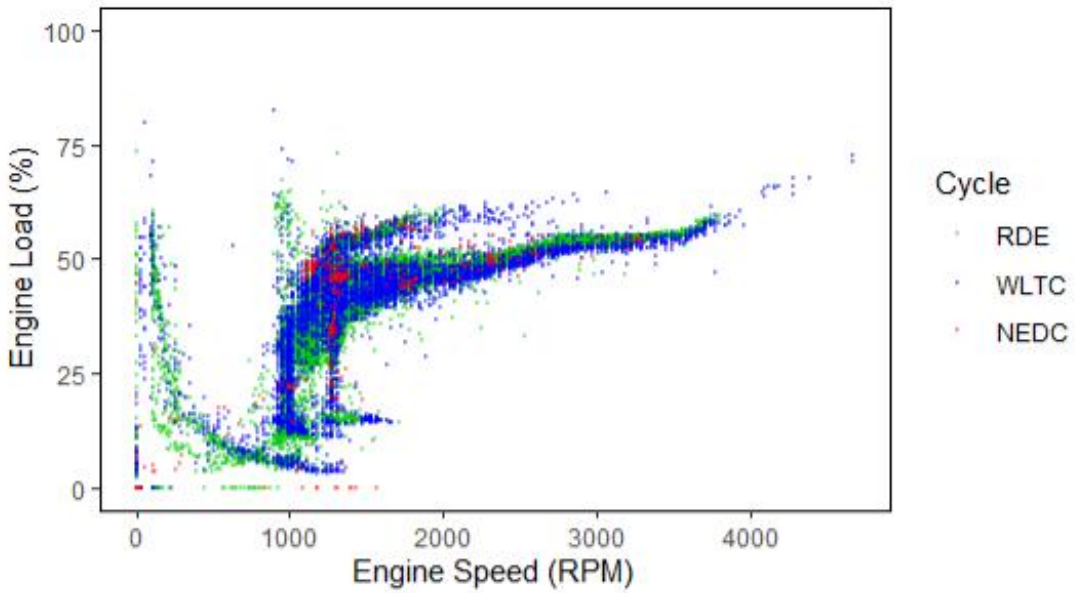

Figure 4.6 Engine load and engine speed points covered by seven repeats of an RDE cycle (green, bottom layer), seven repeats of the WLTC cycle (blue, middle layer), and one run of the NEDC cycle (red, top layer).

Figure 4.7 shows that (at 1Hz resolution) the range of engine operating points covered by the RDE cycle is greater than the WLTC, particularly at lower engine loads and speeds. However, there are two areas of combined high speed and load that extend further for the WLTC than the RDE. This is an indication that some sections of the WLTC are more demanding on the engine than the RDE. It should be remembered that the freedom within the RDE means that driver behaviour will have far more bearing on the cycle demands than the WLTC, and so this result shows that it is possible to drive in a less demanding style than the WLTC test and still pass the RDE criteria. This is not necessarily a disadvantage of the RDE test, as it is supposed to supplement rather than replace the WLTC. The RDE test satisfactorily probes areas of the engine load/speed map that are not reached by the WLTC test.

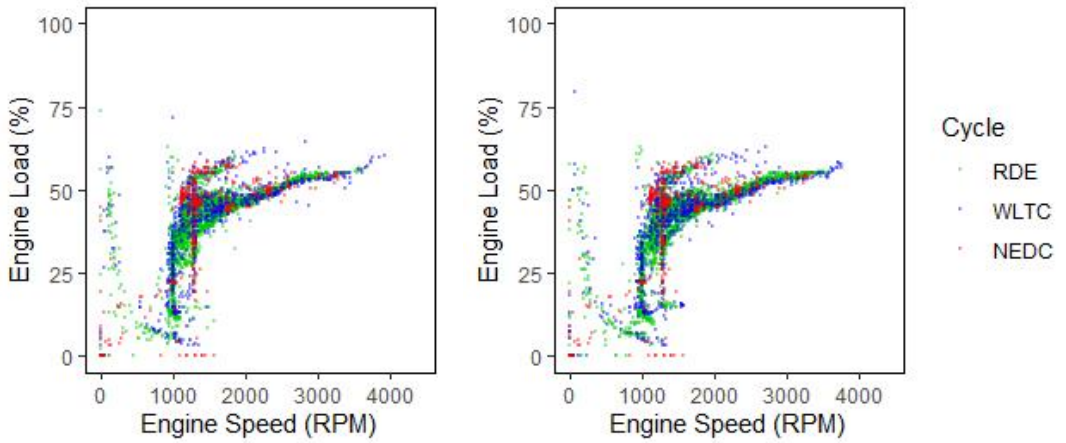

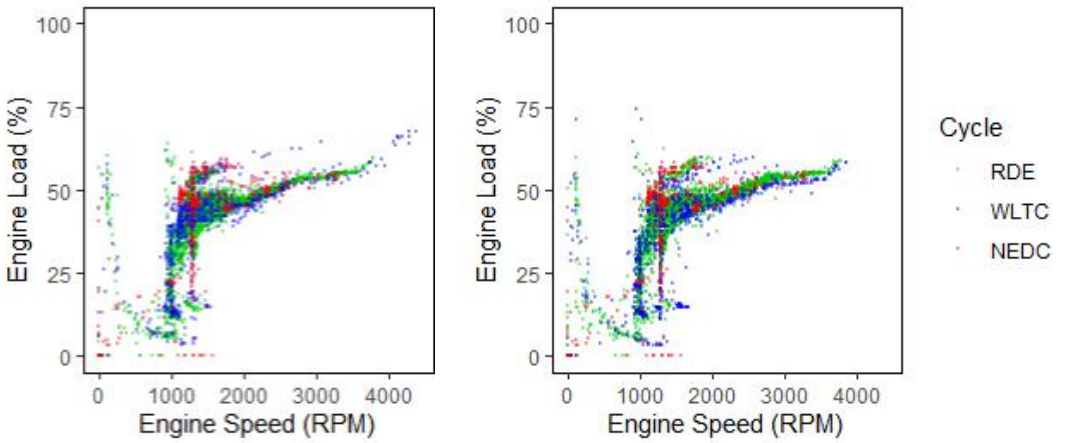

Figure 4.7 Four examples of the engine load and engine speed points covered in an RDE cycle (green, bottom layer), the WLTC cycle (blue, middle layer), and the NEDC cycle (red, top layer).

Most importantly, because the RDE test is performed on real roads, it differs by a greater extent between tests than the WLTC (inferred by the differences between the tests of Figure 4.7), which means that manufacturers have to ensure their vehicles perform well under a wider range of conditions. It should be noted that, generally, there is a wide level of agreement between separate tests. This is testament to the ability of this HEV to combine engine and motor power in a way that leads to increased use of more optimal engine operating points. By comparing these graphs with those published in Donateo & Giovinazzi (2018) given in Figure 4.9a, a much smaller difference is seen between the coverage of engine operating points of the NEDC, WLTC and RDE tests. This is because the HEV can supplement engine demand by the motor, resulting in a smaller range of different operating points being sampled than the diesel vehicle of the previous study.

A plot of vehicle speed versus acceleration is given in Figure 4.8. An example RDE trace (verified as representative of the RDEs presented as a whole) is included here to avoid bias. The plot again indicates that the WLTC has sections that are more demanding than this RDE, while the NEDC is generally the least demanding. The plot looks very similar to that of Donateo & Giovinazzi (2018) given in Figure 4.9b, with the RDE occupying similar regions of the plot in comparison to the WLTC and NEDC, substantiating the reliability of this finding.

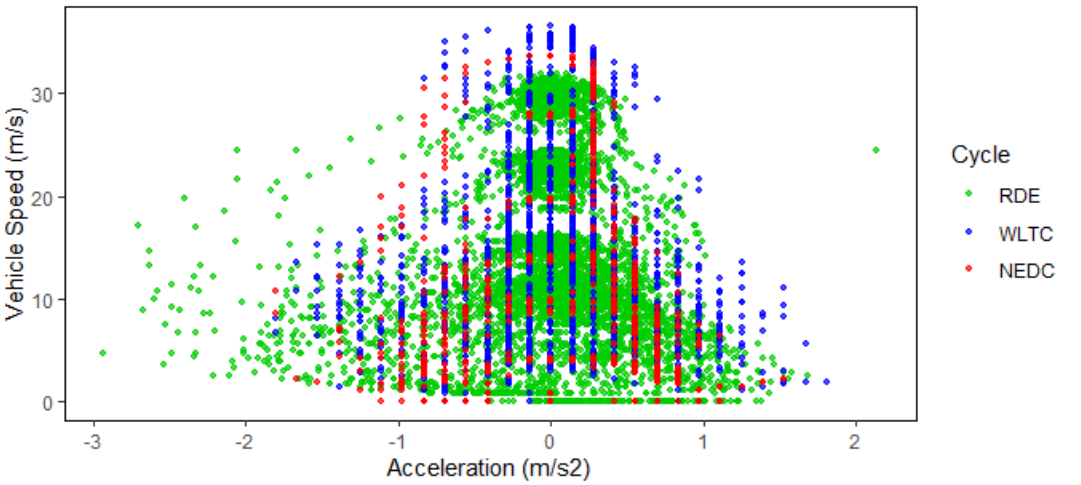

Figure 4.8 Vehicle speed (m/s) versus acceleration (m/s^2) for the NEDC, WLTC and an example RDE drive cycle.

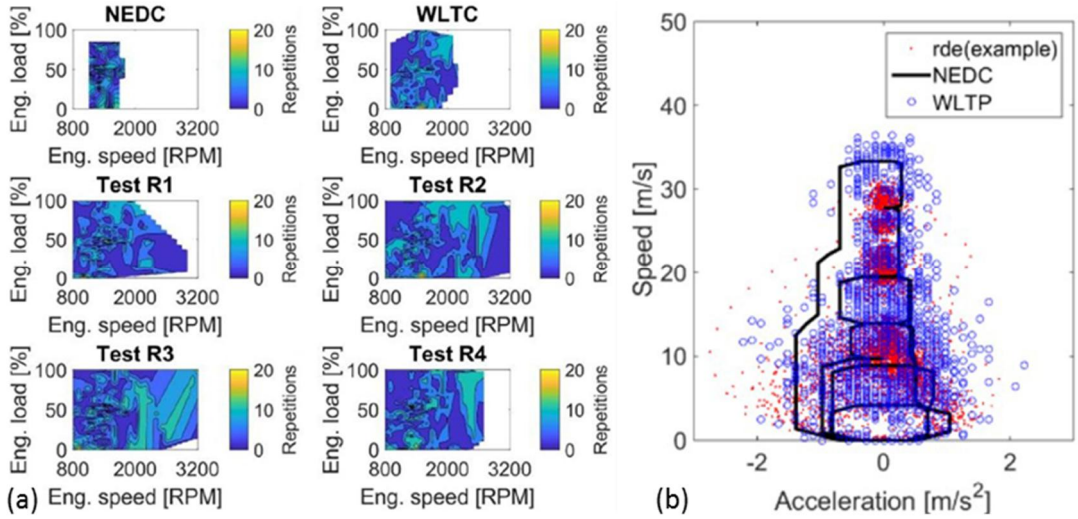

Figure 4.9 (a) Engine load and speed point distributions from the NEDC, WLTC and RDE (Test R1 - Test R4) tests, and (b) speed-acceleration distributions of the NEDC, WLTC and an RDE, published in Donateo & Giovinazzi (2018).

4.2.2 Regulated pollutants

The first part of this section will focus on the CO_2, CO, NO_x, THC and PN emissions differences between the NEDC and WLTC for each test cycle phase, and for the test as a whole. Next, the NEDC, WLTC and RDE total test emissions of CO_2, CO, NO_x and PN will be compared and contrasted, with a detailed look at the transient emissions profile to elucidate the reasons for the differences seen. Finally, the PN size distribution between test cycles will be studied, and a discussion of the suitability of the 23nm diameter PN cut-off will follow.

Figure 4.10 displays the distance-specific mass emission results from chassis dynamometer NEDC and WLTC tests using the Toyota Prius research vehicle, fuelled by an E0 research grade gasoline. As discussed further in Chapter 3 Section 3.8.2, both the NEDC and WLTC are split into three sections for easier comparison with the RDE.

Total (whole cycle) CO_2 emissions were generally comparable, but were 0.2% higher under the WLTC. This HEV result is a smaller increase than that of Duarte et al. (2016) and disagrees with Kim et al. (2019) who witnessed a decrease in CO_2 from their HEV on the WLTC, compared to the NEDC. The results currently presented therefore sit between those of Duarte et al. (2016) and Kim et al. (2019). With regard to CVs, May et al. (2014a), Pavlovic et al. (2016) and Valverde et al. (2019) all present larger CO_2 increases on the WLTC than currently presented. Figure 4.13 gives the results as presented in Valverde et al. (2019), for comparison. It should be noted that the NEDC test currently presented had an initial SOC of 65.5% and net change of -5.5% (i.e. a decrease of 5.5% over whole test) while the WLTC test had an initial SOC of 67.8% with a net change of -0.4%. The fact that the battery lost charge during the NEDC indicates that the perceived increase in the WLTC CO_2 results are greater than those in 'real terms', and Figure 4.14 shows that the mid-section of the drive – where the NEDC CO_2 is much lower than that of the WLTC – was where the greatest loss of battery SOC on the NEDC occurred, and was due to a constant medium vehicle speed period which encouraged the engine to turn off, draining the battery. This NEDC SOC depletion may partly explain why the increase in CO_2 emissions currently presented is not as great as the increases presented by Duarte et al. (2016) and for the CVs. The WLTC (and RDE) are more transient cycles and so do not have this behaviour as often, meaning the SOC is maintained.

The WLTC produced 27% higher CO emissions but 740% lower NO_x emissions, when compared to the NEDC. Literature for CVs generally points to an increase of these emissions over the WLTC compared to the NEDC, though results across literature have also been mixed. The HEV trend in the current work for CO agrees with Marotta et al. (2015) and Valverde et al. (2019), but is in contradiction to the results of May et al. (2014a) and Merkisz et al. (2016a) and Kim et al. (2019). For NO_x, the results presented here are in disagreement with the consensus from the previous literature above for CVs but are in agreement with Kim et al. (2019) for their HEV. The transient NO_x emissions in Figure 4.15c shows that one very large initial NO_x spike on the

NEDC was responsible for the vast majority of reported emissions. THC results were less clear, with 30% increased phase 1 emissions on the WLTC but 23% decreased total cycle emissions. The lower total emissions are in agreement with May et al. (2014a), Merkisz et al. (2016a) and Valverde et al. (2019) for CVs, and with Marotta et al. (2015) and Kim et al. (2019) for HEVs. The results of Valverde et al. (2019) for these species can be seen in Figure 4.13.

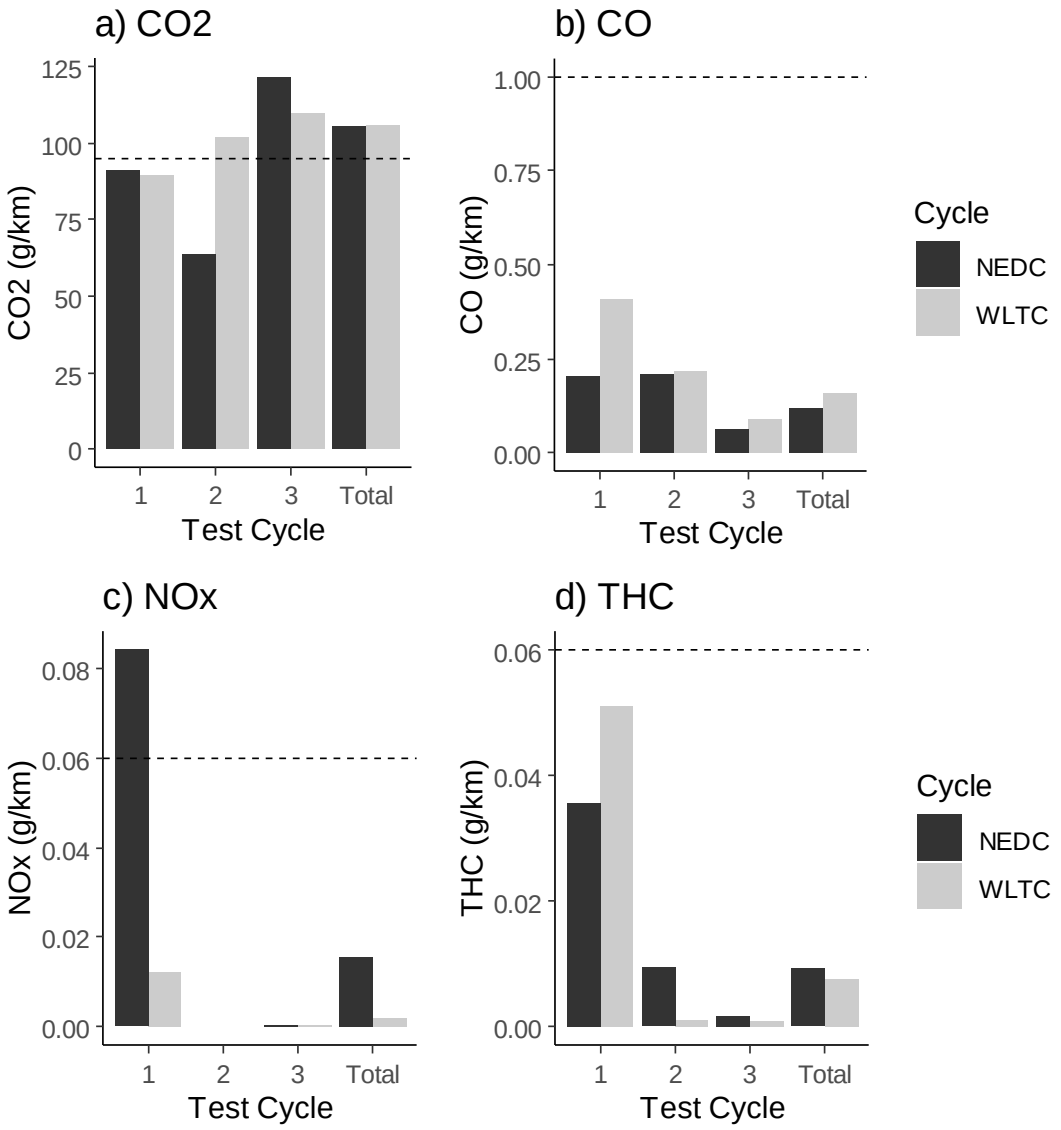

Figure 4.10 Distance-specific THC, CO, NO_x and CO_2 emissions from E0-fuelled NEDC and WLTC test cycles.

The distance-specific PN emissions from the NEDC and WLTC tests are displayed in Figure 4.11. The overall results are very similar between these two test cycles (2% increase under WLTC). The WLTC phase 1 and 3 result in 15% and 23% higher PN emissions respectively, but the WLTC phase 2

results in 12% lower PN emissions, giving total emissions that are slightly higher for the WLTC. This finding agrees with the results of May et al. (2014a) and Valverde et al. (2019) for CVs. The results of Valverde et al. (2019) can be seen in Figure 4.13.

Figure 4.19a and Figure 4.19b display the NEDC and WLTC drive cycles respectively, with vehicle and engine speeds indicated alongside the modal and cumulative PN emissions. These figures show that the phase 1 results are due to the increased transience and stopping behaviour during the urban phase, leading to more hybrid engine stop-start behaviour which is associated with higher levels on PN emissions (see Chapter 6 Section 6.3.2 for more detail). Phase 2 of the WLTC contains more periods of constantly higher speed driving, meaning the vehicle engine stays on for longer periods and the vehicle covers a greater distance, reducing distance-specific emissions from this HEV for this section. Phase 3 of the WLTC contains more transient driving than the NEDC, with lots of acceleration and deceleration points where the engine will turn off and on, again leading to large jumps in PN emission.

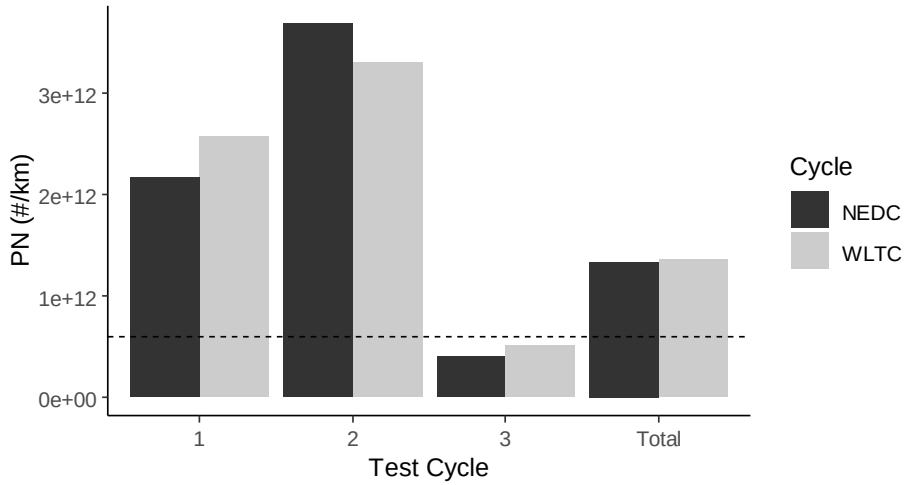

Figure 4.11 Distance-specific PN emissions from E0-fuelled NEDC and WLTC. A dashed line indicates the Euro 6 PN limit of $1.6x10^{11}$ #/km.

Figure 4.12a to Figure 4.12d display the average mass emissions of CO_2, CO and NO_x, and average number emission of PN, per kilometre across the total NEDC, WLTC and RDE test cycles. The Euro 6 fleet-average emission target for CO_2 and pollutant emission limits for CO, NO_x and PN are indicated on the graphs by horizontal dashed lines. The NEDC and WLTC values are from single tests, while the RDE consists of an average from the results of 5 separate repeats of the same RDE route. All tests utilised an E0 research grade fuel. The uncertainty of the RDE values, as calculated from the standard

deviation of the mean, is very small, indicating high repeatability and reliability to these RDE results.

The emission factors of CO_2 are highest for the RDE, followed by the WLTC and then the NEDC (the RDE is 9% higher than the WLTC). This trend is in agreement with the Valverde et al. (2019) study for conventional PFI vehicles, as can be seen by comparison with Figure 4.13. The results contradict Varella et al. (2019), but this latter study utilised an RDE cycle adhering to an older package (Package 2) of the RDE legislation, so is unreliable. The higher on-road CO_2 results compared to NEDC and WLTC agree with May et al. (2014) from non-certification PEMS testing compared to NEDC and WLTC. For CO, the RDE gave the lowest total values (66% decrease compared to WLTC), in agreement with Merkisz et al. (2016a), and Valverde et al. (2019) as can be seen in Figure 4.13. For NO_x, the RDE gave the lowest values again (a 58% decrease compared to WLTC), in agreement with Merkisz et al. (2016a), but in disagreement with Valverde et al. (2019) as can be seen in Figure 4.13. The RDE gave by far the lowest PN (71% decrease compared to WLTC), followed by the NEDC and then WLTC. This is the same trend as that presented by Valverde et al. (2019) for a range of five SI vehicles as can be seen in Figure 4.13, but more exaggerated than their findings. The reasons for all these trends are outlined below.

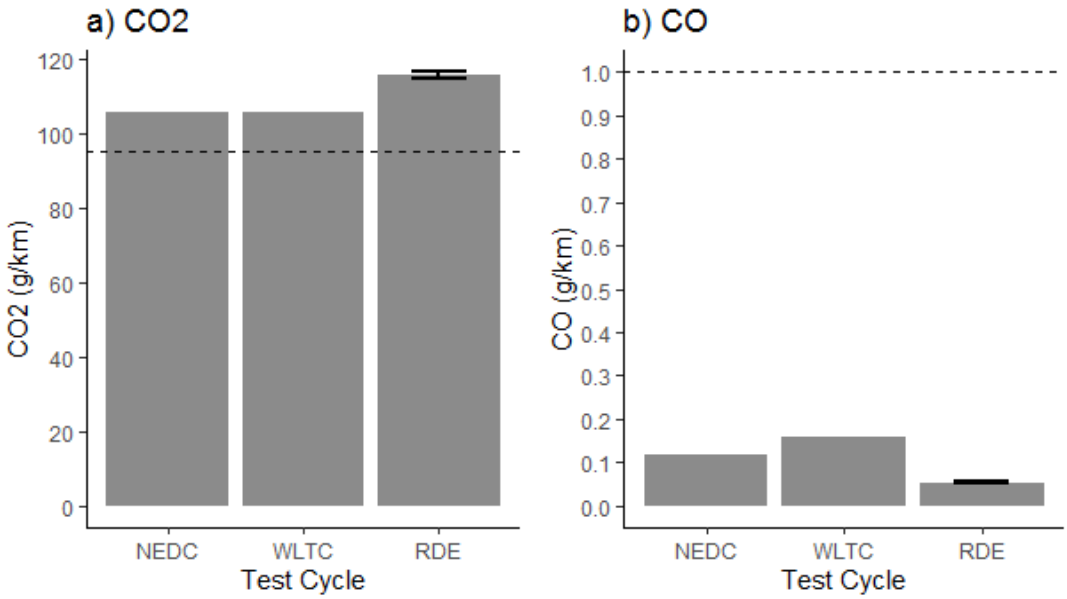

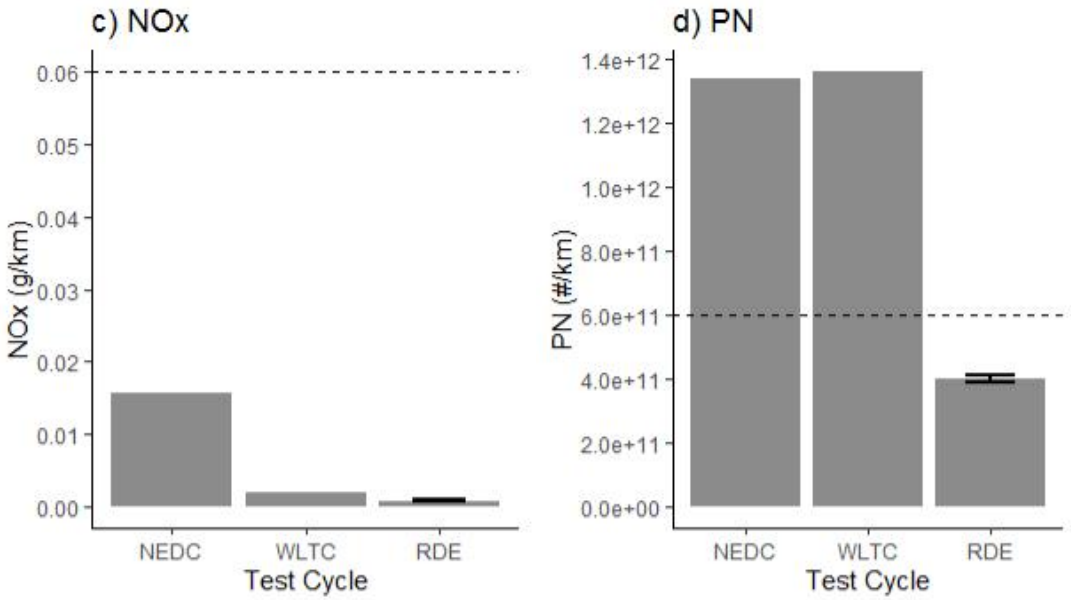

Figure 4.12 Average g/km emission of (a) CO_2, (b) CO and (c) NO_x, and (d) average #/km of PN across the NEDC, WLTC and RDE test cycles.

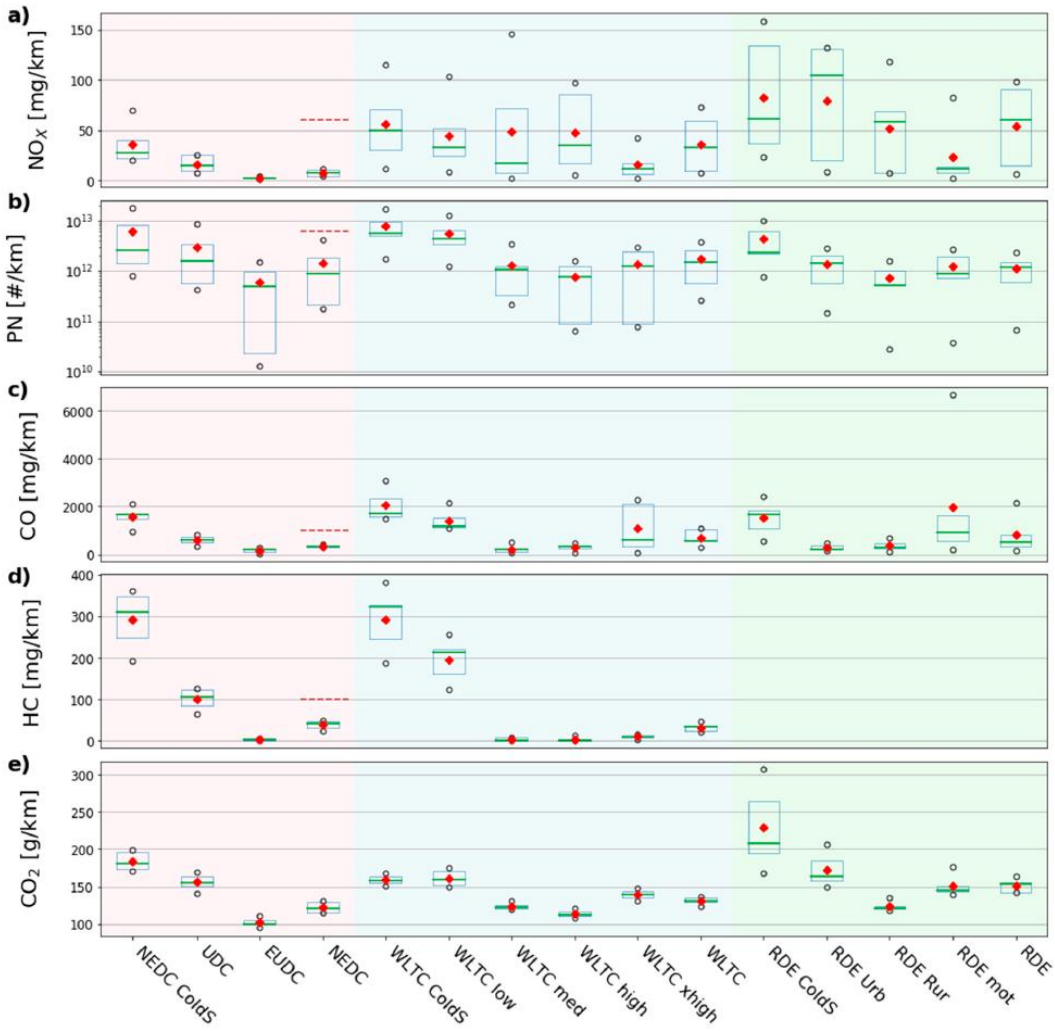

Figure 4.13 SI emission factors from NEDC, WLTC and RDE phases. (a) NOx, (b) PN, (c) CO, (d) HC. Presented by Valverde et al. (2019).

Because of the very high level of agreement between the five RDE tests performed, it was deemed suitable for a single one of these RDE cycles to be randomly selected for more detailed comparison between the NEDC, WLTC and RDE test features in Figure 4.15 to Figure 4.19 below. These plots will be used to elucidate the reasons for the trends presented above. For Figure 5.16 to Figure 5.19 the vehicle speed is on the secondary axis, while engine speed is indicated qualitatively (not corresponding to either y axis), for each plot.

The higher CO_2 emissions of the RDE are a result of the proportionately greater distance covered by less efficient urban driving styles. On top of this, Figure 4.15a shows that the distance-specific emissions, though fairly similar for all three test types, are greater during the urban RDE than the urban sections of the NEDC and WLTC. This is likely caused by the smaller percentage time spent stopped than during either the NEDC or WLTC, in addition to the differing battery SOC behaviour visible for the tests in Figure 4.14.

For NO_x, the majority of emissions are produced in the cold start period, as demonstrated in Figure 4.15c. The far greater total distance covered by the RDE test makes the cold start period a smaller proportion of the test as a whole, thereby rendering the distance-specific emission factors for NO_x smaller than the shorter WLTC and NEDC tests. The magnitude of NO_x emission factors follow the inverse order of test distance for this reason. As mentioned previously, the much greater NO_x emissions of the NEDC test are attributed to one very large event occurring during the cold start period of this test, as can be seen most clearly in Figure 4.18a. Research from CVs suggests that the WLTC and RDE tend to have higher NO_x, due to extra NO_x emissions during increased load and accelerations (Valverde et al. 2019). However, this is not the case for the WLTC and RDE under HEV testing, because the motor can aid the ICE during these periods.

CO emissions are not only produced during cold start, but also when the engine reignites (as discussed further in Chapter 6). The higher number of transient events in the WLTC compared to the NEDC results in a greater number of engine restarts, as presented in Table 4.2 and visible in Figure 4.16. This is the reason that CO has greater distance-specific emissions under the WLTC than the NEDC, despite the longer cold start period of the latter test cycle. This is an important result, as there is disagreement in the literature regarding CO emissions between the WLTC and the NEDC for SI vehicles. It

appears that the additional CO from increased engine restart events on the WLTC indicate HEVs experience increased CO compared to the NEDC, while the inverse is true of the RDE.

As is discussed further in Chapter 6, HEV PN emissions are predominantly produced when the engine reignites, so HEV PN emission factors are heavily related to the number of times the vehicle stops during the test, because this is the condition under which the engine is most likely to fluctuate between on and off. However, the magnitude of PN spike generally increases with the duration for which the engine has been switched off before re-ignition, and so the interplay between these two factors with respect to the distance is the main factor determining PN emission rates. Table 4.2 in Section 4.2.1 showed that the NEDC had the longest percentage time stopped, and the WLTC had the most stops per kilometre, while the RDE had the lowest of both these variables. This has resulted in the WLTC cycle having the largest PN emission factor, followed very closely by the NEDC. The proportionately larger distance covered by rural and motorway styles of driving for the RDE, visible in Figure 4.16, means that this cycles' PN emission factor is by far the lowest. The increased distance covered by the RDE in relation to engine stops is the reason the PN emissions from this HEV on the RDE were smaller than the WLTC and the NEDC by a greater margin than from the SI vehicles presented by Valverde et al. (2019).

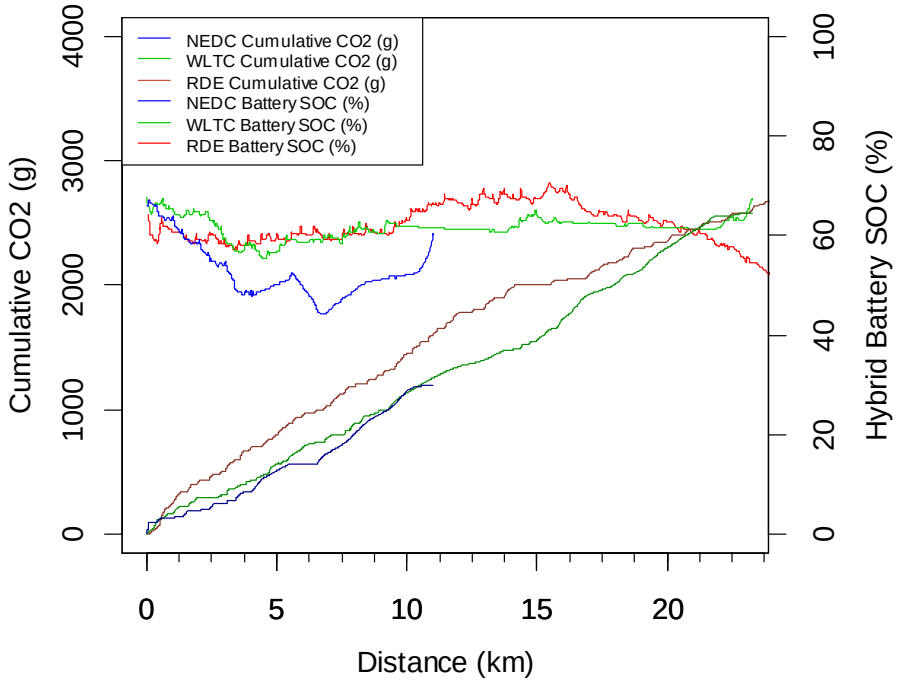

Figure 4.14 Cumulative CO_2 emissions from the NEDC, WLTC and RDE test cycles with distance, alongside the hybrid battery SOC.

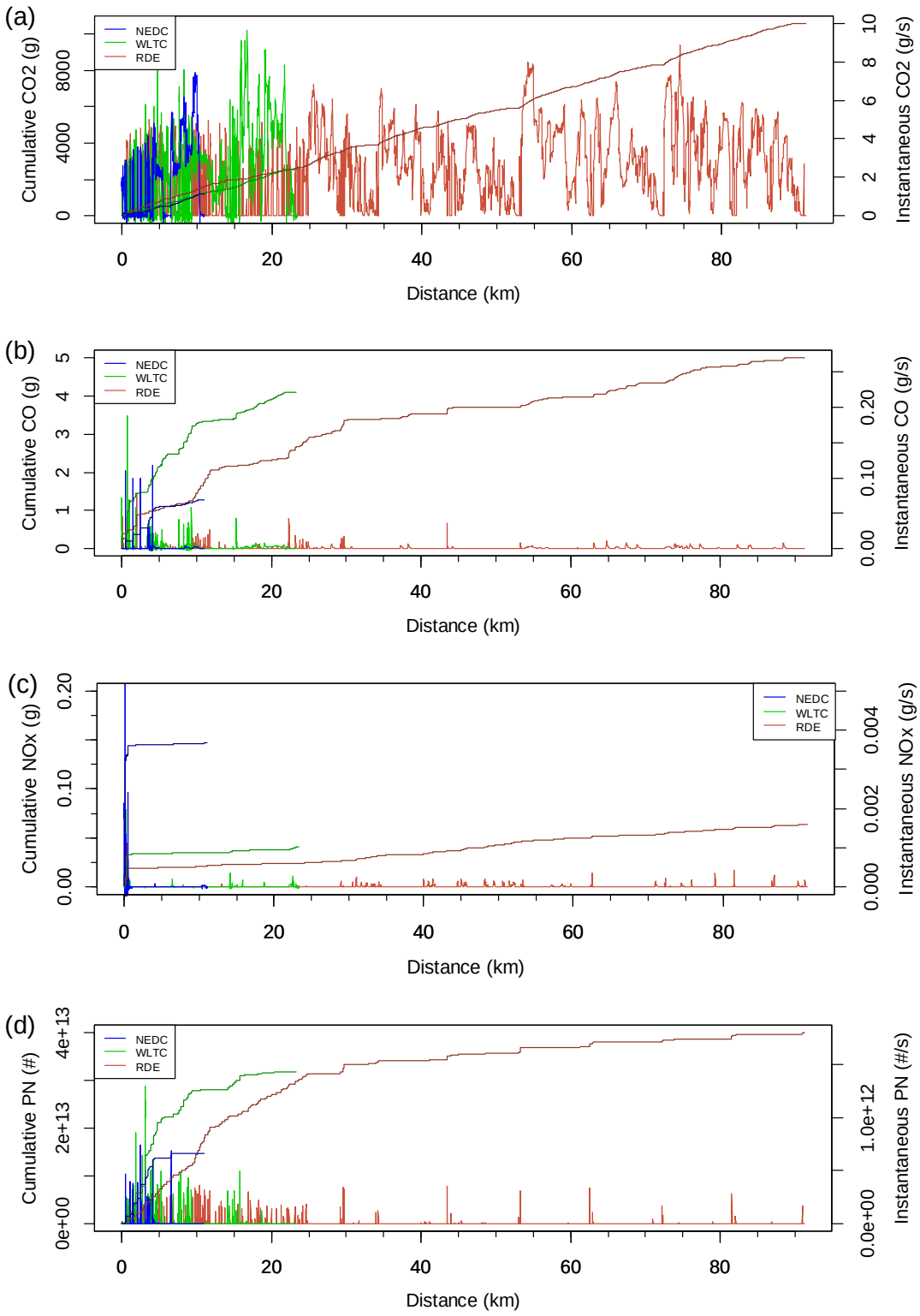

Figure 4.15 Modal and cumulative emissions of (a) CO_2, (b) CO, (c) NO_x and (d) PN, over the NEDC, WLTC and RDE test cycles.

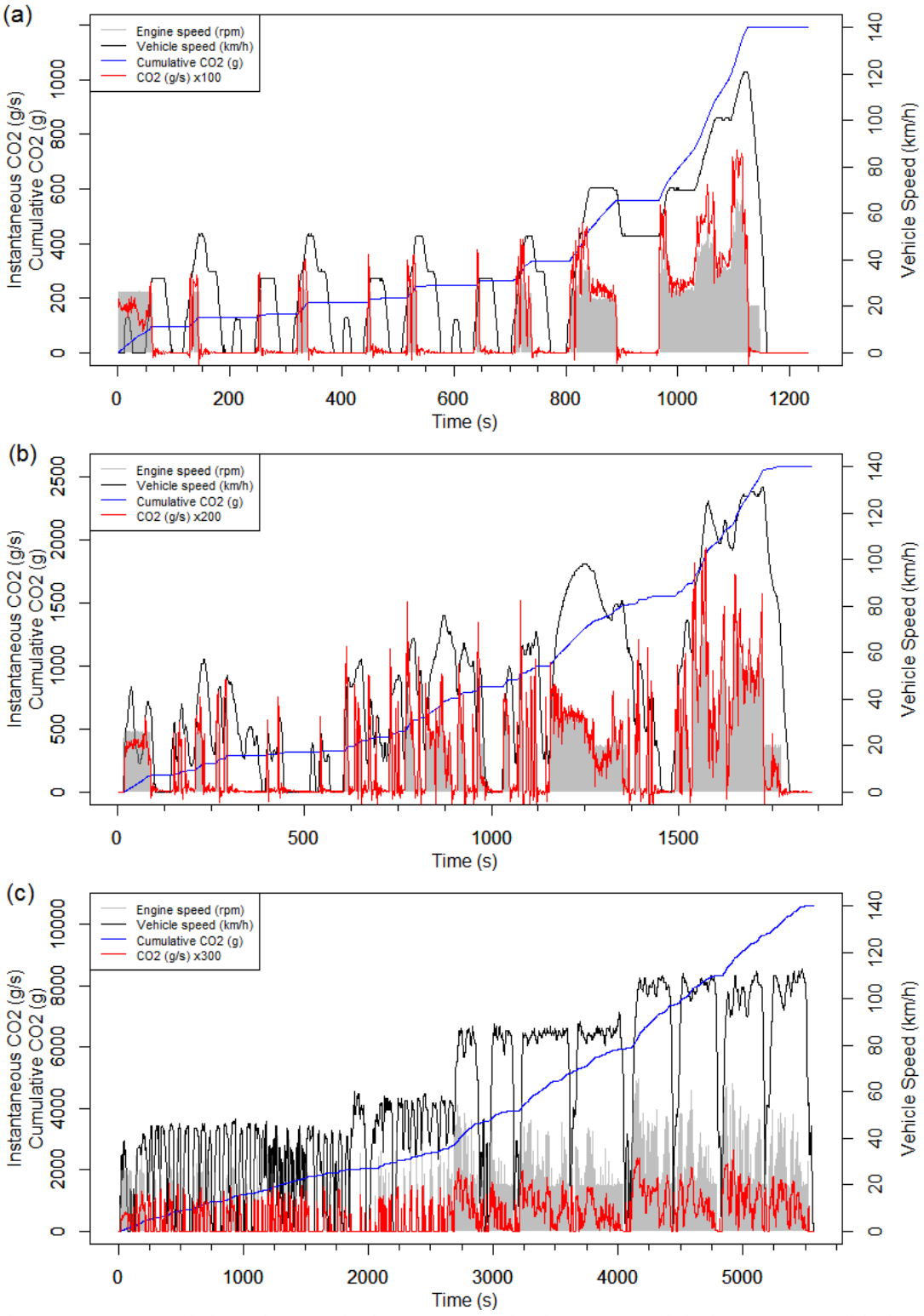

Figure 4.16 Modal and cumulative CO_2 emissions over (a) the NEDC, (b) the WLTC and (c) the RDE.

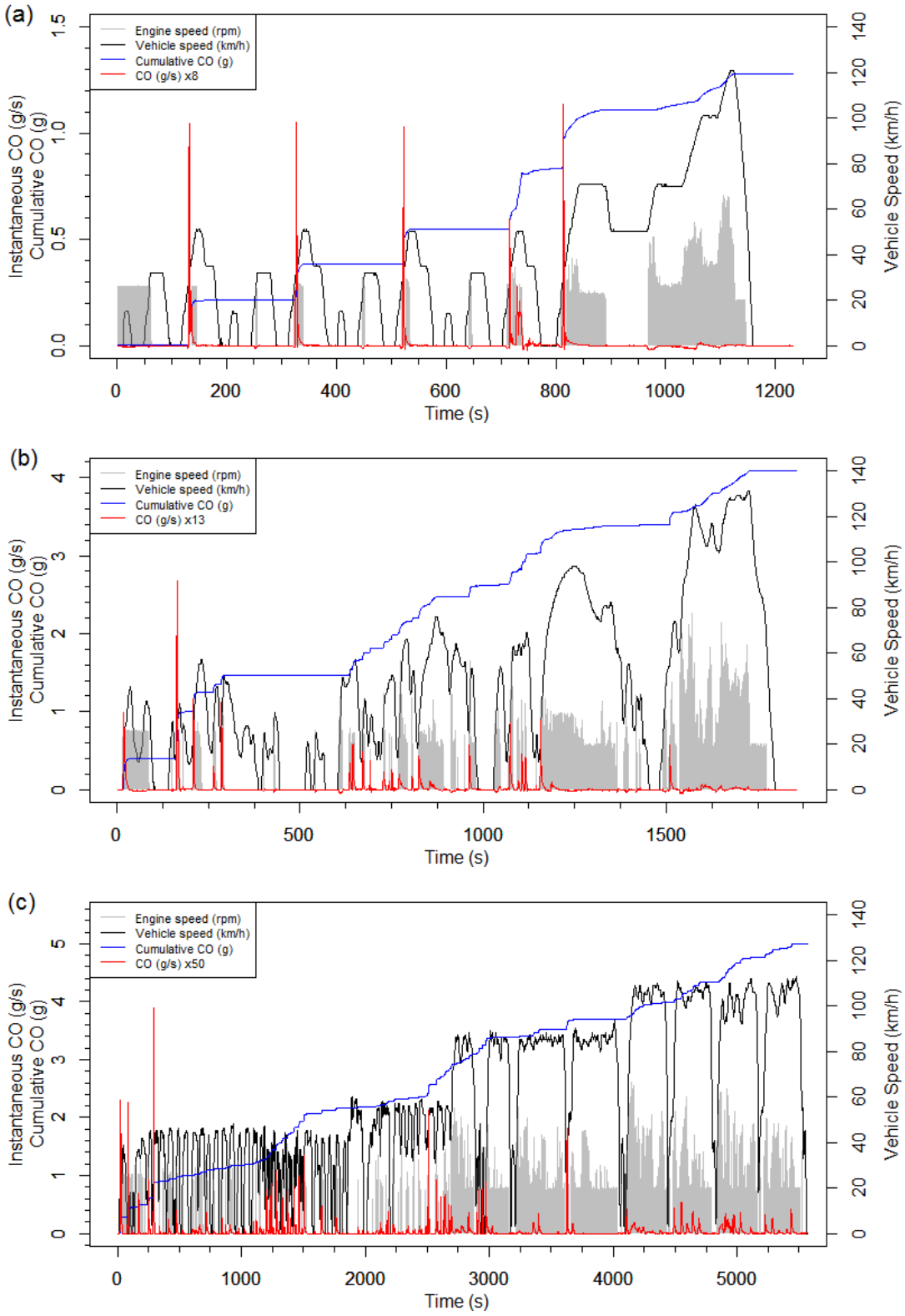

Figure 4.17 Modal and cumulative CO emissions over (a) the NEDC, (b) the WLTC and (c) the RDE.

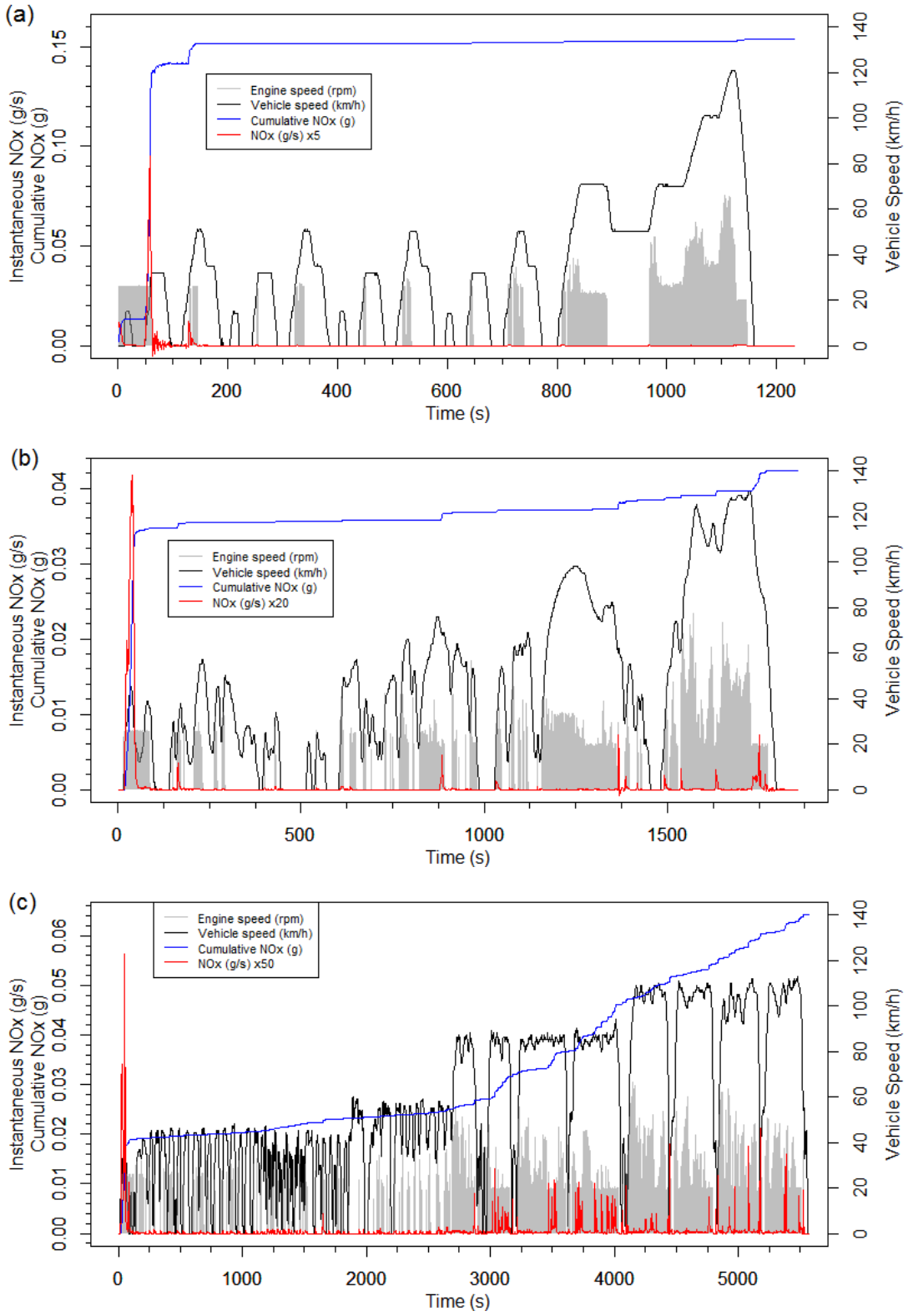

Figure 4.18 Modal and cumulative NO_x emissions over (a) the NEDC, (b) the WLTC and (c) the RDE.

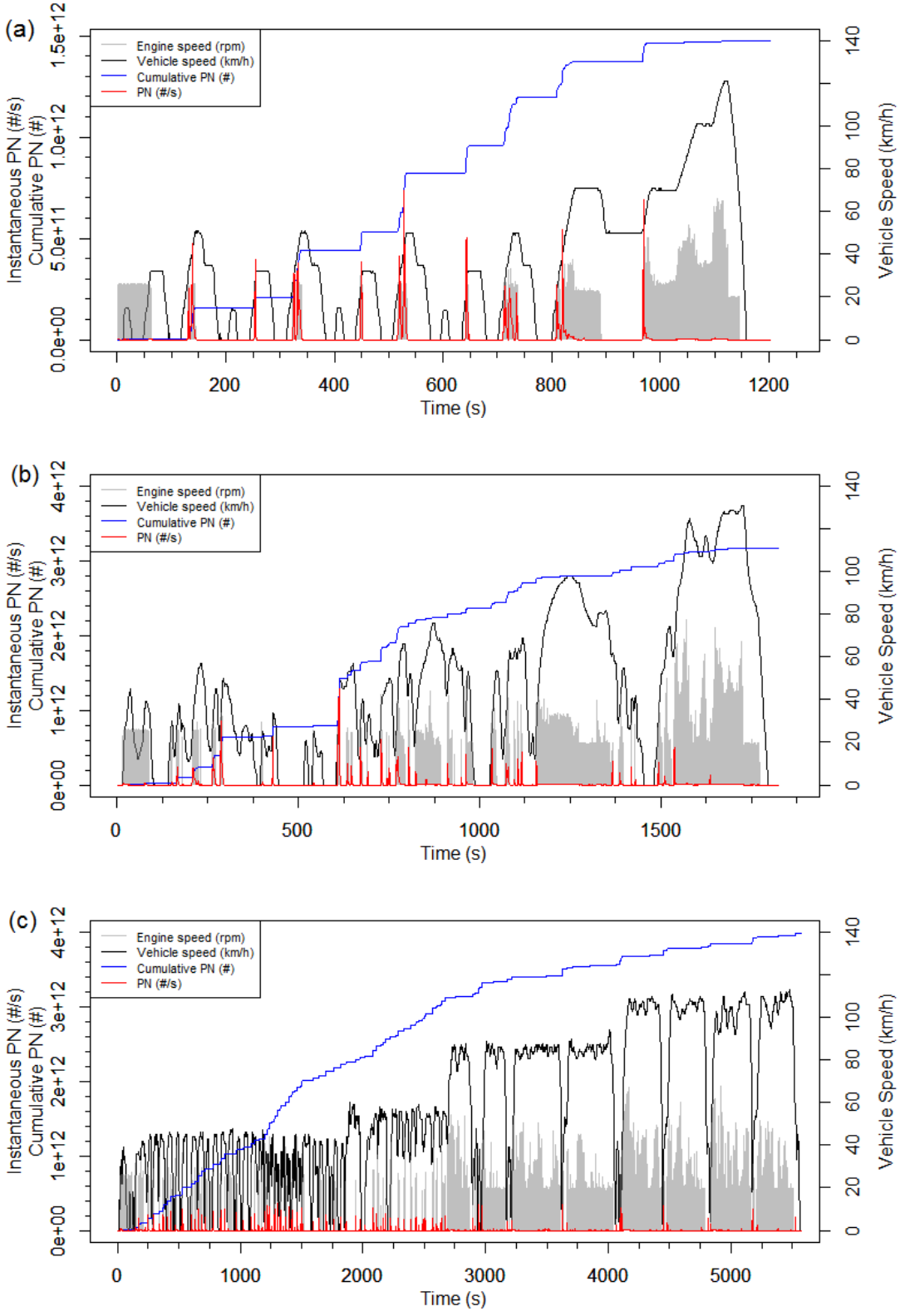

Figure 4.19 Modal and cumulative PN emissions over (a) the NEDC, (b) the WLTC and (c) the RDE.

4.2.2.1 PN size distribution and suitability of the 23nm PN size limit on type approval tests

The size-distributed whole-cycle average PN #/km results from the NEDC, WLTC and RDE-style tests are given in Figure 4.20a, Figure 4.20b and Figure 4.20c respectively. Each test cycle results in a particle number emission factor (#/km) maximum around 50nm, but the RDE-style tests are less unimodal, having secondary maxima occurring either side of this; at 10-15nm and 100-110nm. This finding is in partially contradicts Robinson & Holmén (2011), who reported two distinct modes for their HEV on-road city driving; one again at 50nm but the other at 400nm. However, Giechaskiel et al. (2017) studied the PFI size distribution during engine cold starts of two PFI vehicles, showing one vehicle had a maximum at approximately 10nm, and the other around 100nm; this has similarities to the current work.

In order to investigate the differences in PN distribution across drive modes and cycles, Figure 4.22 shows the PN size distribution for each cycle phase individually. It can be seen that the differences in the total emissions value occur as a result of there being a different distribution in the RDE-style results, which diverge further as the phases continue. Figure 4.23a and Figure 4.23b show the size distribution of PN emissions with time for phase 3 of the shortened RDE-style test cycle, with b showing a smaller scale on the PN axis. During engine operation there is an almost constant low-level of nanoparticle emissions centred around 15nm, and larger diameter (accumulation mode) emissions centred around 110nm. These emissions have a negligible effect on overall size distribution in the NEDC and WLTC test cycles, because of the proportionately larger amount of urban driving styles accompanied by more stop-start behaviour. In the RDE-style test cycle, the higher contribution of steady-state driving means the distribution is far less Gaussian, with two secondary maxima clearly visible in phases 2 and 3 of Figure 4.22. The prevalence of a 10nm nucleation mode particle has been witnessed at high velocities for PFI SI vehicles by Karavalakis et al. (2013), and the appearance of a secondary maximum at around 110nm for higher speed, steady state driving has been witnessed by Christenson et al. (2007) from a First Generation Toyota Prius as shown in Figure 4.21.

It is clear that the type of driving contained within a test cycle has a great impact on the size distribution of HEV PN emissions, which contradicts the conclusions of Robinson & Holmén (2011). Given the narrow range of driving styles included in the earlier study, this new finding has greater reliability. The

more low-speed, stop-start styles of behaviour within a drive cycle, the narrower and more Gaussian the size distribution of PN emissions of an HEV will be, centred around 50nm for this vehicle. Test cycles with prolonged periods of higher speed driving will encourage the engine to engage more constantly, which leads to a broader range (but lower magnitude) of PN distributions.

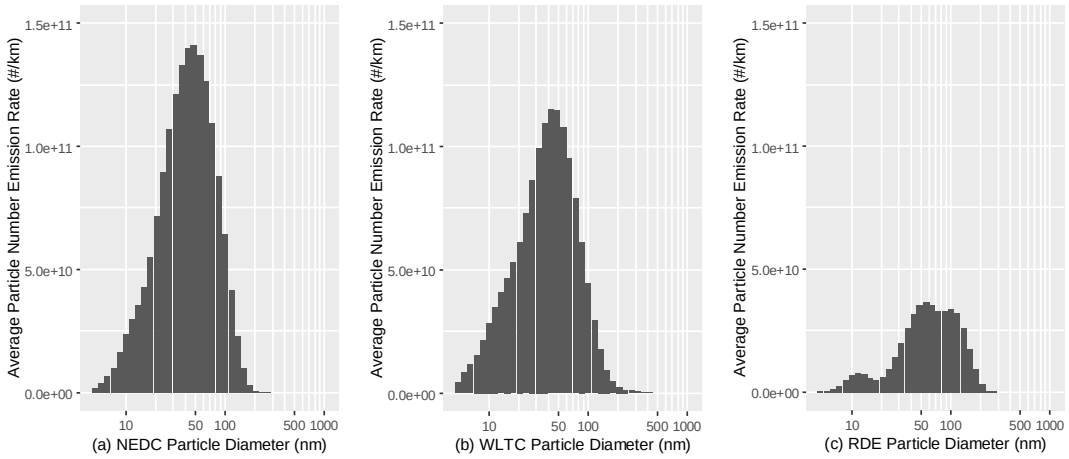

Figure 4.20. Average distance-specific PN size distribution for the NEDC, WLTC and RDE-style drive cycles.

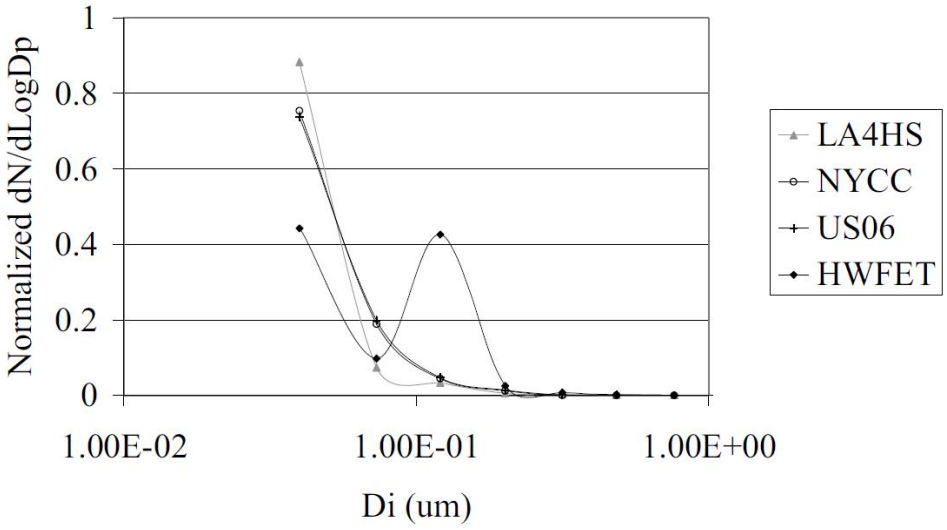

Figure 4.21 PN size distribution from a First Generation Toyota Prius over various test cycles as presented by Christenson et al. (2007).

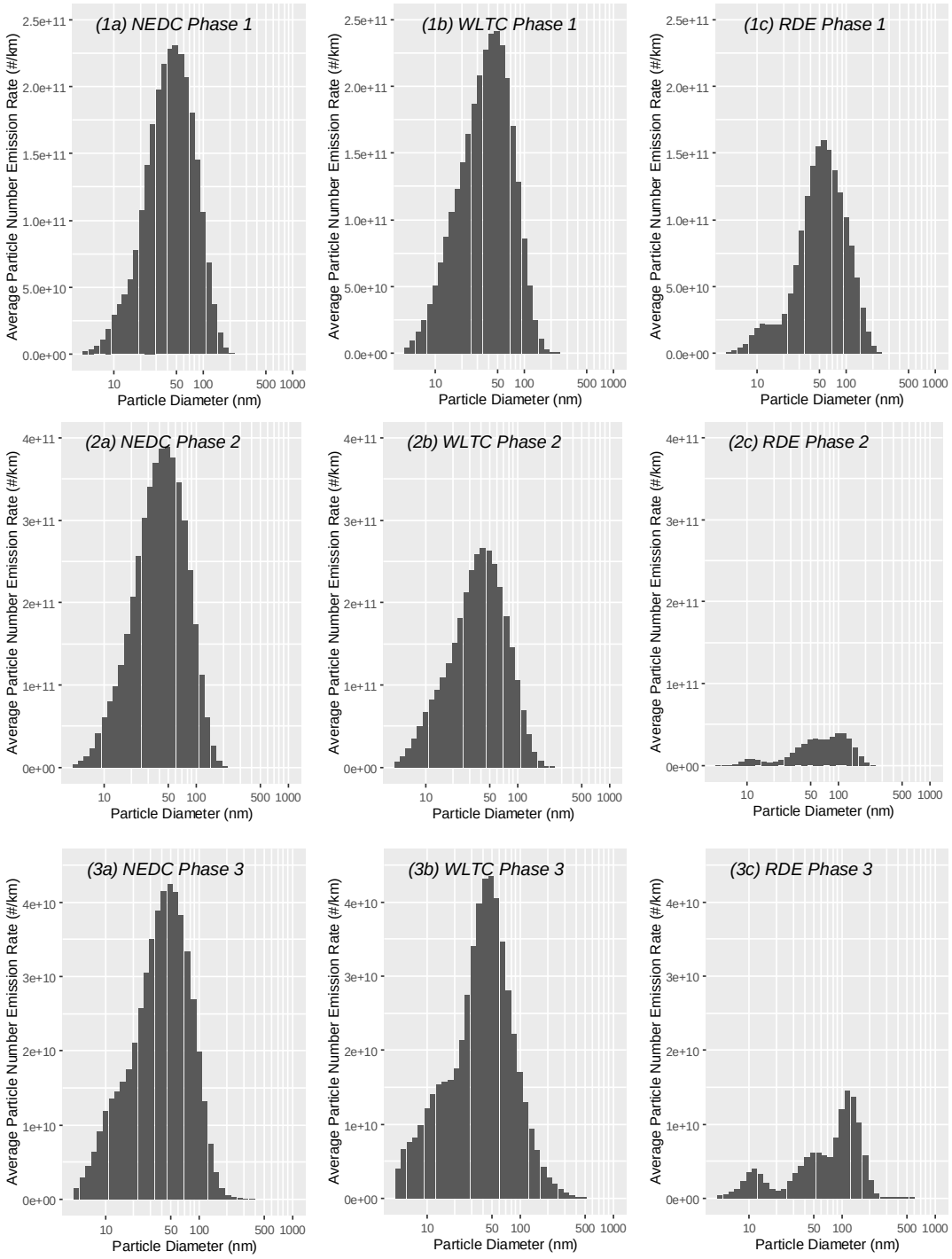

Figure 4.22 Distance-specific PN size distribution of (a) the NEDC, (b) the WLTC and (c) the RDE-style. Phases 1, 2, and 3 given for each.

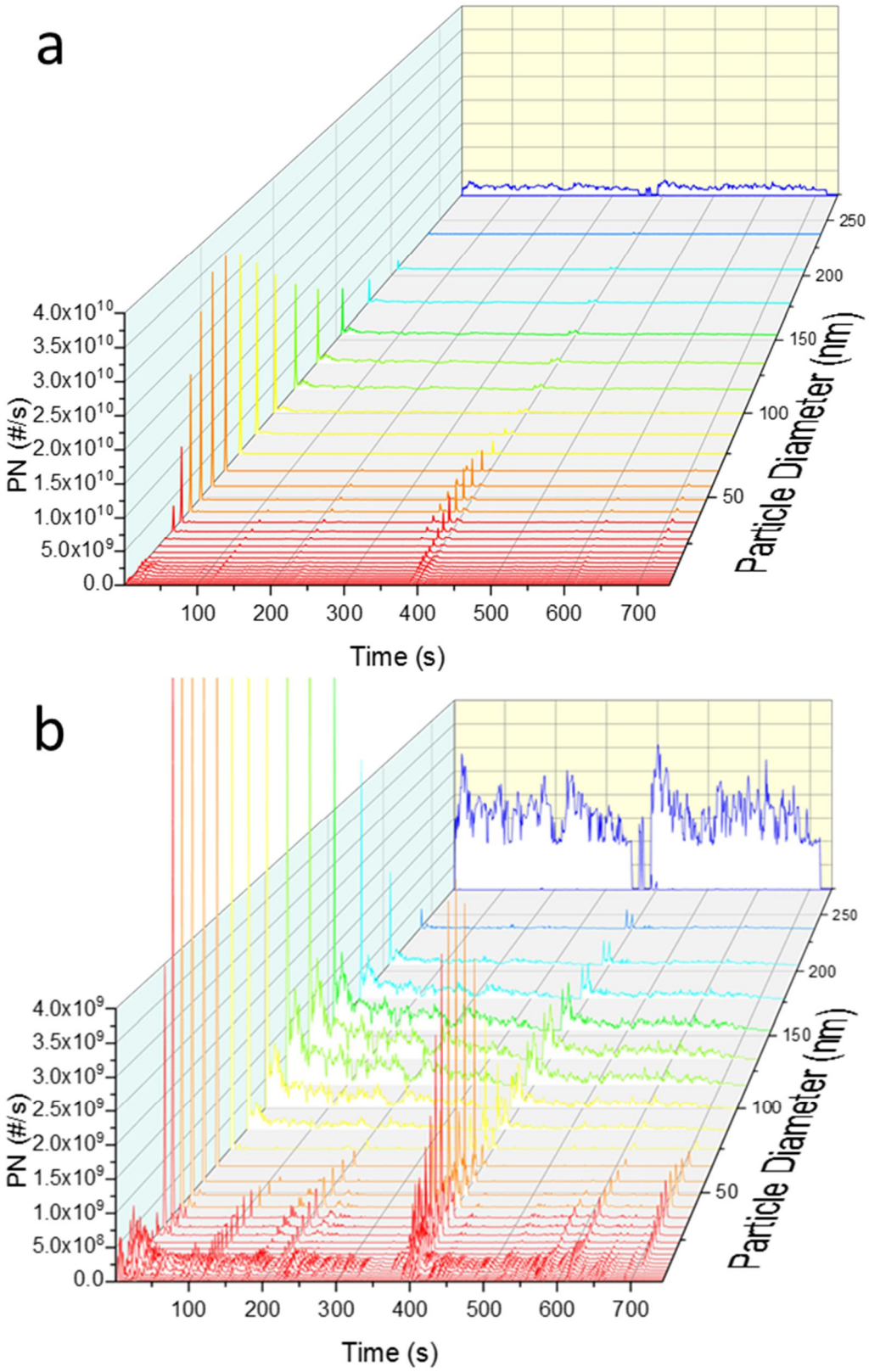

Figure 4.23 (a) Motorway driving PN size distribution, with engine RPM indicated in blue against back wall. (b) shows the y axis scale a magnitude 10 smaller.

4.2.2.1.1 Suitability of the 23nm PN size limit on type approval tests

As discussed in Chapter 2 Section 2.6.2, the type approval legislation currently sets a lower limit to the size of PN counted of 23nm diameter (Giechaskiel et al., 2017). However, legislators are currently debating the possibility of lowering this limit to diameters such as 10nm, in order to capture more of the harmful nanoparticles that can cause such damage when inhaled (Giechaskiel, Lähde, et al., 2019; Giechaskiel, Mamakos, et al., 2019). In order to study the effect that this would have on the PN emission results, the WLTC and RDE-style tests have had their PN_{23nm}, PN_{10nm} and total PN (down to 4.87nm) calculated from size-distributed DMS500 data. The results for the WLTC and RDE-style tests are displayed in Figure 4.24a and Figure 4.24b respectively. For the whole WLTC cycle, the PN results going from a cut-off of 23 nm to 10 nm increased by 25.2% and from a cut-off of 23nm to “total” (4.87nm) PN increased by 31.1%. These differences are much smaller than those witnessed for two PFI SI vehicles on the NEDC and WLTC test cycles in a previous study (Giechaskiel et al., 2017), indicating that HEVs utilising PFI technology cannot be assumed to have the same PN size distribution characteristics as their CV counterparts. For the WLTC cold start phase 1, the increases were similar to the total, standing at 26.5% and 30.7% respectively. For the RDE-style cycle, PN results increased by 9.7% going from 23 nm to 10 nm and 12.1% to total PN. For the urban phase, the increase was similar to that of the total RDE test, standing at 8.7% and 10.5% respectively. There are differences between values for the different test cycles, and this is mainly due to the fact the WLTC was from cold start, while the RDE-style cycle was from warm start. The proportion of sub 23nm particles is larger under cold start conditions.

It is clear that a lowering of the cut-off would increase the reported PN emission results at type approval, thereby encouraging lower PN air pollution levels by forcing car manufacturers to take more action to limit tailpipe PN emissions to ensure vehicles pass the tests. The majority of the difference in emissions is achieved by reducing the cut-off to 10nm, meaning that substantial improvements can be made while still eliminating many of the smallest particles that are so troublesome to measure in a reliable and repeatable manner. By comparison with Giechaskiel et al. (2017), it can be inferred that if PFI vehicles are also made subject to the PN emission regulations, and that the size cut-off is reduced from 23nm to 10nm, that HEV PFI vehicles would see a smaller percentage increase in reported PN as a

result than conventional PFI vehicles. It should be noted that a limitation to the reliability of this conclusion is the assumption of a similar proportion of volatile and non-volatile PN to CVs.

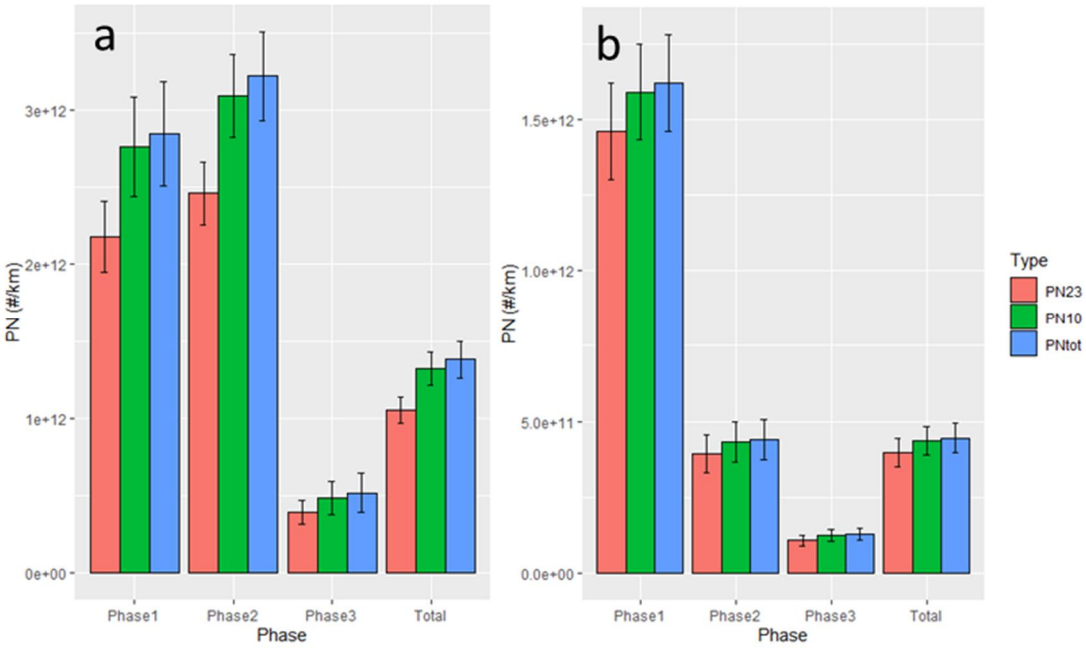

Figure 4.24. PN values comparing diameter cut-offs at 23nm, 10nm and 4.87nm, across phases of (a) the WLTC and (b) RDE-style cycles.

4.3 Chapter 4 Summary

This chapter has compared and contrasted the dynamic properties of the NEDC and WLTC type approval tests with multiple repeats of an RDE test adhering to all requirements outlined in the final version – Package 4 – of the RDE legislation. This began to achieve the first objective outlined in the Refined Aims and Objectives (section 2.11) by satisfying Task 2. The effects of these dynamic properties on the behaviour of an HEV, and the subsequent impact on the reported CO_2, CO, NO_x and PN emissions has been studied for the first time in literature, thereby satisfying Task 3. By comparing findings with previous literature, it has been possible to infer how HEV behaviour has different effects on the emissions compared to CVs. Detailed study of the PN size distribution for HEVs and the suitability of the 23nm PN size cut-off has also been assessed. For the first time, the differences between PN_{23} and PN_{10} results for an HEV running a WLTC test have been quantified.

The trends in the HEV CO_2 emissions over the different test cycles are generally in line with those in previous literature for CVs. The RDE results

were the highest, followed by the WLTC and then the NEDC (with the WLTC and NEDC being very similar). The CO and PN emissions of the HEV showed high sensitivity to both the number of times its engine restarted, and the amount of time that the engine was turned off, meaning that the number of vehicle stops and transients per unit distance had a greater impact on the emissions than have been seen for CVs. This has resulted in lower CO and PN values on the RDE test compared to the WLTC and NEDC than expected from the CV studies to date. The HEV has proven to be less impacted by high load events, therefore the WLTC and RDE cycles do not result in higher NO_x emissions, as other literature on CVs has generally witnessed. Instead, the proportionately smaller contribution of cold start has meant that the NO_x emissions are lower for HEVs on the RDE and WLTC.

With regard to PN size distribution in terms of #/km, the engine restart events of the HEV result in a Gaussian distribution with a maximum around 50nm diameter. The more constant engine operation has a much lower magnitude bimodal distribution with maxima at diameters of 15nm and 110nm. These characteristics result in the RDE having a markedly different distribution to the WLTC and NEDC; the former being less Gaussian than the latter, with a less distinct maximum. By studying the proportion of particles of smaller diameter than 23nm and comparing with values in the literature for CVs, it can be inferred that a tightening of the cut-off diameter currently in the legislation would result in a greater number of particles being detected for HEVs, but likely by a smaller margin than for CVs, due to a smaller proportion of total PN being below the 23nm limit.

The next chapter will go into further detail on the RDE test specifically, including investigating how representative the reported RDE emissions are.

Chapter 5
Real driving emissions (RDE) test properties and results for conventional and hybrid electric spark ignition vehicles

5.1 Introduction

Building on Chapter 4, this chapter will address Objective 1 and Objective 2 as outlined in Section 2.11 of Chapter 2. The drive cycle characteristics and emissions profiles resulting from the RDE test cycle will be studied in depth, analysing how the latest version (Package 4) of the legislation differs from earlier packages, particularly with regard to the reported emissions. This work will show how the RDE test cycle has developed, and allow comparison of different vehicles' results if tested according to different packages of the RDE regulations. This will satisfy Task 4 set out in Chapter 2. Particular attention will be paid to HEVs, in order to partly address Objective 3 set out in Chapter 2. Finally, value of a non-chassis dynamometer test to represent real-world driving will be investigated by comparing an on-road type approval test against a chassis dynamometer test. This will involve investigating whether the urban section of the RDE is a realistic representation of congested city driving, and analysing the RDE repeatability. This section will satisfy Task 5 and Task 6 set out in Chapter 2.

5.2 RDE packages and the effects on the reported results

5.2.1 RDE package results comparisons for a range of vehicles

In Packages 1 and 2 of the RDE test, the reported emission rates were calculated using the MAW method (outlined in Chapter 2 Section 2.7.7). In addition, before the MAW processing was applied to the data, the cold start section of the drive, any periods consisting of vehicle speed <1km/h and any periods where the engine was turned off were removed from the data. In the newer Packages 3 and 4, however, the data undergoes far less additional processing and removal of data to calculate the reported results, as explained in Chapter 2 Section 2.7.7.

In order to study the effect of these processing methods on pollutant emissions across a broad range of vehicles, the RDE test results from the

eight vehicles outlined in Chapter 3 Section 3.6.1 were processed. The values of regulated pollutant emissions across the urban phase and total RDE are compared for each of the four regulated pollutants in this section. It should be noted that the Toyota Corolla vehicle presented in the graphs commenced its RDE test from warm start (engine coolant temperature 84°C), so the comparisons for this vehicle are not complete, and are not incorporated into the calculated percentage differences across methods.

For each vehicle RDE test the time alignment of the data and any necessary corrections were performed. Then the average emission rate per kilometre of CO_2, CO, NO_x and PN was calculated in the four different ways labelled (a) to (e) in the list and flow chart in Figure 5.1 below. For all options, the data was pre-processed according to methods outlined in Chapter 3, Section 3.8.5. The Euro 5 fleet-average emissions target set out in Regulation (EC) 443/2009, and the Euro 5 pollutant emissions limits (measured over the NEDC) – applicable to all but one (Toyota Prius, Euro 4) of the vehicles tested in this campaign – are indicated on the relevant graphs. The figures show the RDE emissions results from the urban section and the whole RDE test, as these are the two results that must be maintained below the respective NTE limits.

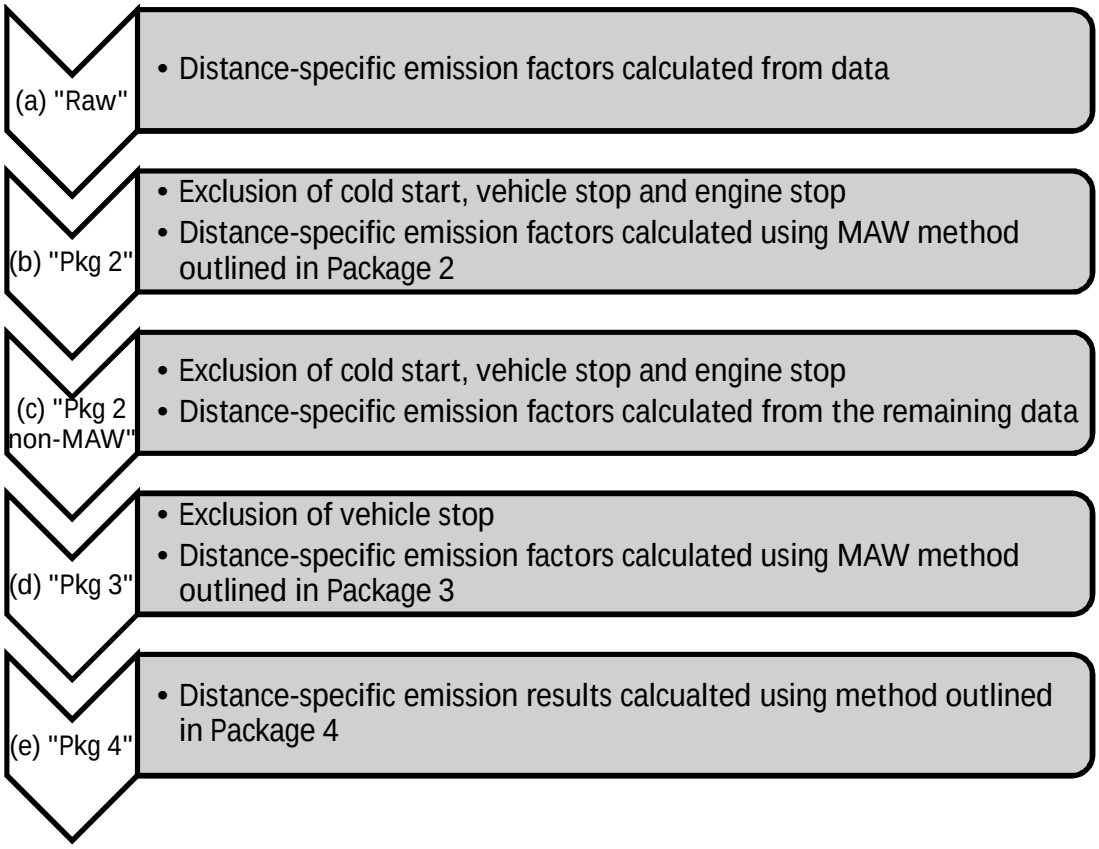

Figure 5.1 Diagram of the data processing steps used in Section 5.2.1.

The processing for the steps in Figure 5.1 are:

(a) No exclusions performed and no MAW processing (called “Raw” in the following figures). Distance-specific averages calculated for the whole RDE test, and each phase separately
(b) According to RDE Package 2, i.e. exclusions above performed, followed by MAW (Package 2) method to calculate final results (called “Pkg2 MAW” in the following figures)
(c) With only the data exclusions of Package 2 applied, and the results calculated from this data without any MAW processing (called “Pkg2 non-MAW” in the following figures)
(d) According to RDE Package 3, i.e. exclusion of vehicle stop sections only, followed by MAW (Package 3) method to calculate final results.
(e) No exclusions performed and no MAW processing, with results calculated according to the method outlined in Package 4 (called “Pkg 4” in the following figures)

5.2.1.1 CO_2

The urban and total emission results from each processing method for CO_2 are given in Figure 5.2 and Figure 5.3 respectively. For the urban section, the raw results show higher CO_2 emission rates than those with the RDE Package 2 exclusions performed, and the MAW processing generally reduces this even further. The Package 4 processing brings the results back to represent those without any package processing, except for the Skoda Octavia, for which a small decrease in urban emissions is seen. The effects for the test cycle as a whole are less distinct, but still show the same general trend for the exclusions.

Processing according to Package 2 decreased reported urban CO_2 by 7±2% but total CO_2 by only 1±0.7%, compared to the raw results. Removal of the MAW processing slightly increased the values, in agreement with results presented by Varella et al. (2019). Processing according to Package 3 slightly decreased values compared to Package 2, by around 1.5±0.5% for both urban and total, but this average difference was almost entirely caused by the HEV Toyota Prius. Package 4, however, with its lack of eliminations or MAW, increased urban and total CO_2 by 10±1% and 2.6±0.5% respectively, relative to Package 3. This brings reported results almost exactly back in line with the raw results, with only one vehicle having a small downward adjustment. The elimination of the MAW processing increased urban CO_2 values by 3±1% but

decreased total values by 2.9±0.2%. The MAW results are affected specifically in two different ways.

Firstly due to the averaging windows, the portions of the drive at the beginning and ends of the data being analysed contribute less to the average than those portions in the middle, because they are included in fewer individual windows. The emissions of these end sections in relation to the middle section of the drive therefore have some impact on whether the reported emissions increase or decrease when the MAW processing is removed. If the emissions at start and end are greater than in the middle, then the reported results will increase when the MAW processing step is removed, and vice versa. Secondly, in addition to this effect, how the CO_2 emissions compare to the characteristic curve is important, because the windows with emissions outside the primary range are weighted down, according to how far from the primary range they are. This was removed from Package 3 MAW methods. The interplay between these two factors determines the overall change seen when the MAW is removed from the processing method for Package 2. Generally, based on the results presented in this section, it appears that the first point has the greater impact on results when the MAW processing is removed.

Inclusion of cold start, vehicle stops, engine stops acts to increase emissions by 7±2% for urban and 4±0.7% for total CO_2 respectively. Engine idling while stationary can increase the distance-specific emissions greatly, due to the lack of distance being made during this time. In addition, some engine efficiency decrease (CO_2 increase) is generally seen during cold start for vehicles due to the warm-up procedures, so this also increases the emissions when included.

There is one vehicle that shows the opposite trend amongst this set of vehicles. The Toyota Prius, because of its hybrid nature, displays lower CO_2 emissions over both urban phase and total RDE test cycle for raw data, Package 3 and Package 4 data, compared to the Package 2 (MAW and non-MAW) handling. This is because the elimination of data where the engine is turned off means that distances of movement with the engine off are not being represented under Package 2, so the reported average emission rates per km travelled for these vehicles under older packages (1 and 2) were greater than the values being represented by the raw data and by newer packages (3 and 4).

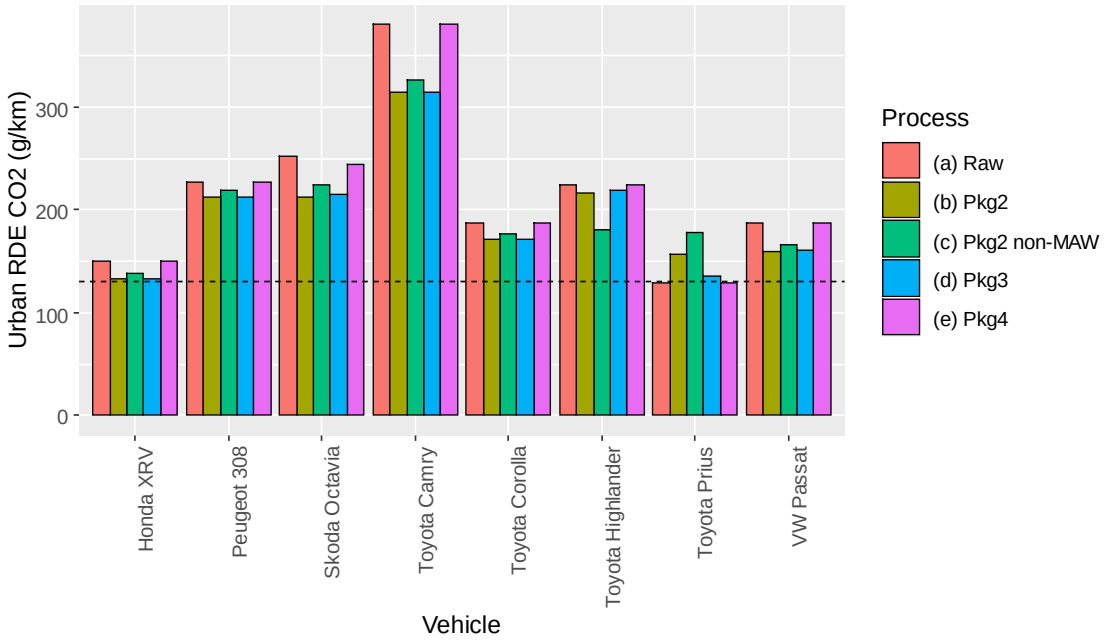

Figure 5.2 Urban RDE CO_2 emissions for a range of SI vehicles under the RDE handling methods outlined in Figure 5.1. The Euro 5 fleet-average emissions target is indicated by a black dashed line.

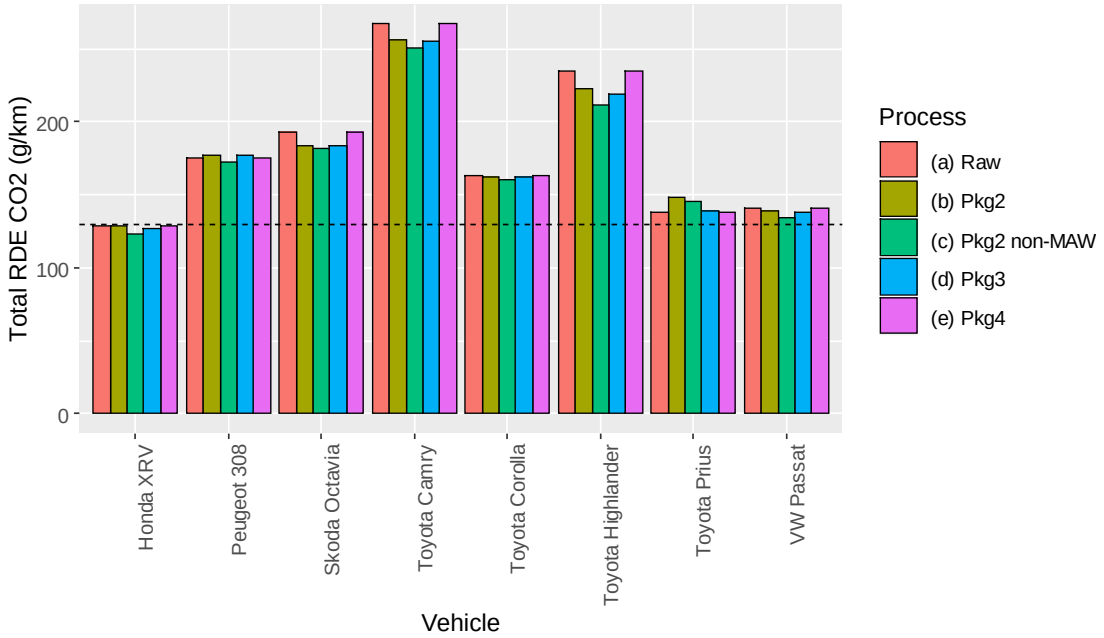

Figure 5.3 Total RDE CO_2 emissions for a range of SI vehicles under the RDE handling methods outlined in Figure 5.1. The Euro 5 fleet-average emissions target is indicated by a black dashed line.

5.2.1.2 CO

Figure 5.4 and Figure 5.5 display the urban and total CO emission results across the five processing methodologies outlined at the beginning of this section. Package 2 processing caused a 50±4% decrease in reported values for urban, and approximately half this decrease for total results, compared to the raw data. Package 3 gave broadly similar CO results to Package 2, while Package 4 gave the same results as the raw data.

The elimination of MAW from the processing had varied effects across vehicle types, while the inclusion of cold start, vehicle stop and engine stop sections led to a general increase in reported results across CVs by 160±90% for urban sections and 17±19% in total. The Prius' urban section was the only vehicle section to see a decrease.

The previous underrepresentation of the beginning and end of the drive caused by the MAW process' averaging windows method is the main driver of the changes seen going from (b) to (c) in the graphs and Figure 5.1. The calculation of pollutant emissions for Package 2 is also dependent on the CO_2 characteristic curve, but one level further removed than for the CO_2 emissions. If pollutant emissions are particularly high during a time where the CO_2 emissions of that window are outside the primary tolerance, then those emissions will be weighted down accordingly. Analysis deemed that the impacts of this step on overall reported values was low compared to other factors. The inclusion of cold start plays the greatest role in increasing the reported emissions going from (b) to (d), while the removal of the MAW processing and its effects was responsible for the change from (d) to (e). From comparison between these factors, we can deduce that the inclusion of cold start, vehicle stop and engine stop has caused the greatest difference in some cases while the MAW has had the greater impact in others. If the cold start section was particularly CO intensive, then it was the former. Otherwise, it was the latter. Generally, it appears that the cold start makes a greater difference, or comparable difference, to the MAW processing. The HEV Prius is the exception, because it actually had lower distance-specific cold start mass emissions than the middle portion of the drive.

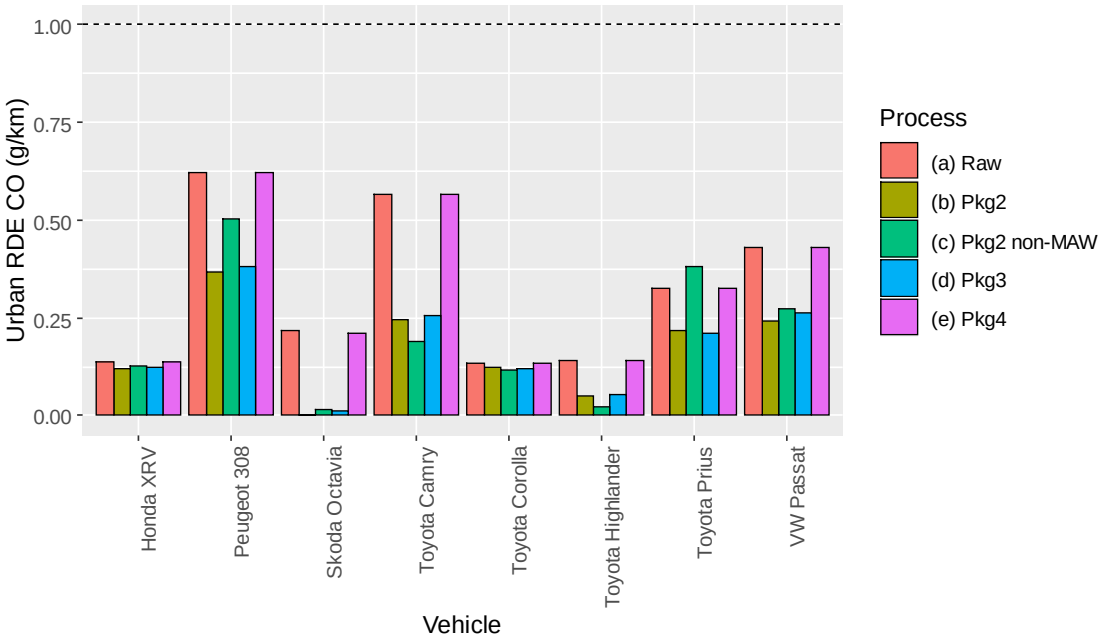

Figure 5.4 Urban RDE CO emissions for a range of SI vehicles under the RDE handling methods outlined in Figure 5.1. The Euro 5/ Euro 6 emission limit is indicated by a black dashed line.

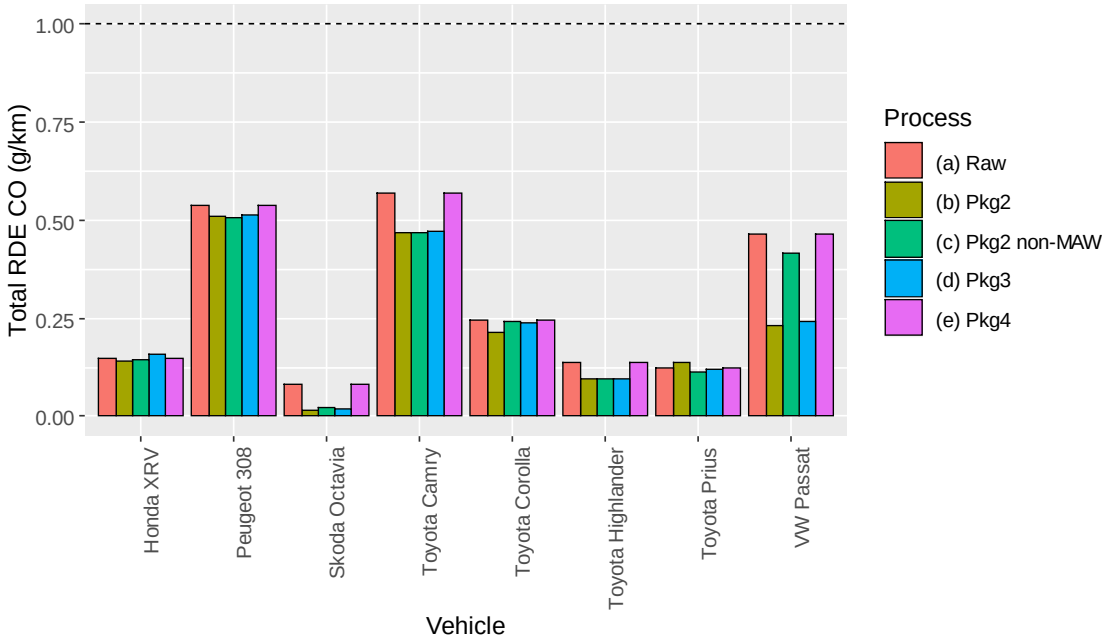

Figure 5.5 Total RDE CO emissions for a range of SI vehicles under the RDE handling methods outlined in Figure 5.1. The Euro 5/ Euro 6 emission limit is indicated by a black dashed line.

5.2.1.3 NO_x

Figure 5.6 and Figure 5.7 display the urban and total NO_x emission results across the five processing methodologies outlined at the beginning of this section. As for CO, the results for NO_x vary greatly from vehicle to vehicle. On average, Package 2 urban emissions were increased by 54±30% but total results decreased by 7±4% compared to raw values, while Package 3 brought increases of 6±3% and 3±1% respectively compared to Package 2. Package 4 brought values back in line with the raw values. It is worth noting that the Peugeot 308 and Toyota Prius were the only vehicles to show an increase for packages 2 and 3, with the other vehicles all having decreased emissions. This will be discussed more below.

On average, the elimination of MAW from the processing decreased Package 2 NO_x results by 25±4% and 7±1% in urban and total RDE respectively, in agreement with Varella et al. (2019). A large proportion of NO_x emissions occur during high speed, high load driving, particularly during parts of the rural section and motorway sections. The MAW acts to make the mid-test sections more influential to the overall emissions than the beginning and end of each test, so when the bulk of NO_x emissions are produced during the middle portion of the RDE test, the emissions are amplified by the MAW. This is the case for the Peugeot 308 and Toyota Prius, skewing the average values mentioned above. If the bulk of the NO_x is emitted toward the end of the motorway phase or during cold start instead, then we see decreased values under the MAW processing.

The inclusion of cold start, vehicle stop and engine stops ((c) to (e) in Figure 5.1) result in less of an increase in emissions compared to for CO for the urban section because NO_x is seen for high speed, high load driving as well as during cold start. The emissions increase was 30±8% in the urban (ignoring Toyota Highlander) and 25±5% for total. The Toyota Highlander was ignored because it suffered one very large emissions event during cold start that was not represented by Package 2 and not well represented by Package 3, skewing the average percentage differences. An increase (or no change) was seen for all vehicles except the HEV. As with CO_2, the HEV Prius shows increased NO_x emissions for Package 2 due to the distance travelled with the engine off being discounted, effectively increasing distance-specific average emission factors. The dominating property for this vehicle is still the centralised NO_x distribution amplification by the MAW technique (Package 2 and 3).

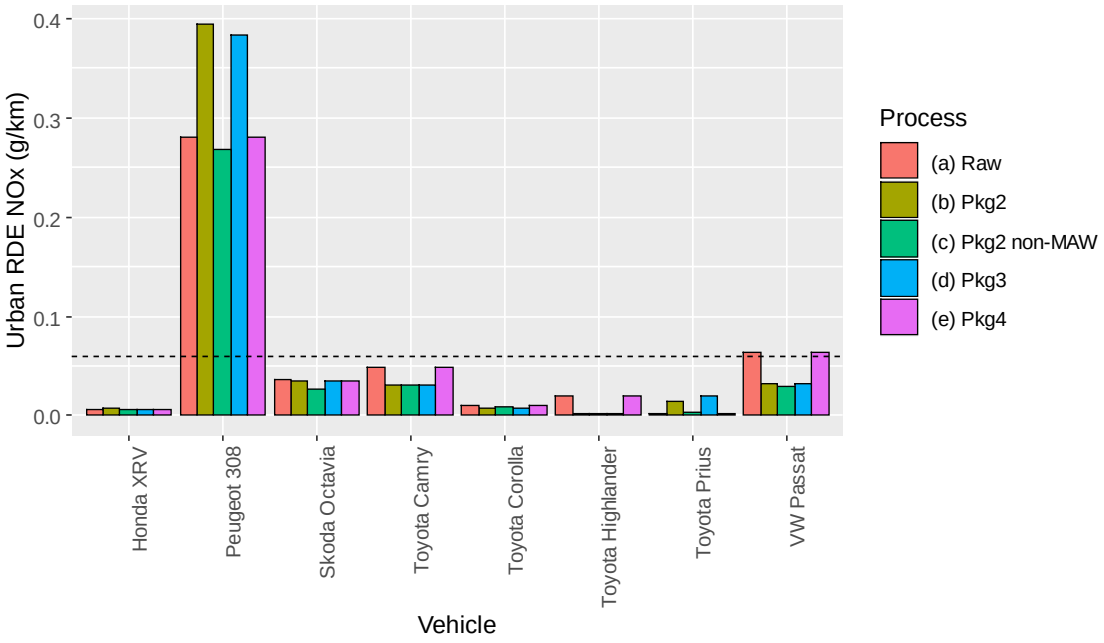

Figure 5.6 Urban RDE NO_x emissions for a range of SI vehicles under the RDE handling methods outlined in Figure 5.1. The Euro 5/ Euro 6 emission limit is indicated by a black dashed line.

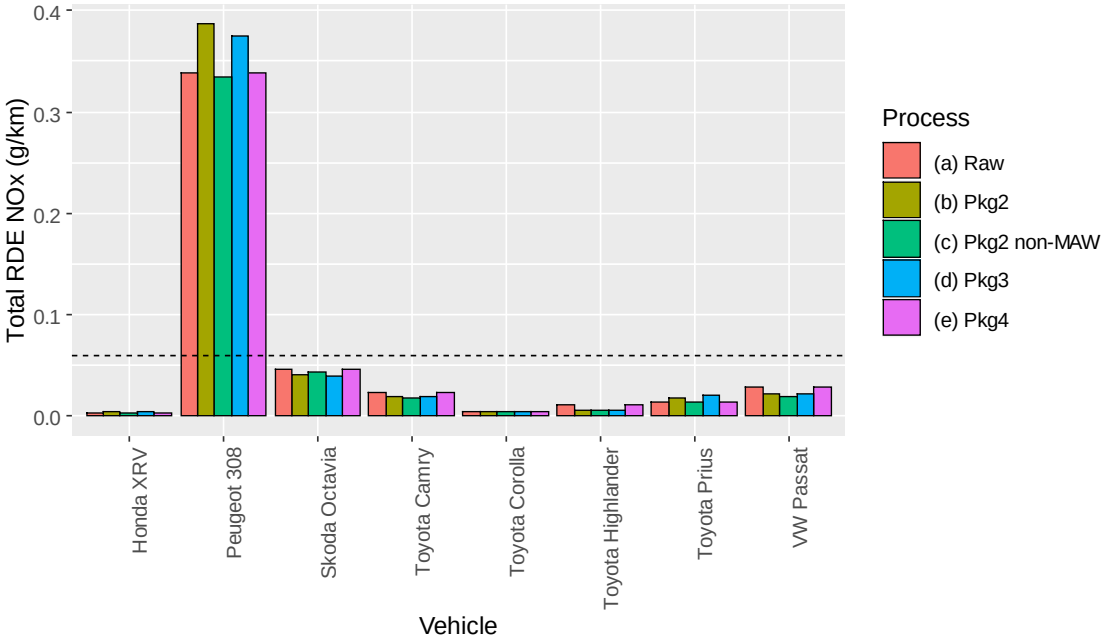

Figure 5.7 Total RDE NO_x emissions for a range of SI vehicles under the RDE handling methods outlined in Figure 5.1. The Euro 5/ Euro 6 emission limit is indicated by black dashed line.

5.2.1.4 PN

Figure 5.8 and Figure 5.9 display the urban and total PN emission results across the three processing methodologies outlined at the beginning of this section. Package 2 processing caused average decreases of 9.5±3% and 5±2% in the urban and total RDE respectively. Package 3 generally increased urban results by 10±4% and decreased total results by 2±2%, while Package 4 brought all figures back to the raw values. The wide variation across vehicles for packages 2 and 3 are reflected in the high levels of associated uncertainty.

The elimination of the MAW technique from Package 2 brought 7±4% and 4±2% increases for the urban phase and the total RDE test respectively. With the inclusion of cold start, vehicle stop and engine stop ((c) to (d) in Figure 5.1) came increases of 13±2% and 4±0.5% respectively (excluding the HEV Prius, for which there was a 16% and 1.4% decrease for urban and total RDE respectively). The results for both urban and total RDE were mixed between vehicles, depending on where the PN spikes were located along the drive. The reported PN is affected by the same variables as CO and NO_x. If there was proportionately increased PN in the urban section stretching beyond the cold start period, or during the high speed, high load conditions toward the end of the motorway section, then the removal of MAW led to increased emissions and vice-versa. Generally the PN distribution over each test cycle was more variable between vehicles, likely due to the mixture of PFI and GDI injection technologies represented. Again, the CO_2 weighting of the MAW had little effect compared to these parameters. Most vehicles saw proportionately larger emissions per km during cold start than the rest of the drive, so these vehicles show an increase in emissions for Package 4 in relation to older packages. The HEV, however, shows a decrease in the urban section when cold start is incorporated, because the inclusion of cold start does not have as large an effect as the inclusion of engine-off distance covered by the vehicle bringing the emission rate per km down. For the HEV RDE test as a whole, these two driving factors appear to balance each other out. The smaller difference seen by the HEV agrees with Kontses et al. (2020), who found a smaller change in PN when cold start was incorporated into test results for HEVs than for CVs.

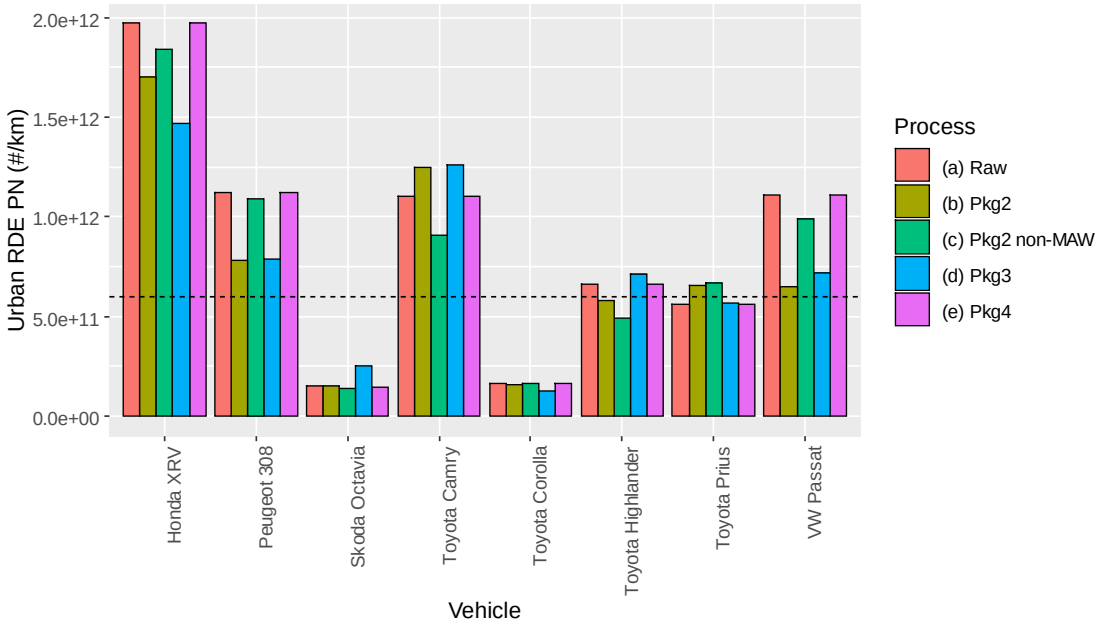

Figure 5.8 Urban RDE PN emissions for a range of SI vehicles under the RDE handling methods outlined in Figure 5.1. The Euro 6 emission limit (for GDI SI vehicles) is indicated by a black dashed line.

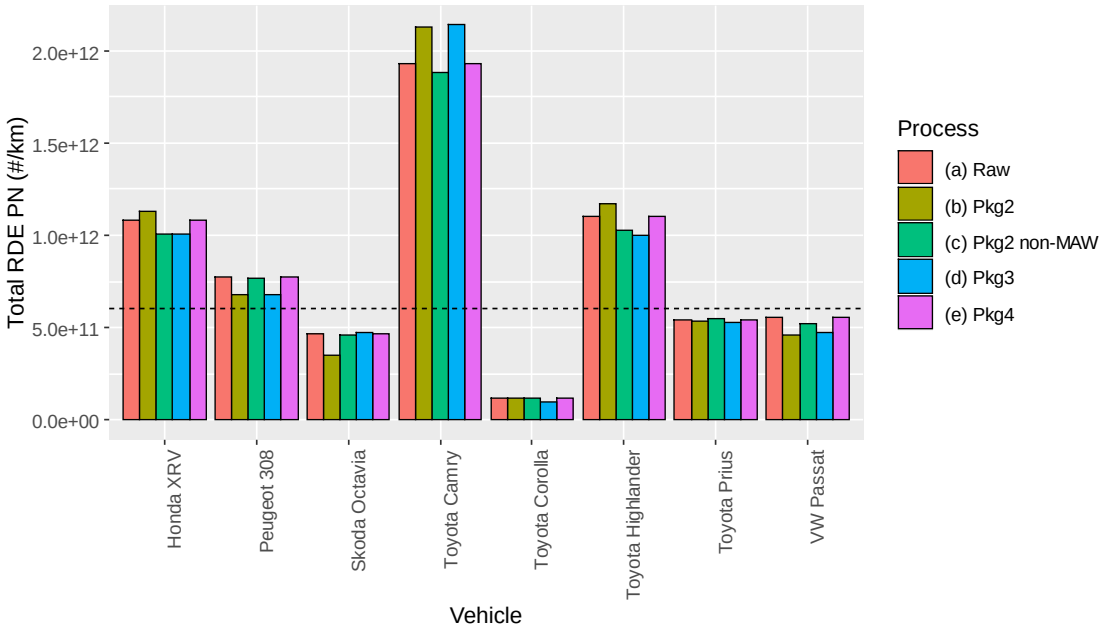

Figure 5.9 Total RDE PN emissions for a range of SI vehicles under the RDE handling methods outlined in Figure 5.1. The Euro 6 emission limit (for GDI SI vehicles) is indicated by a black dashed line.

5.2.1.5 Summary of RDE package effects

Overall, this investigation has shown that the rejection of the MAW technique from RDE processing has resulted in increases in reported emissions of CO_2, CO and PN from the urban phase, and decreases for NO_x. For the RDE test as a whole, decreases of CO_2 and NO_x and increases of CO and PN were seen. As discussed in the preceding paragraphs, the effect of the MAW depends on the interplay between two different variables. The MAW method biases results away from the beginning and end of the drive, with one of these being more affected, depending on the direction of the MAW processing (in Packages 1-2, either direction was permissible). Therefore, both the direction of MAW application and the distribution of emissions across the drive are very important factors. In the data presented here, the MAW runs forwards, so there is no change in bias between Package 2 and 3. Second, the weighting caused by the characteristic curve impacts the CO_2 reported results directly, and the other pollutants indirectly if their emissions show a correlation with CO_2. This latter effect was generally deemed to be relatively small compared to the former except for CO_2, where if larger portions of the drive were either above or below the primary tolerance, the reported CO_2 was changed more significantly.

The inclusion of cold start, vehicle stop and engine stop sections into the RDE test acted to increase the reported emissions across almost all vehicles tested, except the HEV. As these driving sections are seen in real-world driving, one can conclude that the newest package of the RDE legislation acts to make the tests more strict and representative of real-world driving, increasing the difficulty for vehicles to pass, and also allowing HEVs to display all facets of their behaviour.

The COV was high for most of these results, however, due to the wide range of vehicles utilised and the complex range of factors affecting the results, and so it is clear that for different vehicles and different tests, the processing methods were having different overall outcomes for the reported emissions. There is no common trend that can be inferred across all vehicle types for different RDE packages, so it is futile to attempt to create a relation for converting between package results. The HEV tested often had a different pattern of changes to the other vehicles, and so it is important to study the impact of the RDE test on the emissions of this vehicle technology in more detail. This will be completed in the following subsection.

5.2.2 RDE incorporation of cold start, vehicle stop and engine stop – analysis of the effect on a hybrid electric vehicle

The elimination of cold start, vehicle stop and engine stop from the emissions calculation of the RDE test was a large point of contention when first introduced. This was remedied in Packages 3 and 4, so that the final version of the RDE test presented in Package 4 no longer has these eliminations. It is important to investigate the effect that this change has on the emissions of an HEV in detail, to enable more meaningful comparison of RDE reported results for HEVs from different RDE packages.

To this end, the percentage change going from the resultant emission rates with these eliminations, to the resultant emissions rates without them (as in the current RDE Package 4) was calculated, first for each of cold start, vehicle stop and engine stop individually, and then for the three combined. A total of 23 repeats of the same RDE test cycle were used to provide the mean values presented in this section, in order to reduce the uncertainty of the conclusions. The uncertainties presented are the standard error of the mean.

Figure 5.10 below shows the percentage change in reported distance-specific emission factors from RDE data including periods where the engine is switched off (as in packages 3 and 4), when compared against the data where periods of engine speed <50 rpm are excluded (as in packages 1 and 2). Average values across 23 different RDE tests are presented, with error bars calculated as the standard error of the mean for each species/pollutant combination. All distance-specific emission factors in the urban section approximately halved when periods where the engine is turned off are incorporated into the calculation. This does not mean that the total quantities of pollutants halve, but that the total distance that the emissions are counted over doubles while the pollutant emissions stay the same (i.e. the engine is switched off for approximately half of distance covered). For the rural section, this decrease is less than 1%, reflecting the much lower proportion of distance in the rural section with the combustion engine switched off. As the engine is always on for vehicle speeds in the motorway section, there is no change, so motorway phase is not plotted. The total percentage decrease for the test as a whole is around 16% for all pollutants.

Figure 5.11 gives the percentage change in reported distance-specific emission factors from RDE data including periods where the vehicle is stationary (as in Package 4), when compared against the data where periods

of vehicle speed <1 km/h are excluded from the calculation (as in packages 1, 2 and 3). This shows the percentage change in emission rates when periods where the vehicle is stationary (<1km/h) were incorporated into the calculation, compared with when they were excluded. This time we see increases in the gaseous pollutant g/km emission rates, and a very small decrease in the PN number per kilometre emission rates, when sections of <1km/h vehicle speed are incorporated. The increases are due to the emissions produced by the engine when it is idling. Because HEVs utilise stop-start technology, one can assume that the emission rate increase would be greater for a vehicle without this technology, as the quantity of idling would increase comparatively. The change is greatest for CO at 1.9%, followed by $NO/NO_2/NO_x$ at around 1%, and finally CO_2 at 0.6%, for the urban section. The increases seen are mainly because of the Toyota Prius' cold start regime being activated, which maintains the combustion engine at a steady RPM, even when the vehicle is stationary. This also explains why CO and NO_x see the greatest increases, because the TWC is not abating them as effectively during this period of time, so they are being produced in greater quantities than at any other point in the test.

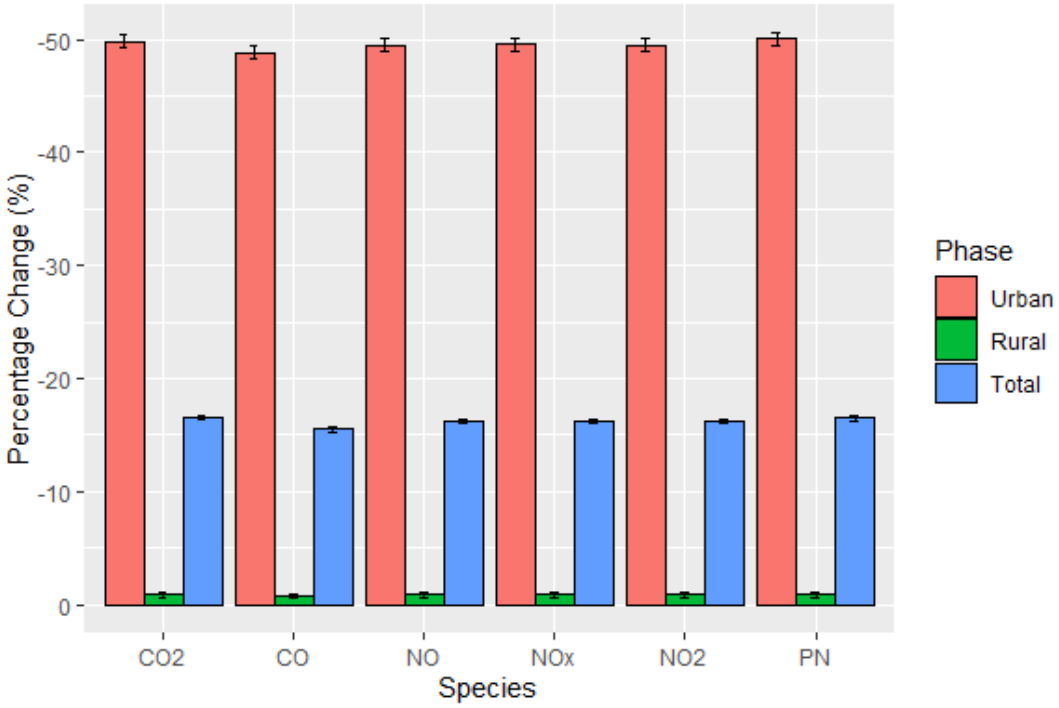

Figure 5.10 Percentage change in g/km emission rates from total RDE (pkg. 4) data compared against the data where periods of engine-off are excluded (as in packages 1 and 2).

The negative result for PN is likely due to the fact that PN emissions are predominantly produced when the engine re-ignites, and not during cold start idling, as we see is the case for CO and NO_x. When the vehicle is travelling between 0-1 km/h, it is still covering distance, so if the pollutant emissions during this period are negligible, as they are for PN, then a decrease in emission rate results. The Toyota Prius strategy tends to 'push-off' in pure electric mode and the engine only ignites as the vehicle accelerates, which usually occurs at a speed greater than 1km. This means that the PN emissions from HEVs were already incorporated into the results under RDE Package 2. It is worth noting that pure-ICE vehicles with stop-start technology would re-ignite when the vehicle is put into gear, before it starts to move, so the PN spike would only be incorporated in Package 3/4. We would therefore expect to see a big increase in the percentage change of PN emissions in the RDE Package 3/4 results compared to Package 2 for pure-ICE stop-start technology vehicles.

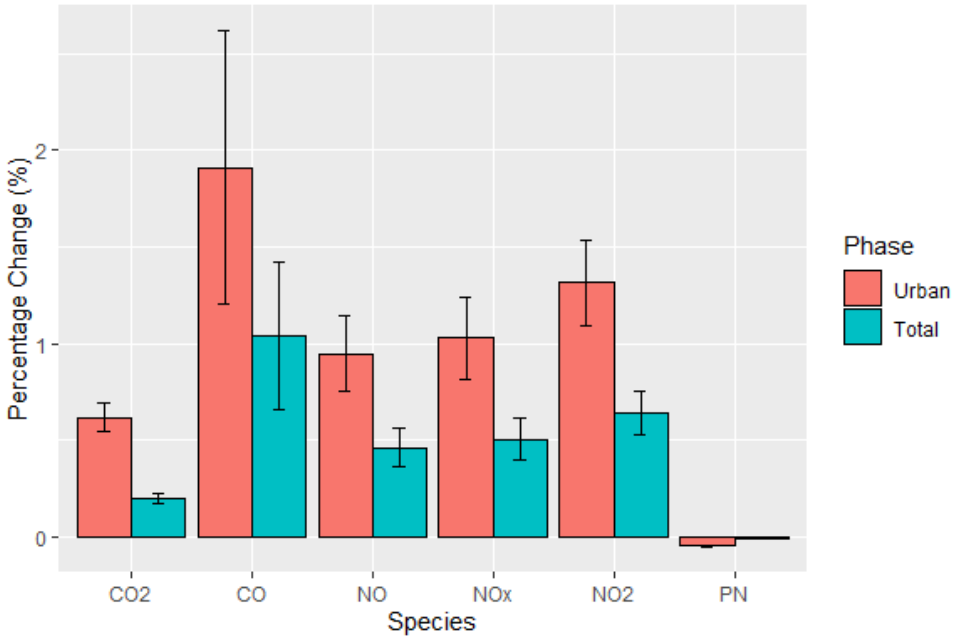

Figure 5.11 Percentage change in reported g/km emission rates from total RDE (pkg. 4) data compared against the data where periods of negligible vehicle speed are excluded (as in packages 1, 2 and 3).

Figure 5.12 displays the percentage changes in emission rates for regulated pollutants that occurred as a result of the inclusion of cold start into the calculation (as in packages 3 and 4). There is a small CO_2 increase penalty seen, which is widely reported in the literature (Alvarez and Weilenmann, 2012; Anderson et al., 2014). Rask et al. (2010) found that cold start incurred a fuel consumption penalty of 10% during a city cycle for the same vehicle,

which is broadly comparable to the CO_2 result reported. This CO_2 increase is smaller than the 55% increase seen by Varella et al. (2019), who studied a range of CI and SI vehicles. All pollutants increased with the inclusion of cold start, with NO_x species seeing the greatest increase. The increase of 252% for NO_x is testament to the high conversion efficiency of the TWC once it has reached light-off temperatures. This NOx increase is larger than the 55% increase seen by Varella et al. (2019). The very large variability in percentage change is predominantly caused by large fluctuations in NO_x emissions during the initial moments after the engine first ignites. This fluctuation was also found in Weiss et al. (2017). The temporal location of NO_x emissions also explains why the reported increases from inclusion of cold start published in Weiss et al. (2017) were not so large – because the MAW process put less emphasis on the beginning of the drive where the cold start emissions reside.

The CO emission increase is the next highest, at 49%. This is a smaller increase because cold start emissions make up a smaller proportion of the total test cycle emissions of CO than NO_x, due to additional CO production during engine restart events (discussed further in Chapter 6 Section 6.3.1). Cold start CO_2 and PN emissions only make up a small proportion of the total emission factor, explaining the proportionately smaller effect of cold start on the production these pollutants. Kontses et al. (2020) calculated an increase of 11.9% PN resulted from the incorporation of cold start into the RDE test procedure. This is close to the average increase of 8.25% displayed in figure 12, with the difference easily attributable to the different test vehicle used. Merkisz et al. (2019) calculated much smaller percentage changes from inclusion of cold start into their RDE test as can be seen by comparison with Figure 5.13, but this study utilised a GDI CV so is not directly comparable.

Figure 5.14 displays the overall percentage change in emission rates per kilometre as a result of the total RDE according to Package 4 (i.e. including vehicle stopped periods, engine-off periods, and cold start) when compared to the data with exclusions required of packages 2 and 3 respectively. The majority of difference originates in the urban section for all species, and the difference between Package 2 eliminations is at least one magnitude greater than that of Package 3 eliminations (vehicle stop) for all except total CO, where the percentage change in Package 2 to 4 transition is approximately three times the Package 3 to 4 transition. NO_x species see an overall increase in pollutant emissions, whereas CO_2 and PN see a decrease with the changes in RDE legislation. Results for CO are mixed, with decrease for the urban

section going from Package 2 to 4 but a small increase over the whole test for this transition, and for both urban and total Package 3 to 4 transitions. The mixture of positive and negative values arises as a result of the interplay between changing mass emissions and changing distances with the different exclusions. The margin of uncertainty for the different species can be high, as a result of the variability of on-road testing, but none of the error bars cross from a positive to negative percentage change or vice versa, so one can be certain of the general trends witnessed for this HEV with the recent RDE package changes. Generally, findings have been in agreement with those of previous literature where comparisons are possible.

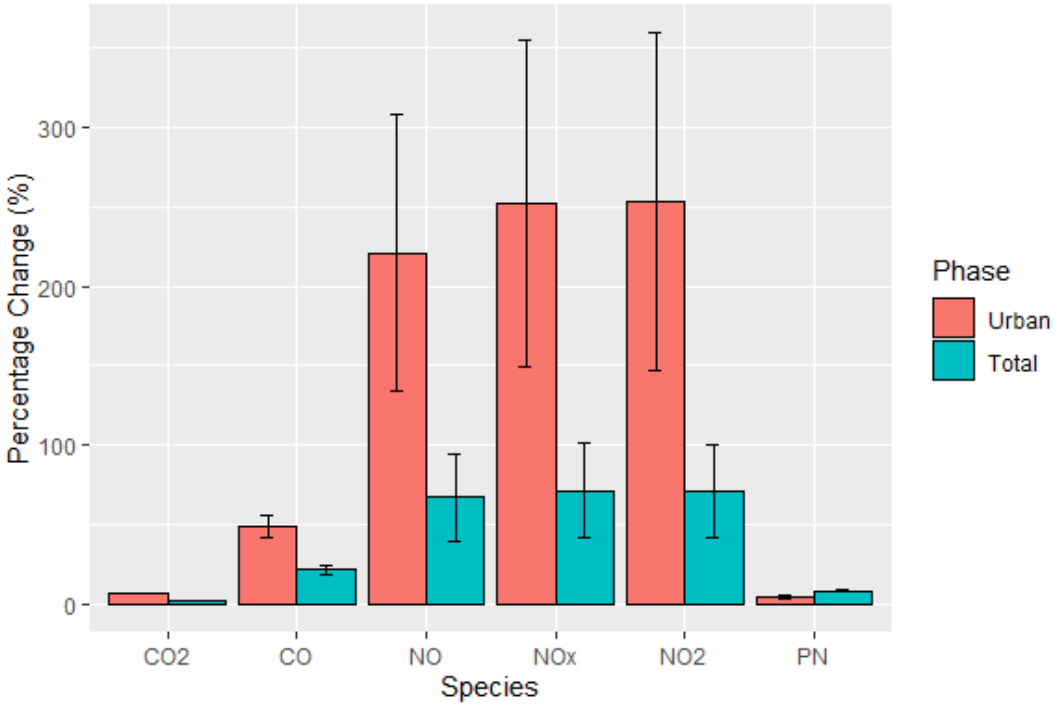

Figure 5.12 Percentage change in reported g/km emission rates from the total RDE (pkg. 4) data compared against the data without cold start included (as in packages 1 and 2).

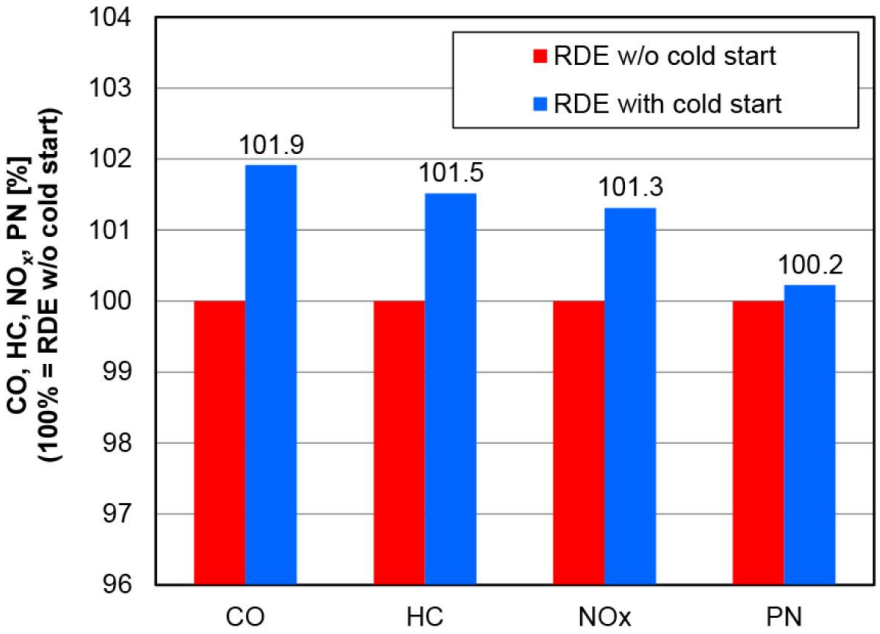

Figure 5.13 RDE pollutant emission results with cold start included, compared to without cold start, presented by Merkisz et al. (2019).

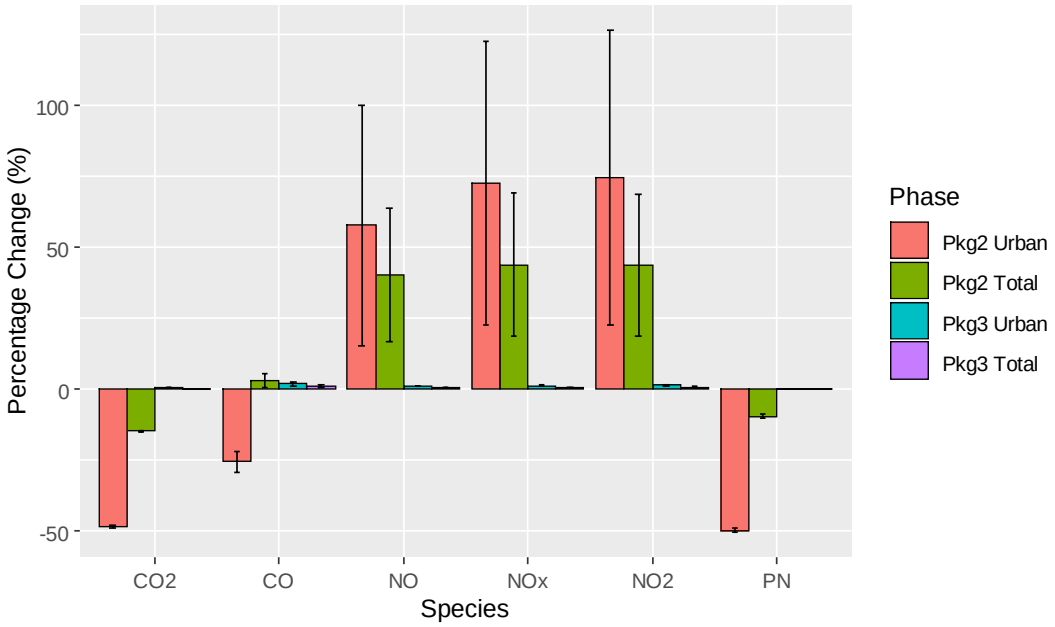

Figure 5.14 Percentage change in reported g/km emission rates from total and urban RDE data (pkg. 4), compared against the data with the exclusions of packages 2 and packages 3.

5.3 Is the RDE representing real-world driving?

5.3.1 Impact of road compared to chassis dynamometer

It is important to assess, for any given drive cycle, how much of an effect the testing methodology has on the dynamic behaviour of the vehicle and therefore the resultant emissions. One key difference between the type approval testing to date and the RDE test is that the latter occurs on real roads, while the former has always been within a lab on a chassis dynamometer.

A new consideration for the RDE test is therefore the effect of road gradient. Whereas for a CV, a gradient will directly affect the load on the engine, for an HEV the gradient is less directly related to load, due to the action of the motor.

Figure 5.15a demonstrates how the battery SOC changes with time over the duration of the three tests (Test 0 in red and Tests 27 and 28 in green and blue respectively), with the vehicle speed and road altitude of Test 0 indicated in grey and black respectively. Note that the altitude has been increased by a value of 50 on the figure, to visually distinguish from vehicle speed. One can see that while the initial and final SOC for the three tests are identical, the changes in SOC are greater for the chassis dynamometer tests. The on-road test maintains its SOC more closely to a median value. In-depth analysis of the portion with greatest divergence in Figure 5.15b shows that the engine was running for different periods of time here between the on-road and on-chassis dynamometer tests, meaning the downhill gradient is the reason for the change in SOC; the regenerative braking system was able to charge the battery effectively as it travelled down the slope, while gravity took load off the motor and allowed the engine to turn off.

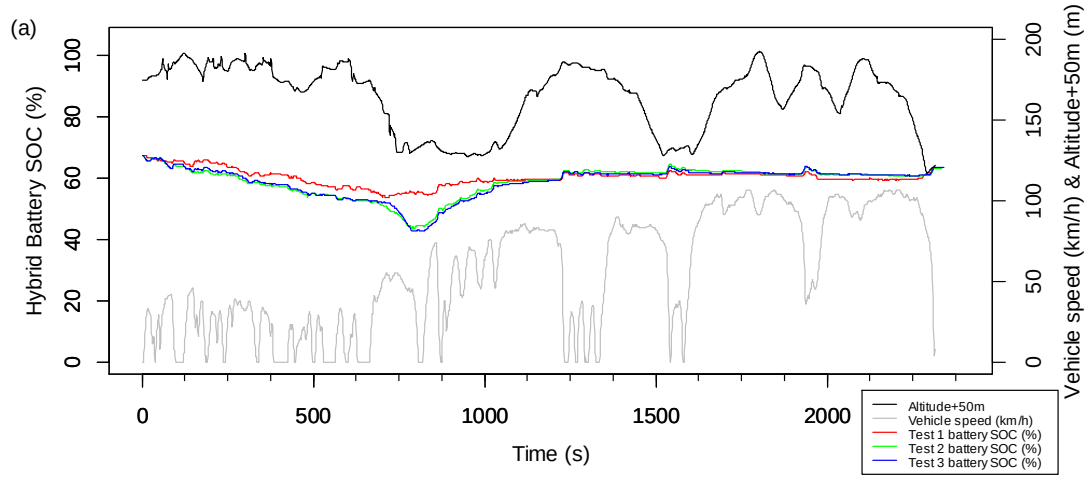

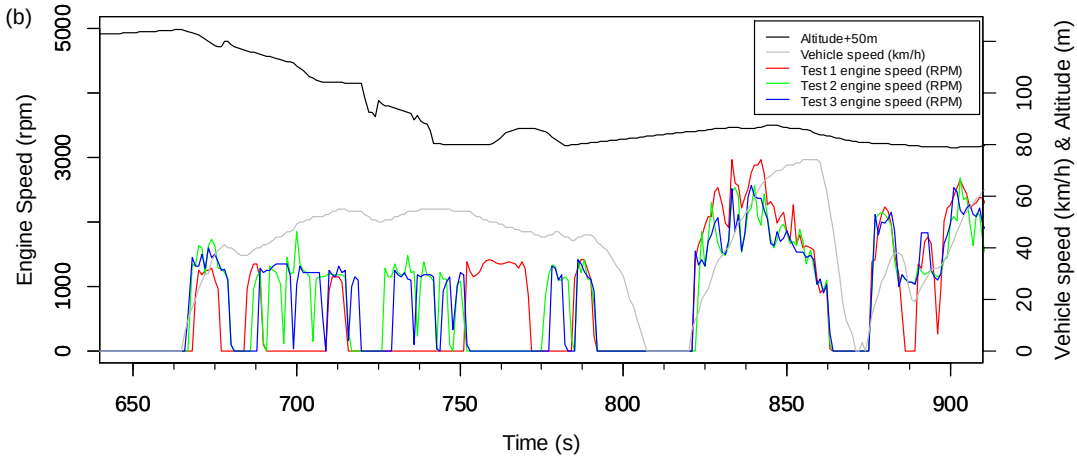

Figure 5.15 (a) Hybrid battery SOC values alongside vehicle speed and altitude (b) The period of greatest SOC divergence between tests, with engine speed values, vehicle speed and altitude.

VSP can be a good indication of powertrain load for testing, so Figure 5.16 gives the VSP distribution of the three tests. All three tests have the expected Gaussian distribution, centred on 4.05 for Test 0, 4.56 for Test 27 and 4.55 for Test 28. The on-road test has a broader VSP distribution than the chassis dynamometer tests, with a greater number of points at the extremes, supporting the finding of broader VSP distribution for on-road tests compared to chassis dynamometer NEDC and WLTC tests presented in Duarte et al. (2016). The previous paper compared sections of road and chassis dynamometer testing with similar VSP values in order to investigate the effects of road gradient, whereas the work presented here is a more direct investigation of the effects of road grade because the speed profiles are exactly the same. From these results, it appears that the differing gradients of an on-road test have a small but appreciable affect.

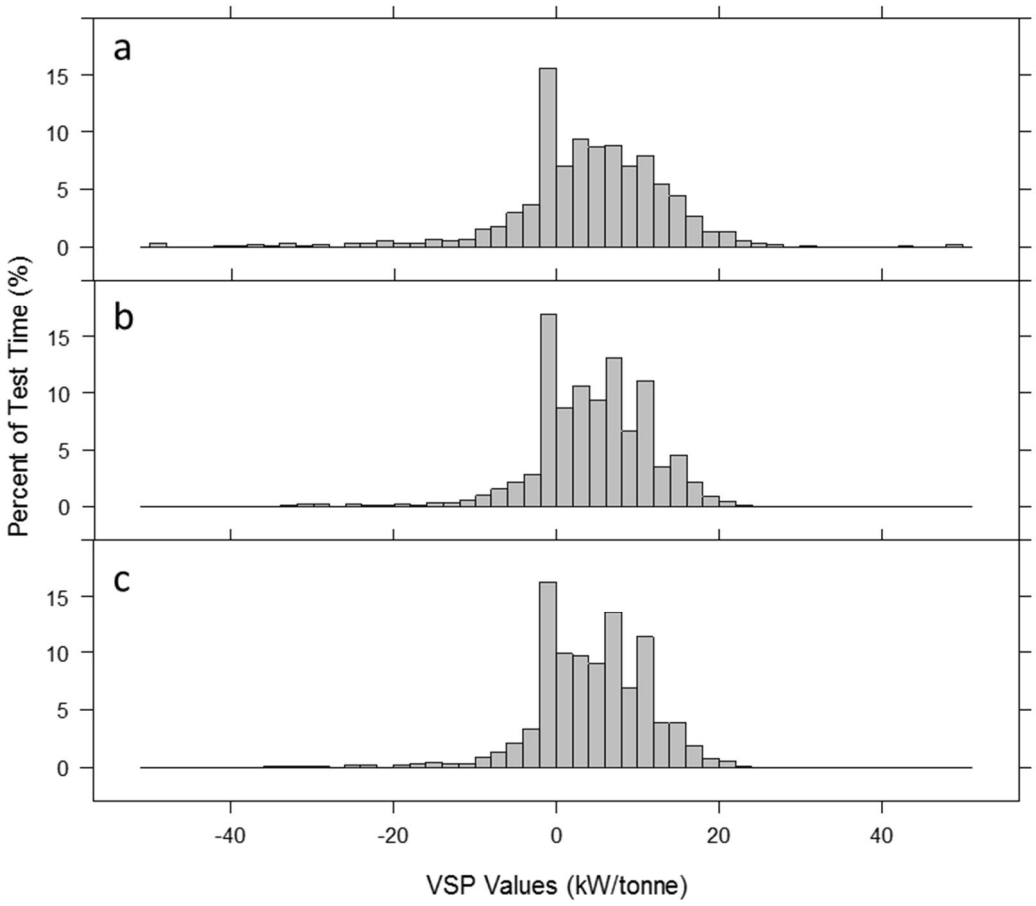

Figure 5.16 VSP distributions for (a) on-road Test 0, (b) chassis dynamometer Test 27 and (c) chassis dynamometer Test 28.

Figure 5.17 shows that the range of torque values attained by the chassis dynamometer repeats of the on-road test do not have very different torque ranges. However, the range of engine speeds extends to higher values for the on-road test than the chassis dynamometer test.

Figure 5.18a, b, c and d show that a higher load is placed on the engine during the on-road test than the chassis dynamometer tests, which is shown to result in more engine activity and greater CO_2 emissions. Figure 5.18a demonstrates that the CO_2 emissions are greatest during periods of uphill driving. This is in agreement with the findings of Duarte et al. (2014), Holmén and Sentoff (2015), Prati et al. (2015), Gallus et al. (2017) and Varella et al. (2019). The phase 1 NO_x in Figure 5.18d emissions are much greater for the chassis dynamometer tests, but the TWC temperature profile for the tests in Figure 5.18c, along with the transient temperature profiles in Figure 5.20a and Figure 5.20b confirm this to be due to a lowered catalyst temperature for these tests compared to the on-road test.

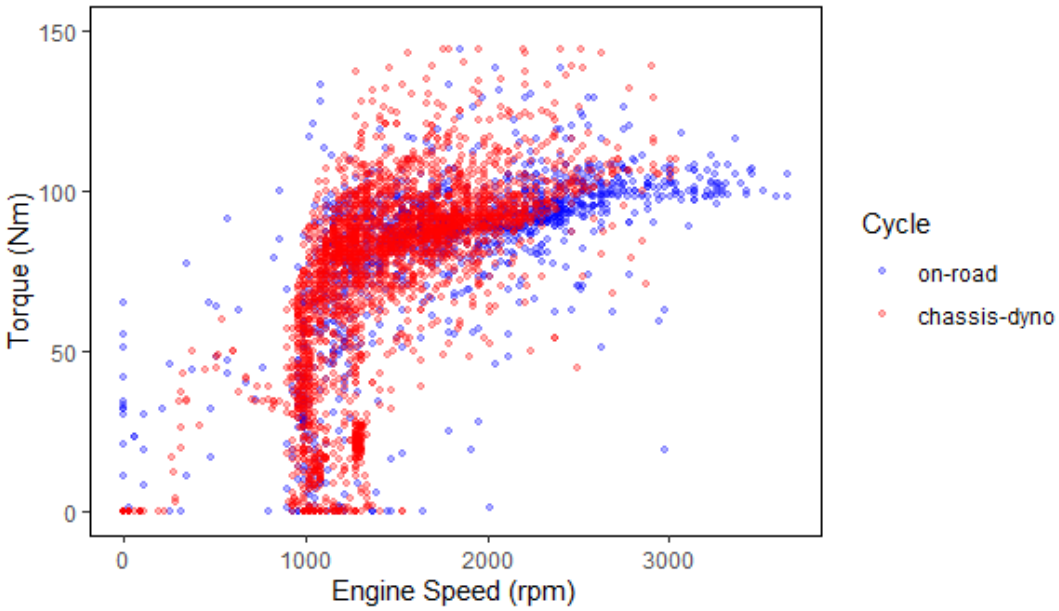

Figure 5.17 Engine torque with engine speed for the on-road drive cycle in blue and the two chassis dynamometer repeats in blue.

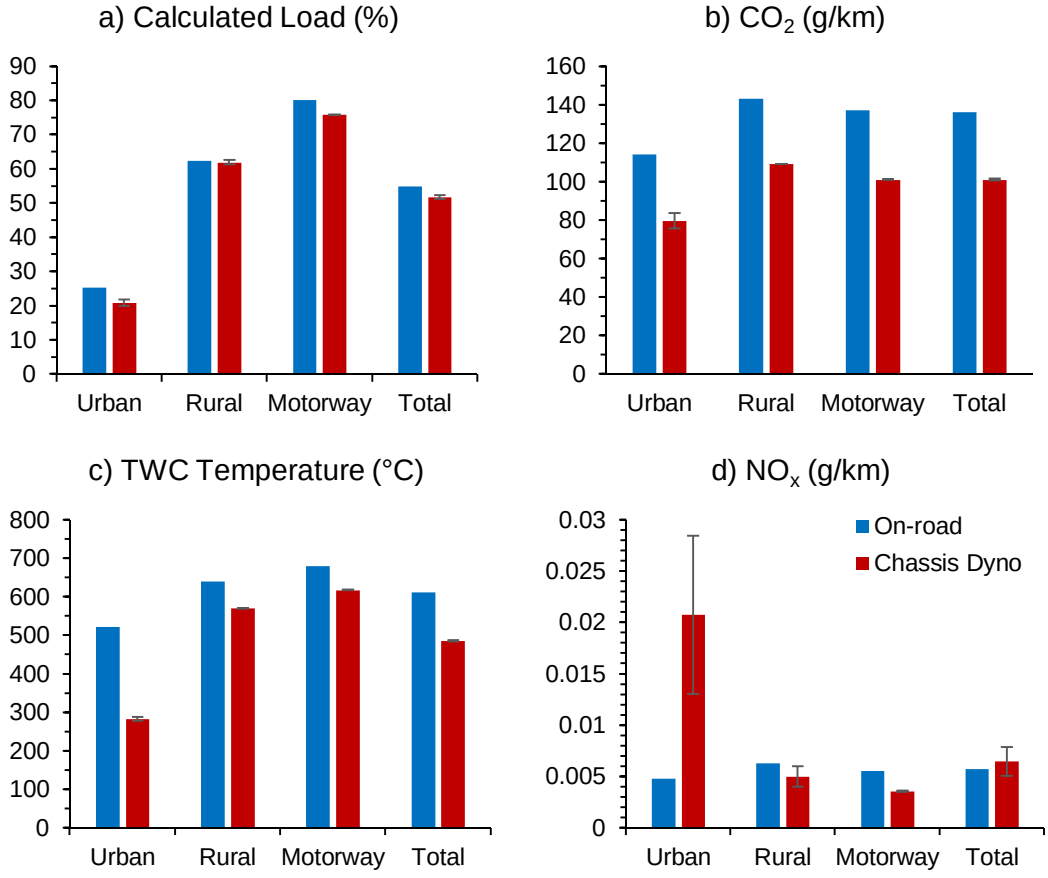

Figure 5.18 (a) Mean calculated load, (b) CO_2 emission rate, c) TWC temperature and d) NO_x emission rate across the 3 phases of the on-road RDE-style drive and two chassis dynamometer repeats.

The NO_x emissions after 1000s of Figure 5.19b (when the engine coolant, catalyst and exhaust temperatures are more comparable between tests) are slightly higher for the on-road test compared to the chassis dynamometer test, clearly associated with periods of uphill driving in the figure. This is in agreement with the findings of Weiss et al. (2011) and Duarte et al. (2014) for HEVs, and Prati et al. (2015), Gallus et al. (2017), Frey (2018) and Varella et al. (2019) for ICEs, from their comparisons between on-road data and chassis dynamometer test cycles.

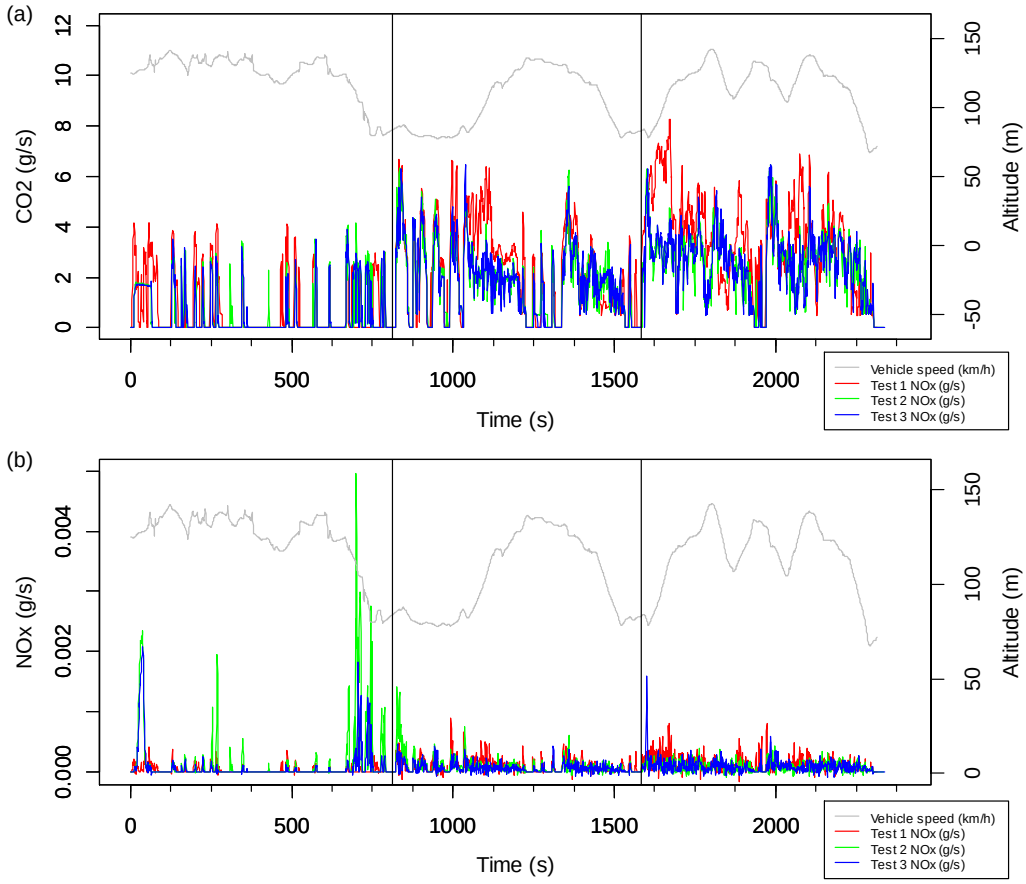

Figure 5.19 (a) CO_2 and (b) NO_x mass emission rates for the on-road and chassis dynamometer tests. Vertical phase divisions are in black, while altitude changes of the on-road test in grey are indexed on the right hand axis.

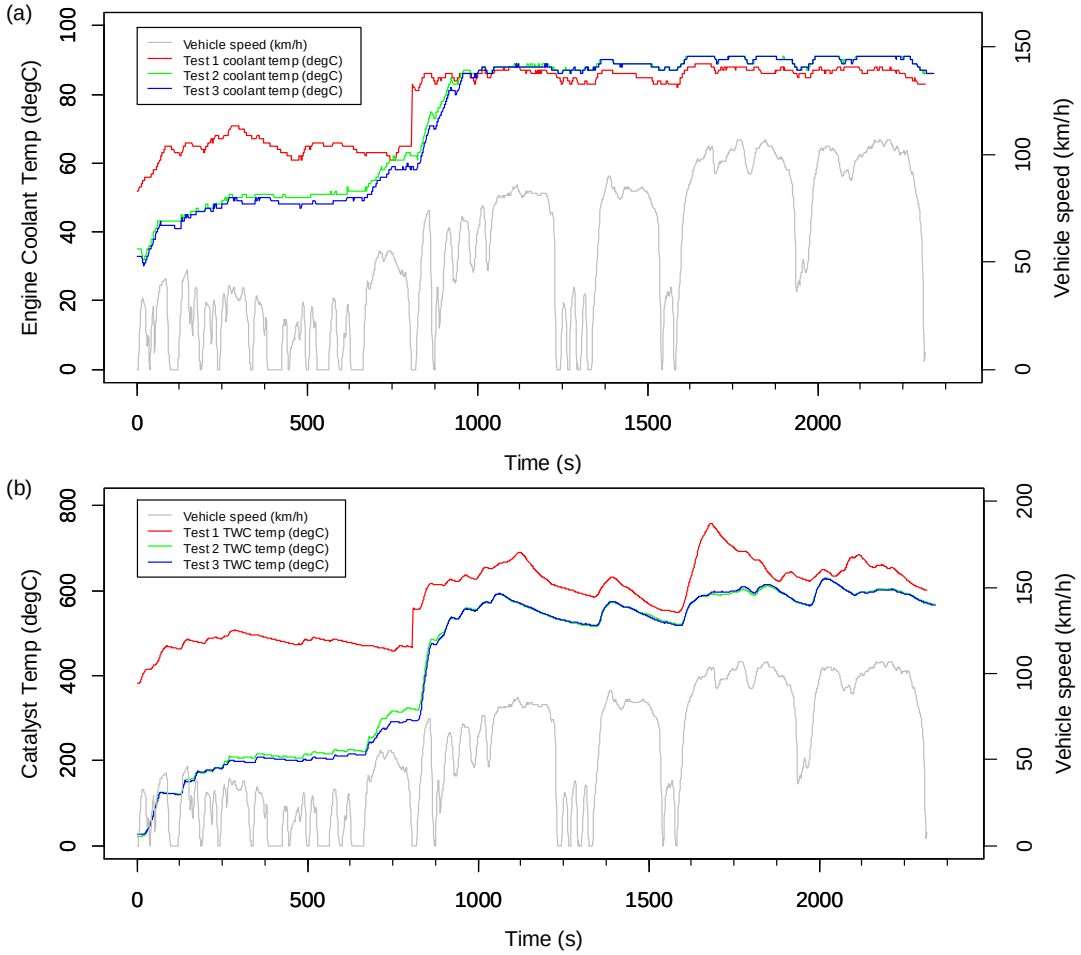

Figure 5.20 (a) Engine coolant temperatures and (b) downstream catalyst temperatures plotted with vehicle speed (grey) for the three tests (Tests 0, 27 and 28).

Figure 5.21 shows that it is during the high engine speed conditions that the greatest emission rates of CO_2 and NO_x are located, thereby explaining where the greater emissions of CO_2 and NO_x occur on real-roads compared to chassis dynamometers.

Overall, this investigation has shown that the more varied requirements on the vehicle during on-road driving result in a wider VSP distribution. Uphill gradients have been shown to result in not only higher CO_2 emissions and therefore fuel consumption, but also higher emissions of NO_x pollution as the load on the engine increases. Generally, findings have been in agreement with those of previous literature where comparisons are meaningful, and indicate that the RDE test does indeed fill a gap in the type approval testing left by only testing on a chassis dynamometer previously.

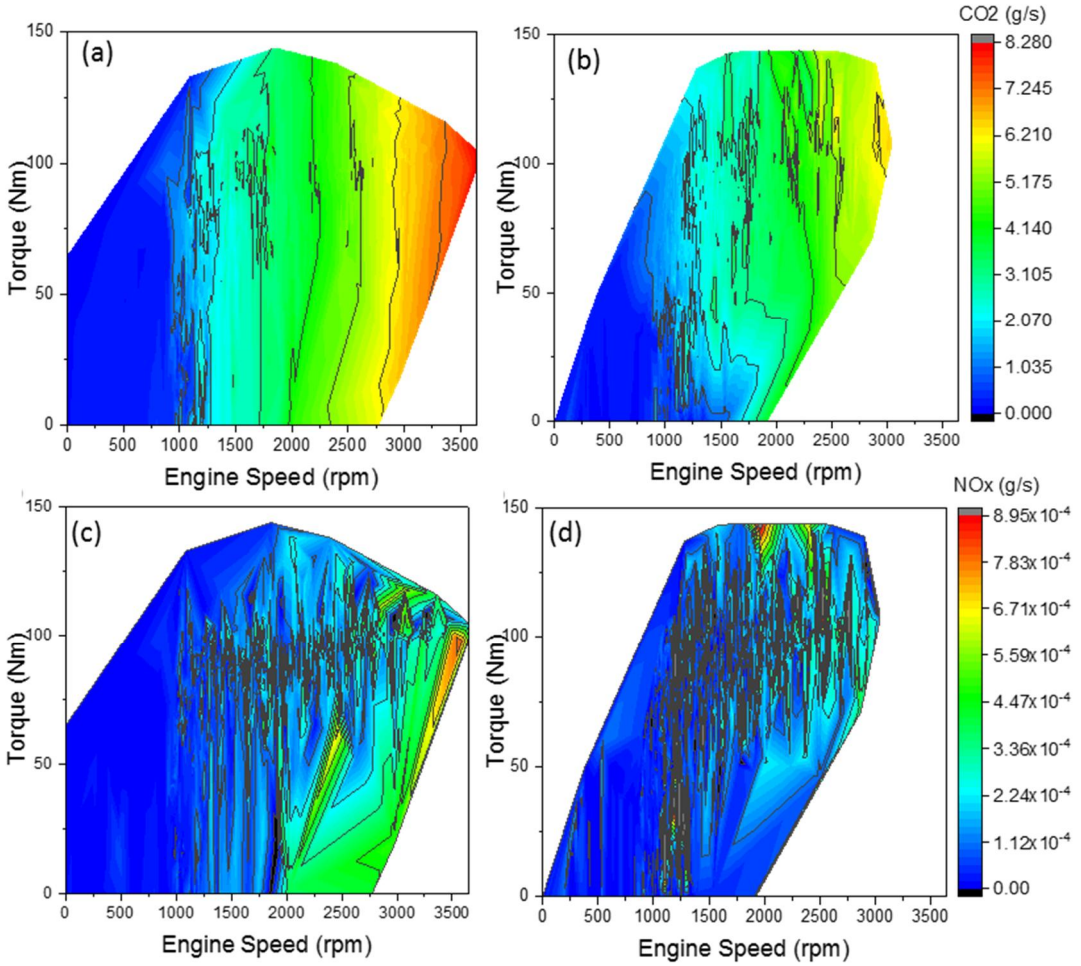

Figure 5.21 Engine maps displaying (a and b) CO_2 and (c and d) and NO_x emissions. (a) and (c) are then on road test while and (b) and (d) are the chassis dynamometer tests.

5.3.2 Does the urban RDE section represent real city driving?

Urban air quality has been one of the major driving factors behind the introduction of the RDE test as an addition to the type approval procedures. Air quality in urban centres has failed to improve in response to the tightening of type approval emissions limits, and it is in these densely populated areas that the impacts of air pollution on public health are most severe. An important factor for the RDE test is therefore that it adequately represents the type of driving seen in urban centres.

5.3.2.1 Dynamic properties

A set of dynamic properties that reflect a vehicle's movement characteristics were selected. The average values of these properties from 26 legislative RDE tests are given in Table 5.1, along with the same values from nine repeats of an alternative real-world urban drive cycle (City Centre route) and

three repeats of an alternative urban and extra-urban drive cycle (Headingley route). Details of these alternative drive cycles are given in Chapter 3 Section 3.5. For each item, the error margins are standard errors calculated from the standard deviation of the mean. As discussed in the Chapter 3 Section 3.5, the City Centre and Headingley tests occur during rush hour times, and were designed to represent the type of driving that commuting vehicles will most likely encounter. It would appear that this is the first time a cold start RDE-compliant test cycle has been compared against cold start city driving. Suarez-Bertoa et al. (2019) conduct real-world drive cycles and compare them with an RDE-compliant cycle, but none of this work studies city driving specifically, nor did Suarez-Bertoa et al. (2019) study an HEV.

One can see that the average speed is nearly half that of the urban section of the RDE route, with the percentage time spent stopped approximately doubled. An RDE route presented in Bodisco & Zare (2019) had a similar average percentage time stopped. The number of individual stops per km is also much lower for the urban section of the RDE test than the real-world urban drives. The RDE route performed five times by Bodisco & Zare (2019) had 1.1 to 1.5 stops per km, so is in the same region as the City Centre drive cycle, demonstrating that the freedom of the RDE boundary conditions currently can allow more representative urban drive sections than was possible on the route designed for the current work. With regards to the maximum speeds, this is lowest for the City Centre test at 46 km/h, with the RDE and Headingley both having the maximum urban speed of 60 km/h (the boundary between urban and rural speeds). The maximum acceleration and deceleration of the RDE is very close to the City Centre values, verifying that these properties are realistic for the RDE.

The time taken for the engine coolant temperature to reach 70°C, widely classified as an indication of the end of the cold start, was much longer for both real-world drives than the RDE test, likely a result of the increased time spent stopped (which, for HEVs and those with stop-start technology, means the engine is likely to be turned off).

The $v.a_{pos}[95]$ and RPA values, however, are identical between the RDE drive and Headingley drive, indicating that the RDE test replicates normal congested city driving for these dynamic values. The City Centre testing was 35% lower, but still within the RPA and $v.a_{pos}[95]$ dynamic boundaries of the RDE test, indicating that these limits for the urban RDE are reasonable.

Table 5.1 Average values of a range of dynamic parameters over repeats of an RDE test and two real-world drive cycles.

	Urban RDE	**City Centre**	**Headingley**
Distance (km)	29.5 ± 0.8	14.3 ± 0.06	11.9 ± 0.2
Urban average speed (km/h)	29 ± 0.3	16 ± 0.6	16 ± 1
Maximum speed (km/h)	60 ± 0	46.4 ±1	60 ± 0
Maximum acceleration (m/s^2)	2.4 ± 0.2	2.5 ± 0.3	1.8 ± 0.1
Maximum deceleration (m/s^2)	-3.2 ± 0.1	-3.2 ± 0.1	-3.1 ±0.3
Stop percentage time (%)	14 ± 0.7	28 ± 2	30 ± 3
Number of stops per km	0.22 ± 0.04	1.4 ± 0.5	0.8 ± 0.5
Time for coolant to reach 70°C (s)	526 ± 18	1277 ± 72	1024 ± 43
Stoppage time during cold start (s)	49 ± 2	159 ± 15	132 ± 4
Urban $v.a_{pos}$[95] (m^2/s^3)	7.8 ± 0.1	5.1 ± 0.2	7.8 ± 0.7
Urban RPA (m/s^2)	0.331 ± 0.004	0.34 ± 0.1	0.331 ± 0.004

The VSP distributions for the three different tests are compared in Figure 5.22a to Figure 5.22c. The RDE test shows a much broader distribution than either of the real-world tests. Over half of VSP points fall within ±5 for both of the real-world test cycles, and values outside this range fall off very quickly. The urban section of the RDE test, however, displays a much slower drop-off in values, indicating that it represents a much broader range of engine operating points.

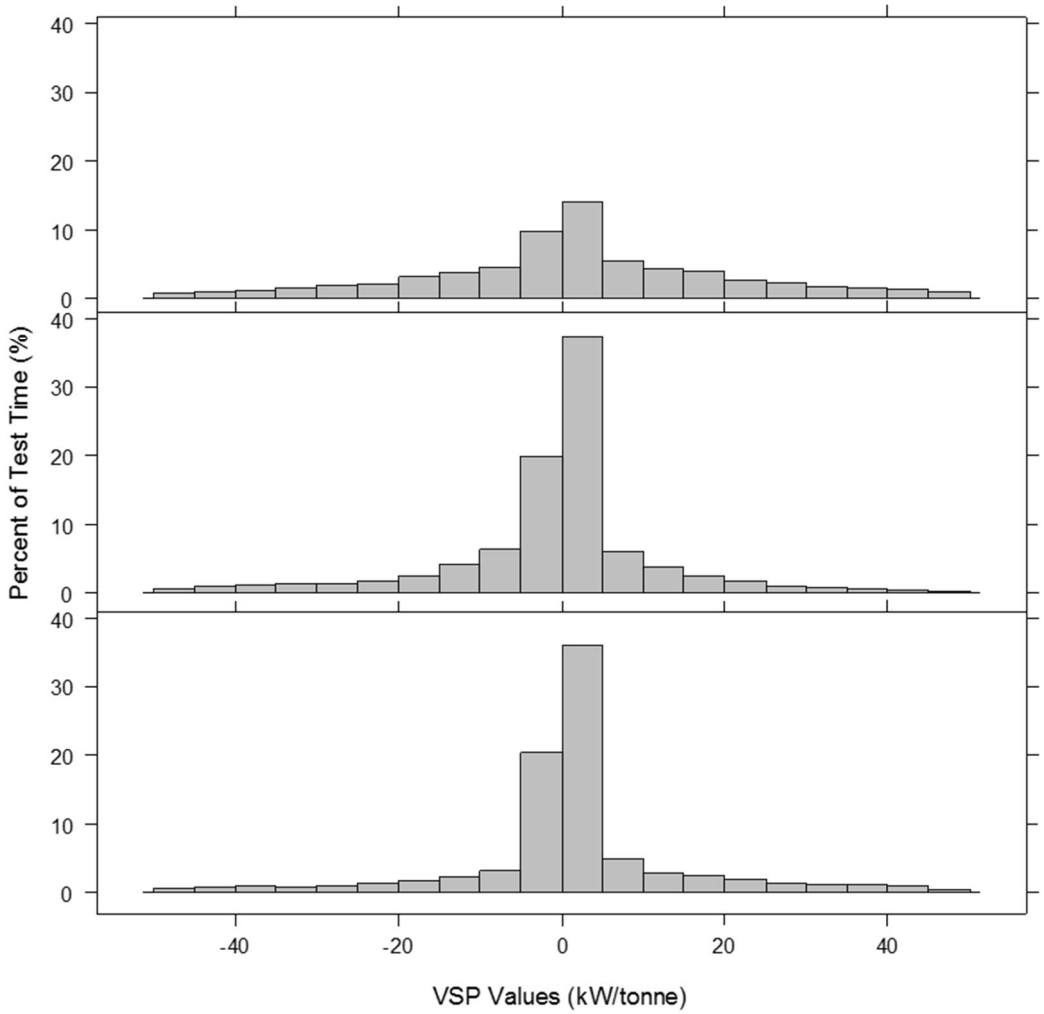

Figure 5.22 VSP average histogram distributions of (a) RDE urban drive sections, (b) City Centre test and (c) Headingley test.

5.3.2.2 Engine properties

Figure 5.23 displays a scatterplot of the engine load and engine speed for the urban RDE compared to the urban Headingley and City Centre drive cycles, differentiated by colour. It can be seen that generally the RDE covers the range of operating points seen in the two real-world drive cycles. There are, however, some mid-load, high engine speed points that do not appear to be as well covered by the RDE as they are by the Headingley route. These areas of the engine map are, however, covered by the RDE, but at higher speeds than 60 km/h, and are therefore not represented here.

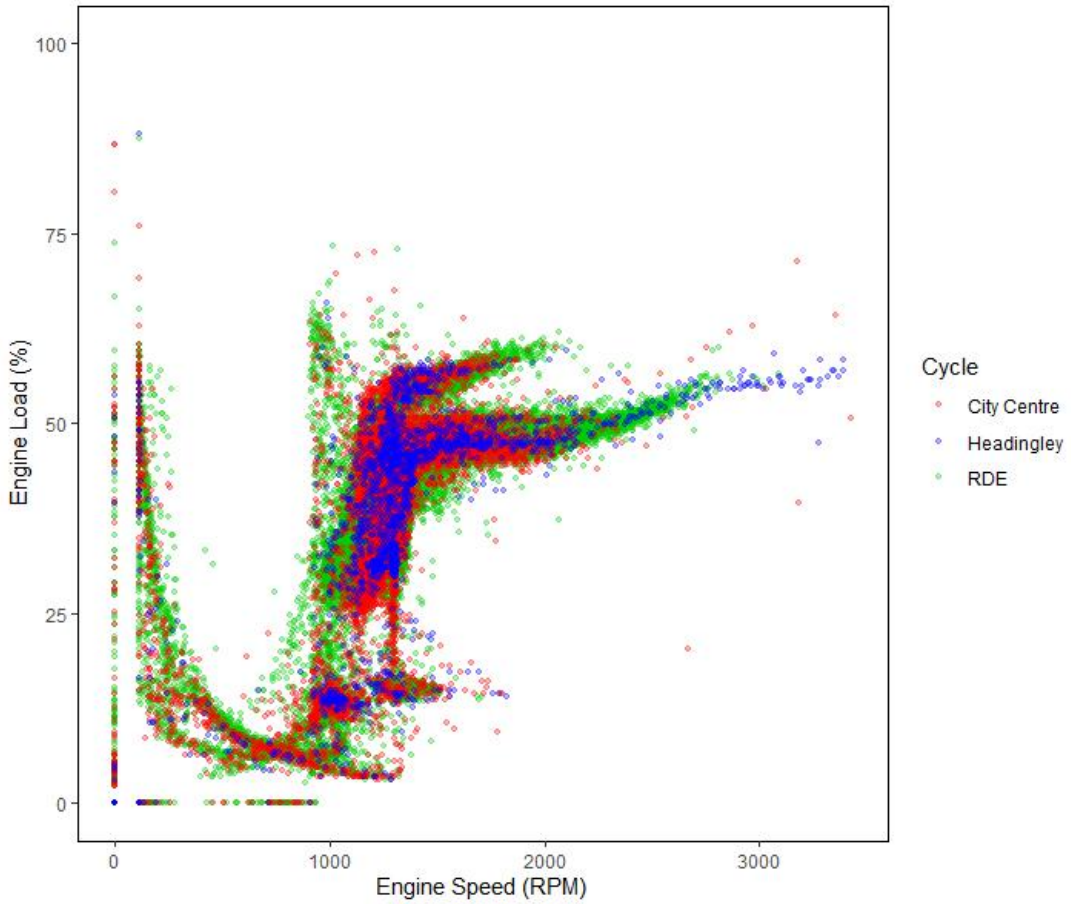

Figure 5.23 Engine load and engine speed operating points covered by the RDE tests, City Centre tests and Headingley test.

Figure 5.24a and Figure 5.24b plot vehicle acceleration against vehicle speed, and engine load against VSP, respectively. They confirm that the urban section of the RDE test covers similar ranges of dynamic and load characteristics seen for the real-world urban test cycles driven under different dynamic conditions, but with the City Centre tests having more outlying points at the extreme values of VSP, engine load, and acceleration (at speeds under 30km/h). The RDE test had more extreme values of acceleration at speeds greater than 30km/h, because a greater proportion of the urban drive occurred at these speeds for the urban section of the RDE than the City Centre and Headingley cycles.

It should be noted that the number of RDE tests represented in Figure 5.23 and Figure 5.24 was over double that of the City Centre tests, and eight times that of the Headingley route. Further random sampling of collections of tests indicated that individual RDE tests generally covered similar ranges as individual City Centre and Headingley tests. A lattice of four example plots is given in Figure 5.25, showing good overlap between VSP/load values for the

three test cycles. Very extreme VSP values are due to errors in GPS height data, rather than very aggressive driving.

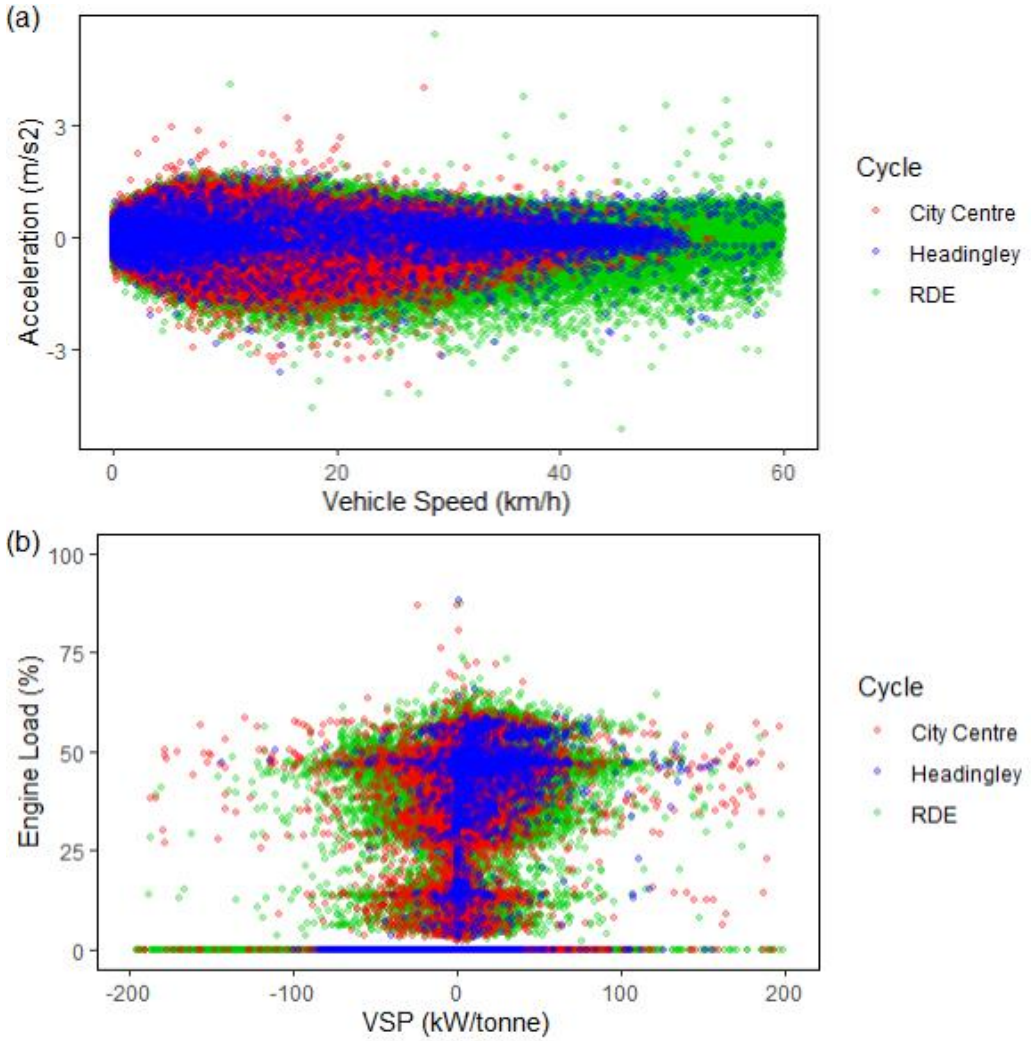

Figure 5.24 (a) Vehicle acceleration versus speed and (b) engine load versus VSP, covered by the RDE tests, City Centre tests and Headingley tests.

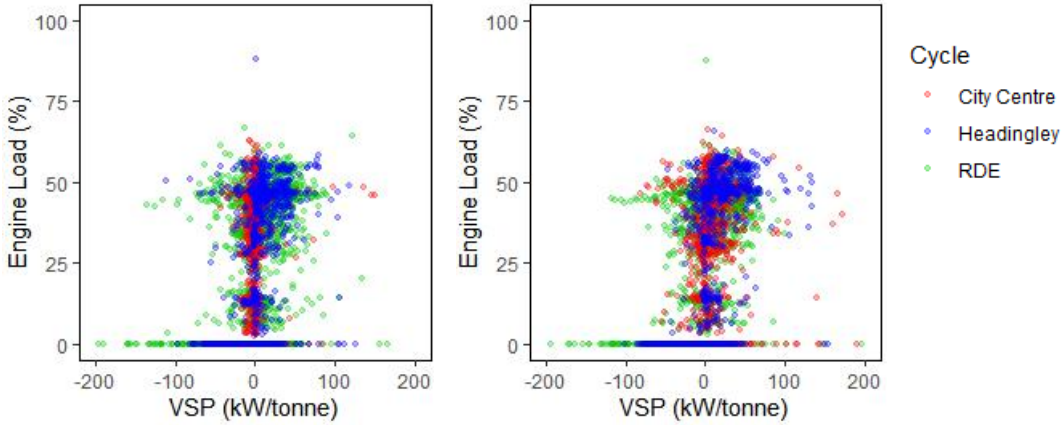

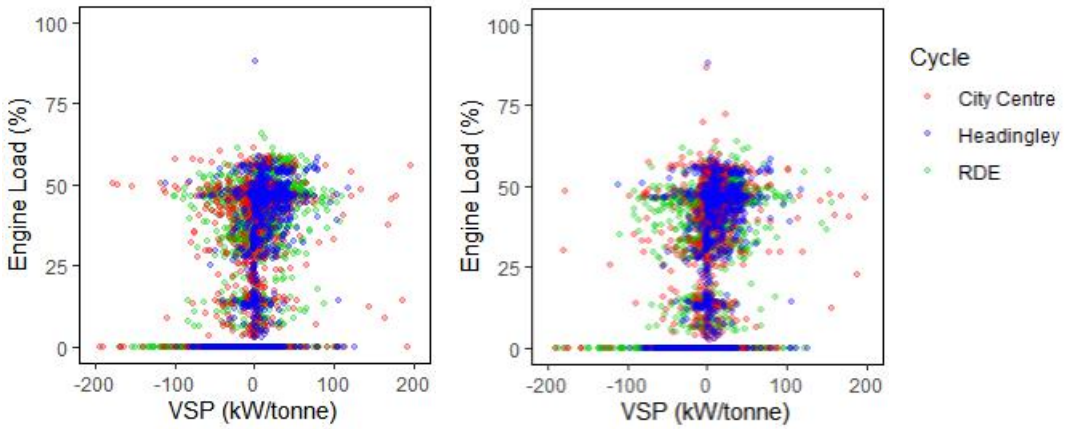

Figure 5.25 A representative selection of 4 comparisons between different individual urban RDE, City Centre and Headingley drive cycles' distributions of engine load with VSP.

5.3.2.3 Tailpipe emissions

The tailpipe emissions also vary for each of the test routes. Figure 5.26a to Figure 5.26d display average regulated pollutant emission factors. Dashed lines indicate the Euro 5 fleet-average emissions target for CO_2 and limits for pollutant emissions, while bars are calculated standard errors. All tests were from cold start and utilised the same tank of E5 UK market fuel. The RDE test gives 8.6±5%, 78±2%, 54±20% and 34±10% lower emission factors of CO_2, CO, NO_x and PN respectively, compared to the City Centre test. These results indicate that the RDE test is not accurately depicting the highly congested conditions that are experienced in most City Centres during rush hour, where the greatest exposure to humans occurs. One can see that the CO_2 produced by this HEV is on the borderline of the fleet-average emissions target, which, as HEVs are widely regarded as being higher-efficiency, is surprising. The CO and NO_x emissions are comfortably below the limit, while the PN emissions exceed the limit (applied to GDI engines only currently). This is clearly an indication that the PN limit should also be applicable to PFI vehicles, not just GDIs, in agreement with Kontses et al. (2020). The greatest PN emissions resulted from the City Centre driving, with emissions almost three times higher than the limit. Given that the greatest exposure to humans occurs in dense urban centres, this finding is particularly important. By studying the transient emissions profiles and the dynamic properties in Table 5.1, it can be inferred that the greater number of stops in the real-world cycles has contributed to the increase in CO and PN, while the increased cold start time has contributed to CO_2, CO and NO_x. No other literature appears to compare RDE test results with real-world driving cycles for HEVs, but the currently presented findings

are in agreement with the majority of literature on the topic of engine stop-start behaviour as discussed in Chapter 2 (e.g. Duarte et al. (2014); Kontses et al. (2020); Robinson & Holmén (2011)), and refutes the assertions of Zhai et al. (2011) that frequent engine-off events improve air quality in urban areas. These HEV behaviours will be investigated more thoroughly in Chapter 6.

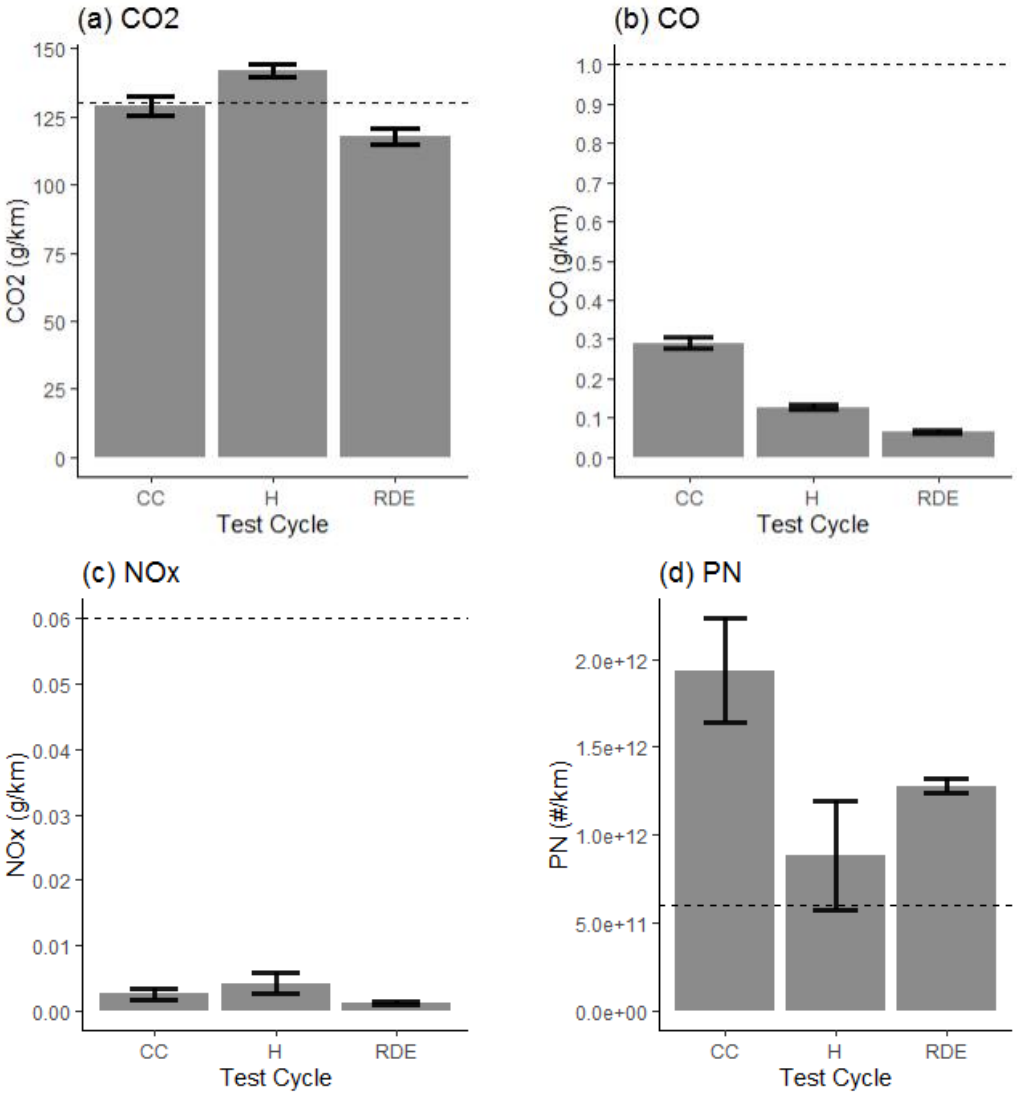

Figure 5.26 Average tailpipe emission rates per km for (a) CO_2, (b) CO, (c) NO_x and (d) PN for the urban drive sections of the City Centre (CC), Headingley (H) and RDE test respectively.

It is also noteworthy that the uncertainty is much lower for the RDE test results for NO_x and PN. This could be partly due to the increased number of RDE tests performed compared to the other test cycles, but also, particularly for PN, is because the increased repeatability of the RDE drive cycle chosen resulted in significantly lower test-to-test variation than the rush hour drive

cycles. The following subsection will focus on the repeatability of the RDE test cycle in more detail.

5.3.3 Repeatability of RDE tests, and variation in RDE results

One of the main reservations regarding the adoption of the RDE emissions test was the issue of repeatability. How can a result be trusted if it cannot be replicated? In order to investigate the repeatability of the RDE test, the spread of values for different properties across 23 RDE replicate tests was plotted, and the COV calculated for the results across tests for each phase. Vertical dashed lines on the latticed histograms indicate the mean value for that property during each phase.

Figure 5.27, Figure 5.28 and Figure 5.29 respectively show that the route gave fairly consistent distances, average speeds and number of seconds spent accelerating for each of the three different test phases. The histogram distributions appear Gaussian in nature, with a maximum near the mean value for each quantity, and decreasing counts further from this maximum. The COV for discrete distances remains within 1-2% for all three phases, indicating that the ability to remain within the desired speed range for the phase in question was high for the route chosen. The COV for average velocities was 6% for urban, 2% for rural and 0.8% for motorway, reflecting the increase in ability for external factors such as congestion and traffic lights more common in built-up areas to effect the vehicle velocity. The COV of the number of seconds spent accelerating for each phase was 4.6%, 14% and 10.5% for urban, rural and motorway phases respectively. The low percent for the urban section will likely be due to the proportionately longer period of time spent stationary in the urban phase. The average values for the number of seconds accelerating match very well to the results of Donateo & Giovinazzi (2018) for all three sections, but the coefficients of variation are different. For urban, they had over double the COV presented above, but then their variation in rural was just less than half, and in motorway driving results were within 2% of the results presented above. These differences will be due to a combination of route choice, traffic levels and driver behaviour. The findings of this thesis are, however, generally in agreement with those of Donateo & Giovinazzi (2018).

The distribution of $v.a_{pos}[95]$ is given in Figure 5.30, and resulted in COV values of 6.4%, 13.7% and 14.4% for urban, rural and motorway phases respectively. The distribution of RPA values, displayed in Figure 5.31 resulted in COV values of 6.2%, 10.3% and 8.7% respectively. The comparison of

$v.a_{pos}$[95] and RPA distributions against average velocities indicates that there was variability in the aggressiveness of driving on top of the variability caused by external factors. This is due to human behavioural changes altering the driving styles from one test to another.

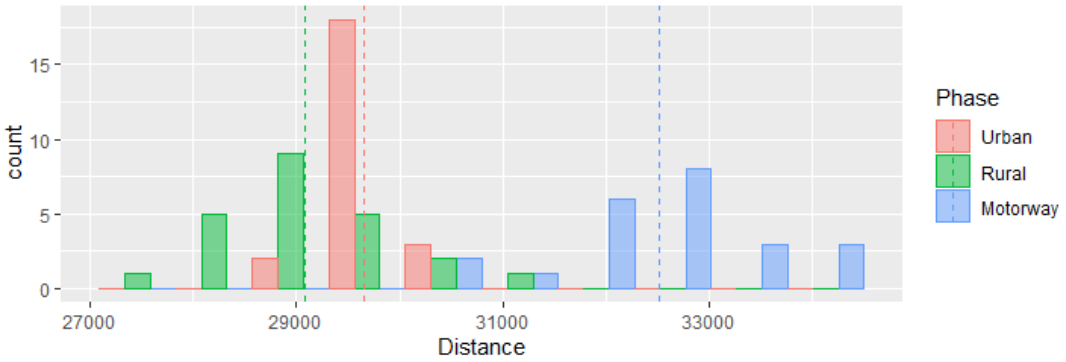

Figure 5.27 Distribution of distances for each of the three RDE phases across 23 replicate RDE tests.

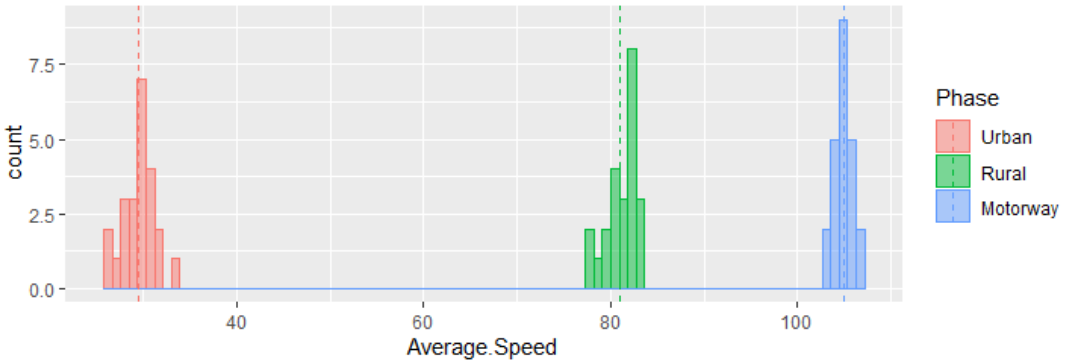

Figure 5.28 Distribution of average speeds for each of the three RDE phases across 23 replicate RDE tests.

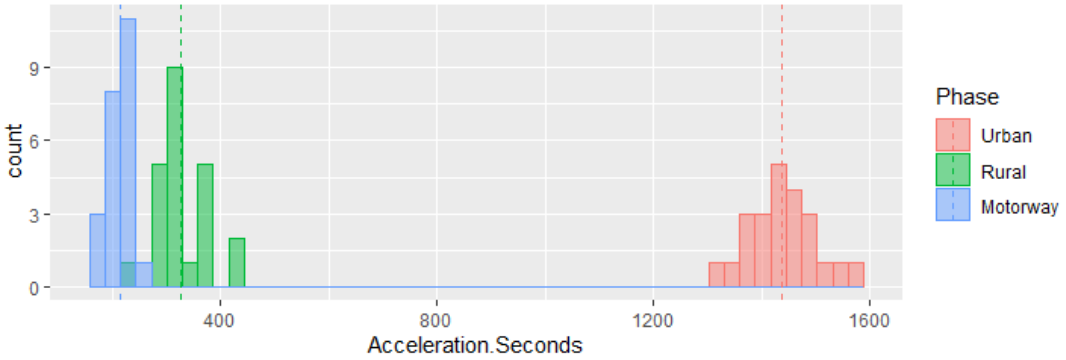

Figure 5.29 Overlapping histogram displaying the distribution of number of seconds the vehicle spent accelerating for each of the three RDE phases across 23 replicate RDE tests.

The total test times in Figure 5.32 showed a 3.8% COV, again with a Gaussian-type distribution about the mean value. Figure 5.33 displays both

distribution of times at vehicle speeds exceeding 100km/h (11.6% COV), and the time taken for the engine coolant of the vehicle to reach 70°C (17.8% COV). The comparatively greater variation of times taken for the engine coolant to reach hot running temperatures is a reflection on the variability of engine strategy employed by the vehicle in reaction to internal factors such as battery SOC, and external factors such as congestion.

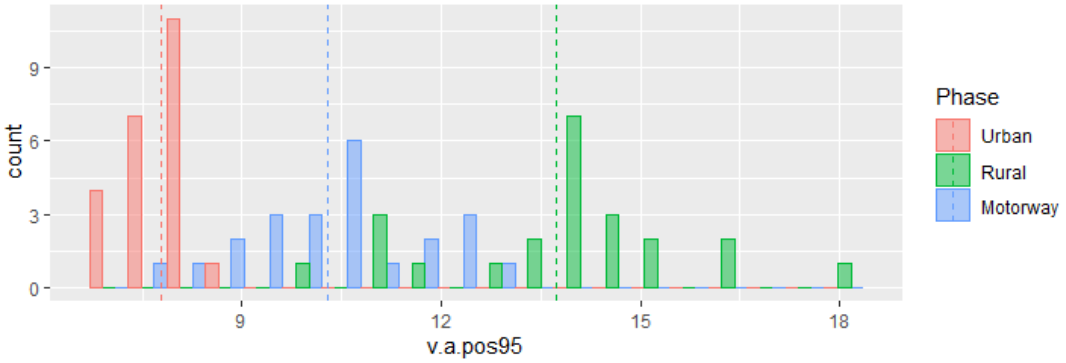

Figure 5.30 Latticed histogram displaying the distribution of $v.a_{pos}[95]$ for each of the three RDE phases across 23 replicate RDE tests.

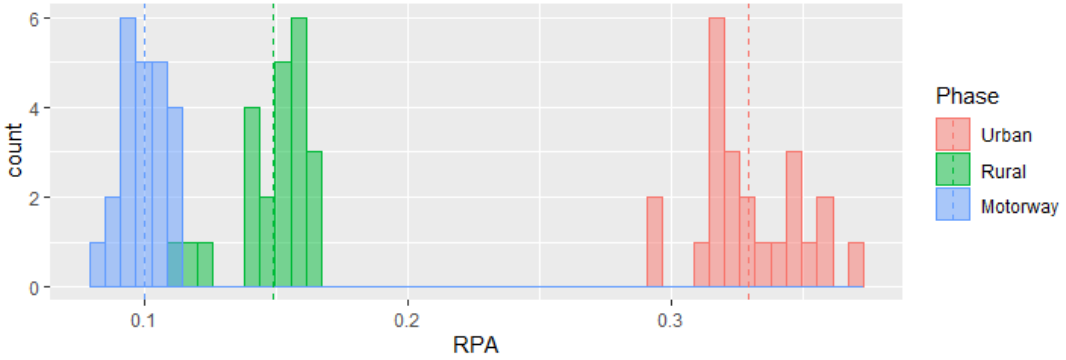

Figure 5.31 Overlapping histogram displaying the distribution of average RPA values for each of the three RDE phases across 23 replicate RDE tests.

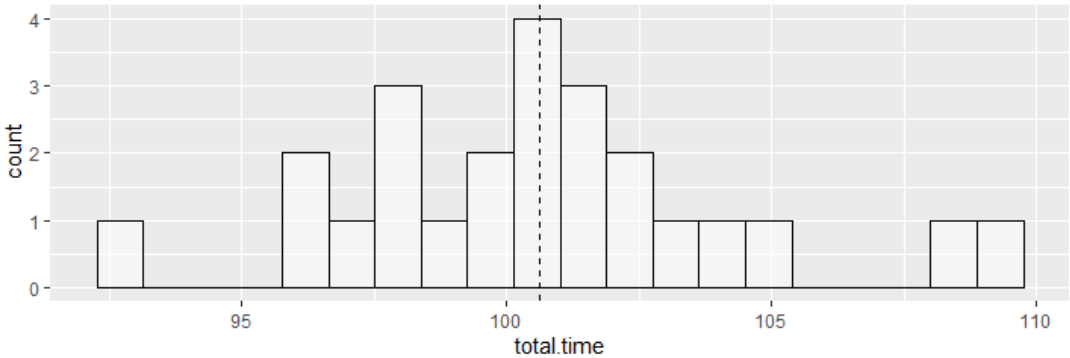

Figure 5.32 Distribution of total test times for 23 replicate RDE tests.

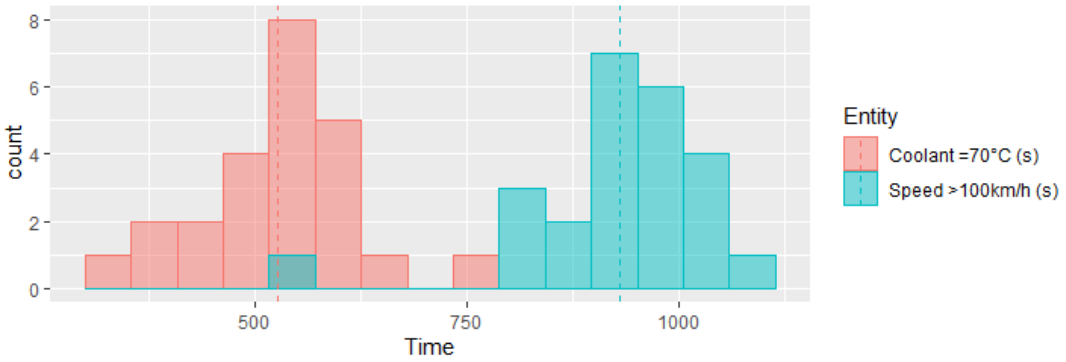

Figure 5.33 Overlapping histograms of time taken for the engine coolant temperature to reach 70°C from cold start, and the number of seconds with vehicle speed above 100km/h, across 23 replicate RDE tests.

Figure 5.34 displays the distribution of CO_2 emission rate values for 5 repeats of the RDE utilising the same fuel. The distributions have reasonable COV values of 5.8%, 7.1% 5.9% and 5.5% respectively for the urban, rural, motorway and total RDE values. Given the variability possible with real-world, on-road testing, particularly for an HEV, these values are perceived as reasonably optimistic for the prospects of the RDE test to give repeatable results.

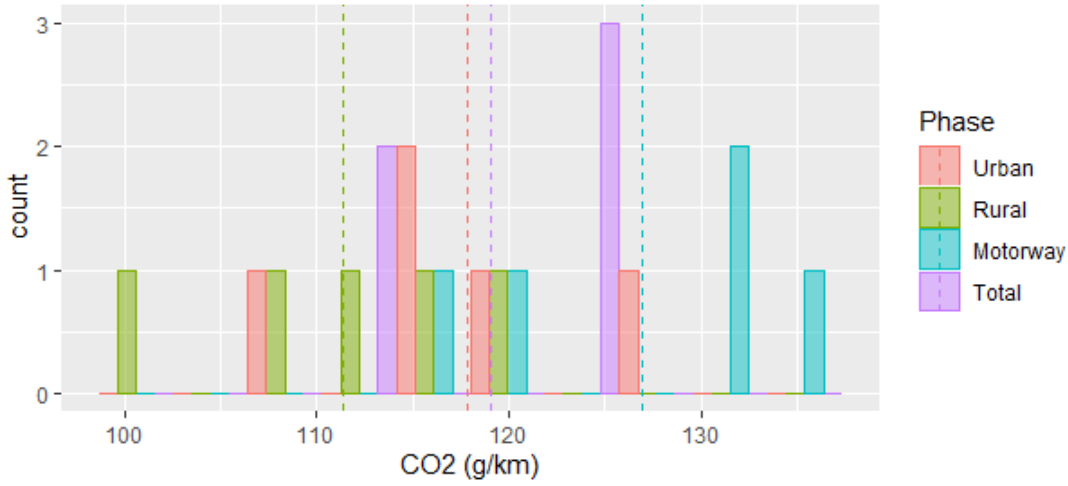

Figure 5.34 Latticed histogram displaying the average CO_2 mass emission rate per km for each phase of the RDE test, and for the test as a whole.

Figure 5.35 shows the COV values of urban CO_2, CO, NO_x and PN emission rates for the RDE, City Centre, and Headingley drive cycles. Unsurprisingly, the CO_2 emissions show the lowest variation, in agreement with Donateo & Giovinazzi (2018). However, the Headingley drive cycle has a variation approximately half that of the RDE and City Centre tests, indicating that the routes chosen for these latter two cycles had a greater variation in traffic behaviour than the former. For CO, the RDE route again had the greatest

variation, while it had the lowest variation for NO_x and PN, particularly the latter. One can conclude from these results that the RDE emission results were no more similar to each other than the other on-road tests performed in urban driving for gaseous pollutant emissions. This is not the case for PN, where more regular traffic patterns due to lower congestion on the roads resulted in more similar engine-use patterns and hence more similar PN between individual RDE tests.

In terms of comparisons between the variation for different pollutants on the RDE, the trend of lowest CO_2, followed by CO and then NO_x is in partial disagreement with the findings of Donateo & Giovinazzi (2018) shown in Figure 5.36, which showed that CO had a higher variation between tests than NO_x. However, their tests were performed with an idle stop-start technology diesel car, and so the different fuel and ICE technology is the likely reason for the different pollutant behaviour seen from the repeated RDE tests by Donateo & Giovinazzi (2018). To the author's best knowledge, no other work has studied repeatability of RDE tests from HEVs.

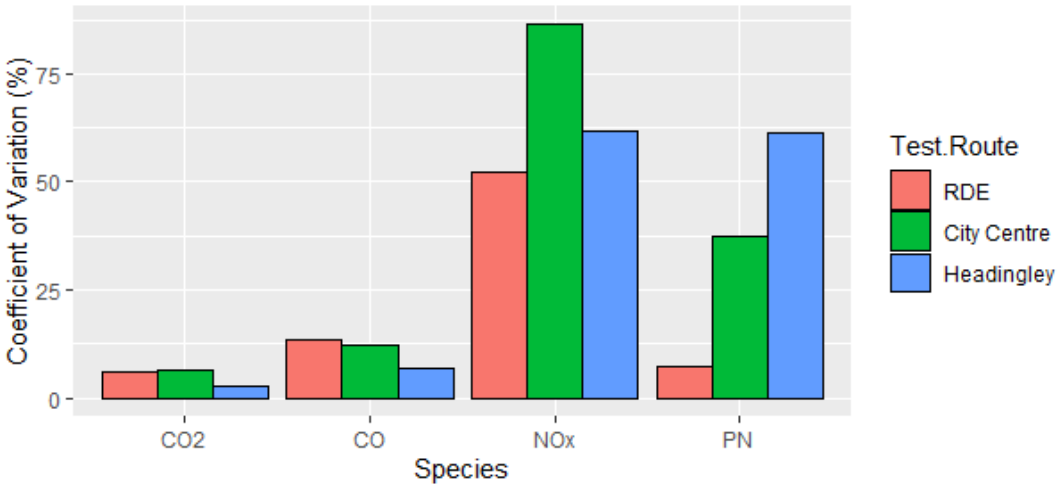

Figure 5.35 Bar chart displaying the COV for regulated pollutant emissions across replicate RDE, City Centre and Headingley tests.

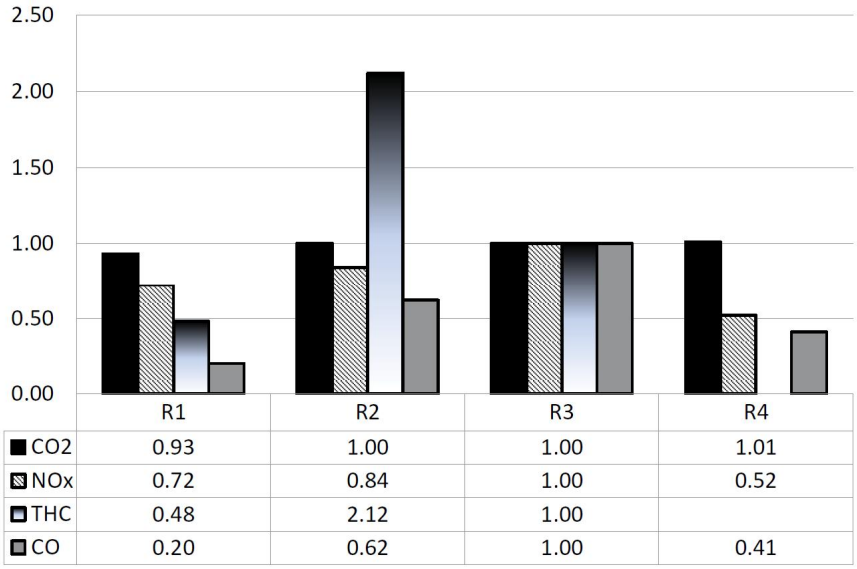

	R1	R2	R3	R4
CO2	0.93	1.00	1.00	1.01
NOx	0.72	0.84	1.00	0.52
THC	0.48	2.12	1.00	
CO	0.20	0.62	1.00	0.41

Figure 5.36 Variation in CO_2, NO_x, THC and CO from four repeated RDE drive cycles (R1-R4), relative to cycle R3, as presented by Donateo and Giovinazzi (2018).

Figure 5.37 displays the COV for the RDE, City Centre, and Headingley test cycles of a wide range of different dynamic properties. The results are mixed, indicating that this RDE test is not generally any more or less dynamically variable than pre-designed test routes being driven during rush hour.

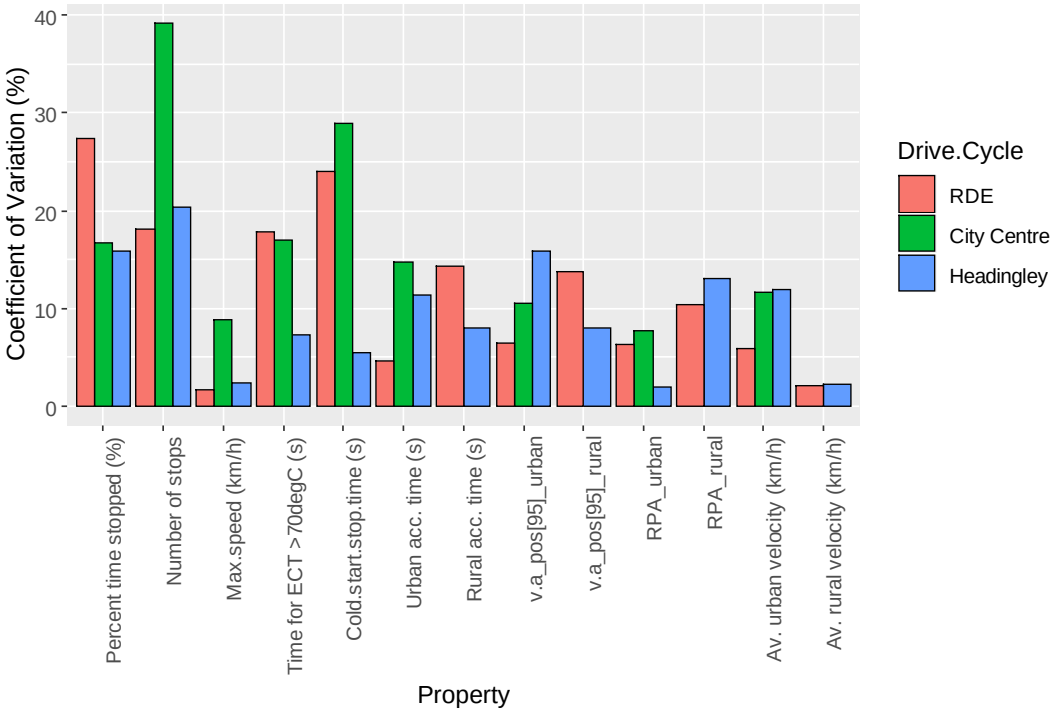

Figure 5.37 Bar chart displaying the COV for a range of dynamic parameters across replicate RDE, City Centre and Headingley tests.

This section has shown that many dynamic properties have good repeatability across multiple repeats of the same RDE test route. This repeatability is not much greater than the repeatability of two different commuting rush hour drive cycles, and does not lead to any greater correlation between emission results.

5.4 Chapter 5 Summary

This chapter has studied the RDE test, its development over time, and its ability to represent real-world driving. Analysis of the results from eight different SI vehicles has shown that there is little common relationship between the reported emissions from analysis according to different RDE packages, across vehicle types. If there were to be a methodology for inferring Package 4 results from earlier package results, knowledge of the transient emissions profile would have to be incorporated. With regard to the exclusion of data required in earlier packages, the greatest difference by far was achieved by the transition from Package 2 to Package 3, with little change being seen going from Package 3 to Package 4.

The newest package of the RDE legislation has proven to be more closely aligned with real-world driving than the older packages. However, the RDE test still does not accurately represent the highly congested conditions that are common in city centres today. This results in the reported emissions from the RDE test being lower than for congested styles of driving where the greatest air quality impacts on health are found. In particular, HEV behaviours have led to an even larger quantity of emissions being produced in these styles of driving currently untouched by either the WLTC or RDE tests.

The next chapter will study these HEV behaviours in more detail.

Chapter 6
Hybrid electric vehicle behaviour and emissions

6.1 Introduction

There are many aspects of an HEV that can mean its engine behaviour is different from a CV. This is the reason to study HEV behaviour and the resultant emissions in detail. This chapter will study the main areas of interest for HEVs (Objective 3 of this thesis, as set out in Section 2.11 of Chapter 2), namely those surrounding catalyst light-off, lambda control during engine stop-start (also called stop-and-go) and the effect of hybrid battery SOC. This will satisfy Tasks 7 and 8 set out in Chapter 2. The repeatability of HEV emissions performance will then be assessed from repeated identical tests, thereby satisfying Task 9.

6.2 Catalyst light-off behaviour

Because of the ability for HEV engines to turn off during driving, there has been some concern surrounding HEV catalyst temperature and hence efficiency. This section will present the results of an investigation into catalyst efficiency (see Chapter 3 Section 3.8.6.5 for details).

Figure 6.1 shows an example WLTC trace of the gas temperature across the TWC, with thermocouple readings of gas temperature at the front face of the first TWC, between the two TWC, and at the rear face of the second TWC, along with TWC monolith temperatures. Engine speed is in black, and the engine warm-up request is indicated in grey along the bottom of the graph. The vehicle engages in a constant engine operation for the first 80s. The engine warm up request causing this is visible as an ECU parameter, and prescribed for all engine key-on, engine ignition-on events that occur with an initial engine coolant temperature lower than 70°C. The approximate 80s duration of this period is slightly longer than previously reported by Rask et al. (2010) (50s) and Anderson et al. (2014) (60s). Given that the former studies were both utilising the same US FTP Urban cycle (also called UDDS), it is unsurprising that the WLTC of the current study results in a different engine warm-up time. Indeed, over the NEDC, the warm-up time was shorter, approximately 65s.

The TWC temperatures show that the gas temperature immediately prior to the first catalyst quickly reaching upwards of 400°C. The TWC block 1 is absorbing heat from the exhaust gases throughout the first few hundred seconds of the test, visible as a convergence of TWC block 1, pre-TWC gas and mid-TWC gas temperatures. The TWC block 1 reaches a thermal equilibrium and light off temperature around 200s into the test.

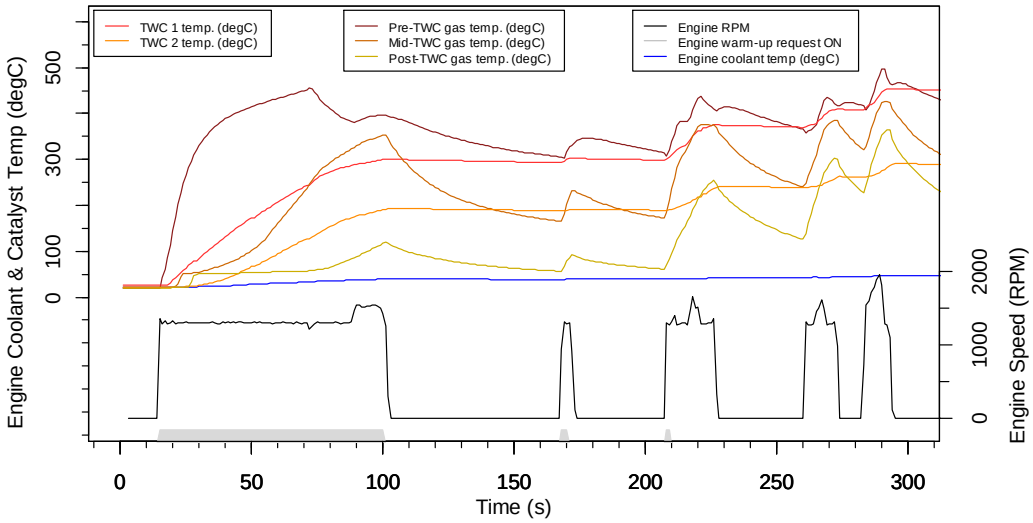

Figure 6.1 First 300s of a WLTC: Gas temperatures across the TWC are given, along with the TWC monolith block 1 and 2 temperatures. Engine coolant temperature is on the same scale, while engine speed and engine warm-up request are represented underneath.

Catalyst efficiency, calculated as the percentage difference between pre-TWC emission rate and post-TWC emission rate, was studied in detail for THC, CO and NO_x. Figure 6.2 gives an example result for CO, demonstrating that the catalyst begins to operate after a very short period of time, even if some breakthroughs occur later in the tests. This indicates that the front face of the TWC is heated sufficiently for a superficial layer to light-off and reduce tailpipe emissions, long before the heat transfers through the monolith and the rest of the catalyst is able to light-off. There is an efficiency drop again at around 160s after the engine has been off. This shows that the TWC did not fully light off during the first 50s of the test, and only lights off completely 200-300s into the test as the temperatures in Figure 6.1 indicated. Note that due to some differences in gas transfer time, the alignment between engine-out and tailpipe measurements is not always perfect, and this can cause some inaccuracies in calculated TWC efficiency.

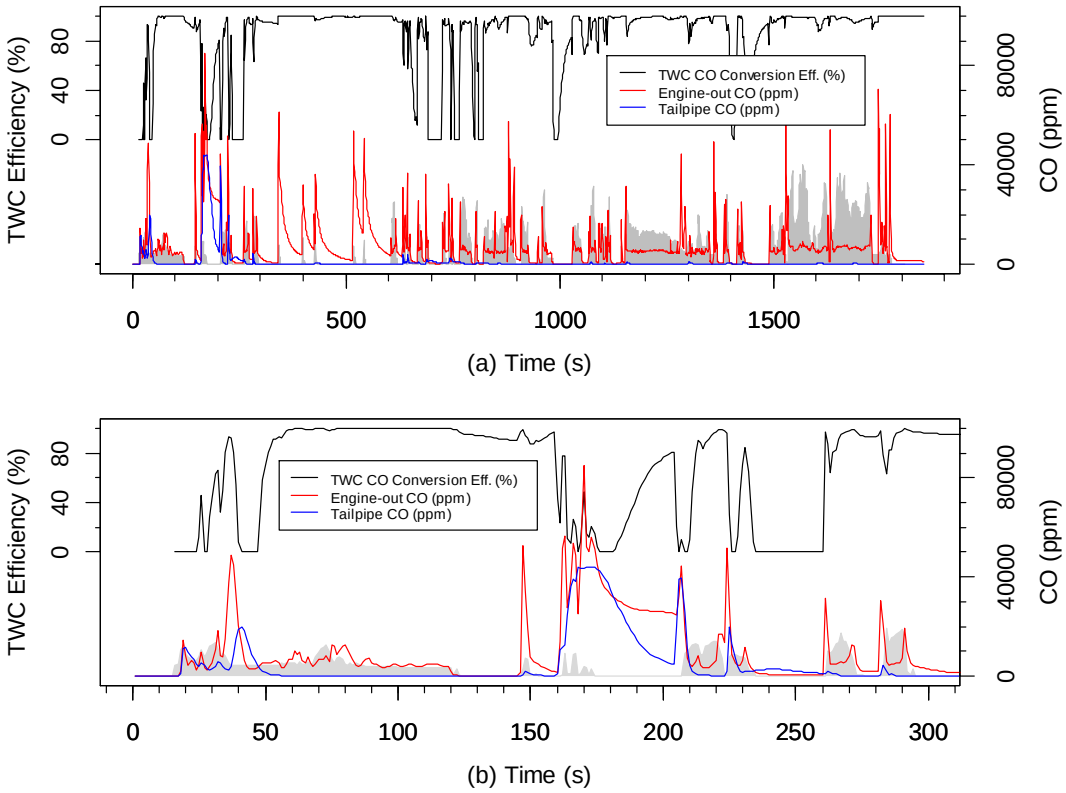

Figure 6.2 WLTC (Test 20) engine-out and tailpipe THC emissions, with calculated catalyst conversion efficiency for THC. (a) Full test and (b) first 300s of a test. Mass air flow rate is indicated qualitatively in grey.

Figure 6.3a, Figure 6.3b and Figure 6.3c capture the cold start section of a representative WLTC test, elucidating the rapidity with which the catalyst begins to abate the engine-out emissions. Within 30s of engine start, the catalyst is converting the engine-out emissions, despite the bulk catalyst temperature being lower than the 200-300°C threshold typical of approximate catalyst light-off (Cant et al., 1998; Gao et al., 2013; Yan et al., 2019). A superficial layer of the TWC, closest to the engine, is sufficiently heated to convert the pollutant emissions. The mid-TWC is displayed as an indicator of catalyst light-off because the cold TWC will absorb heat from the exhaust gas, so once the temperature of gas exiting the first TWC is constantly above light-off temperature, this indicates that the TWC should also have sufficiently heated to light off.

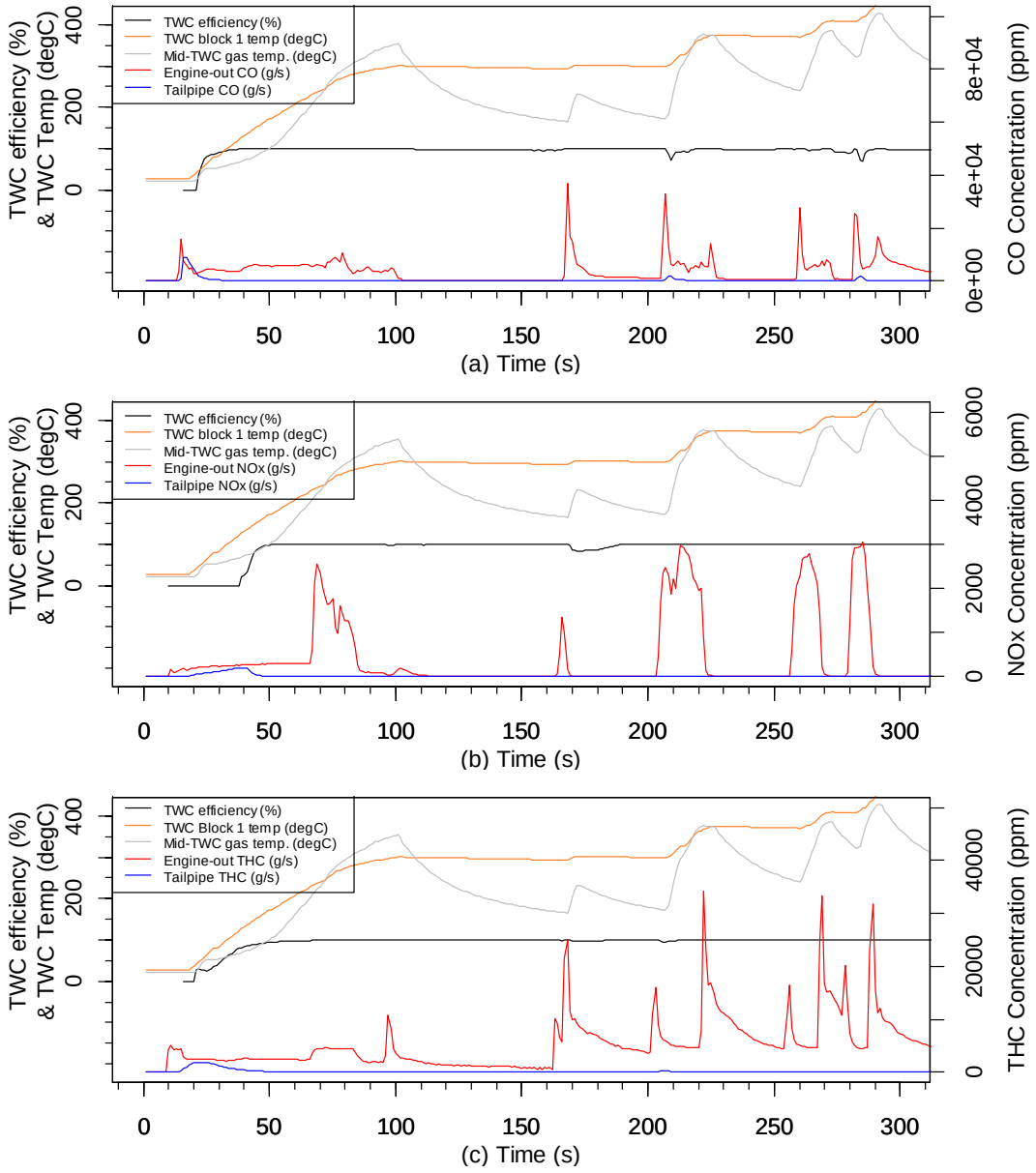

Figure 6.3 Test 23 WLTC engine-out and tailpipe concentration results for (a) CO, (b) NO_x, and (c) THC during first 300s of a cold start test. The TWC conversion efficiency and temperatures are on the primary axis for each.

Table 6.1 displays the average times for which it takes the catalyst to reach 50% and 90% conversion efficiencies for CO, NO_x and THC separately, across six cold start WLTC tests. These values were calculated from the upward curve in efficiency of the catalyst seen once the tailpipe emissions started to decrease compared to the engine-out emissions, as displayed between 40-60s into the example test of Figure 6.2b.

The time for the engine coolant temperature to reach 70°C, and the time for the inlet temperature to reach the thresholds outlined in Watling & Cox (2014)

for 50% and 90% efficiency (325°C and 350°C respectively), are also included for reference. A clear conclusion, as indicated in Figure 6.2, is that the catalyst is able to abate emissions far more quickly than the engine coolant temperature indicates, and at a time more closely aligned with the inlet temperature reaching the thresholds outlined by Watling & Cox (2014). This means that although HEVs may have slower warm-up of their systems due to engine inactivity, this does not appear to significantly affect the TWC emissions abatement capacity. Indeed, Table 6.2 shows the different TWC average temperatures across the 6 replicate tests, proving that the front face of the catalyst is above light-off temperature when the conversion efficiency reaches 90%, while the rest of the TWC remains relatively colder. This indicates that a thin layer of TWC material has lighted off very rapidly and is responsible for the fast abatement of emissions on engine cold start. The average time for 90% conversion efficiency of CO, NO_x and THC was calculated as 47s across tests, so the temperatures given in Table 6.2 can be interpreted as those at this time on average.

Table 6.1 Average time taken to reach different thresholds indicating catalyst light-off.

	Quantity	**Time (s)**
	Engine coolant temperature ≥ 70°C	844 ± 6
50% Efficiency	TWC inlet temperature ≥ 325°C	33.5 ± 4
	CO reduction	33 ± 6
	NO_x reduction	43 ± 1
	THC reduction	39 ± 4
90% Efficiency	TWC inlet temperature ≥ 350°C	43± 10
	CO reduction	38 ± 5
	NO_x reduction	51 ± 3
	THC reduction	52 ±3

Table 6.2 The average temperatures across the catalyst at an average 90% conversion efficiency for CO, NO_x and THC abatement.

Quantity	**Temperature at 90% efficiency (°C)**
TWC block 1 monolith	150 ± 10
TWC block 2 monolith	54 ± 7
TWC front face	366 ± 19
Mid-TWC exhaust gas	75 ± 3
TWC rear face	52 ± 0.3

This section has demonstrated that the point at which the engine coolant temperature reaches 70°C is not a suitable threshold to use to indicate the end of cold start. Surprsingly, neither is the time at which the catalyst monolith or catalyst gas temperatures reach appropriate temperatures. The catalyst lights-off much earlier than these times, which is a finding in agreement with previous studies on the same vehicle (Rask et al., 2010; Anderson et al., 2014). However, as seen in figure 2, this layer can quickly lose temperature if the engine turns back off again, and subsequent spikes in tailpipe emissions can be seen on engine re-ignition during the period of time before the TWC fully lights off at around 200-300s.

As well as ensuring that the catalyst lights-off soon after engine-start, it is also important that after periods of HEV engine-off, the catalyst temperature has not dropped below that required for efficient operation. Figure 6.4a, Figure 6.4b and Figure 6.4c display the THC, CO and NO_x emissions of a WLTC cycle, alongside the average catalyst monolith temperature, average catalyst gas temperature and engine RPM. Between 250s and 600s the engine is on very infrequently, leading to a decrease in catalyst monolith temperature. When the engine restarts, the THC and NO_x emissions that result from the engine are abated by the catalyst, while the CO emissions are not. This behaviour was seen across all tests studied (WLTC, NEDC and RDE-style cycles), indicating that the catalyst does not easily de-light; the temperature was still high enough to abate the emissions. Anderson et al. (2014) stated the same finding for THC from the UDDS cycle tested, but they did witness some breakthrough of NO_x later in the test. The CO emissions were not studied. This means that the TWC may show more varied behaviour across tests for NO_x reduction than THC. The CO emissions that continue to occur into relatively high TWC temperatures are a result of incomplete combustion effects when the engine re-ignited, which is investigated further in Section 6.3.

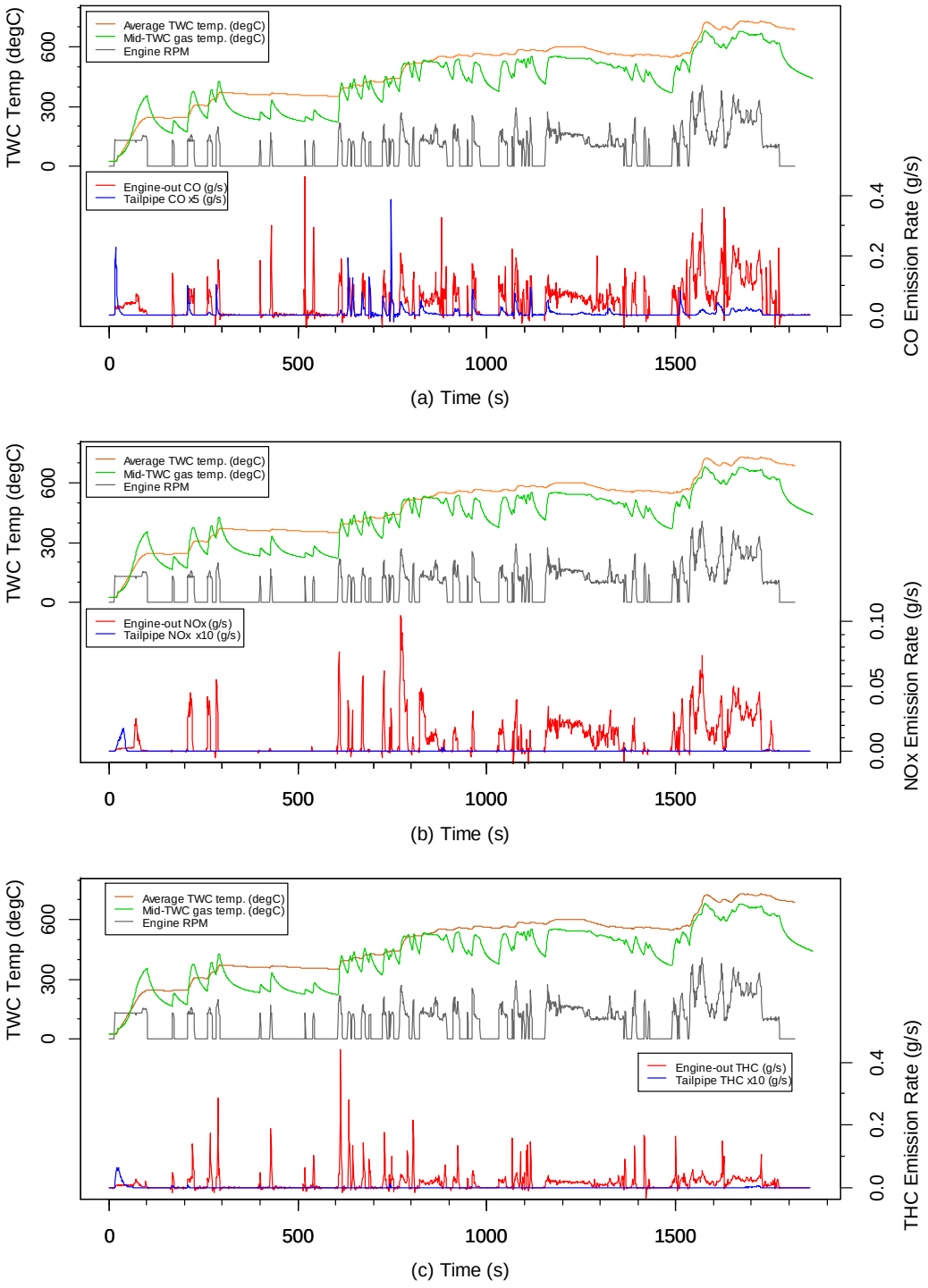

Figure 6.4 Test 23 engine-out and tailpipe emissions of (a) THC, (b) CO and (c) NO_x emissions of a WLTC cycle (the tailpipe CO, NO_x and THC were multiplied by 5, 10 and 10 respectively), alongside the TWC monolith temperature, mid-TWC gas temperature and engine RPM.

6.3 Stop-start behaviour

HEVs, and now many CVs, utilise a technology that automatically turns off the engine when it is not needed. For CVs this is only when the vehicle is stationary and in neutral gear, but for HEVs the engine can turn off more frequently, in conditions such as driving at low speed or load. This section will investigate this stop-start behaviour and the resultant emissions.

6.3.1 Regulated gaseous pollutant emissions

This section will explore the THC, CO and NO_x emission rates for two identical cold start WLTC test cycles, and how this correlates with engine speed, paying particular attention to engine-on and engine-off transitions.

6.3.1.1 THC

Figure 6.5a and Figure 6.6b show tailpipe THC emission rates and cumulative emissions for two WLTC test cycles. There is an emissions spike visible for every engine-start/restart event in the first half of the drive cycle, but after this point, there are no more significant THC emissions seen for engine on events. This is a much longer period of time than witnessed by Anderson et al. (2014), but in agreement with many other investigations of HEV stop-start emissions (e.g. Ng et al. (2001), Christenson et al. (2007)). Overall THC emissions are low, being below the Euro 4, 5 and 6 emissions limit of 0.1 g/km for all tests.

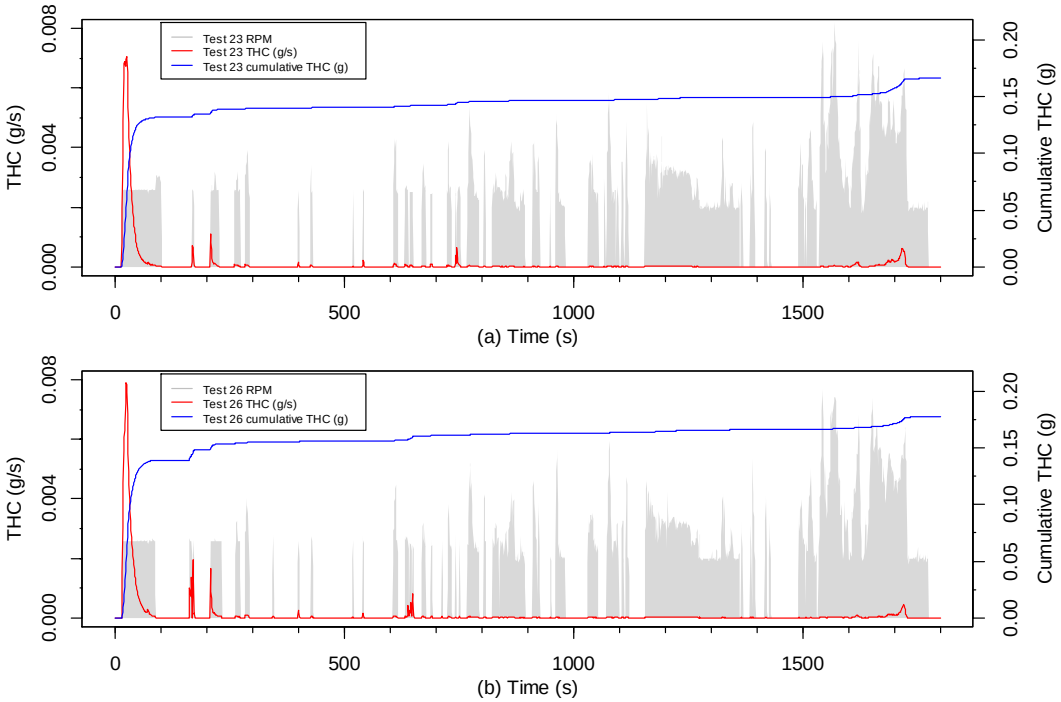

Figure 6.5 Total and cumulative tailpipe THC pollutant emissions from two E10-fuelled WLTC tests. Engine speed is indicated on the plots in grey.

Figure 6.6a and Figure 6.6b show the tailpipe THC emissions for the period from 300-800s of the WLTC, with the engine-out emissions indicated at 1000 times smaller scale for visualisation. Additionally, TWC temperatures measured from assorted positions (Figure 6.6a) and air-fuel ratio (Figure 6.6b) are plotted on the right-hand axis. Figure 6.6a indicates that some of the earlier emissions spikes could be associated with low TWC temperature. Though the monolith is reading over 350°C, the fact that the rear catalyst gas temperature is only 200°C is indicative that the TWC is not fully warmed up. At approximately 600s all catalyst temperatures increase to above 300°C, meaning further emissions are not likely to be related to catalyst temperature. Figure 6.6b indicates that the cause for the increases later in the test are due to an enrichment of the air-fuel ratio during engine starts, with the magnitude of emission breakthrough increasing with the magnitude of diversion into rich air-fuel ratios, visible in green on the figure. In fact, it is possible that all ignition events were rich, but that the four events between 350s and 600s were too short to be registered as such, due to mixing effects within the tailpipe. Huang et al. (2019) also attributed the similar overall THC emissions levels of their HEV to comparable CV as being due to a combination of frequent engine restarts, lowered exhaust gas (i.e. TWC) temperature and reduced effectiveness of the TWC, though the latter two were not measured.

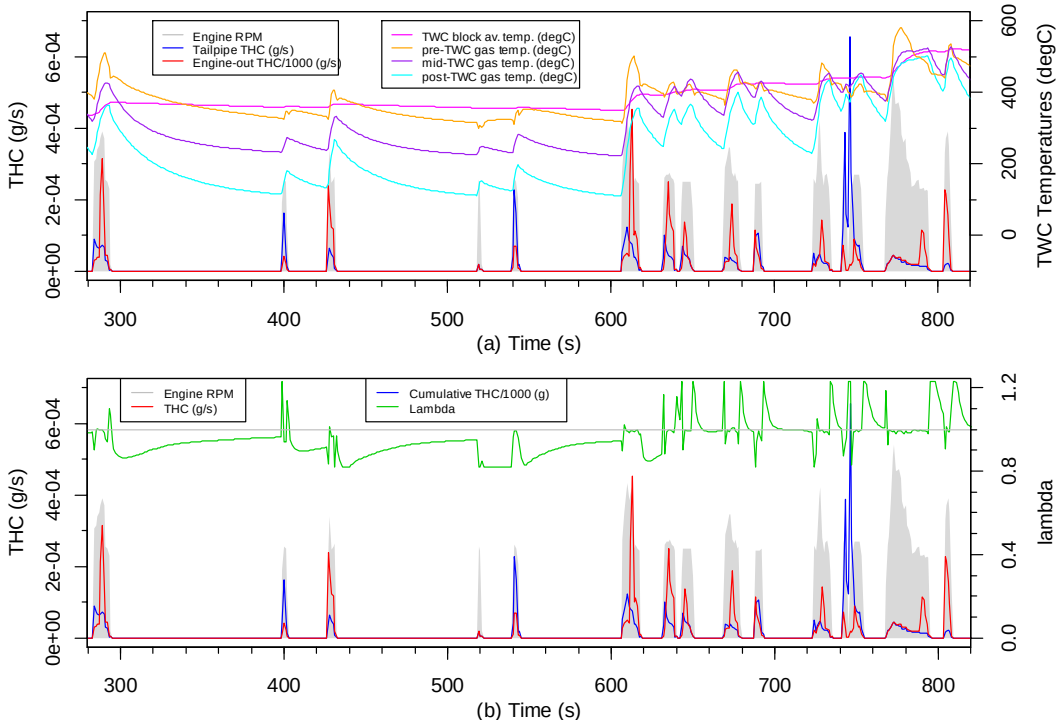

Figure 6.6 Tailpipe THC emissions and engine-out THC emissions for the period from 300-800s of the WLTC alongside indicated engine speed. (a) TWC and gas temperatures around the TWC and (b) air-fuel ratio.

6.3.1.2 CO

Figure 6.7a and Figure 6.6b show the CO emission rates and cumulative emissions for two identical WLTC test cycles. There is an emissions spike visible for almost every engine-start/restart event throughout the duration of the test cycle. The exception here is for some very short duration engine-restart events, for which there are negligible CO emissions. After this engine-off period, the CO emissions are particularly high, so this section deserves deeper analysis, as it is important to investigate the penalty in CO paid when the hybrid engine restarts after a period of engine-off. Finally, it is worth noting that during the highest power-demand sections of the test cycle, we also see CO emissions, in agreement with the findings of Christenson et al. (2007). Note that total CO emission factors were low – all below the Euro 6 limits.

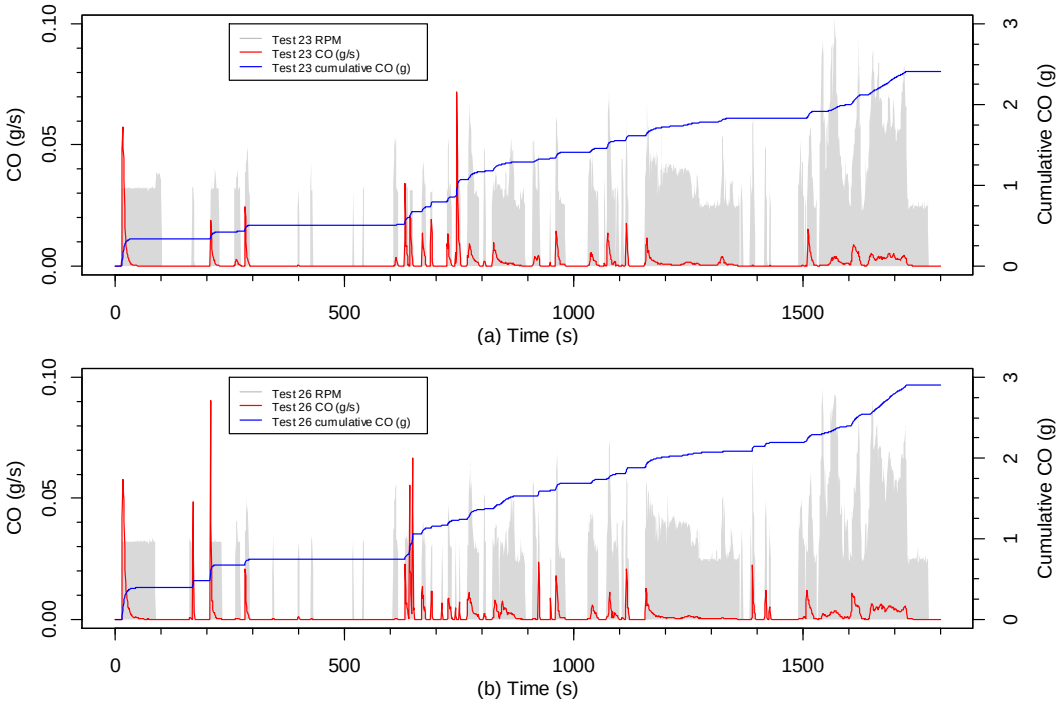

Figure 6.7 Total and cumulative CO pollutant emissions from two WLTC tests fuelled with E10. Engine speed is indicated on the plots in grey.

Figure 6.8a and Figure 6.6b show the engine-out and tailpipe CO emissions for the period from 500-1000s of the WLTC, with catalyst temperatures (measured from assorted positions) plotted on the right-hand axis in Figure 6.8a and lambda in Figure 6.8b. Figure 6.8a conclusively demonstrates that the increase in emissions is not related to the catalyst temperature, because the catalyst is abating the emissions originating from the three engine starts between 500 and 610s, even though this period of time is when the temperatures are lowest. Figure 6.8b confirms that the cause for this increase

in emissions is an enrichment of the air-fuel mixture (lambda<1) for these problematic engine starts. The magnitude of emissions breakthrough is proportional to the magnitude of diversion into rich air-fuel mixtures (note that the lambda values in Figure 6.8b are only meaningful during periods of engine-on activity: When the engine is off, the lambda value increases if fresh air enters the system, or decreases if exhaust gases become trapped in the exhaust system). Huang et al. (2019) also attributed the higher overall CO emissions levels of their HEV to comparable CV as being due to a combination of frequent engine restarts, lowered tailpipe (i.e. TWC) temperature and reduced effectiveness of the oxidation catalyst, though the latter two were not measured.

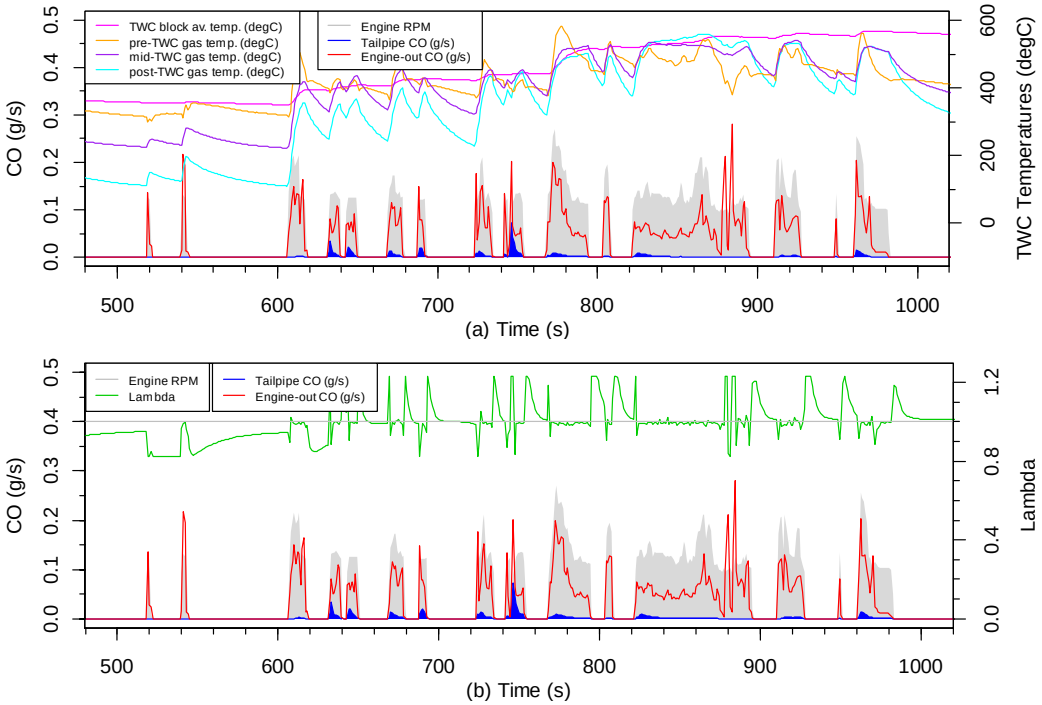

Figure 6.8 Engine-out and tailpipe CO emissions for the period from 500-1000s of the WLTC, alongside engine speed, with (a) TWC average temperature and gas temperatures around the TWC, and (b) lambda.

Figure 6.9a and Figure 6.9b show the CO emissions from an HEV and comparable CV counterpart respectively. The graphs show a portion of the urban phase of an RDE test for each vehicle, after they have warmed out of cold start. The HEV in figure 9a has CO emission events accompanying most engine restart events during this period, while the CV has some CO emissions during periods of constant driving. The overall result is that over the duration of the period shown, the total CO emissions from the HEV are comparable to

the CV, though slightly higher, as shown by comparison of the blue cumulative CO mass emission lines. This finding is in agreement with Huang et al. (2019).

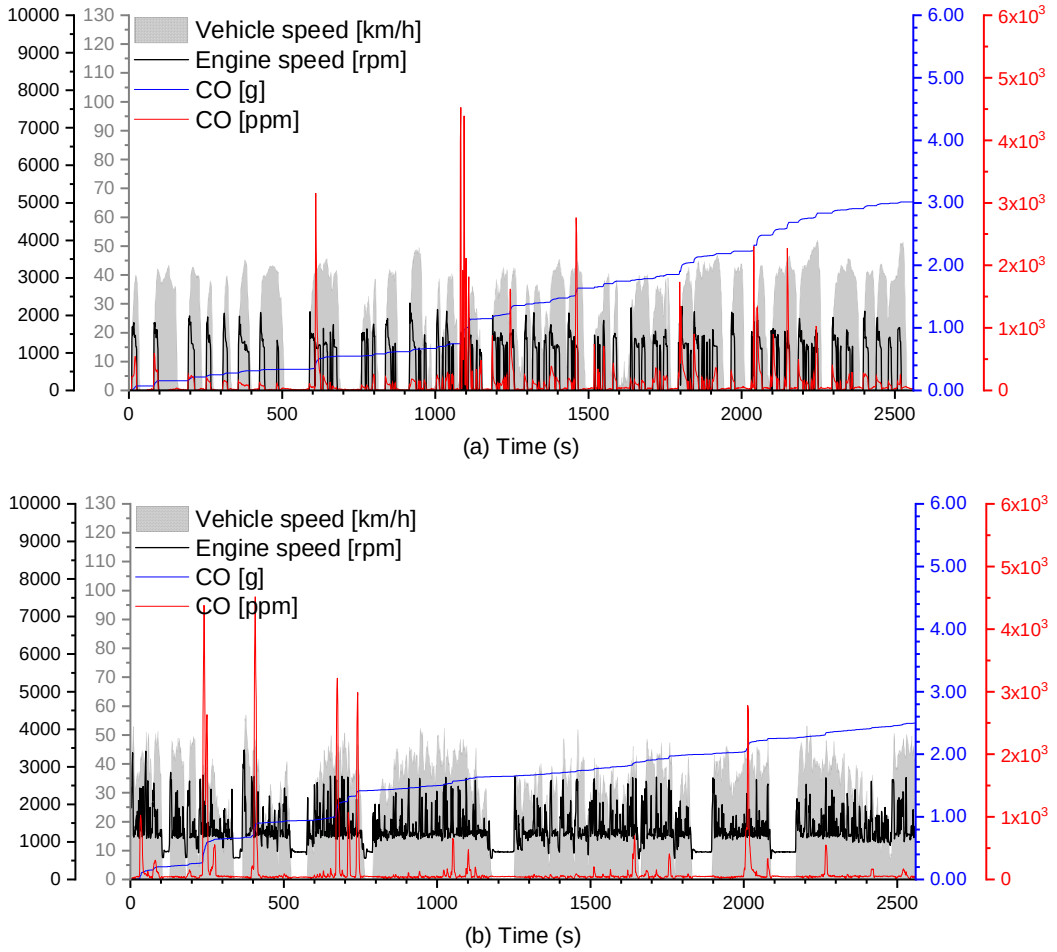

Figure 6.9 Example CO emissions over RDE testing by (a) an HEV Toyota Corolla and (b) a conventional ICE-only Toyota Corolla.

6.3.1.3 NO_x

Figure 6.10a and Figure 6.10b show the NO_x emission rates and cumulative emissions for two identical WLTC test cycles. There are no NO_x emissions associated with engine starts seen once the catalyst light-off period has expired in the lower speed phases, in agreement with Anderson et al. (2014), but some emissions behaviour is visible in the higher-speed phases, associated with engine starts and changes in engine speed. Anderson et al. (2014) did not mention this behaviour, but they only published transient results of the more gentle UDDS cycle.

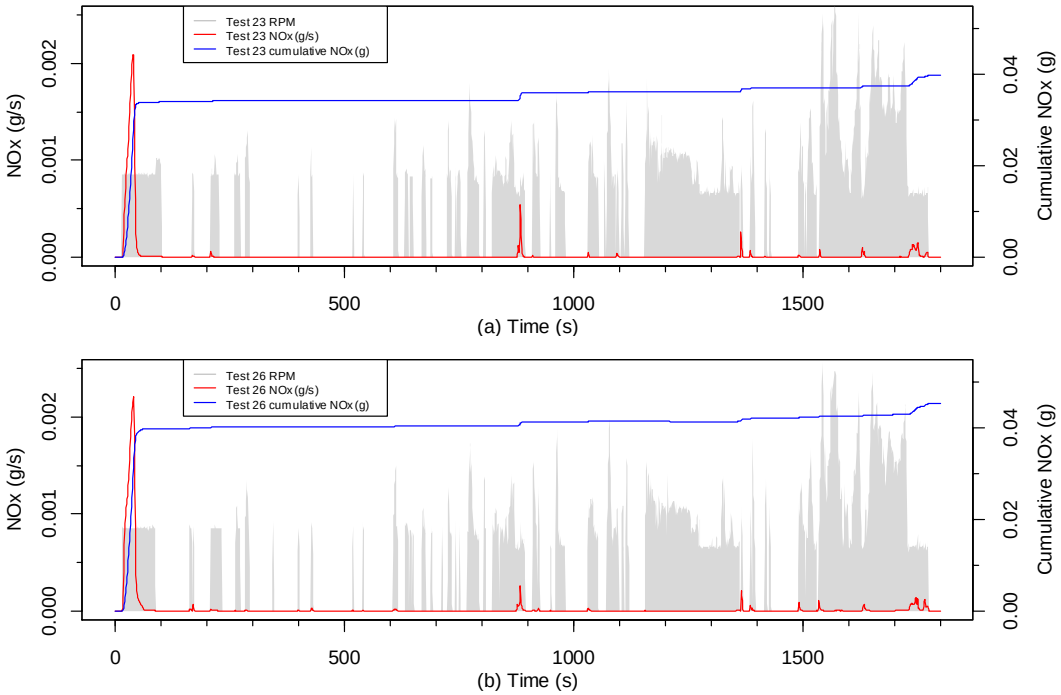

Figure 6.10 Total and cumulative NO_x pollutant emissions from two WLTC tests fuelled with E10. Engine speed is indicated on the plots in grey.

Figure 6.11a and Figure 6.11b confirm that the NO_x emissions spikes later in the drive are not caused by excessive catalyst temperatures (as can occur under high load driving), because the catalyst is shown to be abating the emissions originating from the highest catalyst temperature regions here. Christenson et al. (2007) also observed this NO_x behaviour in their study, but they attributed it to combustion and catalyst temperatures, which were not recorded. Analysis of engine coolant and TWC temperatures in the current study does not support this supposition. Figure 6.11b shows that the events are due to lean combustion events, visible as the air-fuel ratio diverging into the lean region (λ>1). The largest such event occurs as the engine speed decreases at the end of the drive, when load is removed from the engine. Fuel cut-off events, as occur during engine-shutoff or sudden decreases of engine load, can result in lean conditions within the cylinder, which are precipitous for NO_x emission. A recent paper studying HEV transient NO_x emissions at high frequency, saw similar NO_x emissions, and also attributed them to fuel cut-off events, leading to lean conditions in the combustion cylinder (Zhang et al., 2020).

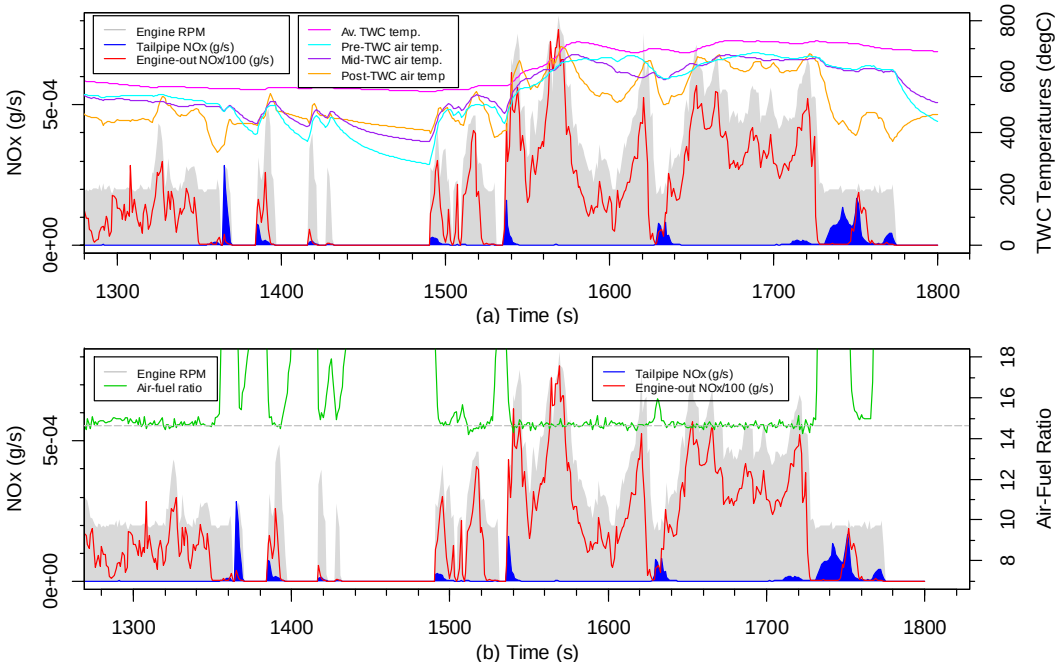

Figure 6.11 Tailpipe NO_x emissions and engine-out NO_x emissions (divided by 100 for scaling), for the period from 300-800s of the WLTC alongside engine speed, with (a) TWC average temperatures and gas temperatures around the TWC, and (b) air-fuel ratio.

6.3.2 PN emissions

The research presented in this section focuses on the PN emissions particularly during engine-starts and restarts, including PN size distribution. Figure 6.12a and Figure 6.12b show the PN emission rates and cumulative emissions for two identical WLTC test cycles. There are spikes in PN associated with the engine starts seen throughout the tests, in agreement with previous literature (e.g. Robinson & Holmén (2011) in Figure 6.13, Wei & Porter (2011), Conger & Holmén (2015) and Kontses et al. (2020)). The PN emission rates seen led to substantial emission factors generally above the Euro 6 emissions limit of $6x10^{11}$ #/km (currently applicable to GDIs only, of all SI vehicles).

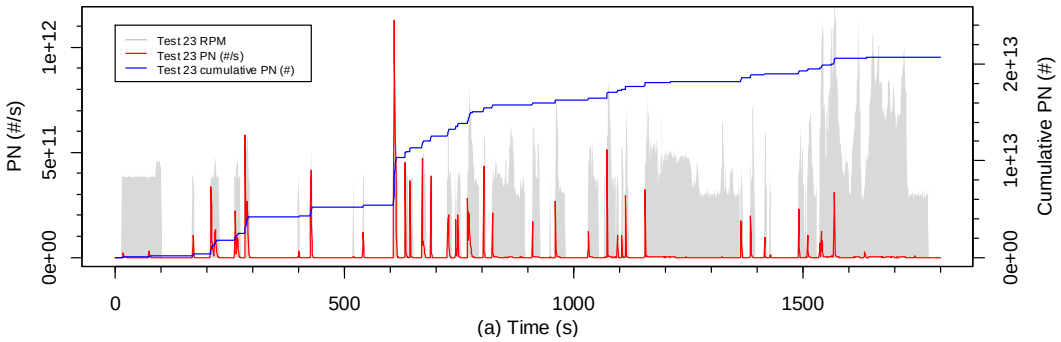

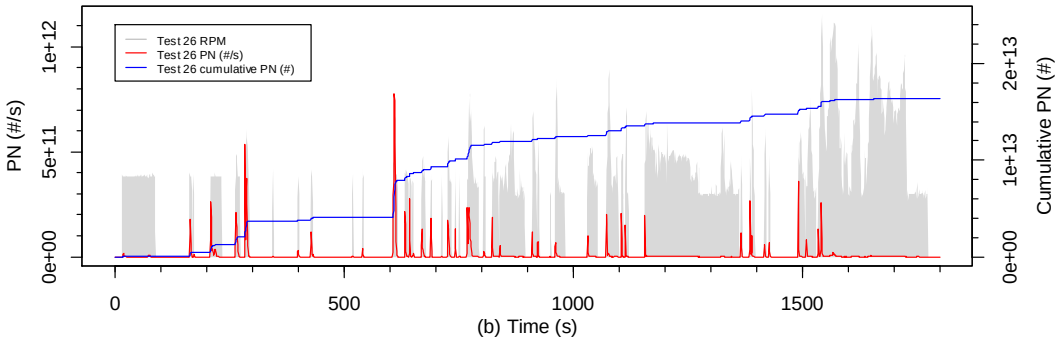

Figure 6.12 Total and cumulative PN emissions from two WLTC tests fuelled with E10. Engine speed is indicated on the plots in grey.

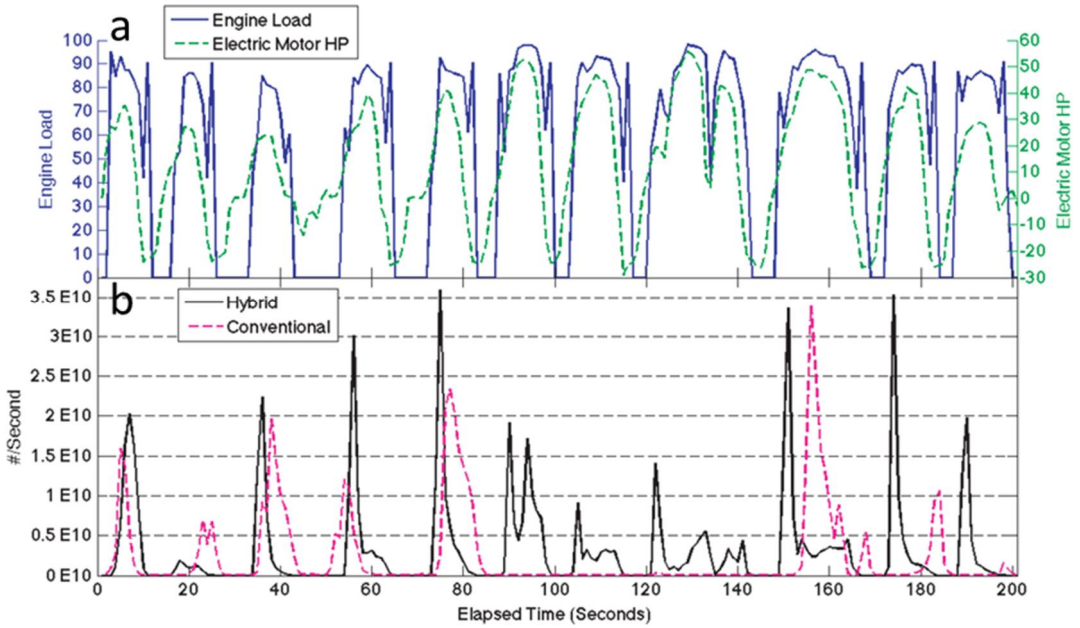

Figure 6.13 (a) Time series HEV engine load and electric motor horsepower of HEV and (b) HEV PN emission rate in bottom figure (with CV plotted as a dashed line for comparison). Source: Robinson and Holmén (2011).

Figure 6.14a confirms that, as expected, the levels of emissions are not being caused by changes in catalyst temperature. Figure 6.14b shows that throughout the test drive, these engine-restart events are often correlated with rich combustion events. Figure 6.14c shows a 500s section in more detail, demonstrating that the PN emissions spikes occur every time the combustion engine ignites under a fuel enrichment strategy, in agreement with the findings of Conger & Holmén (2015). When rich excursions occur during a period of more constant engine activity, no associated PN spikes are seen.

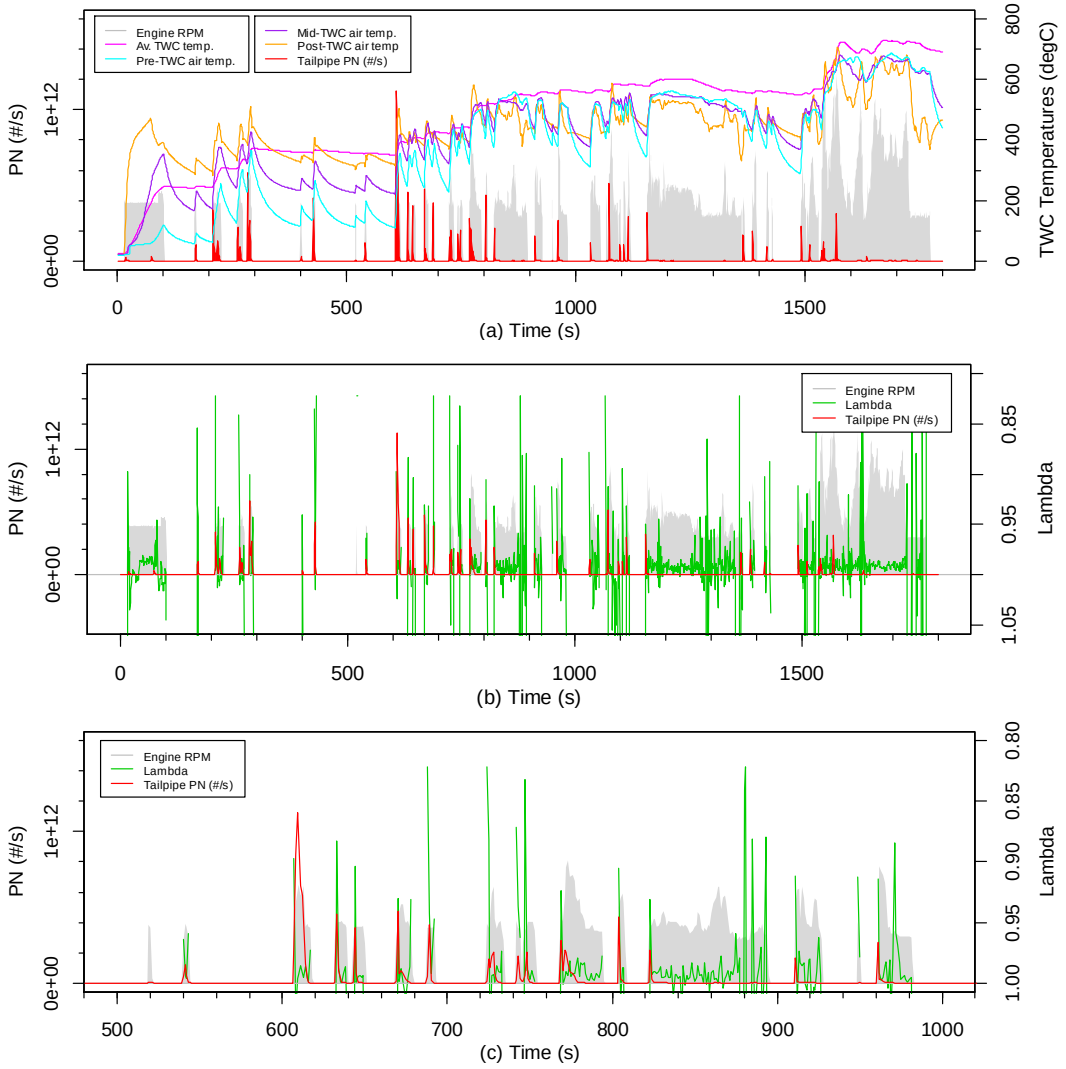

Figure 6.14 Tailpipe PN emissions of the WLTC alongside engine speed, with (a) TWC average temperatures and gas temperatures around the TWC, and (b) lambda. (c) shows the period from 500-1000s of (b).

Figure 6.15a and Figure 6.15b show the PN emissions from an HEV and comparable CV respectively (from the data outlined in Chapter 3 Section 3.6). The graphs show a portion of the urban phase of an RDE test for each vehicle, after they have warmed out of cold start. The HEV in Figure 6.15a has PN emission events on every engine restart event during this period, while the CV has some much lower concentration PN emissions during periods of constant driving. The overall result is that over the duration of the period shown, the cumulative PN emissions from the HEV are over a magnitude greater than for the CV, as shown by comparison of the blue lines and axes. These results agree with Christenson et al. (2007), Wei and Porter (2011), Robinson and Holmén (2011) and Conger and Holmén (2015).

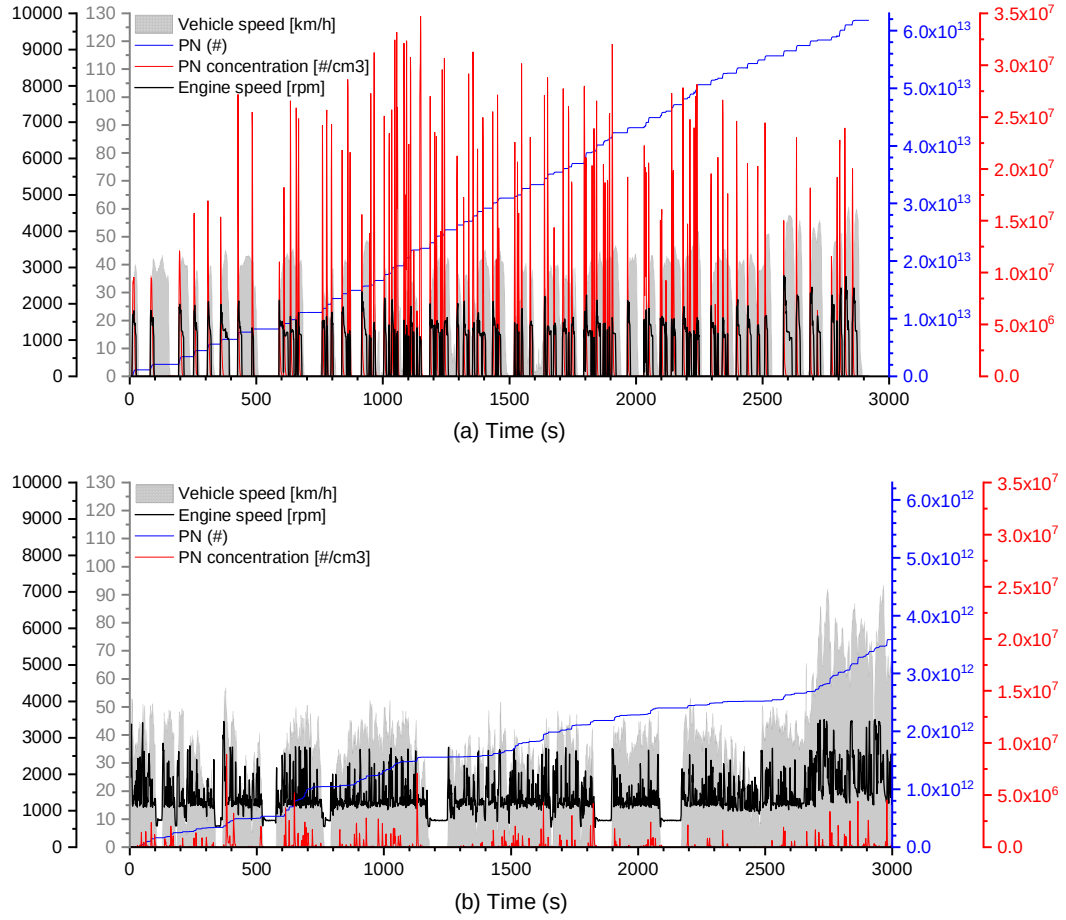

Figure 6.15 Example PN emissions over RDE testing by (a) an HEV Toyota Corolla and (b) a conventional ICE-only Toyota Corolla.

Note that the cumulative PN axis for the CV is (10x) smaller magnitude.

6.3.2.1 PN size distribution of engine re-ignition events

During engine cold start, a bimodal PN size distribution is seen on the initial engine-start event, with a large maximum around 15nm and a shoulder around 50nm. This is demonstrated in Figure 6.16a and Figure 6.16b.

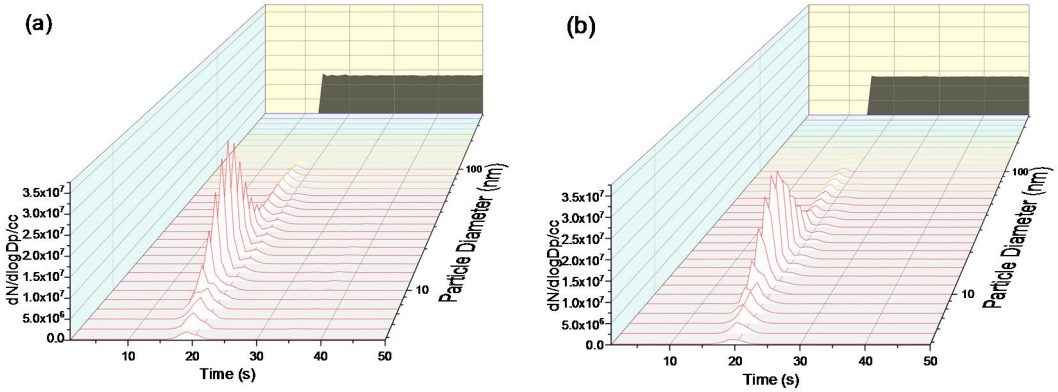

Figure 6.16 PN distribution over first 50s of cold start WLTC Tests 23 (a) and 26 (b). Engine speed is indicated on the back wall (at 10000x scale).

An important question for HEVs is whether the large spike in smaller particles seen for some tests during the initial engine-start event are occurring for subsequent stop-start events. An investigation into all engine-start/restart events during the test cycles showed that once the engine is hot, the nano-particle PN spike at the smallest diameters is not seen when the engine undergoes re-ignition. Two representative examples are given in Figure 6.17a and Figure 6.17b, each showing the first 800s of a cold start WLTC test. Notably, the 15nm diameter emissions spike observed on initial engine-start is not seen for subsequent engine-restart events. The PN size distribution is shifted to larger diameters, with a maximum at approximately 55nm. The smallest particles are likely to be unburnt fuel fractions arising from the inhomogeneous, incomplete combustion of rich air-fuel mixtures within the cold combustion chamber (Eastwood, 2008; Raza et al., 2018). After the initial start-up, any subsequent engine activity occurs within a hot combustion chamber so the fuel is fully vaporized. The fuel enrichment conditions on engine-restart can still lead to soot, which is generally of the larger sizes visible throughout the rest of the test (Eastwood, 2008).

It is worth noting that the volume concentration of these subsequent spikes is actually greater than the initial ignition event in these cases, though this is not always the case, as will be seen in Section 6.5. As far as the author is aware, no previous study has focused on the size distribution of engine restart events specifically. There is some similarity to the findings of Robinson and Holmén (2011), for overall size distribution having a maximum around 50nm, but the secondary maximum at 400nm found in the previous study was not seen at any point in the current testing. Robinson and Holmén (2011) stated that the engine restart events were the source of the approximate 50nm diameter particles, which is also the case currently. There was no transient PNSD data given in the previous paper – only average cycle distributions, which are shown in Figure 6.18 – and without this it is difficult to ascertain when these larger particles were emitted. They are likely due to particle growth via agglomeration, adsorption and condensation. It is possible that the primitive on-road PNSD methodology of the previous study allowed these reactions to occur between the tailpipe and sensor, which would also explain the lower overall PN values from the previous study. Alternatively, it is also possible that the equipment was adversely affected by the vibration of the vehicle in motion as it drove on real roads. Gu et al. (2012) and Costagliola et al. (2013) both studied the PN size distribution from PFI engines and saw similar distributions

to that presented for warm engine behaviour in Figure 6.17, supporting the currently presented findings over those of Robinson and Holmén (2011).

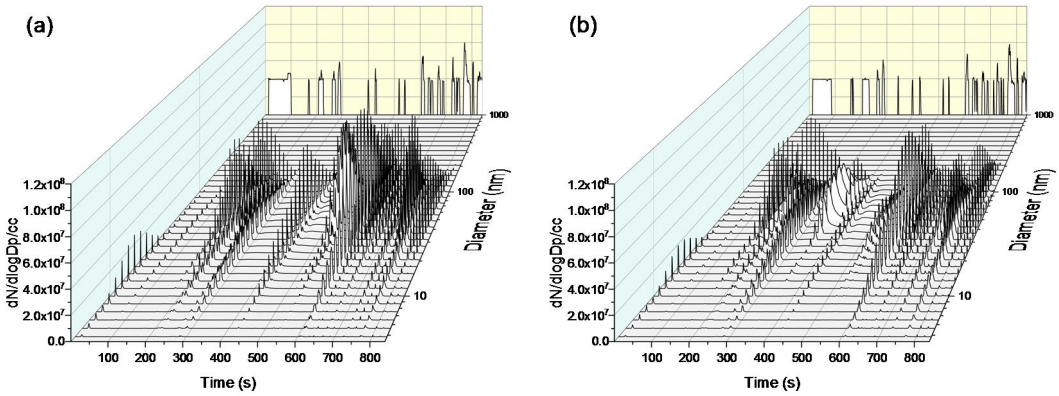

Figure 6.17 Size-distributed PN emission concentrations during the first 800s of cold start WLTC tests (a) Test 23 and (b) Test 26. RPM is indicated on the back wall (at 9x10^4 scale).

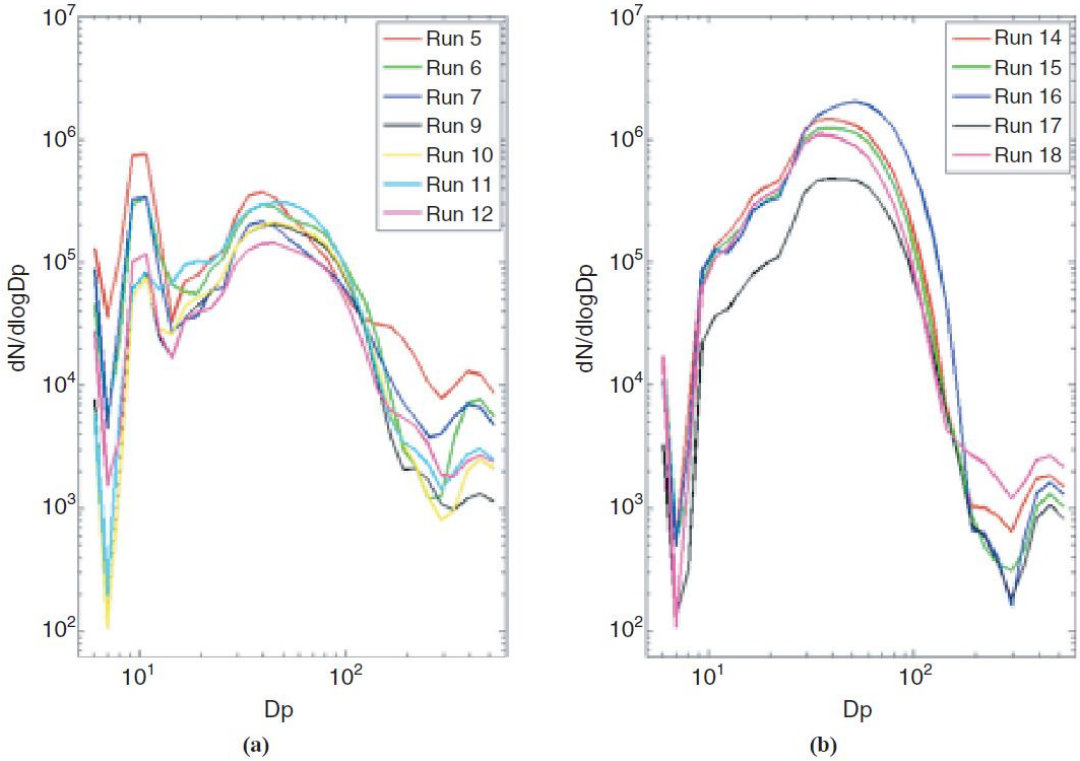

Figure 6.18 Run-by-run mean PN size distributions for (a) CV and (b) HEV, as presented by Robinson and Holmén (2011).

6.3.3 Unregulated pollutants

Figure 6.19a to Figure 6.19g display the tailpipe emissions of a range of non-regulated gaseous pollutants from the HEV using E10 fuel. The engine speed of a representative cold start WLTC test (Test 26) is plotted qualitatively in the

background of each. The results have been verified as representative of the pattern for each pollutant over the repeated cold start WLTC and RDE tests.

Figure 6.19b shows that the ammonia levels increase when the TWC lights off, which has been witnessed previously (Suarez-Bertoa and Astorga, 2016; Suarez-Bertoa et al., 2020). By comparison with Figure 6.19a, the levels of ammonia seem to increase under fuel enrichment conditions, in agreement with previous literature (Suarez-Bertoa and Astorga, 2016; Suarez-Bertoa et al., 2017). This finding is particularly concerning for HEVs, as the enrichment that occurs on engine restart may mean larger quantities of this pollutant are emitted into urban areas as more HEVs are adopted.

Figure 6.19c shows spikes in formaldehyde during engine-start and restart events, but these only last for 200-300s, abating as the vehicle warms up in agreement with Suarez-Bertoa et al. (2020). The emissions of methane in Figure 6.19d are also correlated with engine ignition events, and continue for a more prolonged period. These emissions abate after approximately 700s, opposing the trend presented in Suarez-Bertoa et al. (2020), whereby the highest emissions were seen under the highest speed driving sections later in the test. However, Suarez-Bertoa et al. (2020) referenced fuel enrichment as a causative factor, which has already been proven to occur more frequently during the lower speed stop-start driving than the high speed driving for the HEV results presented. This is not necessarily the case for the CVs of the previous study, hence the difference.

Figure 6.19d demonstrates the tendency for acetylene to only be emitted during the initial (cold start) engine-ignition event, with no other emissions visible thereafter. Ethylene in Figure 6.19f shows similar behaviour, but with small events possible for subsequent re-ignitions during the cold start period. In Figure 6.19g, nitrous oxide shows emissions during engine-restart events only for the first 200-300s, with no emissions visible after the end of cold start, in agreement with Suarez-Bertoa et al. (2020).

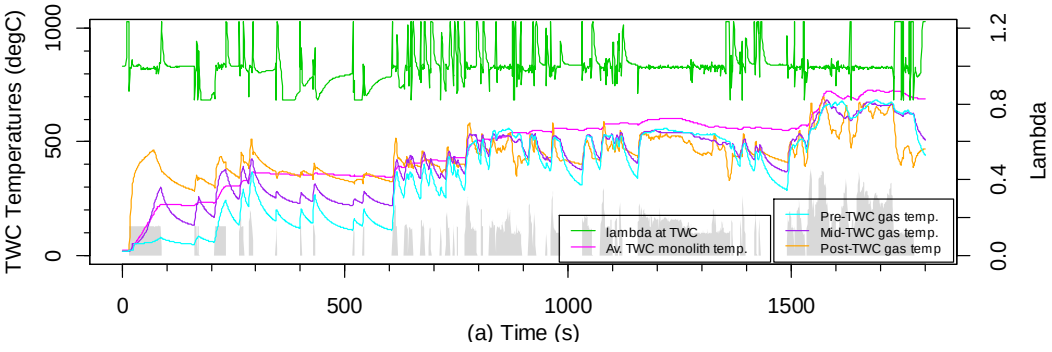

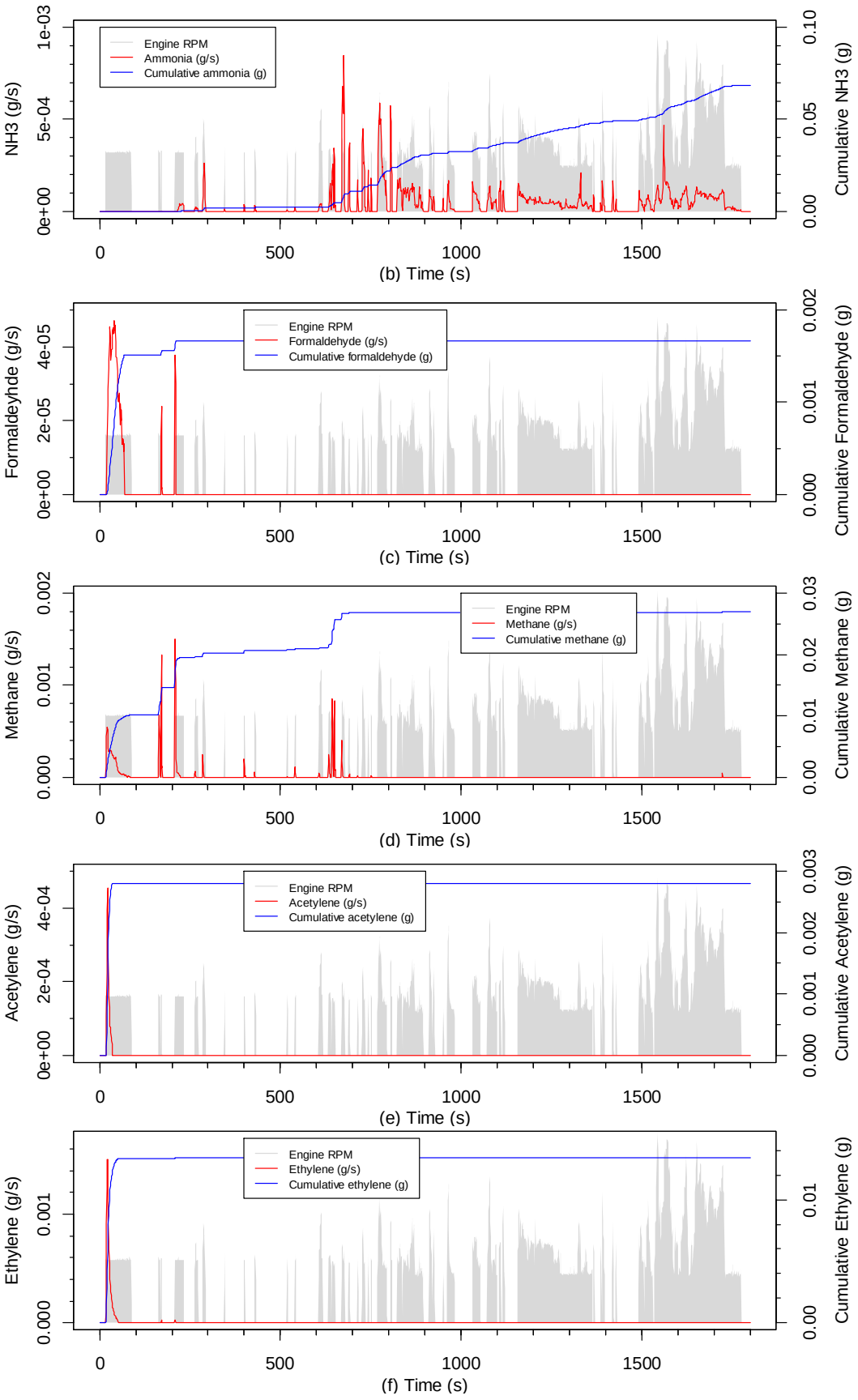
Engine RPM
Ammonia (g/s)
Cumulative ammonia (g)
NH3 (g/s)
Cumulative NH3 (g)
(b) Time (s)
Engine RPM
Formaldehyde (g/s)
Cumulative formaldehyde (g)
Formaldehyde (g/s)
Cumulative Formaldehyde (g)
(c) Time (s)
Engine RPM
Methane (g/s)
Cumulative methane (g)
Methane (g/s)
Cumulative Methane (g)
(d) Time (s)
Engine RPM
Acetylene (g/s)
Cumulative acetylene (g)
Acetylene (g/s)
Cumulative Acetylene (g)
(e) Time (s)
Engine RPM
Ethylene (g/s)
Cumulative ethylene (g)
Ethylene (g/s)
Cumulative Ethylene (g)
(f) Time (s)

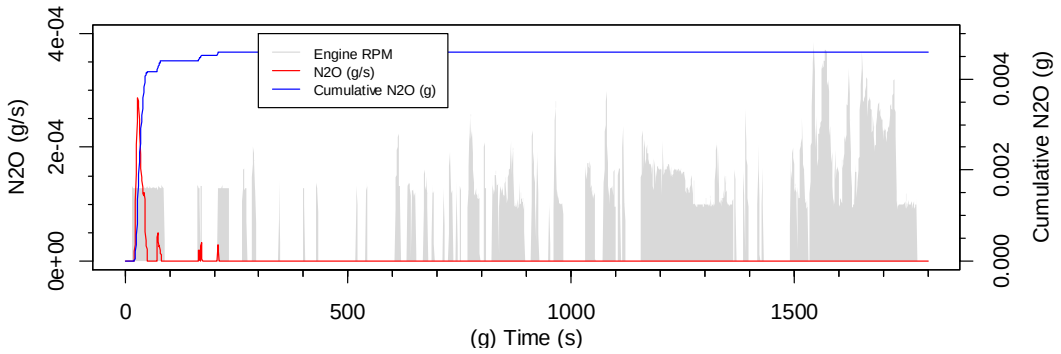

Figure 6.19 Transient and cumulative emissions of ammonia, formaldehyde, methane, acetylene, ethylene and N_2O from a representative WLTC cycle.

The study of further regulated pollutants was possible from E10-fuelled cold start RDE testing utilising an FTIR for mobile tailpipe sampling. Figure 6.20a to Figure 6.20f show representative example plots, with engine speed indicated qualitatively in grey. There is an initial spike on engine cold start, but then no further emissions thereafter of ethane, propane, hexane, benzene, acetaldehyde or 1,3-butadiene. The emissions of SO_2, ethanol and acetic acid were also measured, but values were too low to be detected in either the WLTC or RDE tests. Engine speed is indicated qualitatively in grey on each graph. Suarez-Bertoa and Astorga (2016) reported ethanol and acetaldehyde emissions throughout the cold start period of their cold start E10-fuelled tests, so the work presented currently appears to have lower levels of these pollutants. A possible reason is a lower detection limit of the portable FTIR utilised in the current study compared to a lab FTIR.

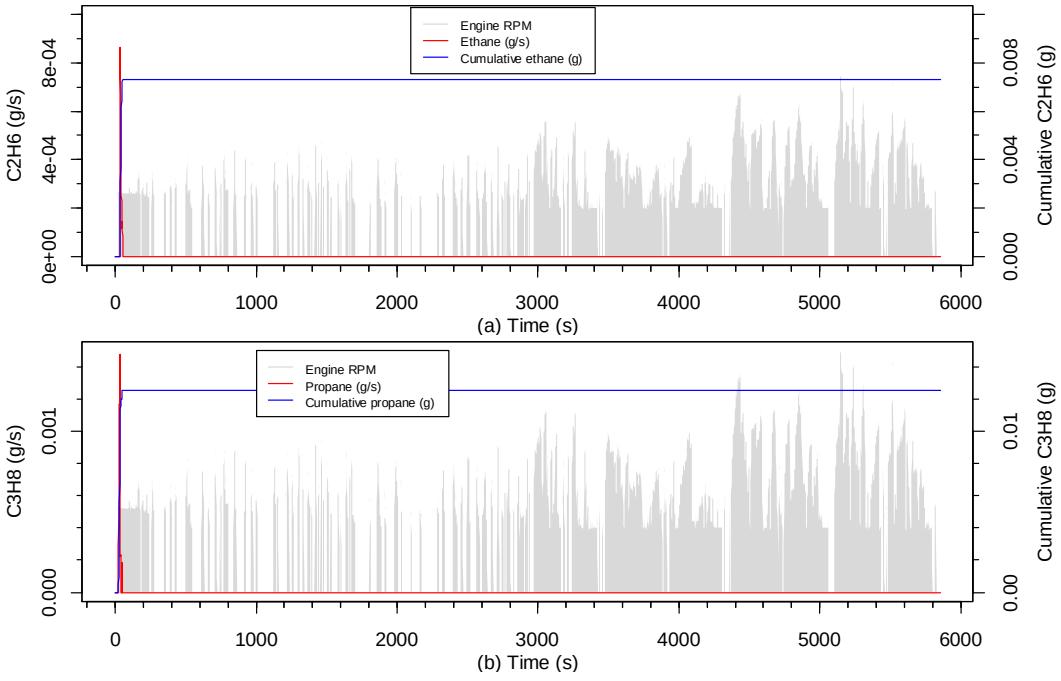

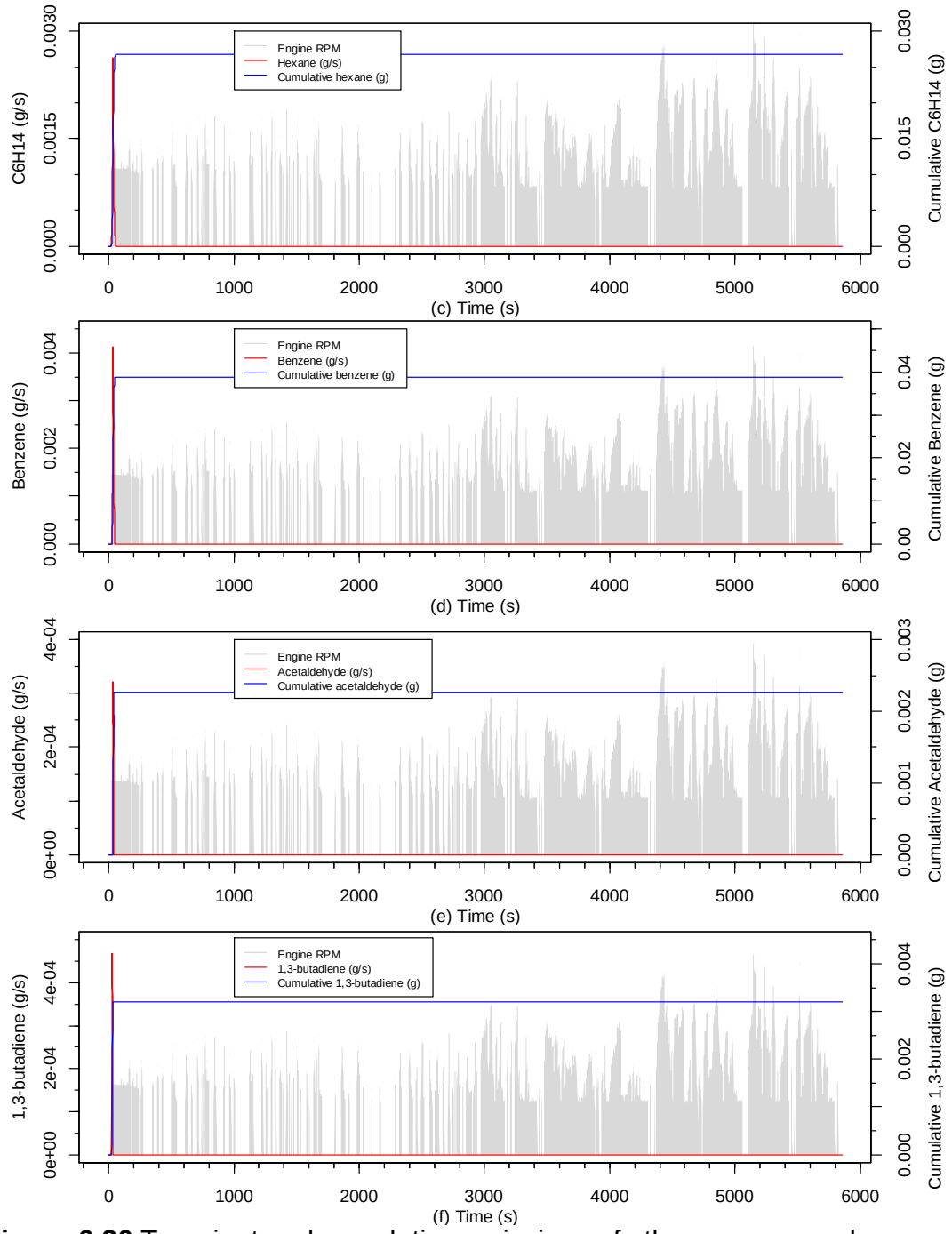

Figure 6.20 Transient and cumulative emissions of ethane, propane, hexane, benzene, acetaldehyde and 1,3-butadiene from a representative RDE test cycle.

6.4 Effects of initial battery SOC

In order to assess the impact of SOC on regulated emissions, the same shortened RDE-style drive cycle was repeated on a chassis dynamometer with 3 different initial SOC values (52.2%, 60.0% and 67.8%) each for 3 different fuels (E0, E10, B10). Though all other parameters were kept as

constant as possible, it should be noted that the initial system temperature was not controlled to a high degree. This means that differences in initial system temperature could have some limited effect on the results (the mean initial engine coolant temperature was 51.1°C with a standard deviation of 7.7°C across the 9 tests; see Chapter 3 Section 3.4.4.3 for more details). Figure 6.21 shows that the different initial SOC values converge over phase 1, such that only phase 1 of the test cycle is substantially affected by differences in initial SOC. In the following analysis, only phase 1 of the drive cycle will be studied. It should be noted that differences in net change of SOC were not accounted for in the subsequent study of CO_2.

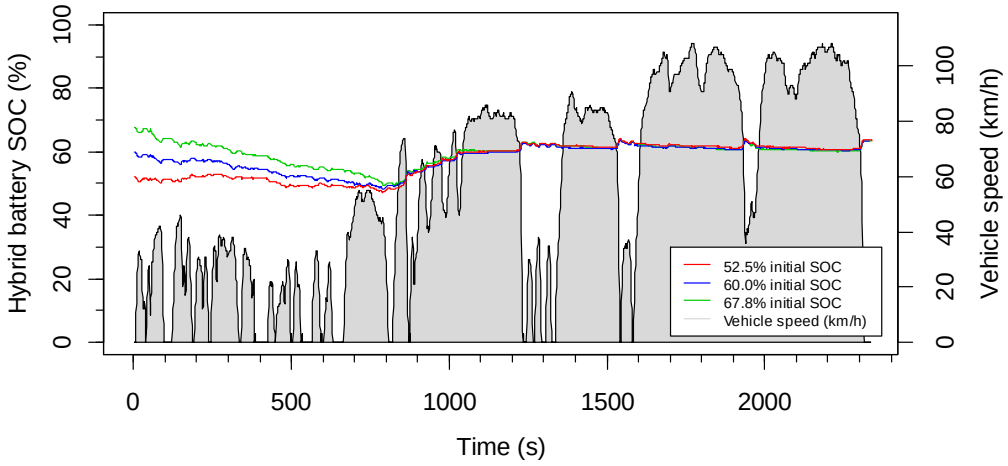

Figure 6.21 The evolution of SOC over a test with different initial SOCs (52.25, 60%, 67.8%). The vehicle speed (km/h) is also given.

In addition to these repeated test cycles, data from 17 repeated cold start RDE tests, each of different initial SOC, was used to investigate the effects of initial SOC on engine behaviour and emissions. The majority of behavioural difference due to differing initial SOC was deemed to occur during the first 300s for these on-road tests, so in subsequent analysis, only this period of the drive cycle was used.

6.4.1 Engine and TWC behaviour

Figure 6.22a, Figure 6.22b, and Figure 6.22c display the engine speeds associated with phase 1 of the chassis dynamometer shortened RDE tests for initial SOCs of 52.2%, 60% and 67.8% respectively. Engine behaviours are similar across tests, though the engine is mildly more active for the lower initial SOC test, in agreement with Cubito et al. (2017).

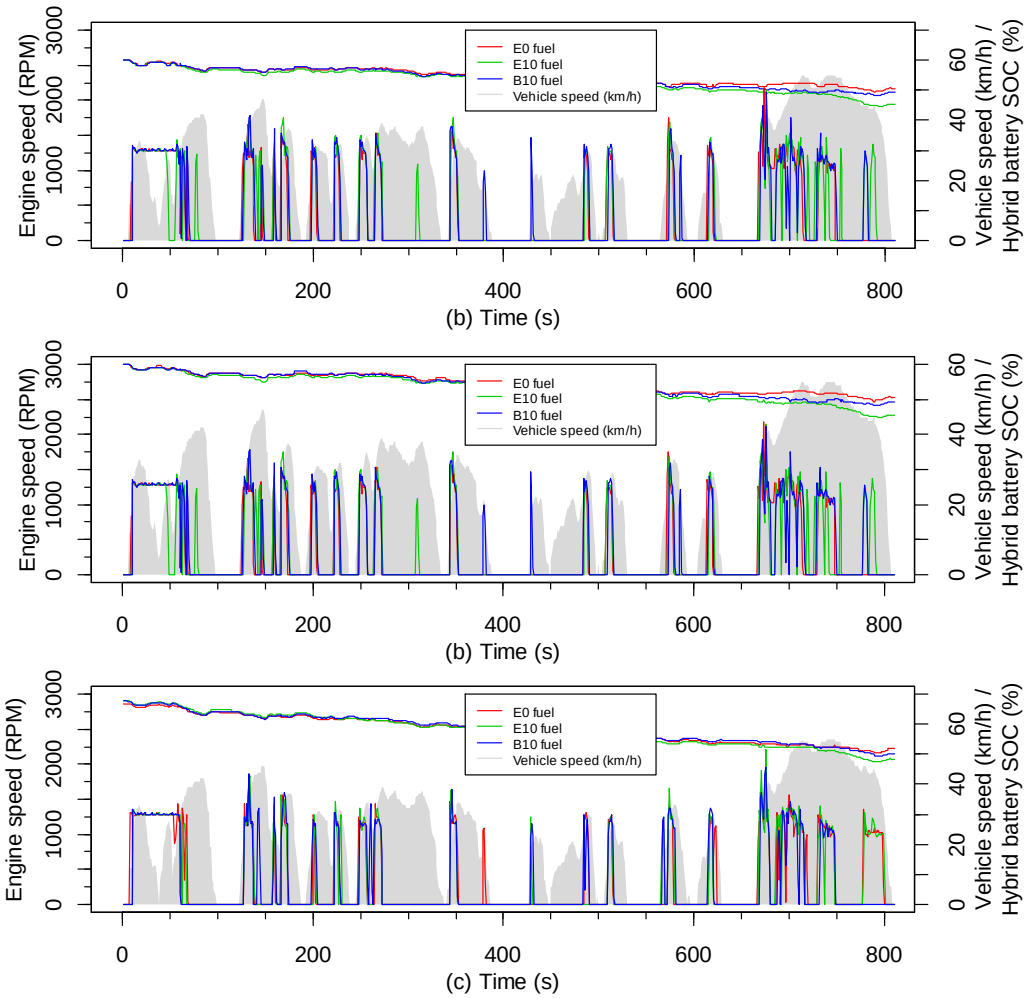

Figure 6.22 Engine speeds and battery SOC for the three tests at (a) 52.2%, (b) 60.0% and (c) 67.8% initial battery SOC value respectively, across three fuel types.

As the speed traces are the same for all of the shortened RDE tests, this set was deemed the most suitable for a direct comparison of engine activity with battery SOC. Figure 6.23a shows that the lower the battery SOC, the more frequently the engine transitions between on and off, while Figure 6.23b shows that the lower the battery SOC the less time the engine is turned off. The first point is in disagreement with Cubito et al. (2017), who reports similar stop-start behaviour for high and low initial SOCs, while the second point agrees with Cubito et al. (2017), and with Duarte et al. (2014). Given that Cubito et al. (2017) studies a different range of SOCs (40% and 56%) and the results are considered for a whole cold start WLTC cycle, some difference is expected. Figure 6.24a shows that the time taken for the TWC to light off decreases for tests commencing from lower battery SOC, because of the increase in engine activity.

Little correlation was seen between the initial SOC and either the time spent with the engine off, or the number of engine deactivations for the on-road RDE tests. This was the case even when these two values were normalised by the time spent stationary and the number of vehicle stops during each test; the real-world conditions are too variable for these relationships to be statistically significant. Similarly, the time taken for the engine coolant temperature to reach 70°C was also quite scattered, but did show a positive correlation that plateaued toward a maximum time at the highest initial SOC values. Figure 6.24b, however, shows that the time for the catalyst to reach 300°C does correlate, with low initial SOCs having faster heating times.

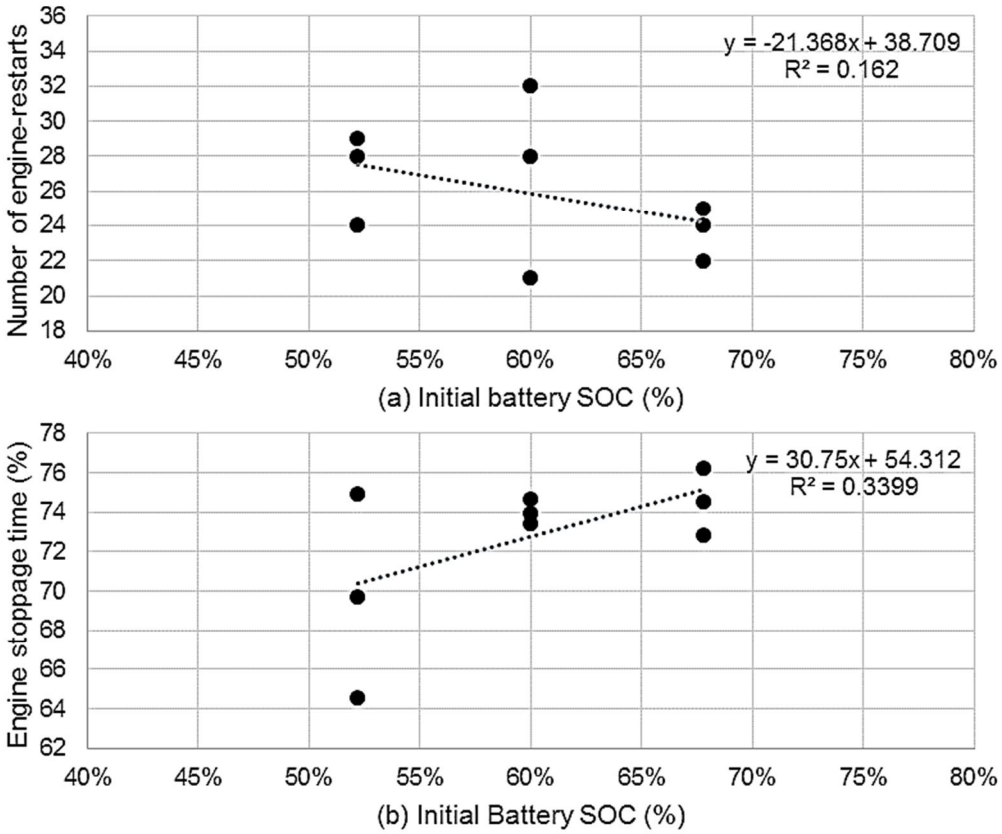

Figure 6.23 Percentage time with the engine deactivated, and number of individual engine-restart events, across phase 1 of the shortened RDE-style test, against initial battery SOC.

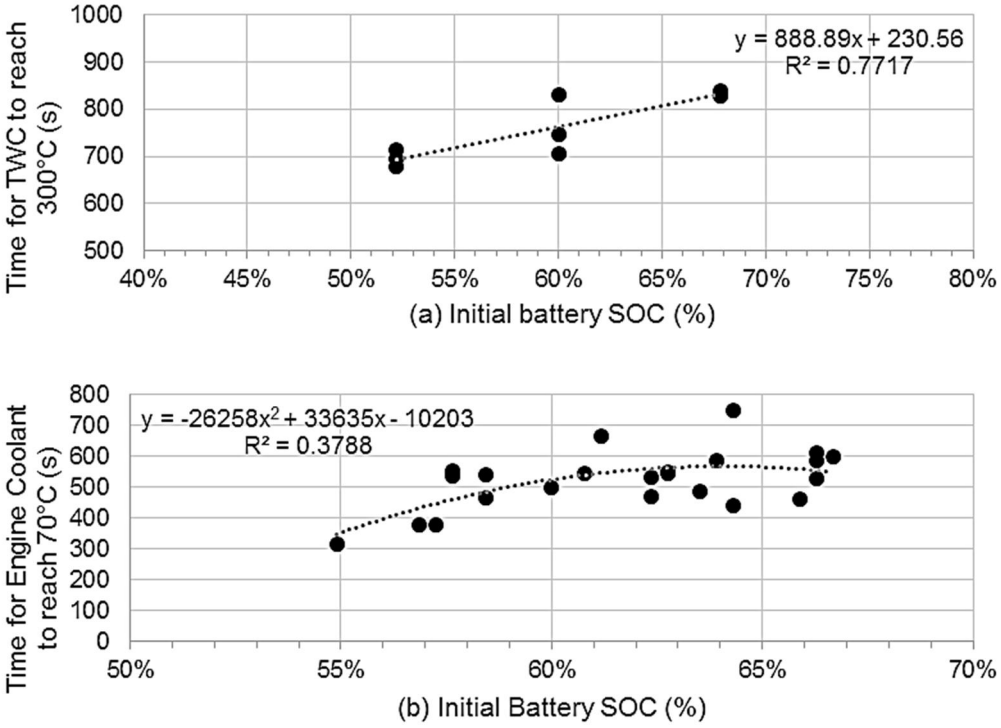

Figure 6.24 (a) Time for TWC to reach 300°C under shortened RDE-style chassis dynamometer tests, and (b) time for engine coolant to reach 70°C under on-road RDE tests, plotted against initial battery SOC.

6.4.2 Emission behaviour

The emission results for phase 1 of the shortened RDE drive cycle are given in Figure 6.25a to Figure 6.25e. For CO_2, the higher the initial SOC value, the lower the CO_2 output because the vehicle is able to rely more heavily on the motor rather than the ICE. This agrees with the results of Fontaras et al. (2008), Loiselle et al. (2010), Favre et al. (2013), Duarte et al. (2014) and Cubito et al. (2017). The results of Duarte et al. (2014) are displayed in Figure 6.27a. The tests with 60.0% initial SOC appear to give the lowest emissions of THC, NO_x and CO, though the standard error uncertainties are large. The trend is likely to be because 60% is approximately the median battery SOC possible for this vehicle, meaning that the vehicle strikes the most optimum balance between TWC light-off time and number of engine-ignition events (Duarte et al., 2014). The results for PN show increased emissions, which are due to the increased number of engine ignition events that occur under low HEV battery SOC, with PN not affected by TWC light-off times. The uncertainties are large for all pollutant species, and this is likely to be due to the low dependence of pollutant emissions on initial SOC, and the fact that pollutants are more affected by initial system temperature, which was not kept

constant (see Chapter 3 Section 3.4.4.3 for details). Previous studies have also failed to find strong correlations of pollutant emissions with SOC (Fontaras et al., 2008; Loiselle et al., 2010; Favre et al., 2013). Duarte et al. (2014) found some indication that CO emissions decreased with SOC, but results for NOx were mixed, as shown in Figure 6.27b and Figure 6.27c respectively.

Figure 6.26a to Figure 6.26d display pollutant emission factors over the first 300s of repeated cold start RDE tests. In Figure 6.26a there is a correlation of decreasing CO_2 emissions for greater initial SOC, while Figure 6.26b indicates a possible minimum in CO occurring around 60% initial SOC. These correlations are both in agreement with the findings from the chassis dynamometer tests in Figure 6.26a and Figure 6.25b. The NO_x and PN results are fairly scattered, which is in agreement with Fontaras et al. (2008) and Favre et al. (2013). Despite all tests commencing from cold start, there are many other changing variables affecting the levels of emissions from these on-road RDE tests, which are having a greater effect than the initial SOC.

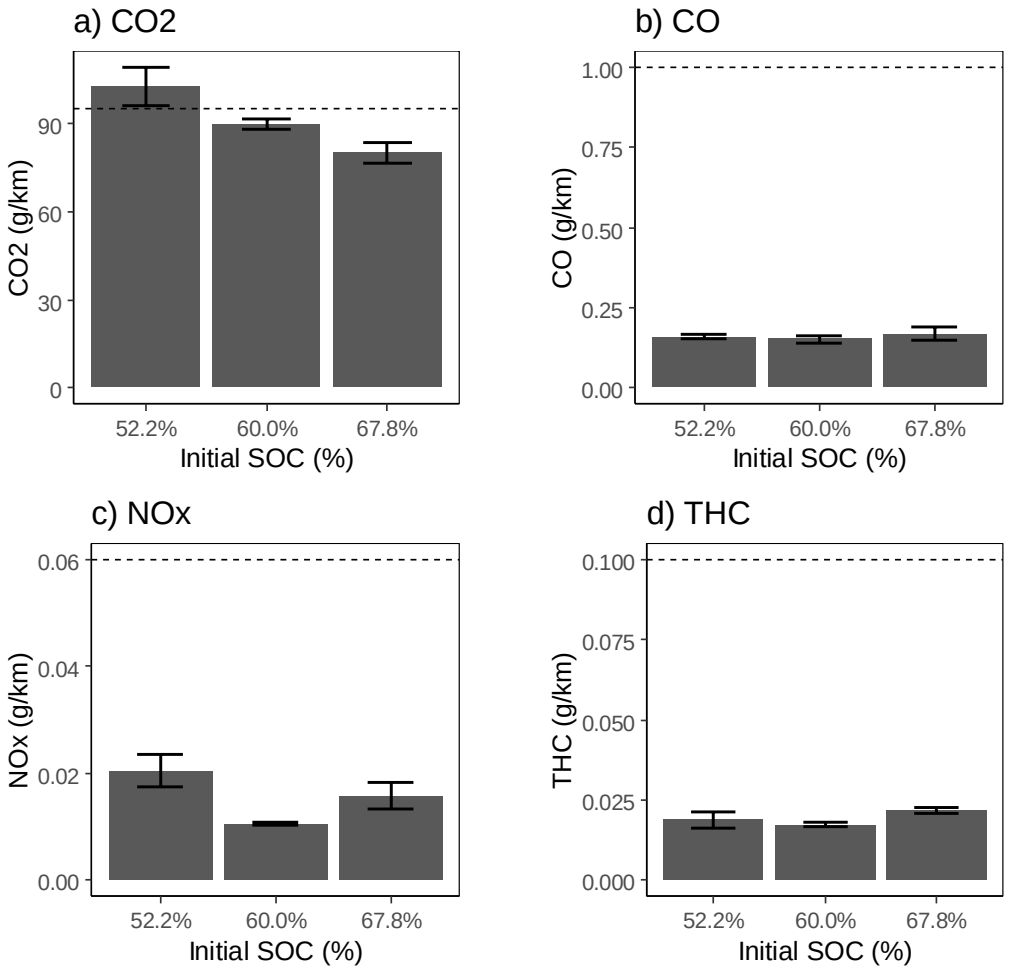

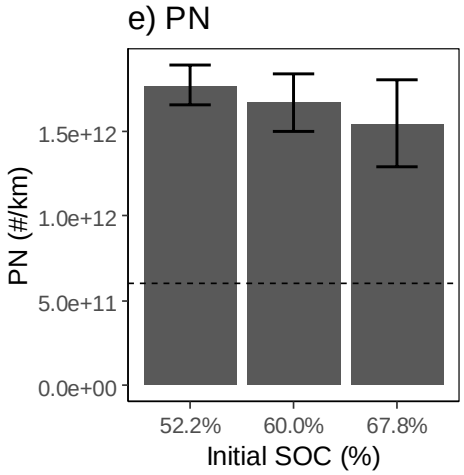

Figure 6.25 Average (a) CO_2, (b) CO, (c) NO_x, (d) THC and (e) PN distributions across replicate shortened RDE-style chassis dynamometer tests with initial battery SOC values of 52.2%, 60.0% and 67.8%.

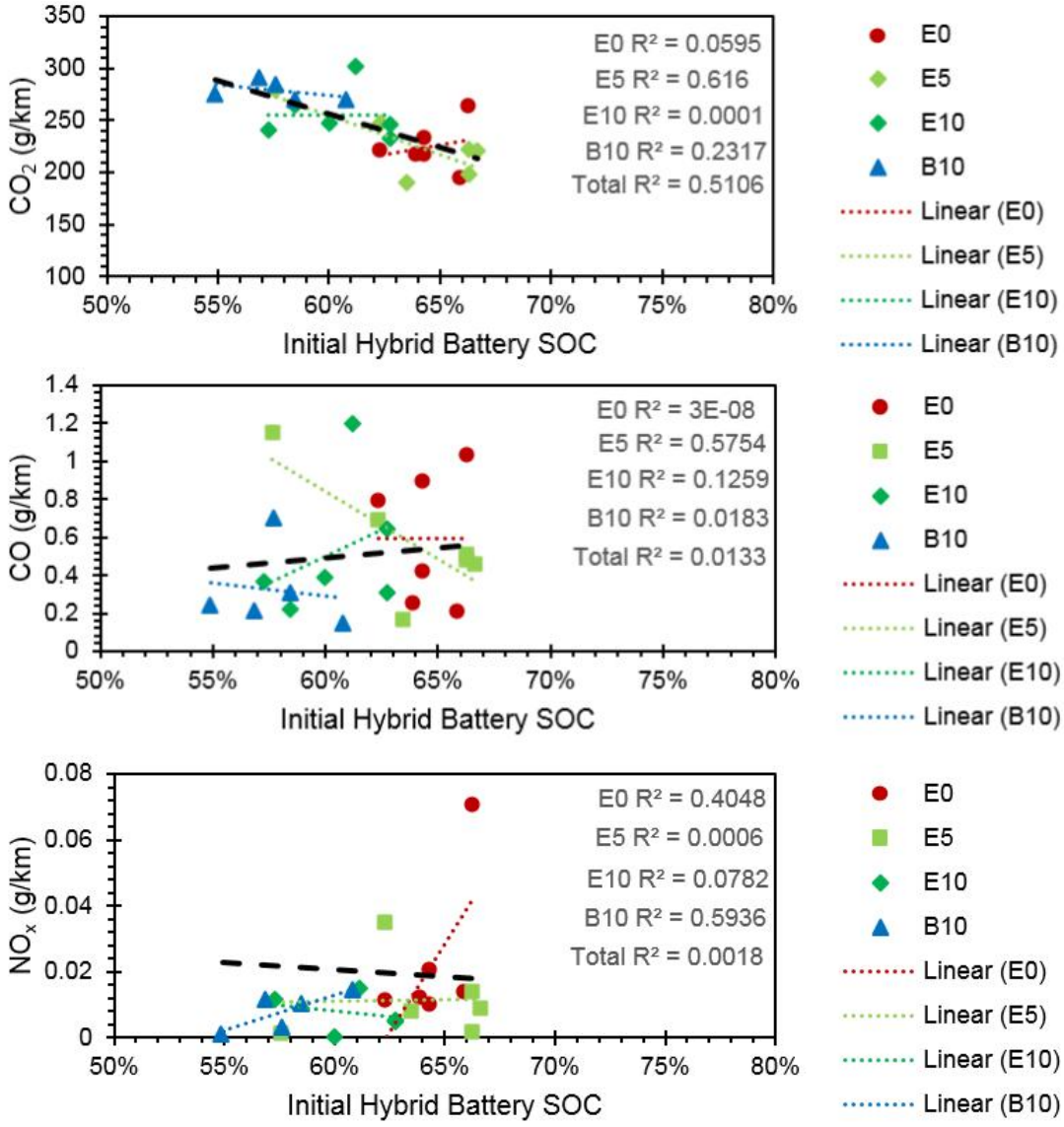

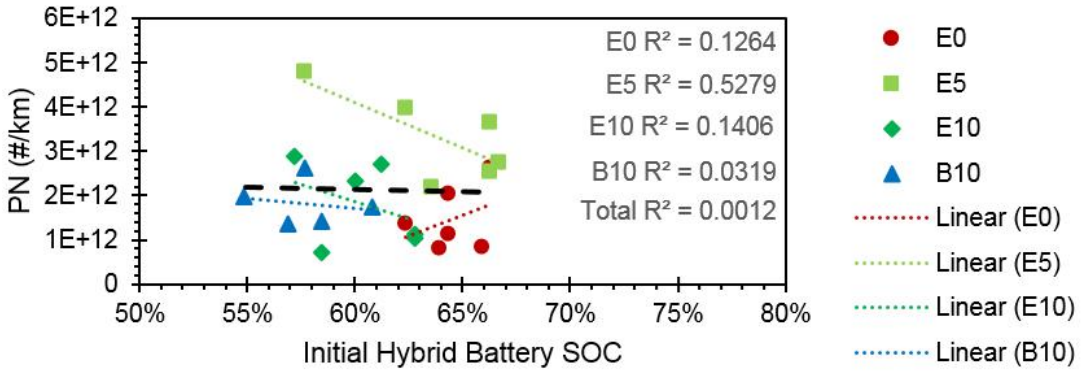

Figure 6.26 Average (a) CO_2, (b) CO, (c) NO_x and (d) PN emission factors across the first 300s of cold start RDE tests with different initial battery SOC values of 52.2%, 60.0% and 67.8%. A line of best fit is drawn for each fuel type individually, with a black line of best fit for the data as a whole.

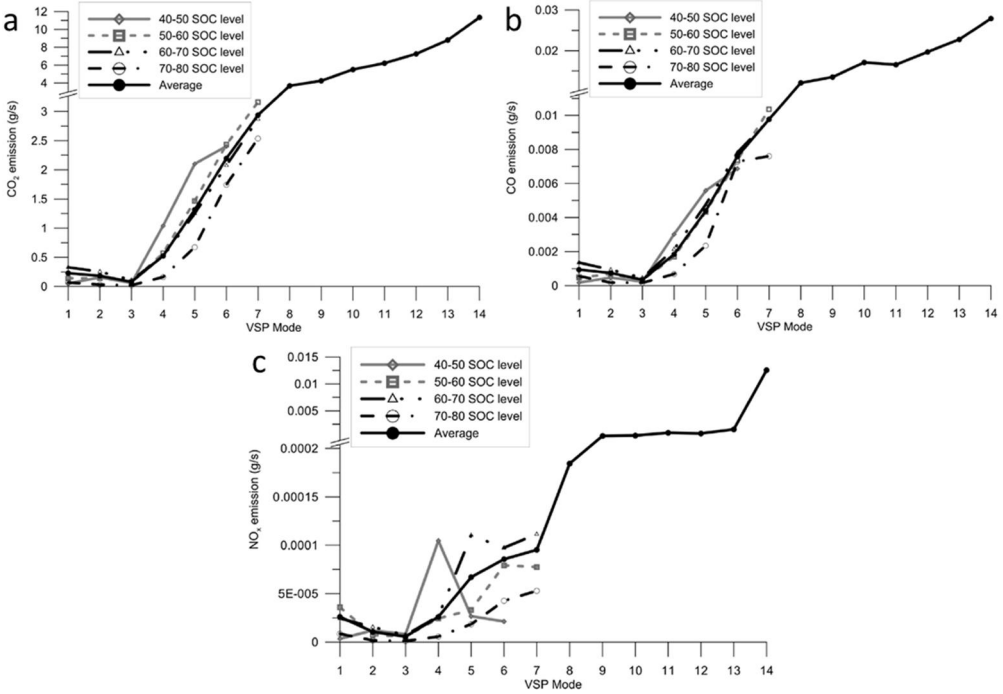

Figure 6.27 CO_2, CO and NO_x emission rates for different SOC values, presented by Duarte et al. (2014).

6.4.2.1 PN size distribution

As discussed in Chapter 4, the engine behaviour over a test can have a large impact on the resultant PN size distribution. During engine restarts, very large transient spikes in PN sized around 50nm occur. During steady engine-on operation, however, lower magnitude constant PN emissions around 15nm and 100-150 nm occur. The interplay between these very different types of particulate emissions dictates the overall PN size distribution. Figure 6.28a, Figure 6.28b and Figure 6.28c give the average distance-specific PN size

distributions from phase 1 of the RDE style test cycle, separated into the three initial SOC values (52.2%, 60% and 67.8% respectively). The lowest battery SOC value gave the broadest full width at half maximum (FWHM), and more prominent secondary maxima/shoulders at 10-15nm and 100-110nm respectively. This is because the engine engages more constant engine-on behaviour under lower SOCs (as explained Chapter 4 Section 4.2.2.1). To the author's best knowledge, no previous work has studied the initial battery SOC effect on PN size distribution.

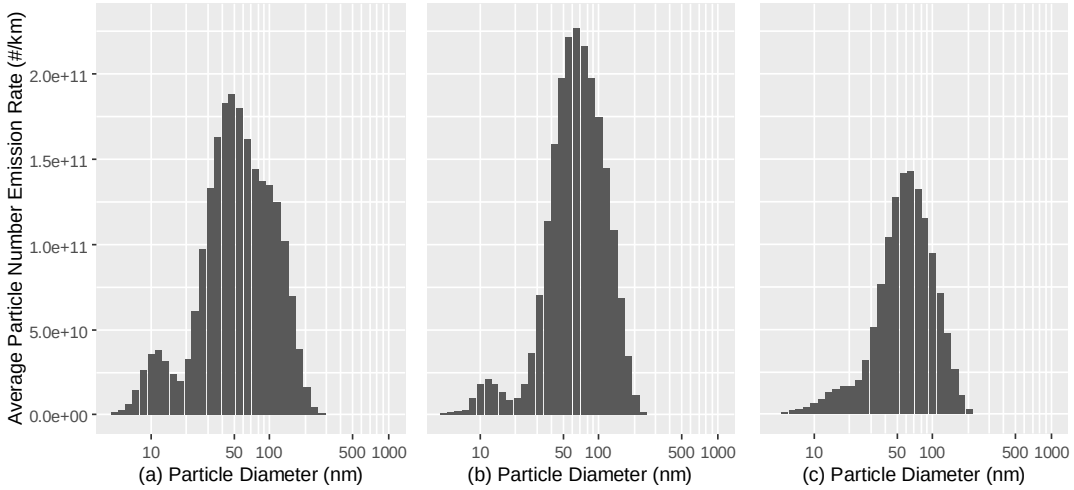

Figure 6.28 Average distance-specific PNSD for phase 1 repeats of the RDE-style cycle with initial SOC values of 52.2%, 60.0% and 67.8% respectively.

6.5 Repeatability of HEV tests

In order to study the repeatability of HEV tests, the spread across a set of 3 identical tests was investigated (named Tests 20, 23 and 26). The same HEV, with the same initial battery SOC (67.8%), with the same fuel (E10) soaked overnight at the same temperature (23°C), underwent the same WLTC drive cycle three times (see Chapter 3 Section 3.4 for further details). The similarities and differences in engine behaviour and emissions will be discussed in this section.

The modal and cumulative emission results are compared between tests for CO_2, THC, CO, NO_x and PN individually in Figure 6.29a to Figure 6.29e respectively. The CO_2 values show a strong correlation, though there are some differences in the initial few hundred seconds (discussed later). All other pollutants show disparity between the three tests, with Test 20 having the greatest emissions of THC, CO and NO_x. Tests 23 and 26 agree fairly well for

these pollutants, with Test 26 continually being slightly higher (closest agreement for THC, followed by NO_x, then CO). The PN and PM results also show Test 20 as having the greatest emissions, but this is then followed, in almost equal increments, by Test 23 and then Test 26. The possible causes for these differences are investigated in the following paragraphs.

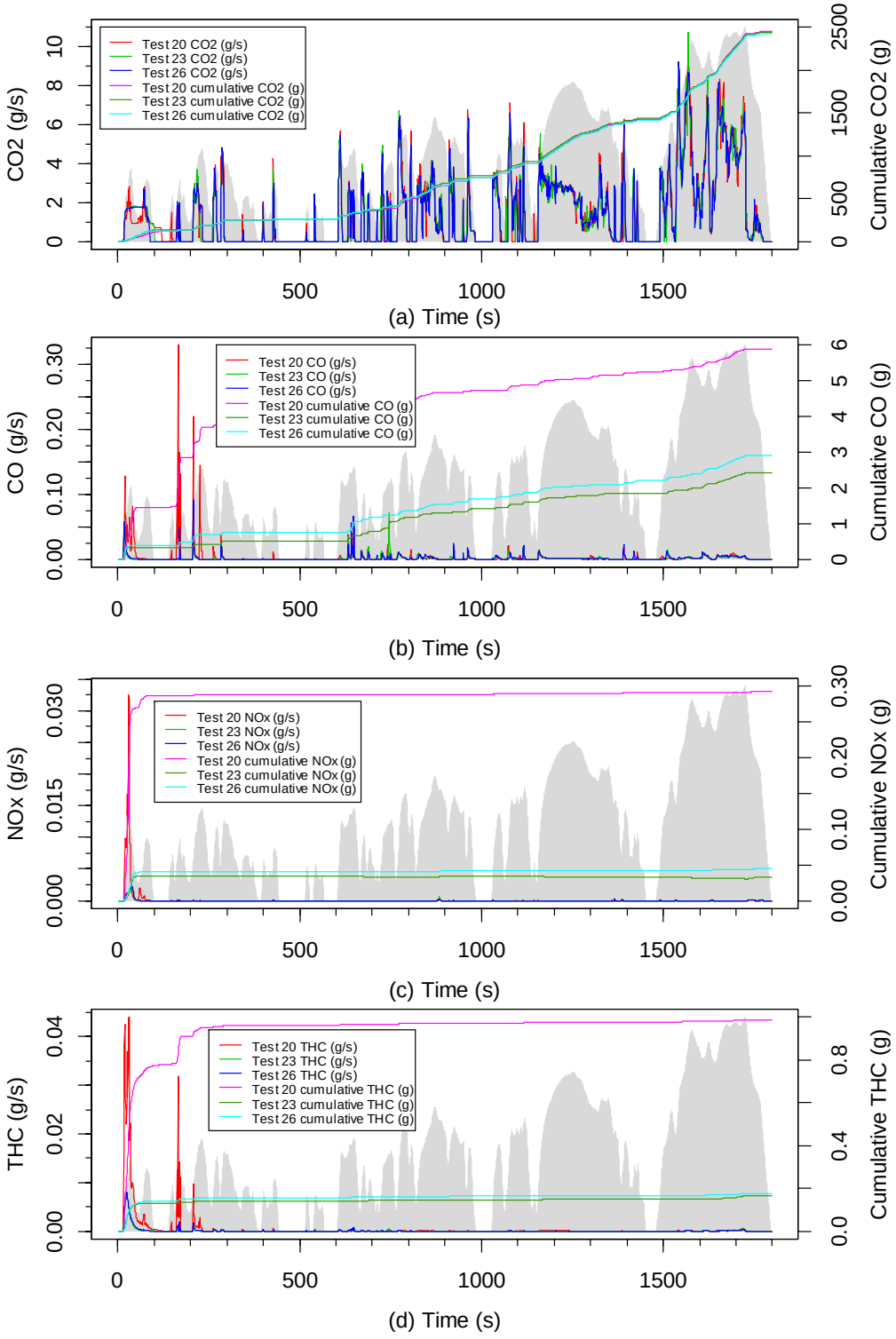

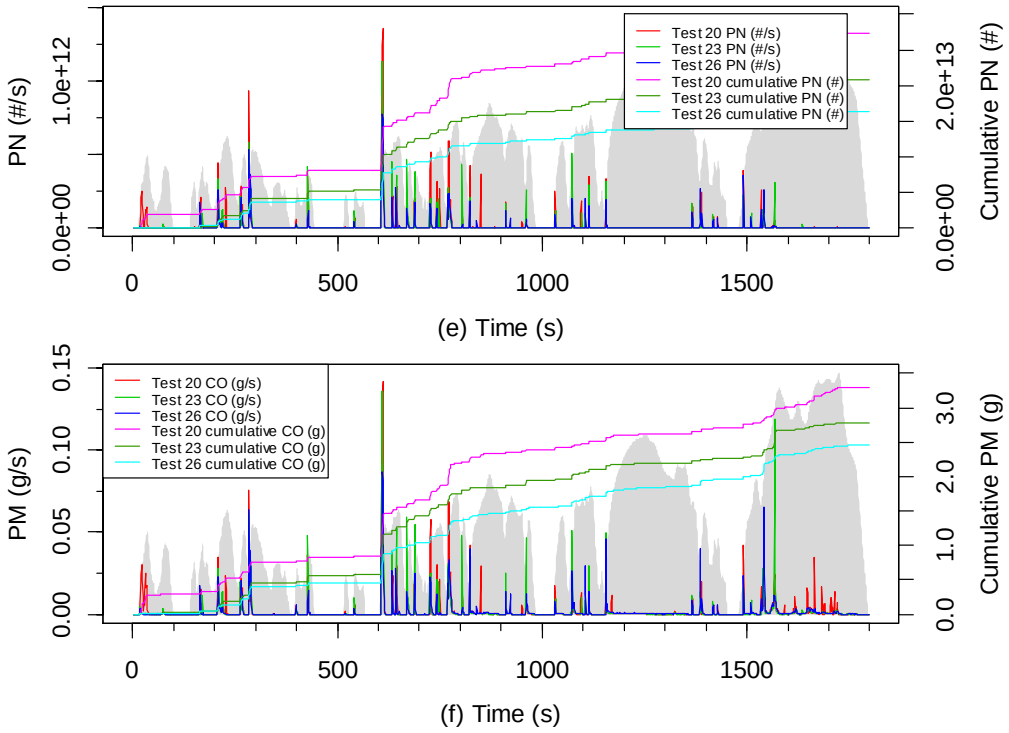

Figure 6.29 Modal and cumulative CO_2, CO, NO_x, THC, PN and PM results from three repeats of the WLTC test cycle under identical conditioning.

The engine speeds across all three tests in Figure 6.30a indicate that, although for the most part the engine turned on and off at the same moments during the test, there were some differences in engine behaviour during the test. These are mostly found during the first 250s of the drive, which is detailed in Figure 6.30b. The engine initiates at the same moment for all three tests, but then turns off at a different time for each test. Test 20, for which the engine remains engaged for longest, also reinitiates for a short period soon after, while the other two tests do not. The majority of difference in regulated emissions occurs during the initial 250s of the drive. There is clearly some difference that is altering the strategy of the vehicle between tests.

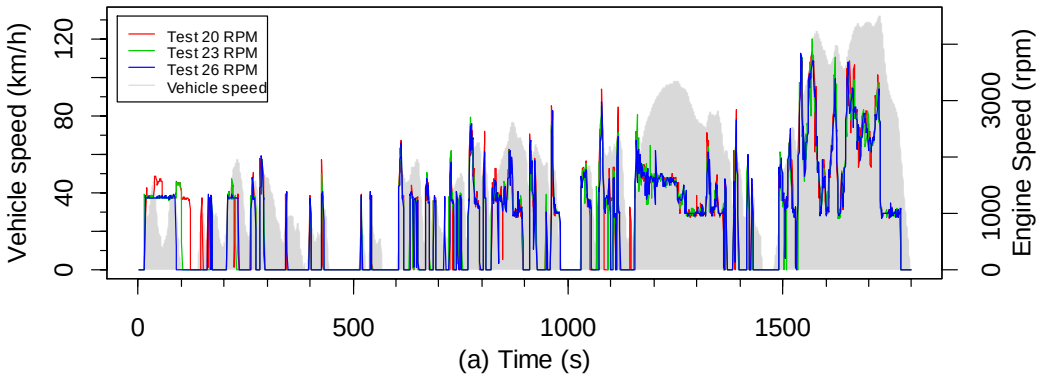

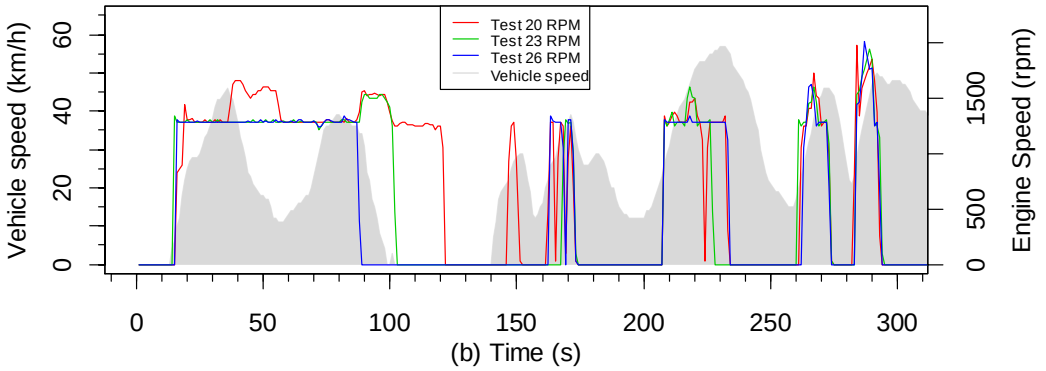

Figure 6.30 Engine speeds of Tests 20, 23, and 26 with vehicle speed (grey). (a) Full test profiles and (b) first 300s of the tests.

Figure 6.31 and Figure 6.32 display the battery SOC, engine coolant temperature and catalyst temperatures across the duration of the tests. The initial SOC values are identical, while the initial engine coolant and catalyst temperatures are each within 1°C difference across tests. The SOCs and temperatures remain just as close to each other throughout the duration of the tests. This suggests that neither SOC nor temperature is the cause for these differences in engine behaviour seen.

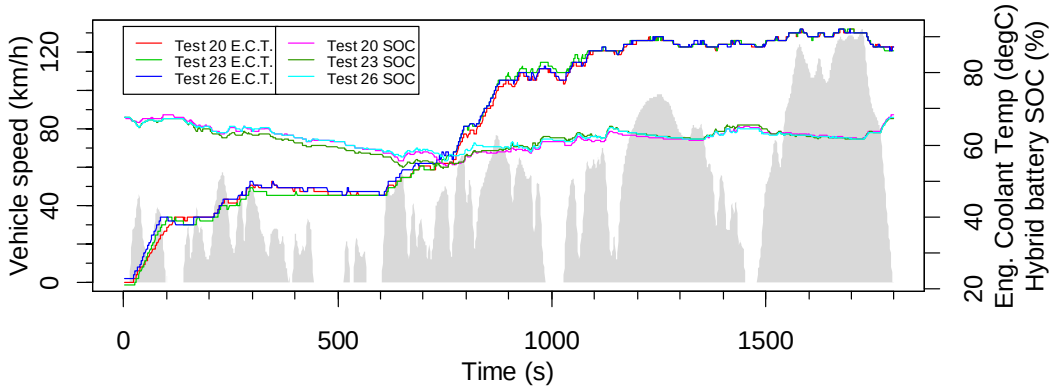

Figure 6.31 Engine coolant temperatures and hybrid battery SOC values of Tests 20, 23, and 26, alongside vehicle speed on the primary axis.

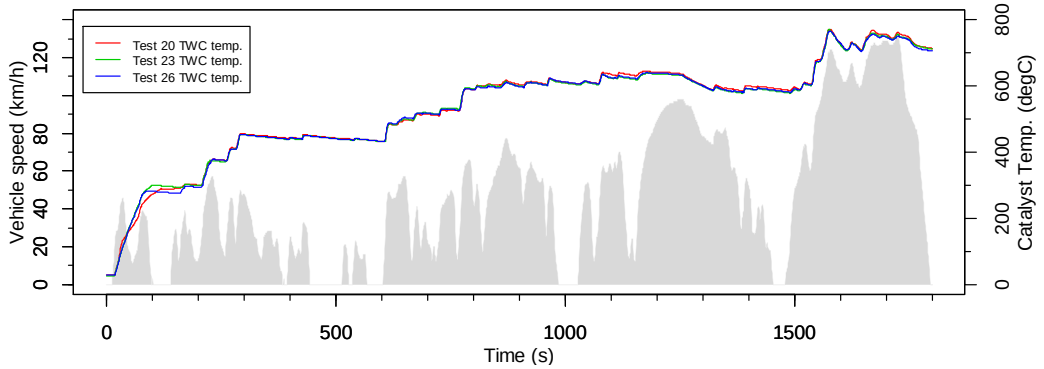

Figure 6.32 Catalyst temperature across Tests 20, 23, and 26, alongside vehicle speed on the primary axis.

Figure 6.33a displays the first 300s of lambda between the two TWC blocks for the three tests, along with corresponding engine speeds on a backdrop of vehicle speed (not associated with any axis). Clearly visible are dips into rich lambda values when the engine is turning on for all three tests. Figure 6.33b to Figure 6.33d show emissions of THC, CO and NO_x respectively. On Test 20 a particularly large spike in THC and CO occurs at exactly the same time as a prolonged period of lambda instability with many excursions into the rich zone, indicating that this is the cause for the emissions. Meanwhile, some NO_x emissions for Test 20 (after the 50s whereby the catalyst was shown to become effective in Section 6.2) are accompanied by an excursion into the lean combustion lambda values, and therefore could be the reason for these NO_x emissions. The same set of behaviours are visible for Tests 23 and 26, although to a lesser degree. The poor control of stoichiometric combustion that this vehicle displays for Test 20 has been shown as a likely reason for the high emissions seen for this test.

During engine cold start, similar bimodal PN size distributions are seen on the initial engine-start event, with maxima at 20 and 50 nm. As previously discussed, the magnitude of this initial PN varies from test to test, despite all measurable parameters being equal between tests. These results are shown in Figure 6.34a and Figure 6.34b.

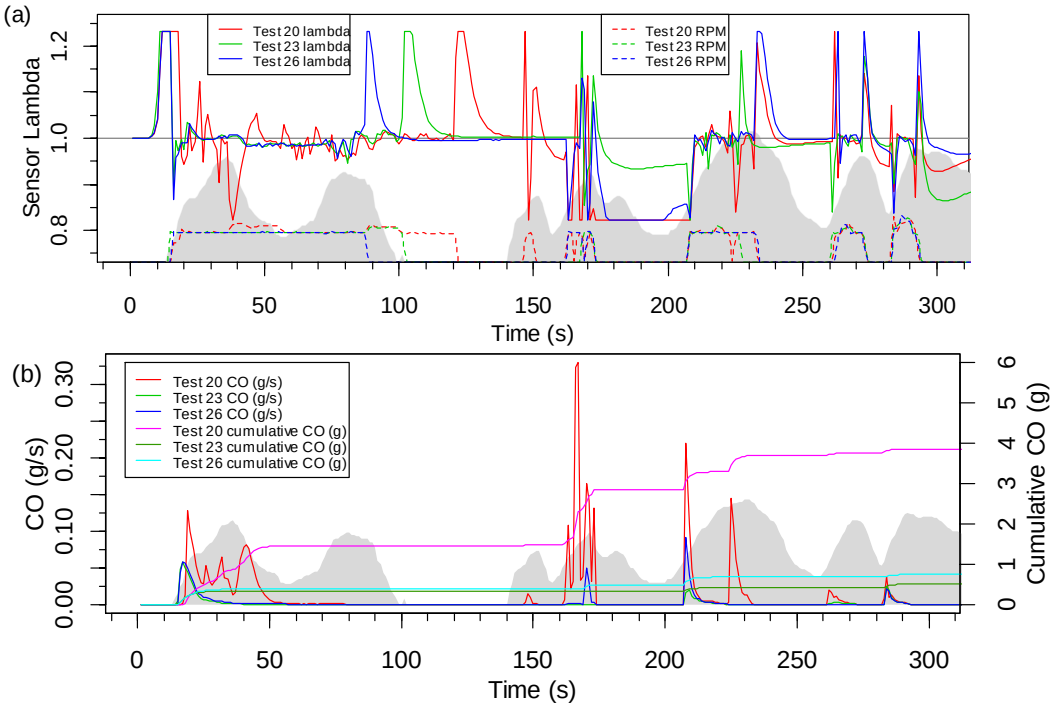

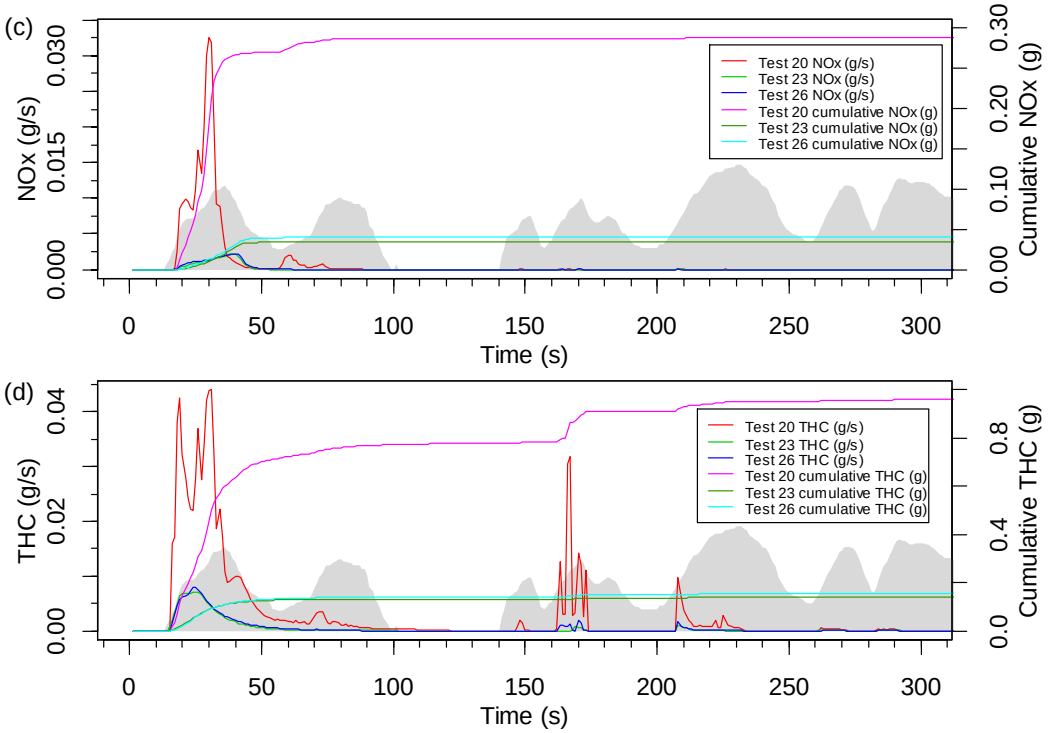

Figure 6.33 Lambda values, THC, CO and NO_x for the period from 0-300s.

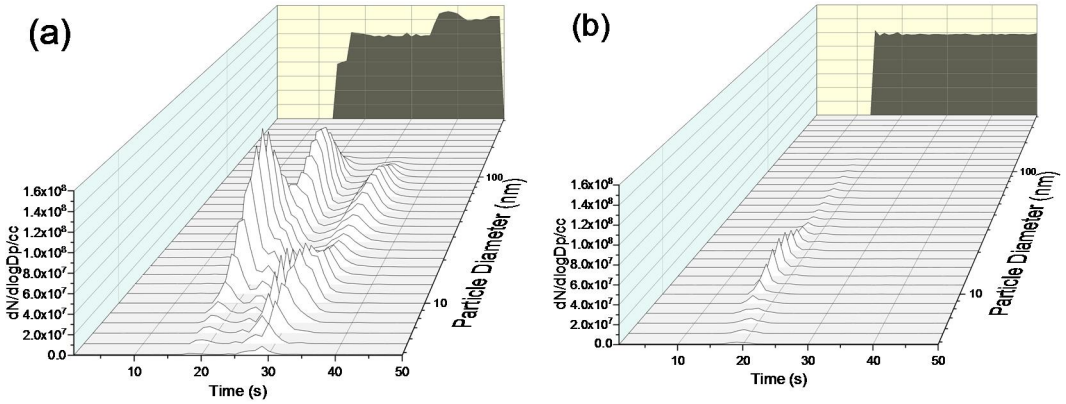

Figure 6.34 First 50s of cold start WLTC (a) Test 20, (b) Test 23. Engine speed is indicated qualitatively on the back wall of each figure.

Figure 6.35a to Figure 6.35f show a range of ECU information for the two tests discussed in Figure 6.34 above. These figures show in more detail that the differences in behaviours are at least partly due to the speed with which the engine fuelling becomes stoichiometric. The reason for the lambda instability in the first test is unclear. In the tests displayed, the lambda instability coincides with some different battery behaviour; the initial battery SOC was constant across all tests, but then drops for Test 20 more rapidly than for other tests. However, this behaviour is not repeated for another high emissions test in the set. One trend across all relevant tests is the fact that those with larger emissions do not lose as much battery SOC in the first 35s as those without,

indicating that the engine is working harder during this time. This conclusion is supported by the fact that the load is higher. The higher load on the cold engine could be the cause of the lambda instability, which is likely leading to the greater pollutant emissions.

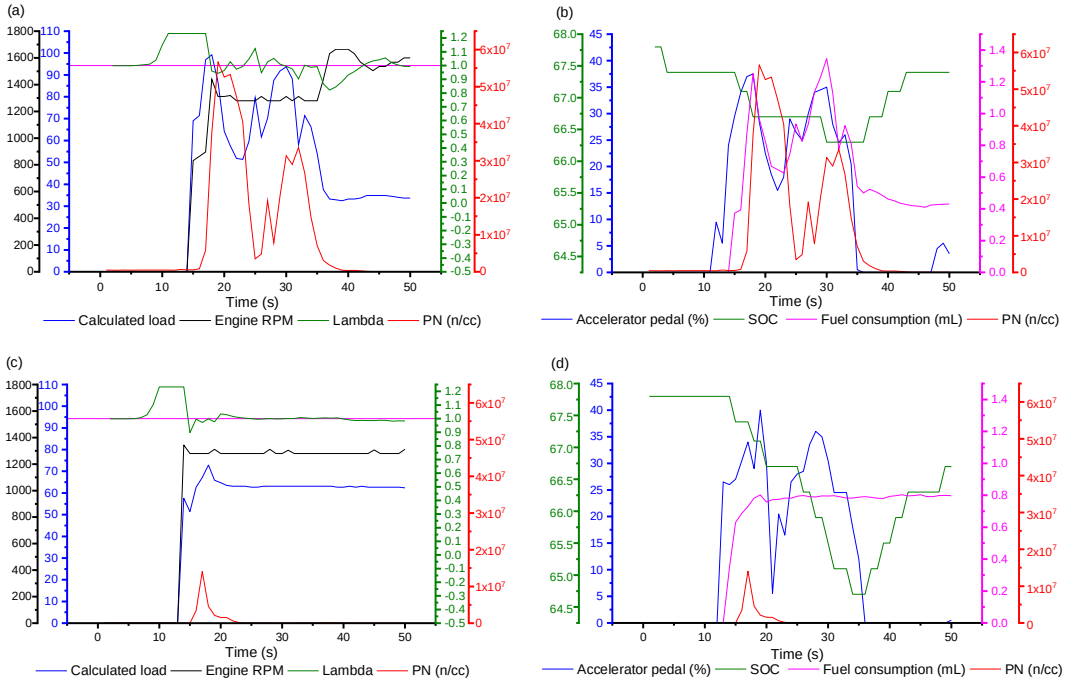

Figure 6.35 ECU parameter readings during first 50s of Tests 20 (a and b) and 23 (c and d) respectively, alongside PN emissions in red.

Figure 6.36a to Figure 6.36d show lambda values, CO, NO_x, THC and PN for a later period of the tests when large spikes of CO and PN were seen. Rich excursions occurring during engine re-ignition tend to be accompanied by a CO and THC spike. This is a major reason for differences in CO between tests; the tests do not have the same enrichment behaviour. This is also true to a degree for NO_x, whereby an event at 880s varies the stoichiometry between tests; the more lean has the greater NO_x emissions. PN emissions, however, are seen to result from almost every single engine-restart event, with the size of resultant spike being less proportional to enrichment. The majority of NO_x and THC difference arises from differences in the initial cold start engine-start event, while the differences are spread throughout the test for CO and PN. Clearly HEVs have a greater capacity for variation under repetitions of the same test cycle with same ambient and vehicle conditions, as has already been considered in previous literature (Bielaczyc et al., 2018). This is an important consideration when assessing the repeatability and reliability of HEV emission results, both in research and at type approval.

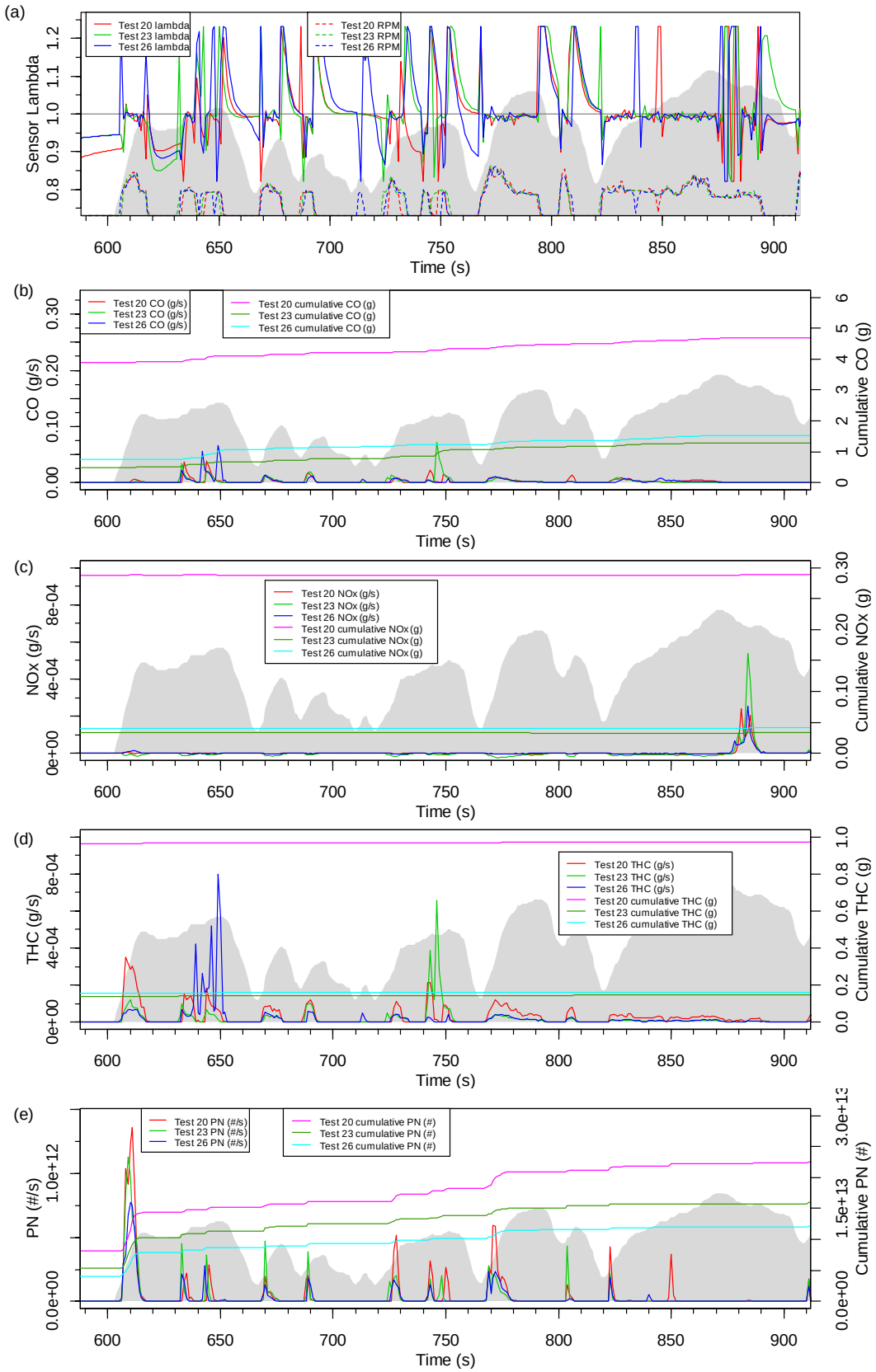

Figure 6.36 (a) Lambda values and RPM, (b) CO, (c) NO_x, (d) THC and (e) PN for the period from 600-900s, with vehicle speed indicated in grey.

6.6 Chapter 6 Summary

The study of TWC behaviour has shown that although HEVs can have longer warm-up times, the TWC retains the ability to quickly reach light-off, an important finding for the emissions profile of HEV technology. Additionally, this study has shown that the TWC has high resistance to cooling effects, maintaining its conversion efficiency after periods of engine-off. However, the pollutant emission penalties associated with engine stop-start events are considerable. The tendency for the vehicle to enter a fuel enrichment strategy on restart has been shown to increase overall emissions of CO, THC, NH_3, methane and PN. The comparison of an HEV with a comparable CV counterpart showed that the CO emissions were not greatly impacted by the stop-start behaviour, but the PN emissions of the HEV were increased by over an order of magnitude due to this behaviour. For PN, this penalty increases total emission factors above type approval limits. This clearly indicates that all HEVs (and not only GDIs, as is currently the case) should have their PN emissions limited by type approval legislation. NH_3 is not currently limited at light duty type approval, so the results presented in this chapter suggest it would be worth adding limits for this species into the regulations. Fuel cut has also been shown to induce NO_x emissions, though not in large enough quantities to risk failure to adhere to current type approval limits. The emission levels of CO and THC were also not large enough to risk a failure at type approval.

The initial battery SOC has been shown to affect the operating strategy of the vehicle, causing the engine to be engaged for a longer period of time, and undergo more stop-start events under lower initial SOCs. This in turn means that the lower the initial battery SOC, the shorter the cold start period. This affects the CO_2 very clearly. Some, notably minor, effects on pollutant emissions were also seen. There is some indication that for the pollutant gases affected by the TWC, having optimum SOCs of around 60% will lead to the lowest levels of emissions, striking the best balance between engine activity and TWC light-off times. For PN, due to the decreased stop-start behaviour, higher initial SOCs have lower associated emissions. The PN size distribution was shown to have a broader FWHM with more prominent secondary maxima/shoulders around 15nm and 100nm under low initial battery SOCs. This is due to the increased steady-state engine operation. The maximum PN size distribution remained centred around 50nm for all tests.

Though the type approval legislation dictates methods to account for differences in net SOC across a test in relation to CO_2 emissions, there is no prescription for the initial charge for (NOVC) HEVs, nor any adjustment to pollutant emissions due to differences in net CO_2. This leaves an area of weakness in the legislation.

With regard to the repeatability of HEV tests, small differences to the vehicle conditioning and operation difficult to control effectively during type approval emissions testing have been shown to cause significant differences in the operating strategies of this HEV. This, in turn, has caused significant differences in pollutant emissions from this HEV, due to the large effect that engine ignition and re-ignition has on these emissions. This is an important result as it has significant bearing on the control measures necessary for strong emissions legislation for HEVs.

The next chapter will study the fuel consumption and pollutant emissions resulting from the increased use of the ethanol and butanol biofuels in gasoline-based fuel blends.

Chapter 7
Influence of biofuels on hybrid electric vehicle emissions

7.1 Introduction

In order for future CO_2 emissions to reduce to a level demanded by emissions targets, both fleet electrification and the increased use of biofuels will likely be required. In the UK, the maximum blending limit has recently been increased from 5% to 10% ethanol in gasoline. In addition to this, research and development into alternative biofuels for blending with gasoline is ongoing. One of the most promising alternative biofuels is butanol, of which n-butanol is one such isomer. The emissions performance of a vehicle depends on a combination of closely intertwined factors such as engine technology, fuel quality and driving conditions (Martini et al., 2010). In order to infer how both the increase to E10 and the uptake of n-butanol to the same percentage (B10) may affect the emissions of HEVs, testing has been performed on a Euro 5 Toyota Prius.

Five WLTC tests, commenced under identical cold start soak and hybrid battery SOC conditions, were used to investigate the impact that E10 and B10 use has on HEV behaviour and emissions. Three different fuels were used: pure gasoline (E0), 10% ethanol in gasoline (E10) and 10% n-butanol in gasoline (B10). Two cycles of the E10 and B10 tests were run, alongside 1 of the E0. In addition to these WLTC results, five repeats each of E0, E5, E10 and B10 fuelled certification RDE tests were used to further clarify how these biofuels impact real-world driving emissions. This chapter addresses Objective 4 as set out in Section 2.11 of Chapter 2, satisfying Task 10 and Task 11.

7.2 Vehicle behaviour

Figure 7.1 below gives an overview of the vehicle, engine and catalyst behaviour for E0, E10 and B10. In Figure 7.1c the temperatures given are the upstream TWC (“TWC 1”), downstream TWC (“TWC 2”) and the engine-out exhaust gas temperature. Each plot shows vehicle speed on the primary y axis. The engine speed profiles show that the biofuels do not cause large differences in engine behaviour, except for a small extra burst of activity

toward the end of the warm-up strategy of the B10 test at 100s into the test, and an additional small duration ignition event at around 350s for E10. The use of these fuels causes small changes to the temperatures visible in Figure 7.1c, but no significant changes to engine coolant temperature in Figure 7.1b. Figure 7.1b shows that the SOC across the three vehicle tests remains consistent, commencing and finishing the tests with the same SOC (within 0.4% of one another). Over the course of the test, the B10 motor appears to be doing more work, visible as a dip in SOC compared to the E0 and E10 tests. Generally, all values appear close to one another. From the first 100s of the three tests, the E10 blend has the lowest exhaust gas temperature, followed by the gasoline test, then the butanol at a marginally higher temperature. From this data, it can be inferred that the combustion temperature is lowest for E10, in agreement with Canakci et al. (2013), and Eyidogan et al. (2010) from PFI chassis dynamometer testing, and also with Masum et al. (2014) under PFI research engine work at low engine speed. The finding that butanol has very similar or slightly higher exhaust gas temperature compared to gasoline is in agreement with Singh et al. (2015) and Varol et al. (2014) from PFI research engine work.

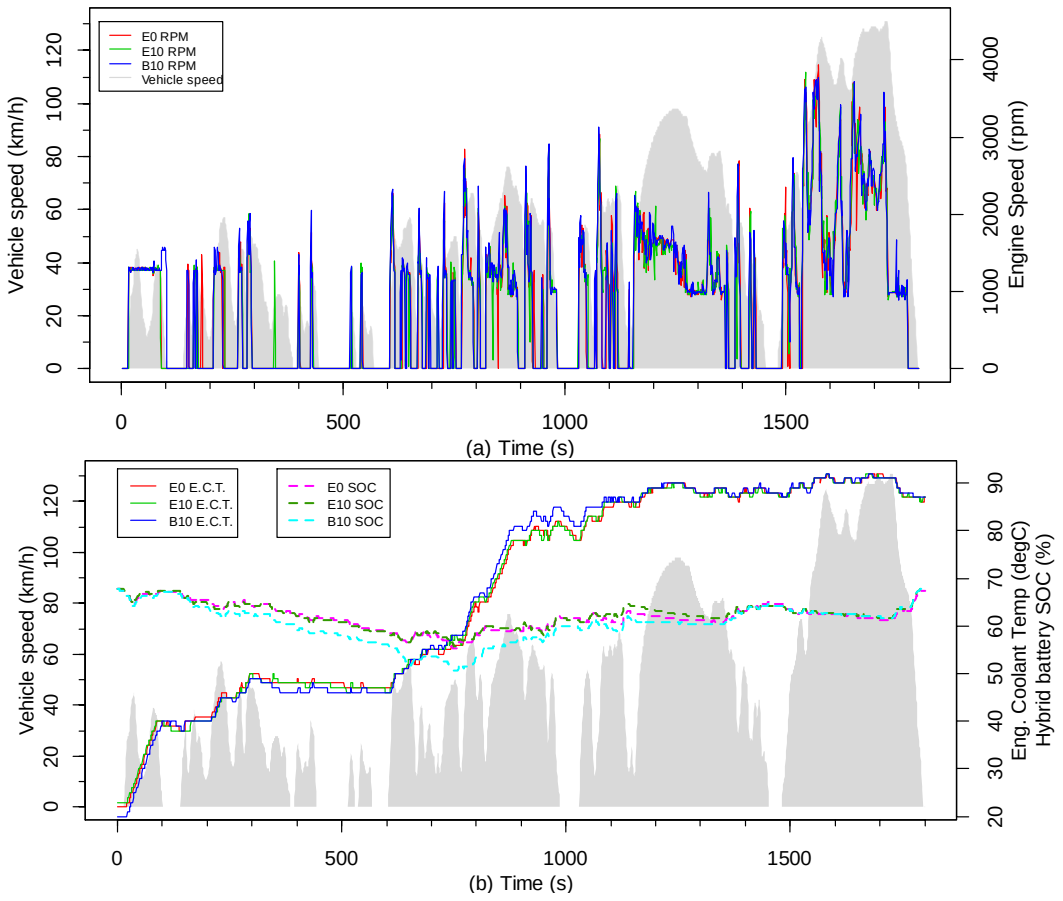

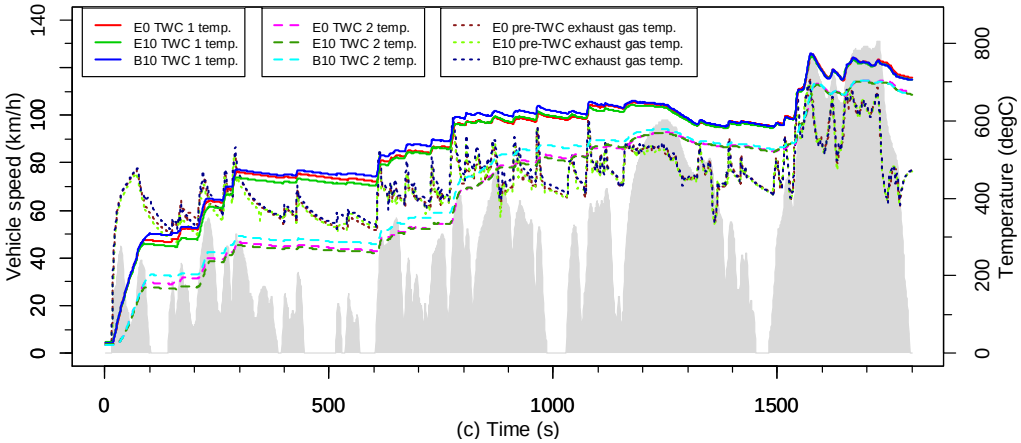

Figure 7.1 One example WLTC test for each of E0, E10 and B10 fuels, outlining (a) Engine speed (b) SOC and engine coolant temperature profiles and (c) Temperatures around the TWC.

7.3 Fuel consumption

While comparisons of tailpipe CO_2 emissions are not meaningful for biofuels due to the large differences in well-to-tank CO_2 emissions, it is useful to study differences in fuel consumption. This is in order to assess whether there is a penalty from the use of these biofuels. As discussed in Chapter 2 Section 2.3, the energy density of both ethanol and butanol is lower than that of gasoline, so some fuel consumption penalty is expected. Little research has been done to assess this penalty for HEVs specifically, but the results presented in Figure 7.2 show that the E10 blend gives the highest results, followed by the B10, with the E0 having the lowest fuel consumption. This result agrees with the results of Liu et al. (2019) CVs, shown in Figure 7.3.

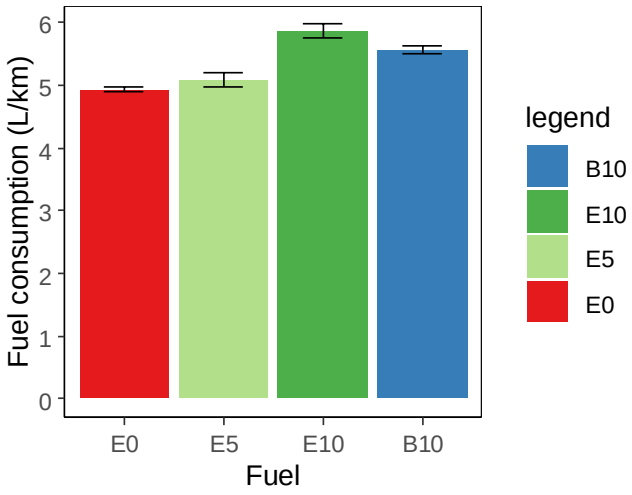

Figure 7.2 Fuel consumption across repeated HEV RDE tests fuelled by E0, E5, E10 and B10. Uncertainties are the standard errors of the distributions.

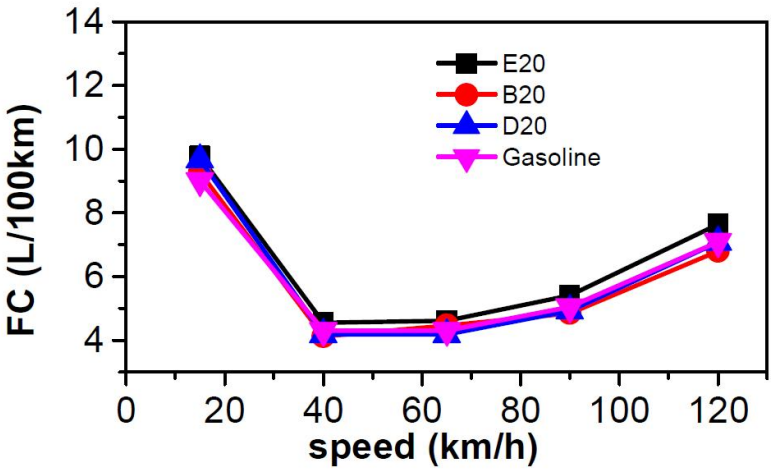

Figure 7.3 Fuel consumption for across a range of steady-speed test points under pure E0 gasoline, E20 and B20 fuel blends as presented by (Liu et al., 2019).

7.4 Regulated gaseous emissions

7.4.1 CO

The WLTC results in Figure 7.4 indicate that both E10 and B10 have decreased CO emissions compared to E0 (by 51% and 33% in phase 1, and 28% and 22% for the total WLTC, respectively), in agreement with Canakci et al. (2013) and Vojtisek-Lom et al. (2015) on chassis dynamometer and Hernandez et al. (2014) on road using PEMS. The results currently presented have the same decreasing CO trend with ethanol blend as the PHEV of Suarez-Bertoa and Astorga (2016), in contrast to their MHEV. The total WLTC emission factor of 110 ± 10 mg/km for E10 currently presented bridges the gap between their PHEV (62 mg/km) and their MHEV (at 238 mg/km) for E10.

Over the total test, both E10 and B10 give very similar CO emission levels to each other, while in the urban section, B10 brought a 36% increase in CO emission levels compared to E10. Vojtisek-Lom et al. (2015) found that the magnitude of emissions reduction from B25 and E15 compared to E0 were similar to one another. Extrapolating from the disparity in percentage blends of this previous study, the results presented below tend toward agreement with this. All three fuels gave emissions below the Euro 6 limit of 1g/km.

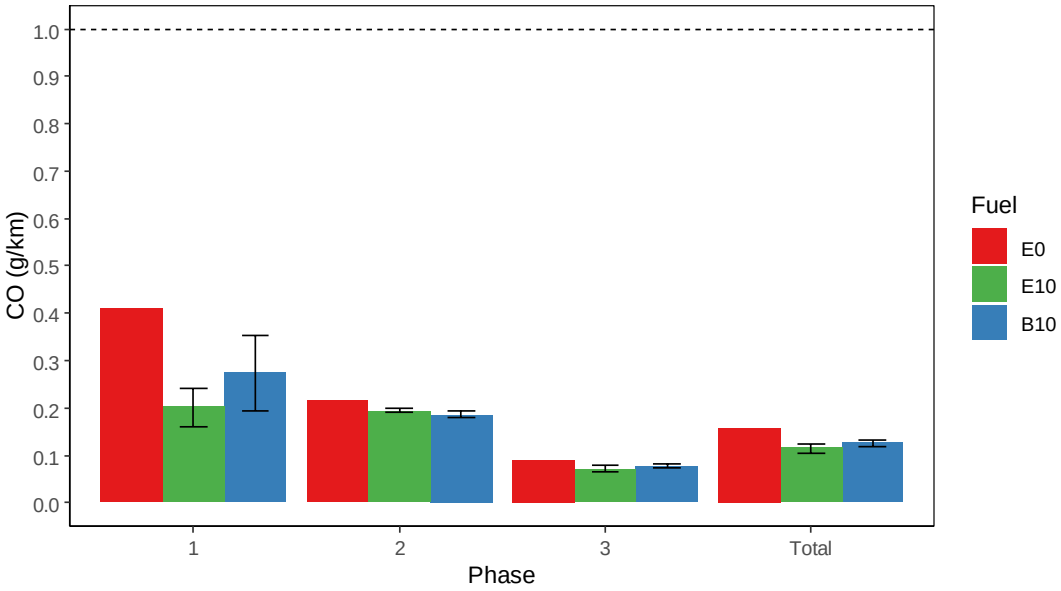

Figure 7.4 WLTC CO pollutant emissions per km from phases 1, 2, 3 and total, for E0, E10 and B10 fuels. The Euro 6 emission limit (1g/km) is indicated by a dashed line on the graph.

Figure 7.5 shows CO emissions from the RDE tests from different blends, with all fuels displaying emission factors far below the Euro 5 and 6 limit of 1g/km. The results show that E0, E10 and B10 follow the same trend as the WLTC for the urban section of the RDE test (21% and 5.5% decreases for E10 and B10 compared to E0), but then E10 – and to a lesser extent, E5 – have greater CO emissions for phases 2 and 3, which are defined as vehicle speed ranges of 60-90km/h and above 90km/h respectively. Canakci et al. (2013) found that at higher vehicle speeds on the chassis dynamometer, SI vehicle CO emissions increased with ethanol blending, so there is some precedent for this observation as the RDE maintains higher average speeds in the rural driving section, and maintains a high speed for much longer in motorway section, than the WLTC (see Chapter 4 Table 4.1).

B10 also has higher emissions over the rural and motorway (and hence whole RDE) compared to E0, but to a lesser degree than E10. Elfasakhany (2014) and Elfasakhany (2017) presented a trend of decreasing CO emissions with n-butanol blends (and ethanol blends) compared to E0 from their single cylinder research engine for low engine speeds, but butanol tests had comparable and higher CO emissions at higher engine speeds. This tendency was also presented by Liu et al. (2019) from their NEDC testing where at low speeds E0 was greater than E20 and B20, while at high speeds E20, then B20 were greater than E0. Previous literature (e.g. Liu et al. (2019) given in Figure 7.1a) has shown that the higher speed driving sections have generally

higher engine speeds, and so the results of Figure 7.5 agree with these references.

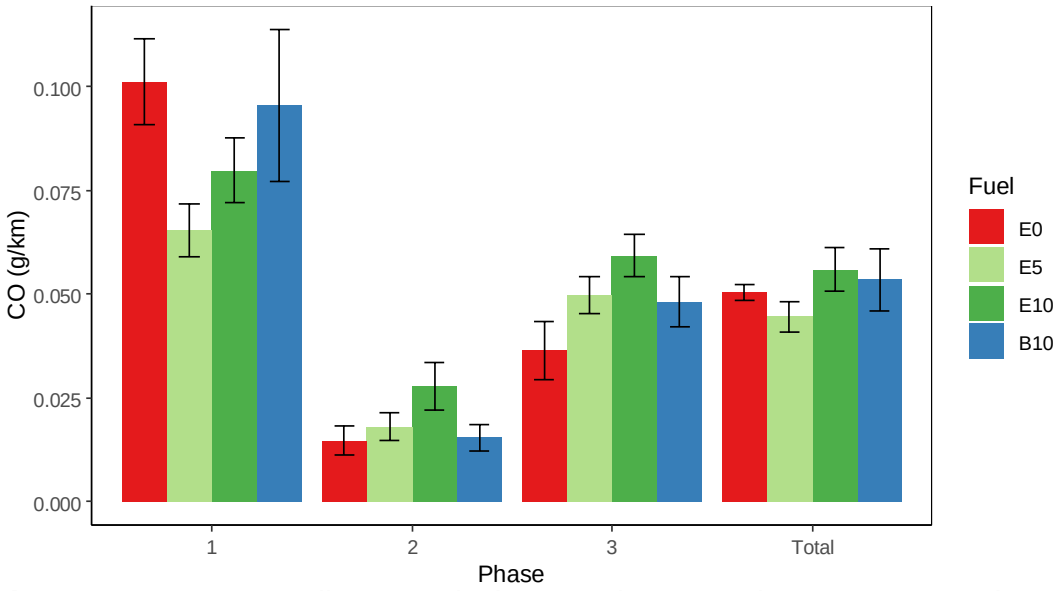

Figure 7.5 RDE CO pollutant emissions per km from phases 1, 2, 3 and total, for E0, E5, E10 and B10 fuels.

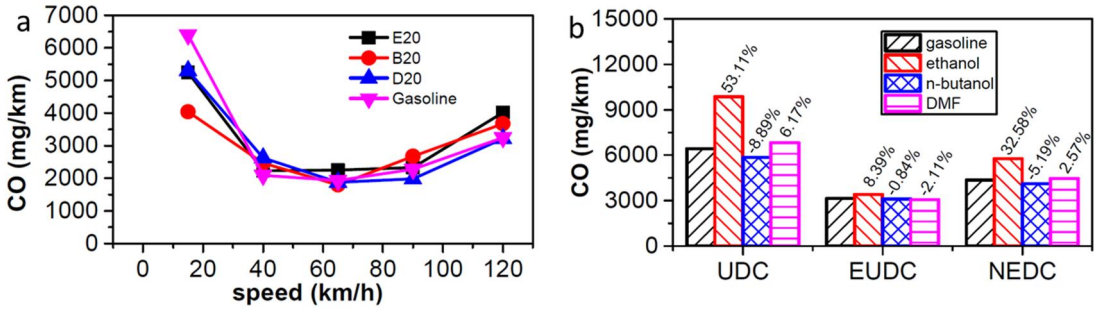

Figure 7.6 CO emissions (a) across a range of steady-speed test points and (b) under NEDC testing, from an SI engine fuelled with pure E0 gasoline, E20 and B20. Presented by Liu et al. (2019).

Figure 7.7a depicting representative transient and cumulative CO emissions from E0, E10 and B10 fuelled tests over the WLTC cycle shows that the magnitude of E0-fuelled CO spikes appear to be generally larger than those from E10 or B10. Li et al. (2017) found that during rich combustion, E10 gave lower levels of CO emissions than E0. As explained in Chapter 6 Section 6.3, engine re-ignition events are often accompanied by fuel enrichment, so these lower emissions under E10 support this finding. Additionally, the cold start emissions appear to be larger for E0 than B10, and E10 has the smallest emissions. These results agree with Liu et al. (2019), who reported improved cold start CO performance resulting from butanol blends to gasoline from a GDI SI engine.

Figure 7.7b shows a range of cumulative CO mass emissions across a selection of nine representative RDE tests (three each of E0, E10 and B10). Little common trend can be seen across repeats with the same fuel, indicating that real-world effects are having a greater impact on the emissions than the fuel type. For this reason, further analysis in the following paragraph will concentrate on the chassis dynamometer WLTC test results where the external conditions were more closely controlled.

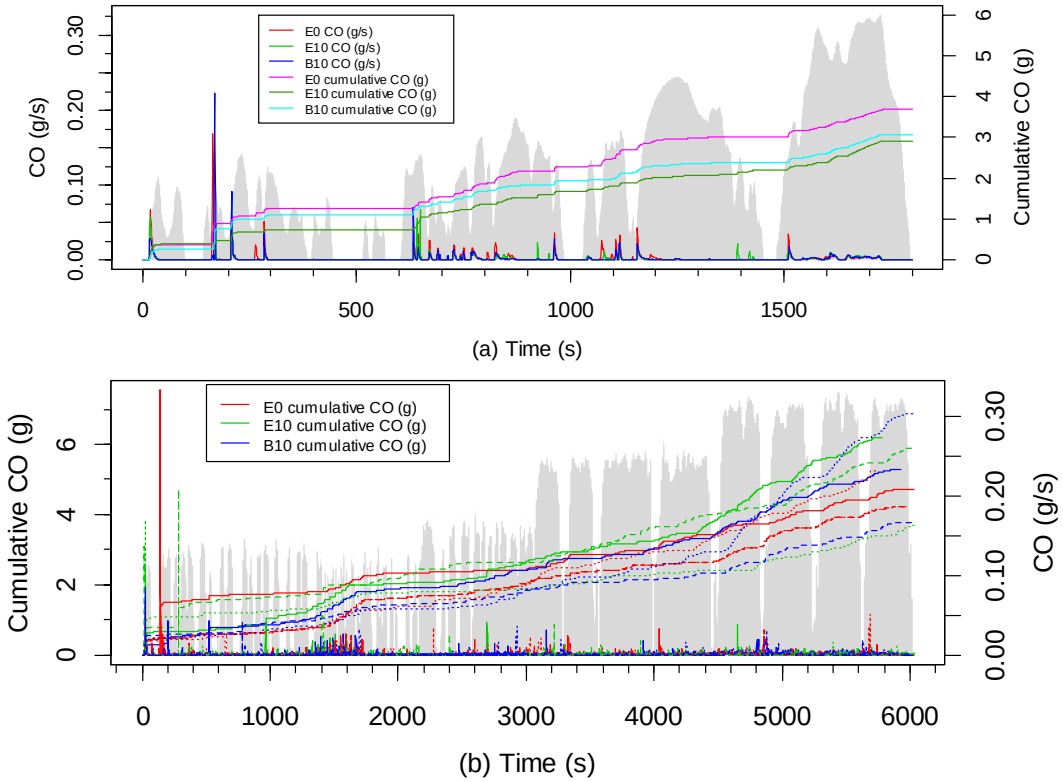

Figure 7.7 (a) CO emissions from WLTC tests fuelled by E0, E10 and B10, with speed indicated in grey. (b) CO emissions across 9 replicate RDE tests (3 each of E0, E10 and B10), with example RDE speed in grey.

The study of air-fuel ratios for the first 300s in Figure 7.8a and Figure 7.8b reveal that there were occasions of fuel enrichment on engine restart that were more common under E0 (then B10, and finally E10). Canakci et al. (2013) attributed the lower CO from ethanol blends at low vehicle speeds to the oxygen in the ethanol molecule contributing to a leaning effect. This theory is supported by the stoichiometry data in Figure 7.8b.

As the cold start impact and number of stops per km are both greater for the WLTC than RDE, this helps explain why the E0 emissions presented are greater under WLTC than RDE testing. An important conclusion for HEVs is therefore that during stop-start driving, increased use of ethanol will bring

about CO emissions decreases, but during higher speed driving, the use of these biofuels can incur greater CO emissions than gasoline. This conclusion supports the results of Suarez-Bertoa and Astorga (2016), who noted that the MHEV they studied saw increased emissions with ethanol blending while their PHEV saw decreased emissions. This would appear to be because the PHEV underwent more engine stop-start behaviour during the test than the MHEV. In the current work the same pattern is true of butanol, but to a lesser degree for both conditions than ethanol.

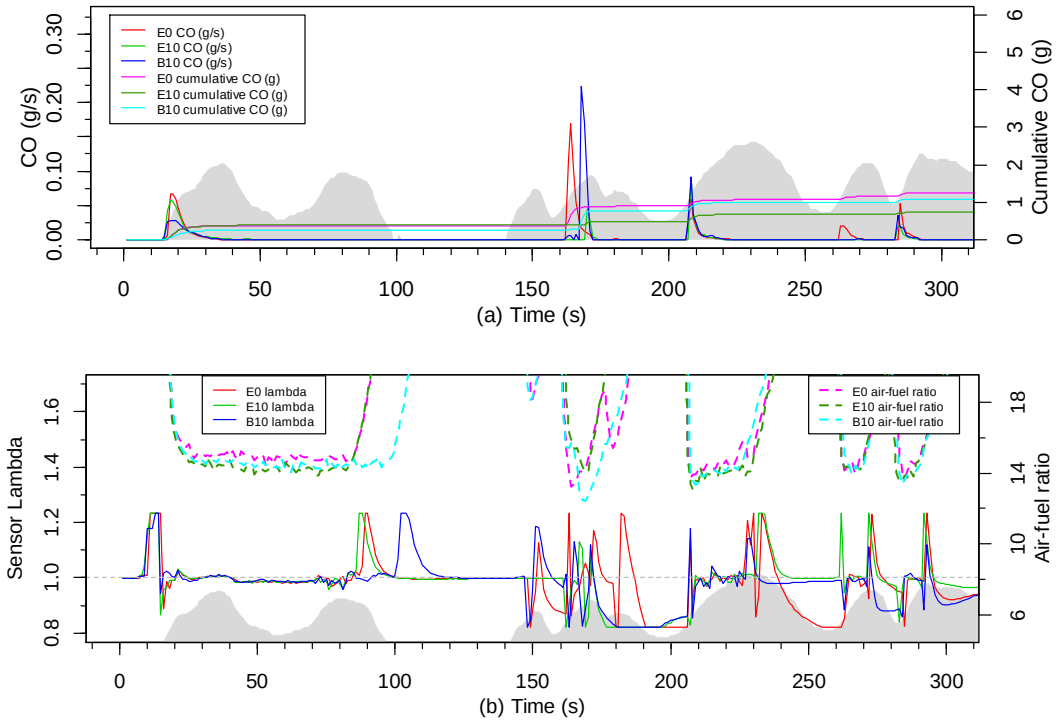

Figure 7.8 (a) First 300s of tests shown in Figure 7.7a (E0, E10 and B10 WLTC tailpipe CO emissions). (b) Lambda and air-fuel ratio for the same period, where lambda values below the grey dashed line represent rich combustion.

7.4.2 NO_x

Figure 7.9 shows that the emissions of NO_x over the WLTC test are very similar across all three fuel types, but are slightly lower under E10 fuelling than B10 and E0 (both of which are approximately equal). The decreases for E10 and B10 respectively against E0 are 1% and 0.2% in phase 1, and 11% and 0.17% for total WLTC. All fuels are far below the Euro 6 emission limit of 0.06g/km.

These results agree with the majority of previous SI work on the topic for E10 and B10 discussed in Chapter 2 Section 2.9. Suarez-Bertoa and Astorga

(2016) also found from their WLTC testing that their NO_x emissions were too close to draw reliable conclusions between E0 and E10. As with CO, the NO_x results of the HEV in the current study bridge the gap between the MHEV and PHEV noted in Suarez-Bertoa and Astorga (2016) for both fuels.

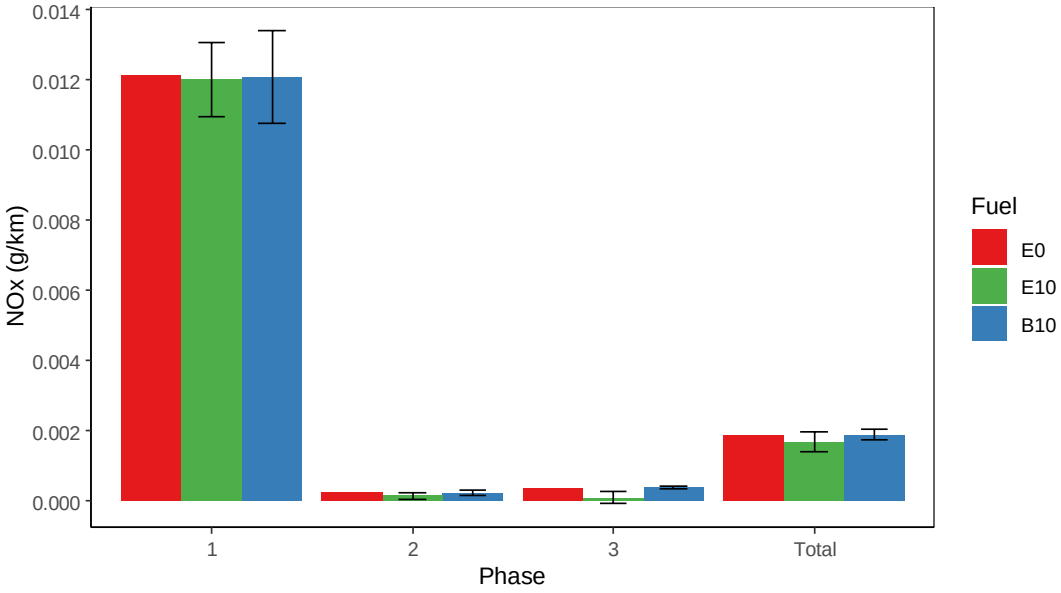

Figure 7.9 WLTC NO_x pollutant emissions per km from phases 1, 2, 3 and total, for E0, E10 and B10 fuels.

Figure 7.10 shows that during RDE testing, the difference in NO_x emissions between fuel types was greater than from the WLTC testing, with most of this difference originating within the urban section. A 36% decrease was witnessed for both E10 and B10 compared to E0 in the urban RDE section, with 24% and 18% lower emissions for E10 and B10 respectively over full RDE. All results are far below the Euro 6 emission limit of 0.06g/km, so this limit is not included in the figure for the sake of scale. The E10 decrease agrees with Canakci et al. (2013) and Kalita et al. (2016), who found that at lower vehicle speeds NO_x emissions decreased with ethanol blend, but as vehicle speed increased more similar emissions levels were seen between fuels. More recently, Liu et al. (2019) found the same for both E20 and B20 compared to E0. One can see the same trend from the data presented. Hernandez et al. (2014) reported little change in NO_x levels between E0 and E10 blends in on-road PEMS testing, so the current work is the first to display from on-road testing the same trend (for converging NO_x as vehicle speed increases) as previously seen on the chassis dynamometer.

Directly comparing ethanol blends to butanol blends utilising an SI vehicle on the chassis dynamometer, Ratcliff et al. (2013) found that B17 gave slightly

higher NO_x emissions than E16, but concluded that the emissions are not greatly affected by these blends. The results in Figure 7.9 and Figure 7.10 concur with this.

Chapter 6 showed that, of the regulated pollutants, NO_x emissions varied the most with initial battery SOC and therefore the differences in initial battery SOC could be affecting the RDE results. Additionally, NO_x is particularly vulnerable to changes in ambient conditions, specifically humidity and rain. As was outlined in Chapter 3 Section 3.7, these ambient conditions were not consistent across testing due to differences in precipitation.

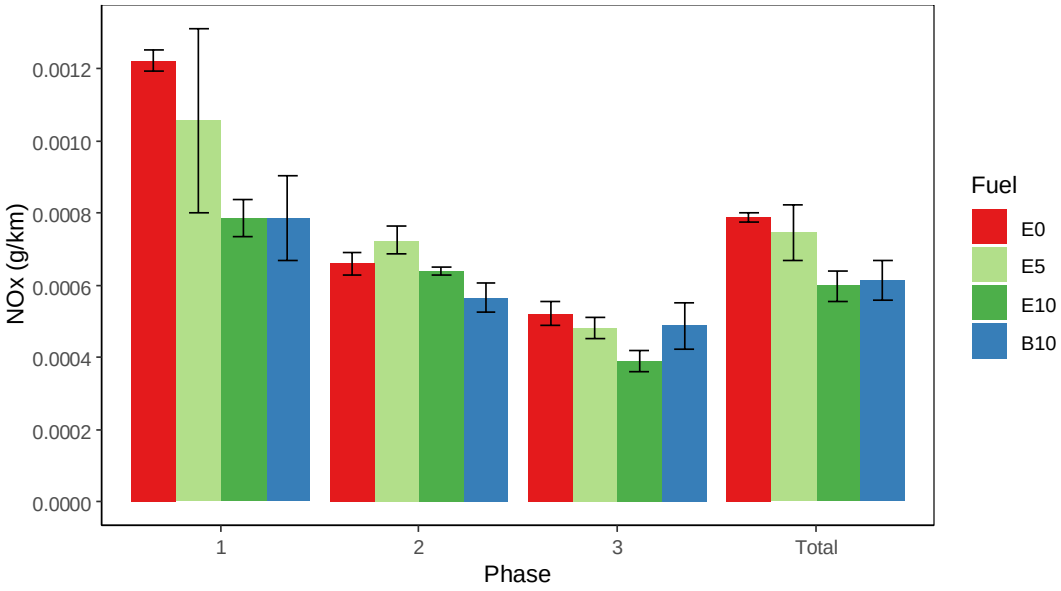

Figure 7.10 RDE NO_x pollutant emissions per km from phases 1, 2, 3 and total, for E0, E10 and B10 fuels.

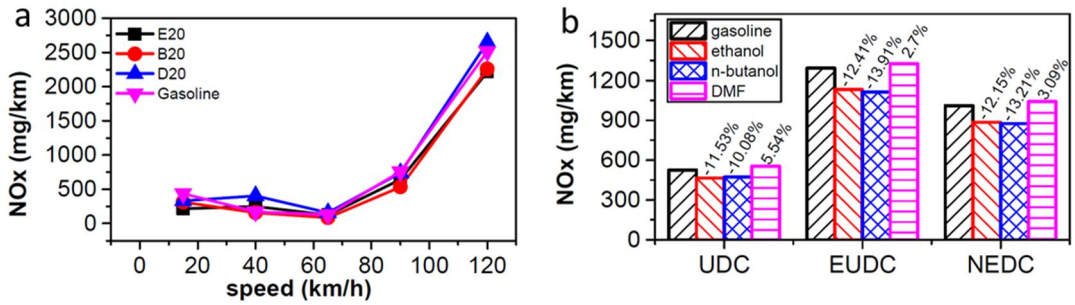

Figure 7.11 NOx emissions (a) across a range of steady-speed test points and (b) under NEDC testing. Results from an SI engine, fuelled with pure E0 gasoline, E20 and B20, as presented by (Liu et al., 2019).

Figure 7.12a shows that the majority of NO_x emissions for all fuels on the WLTC arise from the cold start initial combustion event, before the TWC reaches light off. This also causes the majority of the difference in NOx emissions between biofuels. The NO_x emissions are very similar between

WLTC tests because of the identical ambient conditions, initial HEV SOC and velocity trace being followed. Figure 7.12b shows a sample of RDE NOx results (3 each of E0, E10 and B10). Because the duration of high speed driving is greater on the RDE test, Figure 7.12b shows that the emissions here make up approximately half of total NO_x emissions, but again the emission rates are very similar between fuels for this hot engine operation. The majority of difference for both WLTC and RDE tests comes from the cold start period, where small differences in driving style and ambient conditions on the RDE are having a larger influence than on the WLTC results.

For both test types, the pure gasoline preparations have the highest emissions, followed by nearly all of the B10 preparations, with E10 generally having the lowest resultant NO_x emissions in the cold start section. This trend was also witnessed by Canakci et al. (2013), who attributed the ethanol results to the lower combustion temperature resulting from high latent heat, lower heating value and the extra oxygen content. Given the fact that these properties for butanol generally lie between those of gasoline and ethanol (Serras-Pereira et al., 2013) this would also explain the intermediary butanol results, in agreement with the findings of Broustail et al. (2012) and Ratcliff et al. (2013). Both biofuels could therefore bring about a decrease of NO_x in urban centres, where the greatest exposure to humans occurs.

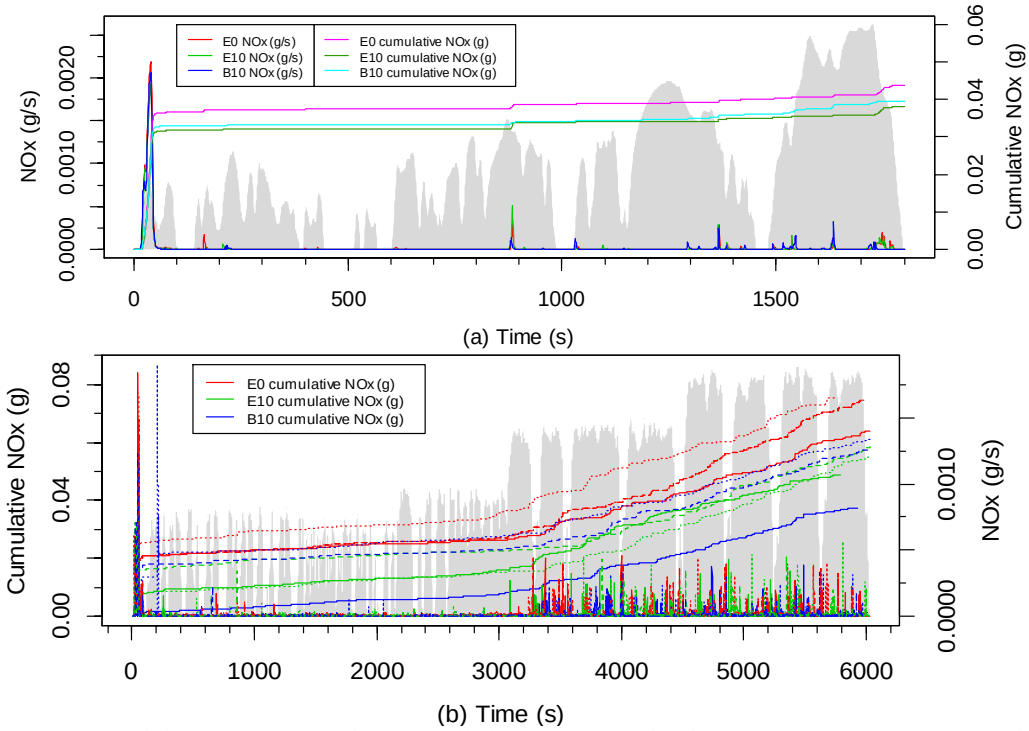

Figure 7.12 (a) E0, E10 and B10 tailpipe NO_x emissions from WLTC tests, (b) tailpipe NO_x emissions across RDE tests, with example speed traces indicated qualitatively in grey.

7.4.3 THC

The emissions of THC over the WLTC test as shown in Figure 7.13 are very similar across all three fuel types, and far below the emissions limit of 0.1g/km, which is not plotted for the sake of scale. THC emissions are slightly lower under E10 fuelling (6% in phase 1, 3% in total WLTC) and comparable under B10 fuelling (1.6% lower under phase 1, but 4% higher under total WLTC) compared to E0. However, all three are within each other's margin for error. The general trend in literature thus far from SI research has been for decreasing THC with ethanol blend strength, though many studies have found mixed results or no change. For example, Ratcliff et al. (2013) also presented mixed results, again indicating that transient cycles do not generally show the clear THC behaviour that steady state testing generally does. Canakci et al. (2013), Elfasakhany (2014) and Liu et al. (2019) found that THC emissions decreased with ethanol and/or butanol blending at lower speeds but then saw a convergence as vehicle speed increased. The results of Liu et al. (2019) are displayed in Figure 7.14, and the speed relationship visible in Figure 7.14a has some similarity with the pattern seen in Figure 7.13.

Suarez-Bertoa and Astorga (2016) also saw little trend in THC emissions with ethanol blending in gasoline for their HEVs. The total WLTC emission factor

of 7.4 ± 0.2 mg/km for E10 presented currently is close to the value 6.8 ± 1 mg/km presented for their PHEV, and bridges the gap between that and their mild parallel HEV (at 13 mg/km).

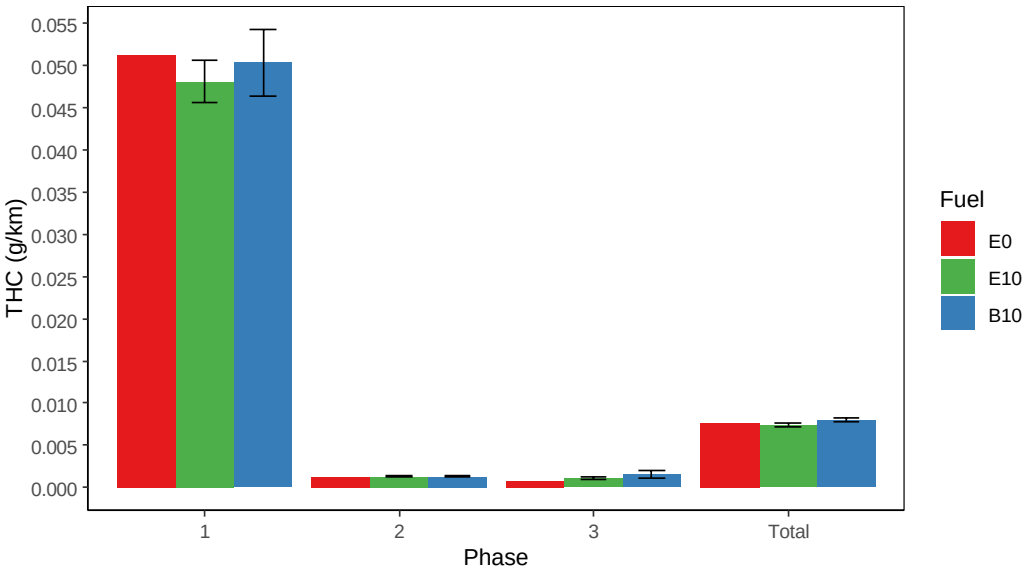

Figure 7.13 WLTC THC pollutant emissions per km from phases 1, 2, 3 and total, for E0, E10 and B10 fuels.

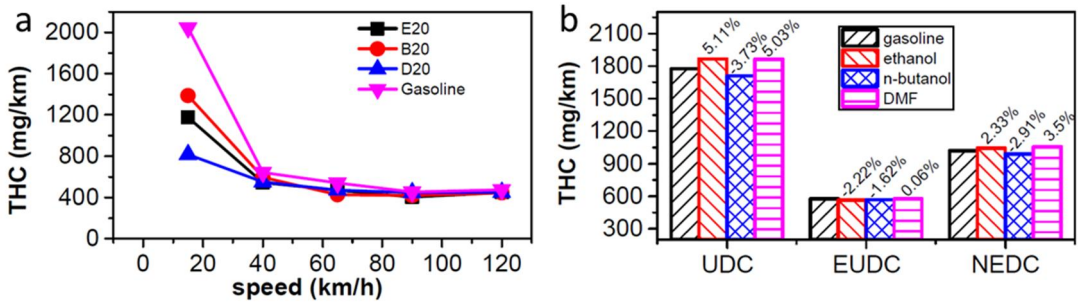

Figure 7.14 THC emissions (a) across a range of steady-speed test points and (b) under NEDC testing, from an SI engine (Liu et al., 2019).

Figure 7.15a gives an example plot of each fuel's WLTC test, while Figure 7.15b concentrates on only the first 300s of this test. Speed traces are indicated in grey. Figure 7.15c shows that the THC emissions are related to rich engine-on events. Therefore, as long as the HEV undergoes stable combustion, the biofuels tested here have minimal impact on THC emissions.

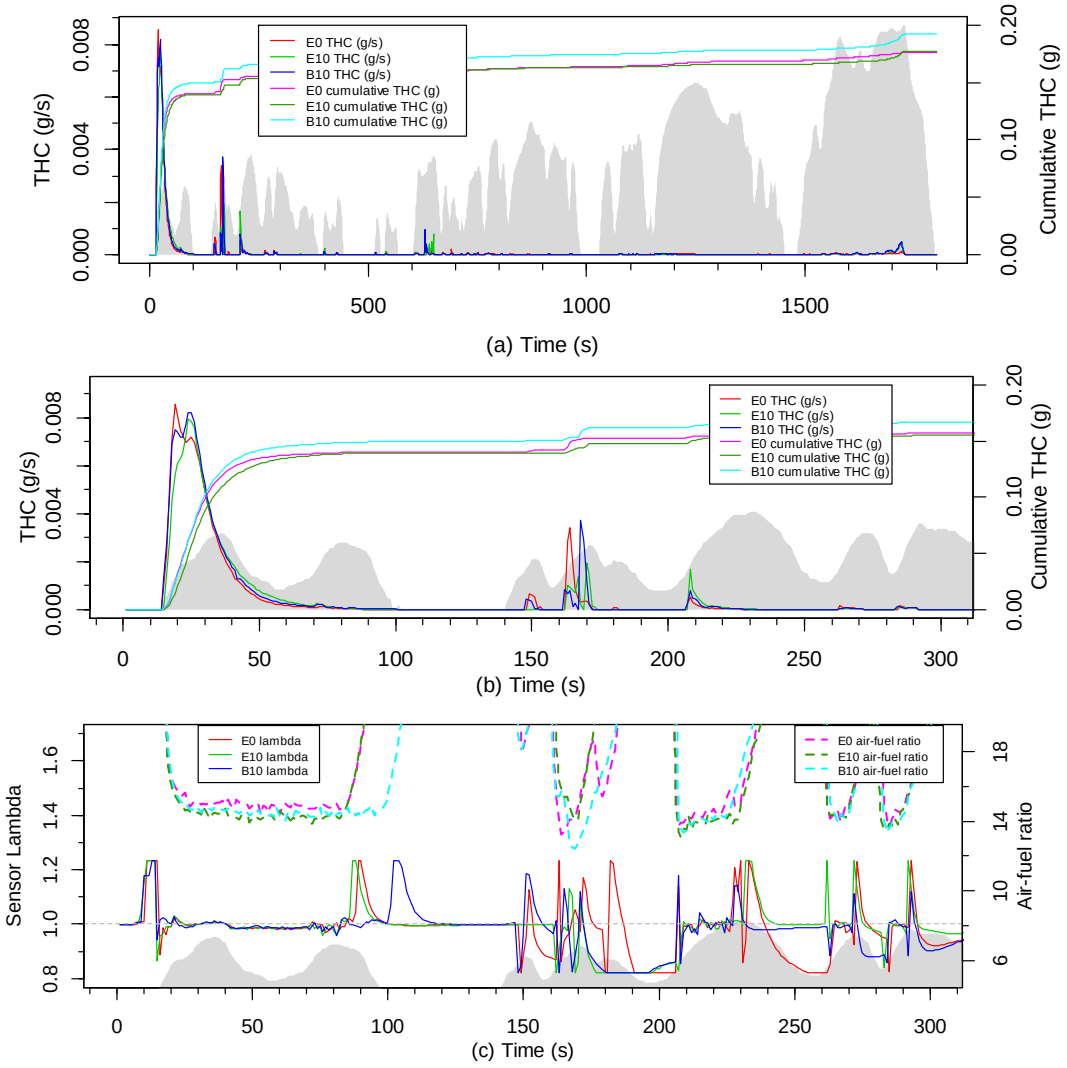

Figure 7.15 (a) Representative E0, E10 and B10 tailpipe THC emissions from (b) First 300s of tests shown in (a), with (c) lambda and air-fuel ratio.

7.5 PN emissions

Figure 7.16 displays the phase and total average PN results measured by DMS500 from five WLTC tests commenced under identical cold start and initial hybrid battery SOC conditions. Average values for each phase are given, along with the Euro 6 limit for applicable SI vehicles. The WLTC PN results are above the Euro 6 limit for all three tested fuels. E0 gave the highest overall PN emissions, followed by B10. E10 consistently gave the lowest results across all phases. In phase 1, E10 and B10 gave 40% and 23% lower results compared to E0, while over the total WLTC these differences were 41% and 21%. The conclusion – that the biofuel blends give the lowest PN emissions, with butanol being higher than ethanol – is in agreement with the consensus of previous literature for CVs, as outlined in Chapter 2 Section 2.9.

As far as the author is aware, no other work has confirmed this behaviour for HEVs under biofuel use.

One can see some convergence between the two biofuels as the speed increases, which is in direct agreement with Liu et al. (2019) from their GDI NEDC testing shown in Figure 7.17a and Figure 7.17b. This indicates that this trend in PN emissions for ethanol and butanol blends at different speeds can be seen from both PFI HEV and ICE GDI vehicles.

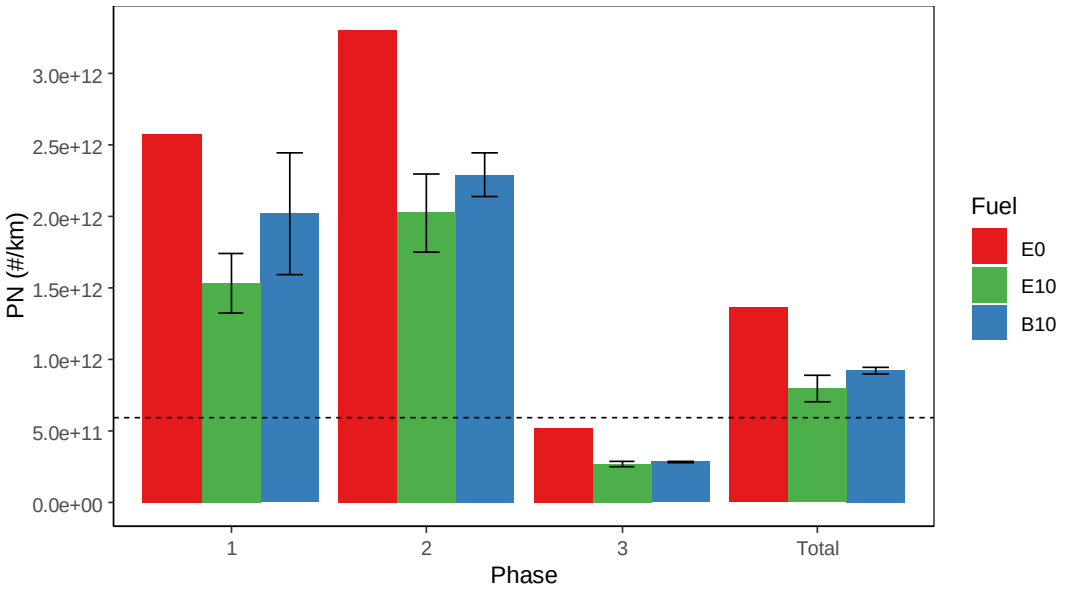

Figure 7.16 WLTC PN pollutant emissions per km from phases 1, 2, 3 and total, for E0, E10 and B10 fuels. The Euro 6 PN emissions limit of $6x10^{11}$ #/km is indicated by a dashed line.

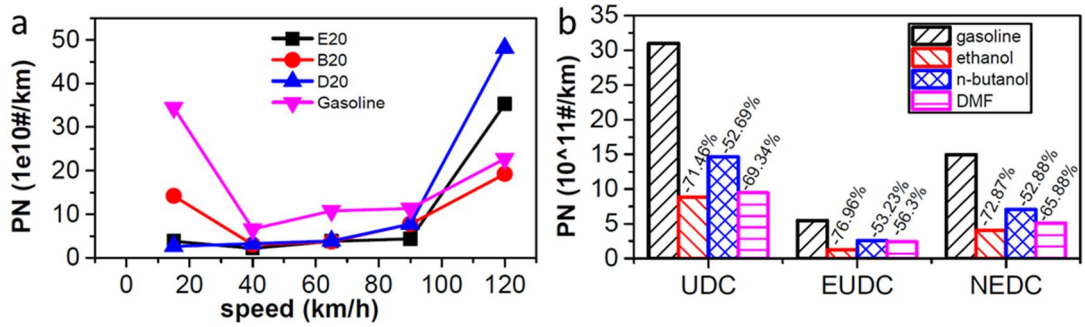

Figure 7.17 PN emissions (a) across a range of steady-speed test points and (b) under NEDC testing. Results from an SI engine, fuelled with pure E0 gasoline, E20 and B20, as presented by (Liu et al., 2019).

The PN results of the RDE tests measured by PEMS in Figure 7.18 appear less clearly distributed, and E10 still maintains the lowest emissions (4% decrease for urban and whole RDE), while E5, surprisingly, has the greatest emissions. B10 shows higher PN emissions generally than E0 (4% increase

over urban, 1% over whole RDE). The error bars for all four fuel types are overlapping, however, indicating that there are too many changing variables between these on-road tests to draw reliable conclusions. The PN behaviour of HEVs is far more dependent on engine behaviour than it is for CVs, because of the stop-start behaviour as explained in Chapter 2 Section 2.8.6. It is therefore unsurprising that on-road testing has not shown such clear correlations between biofuel use and PN emissions for HEVs than previous on-road studies have shown for CVs, such as that presented in Vojtisek-Lom et al. (2015). The urban RDE PN exceeds the Euro 6 limit of $6x10^{11}$#/km

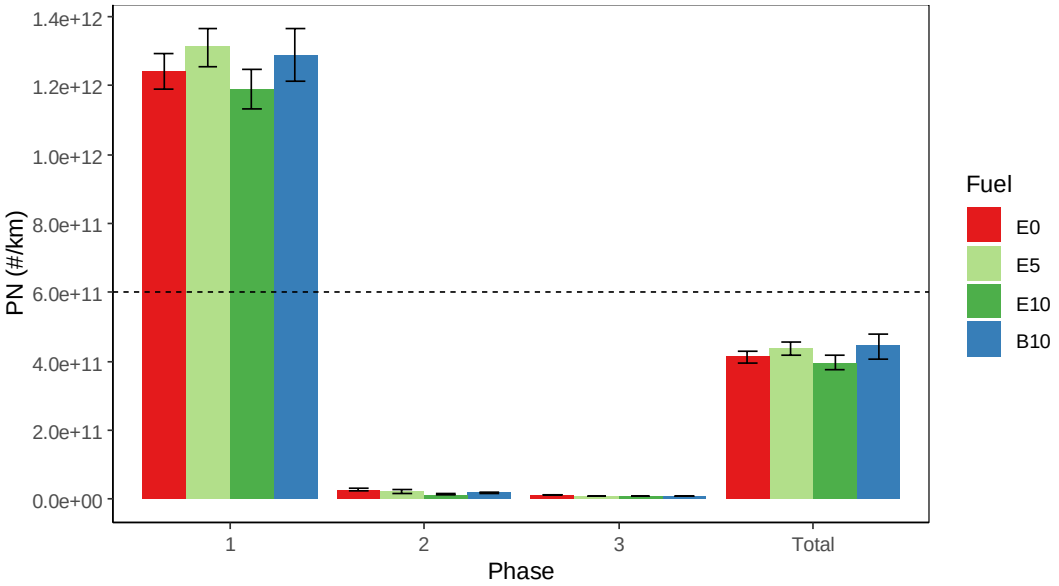

Figure 7.18 RDE PN pollutant emissions per km from phases 1, 2, 3 and total, for E0, E10 and B10 fuels. The Euro 6 PN emissions limit of $6x10^{11}$ #/km is indicated by a dashed line.

Figure 7.19a gives the transient and cumulative PN emissions for three representative E0, E10 and B10 WLTC tests, alongside the vehicle speed indicated qualitatively in grey. This plot clearly indicates that the magnitude of emissions spikes is usually greatest for E0 fuelled tests, followed by B10 and then E10. The frequency of spikes is dictated by the engine-on events, which Figure 7.19c indicates can be the greater cause for differences in PN emission rates under on-road driving such as the RDE. No clear correlation between fuel type and PN emission rate is seen for the RDE tests in Figure 7.19b for this reason, due to differences in the number of engine-on events between tests.

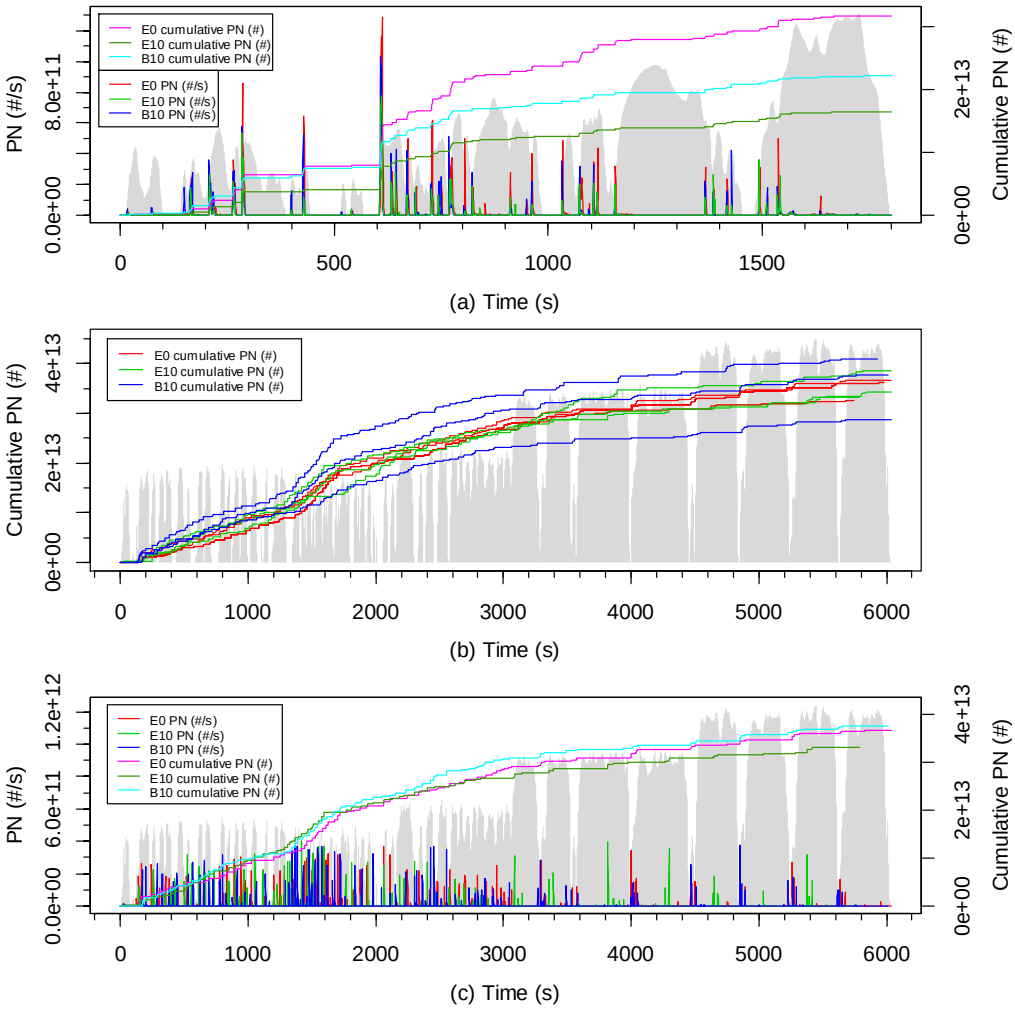

Figure 7.19 (a) Representative E0, E10 and B10 tailpipe PN emissions from WLTC tests, with speed trace indicated qualitatively in grey. (b) Tailpipe PN emissions across 9 replicate RDE tests (3 each of E0, E10 and B10). (c) E0, E10 and B10 tailpipe PN emissions from one representative fuel type example of each RDE test. An example RDE speed trace is indicated qualitatively in grey behind both (b) and (c).

Figure 7.20a and Figure 7.20b indicate that the magnitude of PN emissions is not generally related to the magnitude of diversion into rich combustion. The extra oxygen in the biofuels improves combustion, and allows any soot that has formed to be more easily oxidised (Liu et al., 2019). As ethanol has more oxygen, it reduces soot formation to a greater extent and is the reason for the trend in magnitude of emissions across the three fuels.

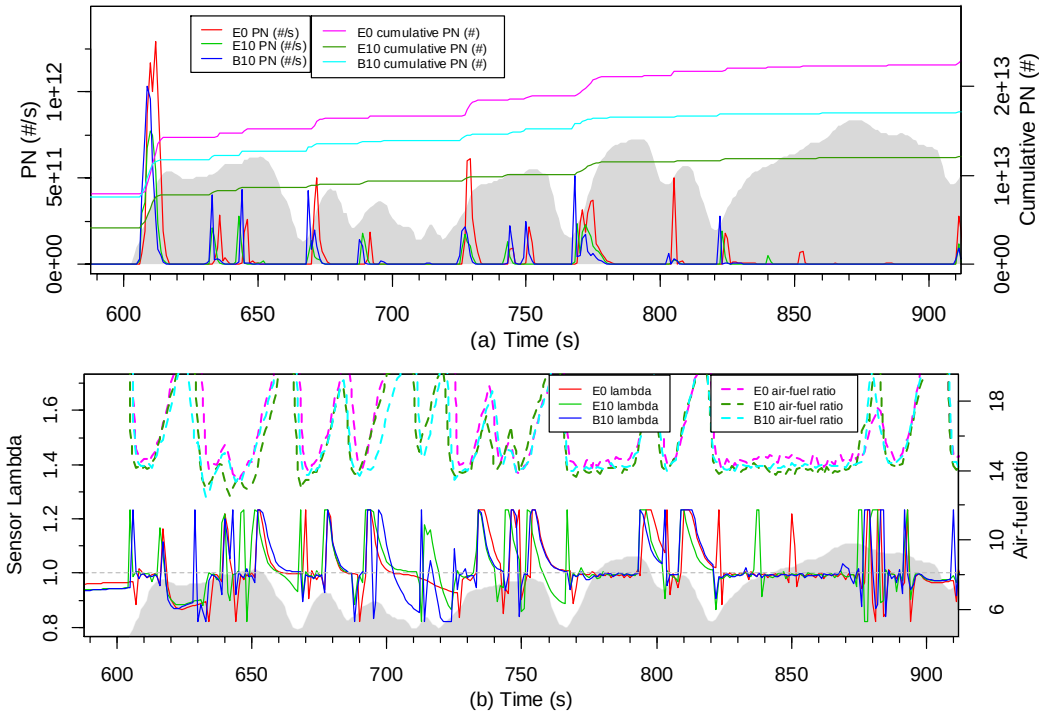

Figure 7.20 (a) 600–900s of tests shown in Figure 7.19a. (b) Lambda and air-fuel ratio for the same period.

7.5.1 Particle number size distribution

The average PNSD resulting from the cold start phase 1 (low speed phase) of the WLTC tests is displayed in Figure 7.21a, Figure 7.21b and Figure 7.21c for E0, E10 and B10 respectively. The distribution for the whole WLTC tests is displayed in Figure 7.22a, Figure 7.22b and Figure 7.22c respectively. Little variation in PNSD is seen, indicating that these three biofuels lead to similar distributions of PN emissions, with a maximum around 40-50nm. Similarly, Gu et al. (2012) did not appear to detect any change in PN size distribution with butanol blends from their PFI research engine. To the author's best knowledge, no study focusing on the PN size distribution changes for an HEV from ethanol and butanol biofuel blends with gasoline has been previously published.

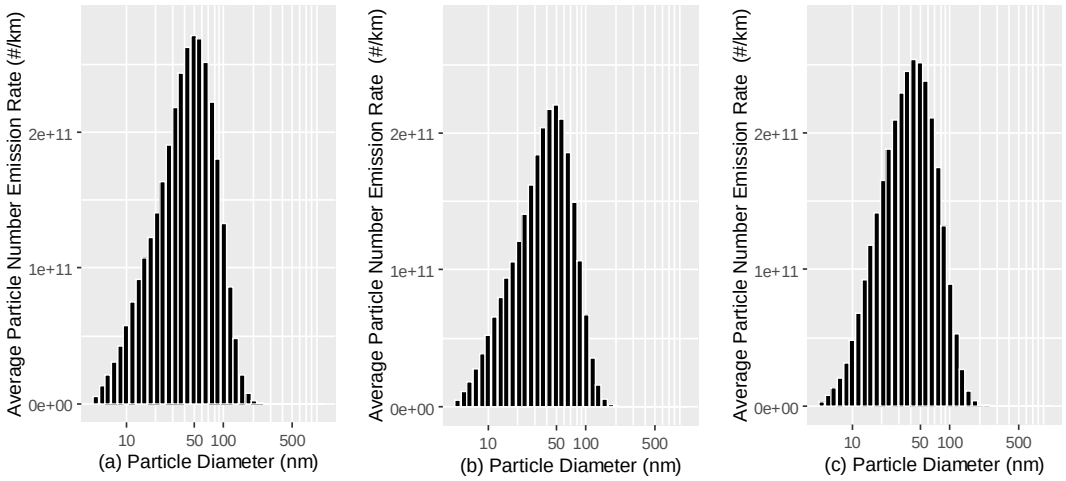

Figure 7.21 Phase 1 WLTC PNSD from (a) E0, (b) E10 and (c) B10 fuelling.

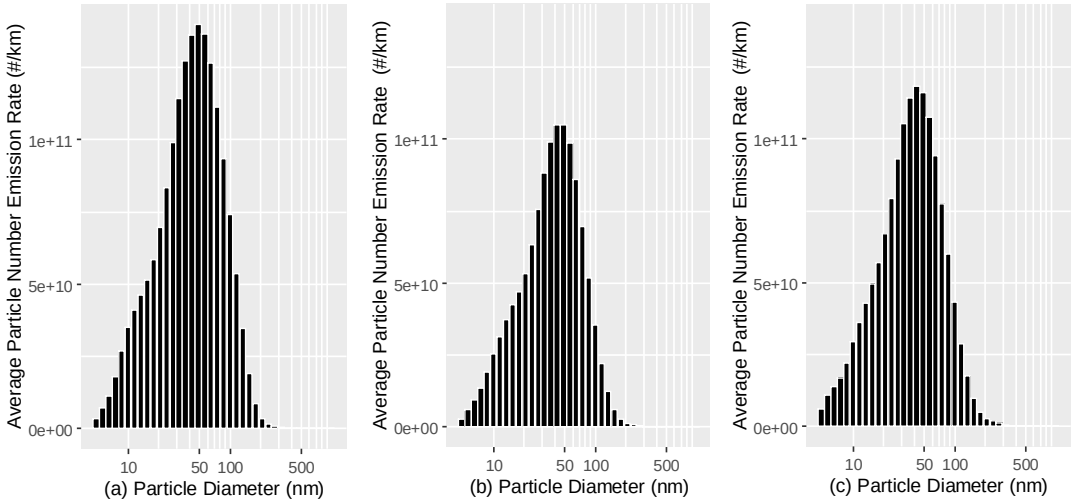

Figure 7.22 Total WLTC PNSD results under E0 (a), E10 (b), B10 (c) fuelling.

7.6 Unregulated gaseous pollutants

When considering the emissions resulting from the use of biofuels, it is important to not only consider the pollutants currently regulated in legislation, but also the toxic pollutants that are not currently regulated, in order to ensure that the emissions of these are not high compared to conventional gasoline. In order to study the unregulated gaseous pollutants, modal FTIR measurements were taken over WLTC chassis dynamometer testing and on-road RDE testing. Each error bar is the standard error of the respective mean.

Figure 7.23a and Figure 7.23b show a range of unregulated pollutant emission factors over both urban (phase 1) WLTC and total WLTC. Error bars are the standard error of the two repeats each for E10 and B10. These plots indicate that urban emissions of NH_3, methane and N_2O all decrease under E10 and

B10 use (60% and 30%, 19% and 14%, 10% and 8% respectively), with E10 showing the greatest reduction. Over the WLTC cycle as a whole, an NH_3 reduction benefit from E10 and B10 both remained. These NH_3 results are in agreement with the conclusions of Suarez-Bertoa and Astorga (2016) for their MHEV, in contradiction to their PHEV. The emissions of methane and N_2O over the complete WLTC are approximately equal between fuel types. Agarwal et al. (2015) and Costagliola et al. (2013) also found inconclusive results for methane, while Agarwal et al. (2015) also found a decrease in N_2O under ethanol blends, for their PFI research engine, visible in Figure 7.27. No previous literature has been found to study N_2O under butanol blends.

Of the VOCs studied, formaldehyde shows increased emissions under E10 in urban driving but decreased emissions overall, compared to E0 (17% increase in phase 1, 28% decrease in total), in agreement with Agarwal et al. (2015) from steady state SI research engine work (shown in Figure 7.27), and Karavalakis et al. (2012) using an SI on chassis dynamometer. B10, meanwhile, is consistently higher by 30% and 20% for phase 1 and total WLTC respectively. The increase in formaldehyde witnessed under B10 fuelling compared to gasoline is in agreement with the general consensus, but the literature to date is divided with regard to the relationship between butanol and ethanol. It should be noted, however, that the uncertainties on these low readings are large.

For 1,3-butadiene, both E10 and B10 appear to give slightly lower urban emission results (25 and 30% lower than E0, respectively), with this difference becoming quite large over the WLTC as a whole (73% and 41% lower). This finding is in agreement with the majority of previous literature where a relationship could be ascertained. Acetylene and ethylene emissions from E10 appear approximately equal to those from E0 for both urban and total WLTC, while B10 shows a 66% and 34% increase in phase 1 for acetylene and ethylene respectively, with 34% and 23% respective increases over the total WLTC (but with large uncertainties on all values). Agarwal et al. (2015) witnessed a decrease in acetylene and ethylene under ethanol blends compared to gasoline, but it is unsurprising that the biofuel blend has been shown to be less influential than other factors, such as engine activity, when considering HEVs on chassis dynamometer testing. The RDE results presented below, however, disagree with the WLTC results, and are in agreement with Agarwal et al. (2015). The increase in ethylene and acetylene under B10 compared to E10 matches the same trend for 25% fuelling

presented by Broustail et al. (2012) from a single cylinder PFI research engine.

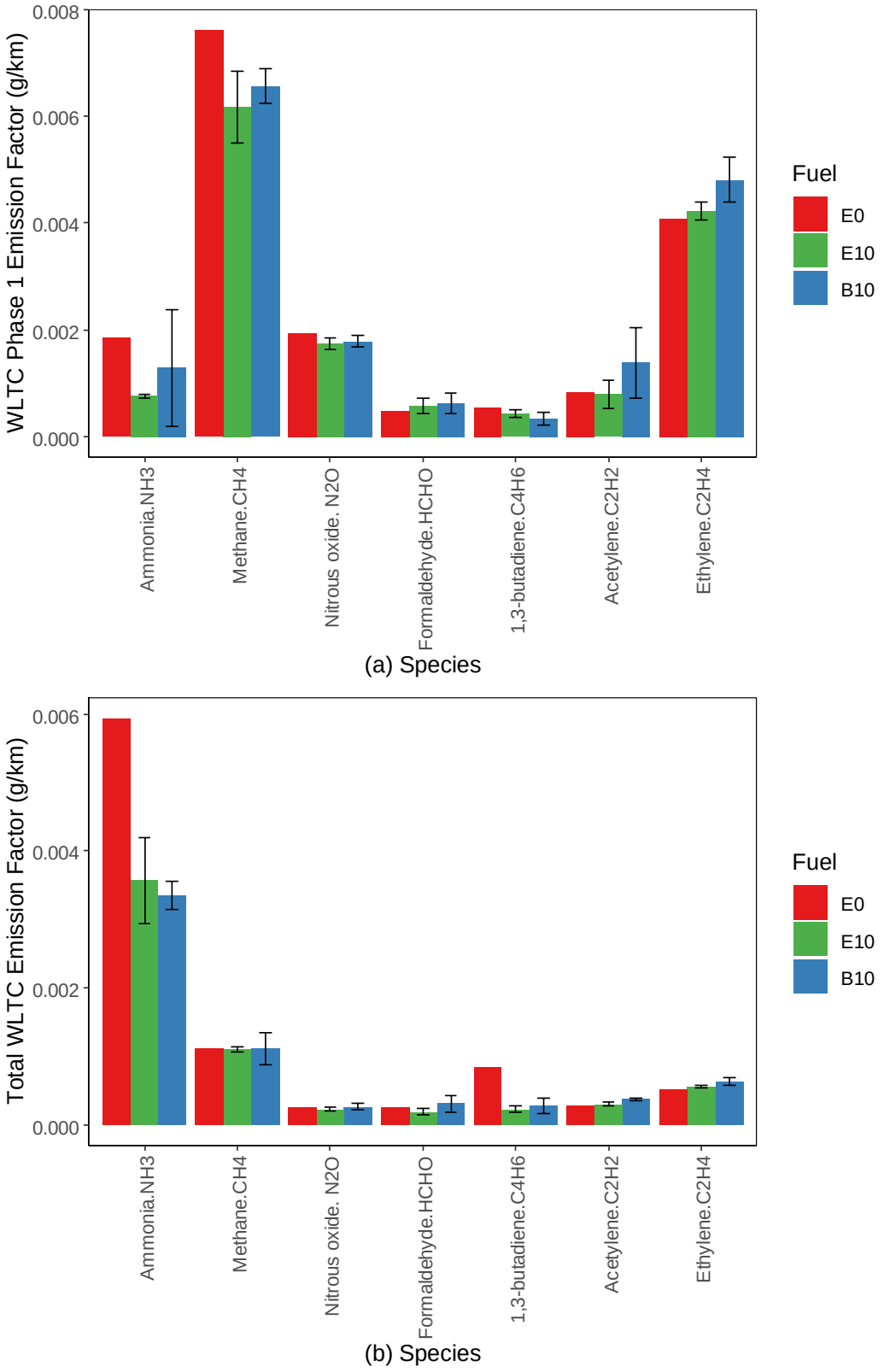

Figure 7.23 (a) Urban (phase 1) and (b) total WLTC emission factors for a range of unregulated gaseous pollutants from E0, E10 and B10 fuels.

A wider range of unregulated pollutants were measured in RDE testing of the same vehicle. The sensitivity of the portable FTIR used for the on-road testing was lower, resulting in only the urban phase having non-negligible emissions for all tested pollutants, except for NH_3 (depicted in Figure 7.25). It should also be noted that the uncertainties under RDE testing are considerable, and any conclusion based on these RDE tests is only indicative and not wholly reliable.

Figure 7.24 gives the urban RDE emission rates of the non-VOC species for E0, E5, E10 and B10 fuelled HEV tests. The results indicate that N_2O remains approximately the same under E10 fuelling as E0 and E5 fuelling (unlike Agarwal et al. (2015) who presented a decrease, visible in Figure 7.27). The uncertainties on the E10 result currently presented are large. The B10 result, however, suggests that N_2O emissions decrease slightly compared to E0 and are approximately the same as E5. Methane emissions show mixed results with large uncertainties, which is the same as many previous studies. Methane does not appear to be a pollutant of new concern with increased biofuel blending. NH_3 emissions decreased slightly under E10 blends but remained similar under B10 fuelling, compared to gasoline and E5. SO_2 results may show increased emissions under B10, and less-so, E10, but uncertainties are large. Agarwal et al. (2015) also found inconclusive results regarding SO_2.

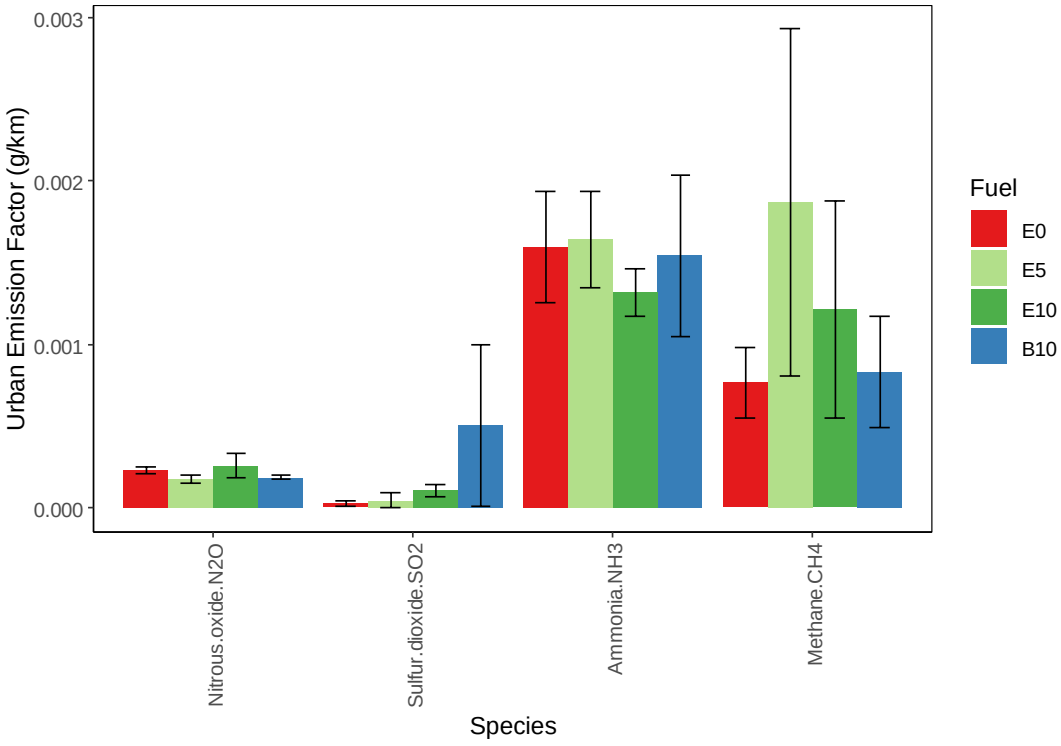

Figure 7.24 Average urban RDE emission factors for a range of unregulated gaseous pollutants from HEV tests utilising E0, E5, E10 and B10 fuels.

Figure 7.25 shows the emission of NH_3 for all three phases and total RDE test, in agreement with the findings of the WLTC testing. The distribution is similar across all phases and suggests decreased emissions from biofuels, with E10 bringing the largest decrease of 28% overall (compared to 5% for B10). These NH_3 results are again in agreement those of with the MHEV in Suarez-Bertoa and Astorga (2016), and in contradiction with their PHEV.

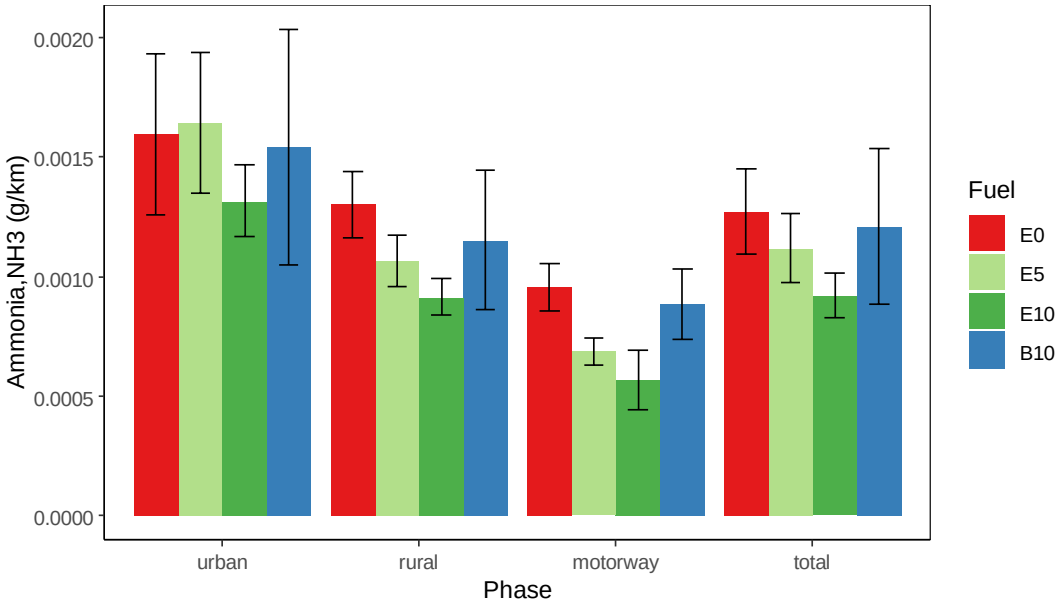

Figure 7.25 Average NH_3 emission factors for each phase of RDE testing of an HEV utilising E0, E5, E10 and B10 fuels.

Figure 7.26a and Figure 7.26b show a selection of VOC emissions from RDE testing, plotted on two separate graphs for easy visualisation. Results indicate that increased use of biofuels leads to decreased ethane, propane, hexane, benzene, acetylene and acetic acid emissions. Agarwal et al. (2015) also witnessed a trend of decreased benzene, acetylene and acetic acid with ethanol blending, but saw a slight increase of propane in their study. These results of Agarwal et al. (2015) are shown in Figure 7.27. E10 and B10 have similar emissions levels for all except acetic acid, where B10 were closer to E0 levels than E10, and acetylene, where no emissions under B10 were seen. Ethylene emissions increased gradually under increased biofuel, with B10 emissions being greater than E10. This finding for butanol is in agreement with Ratcliff et al. (2013).

Results for formaldehyde were mixed, with E5 giving smaller emissions than E0, E10 giving (32%) larger emissions, and B10 giving similar emissions. Agarwal et al. (2015) also witnessed some variation in formaldehyde results for ethanol blends (as presented in Figure 7.27) and Karavalakis et al. (2012)

noted that their trend of increasing formaldehyde with ethanol was weak. Kalita et al. (2016) reported decreased emissions from B10 compared to gasoline, as can be seen in Figure 7.29a, while Costagliola et al. (2013) found increased emissions under B10 compared to gasoline but lower emissions compared to E10. The currently presented results agree with those of Costagliola et al. (2013) as displayed in Figure 7.28.

1,3-Butadiene appears relatively similar or slightly smaller under increased ethanol fuelling, but over double under B10 fuelling (118% higher), than E0 fuelling. Agarwal et al. (2015) also witnessed a trend of decreased 1,3-butadiene with ethanol blending as can be seen in Figure 7.27, while Karavalakis et al. (2012) and Ratcliff et al. (2013) both reported no clear trend. Ratcliff et al. (2013) reported no clear trend in 1,3-butadiene from their chassis dynamometer testing, so this is a new result.

Acetaldehyde shows much larger emissions (1100% increase) under ethanol fuelling, and the increase appears to increase with mixing proportion. This is in agreement with Suarez-Bertoa and Astorga (2016) for their PHEV (they saw no change for their MHEV). Karavalakis et al. (2012) also found distinct increases in acetaldehyde with ethanol blends from SI chassis dynamometer testing. With regard to SI research engines, Varde et al. (2007) found that acetaldehydes increase with ethanol blend, but did not see such a large difference at 10% blending, while Agarwal et al. (2015) (Figure 7.27) did see a noticeable increase at E15. The results presented in Figure 7.26b therefore agree with Agarwal et al. (2015). B10 also caused a large increase in acetaldehyde emissions (790% increase) in agreement with Kalita et al. (2016) as displayed in Figure 7.29b. The increase is a little smaller than the increase under E10, in agreement with Ratcliff et al. (2013) and Costagliola et al. (2013), the latter results of which are displayed in Figure 7.28.

Unsurprisingly, ethanol emissions increase with ethanol content in the fuel (in agreement with Suarez-Bertoa and Astorga (2016)), and are not seen for any of the E0 or B10 tests, which agrees with the trend in Ratcliff et al. (2013).

The increase in benzene and ethylene, under B10 compared to E10 matches the same trend for 25% fuelling presented by Broustail et al. (2012) from a single cylinder PFI research engine. However, this study found B10 also gave higher emissions of formaldehyde and acetylene than E10, in contradiction with the RDE findings (but in agreement with the WLTC findings above).

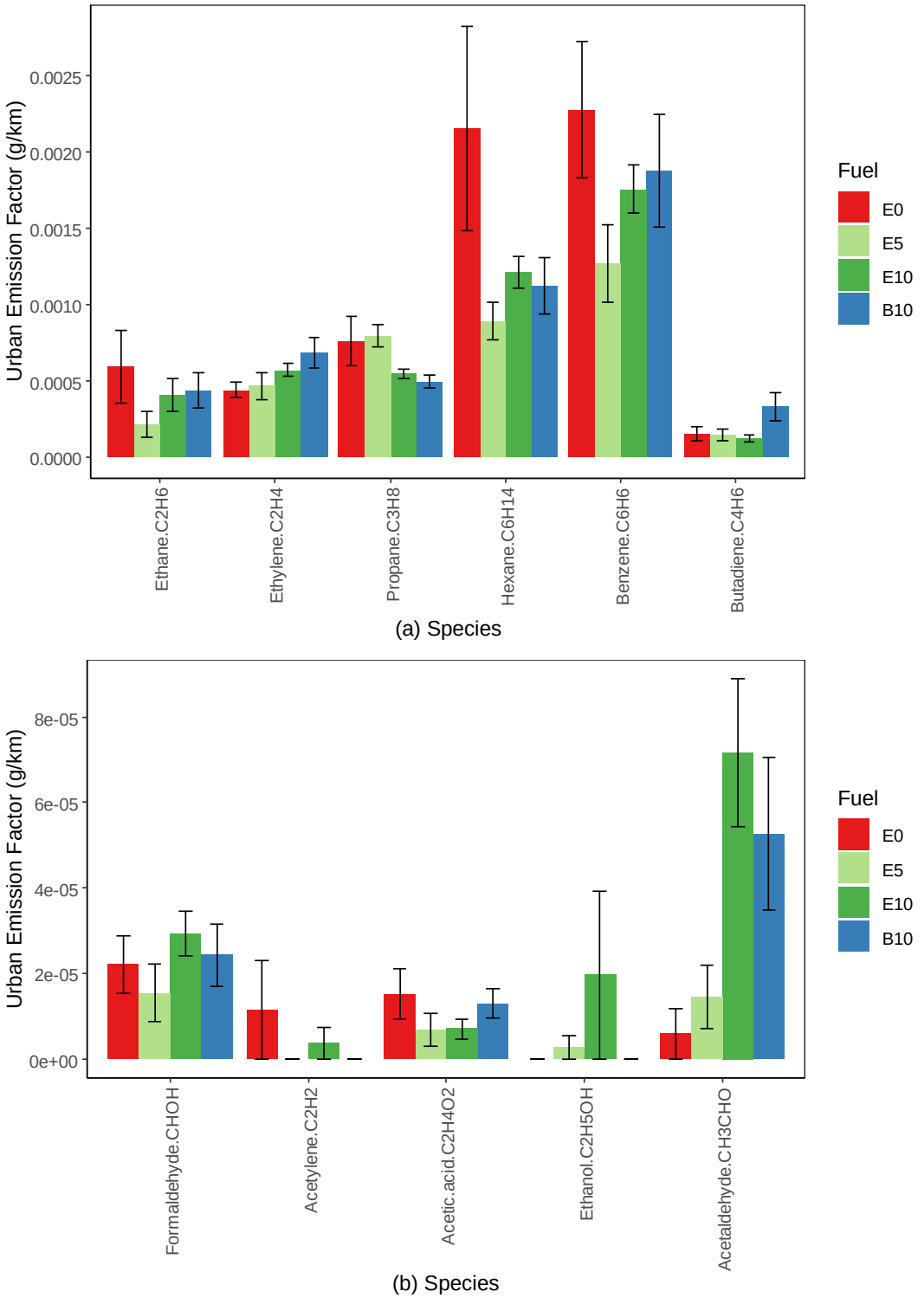

Figure 7.26 Average urban RDE emission factors for a range of unregulated gaseous VOC pollutants arising from HEV tests utilising E0, E5, E10 and B10 fuels.

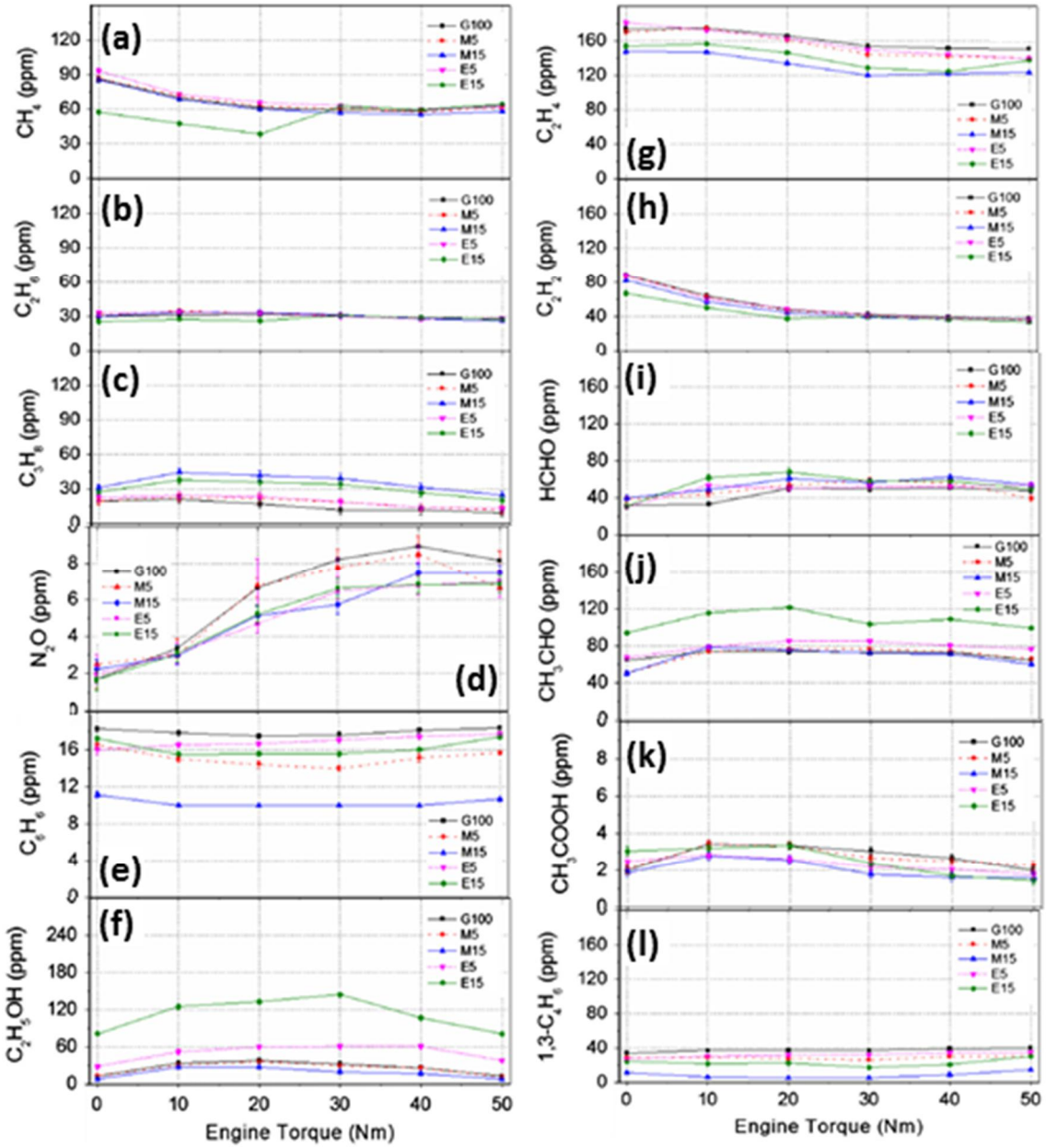

Figure 7.27 A range of unregulated pollutant species emitted from the tailpipe of a PFI engine under E0, E5 and E15 fuels, presented by Agarwal et al. (2015) (edited). (a) methane, (b) ethane, (c) propane, (d) nitrous oxide, (e) benzene, (f) ethanol, (g) ethylene, (h) acetylene, (i) formaldehyde, (j) acetaldehyde, (k) acetic acid, (l) 1,3-butadiene.

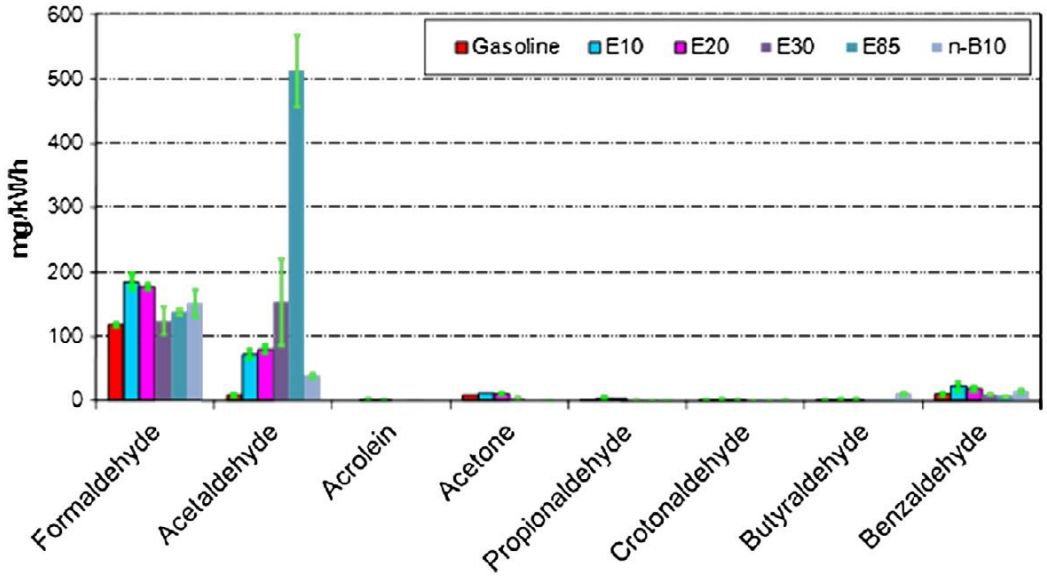

Figure 7.28 Engine-out carbonyl species emissions measured under E0, E10 and B10 fuel blends from an SI vehicle as presented by Costagliola et al. (2013).

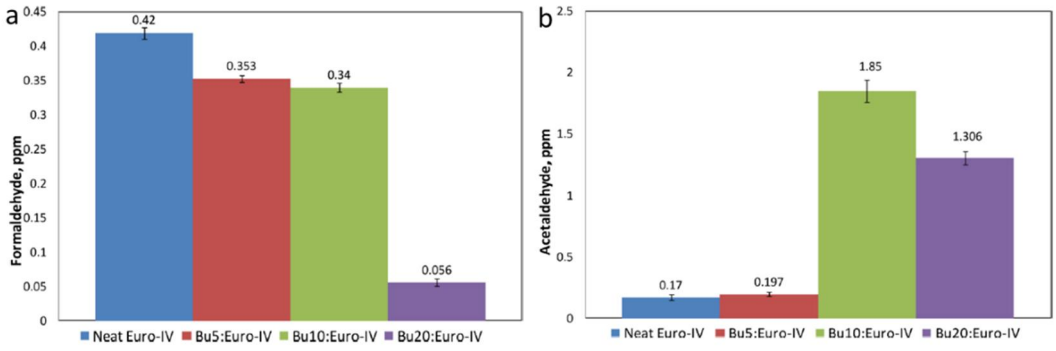

Figure 7.29 (a) formaldehyde and (b) acetaldehyde emissions from a PFI vehicle performing an NEDC test as presented by Kalita et al. (2016).

7.7 Chapter 7 Summary

Through the testing performed over WLTC and RDE tests, it has been confirmed that E10 results in reduced CO and PN emissions compared to E0 gasoline fuel for HEVs. The replacement of gasoline with B10 would also bring about decreases of these pollutants, but not to as great a degree as E10. The RDE results indicate that the decrease in the real world may not be as great as the chassis dynamometer type approval results show. However, this could be an artefact caused by the increased distance of the RDE test minimising the impact of the cold start section, where most of the difference lies. With

regard to NO_x and THC, though both have shown comparable results between fuels for WLTC chassis dynamometer testing, there is some indication that NO_x from HEVs in real-world driving may decrease, by approximately equal percentages for both E10 and B10, compared to E0. The PN emissions over the WLTC cycle showed that the HEV has similar E10 and B10 trends to previous literature for SI ICEs; PN decreases markedly under E10 and B10 use compared to E0 gasoline. However, the HEV has not shown these same PN trends under RDE testing. This is because of the HEVs dependence of PN on engine activity (see Chapter 6 Section 6.3.2); the PN results are very susceptible to differences in any other variables that change the engine speed trace of the vehicle (for example if the initial SOC is different, or the velocity trace is different). This fact is important to note when assessing future experimental HEV PN results.

Additionally, through chassis dynamometer WLTC and on-road RDE testing, it has been demonstrated that the increased use of E10 reduces the majority of unregulated gaseous pollutant emissions, but increases the emission of ethanol, acetaldehyde and formaldehyde. This is in agreement with the vast majority of previous research from both PFI and GDI SI ICE vehicles. Chapter 6 showed that the hybrid nature of HEVs does not impact any of the unregulated pollutant emissions studied, while the current chapter has shown that this is true of both E10 and B10 as well. Furthermore, it has been demonstrated that this HEV sits in between the emissions levels of a PHEV and an MHEV from previous WLTC testing work (Suarez-Bertoa and Astorga, 2016). With regard to B10, it has been shown, for the first time through RDE testing, that formaldehyde and acetaldehyde do not pose any increased risk from the use of B10 than they do from the use of E10. In fact, the evidence points to a slight decrease in the emissions from the use of B10, when compared to E10. It has been indicated that 1,3-butadiene and ethylene may increase under the use of B10 compared to both gasoline and E10, but results are inconclusive, with high uncertainty, so more research is required on these pollutants to draw reliable conclusions.

The next chapter will conclude this thesis by summarising the main findings of this work.

Chapter 8
Conclusion

8.1 Summary

Increased vehicle electrification and biofuel blending both provide promising ways to minimise net CO_2 emissions and therefore reduce the transportation industry's impact on global warming. However, it is important to ensure that these technologies do not further the degradation of local air quality through harmful tailpipe emissions. It is also vital that the type approval test procedures are robust enough to ensure that this is not allowed to occur. The main aim of this work was therefore to investigate the regulated and unregulated pollutant emissions from HEVs, including those using biofuel blends, and to probe how effective the legislated WLTC and RDE tests are at representing their pollutant emission levels.

The objectives of this work, designed to answer the research questions outlined in Chapter 2 Section 2.10, are outlined below for clarity.

1. Investigate HEV drive properties, characteristics and reported emissions resulting from RDE testing compared to legislative type approval test cycles (WLTC and obsolete NEDC), and to real-world on-road driving.
2. Investigate the effect that different packages of RDE legislation have on reported emissions of an HEV.
3. Study in detail the different elements of an HEV that make its behaviour different from a CV, and to qualify and quantify the effect that these behaviours have on the tailpipe emissions.
4. Investigate the impact that the use of low percentage ethanol and butanol blends have on the emissions from an HEV.

These objectives are satisfied sequentially in the results chapters (Chapters 4, 5, 6 and 7) by achieving each of the relevant tasks set in Chapter 2 Section 2.11.3. The main results and contributions to the field of knowledge are outlined below.

8.1.1 Impact of type approval test cycles on emissions

Chapter 4 investigated the properties and emissions resulting from an HEV tested according to the RDE, WLTC and NEDC regulations. The CO_2

emissions of the HEV studied in this chapter over the different test cycles have trends generally in line with previous literature for CVs. The RDE results were approximately 9.5% higher than both the WLTC and the NEDC. The CO and PN emissions of the HEV showed high sensitivity to the number of times its engine restarted, meaning that the number of vehicle stops and transients per kilometre had a greater impact on the emissions than has been seen for CVs in previous literature. This resulted in 66% and 71% lower CO and PN values on the RDE compared to WLTC. The HEV has proven to be less impacted by high load events than CVs, so the WLTC and RDE cycles do not result in higher NO_x emissions, as other literature on CVs has generally witnessed. Instead, the proportionately smaller contribution of cold start has meant that the NO_x emissions are 88% lower for HEVs on the WLTC than NEDC, and RDE is 58% lower than WLTC. No other literature was found to directly compare NEDC, WLTC and RDE Package 4 test results.

Detailed study of the PN size distribution for HEVs across the different test cycles showed that the engine restart events of the HEV result in a Gaussian distribution with a maximum centred around 50nm diameter. The more constant engine operation has a much lower magnitude bimodal distribution with maxima at diameters of 15nm and 110nm. These characteristics result in the RDE having a markedly different distribution to the WLTC and NEDC (the RDE being less Gaussian than the WLTC and NEDC, with a less distinct maximum).

The suitability of the 23nm PN size cut-off for HEVs has also been assessed in unprecedented detail, furthering the knowledge in this field. By studying the proportion of particles of smaller diameter than 23nm and comparing this with values in the literature for CVs, it can be inferred that a tightening of the cut-off diameter currently in the legislation would result in a greater number of particles being detected for HEVs (a 25.2% increase in WLTC PN with 10nm cut-off compared to 23nm cut-off), but by a smaller margin than for CVs.

8.1.2 Real Driving Emissions (RDE) test properties and results

Chapter 5 gave a very detailed investigation into the RDE drive cycle: The drive cycle characteristics and emissions profiles resulting from the RDE test cycle were studied in detail, analysing how the latest version (Package 4) of the regulation differs from earlier packages, particularly with regard to the reported emissions from a range of SI vehicles. Package 4 has shown to be more closely aligned with real-world driving than the older packages.

However, the RDE test still does not accurately represent the highly congested conditions that are so common in city centres today where the greatest air quality impacts on health are found; the RDE test gave 8.6%, 78%, 54% and 34% lower emission factors of CO_2, CO, NO_x and PN respectively, compared to the City Centre test. In particular, HEV behaviours have led to an even larger quantity of emissions being produced in these styles of driving currently untouched by either the WLTC or RDE tests.

The differences of the RDE on-road testing over the WLTC was further elucidated by contrasting an on-road test drive cycle against the same test cycle repeated on a chassis dynamometer. The more varied requirements on the vehicle during on-road driving resulted in a wider VSP distribution. On-road testing had not only higher CO_2 emissions (31% and 36% higher for rural and motorway styles) and therefore fuel consumption, but also higher emissions of NO_x pollution (26% and 58% higher for rural and motorway) as the load on the engine increased. To the author's best knowledge, this is the first such investigation published that directly compares a velocity trace driven on roads with a repeat of it on a chassis dynamometer.

8.1.3 Hybrid electric vehicle (HEV) behaviour and emissions

Chapter 6 studied the main behaviours of interest for HEVs, namely those surrounding catalyst light-off and lambda control during engine stop-start (also called stop-and-go) behaviour. The study of TWC behaviour showed for the first time that although HEVs can have longer warm-up times, the TWC retains the ability to quickly reach light-off; the TWC reached 90% conversion efficiency within approximately 50s for CO, NO_x and THC. Additionally, the HEV has proven to have high resistance to cooling effects, allowing it to maintain its conversion efficiency after periods of engine-off.

This chapter found that some pollutant emission penalties associated with engine stop-start events are considerable. The tendency for the vehicle to enter a fuel enrichment strategy on restart has been shown to increase overall emissions of CO, THC, ammonia, methane and PN. Comparison of an HEV with a comparable CV counterpart showed that the CO emissions were slightly increased by the stop-start behaviour (20% increase), but the PN emissions of the HEV were increased by over an order of magnitude due to this behaviour (a 1622% increase). For PN, this penalty increases total emission factors above type approval limits, giving a clear indication that all HEVs (not just GDIs, as is currently the case) should have their PN emissions limited by

type approval legislation. Ammonia is not currently limited at light duty type approval, so the results presented in this chapter contribute to the evidence that it may be worthwhile adding limits for this species into the type approval regulations.

The initial battery SOC has proven to affect the operating strategy of the vehicle, causing the engine to be engaged for a longer period of time and undergo more stop-start events under lower initial SOCs. This in turn means that the lower the initial battery SOC, the shorter the cold start period. This has been shown to affect the CO_2 very clearly, and some small effects on pollutant emissions were also seen. There is indication that for the pollutant gases affected by the TWC, having optimum SOCs of around 60% will lead to the lowest levels of emissions, striking the best balance between engine activity and TWC light-off times. For PN, due to the decreased stop-start behaviour, higher initial SOCs have lower associated emissions. Though the type approval legislation dictates methods to account for differences in net SOC change across a test in relation to CO_2 emissions, there is no prescription for the initial hybrid battery SOC of (NOVC) HEVs, nor any adjustment to pollutant emissions due to differences in net SOC change across a test, leaving an area of weakness in the legislation.

8.1.4 Influence of biofuels on HEV emissions

Chapter 7 investigated the pollutant emissions resulting from the use of pure (E0) gasoline, E5, E10 and B10. Through chassis dynamometer WLTC testing, Chapter 7 confirmed that E10 use results in 28% lower CO and 41% lower PN emissions compared to E0 for HEVs, similar to previous literature results for CVs. The replacement of gasoline with B10 would also bring about decreases of these pollutants, but not to as great a degree as E10 (22% lower CO and 21% lower PN from B10, compared to E0). Studying the transient events, these tendencies were most visible during engine-restart events for the HEV. The HEV RDE results indicate that at high vehicle speeds, CO may increase under E10 and, to a lesser degree, B10. Inconclusive PN emissions over the RDE demonstrated that making conclusions about the impact of biofuels on HEV PN emissions from real-world tests is unreliable because the most influential factor is the number of engine re-ignitions. This fact is important to note when assessing future experimental HEV PN results.

With regard to NO_x and THC, though both showed comparable results between fuels for WLTC chassis dynamometer testing, there was some

indication from RDE testing that NO_x emissions from HEVs may decrease for both E10 and B10, compared to E5 and E0 gasoline; E10 and B10 led to 24% and 18% respective decreases of NO_x compared to E0 over the RDE.

Additionally, through chassis dynamometer WLTC and on-road RDE testing, Chapter 7 demonstrated that the increased use of E10 reduced the majority of unregulated gaseous pollutant emissions, but increased the emissions of acetaldehyde and formaldehyde (by 1112% and 32% respectively in the urban section of the RDE), as well as ethanol. This trend is in agreement with the vast majority of previous research from SI vehicles. Chapter 6 showed that the hybrid nature of HEVs do not greatly impact any of the unregulated pollutant emissions studied, and Chapter 7 showed that this is true of both E10 too. With regard to butanol, it was shown for the first time through RDE testing that B10 use does not pose any increased risk to the emissions of formaldehyde and acetaldehyde than is posed through the use of E10; B10 resulted in 792% and 9.8% respective decreases compared to E0 in the urban section of the RDE.

Further, it was demonstrated that this HEV generally sits between the emissions levels of a PHEV and a mild HEV from previous WLTC testing work, which is an expected but important new finding.

8.2 Future work

There are various limitations to the project outlined in this thesis, and these will now be discussed, along with suggestions for further work to remedy these and build on the knowledge already attained.

First, the majority of the research in this thesis was gathered from a single Third Generation Toyota Prius (Euro 5) HEV research vehicle. Though this allowed modification of the vehicle for unprecedented depths of behaviour analysis, the results found should be compared with a wider range of HEVs, including Euro 6 models, to investigate whether the conclusions are applicable to other HEVs, including newer models.

Second, the direct comparison of an HEV with its ICE counterpart was not included in detail during this investigation (though such data was used to validate some conclusions regarding HEV behaviour and emissions in Chapter 6). Therefore in future a deeper investigation into HEV emissions is

possible by making further comparisons between pairs of counterpart HEVs and ICEs.

Third, there were only three test routes used for the RDE testing, and only one of these was repeated multiple times for the same vehicle and with the same driver. This had advantages by allowing a more significant number of RDE-compliant tests to be performed, lowering the uncertainty in the conclusions, particularly regarding biofuel emission effects. However, given that globally the RDE test will be performed in many different locations, and by many different drivers and testing authorities, it would also be useful to perform a broader study analysing the results from more varied RDE tests.

Fourth, the FTIR utilised to measure on-road emissions was not very sensitive at 1Hz frequency, making measurements after cold start difficult. In future, it would be beneficial to conduct further work into the unregulated emissions from an HEV using an FTIR more specialised for on-road transient measurement. It would be particularly beneficial to incorporate this into a biofuels investigation, where the unregulated emissions pose the greatest interest.

Fifth, the lowest sampling frequency that was achievable by all of the various pieces of equipment was 1Hz. The future investigation of transient HEV behaviour and emissions at frequencies greater than 1Hz would allow for even deeper understanding of the HEV behaviours discussed in Chapter 7.

Sixth, the PN and size distribution data was gathered with no VPR system. Therefore, the data is not entirely representative of certification PN values, as the volatiles had not been removed before measurement. In order to conduct a more accurate comparison between RDE and WLTC test results, as well as better analysis of the impact resulting from extension of the PN cut-off from 23nm to 10nm, it would be beneficial to conduct an investigation utilising a VPR system in accordance with the PMP.

Seventh, the investigation into the effect of the chassis dynamometer was only possible with CO_2 and NO_x emissions measurement, due to equipment restraints. In the future it would be beneficial to repeat such an investigation, but with a full suite of emissions measurement equipment on board.

Bibliography

Abarham, M., Hoard, J.W., Assanis, D., Styles, D., Sluder, C.S. and Storey, J.M.E. 2010. An analytical study of thermophoretic particulate deposition in turbulent pipe flows. *Aerosol Science and Technology*. **44**(9), pp.785–795.

Adachi, M. and Nakamura, H. 2013. *Engine Emissions Measurement Handbook*.

Agarwal, A.K. 2007. Biofuels (alcohols and biodiesel) applications as fuels for internal combustion engines. *Progress in Energy and Combustion Science*. **33**(3), pp.233–271.

Agarwal, A.K., Shukla, P.C., Gupta, J.G., Patel, C., Prasad, R.K. and Sharma, N. 2015. Unregulated emissions from a gasohol (E5, E15, M5, and M15) fuelled spark ignition engine. *Applied Energy*. **154**, pp.732–741.

Akimoto, H. 2003. Global air quality and pollution. *Science (New York, N.Y.)*. **302**(5651), pp.1716–1719.

Al-Hasan, M. 2003. Effect of ethanol-unleaded gasoline blends on engine performance and exhaust emission. *Energy Conversion and Management*. **44**(9), pp.1547–1561.

Alvarez, R. and Weilenmann, M. 2012. Effect of low ambient temperature on fuel consumption and pollutant and CO 2 emissions of hybrid electric vehicles in real-world conditions. *Fuel*. **97**, pp.119–124.

Amjad, S., Neelakrishnan, S. and Rudramoorthy, R. 2010. Review of design considerations and technological challenges for successful development and deployment of plug-in hybrid electric vehicles. *Renewable and Sustainable Energy Reviews*. **14**(3), pp.1104–1110.

Anderson, J., Rask, E., Lohse-Busch, H. and Miers, S. 2014. A Comparison of Cold-Start Behavior and its Impact on Fuel Economy for Advanced Technology Vehicles. *SAE International Journal of Fuels and Lubricants*. **7**(2), pp.427–435.

Anderson, J.E., Dicicco, D.M., Ginder, J.M., Kramer, U., Leone, T.G., Raney-Pablo, H.E. and Wallington, T.J. 2012. High octane number ethanol-gasoline blends: Quantifying the potential benefits in the United States. *Fuel*. **97**, pp.585–594.

Anderson, J.E., Hardigan, P.J., Ginder, J.M., Wallington, T.J. and Baker, R.E. 2009. Implications of the energy independence and security act of 2007 for the US light-duty vehicle fleet. *SAE Technical Papers*.

Anderson, L.G. 2012. Effects of Biodiesel Fuels Use on Vehicle Emissions. *Journal of Sustainable Energy & Environment*. **3**, pp.35–47.

Andrews, G.E., Xu, J. and Sale, T. 2002. Influence of catalyst and exhaust system on particulate deposition and release from an IDI diesel passenger car under real world driving. *SAE Technical Papers*. (724).

Atsumi, S., Hanai, T. and Liao, J.C. 2008. Non-fermentative pathways for synthesis of branched-chain higher alcohols as biofuels. *Nature*. **451**(7174), pp.86-U13.

AVL 2010. AVL M.O.V.E GAS PEMS 493 493. , pp.1–5.

AVL 2020. AVL SESAM i60 FT SII. [Accessed 10 August 2020]. Available from: https://www.avl.com/web/guest/-/avl-sesam-i60-ft-multi-component-exhaust-measurement-system.

AVL Emission Testing Systems 2016. AVL Emission Testing Handbook – 2016. , p.80.

Bayindir, K.C., Gozukucuk, M.A. and Teke, A. 2011. A comprehensive overview of hybrid electric vehicle: Powertrain configurations, powertrain control techniques and electronic control units. *Energy Conversion and Management*. **52**(2), pp.1305–1313.

BBC 2020. Petrol and diesel car sales ban brought forward to 2035. *BBC News*. [Online]. Available from: https://www.bbc.co.uk/news/science-environment-51366123#:~:text=A ban on selling new,virtually zero carbon by 2050.

Bergthorson, J.M. and Thomson, M.J. 2015. A review of the combustion and emissions properties of advanced transportation biofuels and their impact on existing and future engines. *Renewable and Sustainable Energy Reviews*. **42**, pp.1393–1417.

Bielaczyc, P., Merkisz, J., Pielecha, J. and Woodburn, J. 2018. A Comparison of Gaseous Emissions from a Hybrid Vehicle and a Non-Hybrid Vehicle under Real Driving Conditions. *SAE Technical Papers*. **2018**-**April**, pp.1–11.

Bielaczyc, P., Szczotka, A. and Woodburn, J. 2014. An overview of emissions of reactive nitrogen compounds from modern light duty vehicles featuring SI engines. *Combustion Engines*. **159**(4159), pp.48–53.

Bodisco, T. and Zare, A. 2019. Practicalities and driving dynamics of a real driving emissions (RDE) Euro 6 regulation homologation test. *Energies*. **12**(12).

Borrion, A.L., McManus, M.C. and Hammond, G.P. 2012. Environmental life cycle assessment of bioethanol production from wheat straw. *Biomass and Bioenergy*. **47**, pp.9–19.

Brook, R.D., Franklin, B., Cascio, W., Hong, Y., Howard, G., Lipsett, M., Luepker, R., Mittleman, M., Samet, J., Smith, S.C. and Tager, I. 2004. Air pollution and cardiovascular disease: A statement for healthcare professionals from the expert panel on population and prevention science of the American Heart Association. *Circulation*. **109**(21), pp.2655–2671.

Broustail, G., Halter, F., Seers, P., Mor??ac, G. and Mounaim-Rousselle, C. 2012. Comparison of regulated and non-regulated pollutants with iso-octane/butanol and iso-octane/ethanol blends in a port-fuel injection Spark-ignition engine. *Fuel*. **94**, pp.251–261.

Cambustion 2009. Particulate Mass Measurement with DMS Series Fast

Spectrometers. , pp.1–8. Available from: https://www.cambustion.com/sites/default/files/instruments/DMS/dms01v05.pdf.

Canakci, M., Ozsezen, A.N., Alptekin, E. and Eyidogan, M. 2013. Impact of alcohol–gasoline fuel blends on the exhaust emission of an SI engine. *Renewable Energy*. **52**, pp.111–117.

Cant, N.W., Angove, D.E. and Chambers, D.C. 1998. Nitrous oxide formation during the reaction of simulated exhaust streams over rhodium, platinum and palladium catalysts. *Applied Catalysis B: Environmental*.

Chatterton, T.J., Hayes, E.T. and Longhurst, J.W.S. 2006. Managing air quality - Are we doing enough? *In*: *WIT Transactions on Ecology and the Environment*., pp.155–164.

Chen, R.H., Chiang, L. Bin, Chen, C.N. and Lin, T.H. 2011. Cold-start emissions of an SI engine using ethanol-gasoline blended fuel. *Applied Thermal Engineering*. **31**(8–9), pp.1463–1467.

Cho, J., Si, W., Jang, W., Jin, D., Myung, C.-L. and Park, S. 2015. Impact of intermediate ethanol blends on particulate matter emission from a spark ignition direct injection (SIDI) engine. *Applied Energy*. **160**, pp.592–602.

Christenson, M., Loiselle, A., Karman, D. and Graham, L.A. 2007. The Effect of Driving Conditions and Ambient Temperature on Light Duty Gasoline-Electric Hybrid Vehicles (2): Fuel Consumption and Gaseous Pollutant Emission Rates *In*: *SAE Technical Paper* [Online]. SAE International. Available from: http://dx.doi.org/10.4271/2007-01-2137.

Ciuffo, B., Marotta, A., Tutuianu, M., Anagnostopoulos, K., Fontaras, G., Pavlovic, J., Serra, S., Tsiakmakis, S. and Zacharof, N. 2015. Development of the Worldwide Harmonized Test Procedure for Light-Duty Vehicles: Pathway for Implementation in European Union Legislation. *Journal of the Transportation Research Board*. (2503), pp 110–118.

Clarke, H. and Ainslie, D. 2019. *Road transport and air emissions* [Online]. Available from: https://www.ons.gov.uk/economy/environmentalaccounts/articles/roadtransportandairemissions/2019-09-16.

Clenci, A., Sălan, V., Niculescu, R., Iorga-Simăn, V. and Zaharia, C. 2017. Assessment of real driving emissions via portable emission measurement system. *IOP Conference Series: Materials Science and Engineering*. **252**(1).

Colvile, R.N., Hutchinson, E.J., Mindell, J.S. and Warren, R.F. 2001. The Transport sector as a source of air pollution. *Atmospheric Environment*. **35**(2001), pp.1537–1565.

Conger, M. and Holmén, B.A. 2015. Characterization of Real-World Particle Number Emissions during Reignition Events from a 2010 Light-Duty Hybrid Electric Vehicle. *Transportation Research Record: Journal of the Transportation Research Board*. **2503**(1), pp.137–146.

Costa, H.L. and Spikes, H. 2014. Effects of Ethanol Contamination on Friction and Elastohydrodynamic Film Thickness of Engine Oils. *Tribology Transactions*. **58**(1), pp.158–168.

Costagliola, M.A., De Simio, L., Iannaccone, S. and Prati, M. V. 2013. Combustion efficiency and engine out emissions of a S.I. engine fueled with alcohol/gasoline blends. *Applied Energy*. **111**, pp.1162–1171.

Crutzen, P.J., Mosier, A.R., Smith, K.A. and Winiwarter, W. 2008. N2O release from agro-biofuel production negates global warming reduction by replacing fossil fuels. *ATMOSPHERIC CHEMISTRY AND PHYSICS*. **8**(2), pp.389–395.

Cubito, C., Millo, F., Boccardo, G., Di Pierro, G., Ciuffo, B., Fontaras, G., Serra, S., Garcia, M.O. and Trentadue, G. 2017. Impact of different driving cycles and operating conditions on CO2 emissions and energy management strategies of a Euro-6 hybrid electric vehicle. *Energies*. **10**(10).

Curtis, L., Rea, W., Smith-Willis, P., Fenyves, E. and Pan, Y. 2006. Adverse health effects of outdoor air pollutants. *Environment International*. **32**(6), pp.815–830.

D'Ippoliti, D., Forastiere, F., Ancona, C., Agabiti, N., Fusco, D., Michelozzi, P. and Perucci, C. a 2003. Air pollution and myocardial infarction in Rome: a case-crossover analysis. *Epidemiology (Cambridge, Mass.)*. **14**(5), pp.528–535.

Daham, B., Andrews, G.E., Li, H., Ballesteros, R., Bell, M.C., Tate, J. and Ropkins, K. 2005. Application of a portable FTIR for measuring on-road emissions. *SAE Technical Papers*. **2005**(724).

DeCarlo, P.F., Slowik, J.G., Worsnop, D.R., Davidovits, P. and Jimenez, J.L. 2004. Particle morphology and density characterization by combined mobility and aerodynamic diameter measurements. Part 1: Theory. *Aerosol Science and Technology*. **38**(12), pp.1185–1205.

Department for Transport 2020. *Introducing E10 Petrol : Consultation*.

Department for Transport 2019. RTFO Guidance Part One: Process Guidance. , pp.1–168.

Department for Transport 2017. *RTFO Guidance Part One Carbon Sustainability Guidance* [Online]. Available from: https://www.gov.uk/government/uploads/system/uploads/attachment_data/file/604627/rtfo-guidance-part-2-carbon-sustainability-guidance-year-10.pdf.

Department for Transport 2016a. The Renewable Transport Fuel Obligations Order Proposed amendments: Moving Britain Ahead.

Department for Transport 2016b. *Vehicle Emissions Testing Programme* [Online]. Available from: https://www.gov.uk/government/uploads/system/uploads/attachment_data/file/548148/vehicle-emissions-testing-programme-web.pdf.

Department for Transport 2016c. *Vehicle Licensing Statistics : Quarter 2 (Apr*

- Jun) 2016 [Online]. Available from: https://www.gov.uk/government/uploads/system/uploads/attachment_data/file/551499/vehicle-licensing-april-to-june-2016.pdf.

Department for Transport and Driver and Vehicle Licensing Agency 2020. Cars(VEH02). [Accessed 15 August 2020]. Available from: https://www.gov.uk/government/statistical-data-sets/veh02-licensed-cars.

Department for Transport, Driver and Vehicle Standards Agency, Office for Low Emission Vehicles and Vehicle Certification Agency 2015. Policy paper 2010 to 2015 government policy: transport emissions. *GOV.UK*. [Online]. [Accessed 6 June 2017]. Available from: https://www.gov.uk/government/publications/2010-to-2015-government-policy-transport-emissions/2010-to-2015-government-policy-transport-emissions.

Dernotte, J., Mounaim-Rousselle, C., Halter, F. and Seers, P. 2010. Evaluation of Butanol-Gasoline Blends in a Port Fuel-injection, Spark-Ignition Engine. *Oil & Gas Science and Technology-Revue D Ifp Energies Nouvelles*. **65**(2), pp.345–351.

Dings, J. 2013. *Mind the Gap! Why official car fuel economy figures don't match up to reality?* [Online]. Available from: https://www.transportenvironment.org/sites/te/files/publications/Real World Fuel Consumption v15_final.pdf.

Donateo, T. and Giovinazzi, M. 2018. Some Repeatability and Reproducibility Issues in Real Driving Emission Tests. *SAE Technical Papers*. (March 2017), pp.1–16.

Duarte, G.O., Gonçalves, G.A. and Farias, T.L. 2016. Analysis of fuel consumption and pollutant emissions of regulated and alternative driving cycles based on real-world measurements. *Transportation Research Part D: Transport and Environment*. **44**, pp.43–54.

Duarte, G.O., Varella, R.A., Gonçalves, G.A. and Farias, T.L. 2014. Effect of battery state of charge on fuel use and pollutant emissions of a full hybrid electric light duty vehicle. *Journal of Power Sources*. **246**, pp.377–386.

Eastwood, P. 2008. *Particulate Emissions from Vehicles*.

Edwards, R. (Jrc/Ies), Larive, J.-F. (Concawe) and Beziat, J.-C. (Renault) 2011. *Well-to-wheels analysis of alternative fuels and powertrains in the European context Version 3c* [Online]. Available from: https://iet.jrc.ec.europa.eu/about-jec/sites/iet.jrc.ec.europa.eu.about-jec/files/documents/wtw3_wtw_report_eurformat.pdf.

Elfasakhany, A. 2014. Experimental study on emissions and performance of an internal combustion engine fueled with gasoline and gasoline/n-butanol blends. *Energy Conversion and Management*. **88**, pp.277–283.

Elfasakhany, A. 2017. Investigations on performance and pollutant emissions of spark-ignition engines fueled with n-butanol–, isobutanol–, ethanol–, methanol–, and acetone–gasoline blends: A comparative study.

Renewable and Sustainable Energy Reviews. **71**, pp.404–413.

Els, P. 2013. *Random Cycle Test vs . Portable Emission Measurement System*.

EPA 2014. Greenhouse gas emissions from a typical passenger vehicle. , pp.1–5.

European Commission 2017. FAQ - Type approval of vehicles. *Growth*. [Online]. [Accessed 20 January 2017]. Available from: http://ec.europa.eu/growth/sectors/automotive/technical-harmonisation/faq-auto_en.

European Commission and Council of the European Union 2016a. Commission Regulation (EU) 2016/427 of 10 March 2016 amending Regulation (EC) No 692/2008 as regards emissions from light passenger and commercial vehicles (Euro 6) (Text with EEA relevance). *Official journal of the European Union*. **82**(31/03/2016), pp.1–98.

European Commission and Council of the European Union 2017. Commission Regulation 2017/1154. *Official journal of the European Union*. **1154**(715), pp.708–732.

European Commission and Council of the European Union 2016b. EC. Commission Regulation (EU) 2016/646 of 20 April 2016 amending Regulation (EC) No 692/2008 as regards emissions from light passenger and commercial vehicles (Euro 6). II. *Official journal of the European Union*. **82**(31/03/2016), pp.1–98.

European Commission and Council of the European Union 2018. RDE IV: Commission Regulation (EU) 2018/1832. *Official Journal of the European Union*. **1832**(692), p.301.

Eyidogan, M., Ozsezen, A.N., Canakci, M. and Turkcan, A. 2010. Impact of alcohol-gasoline fuel blends on the performance and combustion characteristics of an SI engine. *Fuel*. **89**(10), pp.2713–2720.

Faiz, A., Weaver, C.S. and Walsh, M.P. 1996. *Air pollution from motor vehicles.*

Favre, C., Bosteels, D. and May, J. 2013. Exhaust emissions from European market-available passenger cars evaluated on various drive cycles. *SAE Technical Papers*. **6**.

Fontaras, G., Ciuffo, B., Zacharof, N., Tsiakmakis, S., Marotta, A., Pavlovic, J. and Anagnostopoulos, K. 2017. The difference between reported and real-world CO2 emissions: How much improvement can be expected by WLTP introduction? *In*: *Transportation Research Procedia*.

Fontaras, G., Pistikopoulos, P. and Samaras, Z. 2008. Experimental evaluation of hybrid vehicle fuel economy and pollutant emissions over real-world simulation driving cycles. *Atmospheric Environment*. **42**(18), pp.4023–4035.

Foster, H., Baron, R. and Bernstein, P. 2011. *Impact of the Blend Wall Constraint in Complying with the Renewable Fuel Standard* [Online]. Washington DC. Available from:

http://www.motoroilmatters.org/~/media/files/policy/fuels-and-renewables/13-march-rfs/cra_rsf2_blendwallconstraints_final_report.pdf.

Frey, H.C. 2018. Trends in onroad transportation energy and emissions. *Journal of the Air and Waste Management Association*. **68**(6), pp.514–563.

Frey, H.C., Zhai, H.B. and Rouphail, N.M. 2009. Regional On-Road Vehicle Running Emissions Modeling and Evaluation for Conventional and Alternative Vehicle Technologies. *Environmental Science & Technology*. **43**(21), pp.8449–8455.

Fuhs, A. 2009. *Hybrid Vehicles and the Future of Personal Transportation*. Taylor & Francis.

Furey, R. and King, J. 1980. Evaporative and Exhaust Emissions from Cars Fueled with Gasoline Containing Ethanol or Methyl tert-Butyl Ether. *SAE International*.

Gallus, J., Kirchner, U., Vogt, R. and Benter, T. 2017. Impact of driving style and road grade on gaseous exhaust emissions of passenger vehicles measured by a Portable Emission Measurement System (PEMS). *Transportation Research Part D: Transport and Environment*. **52**(2), pp.215–226.

Gao, Z., Daw, C.S. and Smith, D.E. 2013. Comparative Urban drive cycle simulations of light-duty hybrid vehicles with gasoline or diesel engines and emissions controls. *SAE Technical Papers*. **2**.

Gasmet Technologies 2013. Gasmet DX-Series FTIR Gas Analyser Instruction and Operating Manual. . **E1.12**, pp.1–48.

George, I.J., Hays, M.D., Herrington, J.S., Preston, W., Snow, R., Faircloth, J., George, B.J., Long, T. and Baldauf, R.W. 2015. Effects of Cold Temperature and Ethanol Content on VOC Emissions from Light-Duty Gasoline Vehicles. *Environmental Science and Technology*. **49**(21), pp.13067–13074.

German, J. 2015. *Hybrid vehicles: Trends in technology development and cost reduction* [Online]. Washington DC. Available from: http://www.theicct.org/sites/default/files/publications/ICCT_TechBriefNo1_Hybrids_July2015.pdf.

Giechaskiel, B., Commission, E., Ntziachristos, L., Wang, X. and Bergmann, A. 2014. Review of motor vehicle particulate emissions sampling and measurement : From smoke and filter mass to particle number. *Journal of Aerosol Science*. **67**(October 2017), pp.48–86.

Giechaskiel, B., Lähde, T. and Drossinos, Y. 2019. Regulating particle number measurements from the tailpipe of light-duty vehicles : The next step? *Environmental Research*. **172**, pp.1–9.

Giechaskiel, B., Mamakos, A., Woodburn, J., Szczotka, A. and Bielaczyc, P. 2019. Evaluation of a 10 nm particle number portable emissions measurement system (PEMS). *Sensors (Switzerland)*. **19**(24), pp.1–18.

Giechaskiel, B., Riccobono, F., Mendoza-Villafuerte, P. and Grigoratos, T. 2016. *Particle Number (PN) - Portable Emissions Measurement Systems (PEMS): Heavy Duty Vehicles Evaluation phase at the Joint Research Centre (JRC)*. Ispra.

Giechaskiel, B., Riccobono, F., Vlachos, T., Mendoza-Villafuerte, P., Suarez-Bertoa, R., Fontaras, G., Bonnel, P. and Weiss, M. 2015. Vehicle emission factors of solid nanoparticles in the laboratory and on the road using Portable Emission Measurement Systems (PEMS). *Frontiers in Environmental Science*. **3**(DEC), pp.1–17.

Giechaskiel, B., Vanhanen, J., Väkevä, M. and Martini, G. 2017. Investigation of vehicle exhaust sub-23 nm particle emissions. *Aerosol Science and Technology*. **51**(5), pp.626–641.

Godish, T. 1997. *Air Quality* 3rd Ed. Boca Raton: CRC Press LLC.

Graham, L. 2005. Chemical characterization of emissions from advanced technology light-duty vehicles. *Atmospheric Environment*. **39**(13), pp.2385–2398.

Granger, P. and Parvulescu, V.I. 2011. Catalytic NOx abatement systems for mobile sources: From three-way to lean burn after-treatment technologies. *Chemical Reviews*. **111**(5), pp.3155–3207.

Gu, J., Pitz, M., Schnelle-Kreis, J., Diemer, J., Reller, A., Zimmermann, R., Soentgen, J., Stoelzel, M., Wichmann, H.-E., Peters, A. and Cyrys, J. 2011. Source apportionment of ambient particles: Comparison of positive matrix factorization analysis applied to particle size distribution and chemical composition data. *Atmospheric Environment*. **45**(10), pp.1849–1857.

Gu, X., Huang, Z., Cai, J., Gong, J., Wu, X. and Lee, C.F. 2012. Emission characteristics of a spark-ignition engine fuelled with gasoline-n-butanol blends in combination with EGR. *Fuel*. **93**, pp.611–617.

Guerrieri, D.A., Caffrey, P.J. and Rao, V. 1995. Investigation into the Vehicle Exhaust Emissions of High Percentage Ethanol Blends. *SAE International*., pp.85–95.

Gurjar, B.R., Butler, T.M., Lawrence, M.G. and Lelieveld, J. 2008. Evaluation of emissions and air quality in megacities. *Atmospheric Environment*. **42**(7), pp.1593–1606.

He, B.Q., Wang, J.X., Hao, J.M., Yan, X.G. and Xiao, J.H. 2003. A study on emission characteristics of an EFI engine with ethanol blended gasoline fuels. *Atmospheric Environment*.

HEM Data 2020. HEM Data. [Accessed 24 August 2020]. Available from: http://hemdata.com/.

Hergueta, C., Bogarra, M., Tsolakis, A., Essa, K. and Ferreros, J.M. 2017. Butanol-gasoline blend and exhaust gas recirculation, impact on GDI engine out emissions. *Fuel*. **208**, pp.662–672.

Hergueta, C., Tsolakis, A., Herreros, J.M., Bogarra, M., Price, E., Simmance, K., York, A.P.E. and Thompsett, D. 2018. Impact of bio-alcohol fuels

combustion on PM morphology from GDI engines. *Applied Energy*. **230**, pp.794–802.

Hernandez, M., Menchaca, L. and Mendoza, A. 2014. Fuel economy and emissions of light-duty vehicles fueled with ethanol–gasoline blends in a Mexican City. *Renewable Energy*. **72**, pp.236–242.

Heywood, J.B. 1988. *Internal Combustion Engine Fundamentals*. McGraw-Hill Inc.

Holmén, B.A. and Sentoff, K.M. 2015. Hybrid-Electric Passenger Car Carbon Dioxide and Fuel Consumption Benefits Based on Real-World Driving. *Environmental Science and Technology*. **49**(16), pp.10199–10208.

Hooftman, N., Messagie, M., Van Mierlo, J. and Coosemans, T. 2018. A review of the European passenger car regulations – Real driving emissions vs local air quality. *Renewable and Sustainable Energy Reviews*. **86**(July 2017), pp.1–21.

Horiba 2020. Horiba. [Accessed 10 August 2020]. Available from: https://www.horiba.com/en_en/.

Horiba 2017. On-board Emissions Measurement System OBS-ONE-GS Installation and Maintenance Instruction Manual. , pp.1–77.

Houghton, J.T., Meira Filho, L.G., Callander, B.A., Harris, N., Kattenberg, A. and Maskell, K. 1996. *Climate Change 1995, The Science of Climate Change: Summary for Policymakers and Technical Summary of the Working Group I* [Online]. Cambridge. Available from: https://www.ipcc.ch/ipccreports/sar/wg_I/ipcc_sar_wg_I_full_report.pdf.

Hsieh, W.-D., Chen, R.-H., Wu, T.-L. and Lin, T.-H. 2002a. Engine performance and pollutant emission of an SI engine using ethanol–gasoline blended fuels. *Atmospheric Environment*. **36**, pp.403–410.

Hsieh, W.-D., Chen, R.-H., Wu, T.-L. and Lin, T.-H. 2002b. Engine performance and pollutant emission of an SI engine using ethanol–gasoline blended fuels. *Atmospheric Environment*. **36**(3), pp.403–410.

Hu, Z.-Y., Ding, Y.-S. and Song, H. 2015. Life cycle energy, environment, and economy assessment of gasoline and its alternative alcohol fuels *In*: *Energy and Mechanical Engineering: Proceeding of 2015 International Conference on Energy and Mechanical Engineering*. Singapore: Word Scientific, 2016, pp.131–140.

Huang, Y., Surawski, N.C., Organ, B., Zhou, J.L., Tang, O.H.H. and Chan, E.F.C. 2019. Fuel consumption and emissions performance under real driving: Comparison between hybrid and conventional vehicles. *Science of the Total Environment*. **659**, pp.275–282.

ICCT 2015. *European Vehicle Market Statistics Pocketbook 2015/16* [Online]. Berlin. Available from: http://www.theicct.org/sites/default/files/publications/ICCT_EU-pocketbook_2015.pdf.

ICCT 2017. *Real-Driving Emissions Test Procedure for Exhaust Gas Pollutant Emissions of Cars and Light Commercial Vehicles in Europe* [Online].

Available from: https://www.theicct.org/sites/default/files/publications/EU-RDE_policy-update_18012017_vF.pdf%0Ahttps://www.theicct.org/sites/default/files/publications/EU-RDE_policy-update_18012017_vF.pdf%0Ahttps://www.theicct.org/sites/default/files/publications/EU-RDE.

IEA 2011. *Technology roadmap: Electric and plug-in hybrid electric vehicles* [Online]. Available from: http://scholar.google.com/scholar?hl=en&btnG=Search&q=intitle:Technology+Roadmap+-+Electric+and+plug-in+hybrid+electric+vehicles#0.

Intergovernmental Panel on Climate Change 2014. *Climate Change 2014 Mitigation of Climate Change*.

Jiang, Y., Xu, C.M., Dong, F., Yang, Y.L., Jiang, W.H. and Yang, S. 2009. Disruption of the acetoacetate decarboxylase gene in solvent-producing Clostridium acetobutylicum increases the butanol ratio. *Metabolic Engineering*. **11**(4–5), pp.284–291.

Jimenez-Palacios, J.L. 1999. *Understanding and Quantifying Motor Vehicle Emissions with Vehicle Specific Power and TILDAS Remote Sensing* [Online]. Massachusetts. Available from: http://hdl.handle.net/1721.1/44505.

Jin, D., Choi, K., Myung, C.L., Lim, Y., Lee, J. and Park, S. 2017. The impact of various ethanol-gasoline blends on particulates and unregulated gaseous emissions characteristics from a spark ignition direct injection (SIDI) passenger vehicle. *Fuel*. **209**(August), pp.702–712.

Johansson, B. and Åhman, M. 2002. A comparison of technologies for carbon-neutral passenger transport. *Transportation Research Part D: Transport and Environment*. **7**(3), pp.175–196.

Johnson, T. V 2016. Vehicular Emissions in Review. *SAE Int. J. Engines*. **9**(2), pp.1258–1275.

Johnson, T. V 2012. Vehicular Emissions in Review. *SAE Int. J. Engines*. **5**(2), pp.216–234.

Jones, D.T. and Woods, D.R. 1986. ACETONE-BUTANOL FERMENTATION REVISITED. *Microbiological Reviews*. **50**(4), pp.484–524.

Joshi, A. 2020. Review of Vehicle Engine Efficiency and Emissions. *SAE Technical Papers*. **2020**-**April**(April), pp.1–23.

Kadijk, G., Verbeek, M., Smokers, R.T.M., Spreen, J., Patuleia, A., van Ras, M., Norris, J.O.W., Johnson, A., O'Brien, S., Wrigley, S., Pagnac, J., Seban, M. and Buttigieg, D. 2012. *Supporting analysis regarding test procedure flexibilities and technology deployment for review of the light duty vehicle fleet CO2 regulations* [Online]. Brussels. Available from: http://repository.tudelft.nl/view/tno/uuid%3A78728d0b-e657-4b65-a84b-3f6baddbbf84/.

Kageson, P. 1998. Cycle-Beating and the EU Test Cycle for Cars. *European Federation for Transport and Environment*. **98/3**(November 1998), p.10.

Kalita, M., Muralidharan, M., Subramanian, M., Sithananthan, M., Yadav, A., Kagdiyal, V., Sehgal, A.K. and Suresh, R. 2016. Experimental Studies on n-Butanol/Gasoline Fuel Blends in Passenger Car for Performance and Emission. *SAE Technical Papers*. **2016**-**Octob**.

Karavalakis, G., Durbin, T.D., Shrivastava, M., Zheng, Z., Villela, M. and Jung, H. 2012. Impacts of ethanol fuel level on emissions of regulated and unregulated pollutants from a fleet of gasoline light-duty vehicles. *Fuel*. **93**, pp.549–558.

Karavalakis, G., Short, D., Hajbabaei, M., Vu, D., Villela, M., Russell, R., Durbin, T. and Asa-Awuku, A. 2013. Criteria emissions, particle number emissions, size distributions, and black carbon measurements from PFI gasoline vehicles fuelled with different ethanol and butanol blends. *SAE Technical Papers*. **2**.

Khuong, L.S., Zulkifli, N.W.M., Masjuki, H.H., Mohamad, E.N., Arslan, A., Mosarof, M.H. and Azham, A. 2016. A review on the effect of bioethanol dilution on the properties and performance of automotive lubricants in gasoline engines. *Rsc Advances*. **6**(71), pp.66847–66869.

Kim, H.J., Lee, J.T., Lim, Y., Keel, J., Hong, Y. and Roh, H.G. 2019. A comparison on emission characteristics between passenger car using gasoline (Including HEV) and diesel fuel according to the various test mode. *SAE Technical Papers*. **2019**-**March**(March), pp.1–5.

Kim, S., Kondo, K., Otsuki, Y. and Haruta, K. 2017. *A New On-Board PN Analyzer for Monitoring the Real- Driving Condition Basic Performance of OBS-ONE-PN*.

Kittelson, D.B. 1998. Engines and nanoparticles: A review. *Journal of Aerosol Science*.

von Klot, S., Peters, A., Aalto, P., Bellander, T., Berglind, N., D'Ippoliti, D., Elosua, R., Hörmann, A., Kulmala, M., Lanki, T., Löwel, H., Pekkanen, J., Picciotto, S., Sunyer, J. and Forastiere, F. 2005. Ambient air pollution is associated with increased risk of hospital cardiac readmissions of myocardial infarction survivors in five European cities. *Circulation*. **112**(20), pp.3073–9.

Kontses, A., Triantafyllopoulos, G., Ntziachristos, L. and Samaras, Z. 2020. Particle number (PN) emissions from gasoline, diesel, LPG, CNG and hybrid-electric light-duty vehicles under real-world driving conditions. *Atmospheric Environment*. **222**(November 2019).

Lee, J.T., Kim, H., Song, H., Hong, Y.C., Cho, Y.S., Shin, S.Y., Hyun, Y.J. and Kim, Y.S. 2002. Air pollution and asthma among children in Seoul, Korea. *Epidemiology*. **13**(4), pp.481–484.

Lee, S.-M., Cho, M.O., Park, C.H., Chung, Y.-C., Kim, J.H., Sang, B.-I. and Um, Y. 2008. Continuous butanol production using suspended and immobilized Clostridium beijerinckii NCIMB 8052 with supplementary butyrate. *Energy & Fuels*. **22**(5), pp.3459–3464.

Li, T., Chen, X. and Yan, Z. 2013. Comparison of fine particles emissions of

light-duty gasoline vehicles from chassis dynamometer tests and on-road measurements. *Atmospheric Environment*. **68**, pp.82–91.

Li, Y., Gong, J., Deng, Y., Yuan, W., Fu, J. and Zhang, B. 2017. Experimental comparative study on combustion, performance and emissions characteristics of methanol, ethanol and butanol in a spark ignition engine. *Applied Thermal Engineering*. **115**, pp.53–63.

Liu, B. and Frey, H.C. 2015. Variability in Light-Duty Gasoline Vehicle Emission Factors from Trip-Based Real-World Measurements. *Environmental Science and Technology*. **49**(20), pp.12525–12534.

Liu, H., Wang, X., Zhang, D., Dong, F., Liu, X., Yang, Y., Huang, H., Wang, Y., Wang, Q. and Zheng, Z. 2019. Investigation on blending effects of gasoline fuel with n-butanol, DMF, and ethanol on the fuel consumption and harmful emissions in a GDI vehicle. *Energies*. **12**(1845), pp.1–21.

Liu, S., Krewski, D., Shi, Y., Chen, Y. and Burnett, R.T. 2003. Association between gaseous ambient air pollutants and adverse pregnancy outcomes in Vancouver, Canada. *Environmental Health Perspectives*. **111**(14), pp.1773–1778.

Liu, Z.G., Vasys, V.N., Dettmann, M.E., Schauer, J.J., Kittelson, D.B. and Swanson, J. 2009. Comparison of strategies for the measurement of mass emissions from diesel engines emitting ultra-low levels of particulate matter. *Aerosol Science and Technology*. **43**(11), pp.1142–1152.

Loiselle, A., Rostkowski, J., Karman, D. and Graham, L. 2010. The Effect of Driving Conditions and Ambient Temperature on Light Duty Gasoline-electric Hybrid Vehicles (3): Battery Energy. *SAE Technical Paper Series*. **1**(1), pp.776–790.

Lonza, L., Hass, H., Maas, H., Reid, A. and Rose, K. 2011. *EU renewable energy targets in 2020: Analysis of scenarios for transport fuels*.

Luo, Y., Zhu, L., Fang, J., Zhuang, Z., Guan, C., Xia, C., Xie, X. and Huang, Z. 2015. Size distribution, chemical composition and oxidation reactivity of particulate matter from gasoline direct injection (GDI) engine fueled with ethanol-gasoline fuel. *Applied Thermal Engineering*. **89**, pp.647–655.

M. Sabri, M.F., Danapalasingam, K.A. and Rahmat, M.F. 2016. A review on hybrid electric vehicles architecture and energy management strategies. *Renewable and Sustainable Energy Reviews*. **53**, pp.1433–1442.

Maricq, M.M., Podsiadlik, D.H. and Chase, R.E. 1999. Gasoline vehicle particle size distributions: Comparison of steady state, FTP, and US06 measurements. *Environmental Science and Technology*. **33**(12), pp.2007–2015.

Maricq, M.M. and Xu, N. 2004. The effective density and fractal dimension of soot particles from premixed flames and motor vehicle exhaust. *Journal of Aerosol Science*. **35**(10), pp.1251–1274.

Marotta, A., Pavlovic, J., Ciuffo, B., Serra, S. and Fontaras, G. 2015. Gaseous

Emissions from Light-Duty Vehicles: Moving from NEDC to the New WLTP Test Procedure. *Environmental Science and Technology*. **49**(14), pp.8315–8322.

Martini, G., Bonnel, P., Manfredi, U., Carriero, M., Krasenbrink, A., Franken, O., Rubino, L., Bartoli, G.B. and Bonifacio, M. 2010. On-road Emissions of Conventional and Hybrid Vehicles Running on Neat or Fossil Fuel Blended Alternative Fuels *In*: *SAE Technical Paper* [Online]. SAE International. Available from: http://dx.doi.org/10.4271/2010-01-1068.

Masum, B.M., Kalam, M.A., Masjuki, H.H., Palash, S.M. and Fattah, I.M.R. 2014. Performance and emission analysis of a multi cylinder gasoline engine operating at different alcohol–gasoline blends. *RSC Advances*. **4**, pp.27898–27904.

Masum, B.M., Masjuki, H.H., Kalam, M.A., Palash, S.M. and Habibullah, M. 2015. Effect of alcohol-gasoline blends optimization on fuel properties, performance and emissions of a SI engine. *Journal of Cleaner Production*. **86**, pp.230–237.

May, J., Bosteels, D. and Favre, C. 2014. An Assessment of Emissions from Light-Duty Vehicles using PEMS and Chassis Dynamometer Testing. *SAE Int. J. Engines*. **7**(3), pp.1326–1335.

Mensch, A.E. and Cleary, T.G. 2019. Measurements and predictions of thermophoretic soot deposition. *International Journal of Heat and Mass Transfer*. **143**, p.118444.

Merkisz, J., Bielaczyc, P., Pielecha, J. and Woodburn, J. 2019. RDE testing of passenger cars: The effect of the cold start on the emissions results. *SAE Technical Papers*. **2019**-**April**(April), pp.1–13.

Merkisz, J., Fuć, P., Lijewski, P. and Bielaczyc, P. 2010. The Comparison of the Emissions from Light Duty Vehicle in On-road and NEDC Tests. *SAE Technical Paper 2010-01-1298*. **2010**-**01**–**12**, pp.1–12.

Merkisz, J., Pielecha, J., Bielaczyc, P. and Woodburn, J. 2016. Analysis of Emission Factors in RDE Tests as Well as in NEDC and WLTC Chassis Dynamometer Tests. *SAE Technical Paper 2016-01-0980*.

Metzger, K.B., Tolbert, P.E., Klein, M., Peel, J.L., Flanders, W.D., Todd, K., Mulholland, J.A., Ryan, P.B. and Frumkin, H. 2004. Ambient air pollution and cardiovascular emergency department visits. *Epidemiology*. **15**(1), pp.46–56.

Miyanishi, M. 2010. Manufacturing Light Weight Cars. *Steel Research International*. **81**(9), pp.1–8.

Mock, P., German, J., Bandivadekar, A. and Riemersma, I. 2012. *Discrepancies between type- approval and 'real-world' fuel- consumption and CO 2 values: Assessment for 2001-2011 European passenger cars*. Berlin.

Momenimovahed, A. and Olfert, J.S. 2015. Effective Density and Volatility of Particles Emitted from Gasoline Direct Injection Vehicles and Implications for Particle Mass Measurement. *Aerosol Science and Technology*.

49(11), pp.1051–1062.

Myung, C.L. and Park, S. 2012. Exhaust nanoparticle emissions from internal combustion engines: A review. *International Journal of Automotive Technology*. **13**(1), pp.9–22.

Ng, H.K., Anderson, J.A., Duoba, M.J. and Larsen, R.P. 2001. Engine start characteristics of two hybrid electric vehicles (HEVs) - Honda insight and toyota prius. *SAE Technical Papers*. **2001**(724).

Nielsen, D.R., Leonard, E., Yoon, S.-H., Tseng, H.-C., Yuan, C. and Prather, K.L.J. 2009. Engineering alternative butanol production platforms in heterologous bacteria. *Metabolic Engineering*. **11**(4–5), pp.262–273.

Nigam, P.S. and Singh, A. 2011. Production of liquid biofuels from renewable resources. *Progress in Energy and Combustion Science*. **37**(1), pp.52–68.

Nose, H., Inoue, T., Katagiri, S., Sakai, A., Kawasaki, T. and Okamura, M. 2013. Fuel enrichment control system by catalyst temperature estimation to enable frequent stoichiometric operation at high engine speed/load condition. *SAE Technical Papers*. **2**.

O'Driscoll, R., Stettler, M.E.J., Molden, N., Oxley, T. and ApSimon, H.M. 2018. Real world CO2 and NOx emissions from 149 Euro 5 and 6 diesel, gasoline and hybrid passenger cars. *Science of the Total Environment*. **621**(x), pp.282–290.

Office for Low Emission Vehicles 2013. *Driving the Future Today - A strategy for ultra low emission vehicles in the UK* [Online]. Available from: https://www.gov.uk/government/uploads/system/uploads/attachment_data/file/239317/ultra-low-emission-vehicle-strategy.pdf.

OriginLab Corporation 2020. Origin(Pro).

Otsuki, Y., Nakamura, H., Arai, M. and Xu, M. 2015. The methodologies and instruments of vehicle particulate emission measurement for current and future legislative regulations. *Measurement Science and Technology*. **26**(092202).

Parry, T. 2019. *Vehicle Licensing Statistics: Annual 2019* [Online]. Available from: https://assets.publishing.service.gov.uk/government/uploads/system/uploads/attachment_data/file/882196/vehicle-licensing-statistics-2019.pdf.

Pasaoglu, G., Honselaar, M. and Thiel, C. 2012. Potential vehicle fleet CO2 reductions and cost implications for various vehicle technology deployment scenarios in Europe. *Energy Policy*. **40**(1), pp.404–421.

Pavlovic, J., Marotta, A. and Ciuffo, B. 2016. CO2 emissions and energy demands of vehicles tested under the NEDC and the new WLTP type approval test procedures. *Applied Energy*. **177**(2016), pp.661–670.

Peel, J.L., Tolbert, P.E., Klein, M., Metzger, K.B., Flanders, W.D., Todd, K., Mulholland, J. a., Ryan, P.B. and Frumkin, H. 2005. Ambient Air Pollution and Respiratory Emergency Department Visits. *Epidemiology*. **16**(2), pp.164–174.

Pelkmans, L. and Debal, P. 2006. Comparison of on-road emissions with emissions measured on chassis dynamometer test cycles. *Transportation Research Part D: Transport and Environment*. **11**(4), pp.233–241.

Pénard-Morand, C., Charpin, D., Raherison, C., Kopferschmitt, C., Caillaud, D., Lavaud, F. and Annesi-Maesano, I. 2005. Long-term exposure to background air pollution related to respiratory and allergic health in schoolchildren. *Clinical and Experimental Allergy*. **35**(10), pp.1279–1287.

Pfromm, P.H., Amanor-Boadu, V., Nelson, R., Vadlani, P. and Madl, R. 2010. Bio-butanol vs. bio-ethanol: A technical and economic assessment for corn and switchgrass fermented by yeast or Clostridium acetobutylicum. *Biomass & Bioenergy*. **34**(4), pp.515–524.

Pollet, B.G., Staffell, I. and Shang, J.L. 2012. Current status of hybrid, battery and fuel cell electric vehicles: From electrochemistry to market prospects. *Electrochimica Acta*. **84**, pp.235–249.

Poullikkas, A. 2015. Sustainable options for electric vehicle technologies. *Renewable and Sustainable Energy Reviews*. **41**, pp.1277–1287.

Prajapati, K.C., Patel, R. and Sagar, R. 2014. Hybrid Vehicle: A Study on Technology. *International Journal of Engineering Research & Technology*. **3**(12), pp.1076–1082.

Prati, M.V., Costagliola, M.A., Pagliara, F. and Mastantuono, E. 2018. Idling Vehicle Emissions and Fuel Consumption in Urban Use : Influence of the Stop & Start Technology *In*: *2018 IEEE International Conference on Environment and Electrical Engineering and 2018 IEEE Industrial and Commercial Power Systems Europe (EEEIC / I&CPS Europe)*. IEEE, pp.1–4.

Prati, M.V., Meccariello, G., Della Ragione, L. and Costagliola, M.A. 2015. Real Driving Emissions of a Light-Duty Vehicle in Naples. Influence of Road Grade. *SAE Technical Papers*. **2015**.

Price, P., Stone, R., Collier, T., Davies, M. and Scheer, V. 2006. Dynamic Particulate Measurements from a DISI Vehicle: A Comparison of DMS500, ELPI, CPC and PASS. *SAE Technical Paper Series*. **1**.

Price, P., Twiney, B., Stone, R., Kar, K. and Walmsley, H. 2007. Particulate and hydrocarbon emissions from a spray guided direct injection spark ignition engine with oxygenate fuel blends. *SAE Technical Papers*. (724), pp.776–790.

Quiros, D.C., Hu, Shaohua, Hu, Shishan, Lee, E.S., Sardar, S., Wang, X., Olfert, J.S., Jung, H.S., Zhu, Y. and Huai, T. 2015. Particle effective density and mass during steady-state operation of GDI, PFI, and diesel passenger cars. *Journal of Aerosol Science*. **83**, pp.39–54.

R Foundation for Statistical Computing, Vienna, A.I. 3-900051-07-0 2011. R Development Core Team. *R: A Language and Environment for Statistical Computing*. **55**, pp.275–286.

Rask, E., Duoba, M., Lohse-Busch, H. and Bocci, D. 2010. Model Year 2010

(Gen 3) Toyota Prius Level-1 Testing Report. *U.S. Department of Energy*. **2010**(ANL/ES/RP-67317).

Ratcliff, M.A., Luecke, J., Williams, A., Christensen, E., Yanowitz, J., Reek, A. and McCormick, R.L. 2013. Impact of Higher Alcohols Blended in Gasoline on Light-Duty Vehicle Exhaust Emissions. *Environmental Science & Technology*. **47**, pp.13865–13872.

Raza, M., Chen, L., Leach, F. and Ding, S. 2018. A Review of particulate number (PN) emissions from gasoline direct injection (gdi) engines and their control techniques. *Energies*. **11**(6).

Reavell, K., Hands, T. and Collings, N. 2002. A Fast Response Particulate Spectrometer for Combustion Aerosols. *SAE Technical Paper Series*. **1**.

Reichmuth, D.S., Lutz, A.E., Manley, D.K. and Keller, J.O. 2013. Comparison of the technical potential for hydrogen, battery electric, and conventional light-duty vehicles to reduce greenhouse gas emissions and petroleum consumption in the United States. *International Journal of Hydrogen Energy*. **38**(2), pp.1200–1208.

Riley, R. 2016. *Developing Real Driving CO2 Emission Factors for Hybrid Cars Through on Road Testing and Microscale Modelling*.[Online] University of Leeds. Available from: http://etheses.whiterose.ac.uk/17410/1/PhD Thesis Richard Riley 2017.pdf.

Ritz, B., Yu, F., Fruin, S., Chapa, G., Shaw, G.M. and Harris, J.A. 2002. Ambient air pollution and risk of birth defects in Southern California. *American Journal of Epidemiology*. **155**(1), pp.17–25.

Robinson, M.K. and Holmén, B.A. 2011. Onboard, Real-World Second-by-Second Particle Number Emissions from 2010 Hybrid and Comparable Conventional Vehicles. *Journal of the Transportation Research Board*. **2233**(2233), pp.63–71.

Ropkins, K. 2012. pems.utils: Data handling, analysis and visualisation tools for data from portable emissions monitoring systems and other mobile sources.

Sadeghinezhad, E., Kazi, S.N., Sadeghinejad, F., Badarudin, A., Mehrali, M., Sadri, R. and Reza Safaei, M. 2014. A comprehensive literature review of bio-fuel performance in internal combustion engine and relevant costs involvement. *Renewable and Sustainable Energy Reviews*. **30**, pp.29–44.

Sagiv, S.K., Mendola, P., Loomis, D., Herring, A.H., Neas, L.M., Savitz, D.A. and Poole, C. 2005. A time-series analysis of air pollution and preterm birth in Pennsylvania, 1997-2001. *Environmental health perspectives*. **113**(5), pp.602–606.

Saikrishnan, V., Karthikeyan, A. and Jayaprabakar, J. 2017. Analysis of ethanol blends on spark ignition engines. *International Journal of Ambient Energy*. **0**(0), pp.1–5.

Santos, A.C. 2012. The Blend Ethanol/Gasoline and Emission of Gases *In*: G.

Liu, ed. *Greenhouse Gases - Emission, Measurement and Management*. InTech, p.23.

Sarathy, S.M., O??wald, P., Hansen, N. and Kohse-H??inghaus, K. 2014. Alcohol combustion chemistry. *Progress in Energy and Combustion Science*. **44**, pp.40–102.

Sarigiannis, D.A., Karakitsios, S.P., Gotti, A., Liakos, I.L. and Katsoyiannis, A. 2011. Exposure to major volatile organic compounds and carbonyls in European indoor environments and associated health risk. *Environment International*. **37**(4), pp.743–765.

Schauer, J.J. 2015. Design Criteria for Future Fuels and Related Power Systems Addressing the Impacts of Non-CO<inf>2</inf> Pollutants on Human Health and Climate Change. *Annual Review of Chemical and Biomolecular Engineering*. **6**, pp.101–120.

Schobert, H. 2013. Chemistry of Fossil Fuels and Biofuels. *Chemistry of Fossil Fuels and Biofuels*., p.411.

Schriefl, M.A., Longin, M. and Bergmann, A. 2019. Charging-Based PN Sensing of Automotive Exhaust Particles. *Proceedings*. **2**(13), p.805.

Schwelberger, M., Mamakos, A., Fierz, M. and Giechaskiel, B. 2019. Experimental assessment of an electrofilter and a tandem positive-negative corona charger for the measurement of charged nanoparticles formed in selective catalytic reduction systems. *Applied Sciences (Switzerland)*. **9**(6), pp.1–17.

Serras-Pereira, J., Aleiferis, P.G. and Richardson, D. 2013. An analysis of the combustion behavior of ethanol, butanol, iso-octane, gasoline, and methane in a direct-injection spark-ignition research engine. *Combustion Science and Technology*. **185**(3), pp.484–513.

Shancita, I., Masjuki, H.H., Kalam, M.A., Fattah, I.M.R., Rashed, M.M. and Rashedul, H.K. 2014. A review on idling reduction strategies to improve fuel economy and reduce exhaust emissions of transport vehicles. *Energy Conversion and Management*. **88**, pp.794–807.

Sheehan, J.J. 2009. Biofuels and the conundrum of sustainability. *Current Opinion in Biotechnology*. **20**(3), pp.318–324.

Shen, C.R. and Liao, J.C. 2008. Metabolic engineering of Escherichia coli for 1-butanol and 1-propanol production via the keto-acid pathways. *Metabolic Engineering*. **10**(6), pp.312–320.

Sher, E. 1998. *Handbook of Air Pollution from Internal Combustion Engines*. London: Academic Press.

Sileghem, L., Bosteels, D., May, J., Favre, C. and Verhelst, S. 2014. Analysis of vehicle emission measurements on the new WLTC, the NEDC and the CADC. *Transportation Research Part D: Transport and Environment*. **32**, pp.70–85.

Sillman, S. 1999. The relation between ozone, NOx and hydrocarbons in urban and polluted rural environments. *Atmospheric Environment*. **33**(12), pp.1821–1845.

da Silva, R., Cataluña, R., Menezes, E.W. de., Samios, D. and Piatnicki, C.M.S. 2005. Effect of additives on the antiknock properties and Reid vapor pressure of gasoline. *Fuel*. **84**(7), pp.951–959.

Singh, S.B., Dhar, A. and Agarwal, A.K. 2015. Technical feasibility study of butanol-gasoline blends for powering medium-duty transportation spark ignition engine. *Renewable Energy*. **76**, pp.706–716.

Suarez-Bertoa, R. and Astorga, C. 2018. Impact of cold temperature on Euro 6 passenger car emissions. *Environmental Pollution*. **234**, pp.318–329.

Suarez-Bertoa, R. and Astorga, C. 2016. Unregulated emissions from light-duty hybrid electric vehicles. *Atmospheric Environment*. **136**, pp.134–143.

Suarez-Bertoa, R., Mendoza-Villafuerte, P., Riccobono, F., Vojtisek, M., Pechout, M., Perujo, A. and Astorga, C. 2017. On-road measurement of NH3 emissions from gasoline and diesel passenger cars during real world driving conditions. *Atmospheric Environment*. **166**, pp.488–497.

Suarez-Bertoa, R., Pechout, M., Vojtíšek, M. and Astorga, C. 2020. Regulated and non-regulated emissions from euro 6 diesel, gasoline and CNG vehicles under real-world driving conditions. *Atmosphere*. **11**(2), pp.1–18.

Suarez-Bertoa, R., Valverde, V., Clairotte, M., Pavlovic, J., Giechaskiel, B., Franco, V., Kregar, Z. and Astorga, C. 2019. On-road emissions of passenger cars beyond the boundary conditions of the real-driving emissions test. *Environmental Research*. **176**(July), p.108572.

Sustainable Transport Solutions Ltd 2008. *Life Cycle Analysis of Road Transport Biofuels* [Online]. London. Available from: www.camden.gov.uk/ccm/cms-service/download/asset?asset_id=1362395.

Szwaja, S. and Naber, J.D. 2010. Combustion of n-butanol in a spark-ignition IC engine. *Fuel*. **89**(7), pp.1573–1582.

Tao, L., Tan, E.C.D., McCormick, R., Zhang, M., Aden, A., He, X. and Zigler, B.T. 2014. Techno-economic analysis and life-cycle assessment of cellulosic isobutanol and comparison with cellulosic ethanol and n-butanol. *Biofuels, Bioproducts and Biorefining*. **8**(1), pp.30–48.

TSI 2006. Aerosol Instrument Manager Software Manual. . (October), pp.1–113.

Turco, R.P. and Yu, F.Q. 1999. Particle size distributions in an expanding plume undergoing simultaneous coagulation and condensation. *Journal of Geophysical Research-Atmospheres*. **104**(D16), pp.19227–19241.

Tutuianu, M., Bonnel, P., Ciuffo, B., Haniu, T., Ichikawa, N., Marotta, A., Pavlovic, J. and Steven, H. 2015. Development of the World-wide harmonized Light duty Test Cycle (WLTC) and a possible pathway for its introduction in the European legislation. *Transportation Research Part D: Transport and Environment*. **40**, pp.61–75.

Uherek, E., Halenka, T., Borken-Kleefeld, J., Balkanski, Y., Berntsen, T., Borrego, C., Gauss, M., Hoor, P., Juda-Rezler, K., Lelieveld, J., Melas,

D., Rypdal, K. and Schmid, S. 2010. Transport impacts on atmosphere and climate: Land transport. *Atmospheric Environment*. **44**(37), pp.4772–4816.

UK Department for Transport 2013. *Motor fuel composition and content regulations - extension of petrol protection grade requirement*.

United Nations 2014. *Addendum 15 : Global technical regulation No . 15 - Worldwide harmonized Light vehicles Test Procedure* [Online]. Available from: https://www.unece.org/fileadmin/DAM/trans/main/wp29/wp29r-1998agr-rules/ECE-TRANS-180a15e.pdf.

United Nations 2012. Regulation No 83 of the Economic Commission for Europe of the United Nations (UN/ECE) — Uniform provisions concerning the approval of vehicles with regard to the emission of pollutants according to engine fuel requirements. *Official journal of the European Union*. **42**(15/02/2012), pp.1–207.

Valin, H., Peters, D., van den Berg, M., Frank, S., Havlik, P., Forsell, N. and Hamelinck, N. 2015. *The land use change impact of biofuels consumed in the EU Quantification of area and greenhouse gas impacts* [Online]. Available from: https://ec.europa.eu/energy/sites/ener/files/documents/Final Report_GLOBIOM_publication.pdf.

Vallero, D. 2008. Pollutant Formation and Control in Combustion *In*: *Fundamentals of Air Pollution*. Burlington, USA: Academic Press, pp.167–225.

Valverde, V., Mora, B.A., Clairotte, M., Pavlovic, J., Suarez-Bertoa, R., Giechaskiel, B., Astor, C. and Fontaras, G. 2019. Emission factors derived from 13 Euro 6b light-duty vehicles based on laboratory and on-road measurements. *Atmosphere*. **10**(5).

Varde, K., Jones, A., Knutsen, A., Mertz, D. and Yu, P. 2007. Exhaust emissions and energy release rates from a controlled spark ignition engine using ethanol blends. *Proceedings of the Institution of Mechanical Engineers, Part D: Journal of Automobile Engineering*. **221**(8).

Varella, R.A., Duarte, G., Baptista, P., Sousa, L. and Villafuerte, P.M. 2017. Comparison of Data Analysis Methods for European Real Driving Emissions Regulation *In*: *SAE Technical Paper* [Online]. SAE International. Available from: http://doi.org/10.4271/2017-01-0997.

Varella, R.A., Faria, M. V., Mendoza-Villafuerte, P., Baptista, P.C., Sousa, L. and Duarte, G.O. 2019. Assessing the influence of boundary conditions, driving behavior and data analysis methods on real driving CO2 and NOx emissions. *Science of the Total Environment*. **658**, pp.879–894.

Varella, R.A., Ribau, J.P., Baptista, P.C., Sousa, L. and Duarte, G.O. 2019. Novel approach for connecting real driving emissions to the European vehicle laboratorial certification test procedure. *Environmental Science and Pollution Research*. **26**(34), pp.35163–35182.

Varol, Y., Oner, C., Oztop, H.F. and Altun, S. 2014. Comparison of Methanol,

Ethanol, or n-Butanol Blending with Unleaded Gasoline on Exhaust Emissions of an SI Engine. *Energy Sources Part A: Recovery Utilization and Environmental Effects*. **36**(9), pp.938–948.

Vassilev, Z.P., Robson, M.G. and Klotz, J.B. 2001. Outdoor exposure to airborne polycyclic organic matter and adverse reproductive outcomes: A pilot study. *American Journal of Industrial Medicine*. **40**(3), pp.255–262.

Vineis, P., Forastiere, F., Hoek, G. and Lipsett, M. 2004. Outdoor air pollution and lung cancer: Recent epidemiologic evidence. *International Journal of Cancer*. **111**, pp.647–652.

Viorel, I.-A., Szabó, L., Löwenstein, L. and Şteţ, C. 2004. Integrated Starter-Generators for Automotive Applications. *Acta Electrotehnica*. **45**(3), pp.255–260.

Vlachos, T.G., Bonnel, P., Perujo, A., Weiss, M., Villafuerte, P.M. and Riccobono, F. 2014. In-Use Emissions Testing with Portable Emissions Measurement Systems (PEMS) in the Current and Future European Vehicle Emissions Legislation: Overview, Underlying Principles and Expected Benefits. *SAE Int. J. Commer. Veh.* **7**(1), pp.199–215.

Vojtisek-Lom, M., Beranek, V., Klir, V., Stolcpartova, J. and Pechout, M. 2015. Effects of n-Butanol and Isobutanol on Particulate Matter Emissions from a Euro 6 Direct-injection Spark Ignition Engine During Laboratory and on-Road Tests. *SAE International Journal of Engines*. **8**(5), pp.2338–2350.

Vu, T. V., Delgado-Saborit, J.M. and Harrison, R.M. 2015. Review: Particle number size distributions from seven major sources and implications for source apportionment studies. *Atmospheric Environment*. **122**, pp.114–132.

Wallington, T.J., Anderson, J.E., Kurtz, E.M. and Tennison, P.J. 2016. Biofuels, vehicle emissions, and urban air quality. *Faraday discussions*. **189**, pp.121–136.

Watling, T.C. and Cox, J.P. 2014. Factors Affecting Three-Way Catalyst Light-Off: A Simulation Study. *SAE International Journal of Engines*. **7**(3).

Wattrus, M. 2013. Fuel Property Effects on Oil Dilution in Diesel Engines. *SAE International*., pp.794–806.

Weber, B.W., Kumar, K., Zhang, Y. and Sung, C.J. 2011. Autoignition of n-butanol at elevated pressure and low-to-intermediate temperature. *Combustion and Flame*. **158**(5), pp.809–819.

Wei, Q. and Porter, S. 2011. Evaluation of Solid Particle Emissions from Hybrid and Conventional Gasoline Vehicles. *SAE International Journal of Engines*. **4**(1), pp.619–638.

Weilenmann, M., Favez, J.-Y. and Alvarez, R. 2009. Cold-start emissions of modern passenger cars at different low ambient temperatures and their evolution over vehicle legislation categories. *Atmospheric Environment*. **43**(15), pp.2419–2429.

Weiss, M, Bonnel, P., Hummel, R. and Manfredi, U. 2011. *Analyzing on-road emissions of light-duty vehicles with Portable Emission Measurement*

Systems (PEMS) [Online]. Available from: http://www.seefed.eu/uploads/5/5/1/2/5512416/lbna24697enc_002.pdf.

Weiss, Martin, Bonnel, P., Hummel, R., Provenza, A. and Manfredi, U. 2011. On-road emissions of light-duty vehicles in Europe. *Environmental Science and Technology*. **45**(19), pp.8575–8581.

Weiss, M., Paffumi, E., Clairotte, M., Drossinos, Y. and Vlachos, T. 2017. *Including cold-start emissions in the Real-Driving Emissions (RDE) test procedure effects*.

Wong, G.W., Ko, F.W., Lau, T.S., Li, S.T., Hui, D., Pang, S.W., Leung, R., Fok, T.F. and Lai, C.K. 2001. Temporal relationship between air pollution and hospital admissions for asthmatic children in Hong Kong. *Clin Exp Allergy*. **31**(4), pp.565–569.

Wróbel, A., Rokita, E. and Maenhaut, W. 2000. Transport of traffic-related aerosols in urban areas. *Science of the Total Environment*. **257**(2–3), pp.199–211.

Wu, M., Wang, M., Liu, J. and Huo, H. 2008. Assessment of Potential Life-Cycle Energy and Greenhouse Gas Emission Effects from Using Corn-Based Butanol as a Transportation Fuel. *Biotechnology Progress*. **24**(6), pp.1204–1214.

Wu, X., Zhang, S., Wu, Y., Li, Z., Ke, W., Fu, L. and Hao, J. 2015. on–road measurement of gaseous emissions and fuel consumption for two hybrid electric vehicles in Macao. *Atmospheric Pollution Research*. **6**(5), pp.858–866.

Wyman, C. 1996. *Handbook on Bioethanol: Production and Utilization*. CRC Press.

Yan, X. and Boies, A.M. 2013. Quantifying the uncertainties in life cycle greenhouse gas emissions for UK wheat ethanol. *Environmental Research Letters*. **8**(1), p.015024.

Yan, X., Sone, R., Inoue, R., Kusaka, J., Umezawa, K. and Kondo, Y. 2019. Modeling Three-Way Catalyst Converters during Cold Starts and Potential Improvements. *SAE Technical Papers*. (December).

Yang, B., Yao, M., ChengB, W.K., Zheng, Z. and Yue, L. 2014. Regulated and unregulated emissions from a compression ignition engine under low temperature combustion fuelled with gasoline and n-butanol/gasoline blends. *Fuel*. **120**, pp.163–170.

Yang, X., Yang, J. and Lin, T. 2009. The effect of an SI engine using butanol-gasoline blended fuel on performance and enviroment *In*: *2009 International Conference on Energy and Environment Technology, ICEET 2009*., pp.402–405.

Yao, M., Liu, H. and Feng, X. 2011. The development of low-carbon vehicles in China. *Energy Policy*. **39**(9), pp.5457–5464.

Ye, Y., Galbally, I.E. and Weeks, I.A. 1997. Emission of 1,3-butadiene from petrol-driven motor vehicles. *Atmospheric Environment*. **31**(8), pp.1157–1165.

Zahabi, S.A.H., Miranda-Moreno, L., Barla, P. and Vincent, B. 2014. Fuel economy of hybrid-electric versus conventional gasoline vehicles in real-world conditions: A case study of cold cities in Quebec, Canada. *Transportation Research Part D: Transport and Environment*. **32**, pp.184–192.

Zervas, E. and Panousi, E. 2010. Exhaust Methane Emissions from Passenger Cars Repeatability of measurements on the. *Sae Paper 2010-01-2224*.

Zhai, H., Christopher Frey, H. and Rouphail, N.M. 2011. Development of a modal emissions model for a hybrid electric vehicle. *Transportation Research Part D: Transport and Environment*. **16**(6), pp.444–450.

Zhang, Y., Deng, J., Li, Q., Liu, Y., He, B., Hu, Z., Bo, S. and Li, L. 2020. Characteristics of Transient NOx Emissions of HEV under Real Road Driving. *SAE Technical Papers*. **2020**-**April**(April), pp.1–12.

Zhang, Z., Wang, T., Jia, M., Wei, Q., Meng, X. and Shu, G. 2014. Combustion and particle number emissions of a direct injection spark ignition engine operating on ethanol/gasoline and n-butanol/gasoline blends with exhaust gas recirculation. *Fuel*. **130**, pp.177–188.